

University College London

**Application of Pyridazinediones  
in the Construction of Self-  
Immolative Scaffolds for  
Potential Use in Small  
Molecule–Drug Conjugates**

by

Marcos Fernández

Submitted in partial fulfilment of the requirements for the degree of

Doctor of Philosophy

# Declaration

I, Marcos Fernández, confirm that the work presented in this thesis is my own. Where information has been derived from other sources, I confirm that this has been indicated in the thesis.

Marcos Fernández

January 2020

# Impact Statement

The work described in this thesis comprises the design and synthesis of derivatised pyridazinedione cores that include groups necessary and relevant for the construction of small molecule–drug conjugates.

A novel, sulfur-based self-immolative linker has been developed on the thiol-reactive centres of this platform, and such a linker undergoes self-degradation only within conditions mimicking those of the tumour microenvironment. The *N*-handles of the pyridazinedione can be and have been derivatised with PEG, azide and alkyne groups. The versatility and modularity of the pyridazinedione scaffold offers real value in the organic chemistry and chemical biology fields, as it allows for the attachment of four different groups to the same core, with the self-immolative linker able to selectively release cytotoxic and fluorescent cargoes inside cancer cells. This ability to install all the relevant groups for a small molecule–drug conjugate and its precursors on the same central platform has the potential to overcome the often cumbersome and inefficient syntheses associated with other small molecule–drug conjugates which lack this focus on a central scaffold.

Outside academia this work has real implications in the clinic for targeted and personalised cancer therapy. Small molecule–drug conjugates based on the pyridazinedione platform offer the ability to incorporate targeting ligands and cytotoxic drugs on the same molecule, thus combining the cancer-selective and drug-killing component in the same dose, which could be beneficial regarding patient compliance. Moreover, the pyridazinedione's impressive scope allows for its scaffold to be modified for use against virtually any target specific to or overexpressed on cancer cells.

# Abstract

Cancer constitutes one of the leading causes of death worldwide and research in this field is constantly aiming to discover and develop ever more efficient ways in which to treat and manage this disease. For much of the 20<sup>th</sup> century the leading strategy has been that of chemotherapy: a treatment invariably accompanied by undesirable side effects due to its lack of specificity. The field has therefore moved towards targeted-drug delivery, with antibody–drug conjugates (ADCs) having established themselves in this area with great success. Less work however has been undertaken on small molecule–drug conjugates (SMDCs) and this thesis describes the design of SMDC precursors based on the pyridazinedione (PD) molecule, as well as the development of a novel, sulfur-based self-immolative linker which could enable the attachment of drugs and fluorophores to such a construct.

The first primary focus of this work centres around the PD core's thiol reactive centres, with the exploration of whether thioaryl- or thioalkyl-PDs fare better when subjected to human serum- and tumour cell-mimicking conditions. It was found that a bis-thioaryl PD performed best, and its aromatic thiol substituents were subsequently derivatised for the purpose of attaching a fluorophore *via* a novel, sulfur-based self-immolative linker. The release of the fluorophore seen by LC-MS and the turn-on fluorescence observed by fluorescence spectroscopy both confirmed the self-degradative mechanism of this linker.

The second primary objective of this work was to then install groups that are relevant to an SMDC precursor onto the *N*-handles of the PD core, culminating in the successful isolation of di-bromo PEG azide and PEG alkyne PDs. The latter's bromine positions were then substituted with a derivatisable thiol to demonstrate that incorporating three distinct groups onto the same PD platform is possible, thus vindicating its versatility and modularity. Consequently, novel SMDC precursors have been synthesised whose functional groups have potential for future attachment of fluorophores, drugs and tumour-targeting ligands.

# Contents

Declaration	i
Impact Statement	ii
Abstract	iii
Contents	iv
Acknowledgments	vii
Abbreviations	x
<b>Chapter 1 Introduction</b>	<b>1</b>
1.1 Chemotherapy	1
1.1.1 Chemotherapy: Origins	1
1.1.2 Chemotherapy: Antifolates	2
1.1.3 Chemotherapy: Combination Treatments	3
1.2 Targeted Cancer Therapy	4
1.2.1 Targeted Therapy: Monoclonal Antibodies (mAbs)	5
1.2.2 Targeted Therapy: Antibody–Drug Conjugates (ADCs)	7
1.2.3 Targeted Therapy: Small Molecule–Drug Conjugates (SMDCs)	11
1.3 3,6-Pyridazinediones (PDs)	26
1.4 Use of PDs in ADCs	28
1.5 Aims	29
<b>Chapter 2 Synthesis of thio-PDs and appraisal in serum- and cell-mimicking conditions</b>	<b>31</b>
2.1 Appraisal of thio-PDs in serum- and cell-like conditions	32
2.2 Results and discussion	33
2.2.1 Synthesis of the bromo PD scaffolds precursor	33
2.2.2 Synthesis of mono-bromo PD	34
2.2.3 Synthesis of thioaryl PDs from the bromo PD scaffolds	37
2.2.4 Synthesis of thioalkyl PDs from the bromo PD scaffolds	38
2.2.5 Synthesis of a thioaryl-alkyl PD from di-bromo PD	40
2.3 Incubation of bromo- and thio-substituted PDs with HSA	42
2.4 Incubation of thio-PDs with GluSH in cell-like conditions	44
2.4.1 Incubation of thioaryl PDs with GluSH at pH 6.5	45
2.4.2 Incubation of thioalkyl PDs with GluSH at pH 6.5	49
2.4.3 Incubation of thioaryl-alkyl PD with GluSH at pH 6.5	52
2.4.4 Incubation of thioaryl PDs with GluSH at pH 5.0	53

2.4.5	Incubation of thioalkyl PDs with GluSH at pH 5.0	55
2.4.6	Incubation of thioaryl-alkyl PD with GluSH at pH 5.0	57
2.5	Conclusion	60
<b>Chapter 3 Design and appraisal of fluorophore–PDs and a sulfur-based self-immolative release mechanism</b>		<b>61</b>
3.1	Selection of fluorophore for turn-on fluorescence	61
3.2	Results and discussion	63
3.2.1	Synthesis of umbelliferone–PD	64
3.2.2	<sup>1</sup> H NMR and LC-MS studies of umbelliferone–PD + umbelliferone	66
3.3	UV absorption and fluorescence emission of umbelliferone PD and umbelliferone	71
3.4	Incubation of umbelliferone–PD with GluSH	74
3.5	Synthesis of water-soluble variant of umbelliferone PD	79
3.5.1	Attempted synthesis of acetic acid umbelliferone–PD	79
3.5.2	<i>Tert</i> -butyl protection of 7-hydroxycoumarin-4-acetic acid	82
3.5.3	Attempted synthesis of <i>tert</i> -butyl acetic acid umbelliferone PD	83
3.5.4	Attempted synthesis of carboxylic acid umbelliferone–PD	84
3.5.5	Synthesis of <i>tert</i> -butyl carboxylic acid umbelliferone–PD	85
3.5.6	Deprotection of 3- <i>tert</i> -butyl carboxylic acid umbelliferone–PD	89
3.6	Incubation of carboxylic acid umbelliferone PD with GluSH	90
3.7	Fluorescence emission spectroscopy of the carboxylic acid umbelliferone–PD + GluSH incubation	94
3.8	Conclusion	95
<b>Chapter 4 Derivatisation of the <i>N</i>-handles of the pyridazinedione core</b>		<b>96</b>
4.1	Results and discussion	97
4.1.1	Synthesis of azide-alkyne PEG PDs	97
4.2	Conclusion	109
<b>Chapter 5 Conclusions and Outlook</b>		<b>110</b>
5.1	Outlook	111
5.1.1	Extension of the aryl moieties of SMDC precursors 83 and 84	111
5.1.2	Derivatisation of SMDC precursors' azide and alkyne groups	112
5.1.3	Aryl-alkyl self-immolative linkers	113
General Experimental		116

Experimental for Chapter 2	119
Experimental for Chapter 3	271
Experimental for Chapter 4	328
<b>References</b>	<b>358</b>

# Acknowledgements

My PhD is the realisation of a hazy, vague notion I had from at least 4 years of age. Though I did not know then what it meant to be a scientist, my inner chemist manifested itself through my mixing of potions in the garden (mainly consisting of snails, water and mud), to later experimenting with ink, oil and other substances as I got older. Now, over two decades later, I can without a doubt confirm that my PhD journey has been one of the most challenging, yet wondrous experiences of my life. From spending untold hours mixing and analysing “potions” in the lab, to KLB holidays and movie nights, and to the, shall we say, *interesting* lab music we were all subject to (if only the central potato123 computer could talk), these three years would not have even come close to being epic without the presence of all the following legends.

Where to even begin with my supervisor, Professor Vijay Chudasama? Never have I known anyone who cares so much for his students and who gives so much of himself in order that they simply succeed. His constant input, support, and most importantly, the presence he has provided over the duration of my project have been unparalleled. I cannot express just how grateful I am to have had such an outstanding mentor.

Dr Antoine Maruani is the Chudasama Group’s resident idol. Aside from possessing virtually every talent under the sun, his chemistry expertise has been an unfailing source of support whenever I had problems or issues regarding my project. He will be sorely missed, but not as much as his tiger cakes.

Dr Daniel Richards’ iconic height, laugh and sarcasm will be remembered and appreciated for many years to come.

Dr Maximillian Lee’s hilarious humour and impressions have in no small part contributed to the group’s famously amusing and friendly atmosphere, a heritage which the rest of us are keeping alive and passing on to the next generations of Chuds.

My full Iberian brother Dr João Nogueira: that accent and that demeanour, what more needs to be said? I raise my bacalhau com natas to you.



The world would be a better place if everyone were as smiley and friendly as Dr Nafsika Forte.

The lab atmosphere is all the more pleasant and relaxed as a consequence of my half Iberian brother André Shamsabadi's affable nature and friendliness. His invaluable assistance with writing and proof-reading has also been hugely appreciated.

Calise Bahou's long, rambling, but immensely entertaining stories will be among the things I miss most from the group.

Faiza Javaid's constant stream of chocolate, ice cream and dessert photos have been a big source of amusement, hunger, and in most cases, envy. Never stop.

The group would not be complete without our gamer lord, Péter Szijj, because of whom I briefly tried my hand at AoE, (which is a Chud rite of passage), and through whom I have come to know of board games I'd never dream could exist.

Though I haven't known them as long, I'd also like to thank Dr Richard Spears, Alexander Furby and Nehaal Ahmed, who have all made a big impression on me in regards to, respectively, how Northern yet sassy one can be, how much general knowledge it's possible for one person to possess, and the bravery it takes to wear trainers costing hundreds of pounds in the lab.

I am also very grateful and lucky to have spent these three years alongside members of the Baker and Sheppard groups, who are just as much a part of the lab family. I can only hope that my future lab environments will be as incredible as this one.

My family deserves special mention, as they've never doubted my determination and have always encouraged me to pursue my own ambitions and dreams. Though they may not be familiar with the field, they've never failed to take a genuine interest in this project and its progression. This thesis is ultimately dedicated to them.

I also wish to extend my gratitude to my examiners, Dr Richard S. Grainger and Dr Kirsten Sander, who have very kindly accepted to read my thesis and carry out my *viva* examination.

I am most thankful to the EPSRC, my funding body, without which I would not have been able to undertake a PhD.

Lastly, I wish to acknowledge the UCL Mass Spectrometry Facility and thank Dr Kersti Karu, Dr Xiaoping Yang and Maggie for their assistance. I am also grateful to Dr Abil Aliev for his help with NMR work.

“Growing apart doesn’t change the fact that for a long time we grew side by side; our roots will always be tangled. I’m glad for that.”

– Ally Condie

# Abbreviations

[ $\alpha$ ] <sub>D</sub>	Specific Rotation
AAZ	Acetaloamide
Ac	Acetyl
ADC	Antibody–Drug Conjugate
ADCC	Antibody-Dependent Cell-Mediated Cytotoxicity
ALL	Acute Lymphoblastic Leukaemia
app.	Apparent
Aq.	Aqueous
Boc	<i>Tert</i> -butyloxycarbonyl (Protecting Group)
BR	Biotin Receptor
CA	Carbonic Anhydrase
<i>Ca.</i>	Circa
Calcd.	Calculated
CDC	Complement-Dependent Cytotoxicity
CuAAC	Copper Azide-Alkyne Cycloaddition
d	Doublet
Da	Dalton
DAVLBH	Desacetylvinblastine Monohydrazide
DCC	<i>N,N'</i> -Dicyclohexylcarbodiimide
DCU	Dicyclohexylurea
dd	Doublet of Doublets
DHFR	Dihydrofolate Reductase
DMAP	4-Dimethylaminopyridine

DMF	<i>N,N</i> -Dimethylformamide
DNA	Deoxyribonucleic Acid
Dox	Doxorubicin
d.t.	Decomposition Temperature
EDC·HCl	<i>N</i> -(3-Dimethylaminopropyl)- <i>N'</i> -ethylcarbodiimide hydrochloride
Et	Ethyl
ES	Electrospray
Eq.	Equivalents
FA	Folic acid
Fab	Fragment Antigen-Binding
FDA	Food and Drug Administration
FR	Folate Receptor
GluSH	Glutathione
GPI	Glycosylphosphatidylinositol
HRMS	High-Resolution Mass Spectrometry
HSA	Human Serum Albumin
ID/g	Injected Dose per Gram of Tissue
IgG	Immunoglobulin G
IR	Infrared
<i>J</i>	Coupling Constant
LC-MS	Liquid Chromatography–Mass Spectrometry
LRMS	Low-Resolution Mass Spectrometry
m	Multiplet
mAb	Monoclonal Antibody

Me	Methyl
MMAE	Monomethylauristatin E
m.p.	Melting Point
MS	Mass Spectrometry
NMR	Nuclear Magnetic Resonance
p	Pentet
PBS	Phosphate-Buffered Saline
PD	Pyridazinedione
PEG	Polyethylene Glycol
Pet.	Petroleum Ether
PFS	Progression-Free Survival
ppm	Parts Per Million
PSMA	Prostate-Specific Membrane Antigen
q	Quartet
quant.	Quantitative
RFT-1	Reduced-Folate Transporter 1
RME	Receptor-Mediated Endocytosis
ROS	Reactive Oxygen Species
s	Singlet
sat.	Saturated
SMDC	Small Molecule–Drug Conjugate
SPAAC	Strain Promoted Azide-Alkyne Cycloaddition
SPECT	Single-Photon Emission Computerised Tomography
t	Triplet
TFA	Trifluoroacetic Acid

THF	Tetrahydrofuran
TIC	Total Ion Current
TLC	Thin-Layer Chromatography
TTDDS	Tumour-Targeted Drug Delivery System
TubBH	Tubulysin B Hydrazide
UCL	University College London
UV	Ultraviolet
UV–Vis	Ultraviolet–Visible Spectrophotometry

# Chapter 1 Introduction

## 1.1 Chemotherapy

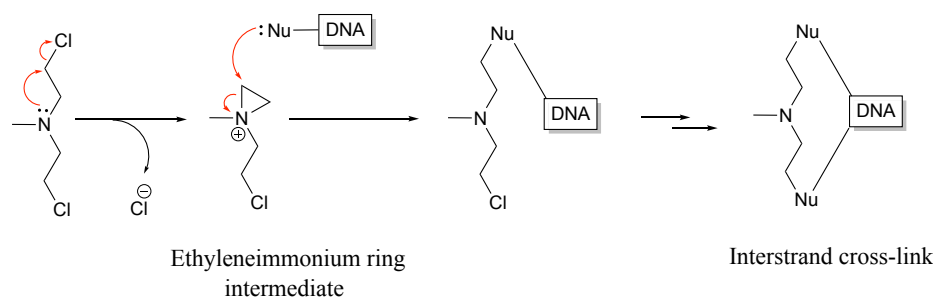
Cancer comprises a group of more than 200 diseases whose defining characteristics constitute the uncontrolled growth of abnormal cells and their potential to invade other parts of the body, often resulting in death if left untreated.<sup>1</sup> In the US, cancer is the second most frequent cause of death and it remains a leading source of fatality worldwide.<sup>2</sup> For much of the 20<sup>th</sup> century, chemotherapy has dominated cancer treatment,<sup>3</sup> but in recent decades tumour-targeted drug delivery systems (TTDDSs) have emerged,<sup>1</sup> exhibiting the ability and potential to treat this disease with superior specificity.

### 1.1.1 Chemotherapy: Origins

Despite the emergence of the aforementioned tumour-targeted cancer treatments, chemotherapy remains the most widely practised treatment of cancer. The basic proof of concept for this type of therapy was demonstrated almost eight decades ago, when in 1942, American scientists Louis Goodman and Alfred Gilman used chlormethine (a nitrogen mustard) to treat a patient afflicted with non-Hodgkin's lymphoma. Although the patient exhibited initial regression of the lymphatic masses, the remission was short-lived, with the disease recurring a few weeks later. Nonetheless, the basic principle of chemotherapy was established: namely, that tumour regression can be induced by the systemic administration of drugs.<sup>4</sup>

The same two scientists next set out to uncover the molecular action that chlormethine exerted on cancerous cells, discovering that it reacted with the electron-donating portions of DNA *via* an alkylating ethyleneimmonium ring intermediate (Scheme 1).<sup>4</sup> This crosslinking of DNA strands induces apoptosis, and although the formation of a covalent bond between chlormethine and DNA was not discovered until later on, experiments like this one revealed the greater susceptibility of tumours to certain toxic agents compared to healthy tissues, despite the reason for this phenomenon being still unknown at the time.<sup>4</sup> Unfortunately, any success that nitrogen mustards may have

initially enjoyed was short-lived, as tumour cells quickly developed resistance to this class of compounds.



Scheme 1. Chlormethine's alkylation of DNA *via* the ethyleneimmonium ring intermediate.

## 1.1.2 Chemotherapy: Antifolates

An alternative approach to cancer treatment was investigated by Sydney Farber in the mid-1940s, who found that patients who suffered from megaloblastic anaemia were deficient in the vitamin B<sub>9</sub>, folic acid, and that the administration of this vitamin to children who presented acute lymphoblastic leukaemia (ALL) stimulated the proliferation of ALL cells.<sup>5</sup> Farber developed the drug methotrexate (Figure 1), which achieved brief remission in children with ALL, and Roy Hertz discovered that methotrexate alone was sufficient to cure choriocarcinoma (a cancer of the placenta), making this the first solid cancer in humans to be cured by drug therapy.<sup>4,6</sup>

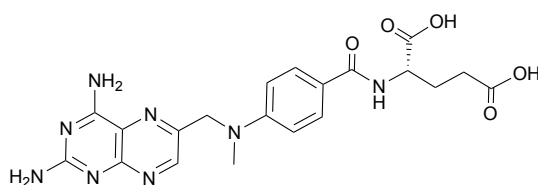


Figure 1. Structure of methotrexate, which was the first drug to cure the solid cancer choriocarcinoma in humans.

It was not until 1958 that Frank Heunneken and Michael Osborn found that the mechanism of action exhibited by antifolate drugs consisted of the inhibition of dihydrofolate reductase (DHFR),<sup>7,8</sup> which includes methotrexate after it is taken up into cells *via* the reduced-folate transporter 1 (RFT-1). While methotrexate is still the main drug employed in therapies for patients with ALL, choriocarcinoma and osteosarcoma, the study of this drug's loss of efficacy due to mutations in RFT-1 and



other aspects of its uptake and cell-killing pathways has provided invaluable lessons for understanding mechanisms of resistance in other chemotherapeutic agents.<sup>4,9</sup>

### 1.1.3 Chemotherapy: Combination Treatments

By 1965, Emil Freireich, James Holland and Emil Frei discovered that a combination of the antifolate methotrexate, the *vinca* alkaloid vincristine, 6-mercaptopurine and prednisone (together known as the POMP regimen) was able to induce long-term remission in children suffering from ALL.<sup>10</sup> By the late 1960s another regimen known as MOPP (nitrogen mustard, vincristine, procarbazine and prednisone) was shown by Vincent De Vita *et al.* to cure Hodgkin's and non-Hodgkin's lymphoma.<sup>4,11,12</sup> Studies like these and many more found that drugs were most efficacious when used as combination therapies and when employed against smaller volume tumours. It was also discovered that combination therapies fared better than single agent treatments in patients at high relapse risk post-surgical treatment, and in metastatic cancers.<sup>4</sup>

Platinum-based chemotherapy, also originating in the 1960s, was made possible by Barnett Rosenberg's accidental discovery of cisplatin's anticancer properties.<sup>13,14</sup> The FDA (Food and Drug Administration) approved cisplatin in 1978 and since then platinum-based drugs have enjoyed an important role in chemotherapy. They are often used in combination with other antitumour agents, and are still used in almost half of all chemotherapeutic programs today.<sup>14-16</sup>

Notwithstanding the early success of chemotherapy, the major drawback that all forms of the therapy are invariably associated with are acute toxicities which develop as a result of lack of specificity, *i.e.* the administered drugs are indiscriminately lethal towards cancerous and healthy cells alike. This inability of chemotherapeutic drugs to differentiate between healthy and cancerous cells manifests as dose-limiting effects in the patient, thus restricting the dose escalation to what could otherwise constitute highly effective therapeutic regimes (Figure 2).<sup>17-21</sup>

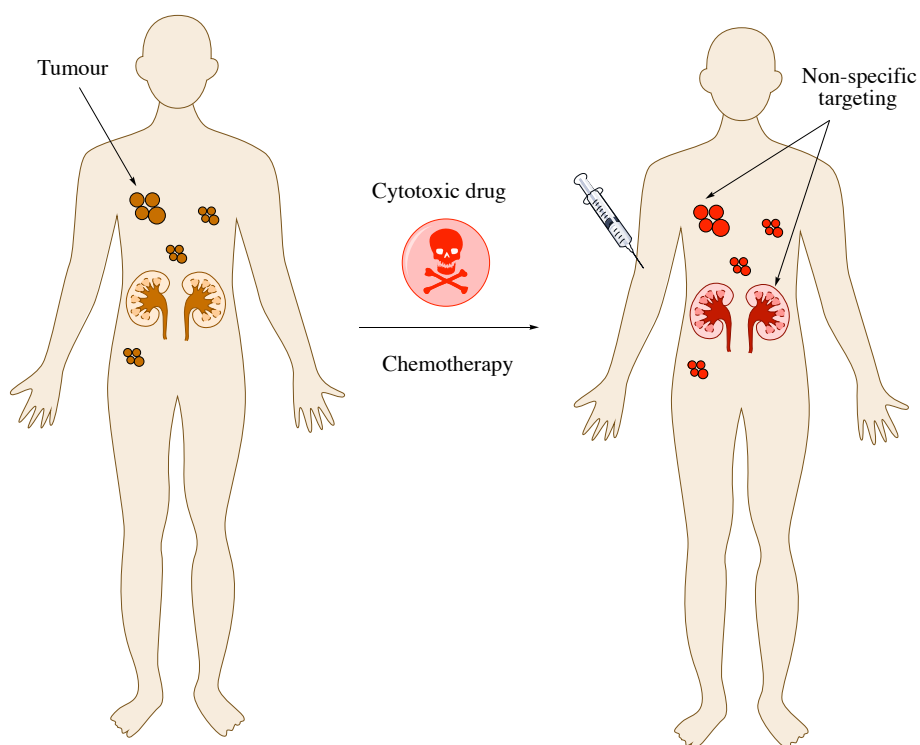


Figure 2. Schematic representation of non-targeted chemotherapy. The red represents the cytotoxicity induced in both tumours and healthy tissues.

The prospect, therefore, of developing ways to treat and manage cancer in a much more selective manner, *i.e.* to minimise off-target toxicity, has always been an attractive one. To this effect, TTDDSs have emerged as a promising alternative.<sup>1</sup>

## 1.2 Targeted Cancer Therapy

TTDDSs largely bypass the adverse side effects characteristic of conventional chemotherapy and maximise cancer cell-selective delivery of the cytotoxic agents. Targeting particular biomarkers that are overexpressed specifically on tumour cells enables the selective delivery of cytotoxic cargo to the cancerous tissue, thereby minimising toxic side effects in the patient and increasing therapeutic index (Figure 3).<sup>22,23</sup>

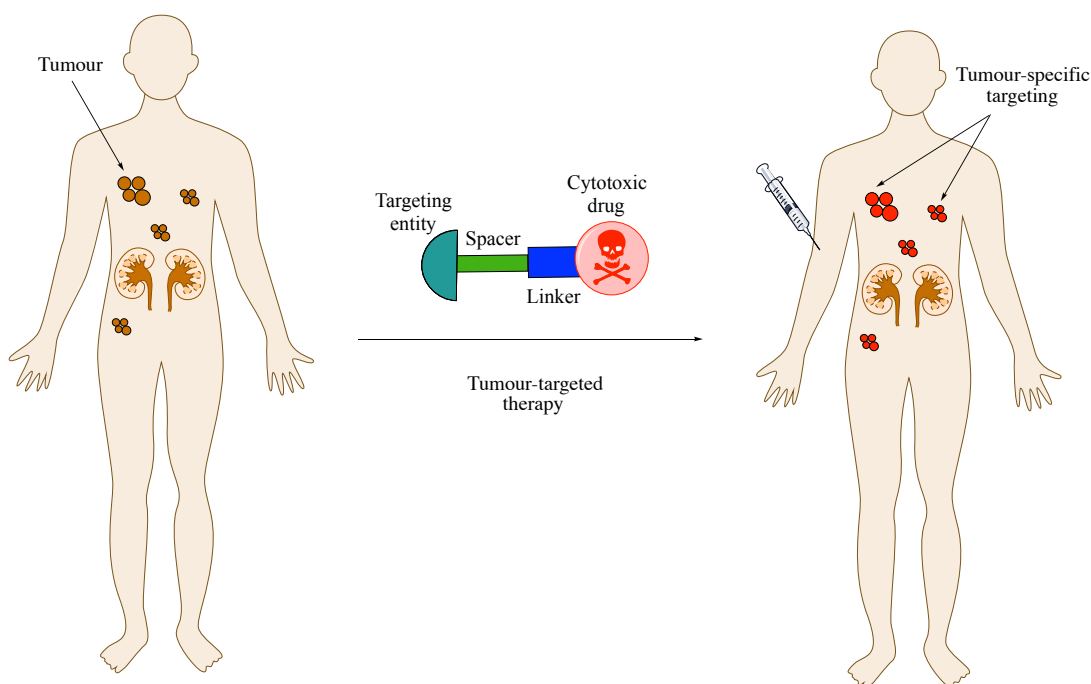


Figure 3. Schematic representation of tumour-targeted therapy, where the drug conjugate is typically composed of a targeting entity, a spacer, a linker and a cytotoxic drug. The red represents the induced cytotoxicity in tumours alone, leaving healthy tissues unaffected.

Another attractive feature of targeted conjugates constitutes the ability to incorporate highly potent warheads, given that the free drug is only cleaved within or in the environment of the malignant cells. This strategy contrasts sharply with chemotherapy, whereby the cytotoxic agent is always administered into circulation in the free (and highly toxic) form, thus excluding the use of large swathes of drugs which would simply be too toxic to use in the patient otherwise. Some of the most common TTDDSs will be discussed in turn below.

### 1.2.1 Targeted Therapy: Monoclonal Antibodies (mAbs)

Monoclonal antibodies (mAbs) (Figure 4) represent an attractive candidate for targeted therapy as they can be generated *in vitro* against a specific antigen overexpressed by the tumour type, inducing cell death by mechanisms such as interference with tumour-cell signalling pathways and antibody-dependent phagocytosis.<sup>3</sup> The first mAb for cancer treatment was approved by the FDA in 1997 for patients with CD-20 positive,

B-cell, low-grade or follicular non-Hodgkin's lymphoma<sup>3,24</sup> and eleven more have been approved since.

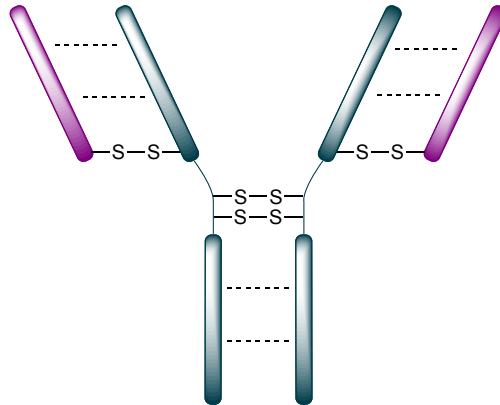


Figure 4. Schematic representation of a mAb.

Another example is that of farletuzumab (MORab003): a fully humanised anti-FR $\alpha$  (FR $\alpha$  is folate receptor  $\alpha$ ) mAb weighing 145 kDa and produced in Chinese hamster ovary cells. This antibody has the added advantages of neither preventing the binding of folic acid to the FR $\alpha$  nor blocking the FR $\alpha$ -mediated FA-transport (FA is folic acid) into the cell.<sup>25,26</sup> The therapeutic potential of farletuzumab has been shown in both *in vitro* and *in vivo* studies. Preclinical *in vitro* studies have demonstrated that upon binding to FR $\alpha$  on tumour cells, farletuzumab promotes tumour cell lysis by various modes of action, including complement-dependent cytotoxicity (CDC) and antibody-dependent cell-mediated cytotoxicity (ADCC). Other mechanisms by which this anti-FR $\alpha$  mAb suppresses cancer cell proliferation activity include sustained autophagy and disruption of the FR $\alpha$  and lyn kinase interaction which curtails intracellular growth signalling.<sup>25,26</sup>

Farletuzumab, in combination with carboplatin/taxane, followed by single-agent farletuzumab maintenance was employed in a phase II study performed in patients with platinum-sensitive recurrent ovarian cancer.<sup>25,26</sup> Single-agent farletuzumab was well-tolerated by the patients, and no additional toxicity was observed when the antibody was administered in combination with chemotherapy. The study also demonstrated an overall improved response rate compared to historical, platinum-based combination chemotherapy regimens.<sup>27-30</sup> Unfortunately, phase III trials in both

platinum-resistant and platinum-sensitive ovarian cancer failed to replicate the promising results of the *in vitro* and *in vivo* studies. Results from a large phase III study in patients with platinum-sensitive recurrent ovarian cancer evaluated farletuzumab in combination with carboplatin and taxane, and was compared with carboplatin/taxane alone. Disappointingly, this trial did not meet the primary end point of improving progression-free survival (PFS).<sup>25,26,31</sup>

Thus, in spite of some modest success enjoyed by monoclonal antibody treatments, they are rarely curative on their own and tend to be administered in conjunction with cytotoxic agents, as described.<sup>3,32</sup>

### **1.2.2 Targeted Therapy: Antibody–Drug Conjugates (ADCs)**

The potential to elevate tumour specificity and enhance efficacy was thus theorised to arise from combining an antibody and a toxic agent in a single conjugate, whereby the exquisite binding selectivity of an antibody could be coupled to the potent toxicity of a chemical warhead. This specificity can be attained by constructing a conjugate that exploits markers which are ideally overexpressed on and are specific to cancerous cells. In this way, the chemical warhead is envisaged to possess a tumour-seeking molecule which does not recognise healthy cells, but which binds selectively to the surface of tumours, causing these to inadvertently internalise the conjugate which can subsequently break down and release the free cytotoxic drug to promote cell death. Therefore, in an effort to enhance the aforementioned site-specific delivery, antibody–drug conjugates (ADCs) were generated by attaching the cytotoxic agents directly to antibodies.

As the name suggests, ADCs consist of a cytotoxic drug conjugated to an antibody, usually *via* a spacer and a cleavable linker (Figure 5).

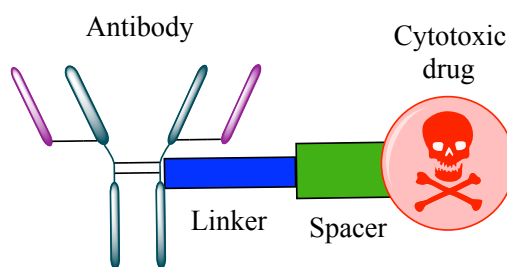


Figure 5. Schematic representation of an ADC. The ADC typically comprises an antibody, a spacer, a linker and a cytotoxic drug payload.<sup>33</sup>

One of the earliest examples of an ADC is BR96-doxorubicin (Figure 6).<sup>32</sup> Despite not being particularly potent, this ADC was developed against breast cancer, which is LeY positive. Consequently, the monoclonal antibody moiety of this drug binds to the LeY tetrasaccharide antigen found on this type of carcinoma<sup>32</sup> and acts as the vehicle for the selective delivery of the cytotoxic agent. Once the conjugate binds to the tumour, it is internalised and the acidic conditions of the late endosome and lysosome cleave the acid labile hydrazone linker, thereby releasing the therapeutic drug doxorubicin (Dox).

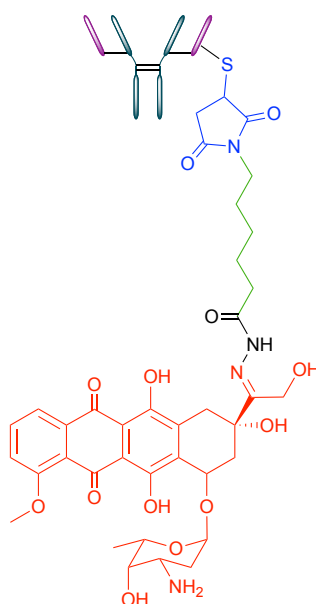


Figure 6. Structure of BR96-doxorubicin, where the Dox portion (red) has been modified to incorporate a hydrazone linker and is conjugated to the antibody *via* an alkyl chain spacer (green) and a succinimide linker (blue).<sup>32</sup>

The bystander effect, despite somewhat undermining the target selectivity of ADCs, is another mechanism of inducing cell death: as described, antigen-positive tumour cells will lead to the binding and internalisation of a specific ADC, but cancer cell efflux

pumps can expel some of the cytotoxic drug.<sup>34</sup> These evacuated cytotoxic drugs can then diffuse into neighbouring tumour cells which may be antigen-negative, as the absence of antigen expression homogeneity is common in solid tumours.<sup>34,35</sup> Moreover, only conjugates possessing cleavable linkers and drugs with suitable logP can contribute to the bystander effect, as the liberated free drug must be able to cross the hydrophobic lipid bilayer of cells. In contrast, conjugates lacking cleavable linkers form charged species when degraded and are therefore often incapable of traversing this same layer.<sup>34,36</sup>

Although some of these early generation ADCs initially showed promising tumour accumulation results in mice, many were subsequently discontinued at various stages in clinical trials as they failed to produce clinically meaningful therapeutic activity.<sup>3</sup> Reasons for this included their low *in vitro* potency and the observation that conjugation significantly reduced the potency as opposed to that of the free drug. In light of this, the field of ADCs has moved towards the use of extremely potent drug payloads that can neutralise cancerous cells at subnanomolar concentrations.<sup>37</sup> Examples of such ADCs that are currently used in cancer treatments are brentuximab vedotin and trastuzumab emtansine, for last-line Hodgkin's lymphoma and HER2-positive breast cancer respectively.<sup>37</sup> Brentuximab vedotin, whose cytotoxic agent is monomethylauristatin E (MMAE), in particular exhibits significant efficacy. Of patients who failed multidrug chemotherapy, 87% presented overall responses when treated with brentuximab vedotin, and 57% of these were complete responses, with a PFS of 12.6 months.<sup>37</sup>

A further example of an ADC that has exhibited some clinical success is IMGN853, a construct composed of (1) an anti-FR $\alpha$  antibody, (2) DM4, an antimitotic agent and (3) a disulfide-based linker that connects the drug to the antibody (Figure 7).<sup>31</sup>

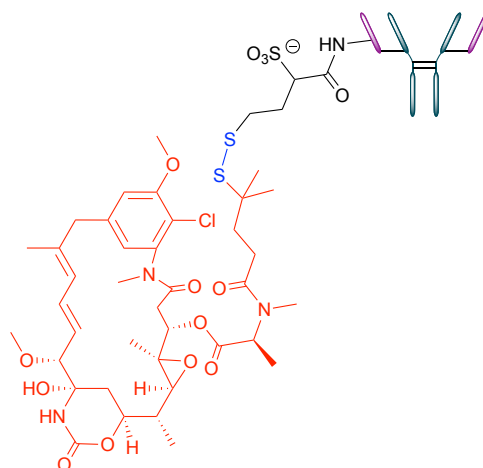


Figure 7. Structure of IMGN853. The anti-FR $\alpha$  antibody is conjugated to the DM4 drug (red) *via* a self-immolative disulfide linker (blue).

After binding to FR $\alpha$ , IMGN853 is internalised *via* receptor-mediated endocytosis (RME), and ensuing enzymatic degradation of the antibody and linker releases the DM4 drug, which induces cell-cycle arrest and death by inhibiting tubulin polymerisation and microtubule assembly. IMGN853 has demonstrated anti-tumour activity and is currently being assessed in the Phase II FORWARD I trial as a single-agent therapy for patients with FR $\alpha$ -positive platinum-resistant ovarian cancer. This ADC is also being tested in combination regimens for FR $\alpha$ -positive ovarian cancer in the Phase 1b/II FORWARD II trial. This ADC represents the only one of its type to target the FR $\alpha$ .

Notwithstanding the success of some ADCs in modern cancer treatment, these conjugates have a number of drawbacks, one being the antibody component's potential to illicit unwanted immunogenic responses *in vivo*.<sup>38</sup> Another disadvantage constitutes the costly production of antibodies, which can take up to 75% of the conjugate manufacturing cost.<sup>23,39</sup> Furthermore, antibodies' large size renders deep tissue penetration slow and inefficient<sup>40,41</sup> with typically over 99% of the administered conjugate not reaching the tumour.<sup>37</sup> In fact, the best immunoglobulin G (IgG) antibodies have only displayed *ca.* 0.01% ID/g (injected dose per gram of tissue) in the tumour after 24 h.<sup>18</sup> This comprises a major limitation of ADCs; undesired toxicities in organs such as the liver and kidneys can result from premature drug release due to the overwhelming majority of the conjugate persisting in the bloodstream, where it can remain in circulation for weeks.<sup>42</sup>



### 1.2.3 Targeted Therapy: Small Molecule–Drug Conjugates (SMDCs)

Small molecule–drug conjugates (SMDCs), which also target markers specific to (or overexpressed on) cancerous cells have emerged as promising alternatives to ADCs (Figure 8).<sup>24–26</sup>

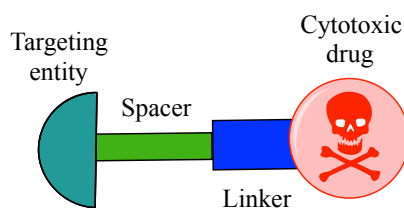


Figure 8. Schematic representation of an SMDC, typically consisting of a cancer targeting ligand, a spacer, a linker and a cytotoxic drug payload.<sup>33</sup>

These smaller ligands aim to selectively deliver drug payloads to tumours and have numerous advantages over their antibody-based analogues. For instance, SMDCs are cost-effective<sup>23</sup> and nonimmunogenic,<sup>40</sup> but the most important unmet need for small-molecule active targeting agents lies in the arenas of imaging and chemotherapy.<sup>43</sup> Moreover, greatly reduced size is another desirable characteristic of SMDCs as compared to antibodies, and this allows for improved penetration into tumours due to easier diffusion in and out of blood vessels, resulting in more efficient and faster arrival of the toxic cargo to the cancerous mass.<sup>44</sup> SMDCs' circulation time is shorter than that of ADCs, with FA-SMDCs for instance, possessing a half-life in the blood of *ca.* 26 mins and consequently minimising the time that the cytotoxic agent spends in the bloodstream.<sup>45</sup> However, the downside of this short half-life means the conjugate must be administered regularly, which is undesirable in regards to patient compliance.

Tumour-targeting receptors in healthy epithelial cells are normally only positioned on the apical surface, and so are inaccessible to parenterally administered drug conjugates owing to intercellular junctions (tight junctions, adherens junctions, desmosomes and gap junctions) that impede small molecules from crossing the epithelium.<sup>33,46</sup> However, upon tumorigenesis the entire architecture of a tumour relative to healthy cells changes: the vasculature becomes disorganised and chaotic and important structural and morphological defects also develop. Among them are basal membrane

modification, abnormal pericyte shape and degradation of smooth muscles that contract and tighten cell junctions.<sup>47,48</sup> The loss of these intercellular junctions gives rise to weak association between endothelial cells,<sup>47</sup> leading to receptors, that were previously restricted to the apical surface, becoming randomly distributed across the surface of the tumour (Figure 9).<sup>33</sup>

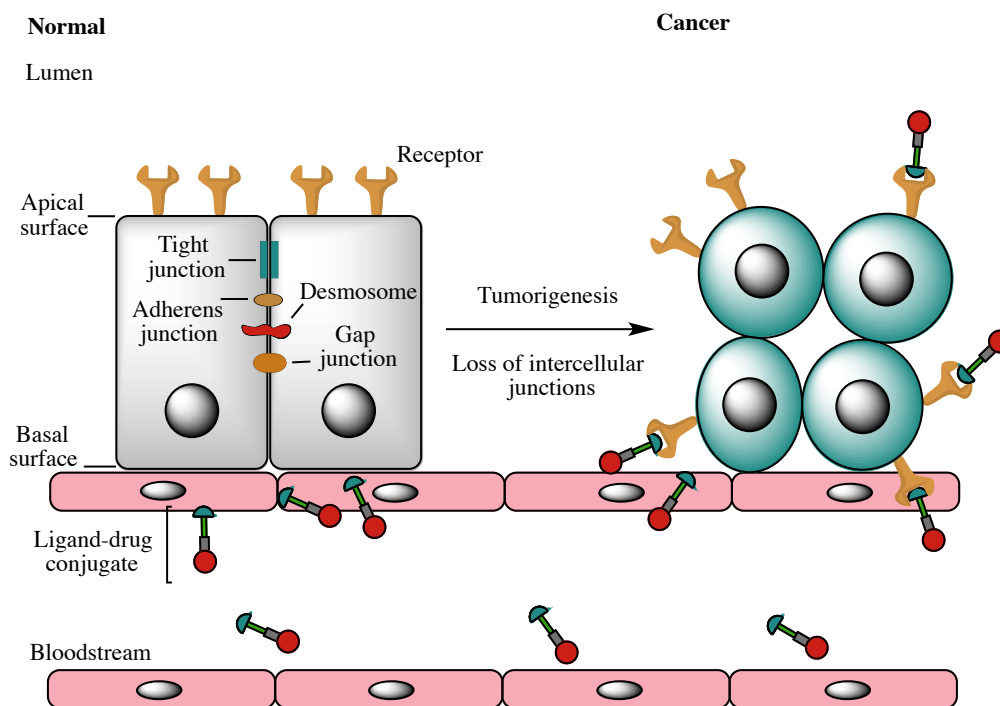


Figure 9. The transformation of healthy epithelial cells to tumour cells and the effect it has on receptor positioning. Upon tumorigenesis, intercellular junctions are lost and receptors become randomly positioned on the tumour cell surface.<sup>33</sup>

As described, antibodies are large, bulky molecules which consequently do not extravasate very well into tissue, so any ADCs on the abluminal side of the blood vessel will only be captured by the tumour receptors that, after random distribution, now point out into the bloodstream. This precludes these conjugates from reaching and neutralising any tumours distantly located from blood vessels.<sup>44</sup> The significantly smaller size of SMDCs alleviates this problem, as they can efficiently diffuse deep into tissue and arrive at tumours located far from the blood supply.

There are many different types of SMDCs, targeted against a large plethora of markers specific to or overexpressed on cancer cells, with just a small selection being discussed below.

### 1.2.3.1 Prostate-Specific Membrane Antigen-targeted SMDCs

Prostate-specific membrane antigen (PSMA) is a surface glycoprotein<sup>49,50</sup> overexpressed on prostatic secretory epithelium cells and prostate cancer,<sup>51</sup> but also found in lower levels on normal cells such as those of the salivary glands, proximal renal tubes and small-intestine brush-border membrane.<sup>43,52,53</sup> PSMA allows the uptake and generation of essential nutrients such as folate and glutamate by displaying carboxypeptidase and folate hydrolase activities.<sup>43,54–56</sup> SMDCs based on targeting PSMA have been reported,<sup>57</sup> such as two small-molecule constructs based on glutamate-urea-lysine that inhibit glutamate carboxypeptidase (Figure 10).<sup>43</sup>

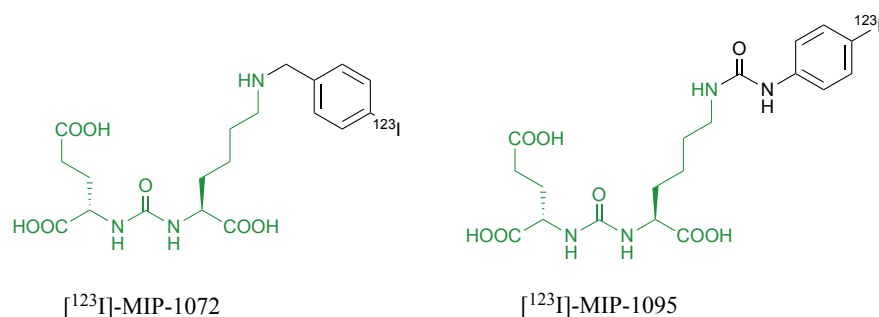
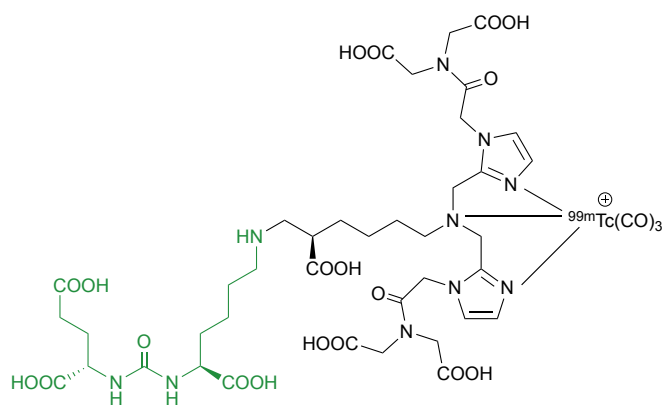


Figure 10. Structures of glutamate carboxypeptidase inhibitors  $[^{123}\text{I}]$ -MIP-1072 and  $[^{123}\text{I}]$ -MIP-1095, with the glutamate-urea-lysine portion shown in green.<sup>43</sup>

Both MIP-1072 and MIP-1095 displayed high binding affinity to PSMA-positive cells ( $K_d = 3.8 \pm 1.3$  and  $0.81 \pm 0.39$  nM respectively) *in vitro* and *in vivo*,<sup>58,59</sup> while exhibiting little to no effects on normal cells and PSMA-negative cancer tissues.<sup>43</sup> MIP-1072 and MIP-1095 have undergone Phase I clinical trials, with both showing brisk localisation at soft tissue and bone cells of metastatic prostate cancer (1–4 hr after administration), with MIP-1072 being cleared from non-targeted cells and circulation five times faster than MIP-1095.<sup>43,60</sup>

Consequently, the structure of MIP-1072 was made more hydrophilic by incorporation of a polar lysine imidazole derivative that included acid groups, as well as employing radionuclide technetium-99m as a labelling agent. This gave rise to  $^{99\text{m}}\text{Tc}$ -MIP-1404 (Figure 11).<sup>43</sup>

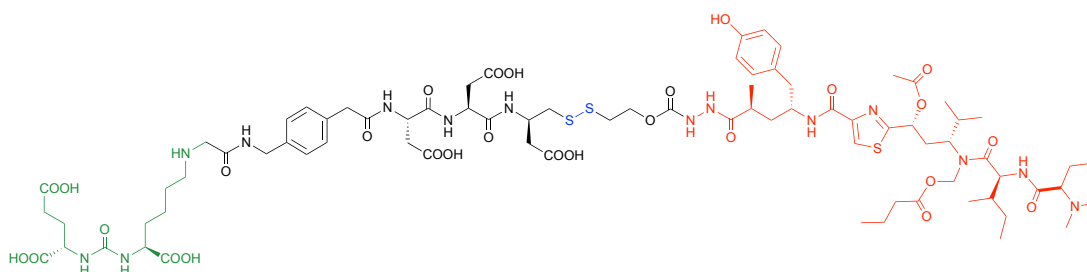


$^{99m}\text{Tc}$ -MIP-1404

Figure 11. Structure of  $^{99m}\text{Tc}$ -MIP-1404, based on imidazole lysine derivatives.<sup>43</sup>

MIP-1404 exhibited superior pharmacokinetic profiles than MIP-1072 and MIP-1095 as well as achieving the best localisation on PSMA-positive tumour xenografts over 4 h.<sup>43,61,62</sup> MIP-1404 was also utilised in Phase I clinical trials for SPECT (single-photon emission computerised tomography) imaging where high specificity and rapid detection were achieved for metastatic prostate cancer in both bone and soft tissue.

EC1169 is a PSMA-SMDC whose drug component is the antineoplastic agent TubBH (Figure 12).



EC1169

Figure 12. Structure of EC1169, possessing a disulfide-based linker (blue) and the antineoplastic drug TubBH (red).<sup>43</sup>

This SMDC was able to leave PSMA-negative cells untouched whilst inhibiting the growth of PSMA-positive tissues *ex vivo*. Use of this SMDC in a tumour xenograft mouse model bearing humanised LNCaP (PSMA-positive) cells caused five of the seven specimens to experience tumour remission with the remaining two being considered cured, as no tumour regrowth was observed for up to 90 days.<sup>43</sup>

### 1.2.3.2 Carbonic Anhydrase IX-targeted SMDCs

Carbonic anhydrase (CA) is a transmembrane zinc metalloenzyme found in cervical cancer HeLa cells.<sup>63</sup> Humans contain a total of 16 different CA isozymes, these being present in tissues ranging from the gastrointestinal tract to the lungs, eyes and skin,<sup>64</sup> with carcinogenesis linked to the isozymes CA-IX and CA-XII.<sup>22,43</sup> The CA-IX isozyme is absent in most healthy tissues save the gallbladder epithelia<sup>65</sup> and the stomach, and is usually overexpressed in breast,<sup>66</sup> colorectal<sup>67</sup> and glioblastoma<sup>68</sup> cancers.<sup>43</sup>

Neri *et al.* conjugated CA inhibitor acetazolamide (AAZ) to the drug duocarmycin, with the SMDC displaying high affinity for the CA-IX receptor. Unfortunately, a human renal-cell carcinoma xenograft model displayed only modest tumour growth inhibition compared to the conjugates that were untargeted.<sup>43,69</sup> When a different drug, namely DM1, was attached to the AAZ, significant tumour shrinkage was observed after a week of consecutive treatment, although regrowth of the tumour masses did occur 20 days after the SMDC had ceased to be administered.<sup>69</sup>

A bivalent analogue of the above was investigated (Figure 13), which performed better than its monovalent conjugate in four main ways. Firstly, no disassociation was observed from cells with a CA-IX-coated surface. Next, the bivalent conjugate accumulated at the tumour site in a quantity three times greater than that of the monovalent analogue. As well as reaching the tumour in greater quantity, bivalent AAZ-maytansinoid DM1 persisted for longer in the tumour mass (post administration showed 40% fluorescence signal for bivalent construct and only 14% for monovalent analogue). Lastly, in a human renal carcinoma SKRC52 xenograft model, ablation of *ca.* 75% of the tumour compared to the initial was observed, with 33% of the treated mice remaining free from disease for up to 90 days.<sup>43,70</sup>

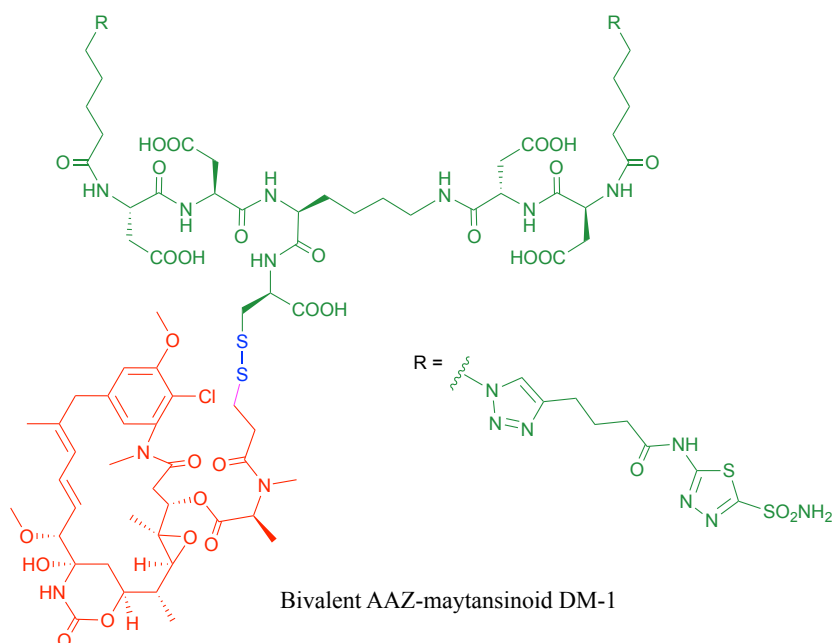


Figure 13. Structure of bivalent AAZ-maytansinoid DM1, possessing a disulfide linker (blue), the CA-IX-targeting AAZ (green), and the drug DM1 (red).<sup>43</sup>

### 1.2.3.3 Biotin Receptor-targeted SMDCs

Another biomarker that has been exploited for small-molecule directed drug delivery is that of biotin, in order to target the biotin receptor (BR)<sup>71</sup> which is necessary for cell growth<sup>72,73</sup> and which is overexpressed on many cancer types, including breast, ovarian, renal, colon and leukaemia.<sup>43,74</sup>

One such example of a biotin-SMDC is SBT-1214, whose drug component is a taxoid (Figure 14). When administered to BR-positive murine leukaemia cells, SBT-1214 exhibited an  $IC_{50}$  of 8.8 nM, compared to the  $IC_{50}$  of 522 nM when this SMDC was incubated with murine leukaemia cells that were BR-negative.<sup>43,75</sup> Chen *et al.* also synthesised fluorescent analogues of SBT-1214 in order to demonstrate that the biotin-taxoid construct underwent preferential accumulation in tumours and that toxic effects on healthy tissues were greatly reduced as a result. These fluorescent studies also found that systemic stability of the construct was heightened by the presence of the disulfide linker.<sup>43,75</sup>

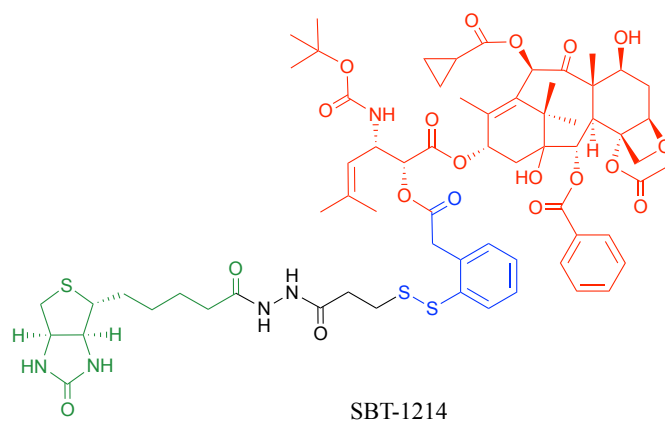


Figure 14. Structure of SBT-1214, possessing a biotin ligand (green), a disulfide-based linker (blue) and a taxoid (red).<sup>43</sup>

There are also examples of dual-warhead biotin-SMDCs, with one construct being tethered to a taxoid and camptothecin (Figure 15). A tetraethylene glycol diamine spacer was also incorporated to confer greater water-solubility to the construct.<sup>76</sup>

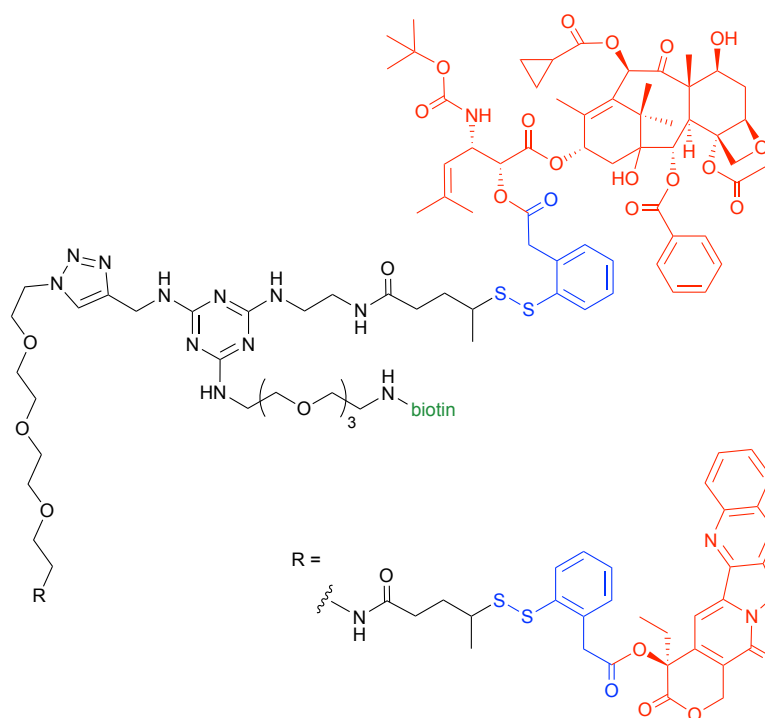


Figure 15. Dual-warhead taxoid-camptothecin biotin-SMDC, possessing a disulfide-based linker (blue) as well as taxoid and camptothecin drugs (both red).<sup>43</sup>

The above SMDC, when administered to BR-positive tumour cells in the presence of glutathione (GluSH), elicited an  $IC_{50}$  of 3.22–9.80 nM as opposed to the  $IC_{50}$  of

705 nM when the SMDC was exposed to normal, BR-negative cells. In addition, the two different drugs delivered to the tumour cells simultaneously *via* the dual-warhead SMDC were found to produce a cooperative effect regarding cell kill.<sup>43</sup>

#### 1.2.3.4 Folate Receptor-targeted SMDCs

Of the many vitamin receptors employed for the selective delivery of cytotoxic cargoes to tumour cells, the FR is one of the most widely studied, making it a promising tumour biomarker for personalised drug delivery.<sup>37</sup> The FR glycoprotein family (35–40 kDa)<sup>77</sup> comprises three isoforms: FR $\alpha$ , FR $\beta$  and FR $\gamma$ . The  $\alpha$  and  $\beta$  variants are attached to the cell membrane *via* GPI (glycosylphosphatidylinositol) anchors, whereas FR $\gamma$  is found only in hematopoietic cells<sup>78</sup> and lacks the GPI component, making it freely soluble.<sup>77</sup> The FR $\beta$  isoform is upregulated on macrophages that participate in inflammatory and autoimmune diseases.<sup>79,80</sup> The FR $\alpha$  has the most potential for targeted cancer therapy as it is overexpressed in a large number of cancers of epithelial origin (including breast,<sup>17</sup> lung, kidney and ovarian<sup>81</sup>) at 10–100 times higher than on healthy cells<sup>17</sup> and in the order of 1–10 million copies per cell.<sup>45</sup> In non-cancerous tissues, the expression and distribution of FR $\alpha$  is largely confined to kidney cells for folate resorption, cells crucial for embryonic development,<sup>77</sup> and the choroid plexus in the brain.<sup>82</sup> Tumours that upregulate FR $\alpha$  do so to maximise vitamin uptake in order to sustain their rapid, uncontrolled and aggressive proliferation: folate is one such vitamin, needed for *de novo* nucleotide synthesis and one carbon methylation reactions inside the cell.<sup>45</sup> Moreover, the number of unoccupied receptors on the cell surface will depend on the recycling rate of the receptor from the endosome, and so in receptor-mediated internalisation pathways it is desirable to have a rapid recycling rate so as to maximise drug capture and uptake.<sup>33</sup> The FR $\alpha$  fulfils this criterion, possessing a receptor recycling rate of 8–12 h<sup>45</sup> and is capable of transporting drug conjugates at a rate of  $3.4 \times 10^5$  molecules cell<sup>-1</sup> h<sup>-1</sup> in KB cells.<sup>44,83</sup> Accordingly, drug conjugates with FA as the targeting entity have been developed. Although only certain positions of the folic acid core scaffold can be modified for attachment to the conjugate, FA–SMDCs retain a high binding affinity for the FR $\alpha$  ( $K_D = 1–10$  nM).<sup>44,84,85</sup>

When an FA-SMDC is injected into the bloodstream, the folate portion of the conjugate acts as the tumour-targeting ligand and binds strongly to FR $\alpha$  receptors on cancer cells which subsequently internalise the SMDC *via* RME. Once the conjugate is



sequestered within an endosome,<sup>45</sup> resident proton pumps result in a slight decrease in pH, altering the FR $\alpha$ 's conformation and allowing the SMDC to detach.<sup>45,86</sup> The late endosome then fuses with the lysosome and intracellular thiols such as GluSH can degrade the conjugate by cleaving the disulfide linker and releasing the cytotoxic drug. This payload can then diffuse out of the endosome into the cytosol where it induces apoptosis; meanwhile, the folate receptors are recycled back to the surface of the cell to engage in further rounds of drug internalisation (Figure 16).<sup>45</sup>

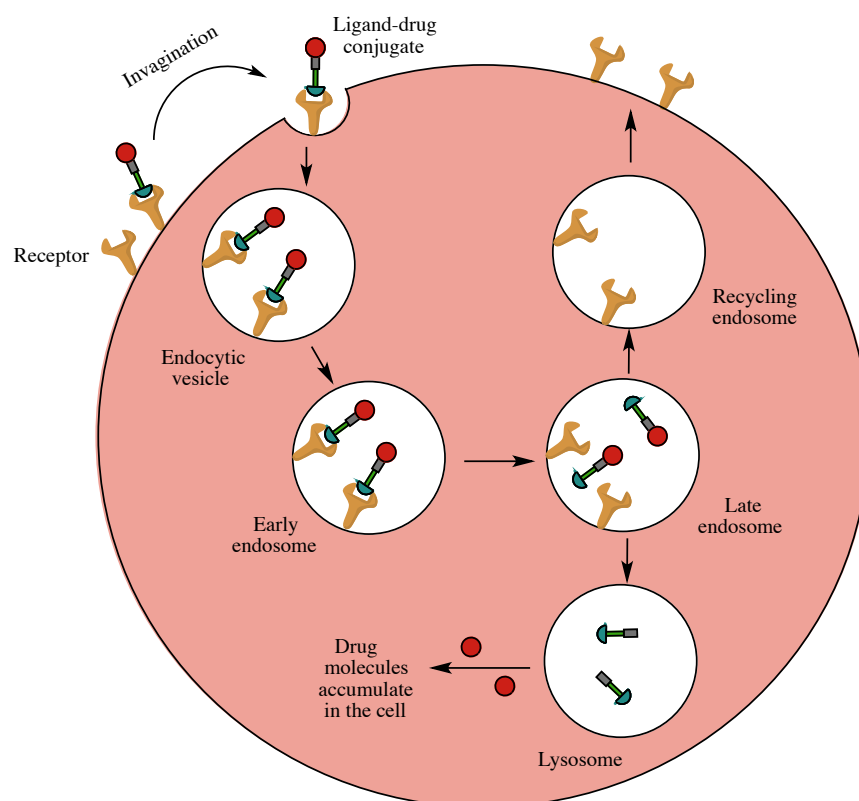


Figure 16. Receptor-mediated endocytosis of an FA–SMDC. The conjugate initially binds to the FR $\alpha$  which forms an invagination and encloses the conjugate in the early endosome. A mild drop in pH changes the receptor's conformation, resulting in SMDC detachment. The late endosome's subsequent fusion with the lysosome leads to degradation of the conjugate and release of the free drug into the cell. The recycling endosome delivers the receptors back to the cell surface.<sup>33</sup>

This rational approach to the design of successful FA–SMDCs manifests as most of these conjugates sharing common features, among them the incorporation of highly potent therapeutic drugs. Measurements of intracellular SMDC concentrations in the range of 1–5  $\mu\text{M}$  suggest that chemical warheads with IC<sub>50</sub> values in the low nanomolar range are necessary to generate meaningful activity against the biological

target of interest.<sup>45</sup>

Other essential characteristics of these drug conjugates include the presence of functional groups which can be modified to permit conjugation to folic acid, and that they possess a low molecular weight for efficient penetration into tumour tissue. The size of FA-SMDCs is typically lower than 2000 Da.<sup>45</sup>

The spacer portion of these drug constructs confers several desirable properties to the conjugate, one being increased hydrophilicity. This is necessary owing to folic acid's rather lipophilic nature and so a hydrophilic spacer, such as a peptide unit in the case of the FA-SMDC EC145, ameliorates the overall water solubility of the drug conjugate. This heightened hydrophilicity also ensures that the SMDC binds exclusively to FR $\alpha$  in lieu of indiscriminately diffusing across the lipophilic membranes of both malignant and benign cells.<sup>45</sup> Another important role provided by the spacer unit is to physically separate the targeting ligand from the cytotoxic agent in order to retain the former's folate receptor binding potential, which without the spacer could be disrupted by the steric hindrance exerted by the close proximity of the drug to the FR $\alpha$ .

Perhaps the most crucial feature of such a design is the presence of a self-immolative or cleavable linker which is highly stable in blood, precluding premature and off-target drug release, but which is unstable inside the acidic endosome and lysosome of a cell, allowing cleavage by intracellular thiols such as GluSH and resulting in concomitant drug release into the cytosol. Folic acid-based SMDCs possessing this self-immolative disulfide bond demonstrate superior activity against FR $\alpha$  expressing cells as compared to non-reducible analogues.<sup>45</sup>

#### **1.2.3.4.1 Vintafolide (EC145)**

Numerous folic acid-based SMDCs have been developed with the aforementioned characteristics and of the several that have reached clinical trials, EC145 (vintafolide) has been the most advanced (Figure 17).<sup>45</sup>

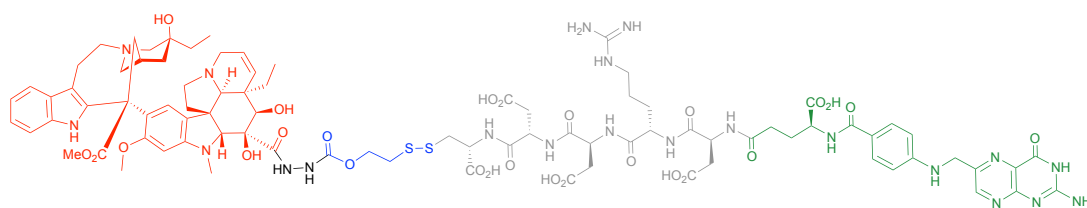


Figure 17. The chemical structure of the FA-based SMDC vintafolide consists of a folate targeting ligand (green), a peptide spacer (grey), a self-immolative disulfide linker (blue) and the potent cytotoxic drug DAVLBH (red).

Leamon *et al.* carried out a study aiming to evaluate the impact of altering three out of the four of vintafolide's constituent elements. They demonstrated that varying the spacer composition, provided that it remained hydrophilic, had minimal effect on the potency of the conjugate. In contrast, bioreleasable linkers that can be cleaved by intracellular thiols such as GluSH in the endosomal milieu are of critical importance for the conjugate's activity and have by far constituted the most successful approach for triggered drug release within the cell.<sup>45</sup> For instance, it was shown that self-immolative disulfide and acyl hydrazone linkers exerted activity both *in vitro* and *in vivo*, whereas vintafolide analogues possessing more stable amide and thioether linkers did not.<sup>87</sup> Furthermore, it was demonstrated that upon substituting DAVLBH with other clinically approved *vinca* alkaloid drugs (vincristine, vindesine, vinorelbine and vinflunine) while retaining the cleavable disulfide linker, that vintafolide was the only variant that exhibited biological activity *in vitro* and *in vivo*. This can be rationalised by considering vintafolide's high potency ( $IC_{50} = 8.44 \pm 1.46$  nM) as compared to the over ten-fold greater  $IC_{50}$  values of all the other drugs ( $IC_{50} > 100$  nM). It was further speculated that the absence of activity observed in the other *vinca* alkaloid forms could be due to a modification in the chemical structure following disulfide reduction and linker release.<sup>87</sup>

Vintafolide has shown promise, both as a single agent, as well as in combination with Dox in two Phase II trials (ovarian and non-small cell lung cancers) and in a randomised open-label Phase II study respectively (platinum-resistant ovarian cancer).<sup>45</sup> It entered Phase III clinical trials in 2010 for advanced stage platinum-resistant ovarian cancer.<sup>88,89</sup> However, this FA-SMDC failed to reach the pre-specified criteria for PFS and as a result, the trial was prematurely terminated. The Phase III trials were unable to demonstrate that the targeted FR therapy was superior to conventional chemotherapeutic methods.

The success of vintafolide, and similar drugs can be rationalised by appreciating its rational design and the spatial and chemical relationships between the tumour-seeking portion of the conjugate and the cytotoxic warhead. It was precisely characteristics such as improving the release properties of the SMDC and the structure-activity relationships of the cytotoxic agent, that were largely ignored during early attempts at developing folate-based drug conjugates and which consequently resulted in their limited success.<sup>45,90</sup>

#### 1.2.3.4.2 Folate-taxoid conjugate

Seitz *et al.* have developed a highly potent next-generation folate-taxoid for use against drug-resistant and drug-sensitive cancer cell lines.<sup>1</sup> This folate-taxoid conjugate (SB-T-1214) incorporates a folic acid targeting moiety and a highly potent taxoid, which is a derivative of the chemotherapeutic drug taxol. Similar to vintafolide, this SMDC possesses a self-immolative disulfide linker, and a hydrophilic PEGylated dipeptide spacer (Figure 18).<sup>1</sup>

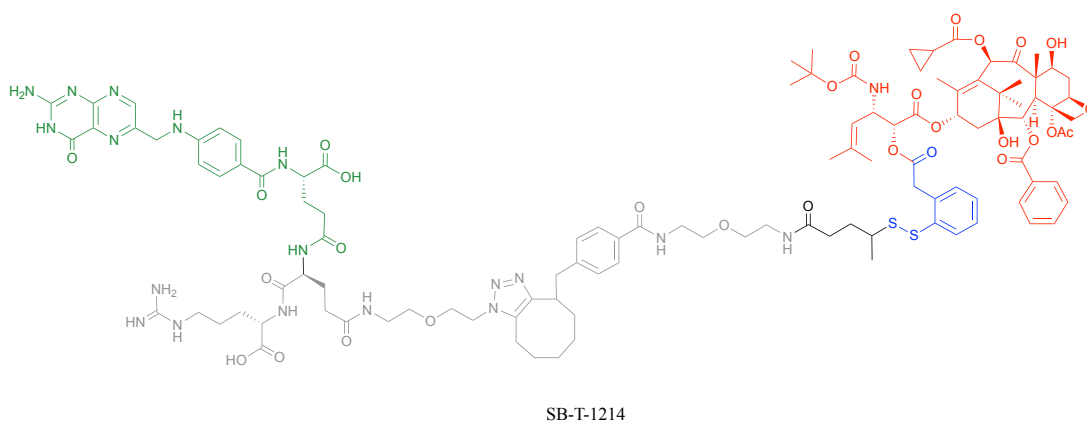


Figure 18. Structure of SB-T-1214, consisting of folic acid as a targeting ligand (green), a solubilising PEG spacer (grey), a disulfide-based linker (blue) and a taxoid (red).<sup>1</sup>

*In vitro* analysis was carried out to compare the activity of the folate-taxoid conjugate SB-T-1214 and the free taxoid drug in FR $\alpha$ -positive and FR $\alpha$ -negative cells. As expected, the free taxoid was highly potent against all cell lines. Conversely, the folate-taxoid conjugate exhibited appreciable cytotoxicity against the FR $\alpha$ -positive cell lines, displaying IC<sub>50</sub> values more than three times smaller than those observed for the FR $\alpha$ -negative cells. This notable potency has been ascribed to the uptake of the

folate–taxoid conjugate occurring *via* RME, an internalisation pathway unaffected by the FA naturally present in the cell culture medium, which suggests that FA required for cell growth is principally shuttled into cells through folate transport proteins in lieu of RME. Further, the folate–taxoid conjugate also exhibited an over 1000-fold decrease in toxicity against healthy cells compared to the free drug. As with vintafolide, the cytotoxic activity of the folate–taxoid conjugate stems from intracellular GluSH-triggered reduction of the disulfide linker to release the free toxic drug.<sup>1</sup> Ideally, for maximum biological activity, the drug should be released in its unmodified form, as with the folate–taxoid conjugate, giving further weight to the speculation that the failure of vintafolide analogues may be due to the liberation of a chemically altered payload.<sup>87</sup> Moreover, the efficient release of the chemical warheads is contingent on the GluSH levels present in the intracellular milieu, the concentration of which can vary in different cell lines. It is therefore important to consider this particular variation when selecting tumour cell lines to be targeted by SMDCs whose activity is dependent on the intracellular GluSH concentration. Partly in view of this potential complication/limitation with certain cancer cells and serum stability questionability, FA–SMDCs have been developed where degradation to release free drug is not mediated by intracellular GluSH.

The above examples comprise a small, but representative, selection of FA–SMDCs from a vast field of conjugates that employ a disulfide linker for cytotoxic drug release. It is of particular relevance to highlight that folate conjugates to many other drugs *via* a disulfide linker, such as maytansinoids,<sup>91</sup> mitomycins,<sup>92</sup> alkaloid/mitomycins,<sup>93</sup> tubulysins<sup>94,95</sup> and camptothecins,<sup>96</sup> have been prepared and appraised.

#### **1.2.3.4.3 Non-disulfide carbon-based FA–SMDCs**

There are a variety of free thiol-containing compounds present in the blood and as such, the disulfide bond in FA–SMDCs is susceptible to cleavage in circulation by these thiols, potentially giving rise to undesired premature drug release. Consequently, alternative approaches have been developed in which the FA–SMDCs do not possess disulfide linkers, a structural property which would ideally minimise off-target drug liberation in the bloodstream. One such example developed by Alsarraf *et al.* is a  $\beta$ -galactosidase-responsive drug conjugate that delivers the potent antineoplastic drug MMAE to cancer cells.<sup>97</sup> This SMDC consists of a galactoside trigger, phenolic and

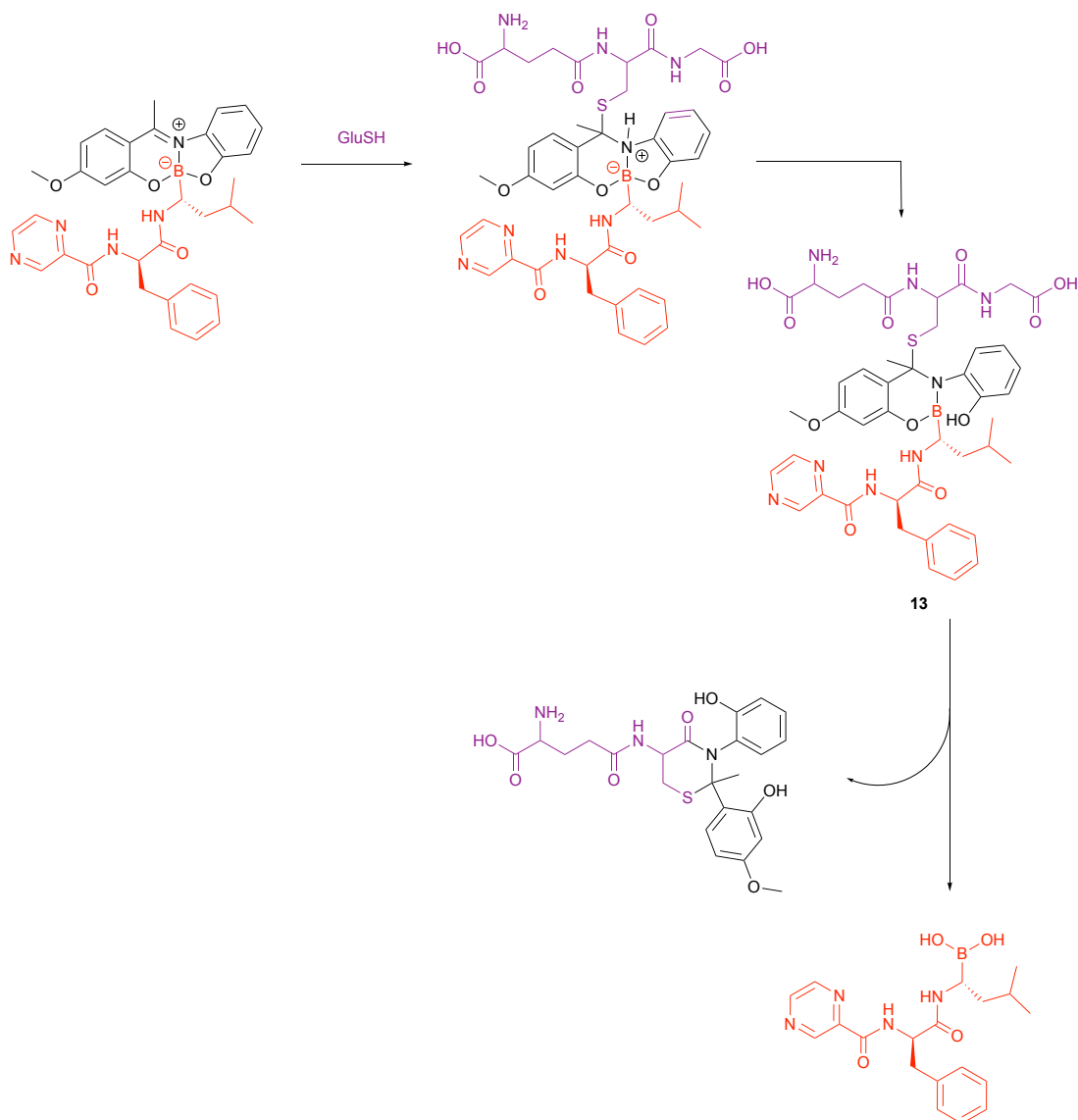
aniline self-immolative linkers, a folic acid targeting ligand and two MMAE molecules centred around a chemical amplifier, enabling a release of two drug molecules *via* a single internalisation and activation pathway. When performing cytotoxic assays on FR $\alpha$ -positive HeLa, SKOV-3 and A2780 cell lines, the aforementioned dual-MMAE conjugate exhibited a *ca.* 2- to 4-fold increase in cytotoxicity as compared to a mono-MMAE conjugate.<sup>26</sup>

A further example of an FA-SMDC that does not bear a disulfide linker and is cleaved by an enzyme is a folate-camptothecin conjugate degraded by the cathepsin B enzyme.<sup>98</sup> In addition to FA-SMDCs that are cleaved by enzymes already present in the tumour milieu, folate-enzyme conjugates have also been developed to deliver an enzyme to the folate receptor of the tumour cell prior to the administration of a prodrug that is converted to the active form by this enzyme. An example of this therapy utilises penicillin-V amidase and a Dox prodrug.<sup>99</sup> Consequently, this work paves the way for the development of a new generation of enzyme-responsive FA-SMDCs that could broaden the scope of selectively targeting FR $\alpha$ -expressing tumours.

#### **1.2.3.4.4 Boron-based FA-SMDCs**

In addition to the commonly employed disulfide and carbon-based linkers for drug release inside the cell, the covalent attachment of boronic acids to Schiff base ligands to yield boronate complexes can also be utilised as a platform to selectively deliver cytotoxic drugs to cancer cells. Gois *et al.* designed such a complex, which comprises the cytotoxic drug bortezomib, PEG chains and folate targeting units (Figure 19).<sup>100</sup>





Scheme 2. Proposed mechanism for GluSH-mediated release of bortezomib from a boron complex core developed by Gois *et al.*<sup>100</sup>

### 1.3 3,6-Pyridazinediones (PDs)

Pyridazinediones (PDs) were first synthesised in 1951,<sup>101</sup> but have only recently emerged as a promising scaffold with which to construct drug conjugates for targeted cancer treatment (Figure 20).

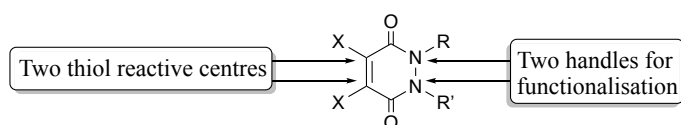
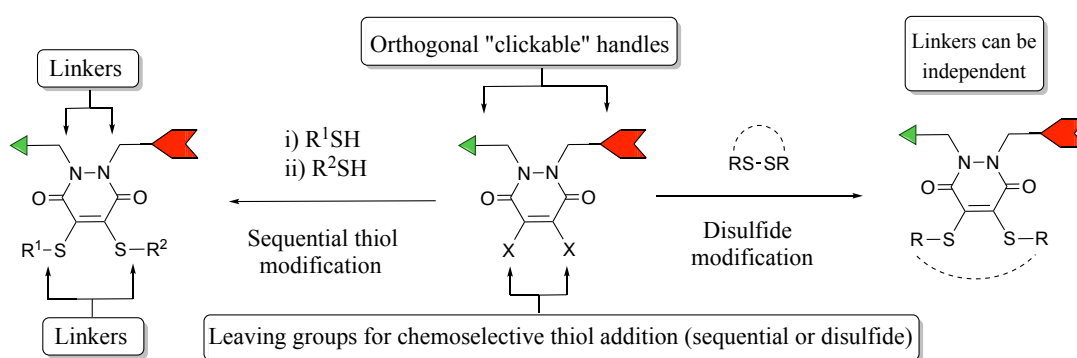


Figure 20. Structure of a PD, a molecule that possesses two centres available for reaction with thiols, as well as two *N*-handles available for further functionalisation.



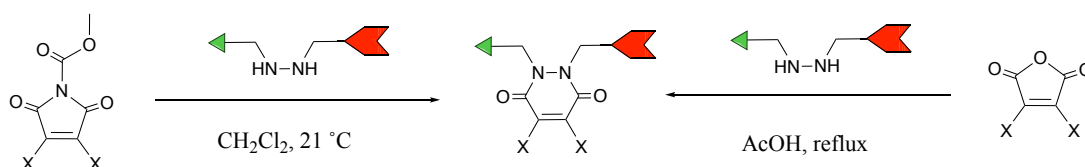
This PD comprises two leaving groups (X) and two orthogonal “clickable” handles.<sup>102</sup> PDs also offer an improved thiol reactivity profile to reagents that are conventionally used to modify thiols, *e.g.* maleimides, exhibiting a tuned-down reactivity profile with superior selectivity, hydrolytic stability and serum stability.<sup>102,103</sup> PDs have also been demonstrated to conjugate different proteins on the same core scaffold, albeit in moderate yield and to date this is limited to protein thiols only.<sup>102,103</sup> The orthogonally reactive “clickable” handles are designed to permit addition of functional moieties of choice in a sequential manner using reliable and aqueous compatible “click” chemistry (Scheme 3).<sup>104</sup>



Scheme 3. Structure and versatility of the PD scaffold.

A challenge in this area is the sequential, controlled addition or modification of non-protein thiols to the PD. For the aforementioned addition of protein thiols, it can be rationalised that the presence of a conjugated protein to one end of the PD’s double bond could allow the relatively facile addition of a subsequent non-protein thiol, (as adding two huge protein thiols to adjacent centres on the PD scaffold is likely to be difficult), resulting in the presence of two very different thiols to each end of the PD’s alkene bond. In contrast, adding a comparatively small, non-protein thiol to one end of the PD carbon–carbon double bond is unlikely to significantly affect the neighbouring carbon’s reactivity, rendering the approach of having two distinct, non-protein thiols on the same PD, a more challenging one.

The synthesis of the PD core is simple and convenient: appropriately substituted maleic anhydrides, or maleimido-carbamates, serve as the starting materials which react with functionalised hydrazines to afford the desired PDs with orthogonal “click” handles (Scheme 4).<sup>105</sup>



Scheme 4. Two established synthetic routes for PDs.

It is possible to conveniently vary the leaving groups (X) by synthesising the corresponding maleic anhydride or maleimidocarbamate, or by nucleophilic displacement of X in the final step.

## 1.4 Use of PDs in ADCs

The Chudasama, Baker and Caddick groups have utilised di-bromo PDs to site-specifically modify native antibodies *via* functional disulfide rebridging to create potent ADCs (Figure 21).<sup>106–108</sup>

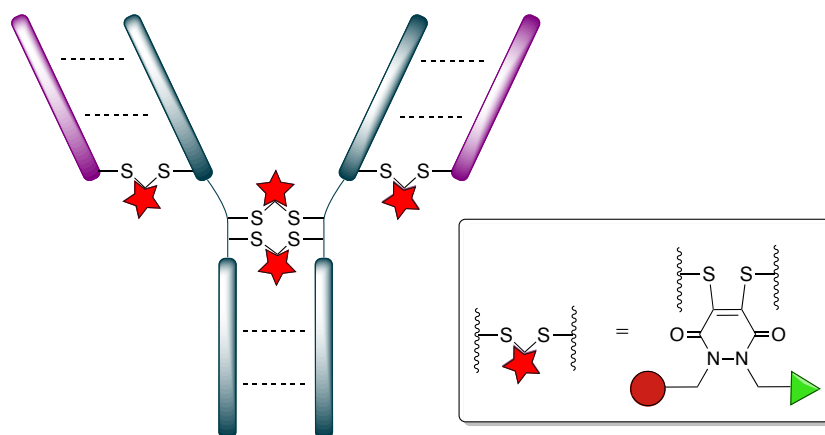


Figure 21. Site-selective modification of antibodies. The native disulfide bonds have been rebridged with PD-based drug conjugates possessing a toxic payload and a functional handle.<sup>107</sup>

Chudasama *et al.* have developed PD-ADCs which comprise an anti-HER2 antibody, di-bromo PDs which rebridge the latter, and the toxic agent Dox. When incubated with HER2-negative MDA-MB-468 cells no toxicity was observed, but the PD-ADCs elicited an  $IC_{50}$  of 2.1–2.8  $\mu\text{M}$  in HER2-positive BT-474 cells. Dox on its own only produced an  $IC_{50}$  of 39 and 10 nM for BT-474 and MDA-MD-468 cell lines respectively, highlighting the greatly increased toxicity exerted by the PD-ADCs, which bind to the HER2 receptors and are thus internalised in the cell.<sup>102</sup>

Chudasama *et al.* have also developed another example of an anti-HER2 PD-ADC, this time incorporating the cytotoxic drug MMAE.<sup>109</sup> This PD-ADC displayed *in vitro* potency over two orders of magnitude greater for HER2-positive human breast cancer HCC1954 cells than for HER2-negative MCF-7 cells. Moreover, in an *in vivo* human breast cancer xenograft model, this PD-ADC gave rise to tumour inhibition after only the first day of therapy, with said inhibition being sustained during and after dosing, with complete regression of the tumours being observed at 18 days after the therapy was initiated. The study was terminated at day 45 and in that time no tumour recurrence occurred.<sup>109</sup>

The desirable properties of PDs, and their success in ADC technology suggest that they can be applied in a similar fashion to the synthesis and structure of SMDC precursors. Moreover, the synthetic approaches of many SMDCs used for cancer treatment that are currently available are rather convoluted and cumbersome.<sup>45,91,94,110</sup>

## 1.5 Aims

As highlighted, PDs have been successfully incorporated into ADC technology and the general aim of this project will be to apply these findings for translation to the development and construction of SMDC precursors for targeted cancer therapy. The structure of a future, complete SMDC is envisaged to consist of a PD core, a tumour-targeting ligand and a water solubilising group to increase hydrophilicity as some tumour-targeting ligands (*e.g.* folic acid) and cytotoxic agents can be rather insoluble in aqueous media (Figure 22).

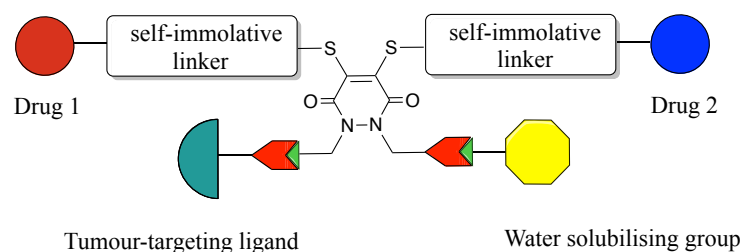


Figure 22. Schematic representation of a PD-based SMDC, where one *N*-handle of the PD has been attached to a tumour-targeting ligand and the other to a water solubilising group. Two distinct cytotoxic agents are conjugated to non-protein thiol substituents *via* self-immolative linkers.

The work in this thesis focuses around two main portions of the PD scaffold. The first centres on the thiol reactive centres of the PD, with the initial objective being to explore whether simple aryl- or alkyl-based thiols affect the scaffold's stability in serum conditions and which of the thiols, if any, is best when said scaffold is subsequently subjected to cell-mimicking conditions. Based on the outcomes of these results, work will then begin on designing a novel thiol-based self-immolative linker, with the purpose of creating a system for future attachment of drugs or fluorophores that could be released selectively inside tumour cells in a self-immolative manner.

The second main portion of this thesis focuses on both *N*-handles of the PD, with the aim to incorporate a water-solubilising group onto one and the installation of groups onto the other that could be further functionalised for the potential future attachment of cytotoxic drugs and/or fluorophores. Functional groups that serve such a purpose could include amines, alkynes and azides, with the latter two able to engage in click and cycloaddition reactions.

Both the described objectives are envisaged to create a system in which three or more different components can be incorporated on the same PD platform, which will hopefully vindicate the modularity and versatility of the PD core in and of itself. Such a construct would also constitute a flexible scaffold where future fluorophore and/or drug attachment could take place on either the thiol reactive centres or the *N*-handles, with both of these cargoes able to undergo self-immolative release under tumour-specific cell conditions.

# Chapter 2 Synthesis of thio-PDs and appraisal in serum- and cell-mimicking conditions

As the first portion of this work intends to focus on the thiol-reactive centres of the PD scaffold, it became pertinent to commence a synthetic route for a small library of thio-substituted PDs. From the outset, it was decided that two main parameters would be considered regarding these PDs: (1) the aromatic or aliphatic nature of the thiols chosen for this library, and (2) mono- and bis-thiol substitution.

As for the first parameter, it became clear that both aromatic *and* aliphatic thiols must be employed to achieve a fair comparison between thioaryl- and thioalkyl PDs when both are subjected to serum- and cell-like conditions. To this end, thiophenol **10** and *N*-(*tert*-butoxycarbonyl)-L-cysteine methyl ester **13** have been selected as simple, yet model aromatic and aliphatic thiols respectively. Aside from the nature of the thiol portion of this PD library, it was decided to explore whether the presence of mono- or bis-thiol substitution on the PD scaffolds would have any effect on their reactivity and stability.

Consequently, it is envisaged that the library of thioaryl- and thioalkyl PDs will comprise mono- and bis-thioaryl PDs **11** and **12**, mono- and bis-thioalkyl PDs **14** and **15** as well as the mixed thioaryl-alkyl PD **17** (Figure 23).

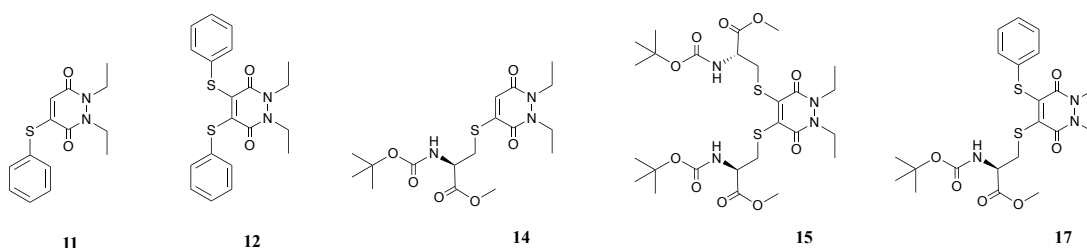


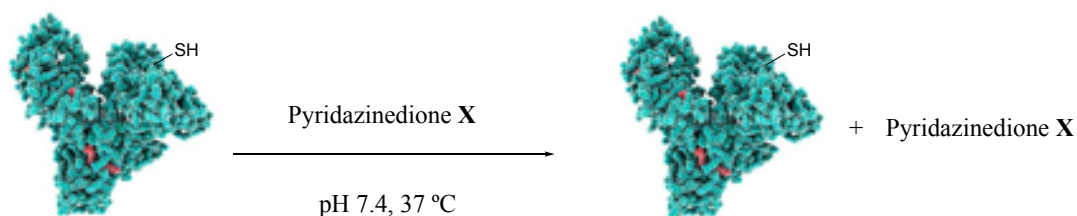
Figure 23. Library of mono- and di-substituted thioaryl- and thioalkyl PDs, as well as the mixed thioaryl-alkyl variant.

Chudasama *et al.* have developed synthetic routes to diethyl mono-bromo PD **5** and di-bromo PD **8**<sup>103</sup> and thus these two will act as the precursors to all the five thio-PDs,

with the plan to mix PDs **5** and **8** with the relevant thiol in order to form thio-PDs **11**, **12**, **14** and **15**. For the synthesis of thioaryl-alkyl PD **17** it is posited that a stepwise addition will be necessary: protected cysteine **13** will be added first in the hope that it only substituted one bromine atom of di-bromo PD **8**, followed by addition of thiophenol **10** to replace the remaining bromine.

## 2.1 Appraisal of thio-PDs in serum- and cell-like conditions

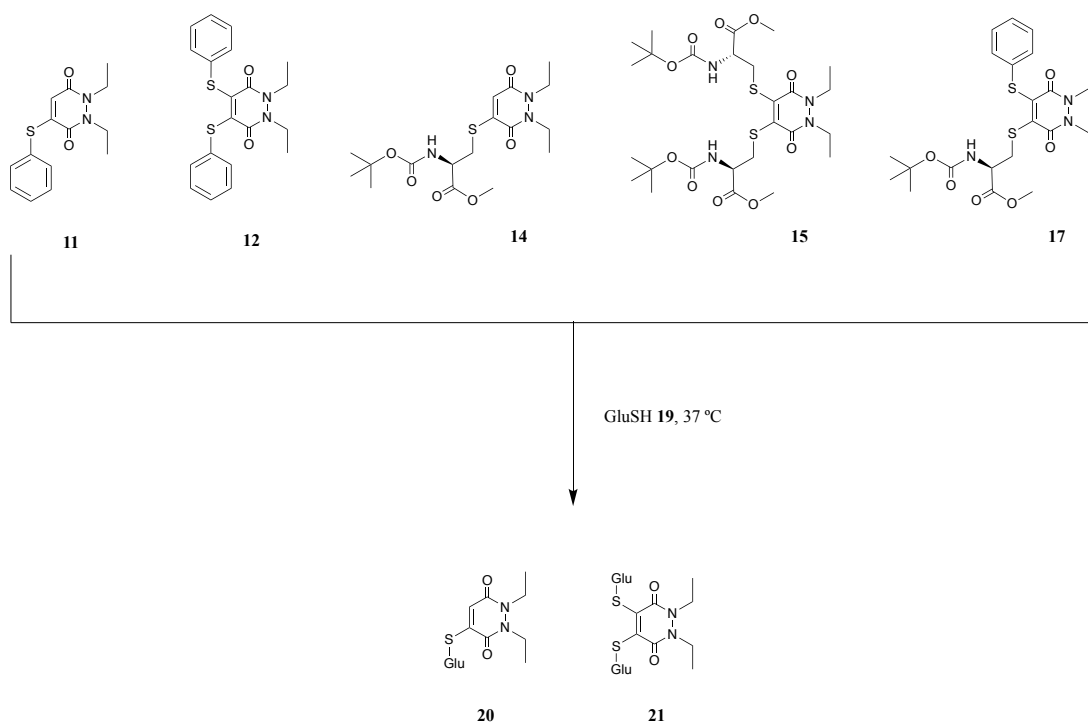
As an ideal SMDC remains stable in the bloodstream and only releases its toxic cargo once inside the tumour environment, the next step in this work will involve subjecting the five synthesised thio-PDs to serum-like conditions. As human serum albumin (HSA) constitutes the most abundant blood thiol as well as containing a free cysteine (Cys-34), incubation of the latter with the five thio-PDs will be undertaken to investigate whether this free cysteine attacks and replaces any of the PDs' thiol-reactive centres, with the ideal scenario resulting in no reaction (Scheme 5).



Scheme 5. Schematic representation of a PD (where X = **11**, **12**, **14**, **15** and **17**) incubated with HSA, and ideally the absence of reaction.

Assuming all five thio-PDs are stable to HSA, the final step in testing their suitability for intracellular cargo release will involve incubation with GluSH **19** in order to mimic tumour cell-conditions, with the ideal situation this time being instability of the thio-PDs and thus susceptibility of their thiol groups to substitution by GluSH **19**'s free thiol (Scheme 6).

It is hoped that if not the HSA incubation, then the subjection of the thio-PDs to GluSH **19** will reveal which, if any, of the five is the most suitable candidate to be taken forward in the derivatisation of the thiol groups for the construction of the self-immolative linker for drug or fluorophore attachment.

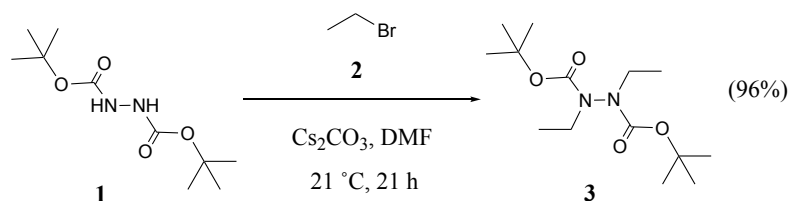


Scheme 6. Envisaged incubation of thio-PDs **11**, **12**, **14**, **15** and **17** with GluSH **19** and desired substitution of the thio-PDs' thiol groups by GluSH **19** to form PDs **20** and **21**.

## 2.2 Results and discussion

### 2.2.1 Synthesis of the bromo PD scaffolds precursor

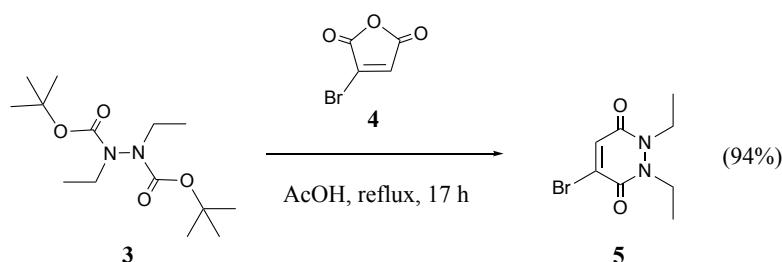
In order to obtain 1,2-diethyl-3,6-pyridazinediones scaffolds, it was first necessary to synthesise di-boc diethyl hydrazine **3**, the diethyl precursor to these PDs. This was achieved using literature conditions: alkylation of boc-protected hydrazine **1** with bromoethane **2** at 21 °C for 21 h, affording di-boc diethyl hydrazine **3** in 96% yield (Scheme 7).



Scheme 7. Synthesis of di-boc diethyl hydrazine **3** from boc-protected hydrazine **1** and bromoethane **2**.

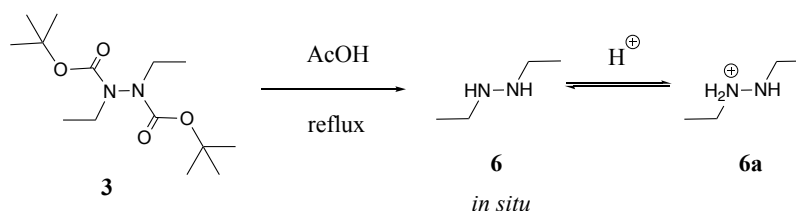
## 2.2.2 Synthesis of mono-bromo PD

With di-boc diethyl hydrazine **3** in hand, the bromo PD scaffolds could be made, with the mono-variant, mono-bromo PD **5**, being synthesised first, using the established procedure as described by Mizzoni *et al.* in 1951.<sup>101</sup> PD **5** is formed in a condensation reaction with bromomaleic anhydride **4** under reflux in acetic acid (Scheme 8).



Scheme 8. Synthesis of mono-bromo PD **5** from di-boc diethyl hydrazine **3** and bromomaleic anhydride **4**.

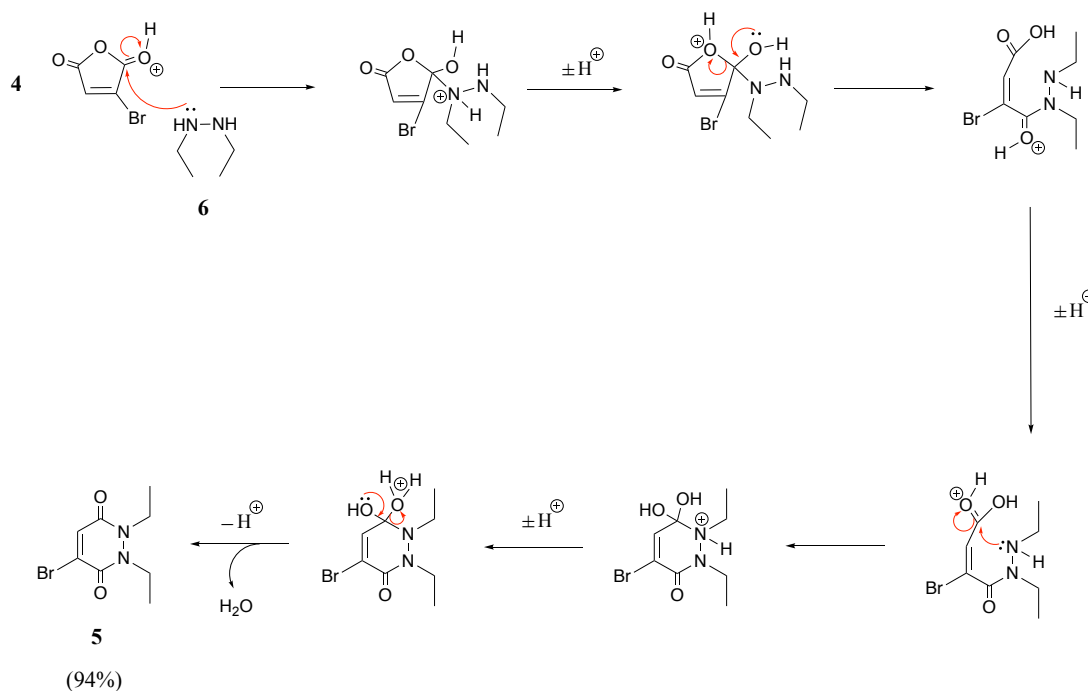
This reaction proceeds *via* the *in situ* acid-mediated boc-deprotection of di-boc diethyl hydrazine **3**, forming diethyl hydrazine **6**. As this formed hydrazine is refluxing in acidic conditions, it exists in equilibrium with its protonated form **6a**. (Scheme 9).



Scheme 9. *In situ* formation of diethyl hydrazine **6** *via* acidic boc-deprotection of di-boc diethyl hydrazine **3** and the equilibrium of the former with its protonated form **6a**.

Once diethyl hydrazine **6** has formed *in situ* it can attack bromomaleic anhydride **4** in a ring-opening and subsequent ring-closing mechanism to afford mono-bromo PD **5** in an excellent 94% yield (Scheme 10).

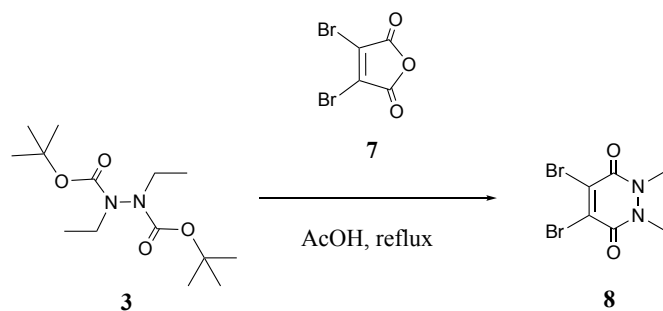




**Scheme 10.** Proposed mechanism of mono-bromo PD **5** formation.

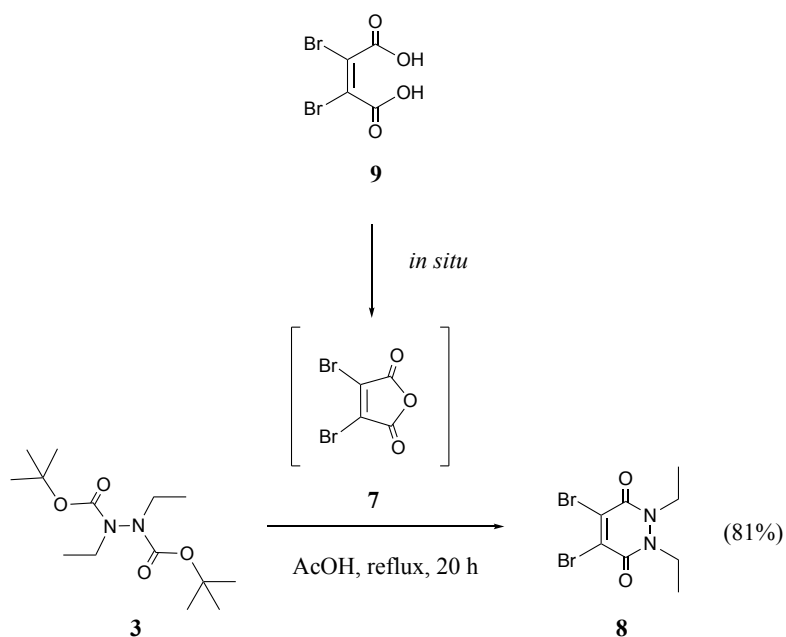
The first step of this mechanism, where diethyl hydrazine **6** attacks bromomaleic anhydride **4**, could be regioselective to some extent due to the C–Br bond being alpha to one carbonyl group and beta to the other. The Br substituent's inductive electron withdrawing effect renders the alpha carbonyl slightly more electropositive and therefore more susceptible to nucleophilic attack. In this particular mechanism it is of no concern which carbonyl group is attacked first because hydrazine **6** is symmetrical, but Chudasama *et al.* have shown that an unsymmetrical hydrazine with a bulky and non-bulky substituent afforded a *ca.* 60:40 mixture of regioisomers when reacted with bromomaleic anhydride **4**, the major isomer being where the *N*-bulky group ends up beta to the C–Br bond of the pyridazinedione.<sup>111</sup>

Once the mono-bromo PD scaffold had been isolated, di-boc diethyl hydrazine **3** was then also employed in the synthesis of di-bromo analogue of mono-bromo PD **5**. Traditionally the formation of di-bromo PD **8** has been achieved by reaction of di-boc diethyl hydrazine **3** with dibromomaleic anhydride **7** (Scheme 11).



Scheme 11. Traditional condensation route for the synthesis of di-bromo PD **8** from di-boc diethyl hydrazine **3** and dibromomaleic anhydride **7**.

A drawback of this procedure is that dibromomaleic anhydride **7** must first be synthesised using elemental bromine and high temperature and pressure conditions. To avoid having to employ these unfavourable reaction conditions in the laboratory, it was decided to utilise commercially available dibromomaleic acid **9** to form di-bromo PD **8** (Scheme 12). The reaction proceeded in analogous conditions used to form mono-bromo PD **5**.



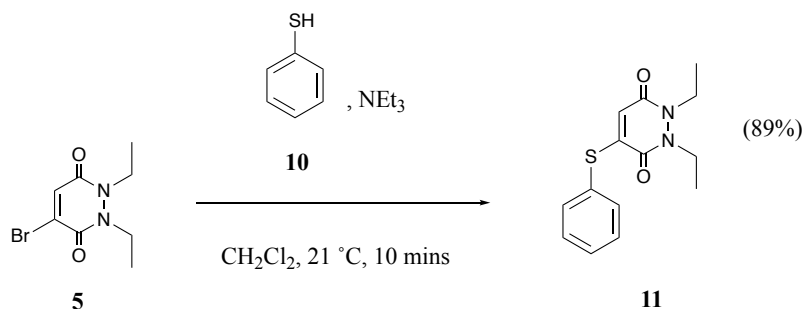
Scheme 12. Synthesis of di-bromo PD **8** from di-boc diethyl hydrazine **3** and dibromomaleic acid **9**.

The reaction in Scheme 12 proceeds *via* the initial acid-mediated ring-closing of dibromomaleic acid **9** to form dibromomaleic anhydride **7** *in situ*.<sup>112</sup> Once this anhydride has formed, the deprotected hydrazine **6** can attack the dibromomaleic anhydride **7**, following the same mechanism as depicted in Scheme 10.

PDs **5** and **8** could then form the basis of a small library of both thioaryl- and thioalkyl-substituted PDs.

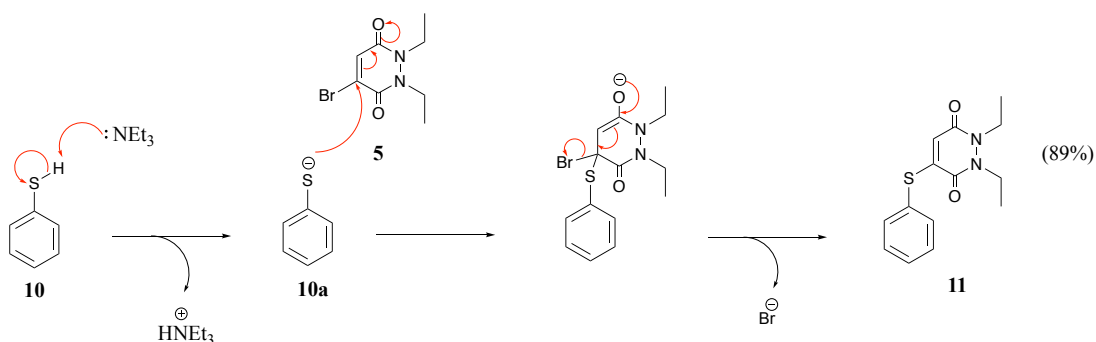
### 2.2.3 Synthesis of thioaryl PDs from the bromo PD scaffolds

As a long-term goal of this project is to attach cytotoxic drugs or fluorophores to thiol-based linkers on PDs, it was incumbent to generate and appraise a library of both thioaryl- and thioalkyl-substituted PDs in order to gauge which groups are more suitable for drug delivery and release as they have very different reactivity profiles (*i.e.* aryl thiols are more easily substituted as one may expect). The first of these PDs to be synthesised was mono-thioaryl PD **11** and this was achieved by reacting mono-bromo PD **5** with thiophenol **10** to afford the mono-thioaryl PD **11** in a high yield of 89% (Scheme 13).



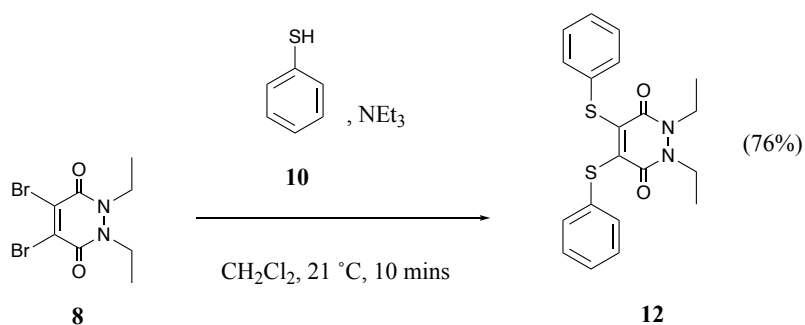
Scheme 13. Synthesis of mono-thioaryl PD **11** from mono-bromo PD **5** and thiophenol **10**.

The reaction is thought to proceed through an addition-elimination mechanism (Scheme 14). The bromine-bearing carbon of PD **5** is rather electropositive owing to the inductively electron withdrawing nature of the bromine atom. Consequently, it is thought to be the carbon that is attached to bromine that is the most susceptible to nucleophilic attack by the thiolate, with the resulting enolate leading to the expulsion of bromide (*i.e.* addition-elimination mechanism) to afford mono-thioaryl PD **11**.



Scheme 14. Formation of mono-thioaryl PD **11** from mono-bromo PD **5** and thiophenol **10** via a proposed addition-elimination mechanism.

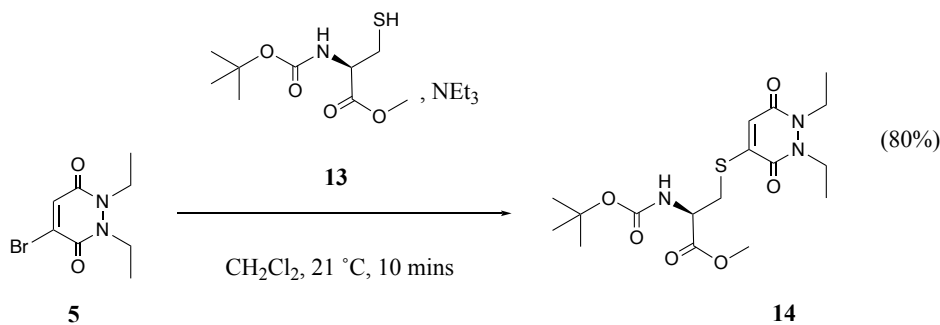
As the synthesis of mono-thioaryl PD **11** was achieved in very good yield after only 10 mins of stirring, the same procedure, with an excess of thiol, was employed for the synthesis of bis-thioaryl PD **12** (Scheme 15). A final yield of 76% for PD **12** was achieved without the need for further optimisation.



Scheme 15. Synthesis of bis-thioaryl PD **12** from di-bromo PD **8** and thiophenol **10**.

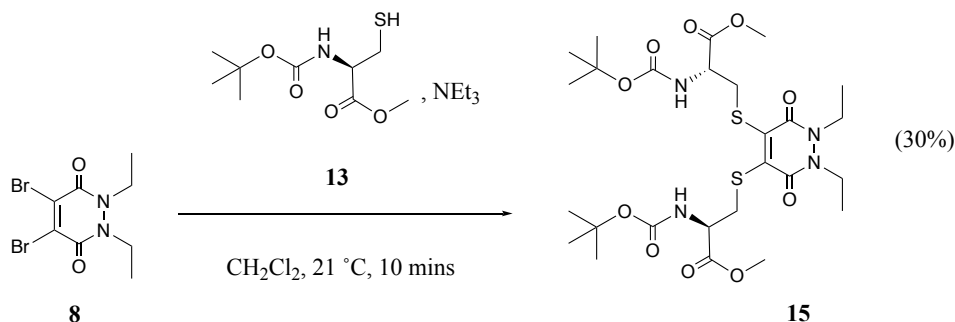
## 2.2.4 Synthesis of thioalkyl PDs from the bromo PD scaffolds

With the thioaryl PDs **11** and **12** in hand, the next aim consisted of synthesising the corresponding alkyl variants; encouraged by the successful and relatively high yielding syntheses of the former, the same conditions were employed in the formation of the mono-thioalkyl PD **14** from mono-bromo PD **5** and protected cysteine **13** (Scheme 16). This reaction proceeded with a very good yield of 80% despite the now smaller difference in  $pK_a$  values between protected cysteine **13** and triethylamine (10.0 and 10.8 respectively), meaning that not as great a proportion of protected cysteine **13** would be deprotonated as thiophenol **10** had been under the same reaction conditions.



Scheme 16. Synthesis of mono-thioalkyl PD **14** from mono-bromo PD **5** and protected cysteine **13**.

As the synthesis of mono-thioalkyl PD **14** had proved successful, di-bromo PD **8** was subjected to the same reaction conditions in an attempt to afford the bis-thioalkyl PD **15** in similar yield (Scheme 17). Disappointingly, the trend observed for PDs **11**, **12** and **14** where excellent yields were obtained after stirring in  $\text{CH}_2\text{Cl}_2$  at  $21\text{ }^\circ\text{C}$  for just 10 mins, did not continue for bis-thioalkyl PD **15**, with an isolated yield of only 30% being achieved – mainly as a consequence of low conversion of di-bromo PD **8** (53% recovery). The steric bulk of the adjacent alkyl thiol groups on PD **15** may play a role in the rather low yield observed after 10 mins stirring.

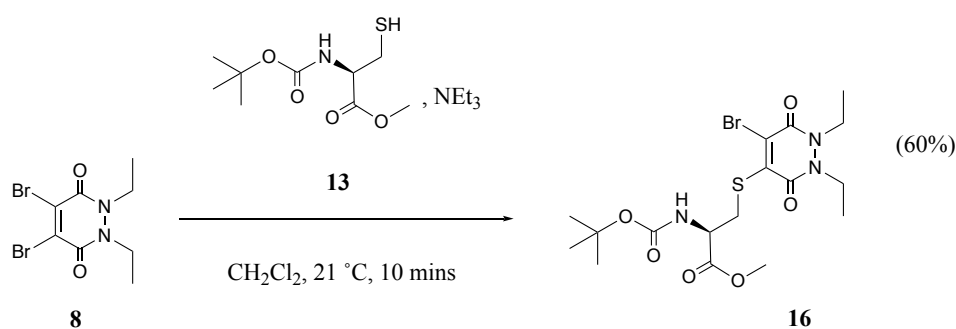


Scheme 17. Initial synthesis attempt of bis-thioalkyl PD **15** from di-bromo PD **8** and protected cysteine **13**.

In an effort to increase the yield of PD **15**, the reaction was repeated over a longer time period. After 65 h stirring at  $21\text{ }^\circ\text{C}$ , analysis by TLC suggested bis-thioalkyl PD **15** as the major product, and the reaction was stopped and worked up at this point. The yield after 65 h amounted to 59%: almost double that to what was achieved after the 10 min time point. As the aim of this section of the project was simply to generate a small library of PDs, further attempts at optimising the yield of bis-thioalkyl PD **15**, perhaps by investigating the use of an alternative (stronger) base and heating to higher temperatures, were not carried out.

## 2.2.5 Synthesis of a thioaryl-alkyl PD from di-bromo PD

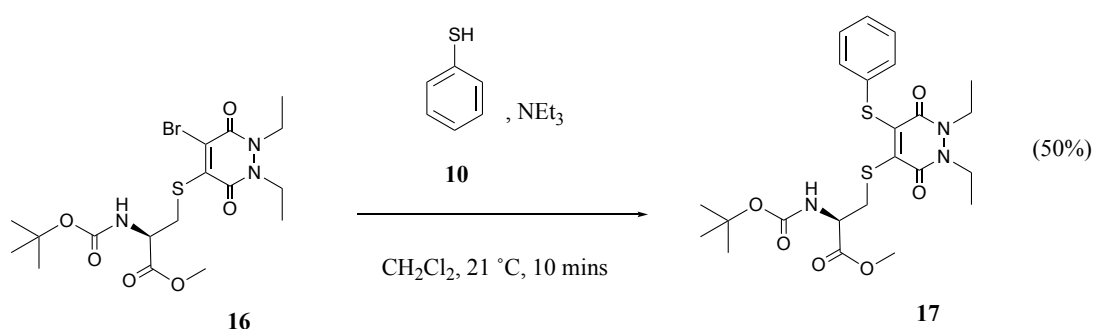
As far as the small PD library was concerned, the initial plan had been to only synthesise the above four PDs: two thioaryl-based (**11** and **12**) and two thioalkyl-based variants (**14** and **15**). However, once these had been isolated, the prospect arose of synthesising a thioaryl-alkyl analogue and including it in subsequent studies alongside PDs **11**, **12**, **14** and **15**. Unlike the synthesis of these last four, that of the mixed variant was carried out in two steps, the first being mono-addition of protected cysteine **13** to di-bromo PD **8** (Scheme 18).



Scheme 18. Synthesis of mono-bromo mono-thioalkyl PD **16** from di-bromo PD **8** and protected cysteine **13**.

While for the syntheses of PDs **11**, **12**, **14** and **15**, the protected cysteine **13** was added at once and the resulting reactions stirred for 10 mins, for the synthesis of PD **16**, protected cysteine **13** (1 eq.) was added to the reaction dropwise over 10 mins. The bromine-bearing carbons of di-bromo PD **8** are highly reactive to nucleophilic attack and so the dropwise addition was employed to maximise mono-addition to PD **8** instead of substituting both of its bromine atoms. The previously observed slow formation of bis-thioalkyl PD **15** did give some hope that formation of PD **16** would be feasible. Initial TLC analysis (90:10 EtOAc/ $\text{CH}_2\text{Cl}_2$ ) of the crude reaction mixture revealed just “one product” spot, but its slightly smeared nature exposed the possibility of the spot containing overlapping species. Consequently, a vast range of solvent systems were investigated, including the use of toluene, diethyl ether and chloroform, which found that only 40:60 and 30:70 EtOAc/ $\text{CHCl}_3$  produced a viable separation between the species for effective purification by flash column chromatography. Spotting the previously isolated bis-thioalkyl PD **15** on the same TLC plate confirmed its identity as one of the two species in the crude reaction mixture, highlighting the

high predicted reactivity of the bromine-bearing carbons on di-bromo PD **8**, and demonstrating that even dropwise addition of one equivalent of nucleophile generates some di-substituted product. After purification, mono-bromo mono-thioalkyl PD **16** was obtained in a moderate yield of 60%. As the aim of this synthesis was purely to isolate a thioaryl-alkyl PD, no further attempts to optimise the yield of this reaction were carried out, such as diluting and cooling the mixture, longer dropwise addition time of protected cysteine **13** or using lower equivalents of the same. Instead, mono-bromo mono-thioalkyl PD **16** was brought forward in the synthesis of thioaryl-alkyl PD **17** (Scheme 19).

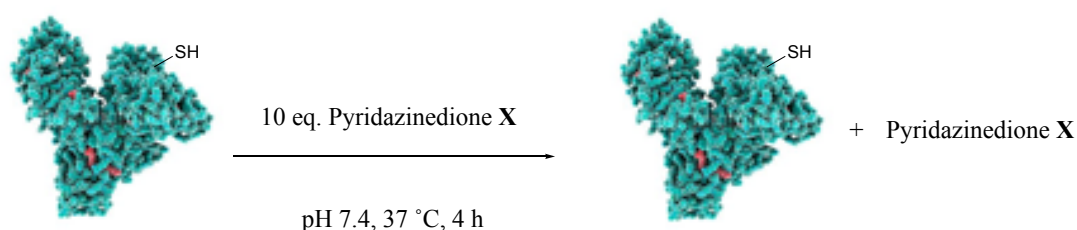


Scheme 19. Synthesis of thioaryl-alkyl PD **17** from mono-bromo mono-thioalkyl PD **16** and thiophenol **10**.

For this synthesis, the bromine-bearing carbon was thought to be far more reactive than the thioether site, and TLC analysis of the reaction after 10 mins showed mainly the presence of thioaryl-alkyl PD **17**, which was isolated in 50% yield. The stepwise synthesis of this thioaryl-alkyl PD is designed to proceed, as shown, by initial addition of the protected cysteine **13** first to di-bromo PD **8** (Scheme 18) in lieu of adding thiophenol **10** first. This rationale is based on thiophenol **10** being a better leaving group than protected cysteine **13**. Thus, if the synthesis order were to be reversed: if 1 eq. of thiophenol **10** were to be added first to di-bromo PD **8** to generate the mono-substituted aryl analogue of **16**, subsequent addition of protected cysteine **13** may have, after substituting the remaining bromine, also displaced the thioaryl group due to the latter's stabilised nature as a leaving group. This synthesis order would probably result in the formation of bis-thioalkyl PD **15** in place of the desired thioaryl-alkyl PD **17**.

## 2.3 Incubation of bromo- and thio-substituted PDs with HSA

With PDs **11**, **12**, **14**, **15** and **17** successfully isolated, they were incubated with HSA in serum-mimicking conditions (Scheme 20). As has been described, the optimal scenario was to observe no reaction between the thio-substituted PD scaffolds and HSA because an ideal SMDC would be stable in the bloodstream and only degrade and release its cargo once inside the tumour cell environment.



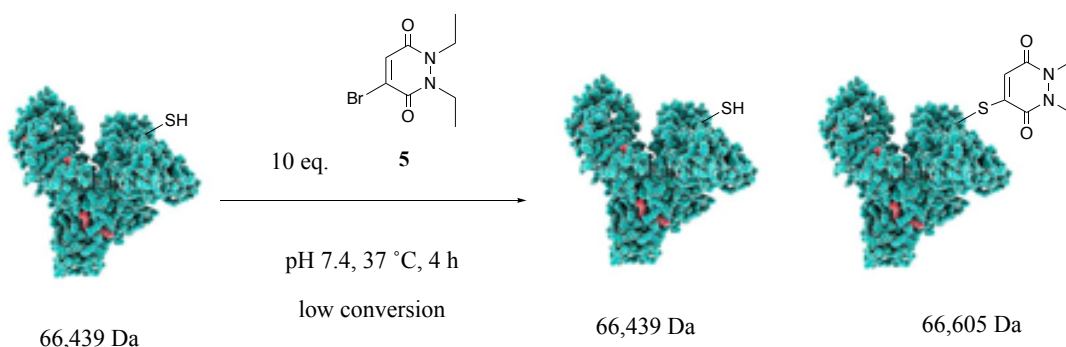
Scheme 20. Schematic representation of PD **X** (where **X** = **5**, **8**, **11**, **12**, **14**, **15** and **17**) incubated with HSA, and ideally the absence of reaction for thio-PDs **11**, **12**, **14**, **15** and **17**.

HSA was selected because it is the major blood thiol, with a total blood plasma concentration of 400–500  $\mu\text{M}$  as compared to 4–5  $\mu\text{M}$  GluSH.<sup>113</sup> Human albumin's free cysteine-34 (Cys-34) represents 80–90% of human plasma's thiol concentration and it is also the most reactive thiol in blood plasma, having a  $\text{pK}_a$  of  $\sim 7$  whereas those of GluSH and cysteine are 8.9 and 8.5 respectively.<sup>113</sup> In order to simulate blood plasma conditions, PDs **11**, **12**, **14**, **15** and **17** (10 eq. of each) were all incubated at 37  $^\circ\text{C}$  with HSA (57  $\mu\text{M}$ ) at pH 7.4 for 4 h. The HSA's concentration of 57  $\mu\text{M}$  was considered pertinent for such studies, as it is a very sticky protein and higher concentrations can lead to the blockage and breakdown of spectroscopic equipment. It was also decided at this juncture, to appraise the reactivity of mono- and di-bromo PDs **5** and **8** with HSA as this had not been previously appraised and this site-selective modification of albumin is an important field in itself – it would also be interesting to see the inherent difference in reactivity between these PDs.

Reaction between HSA and the mono-bromo and di-bromo PDs (**5** and **8** respectively) was observed. Incubation of mono-bromo PD **5** (10 eq.) with HSA was found to give

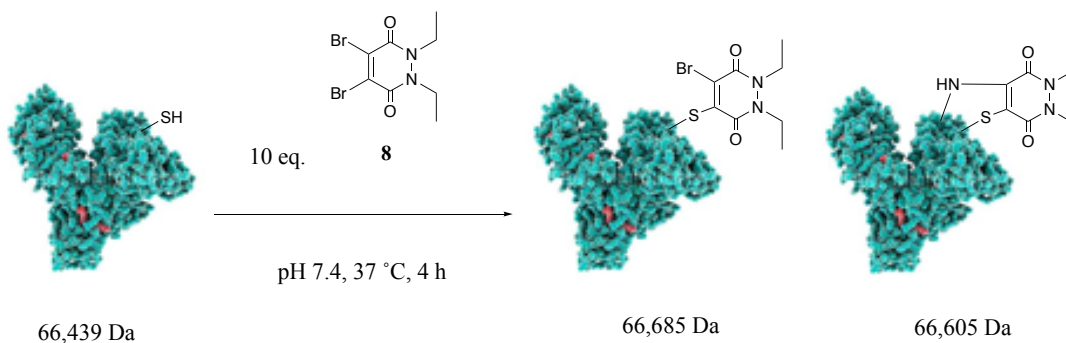


rise to one new species: the conjugation product, but in a low conversion of *ca.* 40% (Scheme 21).



Scheme 21. Reaction between HSA and mono-bromo PD **5**.

Subsequently, 10 eq. of di-bromo PD **8** were incubated with HSA, and this produced two substitution products. Moreover, unlike the incubation with mono-bromo PD **5**, no native albumin was present in the spectrum (Scheme 22).



Scheme 22. Reaction between HSA and di-bromo PD **8**.

The absence of native HSA in the spectrum suggests that di-bromo PD **8** is more reactive than its mono-bromo analogue **5**. Furthermore, in addition to the expected mono-substituted product (66,685 Da), a di-substituted species (66,605 Da) was detected, the former being the substitution product of one bromine by albumin's Cys-34 and the latter comprising the substitution product of one bromine by the same Cys-34 and the second by a Lysine-41 residue 9.5 Å away.<sup>114</sup>

Gratifyingly, no reaction was observed between HSA and thio-PDs **11**, **12**, **14**, **15** and **17**, corroborating previously reported results that thio-PDs are stable in blood mimicking conditions.<sup>106</sup> As a further positive control to the reaction of HSA with PDs **5** and **8**, maleimide **18** was incubated with HSA alongside PDs **11**, **12**, **14**, **15** and **17**

under identical conditions. Maleimides are substantially more reactive than PDs and are known to react with HSA,<sup>115</sup> therefore conjugation between maleimide **18** and the major blood thiol was expected, and indeed observed. As FA–SMDCs, the most studied SMDCs, have a blood circulation half-life of 26 mins,<sup>45</sup> a substantially longer incubation time point of 4 h was deemed more than appropriate to demonstrate the pyridazinedione core's excellent stability in human blood serum-like conditions. Similarly, a large excess of each PD (10 eq.), an unrealistic surplus of what would be present in the blood with an administered drug, was used to establish the same.

## 2.4 Incubation of thio-PDs with GluSH in cell-like conditions

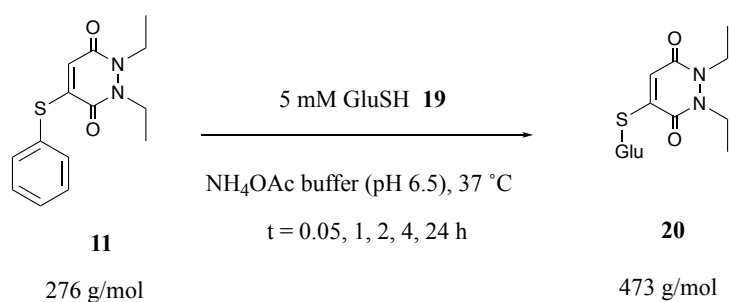
Once the human blood serum-like stability of PDs **11**, **12**, **14**, **15** and **17** had been demonstrated, the next logical step in their appraisal for being suitable scaffolds regarding an SMDC construct involved incubation of these thio-PDs with GluSH **19**. The reasoning for selecting GluSH **19** stemmed from the abundant literature on this thiol being predominant in the intracellular milieu<sup>116,117</sup> (*i.e.* where the SMDC would reside post-internalisation) and its ability to cleave disulfide bonds in SMDCs to liberate the free drug.<sup>1,116,118</sup> Notwithstanding the absence of disulfide bonds in PDs **11**, **12**, **14**, **15** and **17**, it was expected that GluSH **19** *would* react with these thio-PDs, by instead engaging in addition–elimination reactions with the PD scaffolds and expelling the thioaryl and thioalkyl moieties.

It was reasoned that the three main parameters of this study to replicate intracellular conditions would consist of temperature, concentration of GluSH **19**, and the pH of the solution. Internal body temperature of 37 °C was selected, as is consistent in the field. The concentration of extracellular GluSH concentration is known to lie between 1 µM and 10 µM, whereas that of intracellular GluSH is around 1000 times greater, in the range of 1 mM to 10 mM.<sup>116,119–121</sup> In light of this, an intermediate intracellular GluSH concentration of 5 mM was considered appropriate for the study. Moreover, since the HSA studies employed an excess of PDs (10 eq.) to demonstrate their stability in blood, their expected instability when exposed to intracellular GluSH **19** called for the situation to be reversed, in that it would be GluSH **19** used in excess (10 eq.), in order to mimic the large excess of this thiol inside a cell relative to intracellular drug

concentration. Consequently, the cell-mimicking conditions of this study would involve PDs **11**, **12**, **14**, **15** and **17** being at 0.5 mM relative to GluSH **19**. As many SMDCs are internalised by cells *via* RME, most drug conjugates must necessarily pass through the early endosome before being degraded in the late endosome/lysosome. The pH extremes of the early endosome and late endosome/lysosome are around 6.5 and 4.9–5.0 respectively<sup>122–125</sup> and thus it was decided to incubate PDs **11**, **12**, **14**, **15** and **17** with GluSH **19** at pHs 6.5 and 5.0.

### 2.4.1 Incubation of thioaryl PDs with GluSH at pH 6.5

With the relevant conditions in mind, it was decided to begin the study with the thioaryl PDs **11** and **12** as these were expected to be the most reactive. Mono-thioaryl PD **11** was thus incubated with 5 mM GluSH **19** at 37 °C and at pH 6.5 (Scheme 23).



Scheme 23. Expected reaction between mono-thioaryl PD **11** and GluSH **19** at pH 6.5.

Five time points were taken of these incubations to determine how quickly substitution was occurring and the samples were analysed by LC-MS. For the incubation of mono-thioaryl PD **11** and GluSH **19**, the GluSH-substituted PD **20** of molecular weight 473 g/mol was expected to be observed. At t = 0.05 h (sample run on LC-MS as soon as possible after mixing all reagents), no reaction had taken place (Figure 24).

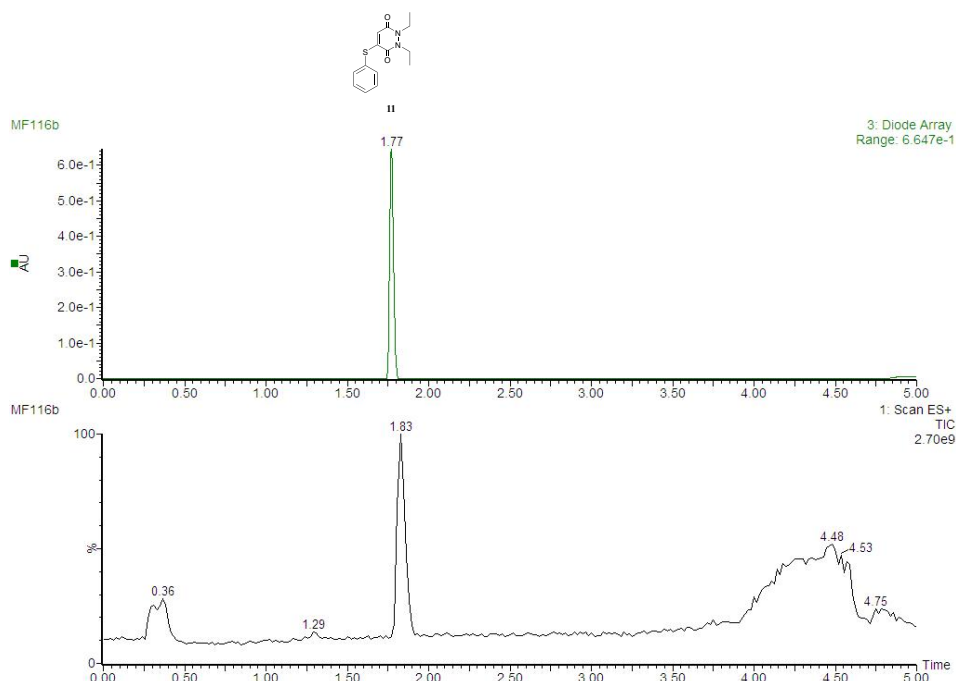


Figure 24. TIC and UV trace of the incubation of mono-thioaryl PD **11** and GluSH **19** at  $t = 0.05$  h at pH 6.5, where no substitution by GluSH **19** has taken place.

As can be seen from Figure 14, at  $t = 0.05$  h, the only visible peak in the UV trace (at 1.77 mins) is unreacted mono-thioaryl PD **11**, with the peak in the TIC at 0.36 mins corresponding to unreacted GluSH **19**. Gratifyingly, formation of GluSH PD **20** was visible at  $t = 1$  h, but surprisingly, the reaction remained incomplete at  $t = 24$  h, yielding a mixture of GluSH PD **20** and unreacted mono-thioaryl PD **11** (Figure 25).

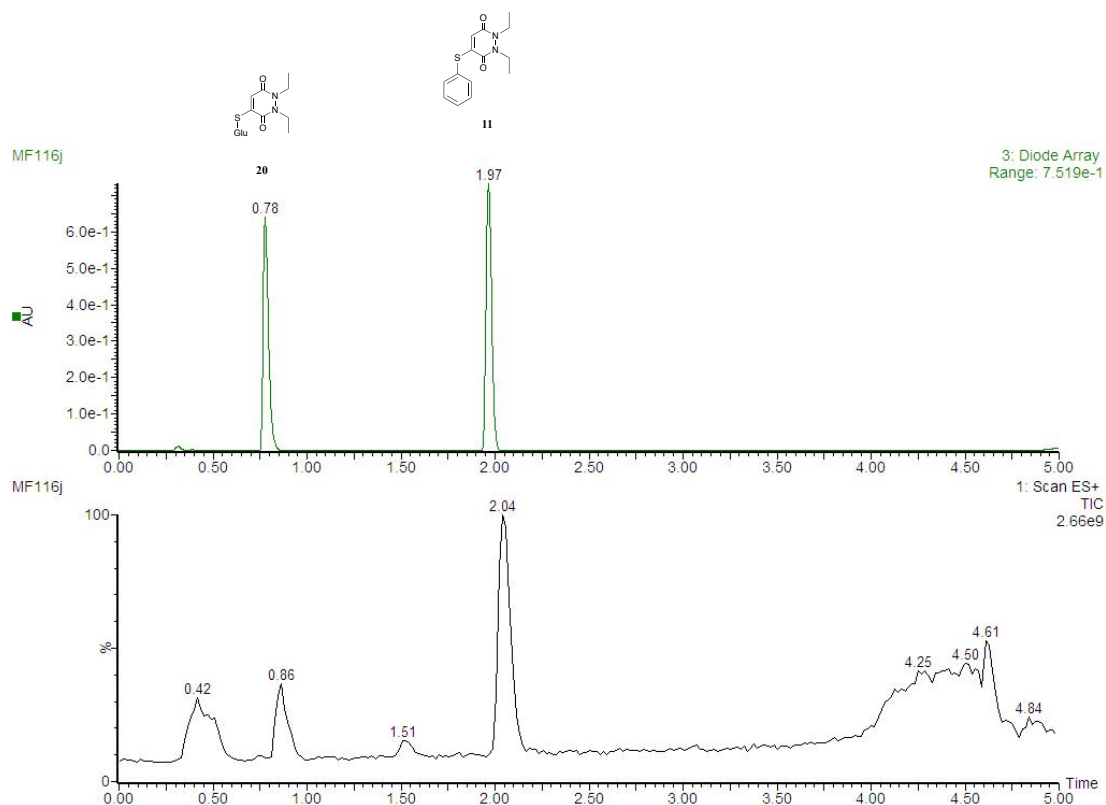
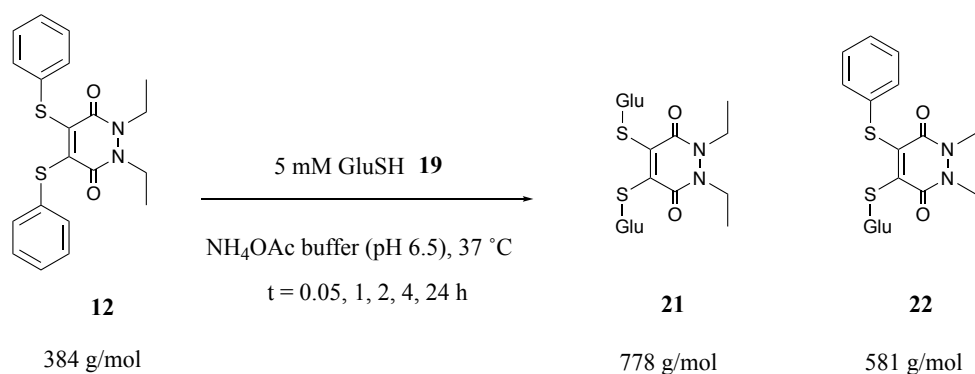


Figure 25. TIC and UV trace of the incubation of mono-thioaryl PD **11** and GluSH **19** at  $t = 24$  h at pH 6.5, where PD **11** has not been fully consumed.

Once this study was complete, it was repeated with the bis-thioaryl PD **12** (Scheme 24). As PD **12** has two aryl groups, the incubations were expected to yield a mixture of the mono-GluSH-substituted product **22** and the bis-GluSH PD **21**. However, it was not known whether the presence of two aryl groups on the PD scaffold would have any effect on the kinetics of the substitution by GluSH **19**.

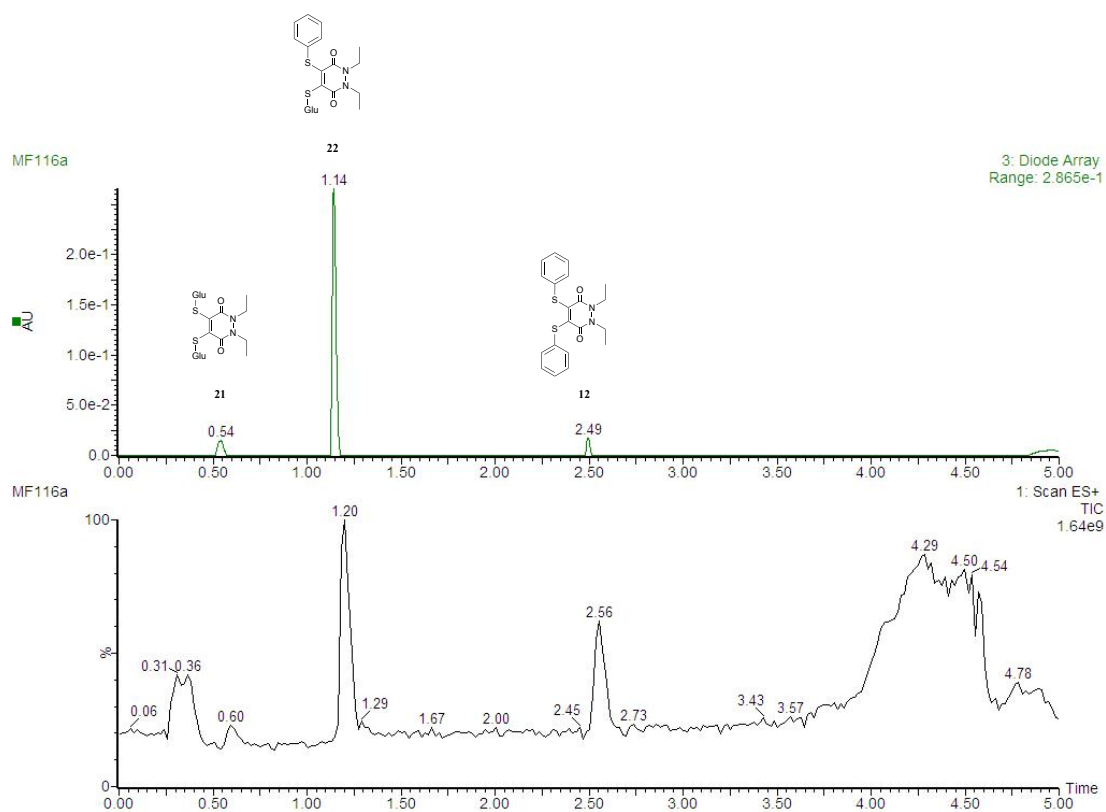


Scheme 24. Expected reaction between bis-thioaryl PD **12** and GluSH **19** at pH 6.5.

Interestingly, the  $t = 0.05$  h time point of this reaction showed both mono-addition and double-addition product (PDs **22** and **21** respectively). The far larger UV peak of the

mono-addition species **22** at this time point suggests that more of it was formed in the initial reaction. However, within 2 h the double-addition product **21** became the main species and the UV signal of mono-addition product **22** could not be observed anymore. The next time point of 4 h shows that the sole product species consisted of double-addition PD **21** (Figure 26).

(a)



(b)

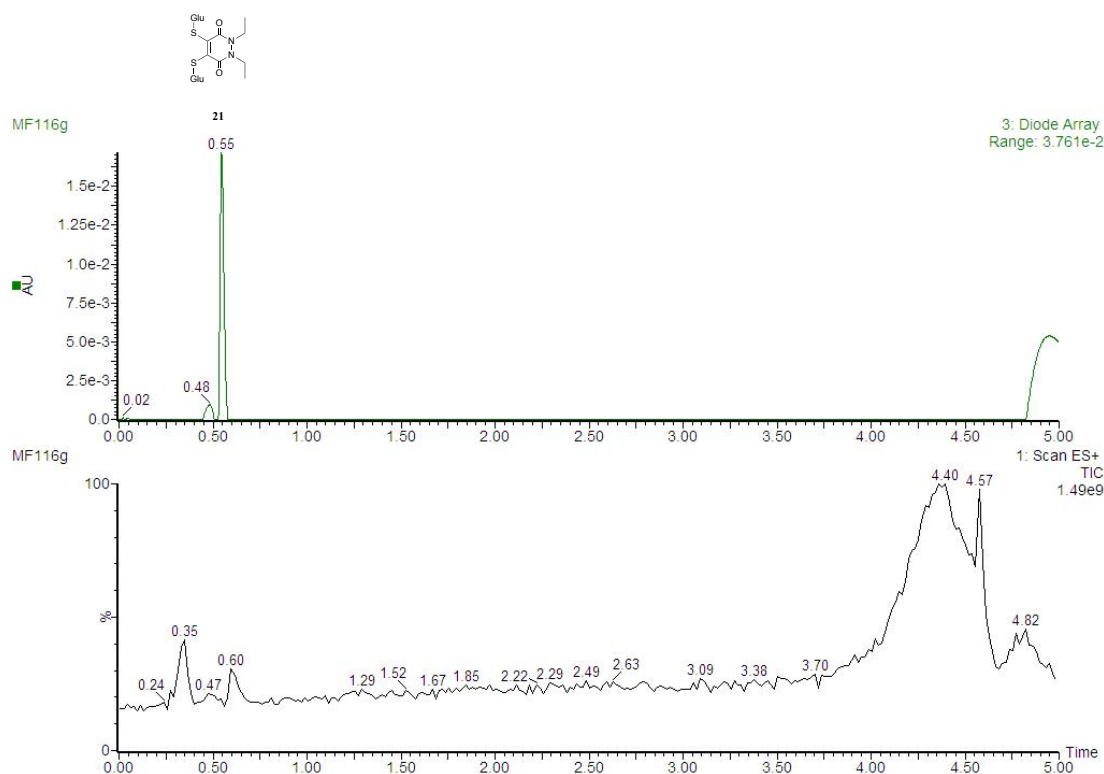
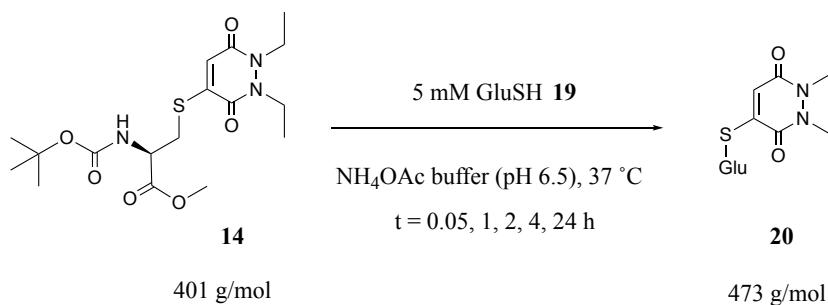


Figure 26. TIC and UV trace of the incubation of bis-thioaryl PD **12** and GluSH **19** at (a)  $t = 0.05$  h and (b)  $t = 4$  h, at pH 6.5.

It is of note that the bis-thioaryl PD **12** is more reactive than the mono-thioaryl PD **11**, following the same trend as the bromo PDs **5** and **8**, where the di-bromo PD **8** reacted fully with HSA and mono-bromo PD **5** did not.

## 2.4.2 Incubation of thioalkyl PDs with GluSH at pH 6.5

Once the GluSH incubations at pH 6.5 had been carried out with the thioaryl PDs **11** and **12**, the thioalkyl variants **14** and **15** were subjected to the same conditions. It was predicted that GluSH substitution would be slower and less efficient due to the alkyl thiol moieties being poorer leaving groups than the thiophenol portions of PDs **11** and **12**. The studies began with the incubation of GluSH **19** with mono-thioalkyl PD **14** (Scheme 25).



Scheme 25. Expected reaction between mono-thioalkyl PD **14** and GluSH **19** at pH 6.5.

As predicted, mono-thioalkyl PD **14** was significantly less reactive towards GluSH substitution than mono-thioaryl PD **11**. Substitution by GluSH **19** was not observed until  $t = 4$  h time point, and even after 24 h the difference in the relative proportion in the UV trace of PD **20** to PD **14** was greater than the same relationship of PD **20** to mono-thioaryl PD **11** (Figure 27).

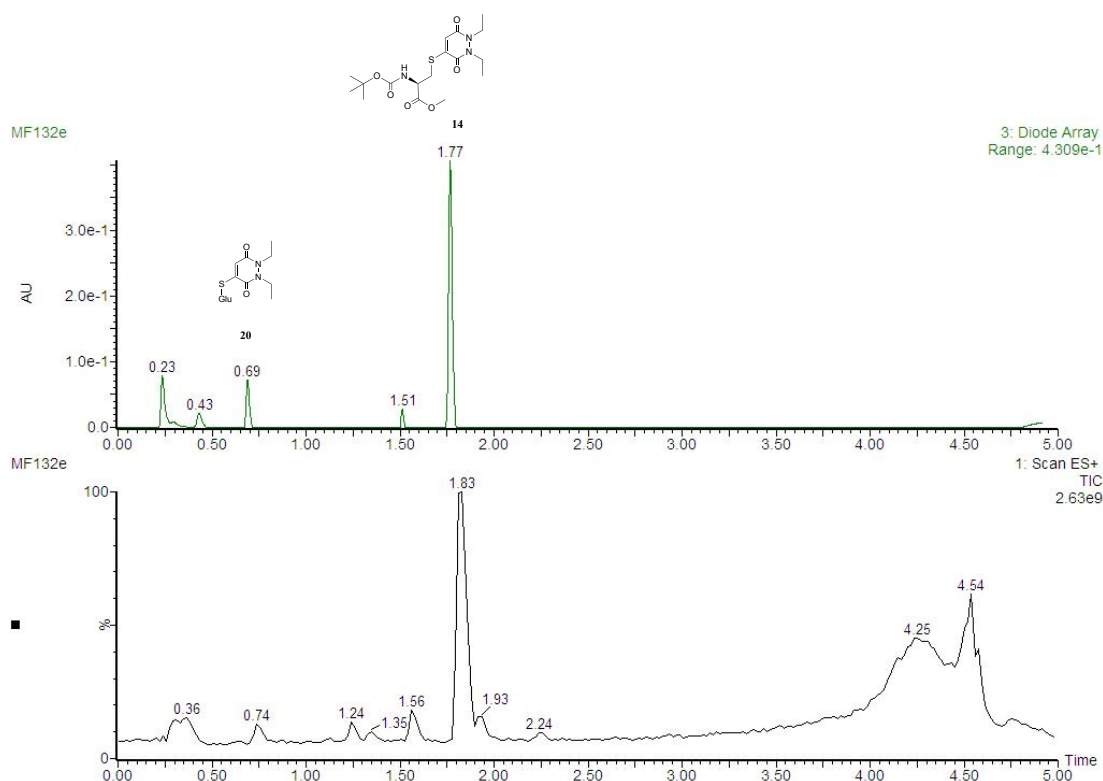
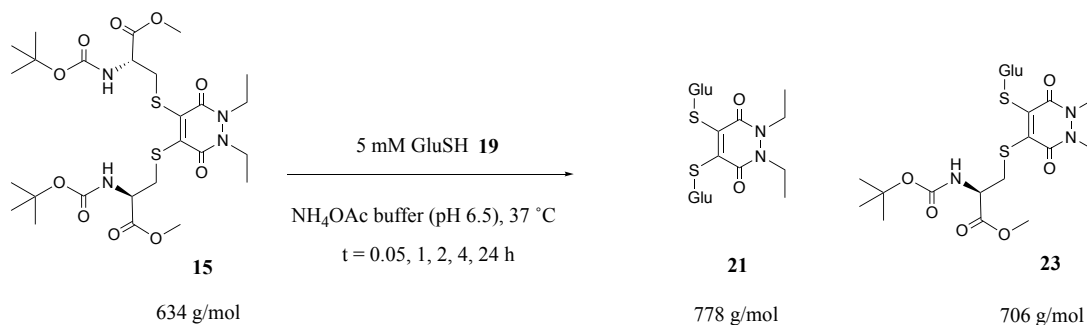


Figure 27. TIC and UV trace of the incubation of mono-thioalkyl PD **14** and GluSH **19** at  $t = 24$  h at pH 6.5.

Bis-thioalkyl PD **15** was subsequently incubated with GluSH **19**. As in both the bromo and thioaryl PDs' cases, *i.e.* the di-substituted analogues being more reactive than the



mono variant, the same trend was expected to continue with bis-thioalkyl PD **15** relative to mono-thioalkyl PD **14** (Scheme 26).



Scheme 26. Expected reaction between bis-thioalkyl PD **15** and GluSH **19** at pH 6.5.

The greater reactivity of bis-thioalkyl PD **15** compared to mono-thioalkyl PD **14** was confirmed immediately at t = 0.05 h upon the observation of the formation of mono-substituted PD **23**. However, this superior reactivity did not lead to bis-GluSH PD **21** being the sole product observed after 24 h (as it had been for the reaction of bis-thioaryl PD **12**) (Figure 28).

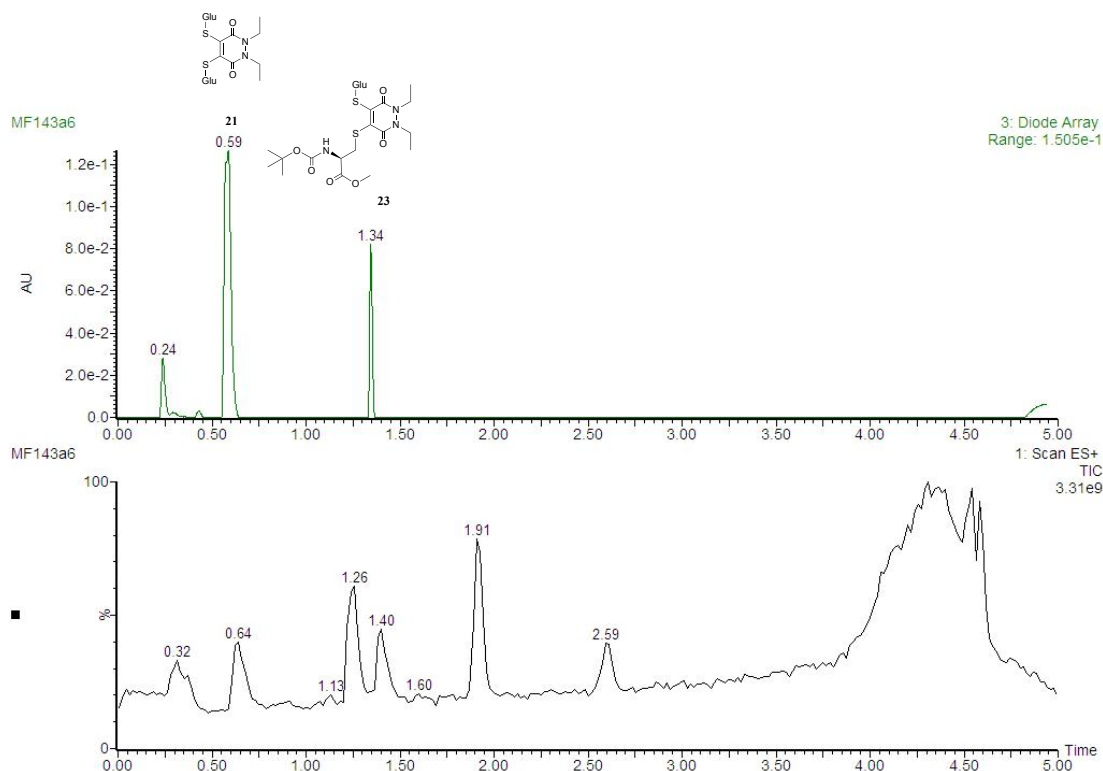
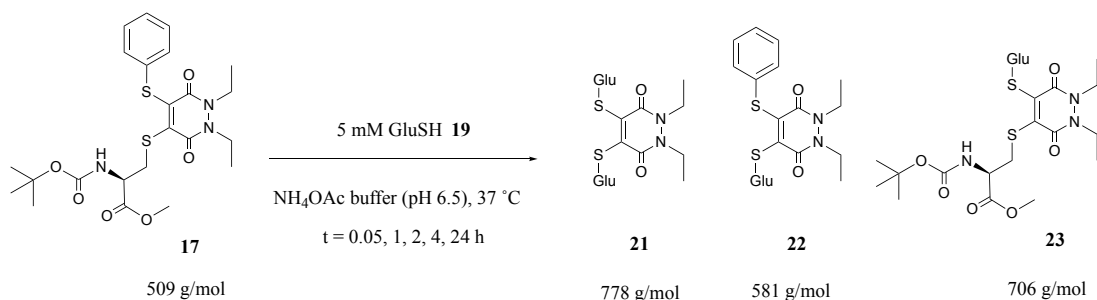


Figure 28. TIC and UV trace of the incubation of PD **15** and GluSH **19** at t = 24 h at pH 6.5.

### 2.4.3 Incubation of thioaryl-alkyl PD with GluSH at pH 6.5

The final PD to be incubated with GluSH **19** at pH 6.5 was thioaryl-alkyl PD **17** (Scheme 27). The di-substituted nature of this PD, with one of the substituents being a thioaryl group might be expected to have a reactivity greater than that of bis-thioalkyl PD **15**, but lesser than bis-thioaryl PD **12**. At  $t = 0.05$  h, double substitution by GluSH (PD **21**) was observed, as were both mono-substituted products **22** and **23**.



Scheme 27. Expected reaction between thioaryl-alkyl PD **17** and GluSH **19** at pH 6.5.

By the 24 h time point, PD **22** was no longer visible in the UV trace, which can be rationalised by quicker and more efficient substitution of the second thioaryl group by GluSH **19** than the alkyl thiol moiety of PD **23**. Consequently, at 24 h post-incubation of thioaryl-alkyl PD **17** with GluSH **19**, the major product was bis-GluSH PD **21**, but there also remained some unreacted PD **23** (Figure 29). The UV signal at 0.72 mins corresponds to di-substituted PD **21** and the peak at 0.87 mins in the UV contains some GluSH **19** and as well as some bis-GluSH PD **21**.

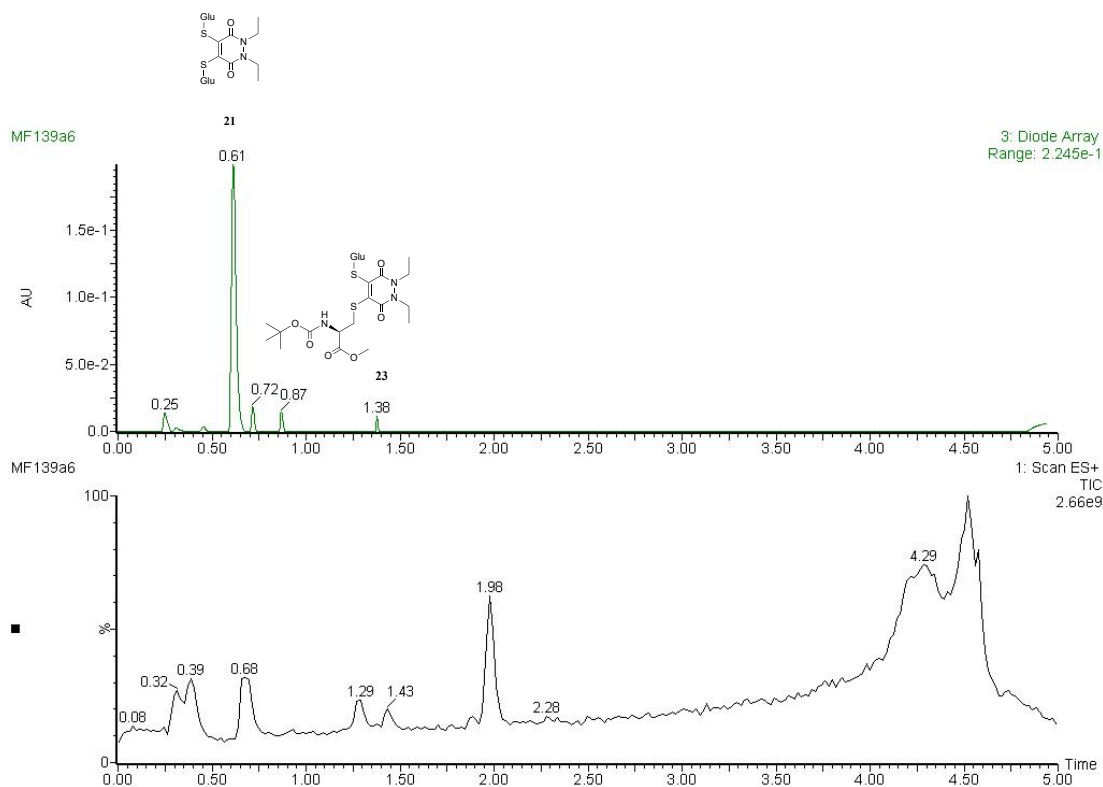


Figure 29. TIC and UV trace of the incubation of thioaryl-alkyl PD **17** and GluSH **19** at  $t = 24$  h at pH 6.5.

The conclusion drawn from the incubations of PDs **11**, **12**, **14**, **15** and **17** with GluSH **19** at  $t = 0.05$ , 1, 2, 4, 24 h was that bis-thioaryl PD **12** is the best candidate for an SMDC scaffold. This is due to there being complete substitution of both thioaryl moieties of PD **12** by GluSH **19** at  $t = 4$  h, with none of the other PDs being fully substituted by GluSH **19**, even after 24 h.

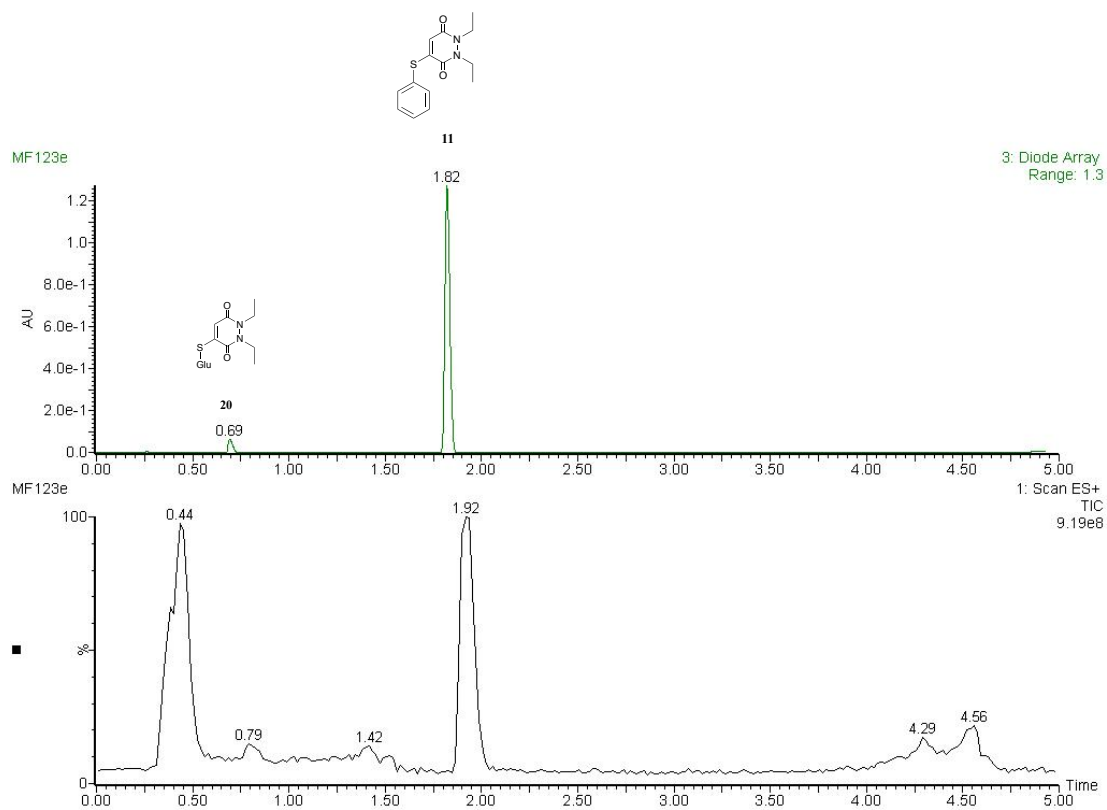
#### 2.4.4 Incubation of thioaryl PDs with GluSH at pH 5.0

Once the GluSH incubations has been conducted at pH 6.5, they were repeated at pH 5.0 using the same 5 time points, temperature and GluSH concentration. The established trend in reactivity of the PDs to GluSH **19** was expected to remain the same, in that bis-thioaryl PD **12** was predicted to still react the most quickly and completely. However, the time this would take was speculated to be longer, as at pH 5.0 a greater proportion of the GluSH would be protonated and thus its nucleophilic character lowered.

The studies showed that lowering the pH from 6.5 to 5.0 indeed reduces the reactivity of GluSH **19**, and although bis-thioaryl PD **12** was not fully consumed after 4 h,

virtually fully complete GluSH substitution had taken place after 24 h. On the other hand, mono-thioaryl PD **11** showed only a small proportion of substitution product at the same time point (Figure 30).

(a)



(b)

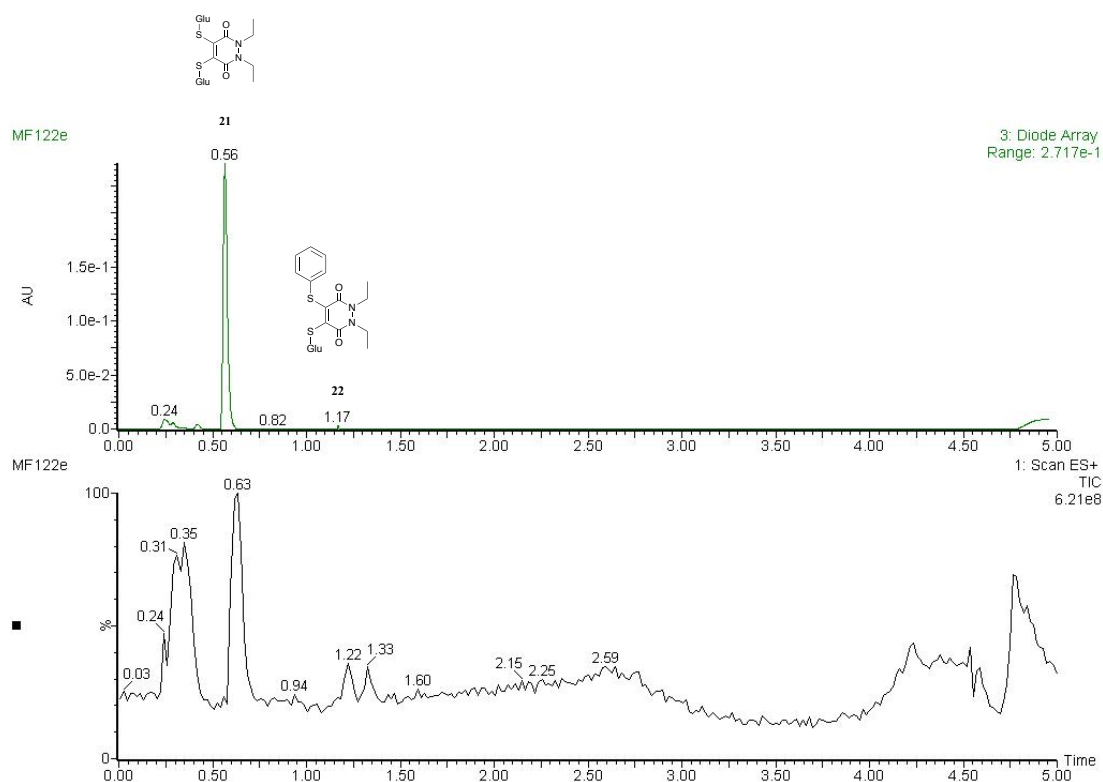
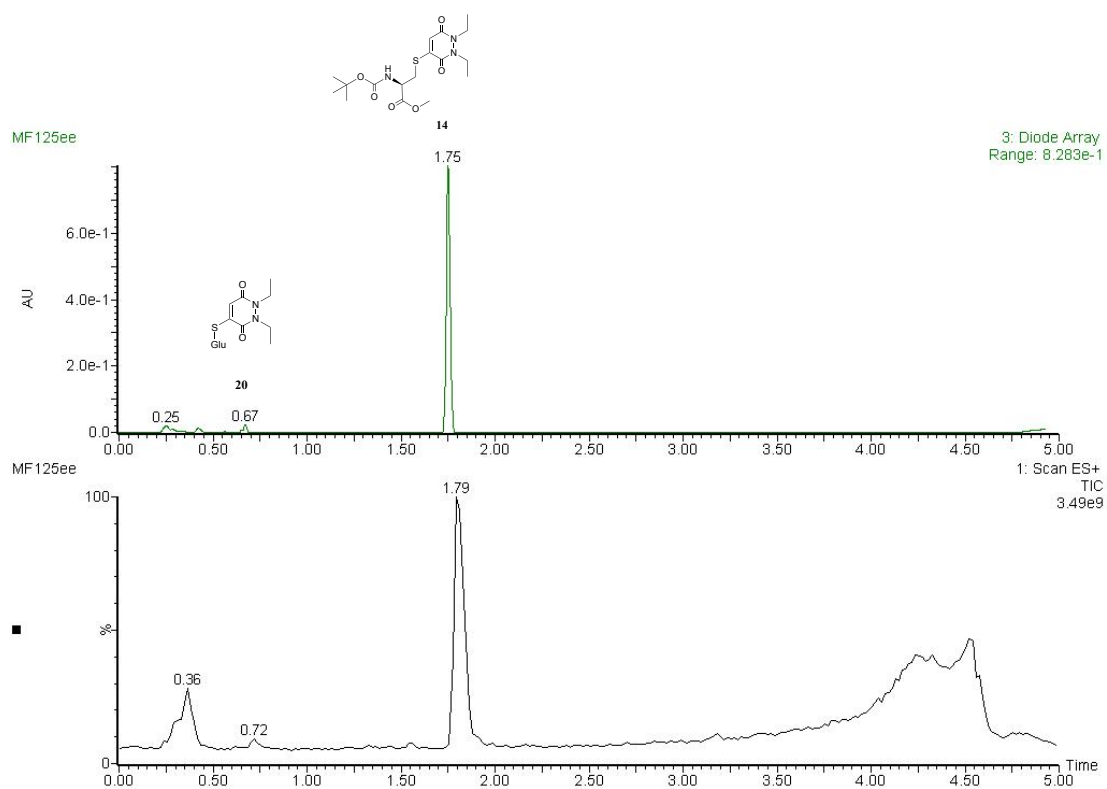


Figure 30. TIC and UV trace of the incubation of GluSH **19** and (a) mono-thioaryl PD **11** at  $t = 24$  h and (b) bis-thioaryl PD **12** at  $t = 24$  h, both at pH 5.0.

## 2.4.5 Incubation of thioalkyl PDs with GluSH at pH 5.0

Given very little reaction of mono-thioaryl PD **11** was observed at pH 5.0, it was predicted that this trend would be observed for the mono-thioalkyl PD **14**, whereas bis-thioalkyl PD **15** was expected to be slightly more reactive. As can be seen from the TIC and UV traces, the UV signal of substitution product PD **20** after 24 h was minuscule compared to that of unreacted mono-thioalkyl PD **14**. Whilst the reactivity of bis-thioalkyl PD **15** was greater than that of PD **14**, it had still not been fully consumed after 24 h and the remaining species were a mixture of both mono- and di-substituted GluSH products (PDs **23** and **21** respectively), rather than the desired sole presence of bis-GluSH PD **21** (Figure 31).

(a)



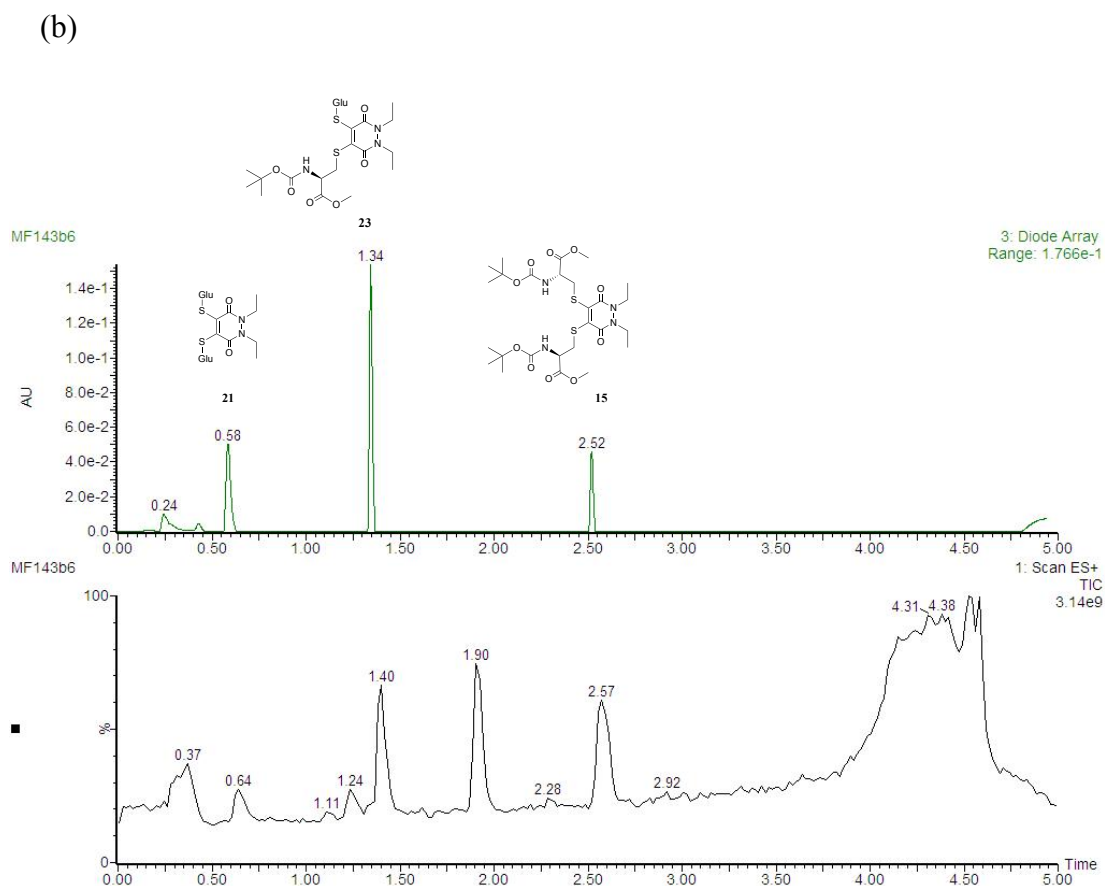


Figure 31. TIC and UV trace of the incubation of GluSH **19** and (a) mono-thioalkyl PD **14** at  $t = 24$  h and (b) bis-thioalkyl PD **15** at  $t = 24$  h, both at pH 5.0.

## 2.4.6 Incubation of thioaryl-alkyl PD with GluSH at pH 5.0

Regarding thioaryl-alkyl PD **17**, the level of GluSH substitution at pH 5.0 was also reduced as compared to that at pH 6.5. In the less acidic conditions, only PDs **23** and **21** were observed in the UV trace at  $t = 4$  h. In contrast, when this study was replicated at pH 5.0, the  $t = 4$  h time point showed the presence of PDs **21**, **22** and **23**, confirming that the more acidic conditions slowed down the conversion of PD **22** to bis-GluSH PD **21**. The  $t = 24$  h time point also showed a fairly large proportion of PD **23** relative to bis-GluSH PD **21** (Figure 32).

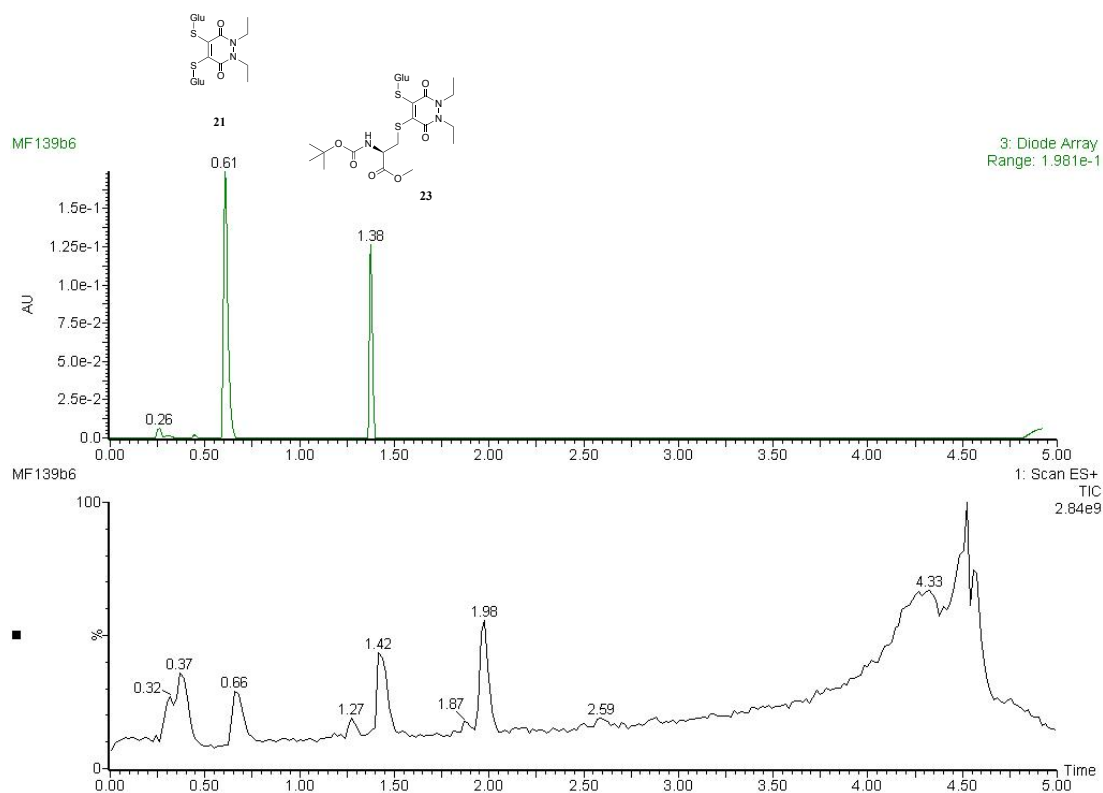
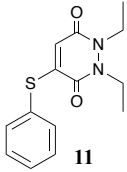
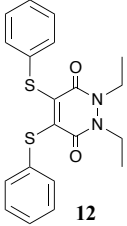
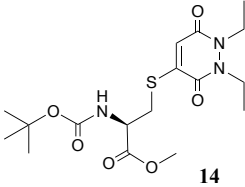
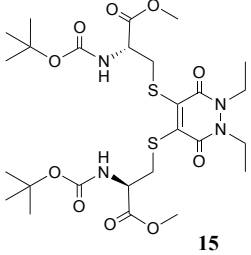
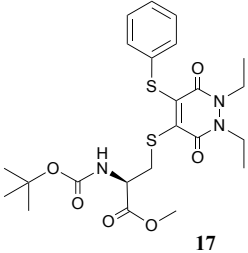


Figure 32. TIC and UV trace of the incubation of thioaryl-alkyl PD **17** and GluSH **19** at  $t = 24$  h at pH 5.0.

While this study demonstrated that GluSH **19**, as expected, is less reactive at pH 5.0 than at pH 6.5, it has also confirmed the superior reactivity of bis-thioaryl PD **12** in regards to producing entirely fully substituted or almost entirely fully substituted PD **21** at the representative intracellular pH extremes of 6.5 and 5.0 respectively after 24 h. Results for all the PDs and studies carried out are shown below (Table 1).



Entry	PD	HSA	GluSH pH 6.5	GluSH pH 5.0
1	 11	Stable after 4 h ✓	Incomplete substitution after 24 h ✗	Incomplete substitution after 24 h ✗
2	 12	Stable after 4 h ✓	Complete substitution after 4 h ✓	Incomplete substitution after 24 h ~ <sup>a</sup>
3	 14	Stable after 4 h ✓	Incomplete substitution after 24 h ✗	Incomplete substitution after 24 h ✗
4	 15	Stable after 4 h ✓	Incomplete substitution after 24 h ✗	Incomplete substitution after 24 h ✗
5	 17	Stable after 4 h ✓	Incomplete substitution after 24 h ✗	Incomplete substitution after 24 h ✗

<sup>a</sup> ~ = almost complete

Table 1. Summary of results from incubating PDs 11, 12, 14, 15 and 17 at 37 °C with HSA and GluSH 19 at pHs 6.5 and 5.0.

## 2.5 Conclusion

In conclusion, simple aromatic and alkyl thiols were installed on the basic diethyl PD scaffold, with the result of successfully synthesising a small library of mono- and di-substituted thioaryl and thioalkyl PDs, as well as a mixed thioaryl-thioalkyl variant. All of these thio-PDs were then demonstrated to be stable in human blood-mimicking conditions, as is desired for a future SMDC. The same five PD platforms were then subjected to cell-mimicking conditions, where, in contrast, GluSH-triggered breakdown was desired, and indeed gratifyingly observed. In both pH employed the bis-thioaryl PD **12** performed the best, showing the quickest complete release of its thiophenol moieties.

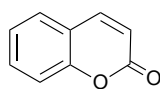
# Chapter 3 Design and appraisal of fluorophore–PDs and a sulfur-based self-immolative release mechanism

## 3.1 Selection of fluorophore for turn-on fluorescence

As it has been established in Chapter 2 that bis-thioaryl PD **12** was the optimal scaffold from the ones tested in regards to thiol release in endosome-mimicking conditions (in both pH studies) and serum stability, attention then turned to derivatising the thioaryl moieties of this PD backbone for the purpose of creating a GluSH-triggered cleavable, self-immolative linker. The future function of such a linker could include the attachment of one or more cytotoxic drugs to the PD scaffold, with the self-immolative linkage allowing detachment of the drug-carrying portion inside a tumour cell and subsequent self-immolative release of the “free” drug itself.

Such a self-immolative linker could also be used to attach a fluorophore for the purposes of imaging, and this self-immolative breakdown could be demonstrated using a releasable fluorophore in lieu of a cytotoxic agent. More specifically, a turn-on fluorophore probe was selected for this investigation. In this way, it was hoped the fluorophore would display little to no fluorescence when attached to the linker construct, but *would* fluoresce when released *via* the self-immolative breakdown, permitting the monitoring of this mechanism both by LC-MS and fluorescence spectroscopy.

Research on suitable fluorophore selection was focussed on coumarin derivatives as there is abundant literature on this class of molecules being utilised in diverse fields and applications, including those of photochemistry, as photo-releasable templates, laser dyes and anti-tumour agents.<sup>126–130</sup> Notwithstanding the widely employed coumarin core for the aforementioned applications, coumarin itself (**24**, Figure 33) only displays very weak fluorescence owing to the nature of its first singlet state ( $^1n\pi^*$ ); and is thus of little value for use as a fluorophore when underivatised.<sup>126</sup>

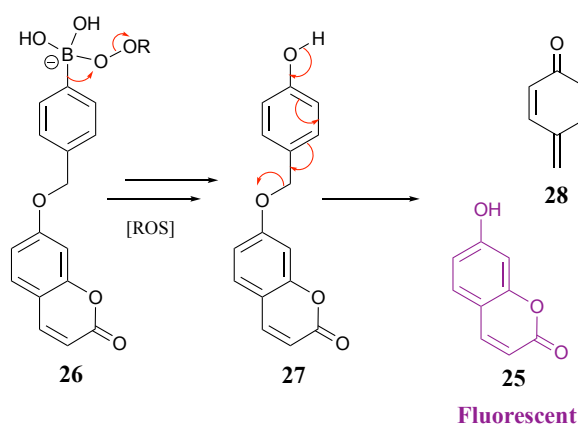


24

Figure 33. Structure of coumarin **24**.

However, abundant literature exists on the use of 7-hydroxy-coumarin (also known as umbelliferone) and its analogues as fluorescent probes.<sup>131–134</sup> Moreover, it is known that the strong fluorescence emission of umbelliferone **25** can be greatly diminished by alkylating the OH group,<sup>126</sup> satisfying the requirement for the selected fluorophore to display turn-on fluorescence.

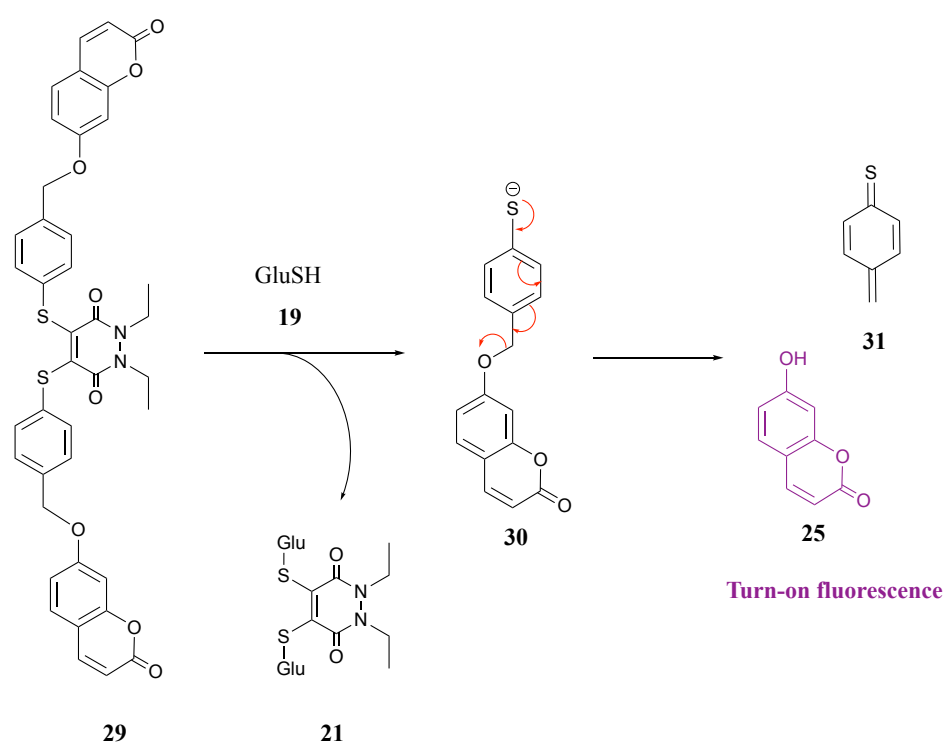
Analysing the literature concerning turn-on fluorescence *via* the self-degradative release of a fluorophore showed that Van Bittner *et al.* developed a self-immolative phenolic-based construct that releases luciferin.<sup>135</sup> Gois *et al.* modified this phenolic-based linker to self-immolatively release umbelliferone **25** instead from a boronate complex, and which was successfully employed to image human breast cancer cells using fluorescence microscopy (Scheme 28).<sup>100</sup>



Scheme 28. Boronate complex **26** developed by Gois *et al.* that is transformed to species **27**, which can subsequently undergo self-immolative degradation to release the fluorescent umbelliferone **25**.<sup>100</sup>

## 3.2 Results and discussion

Taking inspiration from both these systems, it was decided to apply a related but novel strategy to the thiophenol system of bis-thioaryl PD **12**, in which umbelliferone **25** would be incorporated into the structure of umbelliferone–PD **29**. As with bis-thioaryl PD **12**, it was hoped that the incubation of umbelliferone–PD **29** with GluSH **19** would proceed *via* an addition-elimination reaction in which linker species **30** is expelled, followed by self-immolative degradation to release umbelliferone **25** in a manner analogous to that employed by Gois *et al.* (Scheme 29).



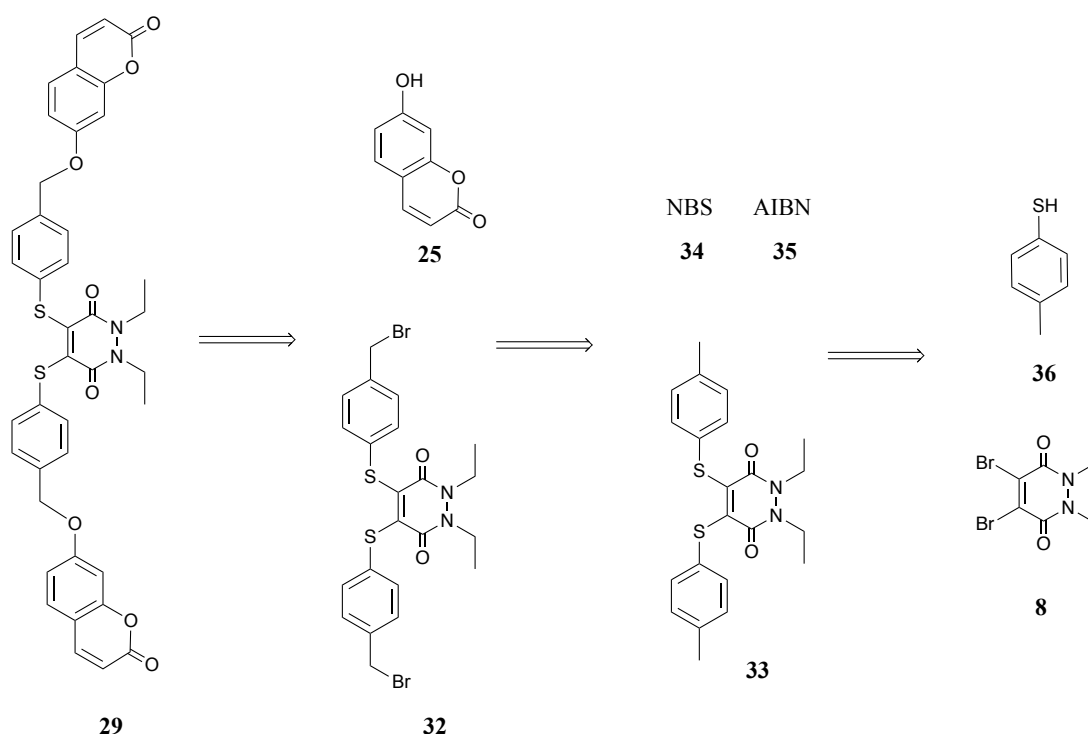
Quenched fluorescence

Scheme 29. Ideal reaction of umbelliferone–PD **29** with GluSH **19** and proposed self-immolative breakdown of **30** to release fluorescent umbelliferone **25**.

Consequently, the main objective in synthesising umbelliferone–PD **29** and incubating with GluSH **19** would be to gauge whether a thiophenol-based self-immolative linker would degrade in the same manner as Gois' phenol-based analogue.

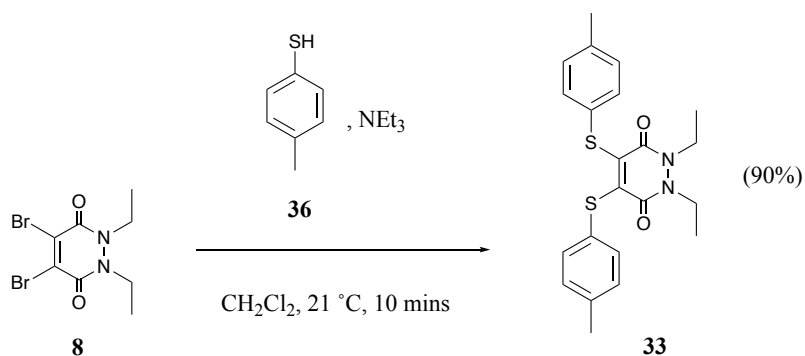
### 3.2.1 Synthesis of umbelliferone–PD

A simple retrosynthetic analysis of umbelliferone–PD **29** reveals that the attachment of the umbelliferone moiety to the thiol-based linker could proceed *via* displacement of a good leaving group such as bromide in an  $S_N2$  reaction by the phenolic functionality on umbelliferone **25**. The brominated species **32** could in turn be obtained by radical bromination of bis-4-methylbenzenethiol PD **33** using *N*-bromosuccinimide **34** (NBS) and azobisisobutyronitrile **35** (AIBN). It was envisioned that the synthesis of PD **33** could be achieved from the reaction of di-bromo PD **8** and 4-methylbenzenethiol **36** (Scheme 30).



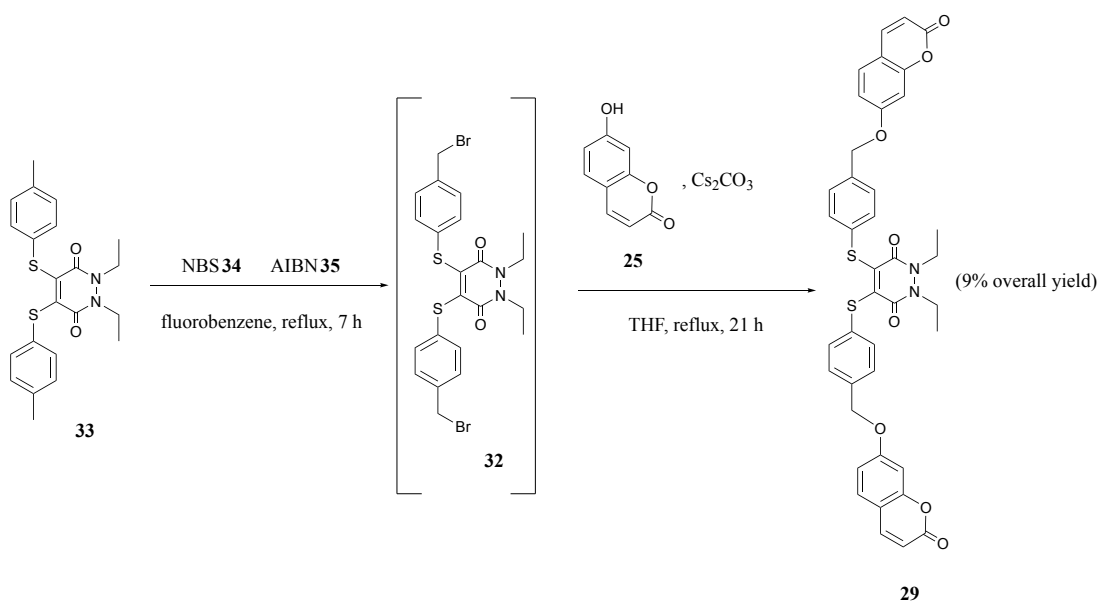
Scheme 30. Retrosynthetic analysis of umbelliferone–PD **29**.

Consequently, the first step in the synthesis of umbelliferone–PD **29** consisted of reacting di-bromo PD **8** with 4-methylbenzenethiol **36** in  $\text{CH}_2\text{Cl}_2$  (Scheme 31). The mixture was stirred at 21 °C for 10 mins to yield bis-4-methylbenzenethiol PD **33** in an excellent yield of 90%.



Scheme 31. Synthesis of bis-4-methylbenzenethiol PD **33** from di-bromo PD **8** and 4-methylbenzenethiol **36**.

Once bis-4-methylbenzenethiol PD **33** had been isolated and purified, it was taken forward in a bromination step using NBS **34** and AIBN **35**. Despite the TLC analysis of this reaction suggesting that only one product spot had formed,  $^1\text{H}$  NMR of the post work-up crude residue revealed that this single spot contained several unidentified impurities, some unreacted PD **33**, but also peaks corresponding to the expected brominated product **32**. At this stage, nonetheless, the crude residue was subsequently reacted with umbelliferone **25** in an attempt to make some of desired umbelliferone–PD **29** (Scheme 32); it was hoped that isolating umbelliferone–PD **29** from by-products might be easier than isolating PD **32** from by-products. After purification by preparative TLC, 18 mg of material was obtained in 9% overall yield, with  $^1\text{H}$  NMR and HRMS confirming its identity as umbelliferone–PD **29**.



Scheme 32. Synthesis of umbelliferone–PD **29** from PD **32**, umbelliferone **25**, NBS **34**, AIBN **35** and bis-4-methylbenzenethiol PD **33**.

### 3.2.2 $^1\text{H}$ NMR and LC-MS studies of umbelliferone–PD + umbelliferone

With umbelliferone–PD **29** in hand it was then decided to carry out an incubation of this PD with GluSH **19** using the same environment as that of the early endosome (pH 6.5) and temperature (37 °C). A concentration of PD (0.5 mM) and concentration of GluSH (5 mM) were employed, *i.e.* analogous conditions to the incubations of GluSH **19** with PDs **11**, **12**, **14**, **15** and **17**. However, in the interests of conserving as much material as possible due to only isolating 18 mg of umbelliferone–PD **29**, it was deemed reasonable to half the number of time points ( $t = 4$  and 24 h) for this study relative to the five time points conducted for PDs **11**, **12**, **14**, **15** and **17** ( $t = 0.05$ , 1, 2, 4 and 24 h).

As it was planned in advance that the incubation of GluSH **19** with umbelliferone–PD **29** would be monitored by both LC-MS and fluorescence spectroscopy, the LC-MS UV trace area ratio between umbelliferone–PD **29** and umbelliferone **25** (the fluorescent molecule expected to be released upon self-immolative degradation) was considered an important piece of data to obtain prior to the incubation. In this way, during the incubation of umbelliferone–PD **29** with GluSH **19**, the UV area ratios of umbelliferone–PD **29** to umbelliferone **25** at  $t = 4$  and 24 h could be utilised to calculate the proportion of the umbelliferone–PD **29** that had been cleaved.

In order to be able to make comparisons of UV area ratios, an initial known ratio of umbelliferone–PD **29** and umbelliferone **25** was required. To this end, it was decided to attempt to make a 1:1 solution of both molecules and then measure the relative UV area ratios. However, as only 18 mg of umbelliferone–PD **29** had been isolated, the ratio of this mixture was to be verified by  $^1\text{H}$  NMR so as to eliminate any errors associated with having to weigh small amounts ( $< 1$  mg) of said PD. In light of this, it was not *necessary* for the solution of these two molecules in deuterated solvents to be exactly 1:1 *per se*, rather it was hoped to be *ca.* 1:1, with  $^1\text{H}$  NMR integrations being used to calculate the exact ratio.

An initial obstacle to this objective was noting that, due to their fairly different structures (Figure 34), the only common laboratory solvent that both umbelliferone–PD **29** and umbelliferone **25** fully dissolved in was THF. As deuterated THF is rather



expensive and was not available in the laboratory at that time, two-solvent mixtures were investigated, with a 2:1 ratio of CD<sub>3</sub>OD/CDCl<sub>3</sub> found to dissolve both molecules fully.

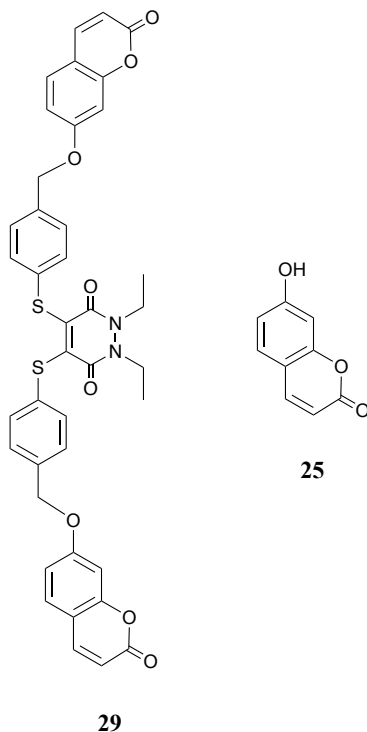


Figure 34. Structures of umbelliferone–PD **29** and umbelliferone **25**.

With this solvent system now in hand, an attempt to prepare a *ca.* 1:1 solution of both umbelliferone–PD **29** and umbelliferone **25** in 2:1 CD<sub>3</sub>OD/CDCl<sub>3</sub> was undertaken, where both molecules were calculated to be at a concentration of *ca.* 0.5 mM, so as to be representative of the umbelliferone–PD **29** concentration when incubated with GluSH **19**. An <sup>1</sup>H NMR spectrum was obtained of this mixture (Figure 35).

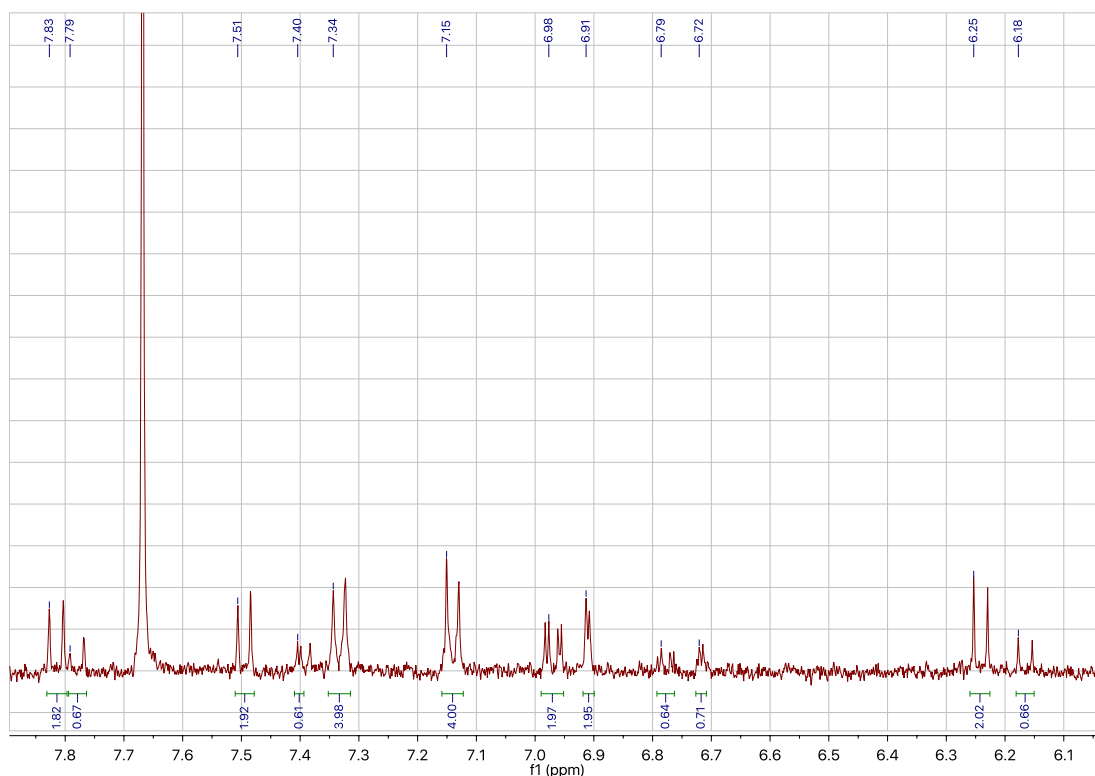
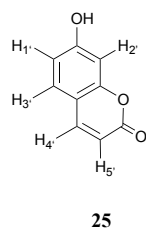
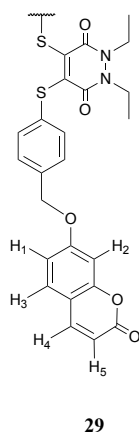


Figure 35.  $^1\text{H}$  NMR spectrum of umbelliferone–PD **29** and umbelliferone **25** in 2:1  $\text{CD}_3\text{OD}/\text{CDCl}_3$  where the ratio of umbelliferone–PD **29** to umbelliferone **25** was presumed to be 1:1 prior to integration analysis.

Upon analysing this  $^1\text{H}$  NMR spectrum it became clear from the integration values that the two molecules were only near equimolar concentrations, most likely due to the balance error associated with weighing such small amounts of umbelliferone–PD **29**. As the umbelliferone moiety is the only common structural portion shared by both umbelliferone–PD **29** and umbelliferone **25**, it was necessary to compare only the integration values of the peaks arising from this moiety in order to calculate the true ratio of these molecules in solution (Table 2).



Chemical shift and splitting of umbelliferone–PD <b>29</b> peak	Chemical shift and splitting of corresponding umbelliferone <b>25</b> peak	Original ratio of integration values <b>29:25</b>	True ratio of integration values <b>29:25</b>
7.83 ppm, d, H <sub>4</sub>	7.79 ppm, d, H <sub>4</sub> '	1.82:0.67	0.91:0.67 = <b>1.4:1</b>
7.51 ppm, d, H <sub>3</sub>	7.40 ppm, d, H <sub>3</sub> '	1.92:0.61	0.96:0.61 = <b>1.6:1</b>
6.98 ppm, m, H <sub>1</sub>	6.79 ppm, m, H <sub>1</sub> '	1.97:0.64	0.99:0.64 = <b>1.5:1</b>
6.91 ppm, d, H <sub>2</sub>	6.72 ppm, d, H <sub>2</sub> '	1.95:0.71	0.98:0.71 = <b>1.4:1</b>
6.25 ppm, d, H <sub>5</sub>	6.18 ppm, d, H <sub>5</sub> '	2.02:0.66	1.01:0.66 = <b>1.5:1</b>

Table 2. Chemical shifts, splittings of umbelliferone–PD **29** and umbelliferone **25** in addition to the original and true integration value ratios.

As umbelliferone–PD **29** contains two umbelliferone moieties, halving the integrations of the former's peaks was required in order to obtain the true ratio of the two species. The two doublets at 7.34 ppm and 7.15 ppm could be ignored as they comprise the thiophenol moiety aromatic protons of umbelliferone–PD **29**, and these have no equivalent peaks on umbelliferone **25**. An average of the ratios shown in red was then taken to obtain the result that in this solution, umbelliferone–PD **29** and umbelliferone **25** were at a ratio of 1.5:1. This same NMR solution was then analysed on the Waters

LC-MS (C18 column) in order to compare the UV area ratios (Figure 36). As can be seen from the UV trace peaks, umbelliferone **25** had a retention time of 0.96 mins whereas umbelliferone–PD **29** came off the column at 2.81 mins (an unrelated column impurity was observed at 1.83 mins); the UV area ratio of **29:25** is 78,974:26,676. Adjusting this area to take into account the previously calculated ratio of **29:25** in this solution of 1.5:1 yielded a UV area ratio of 52,649:26,676 which simplifies to a ratio of *ca.* 2:1 if the molecules were equimolar. Therefore if a solution of umbelliferone–PD **29** and umbelliferone **25** were analysed on the LC-MS where the ratio of the two molecules were exactly 1:1, the UV peak area of the former would be approximately twice as great as that of the latter.

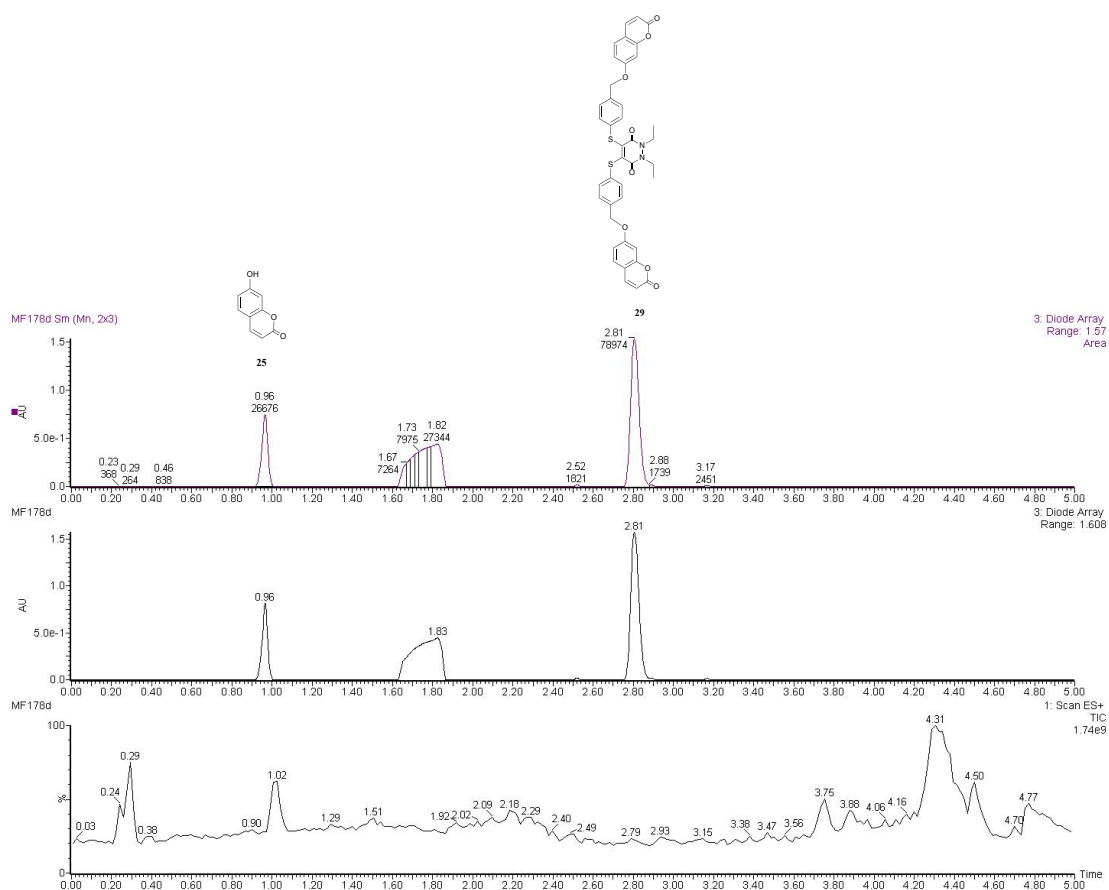


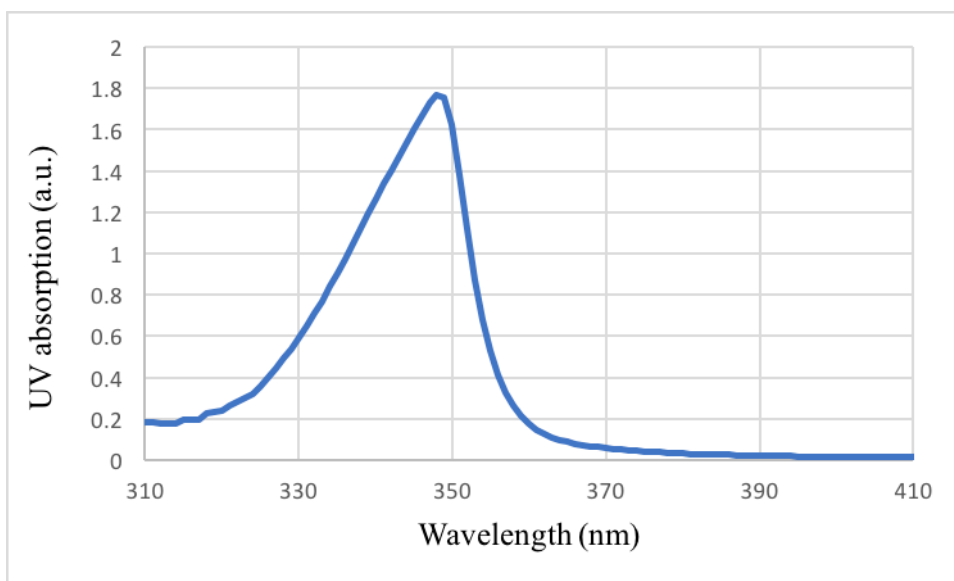
Figure 36. TIC, UV trace and area of UV trace peaks of 1.5:1 solution of umbelliferone–PD **29** and umbelliferone **25** in 2:1 CD<sub>3</sub>OD/CDCl<sub>3</sub>.

### 3.3 UV absorption and fluorescence emission of umbelliferone PD and umbelliferone

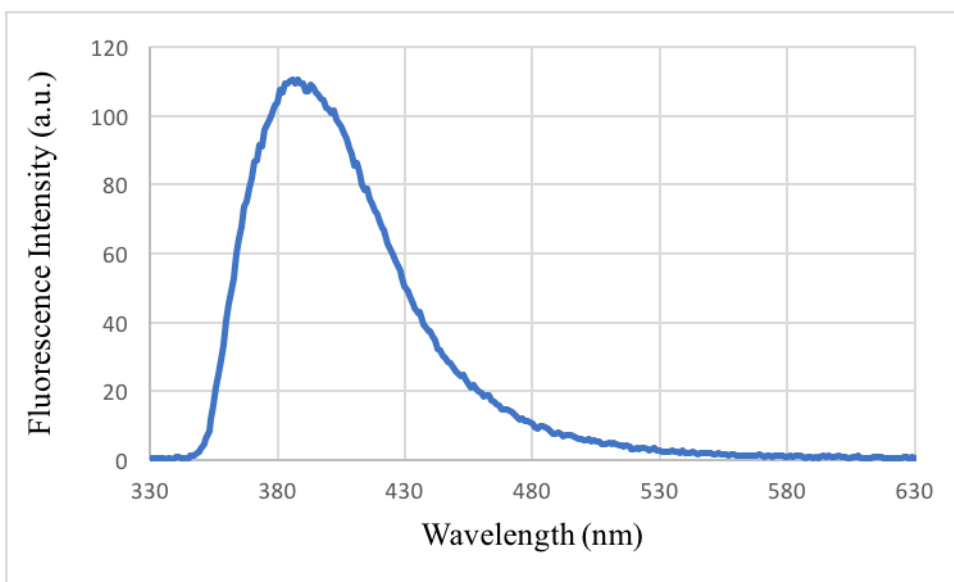
While the isolated 18 mg of umbelliferone–PD **29** was thought to not comprise enough material to conduct both LC-MS and fluorescence studies on the incubation with GluSH **19**, umbelliferone–PD **29** and umbelliferone **25** were nonetheless tested separately before the incubations in order to be sure that, when at the same concentration, the fluorescence emission of umbelliferone **25** was substantially greater than that of umbelliferone–PD **29**. This is because in PD **29**, the umbelliferone portion's phenol group is substituted with something other than H, which should eliminate any fluorescence. To this end, THF was employed to make 1 mM solutions of both umbelliferone–PD **29** and umbelliferone **25**, whose UV absorption wavelengths and fluorescence emission wavelengths were then measured.

As mentioned, in an ideal scenario it was expected that the fluorescence intensity of umbelliferone **25** would be substantially greater than that of umbelliferone–PD **29**, otherwise the value of umbelliferone **25** (or analogues of umbelliferone **25**) as a turn-on fluorophore probe would be nullified. Gratifyingly, this is what was observed: the maximum UV absorption of umbelliferone **25** occurred at 348 nm and when excited at this same wavelength produced a maximum fluorescence emission at 388 nm with an intensity of 111 a.u. Conversely, the UV absorption maximum of umbelliferone–PD **29** occurred at 342 nm and when excited at this wavelength produced a maximum fluorescence emission at 344 nm with an intensity of only 9 a.u., over 10 times less intense than the fluorescence emission reading obtained for umbelliferone **25** (Figure 37).

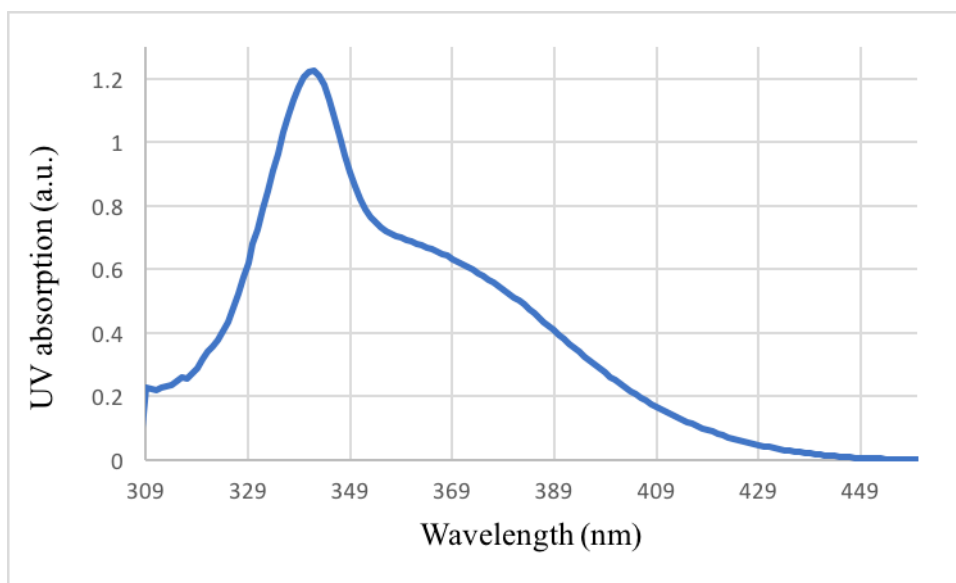
(a)



(b)



(c)



(d)

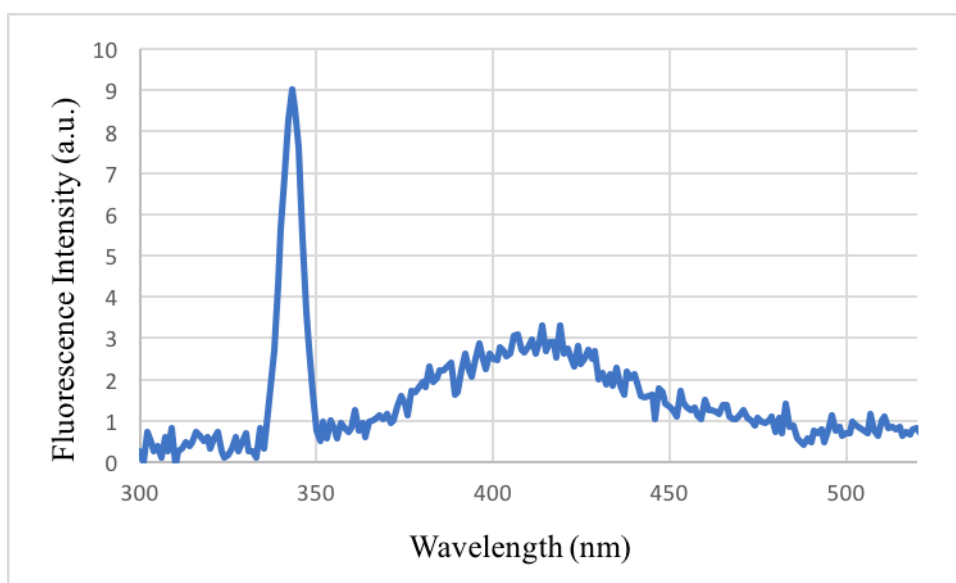


Figure 37. (a) UV absorption spectrum of umbelliferone **25**, with a maximum UV absorption wavelength of 348 nm and  $\epsilon_{348} = 1770 \text{ M}^{-1}\text{cm}^{-1}$ , (b) fluorescence emission spectrum of umbelliferone **25** when excited at 348 nm, producing a maximum fluorescence emission wavelength at 388 nm with an intensity of 111 a.u., (c) UV absorption spectrum of umbelliferone–PD **29**, with a maximum UV absorption wavelength of 342 nm and  $\epsilon_{342} = 1230 \text{ M}^{-1}\text{cm}^{-1}$  and (d) fluorescence emission spectrum of umbelliferone–PD **29** when excited at 342 nm, producing a maximum

fluorescence emission wavelength at 344 nm with an intensity of 9 a.u. All samples were at a concentration of 1 mM in THF.

### 3.4 Incubation of umbelliferone–PD with GluSH

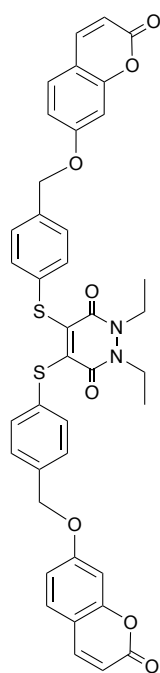
Once the UV area ratios and fluorescence emission values of umbelliferone–PD **29** and umbelliferone **25** had been measured, the subsequent step (as highlighted at the beginning of section **3.2**), involved incubating umbelliferone–PD **29** with GluSH **19** using the same conditions as with PDs **11**, **12**, **14**, **15** and **17** for the early endosome-mimicking conditions: PD at 0.5 mM, GluSH **19** at 5 mM, 37 °C and pH 6.5 (Figure 38). As the incubations of the aforementioned five PDs had been conducted in 5% organic solvent and 95% aqueous GluSH buffer, this same ratio of organic solvent to buffer was conserved for the incubation of umbelliferone–PD **29** with GluSH **19**. However, while the organic solvent used in the incubations for PDs **11**, **12**, **14**, **15** and **17** was MeCN, THF had to serve the role as the organic solvent for the umbelliferone–PD **29** stock solution as it was the only common laboratory solvent that this PD fully dissolved in; not surprising in view of the “greasy” umbelliferone core.

Unlike the incubations carried out with PDs **11**, **12**, **14**, **15** and **17**, when the stock solution of umbelliferone–PD **29** in THF was added to the aqueous GluSH buffer, some mild cloudiness was observed, suggesting that some of the umbelliferone–PD **29** and/or any species formed were crashing out of solution. As the cloudiness was still minor, it was decided to continue with the incubation and wait until the first 4 h time point to judge whether the reaction mixture was still suitable for analysis on the LC-MS.

Gratifyingly, at  $t = 4$  h, the reaction appeared homogeneous, and after passing some reaction solution through a 0.22  $\mu\text{m}$  filter for good measure, analysis could be carried out by LC-MS without fear of blocking or damaging the instrument (Figure 38).

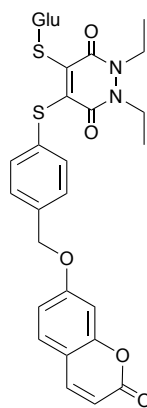
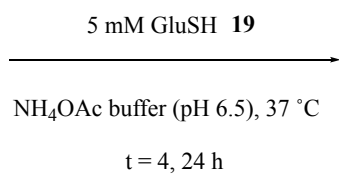


(a)



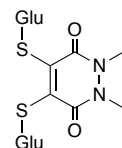
**29**

732 g/mol



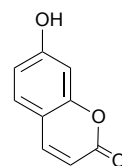
**37**

755 g/mol



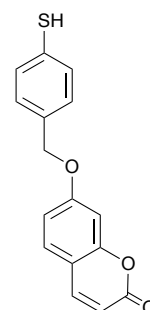
**21**

778 g/mol



**25**

162 g/mol



**30**

284 g/mol

(b)

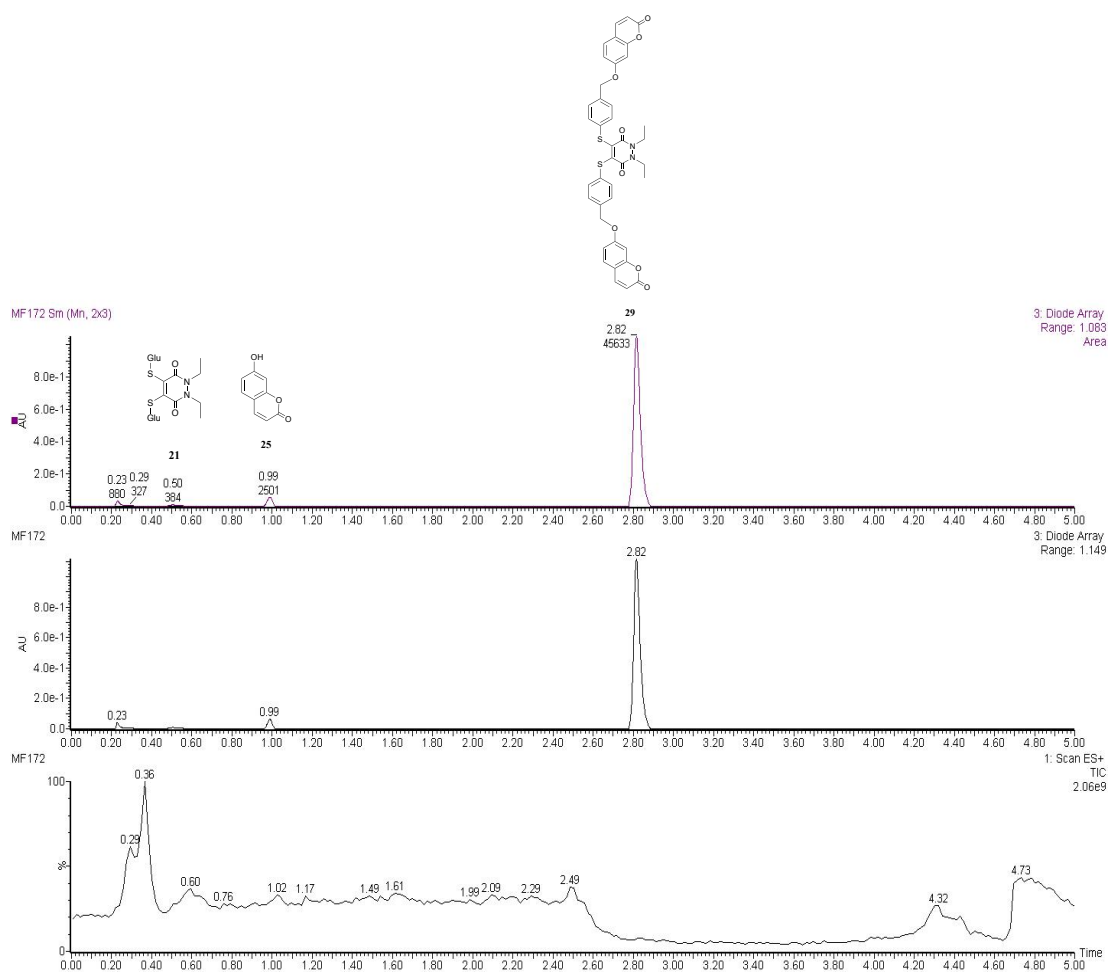


Figure 38. (a) Reaction of umbelliferone–PD **29** with GluSH **19** at pH 6.5 and the masses of the principle expected products formed and (b) TIC, UV trace and UV trace area of the incubation of umbelliferone–PD **29** with GluSH **19** at  $t = 4$  h at pH 6.5 and  $37^{\circ}\text{C}$ .

This result at the 4 h time point was both disappointing and pleasing at the same time. It was disappointing because as can be noted from the UV trace, the majority of the sample contained unreacted umbelliferone–PD **29**. This is in sharp contrast to the incubation of bis-thioaryl PD **12** with GluSH **19** at pH 6.5, where almost complete substitution of the PD thioaryl moieties by GluSH **19** had occurred after this time. This reduction in reactivity of umbelliferone–PD **29** relative to the bis-thioaryl PD **12** it was modelled on may be due to the lack of complete solubility of the former in the 5% organic solvent and 95% buffer system. Although the solution appeared clear to the naked eye at  $t = 4$  h, the fact that cloudiness had been observed immediately upon addition of umbelliferone–PD **29** to the GluSH buffer, allowed for the possibility that

some of this insolubility remained for the entire duration of the incubation, even if undetected by eye.

The positive result of this time point stemmed from observation of the appearance of released umbelliferone **25** at 0.99 mins, which confirmed the proposed self-immolative mechanism as depicted in Scheme 29. This demonstrated that Gois *et al.*'s phenolic-based self-immolative degradation mechanism can be applied to sulfur-based analogues. There was also some bis-GluSH PD **21** present at 0.50 mins, further confirming that addition-elimination of GluSH **19** to umbelliferone-PD **29** did take place. Gratifyingly, no mass of 285 g/mol was observed, which would correspond to the theoretical non-self-immolative broken down thiol-umbelliferone **30** expelled upon addition-elimination of GluSH **19**, see Figure 38.

Concerning the UV areas, Figure 38 shows **29:25** at a ratio of 45,633:2,501. As it was previously calculated that the UV area ratio of **29:25** was *ca.* 2:1 when both molecules were equimolar, the UV area ratios signify that the ratio of **29:25** was *ca.* 9.1:1 at  $t = 4$  h.

The same reaction mixture was then analysed by LC-MS at  $t = 24$  h (Figure 39). As expected at  $t = 24$  h, the UV peak corresponding to released umbelliferone **25** had increased in area whereas that of unreacted umbelliferone-PD **29** had decreased. As with the 4 h time point, no thiol-umbelliferone **30** was observed. At  $t = 24$  h, the UV area ratio of **29:25** was 4,539:7,825 demonstrating that the ratio of **29:25** had changed to 1:3.4, showing 77% cleavage of umbelliferone-PD **29** after 24 h. It must however, be taken into account that these values cannot be considered of the utmost accuracy due to the fact that some species may not completely soluble considering that initial cloudiness was observed upon addition of umbelliferone-PD **29** to the aqueous GluSH buffer. However, as the reaction solution appeared clear at  $t = 4$  h and beyond, these UV area ratios can be assumed to be of reasonable accuracy.

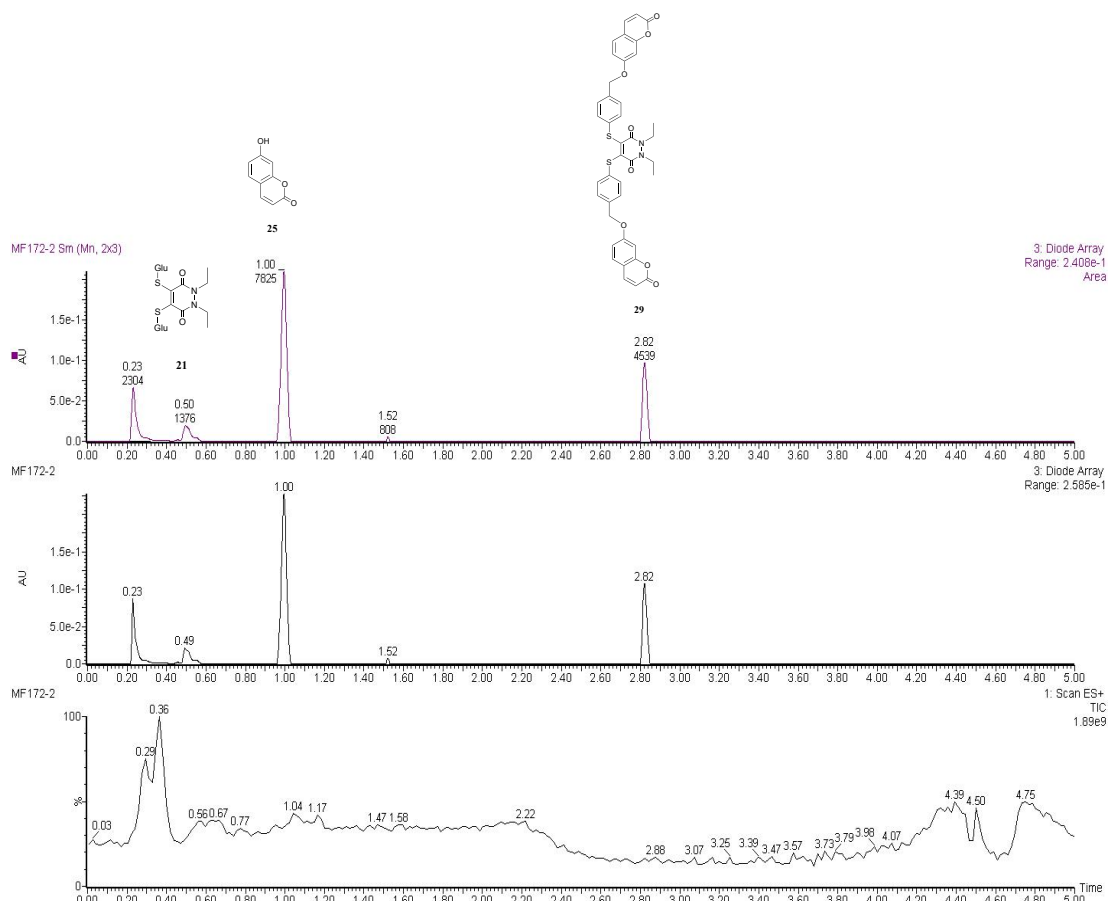


Figure 39. TIC, UV trace and UV trace area of the incubation of umbelliferone–PD **29** and GluSH **19** at  $t = 24$  h at pH 6.5 and  $37$  °C.

Due to observing a reaction suspension when umbelliferone–PD **29** was added to the aqueous GluSH buffer, the same incubation was repeated five more times where the organic portion of the solvent consisted of 5% DMF, 10% DMF, 10% MeCN, 20% MeCN and 10% THF respectively. None of these incubations were successful, either as a result of the organic solvent giving an incorrect mass extraction for expelled umbelliferone (in the case of DMF), or due to abundant crashing out of solid (in the case of the MeCN and 10% THF), rendering analysis by LC-MS inappropriate.

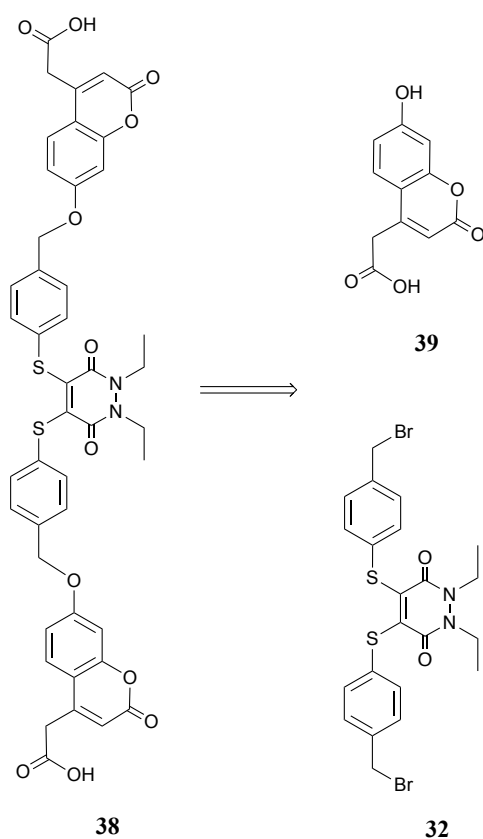
It was decided that as the initial partial insolubility of umbelliferone–PD **29** when added to the 95% aqueous GluSH buffer compromised the accuracy of any LC-MS readings, it would not be re-synthesised on a larger scale to repeat the studies.

Investigation was instead carried out into using more water-soluble analogues of umbelliferone–PD **29** analogues so that solubility in buffer of the final molecule would be greater.

## 3.5 Synthesis of water-soluble variant of umbelliferone PD

### 3.5.1 Attempted synthesis of acetic acid umbelliferone–PD

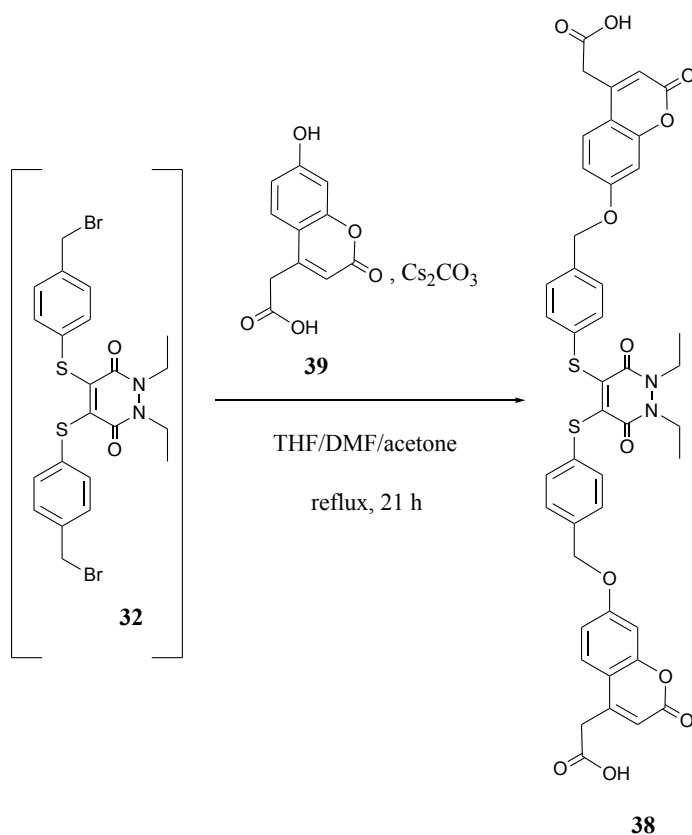
As previously mentioned in section 3.4, the fact that umbelliferone–PD **29** suffered from lack of initial solubility when added to GluSH buffer, and finding that this problem was only aggravated when utilising other organic solvents such as MeCN and DMF and even THF in percentages higher than 5, spurred work to focus on synthesising a more water-soluble, acetic acid umbelliferone–PD **38** (Scheme 33).



Scheme 33. Retrosynthetic analysis of acetic acid umbelliferone–PD **38** from PD **32** and 7-hydroxycoumarin-4-acetic acid **39**.

As with umbelliferone–PD **29**, the synthesis of acetic acid umbelliferone–PD **38** was envisaged from reacting brominated PD **32** and commercially available 7-hydroxycoumarin-4-acetic acid **39**. Although the desired PD **38** is hypothetically formed from the phenolic hydroxyls of compound **39** displacing the bromine atoms of PD **32**, 7-hydroxycoumarin-4-acetic acid **39** contains an additional carboxylate hydroxyl which could become deprotonated during the reaction and potentially also undergo an S<sub>N</sub>2 reaction at the bromine-bearing carbons of PD **32**. From the outset therefore, it was kept in mind that the carboxylate hydroxyl of 7-hydroxycoumarin-4-acetic acid **39** may potentially require protection.

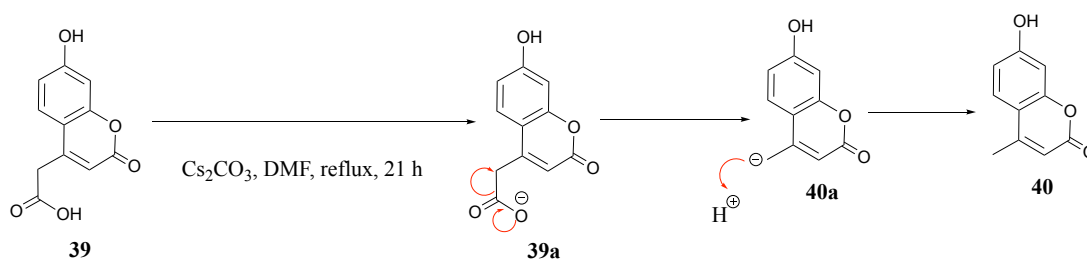
Before proceeding with protection strategies however, it was decided to test the reaction between PD **32** and 7-hydroxycoumarin-4-acetic acid **39**. Three reactions of PD **32** and compound **39** was conducted in parallel, with cesium carbonate as base and in three solvents: THF (as that solvent had been used to synthesise umbelliferone–PD **29**), DMF and acetone, all under reflux (Scheme 34).



Scheme 34. Potential formation of acetic acid umbelliferone–PD **38** from 7-hydroxycoumarin-4-acetic acid **39** and PD **32**.

Although the  $pK_a$  of the carboxylate hydroxyl of compound **39** is not present anywhere in the scientific literature, it can be assumed to be in 4–5 region by considering acetic acid's  $pK_a$  value of 4.8. In contrast, the phenolic hydroxyl of compound **39** has a  $pK_a$  of 7.8.<sup>136</sup> It was thus expected that in the above THF, DMF and acetone reactions, more of the carboxylate hydroxyl than phenolic hydroxyl of compound **39** would be deprotonated, potentially leading to a mixture of products: acetic acid umbelliferone–PD **38** linked to 7-hydroxycoumarin-4-acetic acid **39** through the phenolic oxygen and another PD attached to **39** through the carboxylate oxygen. Despite this, it was hoped that the phenolate's relative instability/higher reactivity when compared to the carboxylate portion of **39** would drive the phenolate position to react more quickly with PD **32** in an  $S_N2$  reaction and thus yield a greater proportion of PD **38** as opposed to the potential PD linked to 7-hydroxycoumarin-4-acetic acid **39** *via* the carboxylate.

TLC analysis of both the THF and acetone reactions after 21 h showed that no reaction had taken place and flash column chromatography was employed to recover the unreacted starting materials. In contrast, TLC analysis of the DMF reaction showed the presence of a new product spot. Purification and analysis of this compound revealed its identity not as desired acetic acid umbelliferone–PD **38**, but rather as 4-methylumbelliferone **40**, which must have occurred *via* a decarboxylation reaction of 7-hydroxycoumarin-4-acetic acid **39** (Scheme 35).

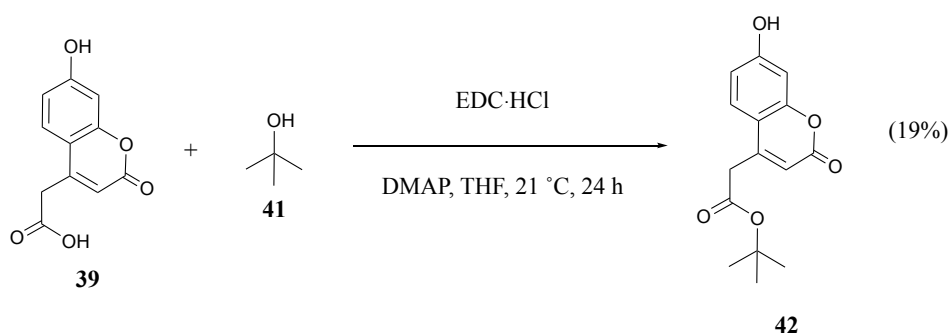


Scheme 35. Formation of 4-methylumbelliferone **40** from the decarboxylation of 7-hydroxycoumarin-4-acetic acid **39**.

It was disappointing that none of these reactions had seen an  $S_N2$  displacement of the bromine on PD **32**, even in the case of the DMF reaction where the potentially competing carboxylate hydroxyl had been eliminated. In light of these results, it was subsequently decided to protect the carboxylic acid portion of compound **39** to appraise whether this would minimise or eliminate decarboxylation and potentially permit only the phenolic position to react with PD **32**.

### 3.5.2 *Tert*-butyl protection of 7-hydroxycoumarin-4-acetic acid

The *tert*-butyl group was chosen to this end as it is commonly employed to protect carboxylic acids and able to be removed fairly easily under acidic conditions. 7-hydroxycoumarin-4-acetic acid **39** was therefore protected using *tert*-butanol **41**, *N*-(3-dimethylaminopropyl)-*N*'-ethylcarbodiimide hydrochloride (EDC·HCl) and 4-dimethylaminopyridine (DMAP), using the only conditions from the literature that employed compound **39** as a reagent (Scheme 36).<sup>137</sup> The use of EDC·HCl is preferable to *N,N'*-dicyclohexylcarbodiimide (DCC) as the urea by-product of the former is water soluble and can thus be easily removed in an aqueous work-up, whereas dicyclohexylurea (DCU) is soluble in organic solvents and can often require several rounds of cooling and filtration to remove it completely from the desired product.



Scheme 36. Synthesis of *tert*-butyl 2-(7-hydroxy-2-oxo-2H-chromen-4-yl)acetate **42** from EDC·HCl, DMAP, *tert*-butanol **41** and 7-hydroxycoumarin-4-acetic acid **39**.<sup>137</sup>

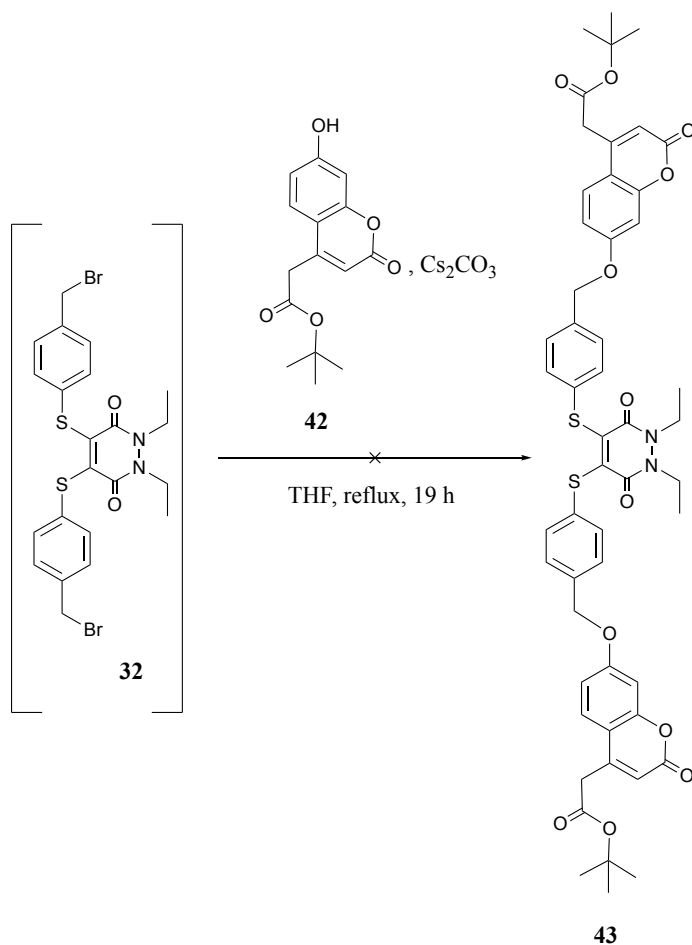
The obtained yield of **42** in 19% was lower than the 30% yield obtained in the literature protocol. The latter provides no rationale for this low yield, be it from low conversion of 7-hydroxycoumarin-4-acetic acid **39** and/or formation of side products. In the case of compound **42**'s synthesis, the low yield can be explained by two main factors: (1) incomplete conversion of compound **39** (65% recovery) and (2) formation of 4-methylumbelliferone **40** as a side product. Consequently, once 7-hydroxycoumarin-4-acetic acid **39** is deprotonated by EDC·HCl, the decarboxylation pathway to produce **40** competes with the expected nucleophilic attack of the carboxylate on EDC·HCl.



A further complication of this 4-methylumbelliferone **40** side product was that in most solvent systems it was inseparable from desired compound **42** by TLC. The largest separation between **40** and **42** was achieved by employing 50:50 EtOAc/Toluene, and even then, the separation ( $R_f$  **40** = 0.4,  $R_f$  **42** = 0.5) rendered separation of the two species by flash column chromatography impossible. Accordingly, the species needed to be isolated by preparatory TLC, with some product having to be sacrificed due to the two smeared spots overlapping. All of these factors of: (1) incomplete conversion of 7-hydroxycoumarin-4-acetic acid **39**, (2) side product formation of decarboxylated **40** and (3) sacrificing a portion of the overlapping species during preparatory TLC, can be rationalised to contribute to the low final yield of 19%.

### 3.5.3 Attempted synthesis of *tert*-butyl acetic acid umbelliferone PD

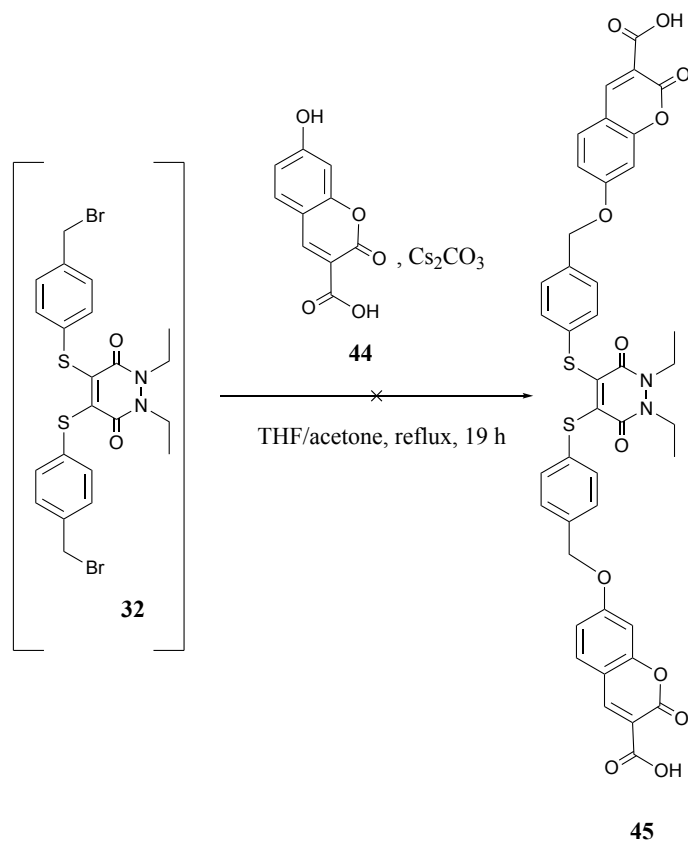
With *tert*-butyl protected **42** in hand, it was then reacted with PD **32** in the hope that the latter's bromine groups would be displaced by the only free hydroxyl of **42** (Scheme 37). While analysis by TLC showed full consumption of PD **32**, the  $^1\text{H}$  NMR spectrum of the new spot isolated from the column proved inconclusive: there were peaks indicating the presence of the PD **43** quartet and some of its **42** portion protons. However, some of the thiophenol region's doublets were absent as well as there being no obvious peak corresponding to the  $\text{CH}_2\text{-O}$  protons linking the thiophenol moiety to **42**. What this study had shown, was that *tert*-butyl protection of the carboxylic acid group of **42** had at least led to the appearance of a new product spot when reacted with PD **32**, which although not the desired PD **43**, was somewhat encouraging in that it was thought that conditions could be found to cause the desired reaction to proceed. As compound **42** could only be synthesised on fairly small amounts due to the low conversion of **39**, attention was turned to utilising a related analogue of the latter, but one which lacked the intermediate  $\text{CH}_2$  group between the aromatic ring and the carboxylic acid group, so as to eliminate the possibility of decarboxylation.



Scheme 37. Potential formation of PD **43** from compound **42** and PD **32**.

### 3.5.4 Attempted synthesis of carboxylic acid umbelliferone–PD

With the above idea in mind, 7-hydroxy-coumarin-3-carboxylic acid **44** was purchased and although its related analogue **39** had not reacted when unprotected with PD **32**, it was decided to give **44** a fair chance to gauge whether its slightly different structure to **39** would lead to a successful S<sub>N</sub>2 reaction on the bromine-bearing carbon atoms of PD **32** without having to protect the carboxylic acid group. Thus, two parallel reactions were run, one in THF and the other in acetone, in which **44** was mixed with PD **32** (Scheme 38). As with the three reactions depicted in Scheme 34, **44** did not react with PD **32** in either THF or acetone, with TLC analysis showing unreacted starting materials and the absence of a new product spot.

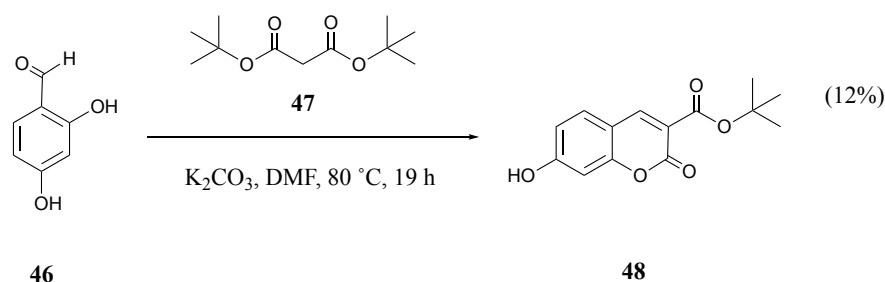


Scheme 38. Potential formation of carboxylic acid umbelliferone–PD **45** from 7-hydroxy-coumarin-3-carboxylic acid **44** and PD **32**.

### 3.5.5 Synthesis of *tert*-butyl carboxylic acid umbelliferone–PD

It was subsequently decided that the next step would involve *tert*-butyl protection of the acid group of 7-hydroxy-coumarin-3-carboxylic acid **44**, as this protection had been the only method so far that had produced a new spot when **42** was reacted with PD **32**. However, as 7-hydroxy-coumarin-3-carboxylic acid **44** is very expensive and was in low reserve in the laboratory at the time, rather than attempt a *tert*-butyl protection directly, its synthesis was achieved from 2,4-dihydroxybenzaldehyde **46** and di-*tert*-butyl malonate **47** (Scheme 39). Although rather low yielding, the advantage of this reaction as opposed to the synthesis of **42**, is that 3-*tert*-butyl carboxylic acid umbelliferone **48** can be separated easily from the starting materials and can be obtained by column chromatography, in contrast to the prep TLC purification necessary to isolate compound **42**, a method which is both time consuming and limited by the low amount of product that can be loaded onto and recovered from the plate. In contrast, 3-*tert*-butyl carboxylic acid umbelliferone **48** could be isolated fairly easily

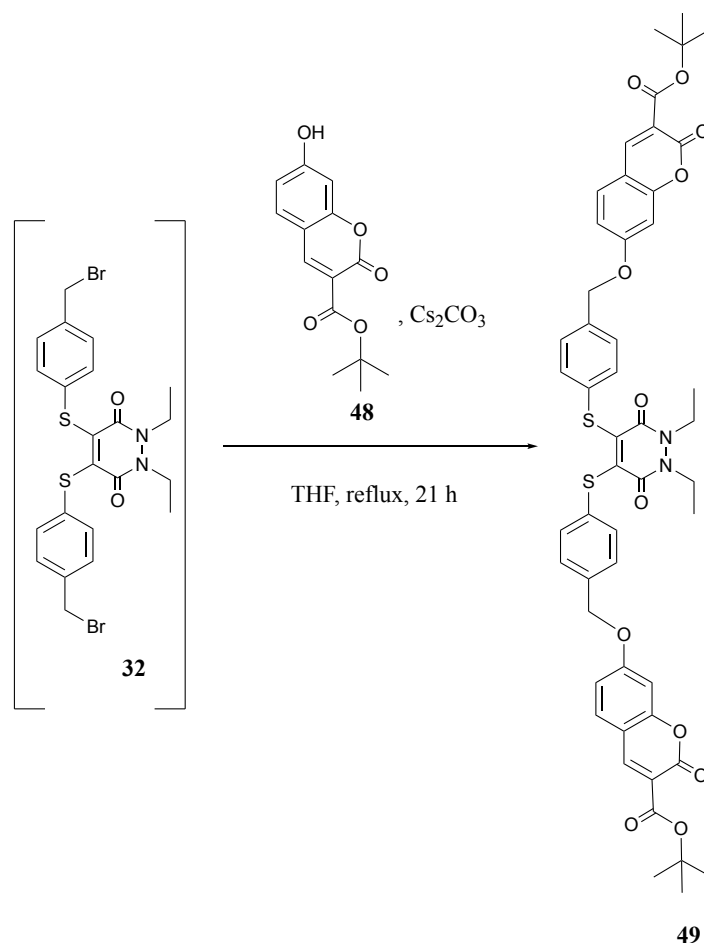
from multiple parallel reactions so as to end up with a combined mass of **48** for reactions to be performed on > 30 mg scales.



Scheme 39. Synthesis of 3-*tert*-butyl carboxylic acid umbelliferone **48** from 2,4-dihydroxybenzaldehyde **46** and di-*tert*-butyl malonate **47**.

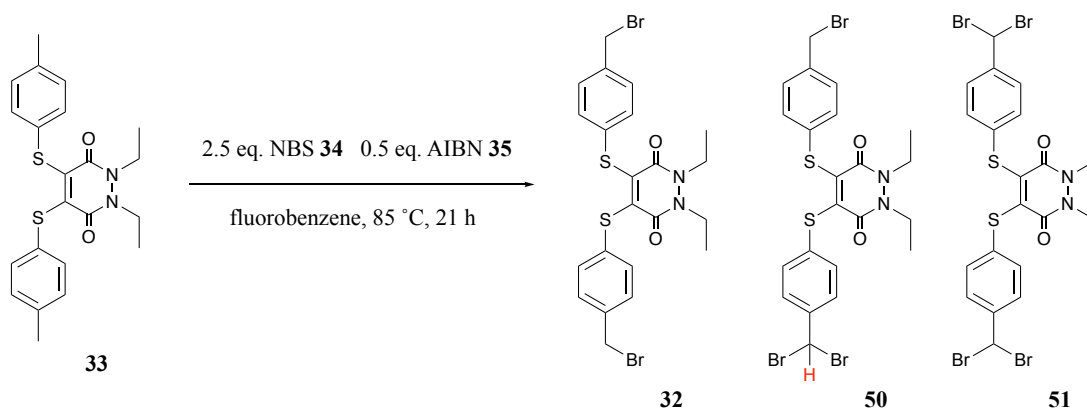
With 3-*tert*-butyl carboxylic acid umbelliferone **48** in hand, it was chosen to engage in one of the last few attempts at reaction with PD **32**, and if said reactions produced no sign of the desired product, then some alternative route would have to be found to synthesise a PD capable of dissolving in buffer. Thus, as in previous analogous reactions, 3-*tert*-butyl carboxylic acid umbelliferone **48** was reacted with PD **32** in THF (Scheme 40). The first attempt at this reaction involved employing *ca.* 3 eq. of **48** relative to PD **32**, and TLC analysis after stirring in THF under reflux for 21 h showed no reaction. The second attempt at this reaction involved drastically lowering the eq. of **48** administered to the solution (*ca.* 0.8 eq.), to gauge whether this produced any desired 3-*tert*-butyl carboxylic acid umbelliferone–PD **49** whatsoever. Very surprisingly, TLC analysis showed the appearance of a single new spot and aside from a few impurities, the <sup>1</sup>H NMR spectrum showed every expected peak of the desired PD **49**, with the sole problem being the overintegration of the PD **49**'s quartet and triplet to roughly double what they should be.

This unexpected observation exposed the possibility of the spectrum containing two or more very similar species, which could be causing this overintegration, and which could have their origin in PD **32**, which was never purified and instead always telescoped crude into reactions.



Scheme 40. Proposed synthesis of 3-*tert*-butyl carboxylic acid umbelliferone–PD 49 from 3-*tert*-butyl carboxylic acid umbelliferone 48 and PD 32.

Previously, when synthesising PD 32, the sole object had been to completely consume its precursor: bis-4-methylbenzenethiol PD 33, and it had been found that employing 2.5 eq. NBS 34 and 0.5 eq. AIBN 35 in fluorobenzene at 85 °C for 21 h had been enough to achieve this. However, it was consistently found that consumption of 33, as well as forming the desired PD 32, invariably led to the formation of a peak at 6.60 ppm in the  $^1\text{H}$  NMR spectrum, indicating the formation of a doubly brominated methyl group and thus a mixture of inseparable products (Scheme 41). The species with a methyl group that had been doubly brominated thus presents two  $\text{S}_{\text{N}}2$  centres on the same carbon, and could go some way to explaining why formation of PD 49 contained overintegrated signals, as if there were two or more extremely similar species mixed together inseparably.



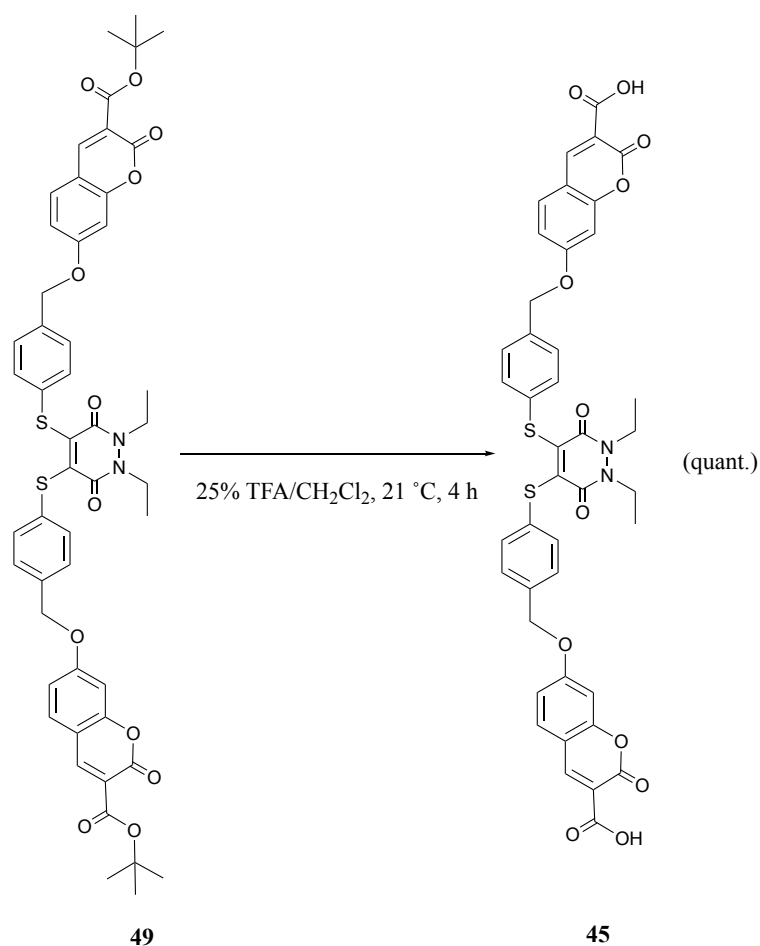
Scheme 41. Potential mixture of products obtained when reacting bis-4-methylbenzenethiol PD **33** with 2.5 eq. NBS **34** and 0.5 eq. AIBN **35**. Proton shown in red corresponds to the signal seen at 6.60 ppm in the  $^1\text{H}$  NMR ( $\text{CDCl}_3$ ).

Thus, it was decided that conditions would be modified in an effort to eliminate formation of the 6.60 ppm peak, even if that meant having to sacrifice full consumption of bis-4-methylbenzenethiol PD **33**. Consequently, the first conditions involved only modifying the eq. of NBS **34**, namely, from 2.5 eq. to 2 eq. The eq. of AIBN **35** were kept the same (0.5 eq.), as well as the reaction temperature of 85 °C. After 21 h, the  $^1\text{H}$  NMR spectrum showed, as expected, some unreacted PD **33**, but there was a small peak visible at 6.60 ppm, suggesting some overbromination had still occurred. The reaction was then repeated, but this time only the temperature of the reaction was modified, being reduced from 85 °C to 60 °C, and after 21 h there was virtually no peak visible at 6.60 ppm.

It was subsequently decided to gauge whether this non overbrominated mixture, when reacted with 3-*tert*-butyl carboxylic acid umbelliferone **48**, would produce the desired 3-*tert*-butyl carboxylic acid umbelliferone–PD **49**, this time with correct integration values. So, as before, the PD **32** mixture, was reacted with *ca.* 0.8 eq. 3-*tert*-butyl carboxylic acid umbelliferone **48**, which *was* finally successful in isolating the desired 3-*tert*-butyl carboxylic acid umbelliferone–PD **49** in 23% yield, with all integrations being correct this time.

### 3.5.6 Deprotection of 3-*tert*-butyl carboxylic acid umbelliferone–PD

With 3-*tert*-butyl carboxylic acid umbelliferone–PD **49** in hand, it then became pertinent to perform a *tert*-butyl deprotection in order to liberate its carboxylic groups and test whether this final PD structure was more water-soluble than umbelliferone–PD **29**. Consequently, 3-*tert*-butyl carboxylic acid umbelliferone–PD **49** was subjected to 25% TFA/CH<sub>2</sub>Cl<sub>2</sub> at 21 °C and monitored by TLC. After 4 h stirring, TLC analysis showed full consumption of PD **49**, with the desired carboxylic acid umbelliferone–PD **45** being isolated in quantitative yield (Scheme 42).

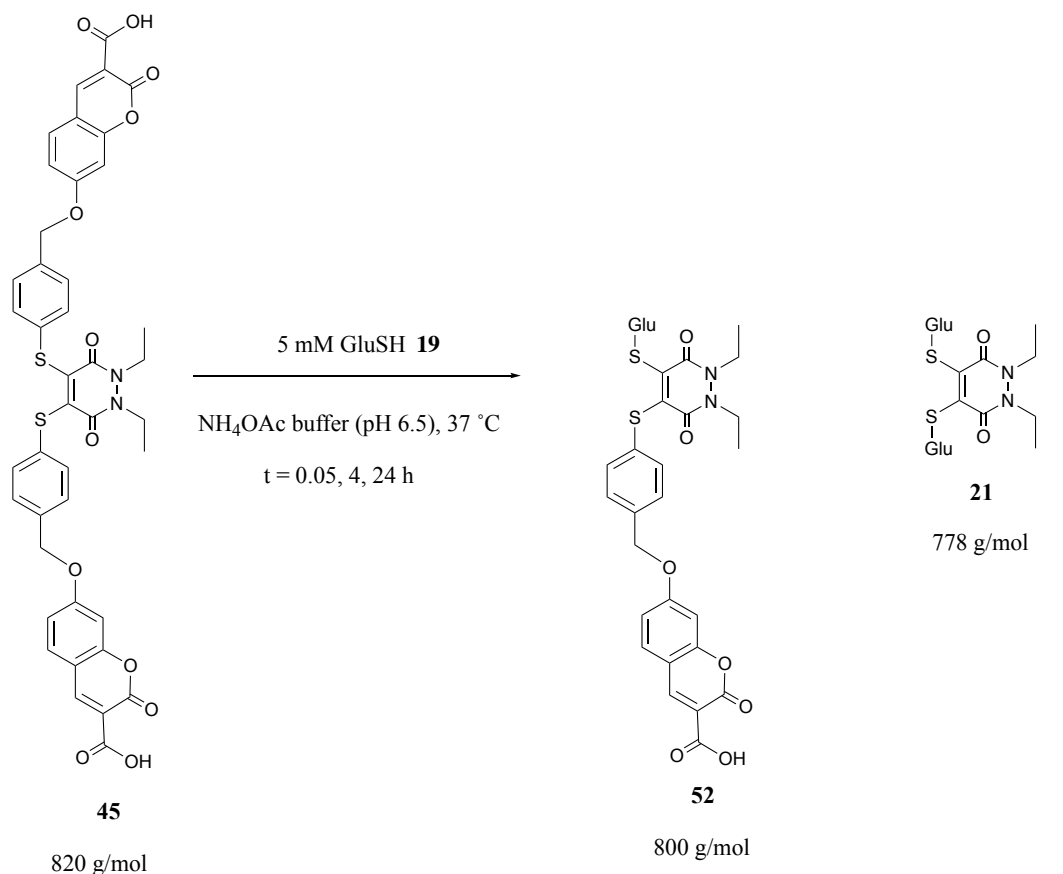


Scheme 42. Formation of carboxylic acid umbelliferone–PD **45** from 3-*tert*-butyl carboxylic acid umbelliferone–PD **48** when stirred in 25% TFA/CH<sub>2</sub>Cl<sub>2</sub>.

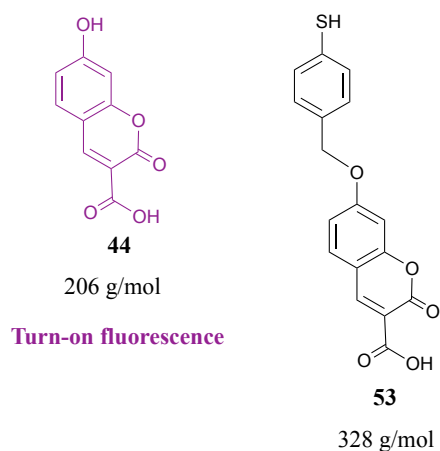
### **3.6 Incubation of carboxylic acid umbelliferone PD with GluSH**

Now that carboxylic acid umbelliferone–PD **45** had finally been isolated, it was time to test whether the addition of a carboxylic acid group on each umbelliferone moiety had been enough to ensure the PD did not crash out of solution, as had been the case with umbelliferone–PD **29**. As with previous incubations, PD **45** was made up to a final concentration of 0.5 mM relative to 5 mM of GluSH **19**, with the reaction conducted in a 5% DMSO/ammonium acetate buffer mixture, pH 6.5, 37 °C, and taking three time points: 0.05, 4 and 24 h (Scheme 43).





#### Quenched fluorescence



Scheme 43. Incubation of carboxylic acid umbelliferone–PD **45** with GluSH **19** at pH 6.5 and 37 °C, and potential products of the reaction.

Gratifyingly, when PD **45** was added to the buffer mixture, no reaction suspension was observed, suggesting good water solubility of PD **45**. As can be seen from Figure 40, though there is still some starting material **45** at the t = 0.05 h time point, there is also a significant UV peak corresponding to mono-substituted GluSH PD **52** at 1.50 mins.

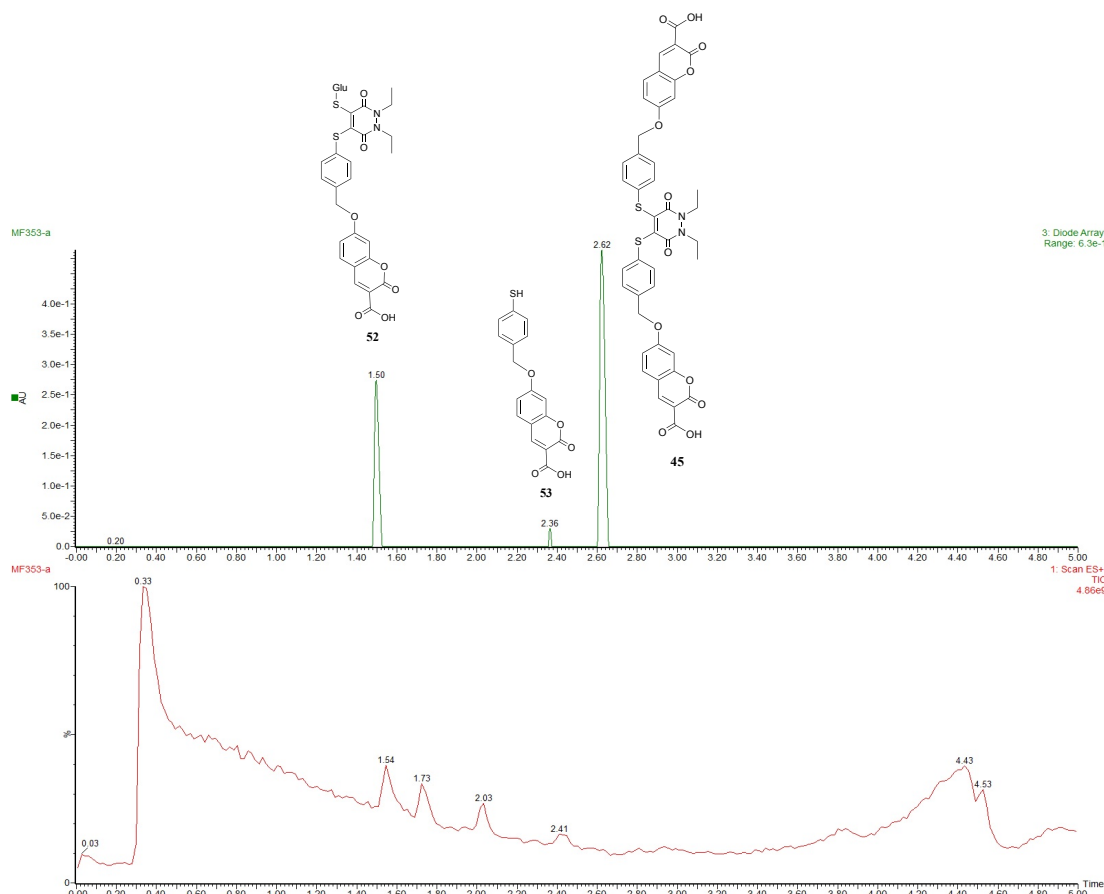


Figure 40. TIC, UV trace and UV trace area of the incubation of carboxylic acid umbelliferone–PD **45** and GluSH **19** at  $t = 0.05$  h at pH 6.5 and 37 °C.

It can also be seen from the TIC trace that a species elutes off the column at 2.36 mins, and has a mass of 329 g/mol, which corresponds to the intact self-immolative linker **53**. In an ideal scenario, none of this linker would be observed even at  $t = 0.05$  h, as it is supposed to undergo self-immolative cleavage as soon as it is formed. However, as the UV peak is small, it was hoped that this suggested only a small amount of intact linker **53** present at this time, and it was further hoped that it would be completely absent from both the TIC and UV trace by the  $t = 4$  h time point. Gratifyingly, this is exactly what occurred: no intact linker **53** was observed even in the TIC trace at the  $t = 4$  h time point, insinuating that although present in potentially small quantities at  $t = 0.05$  h, it degrades quickly enough for it to be absent from the reaction mixture just under 4 h later. Consequently, the disappearance by the  $t = 4$  h time point of linker **53** inevitably lead to the presence of a new UV trace peak corresponding to the self-immolatively released fluorophore **44**, confirming PD **45**'s ability to act as the conduit for GluSH-triggered turn-on fluorescence. By  $t = 24$  h, the main species observed in the UV trace were fluorophore **44** at 1.04 mins and bis-

GluSH PD **21** at 0.57 mins (Figure 41), confirming the similarity in reactivity of carboxylic acid umbelliferone–PD **45** and the much structurally simpler bis-thioaryl PD **12**, both of which were the only PDs incubated with GluSH **19** at pH 6.5 which were completely consumed at the  $t = 24$  h time point. The peaks at 1.74 and 2.03 mins in the TIC, and at 3.79 mins in the UV of Figure 41 are impurities which were consistently present, and thought to be unrelated to the species of interest.

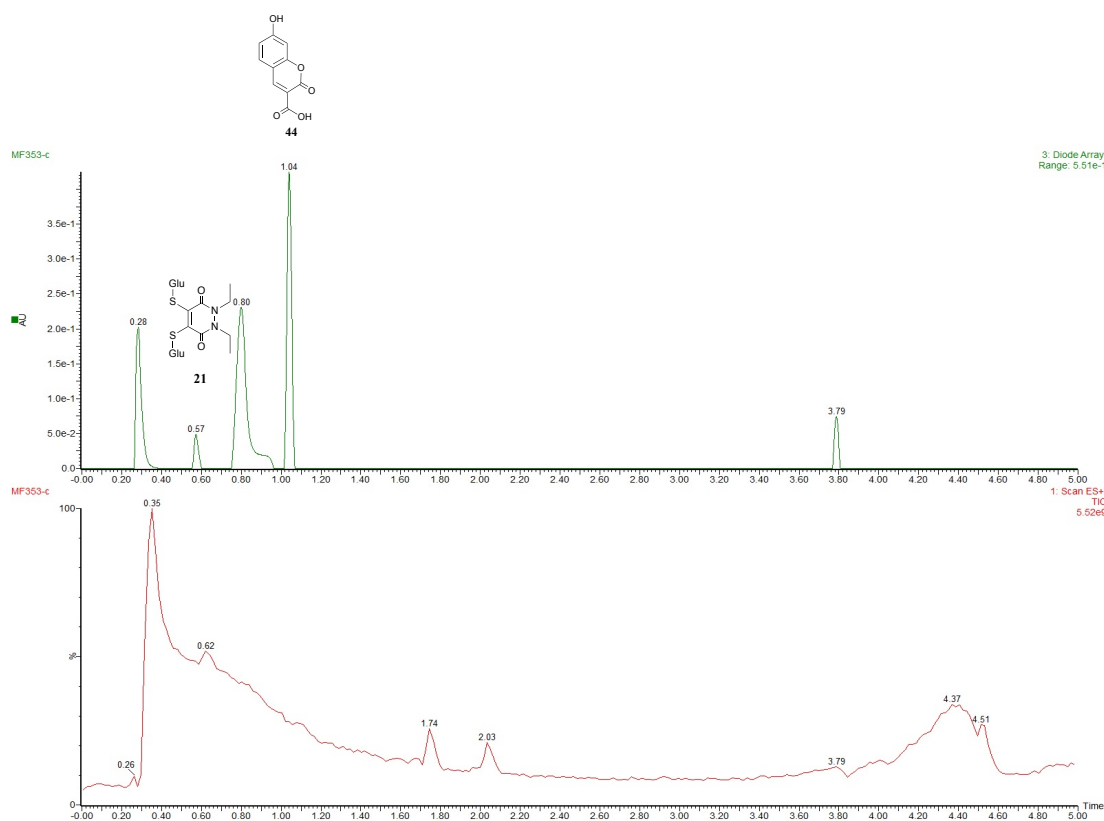


Figure 41. TIC, UV trace and UV trace area of the incubation of carboxylic acid umbelliferone–PD **45** and GluSH **19** at  $t = 24$  h at pH 6.5 and 37 °C.

### 3.7 Fluorescence emission spectroscopy of the carboxylic acid umbelliferone–PD + GluSH incubation

Now that the successful self-immolative release and thus turn-on fluorescence of species **44** from carboxylic acid umbelliferone–PD **45** had been demonstrated by masses using LC-MS, specifically the turn-on fluorescence nature of this incubation was corroborated by monitoring its fluorescence emission. As any increase in fluorescence would necessarily be due to the appearance of fluorophore **44**, it was first required to measure the latter's maximum UV absorption, and its subsequent maximum fluorescence emission when excited at this absorption wavelength. When subjected to UV–Vis spectroscopy, it was found that fluorophore **44** has a maximum UV absorption at 335 nm, and that its maximum fluorescence emission when excited at this wavelength occurs at 447 nm.

Consequently, at each time point that a portion of the carboxylic acid umbelliferone–PD **45** + GluSH **19** incubation was removed for LC-MS analysis, a second portion was taken destined for fluorescence emission spectroscopy. The reaction sample was excited at 335 nm and the increase in fluorescence measured across the three time points ( $t = 0.05, 4$  and  $24$  h) (Figure 42). As can be seen from the figure, the fluorescence emission spectroscopy indeed shows turn-on fluorescence as the concentration of the self-immolatively released fluorophore **44** increases. There is little difference in fluorescence intensity between the carboxylic acid umbelliferone–PD **45** control and the  $t = 0.05$  h time point, but by  $t = 4$  h, the fluorescence emission intensity has increased drastically from 25.8 a.u. to 165.1 a.u., with the rise being less pronounced between 4 h and its value of 199.6 a.u. after 24 h. The rise in fluorescence emission between the  $t = 4$  and 24 h time points, though relatively small, can perhaps be explained by incomplete reaction at  $t = 4$  h: at this time point there is still some unreacted PDs **45** and **52** in solution.

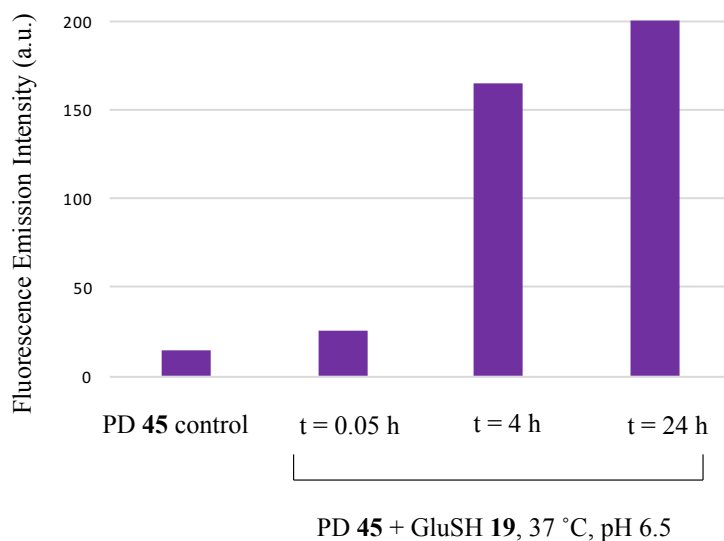


Figure 42. Fluorescence emission spectroscopy of the carboxylic acid umbelliferone PD 45 + GluSH 19 incubation, at  $t = 0.05$ , 4 and 24 h when excited at 335 nm. PD 45 was used as a control.

### 3.8 Conclusion

In conclusion, this thesis' focus on the two thiol reactive centres of the PD core has culminated in the successful synthesis of two fluorophore-PDs **29** and **45** by derivatising the thioaryl groups of bis-thioaryl PD **12**. A novel, sulfur-based self-immolative linker which was inspired by Van Bittner *et al.* and Gois *et al.* was designed to attach the fluorophores to the PD's thiol moieties, with successful self-immolative release of the fluorophore being observed when the PDs were subjected to tumour cell-mimicking conditions. The first umbelliferone-PD **29** was important in proving that the sulfur-based self-immolative mechanism worked, with the release of umbelliferone **25** on LC-MS demonstrating the fact. Unfortunately, umbelliferone-PD **29** displayed suboptimal buffer solubility, limiting its use as a viable SMDC precursor. In an effort to solve these solubility issues a second fluorophore-PD **45** incorporating carboxylic acid functional groups was synthesised. As well as dissolving fully in buffer, the reactivity of fluorophore-PD **45** closely mirrored that of the simpler PD it was based on: bis-thioaryl PD **12**. The turn-on fluorescence of the reaction between fluorophore-PD **45** and GluSH **19** was confirmed both by LC-MS and fluorescence emission spectroscopy.

# Chapter 4 Derivatisation of the *N*-handles of the pyridazinedione core

The outstanding scope of the PD scaffold has been demonstrated extensively by research conducted in the Chudasama and Caddick groups,<sup>102,111,138</sup> with the *N*-handles of the PD core able to incorporate alkynes and azides<sup>111</sup> than can be utilised in “click” reactions for the attachment of cytotoxic drugs such as Dox,<sup>139</sup> fluorescent dyes such as AlexaFluor488<sup>TM</sup> and sulfo-cyanine5 azides<sup>107,139</sup> and porphyrin analogues.<sup>138</sup> “Click” chemistry generally refers to high-yielding reactions that can occur under benign solvent conditions and which form minimal by-products.<sup>140,141</sup> In addition, “click” reactions are noted for a strong thermodynamic driving force which gives rise to rapid and selective formation of a single product. Further, this type of reaction tends to proceed *via* bioorthogonal pathways and as a result has enjoyed widespread use in protein modification.<sup>142,143</sup>

Maruani *et al.* have developed a “dual click” strategy that allows for the site-selective dual modification of proteins.<sup>102</sup> They achieved this by synthesising a PD incorporating both a terminal and strained alkyne on the adjacent *N*-handles (Figure 43).

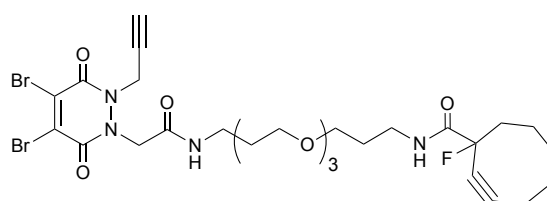


Figure 43. Structure of the “dual strategy” PD developed by Maruani *et al.*<sup>102</sup>

The structure of this PD allows for the sequential addition of different targets to the same PD core: a copper azide-alkyne cycloaddition (CuAAC) on the terminal, non-strained alkyne, and a copper-free strain promoted azide-alkyne cycloaddition (SPAAC) “click” on the cyclooctyne.<sup>102</sup>

As a result, this chapter will focus on the construction of an SMDC precursor, in which particular focus will centre on derivatising the PD core’s *N*-handles to alkynes, azides and PEG groups.

## 4.1 Results and discussion

### 4.1.1 Synthesis of azide-alkyne PEG PDs

While the structure of the carboxylic acid umbelliferone–PD **45** was well-suited for demonstrating that GluSH can substitute its thioaryl moieties and lead to turn-on fluorescence *via* self-immolative cleavage, it was kept in mind that this PD scaffold could have potential use in an SMDC. In an effort to synthesise a molecule that more closely resembled an SMDC precursor, it was reasoned that the diethyl portions of PD **45** could be substituted for more relevant handles. For instance, one diethyl group could be substituted for an amide linkage, useful for the potential attachment of a targeting ligand (such as folic acid), and “click” reactions if we installed a click handle. The other diethyl moiety could be exchanged for a simple PEG group, whose function would be to aid the water solubility of the construct in the presence of any hydrophobic drugs, fluorophores or targeting ligands. With this in mind, it was decided that a construct resembling **54** could be a good objective to work towards (Figure 44).

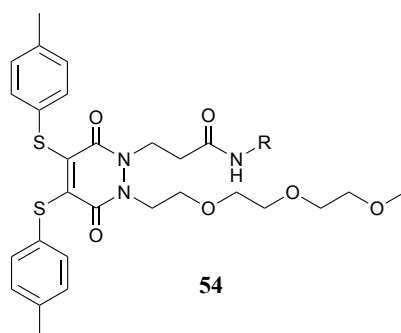
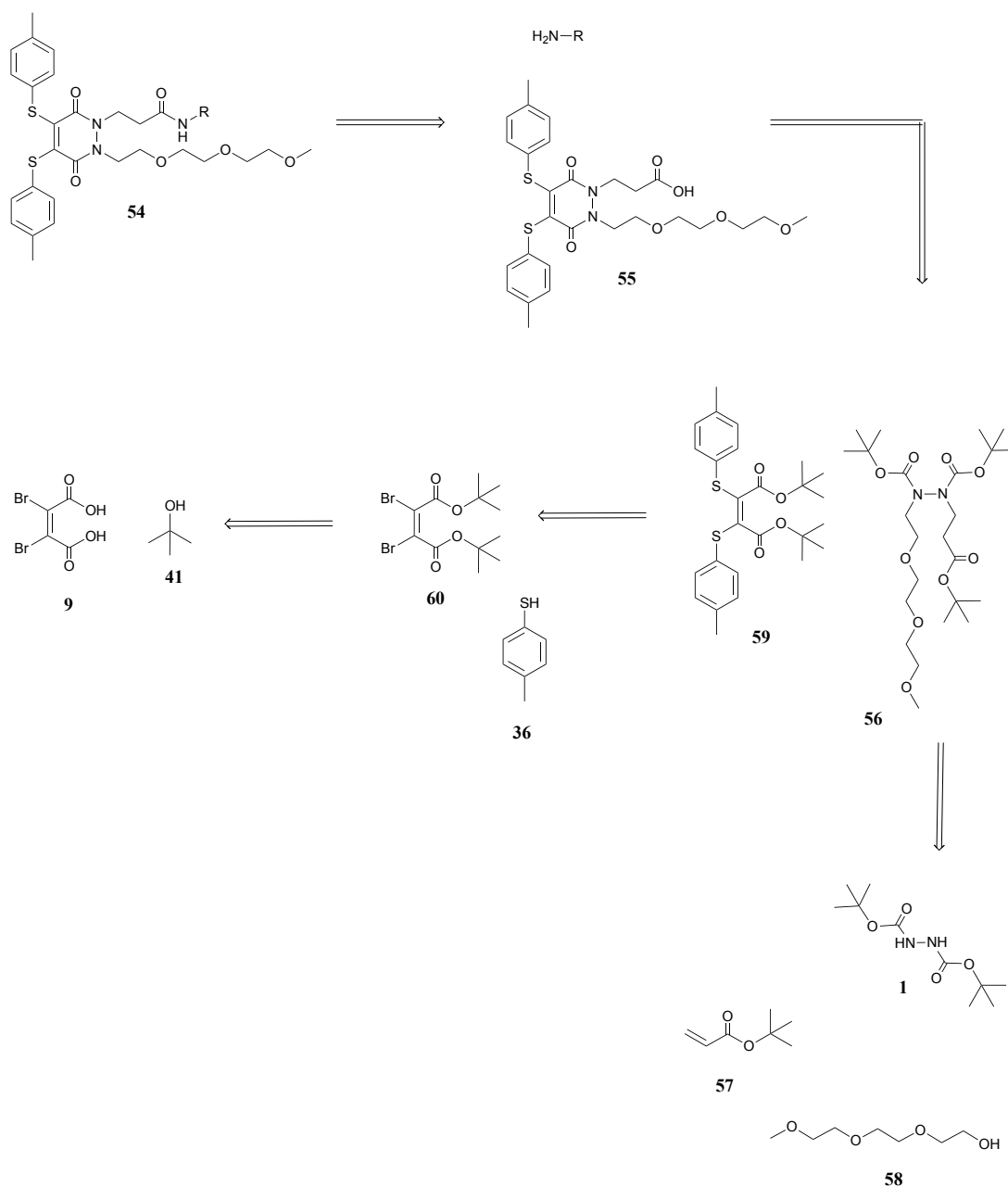


Figure 44. Structure of construct **54**: the PD scaffold’s diethyl handles have been exchanged for an amide linkage and a simple PEG group.

As carboxylic acids had been successfully *tert*-butyl-protected in this project (see Scheme 36), a retrosynthetic analysis was performed on compound **54** (Scheme 44). It was envisaged that the forward reaction of said analysis could consist of a *tert*-butyl protection of dibromomaleic acid **9**, followed by 4-methylbenzenethiol **36** addition to give species **59**. This could then be condensed with hydrazine **56** to give acid PEG PD **55**. The latter could subsequently be subjected to amide coupling conditions in order to afford the desired construct **54**. It was also noted that hydrazine **56** would need to be synthesised over several steps.



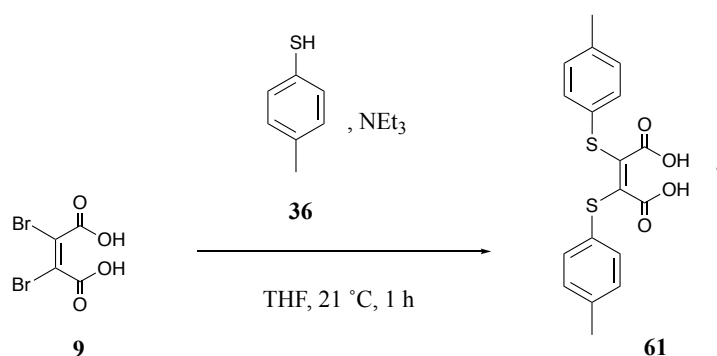
Scheme 44. Retrosynthetic analysis of SMDC precursor **54**.

#### 4.1.1.1 Attempted *tert*-butyl protection of dibromomaleic acid

As described, the first step of the synthesis constitutes the *tert*-butyl protection of dibromomaleic acid **9**, so that its bromine atoms can be subsequently substituted by 4-methylbenzenethiol **36** (Scheme 44). The *tert*-butyl protection was proposed as free carboxylic acid groups could potentially be adversely affected by the other reagents and/or make the final product of this step difficult to purify. However, it was decided to undertake an initial reaction without protection of the carboxylic acid groups to



gauge whether these would survive and whether an acid protection step would be warranted in the first place (Scheme 45).



Scheme 45. Potential formation of 2,3-bis(*p*-tolylthio)maleic acid **61** from 4-methylbenzenethiol **36** and dibromomaleic acid **9** in the absence of *tert*-butyl protection of the acid groups.

As the carboxylic acid OH groups of dibromomaleic acid **9** have a lower pK<sub>a</sub> than the thiolate of 4-methylbenzenethiol **36**, it was envisaged that the thiolate may engage in two competing pathways: substitution of the bromine atoms of compound **9** as well as deprotonation of its acidic protons. The latter pathway in and of itself was not thought to be problematic as a work-up could quench any remaining carboxylate, however, in light of the decarboxylation pathway observed for compound **39** once its OH had been deprotonated (Scheme 35), it was kept in mind that a similar reaction could take place here too.

As a result, it was decided to pre-mix a 1:1 mixture of thiol **36** and NEt<sub>3</sub> and subsequently add this to dibromomaleic acid **9** (final solution contained 1 eq. dibromomaleic **9** and 2 eq. thiol **36**) and monitor by TLC until full consumption of **9** was observed.

After stirring for 1 h at 21 °C, no remaining dibromomaleic acid **9** was visible by TLC and 2 new product spots were present. As in the case of the synthesis of compound **42**, the similarity in R<sub>f</sub> values of these two species meant they had to be separated by preparatory TLC. Upon isolation and characterisation, the higher spot was found to be the mono-decarboxylated compound **62**. Such little material was recovered from the bottom spot that full spectroscopic data could not be obtained. However, due to the two aromatic region doublets seen in the <sup>1</sup>H NMR spectrum (as opposed to the

aromatic region multiplets seen in the  $^1\text{H}$  NMR spectrum of **62**) and mass spec analysis, the bottom spot was tentatively assigned as compound **63** (Figure 45).

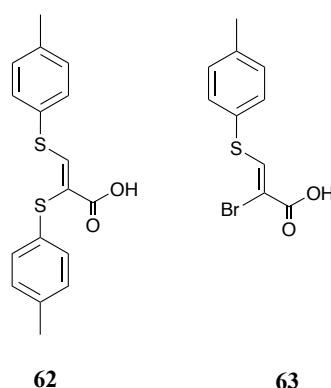
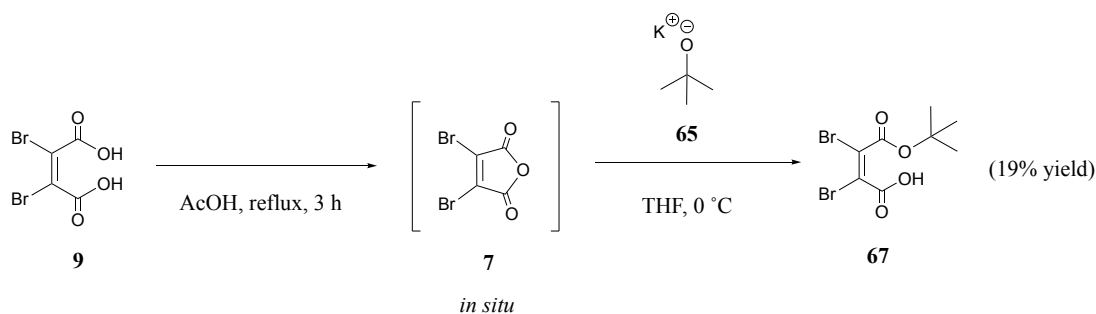


Figure 45. Mono-decarboxylated acid **62** and tentatively mono-decarboxylated mono-bromo compound **63**.

The results of this experiment, especially the fact that none of the desired compound **61** was formed, suggested that the carboxylic acid groups needed to be protected in order to avoid decarboxylation. An initial search of the literature revealed that no published protocols exist for the *tert*-butyl protection of dibromomaleic acid **9**. The only protocols that exist for the *tert*-butyl protection of the non-brominated analogue of dibromomaleic acid **9**, maleic acid, utilised sulfuric acid and isobutene gas,<sup>144,145</sup> and this last reagent was not stocked in the laboratory. It was thus decided to submit dibromomaleic acid **9** to the same *tert*-butyl protection conditions employed to transform compound **39** to **42** (Scheme 46). Despite the TLC of this reaction showing a single product spot after 24 h,  $^1\text{H}$  NMR analysis post-purification showed a complex, unidentifiable mixture as well as absence of the characteristic *tert*-butyl protons peak at *ca.* 1.43–1.48 ppm. The  $^{13}\text{C}$  NMR spectrum also lacked the quaternary *tert*-butyl signals that come at *ca.* 80–82 ppm.

The reaction was repeated by pre-stirring dibromomaleic acid **9** with EDC·HCl at 0 °C for 1 h in lieu of the 30 mins for the first reaction, but the result was the same: very complex NMR spectra that lacked the characteristic *tert*-butyl signals.



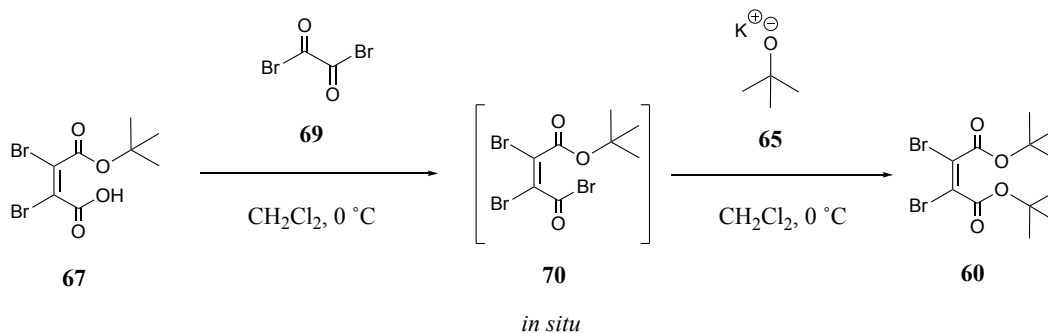


Scheme 48. Synthesis of (*Z*)-2,3-dibromo-4-(*tert*-butoxy)-4-oxobut-2-enoic acid **67** from potassium *tert*-butoxide **65** and dibromomaleic anhydride **7**, formed *in situ* from dibromomaleic acid **9**.

With compound **67** in hand, it was decided not to attempt to install the second *tert*-butyl group using the standard conditions of *tert*-butanol **41**, EDC·HCl and DMAP. If, as rationalised, the reaction shown in Scheme 46 had proved unsuccessful due to the steric hindrance imposed by having two close oxygens bound to EDC·HCl, then the same outcome was thought to be likely in this case too. Instead, an attempt was made to transform the remaining carboxyl into an improved leaving group which could then be substituted by potassium *tert*-butoxide **65**. Once again, a search of the literature was undertaken and a synthesis was found in which an  $\alpha,\beta$ -unsaturated carboxylic acid was first converted into an acyl chloride using oxalyl chloride **68** (*in situ*) and then treated with potassium *tert*-butoxide **65** to give the *tert*-butyl protected acid.<sup>148</sup> As compound **67** contains bromines, it was decided not to employ oxalyl chloride **68** as it was reasoned that the expelled chloride atoms could potentially substitute the bromine atoms of **67**. Thus, oxalyl bromide **69** was chosen instead for conversion of **67** into an acyl bromide and subsequent addition of potassium *tert*-butoxide **65** to yield the desired, doubly *tert*-butyl protected species **60** (Scheme 49).

This reaction was attempted twice and the major issue encountered was that acyl bromide **70** was not UV active and stained extremely poorly on TLC, as well as being rationalised to be readily prone to hydrolysis. It was therefore difficult to be certain when it had formed. Instead, TLC monitoring focused on the consumption of **67**. In the first reaction, TLC analysis showed that **67** had been fully consumed after 2 h of stirring with oxalyl bromide **69**, so potassium *tert*-butoxide **65** was then added and the reaction was stirred for 30 mins at 0 °C. After this time, the TLC revealed an extremely faint product spot (not UV-active) and the crude material was subjected to flash

column chromatography. However, the attempted isolation of this spot proved challenging due to staining very poorly and therefore being very difficult to visualise by TLC. The collected fractions showed no presence of the desired **60**.



Scheme 49. Proposed formation of compound **60** from potassium *tert*-butoxide **65** and *in situ* formation of acyl bromide **70** from oxalyl bromide **69** and (Z)-2,3-dibromo-4-(*tert*-butoxy)-4-oxobut-2-enoic acid **67**.

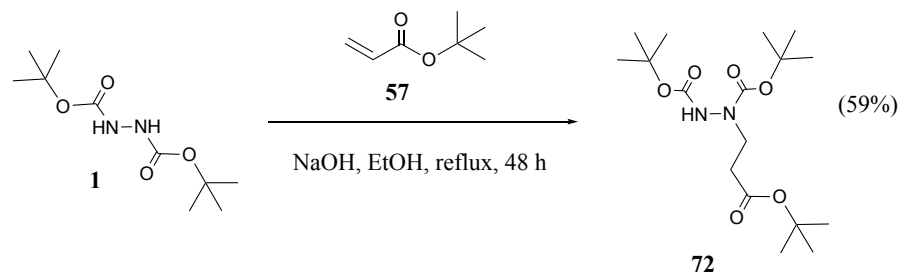
When the reaction was attempted for the second time, it was noted that unlike the first, starting material **67** had not been fully consumed after 2 h of stirring with oxalyl bromide **69**. Acyl bromide formation from a carboxylic acid should occur rather quickly and so potassium *tert*-butoxide **65** was added to the solution in any case. It was decided not to wait for full consumption of **67** because this reaction produces HBr **71**, which could potentially remove the *tert*-butyl group of **67** and/or remove the *tert*-butyl groups of any potentially formed **60**.

As with the first reaction, a new product spot was observed by TLC (alongside unreacted compound **61**), but proved difficult to visualise and none of the fractions obtained after flash column chromatography were shown to contain the desired compound **60** by  $^1\text{H}$  NMR analysis.

#### 4.1.1.2 Synthesis of di-bromo PEG acid PD

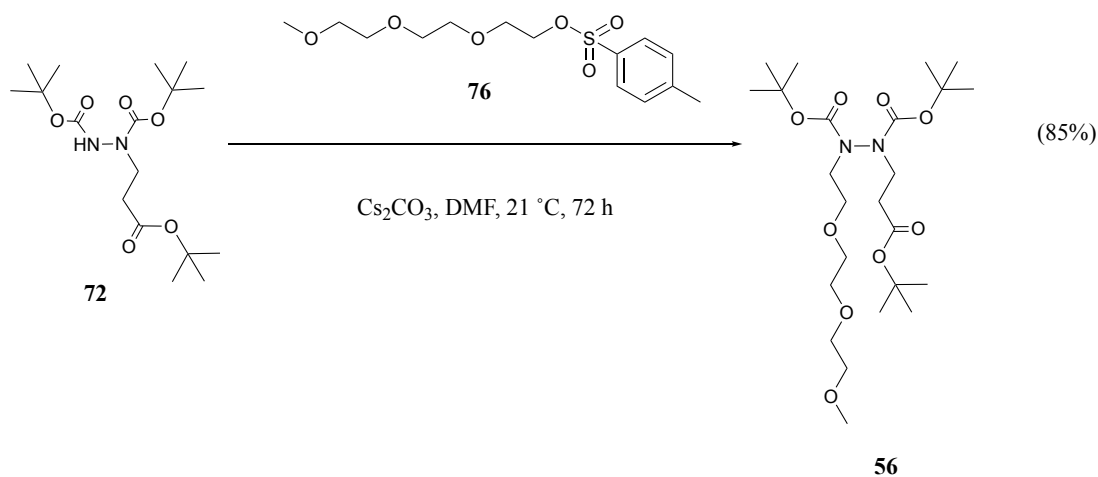
At this stage in the project the choice was made to abandon the efforts to doubly *tert*-butyl protect dibromomaleic acid **9** as all the attempts had proven unsuccessful and a significant amount of time had been spent on this endeavour. An alternative synthesis was proposed: reacting dibromomaleic acid **9** directly with hydrazine **56**, making it pertinent to commence the latter's synthesis from commercially available boc-

protected hydrazine **1**. Consequently, boc-protected hydrazine **1** was reacted with *tert*-butyl acrylate **57** over 48 h to afford mono-substituted boc-protected hydrazine **72** (Scheme 50).



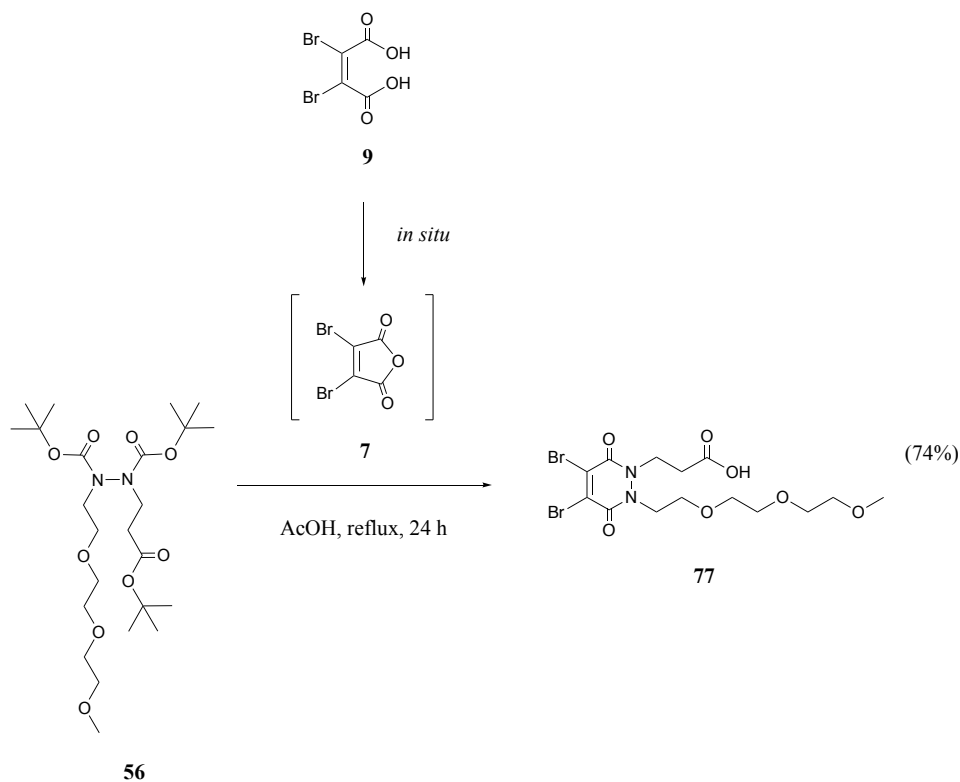
Scheme 50. Synthesis of mono-substituted boc-protected hydrazine **72** from *tert*-butyl acrylate **57** and boc-protected hydrazine **1**.

For the next step of installing a simple PEG group onto **72**, it was thought that triethylene glycol monomethyl ether **58** could be reacted with methanesulfonyl chloride **73** and that the methanesulfonyl portion of the resulting PEG **74** could act as a leaving group when attacked by the NH of hydrazine **72**. However, no reaction occurred between methanesulfonyl PEG **74** and hydrazine **72**, despite many conditions being trialled in an attempt to get the reaction to proceed (bases such as cesium carbonate, NaOH and NaH. Solvents such as DMF, EtOH and THF. Temperatures ranging from 21 °C to 78 °C). It was then decided to synthesise a PEG with a better sulfur-based leaving group, and to this end triethylene glycol monomethyl ether **58** was reacted with 4-methylbenzenesulfonyl chloride **75** and the resulting PEG **76** was added to hydrazine **72** to afford the desired doubly-substituted boc-protected hydrazine **56** in an excellent yield of 85% (Scheme 51).



Scheme 51. Synthesis of doubly-substituted boc-protected hydrazine **56** from PEG **76** and mono-substituted boc-protected hydrazine **72**.

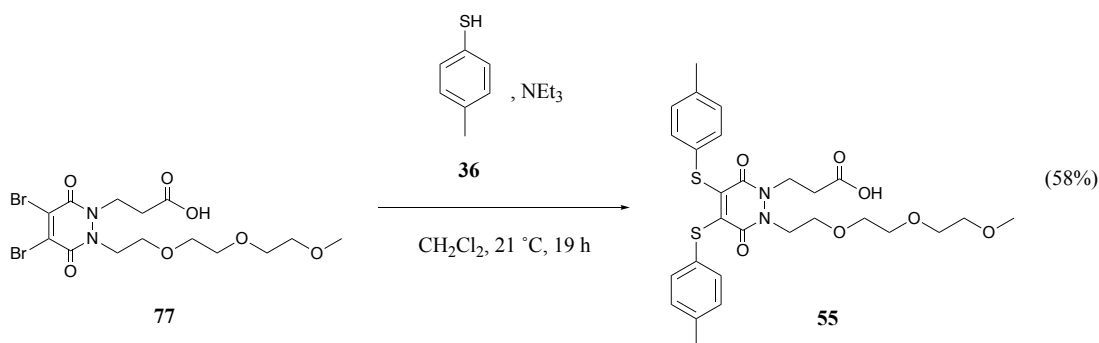
With this hydrazine in hand it was then reacted with dibromomaleic acid **9** in AcOH, where dibromomaleic anhydride **7** forms *in situ*. At the same time, all of the *tert*-butyl groups of hydrazine **56** should become deprotected under these acidic conditions, liberating the NHs to attack anhydride **7**. The desired di-bromo PEG acid PD **77** was obtained in 74% yield (Scheme 52).



Scheme 52. Synthesis of di-bromo PEG acid PD **77** from dibromomaleic anhydride **7** (formed from dibromomaleic acid **9** *in situ*) and hydrazine **56**.

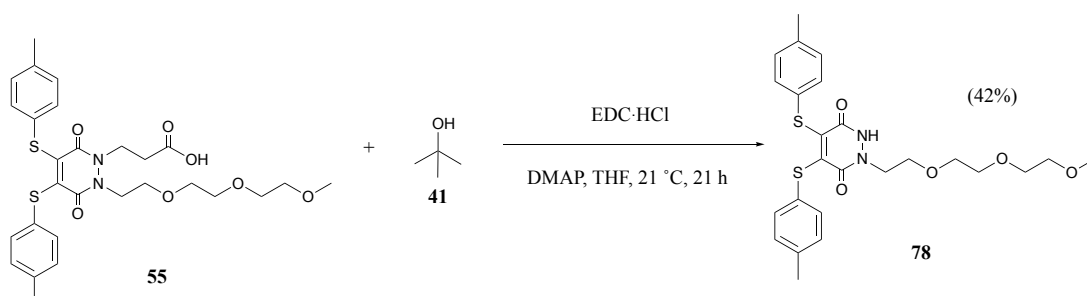
### 4.1.1.3 Synthesis of di-thiol PEG acid PD

The subsequent step, then, and the one prior to the amide couplings, was to add the aromatic thiols in the likely case they would substitute the bromine atoms of di-bromo PEG acid PD **77**. When 4-methylbenzenethiol PD **36** was added to the latter, the desired bis-thiol PEG acid PD **55** was, as expected, isolated, in a moderate yield of 58% (Scheme 53).



Scheme 53. Synthesis of bis-thiol PEG acid PD **55** from 4-methylbenzenethiol **36** and di-bromo PEG acid PD **77**.

Now that thiol **36** had been shown to indeed substitute the bromine positions of **77** as expected, it was decided to attempt a *tert*-butyl protection of the acid group. This was done in an effort to show that this functionality could be masked in order to render easier purification of a construct that, for instance, underwent modifications to the thiol portions (such as bromination, attachment of fluorophore etc.). If achieved, the acid would be able to be deprotected after these transformations had taken place. To this end, the previously employed reagents of *tert*-butanol **41**, EDC·HCl and DMAP were employed in an effort to protect bis-thiol PEG acid PD **55** (Scheme 54).



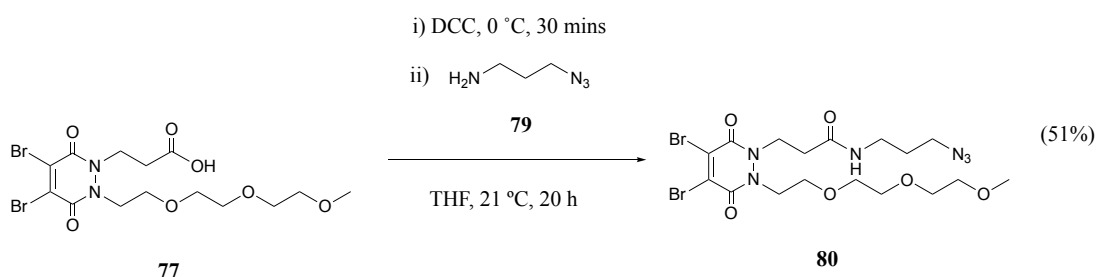
Scheme 54. Unexpected formation of **78** via loss of the propanoic acid chain when bis-thiol PEG acid PD **55** was reacted with EDC·HCl, DMAP and *tert*-butanol **41**.



As can be seen in Scheme 54, no protected product was isolated and only PD **78** was observed, where bis-thiol PEG acid PD **55** lost the entirety of its *N*-propanoic acid portion. At this stage, the decision was made to abandon protection attempts and press forward with amide couplings.

#### 4.1.1.4 Azide and alkyne amide couplings on di-bromo PEG acid PD

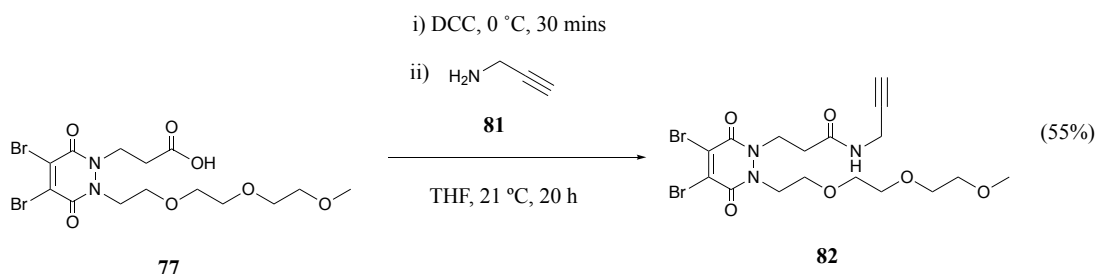
To this end, di-bromo PEG acid PD **77** had to be re-synthesised, with the syntheses of its precursor hydrazines **72** and **56** taking 72 h and 48 h respectively. When PD **77** was finally isolated, it was decided to conduct the amide couplings at this point, as it had already been shown that 4-methylbenzenethiol **36** successfully substituted PD **77**'s bromines, and so this substitution reaction did not need to be repeated. It was considered a better use of time to show that the amide couplings worked, and then, if there were time and material left over, to add a thiol in the last step of the SMDC precursor synthesis. As a result, it was decided to employ previously synthesised 3-azido-1-propanamine **79** for the first amide coupling, as adding an azide to PD **77**'s scaffold could constitute the installation of a very useful handle for subsequent click reactions. Di-bromo PEG acid PD **77** was activated with DCC at 0 °C for 30 mins, after which time 3-azido-1-propanamine **79** was added and the reaction mixture stirred at 21 °C for a further 20 h. This yielded the desired di-bromo PEG azide PD **80** in a 51% yield (Scheme 55).



Scheme 55. Synthesis of di-bromo PEG azide PD **80** from 3-azido-1-propanamine **79** and di-bromo PEG acid PD **77**.

Once the di-bromo PEG azide PD **80** had been successfully isolated, a second amide coupling to PD **77** was envisaged. The amine chosen was propargylamine **81**, due to the fact that installing an alkyne functionality on PD **77** would be complementary to the azide functionality of PD **80**, with both alkynes and azides able to undergo “click” reactions. Consequently, PD **77** was reacted with propargylamine **81** under identical

conditions utilised for the synthesis of PD **80**, with di-bromo PEG alkyne PD **82** being obtained in a slightly higher yield of 55% than the 51% isolated of di-bromo PEG azide PD **80** (Scheme 56).



Scheme 56. Synthesis of di-bromo PEG alkyne PD **82** from propargylamine **81** and di-bromo PEG acid PD **77**.

Once both the azide- and alkyne-based di-bromo PEG PDs **80** and **82** had been isolated, it was recognised that the final step in constructing a potential SMDC precursor was to substitute the bromine positions with an aromatic thiol. As the methyl group of 4-methylbenzenethiol **36** had been shown to permit functionalisation in order to construct fluorophore-PDs, this same thiol was selected for addition to PDs **80** and **82**. After just 10 mins stirring at 21 °C, bis-thioaryl PEG azide PD **83** and bis-thioaryl PEG alkyne PD **84** were isolated in 82% and 85% yield respectively (Figure 46).

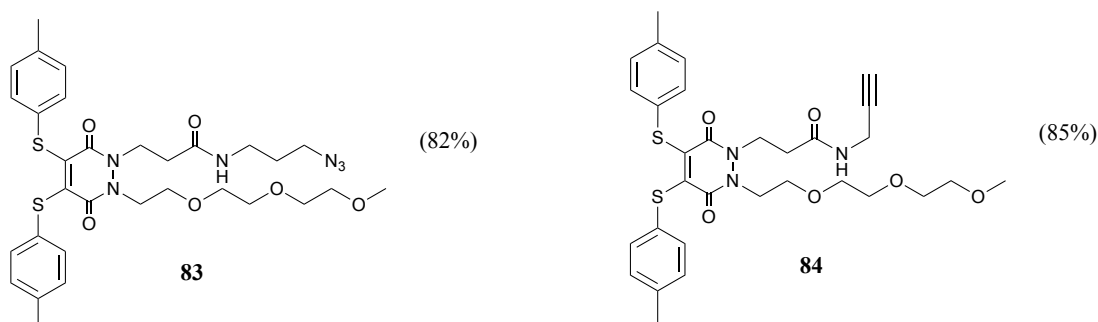


Figure 46. Structures of bis-thiol PEG azide PD **83** and bis-thiol PEG alkyne PD **84**.

The fact PDs **83** and **84** were obtained in excellent yields after only 10 mins stirring at 21 °C, confirms the high reactivity of their bromine positions, and demonstrates that this reactivity is not adversely affected by the PD's PEG, alkyne and azide groups. In fact, the yields of these structurally complex and derivatised bis-thioaryl PDs were higher than that achieved for the simple diethyl bis-thioaryl PD **12** (76%) after 10 mins stirring at 21 °C. It was gratifying to see, at this final stage in the project, that the bis-thioaryl PDs **83** and **84** had been synthesised in a similarly high yield to the bis-

thioaryl PD **12**, a molecule on which much of the self-immolative design of carboxylic acid umbelliferone–PD **45** had been based. Furthermore, PDs **83** and **84** can be considered to be SMDC precursors, containing the PEG group to aid solubility of hydrophobic drugs and tumour-targeting ligands; the alkyne and azide groups for “click” reactions in order to install a fluorophore or tumour-targeting ligand; and the aromatic thiol moieties, also available for further derivatisation in order to attach drugs or fluorophores that could be self-immolatively released under tumour-specific conditions.

## 4.2 Conclusion

In conclusion, this portion of the thesis focussed on the *N*-handles of the PD core and has resulted in the successful synthesis of di-bromo acid-, azide- and alkyne PEG PDs. The initial strategy of making these constructs consisted of the attempted *tert*-butyl protection of dibromomaleic acid **9** so that the thiol moieties could be added and potentially derivatised first, with hydrazine condensation to form the PD being the final step in the synthesis. The unsuccessful *tert*-butyl protection of both acid groups of dibromomaleic acid **9** led to the conception of a reverse strategy in which the condensation of the derivatised hydrazine and dibromomaleic acid **9** to form the PEG acid PD would constitute the first step, followed by the final addition of the relevant thiols. This reversal proved to be successful, with the versatilities of the final SMDC precursors **83** and **84** demonstrated by possessing three distinct groups on the same PD platform, all of which are relevant to the future design of a complete SMDC.

## Chapter 5 Conclusions and Outlook

In conclusion, the two defining portions of the 3,6-PD platform have been developed and extended in such a way as to enable the successful construction of SMDC precursors. The first of these said portions, the thiol reactive centres of the PD, were reacted with aryl- and alkyl-thiols, which were subsequently subjected to both human blood-mimicking and two (pHs 6.5 and 5.0) intracellular conditions. All the thio-PD constructs were stable in the human-blood conditions, as desired, and all experienced some degree of GluSH-triggered degradation when incubated under tumour cell-specific conditions, with bis-thioaryl PD **12** outperforming the other four candidates by a significant margin. The thio-PDs' stability in blood serum and instability inside conditions similar to those inside a cell are exactly the characteristics desired in an optimal SMDC, and thus also in an ideal SMDC precursor. The thioaryl moieties of PD **12** were then derivatised in order to synthesise fluorophore-PDs, where the fluorophore component was attached to the PD *via* a novel, sulfur-based self-immolative linker. Incubation of these fluorophore-PDs under intracellular conditions demonstrated the correct functioning of this self-degradation release mechanism, with the release of the fluorophore and thus turn-on fluorescence of the incubation able to be tracked both by LC-MS and fluorescence spectroscopy.

The second portion of the PD platform to be explored in this thesis were its *N*-handles, which had been kept as simple diethyl groups while work had been conducted on the thiol reactive centres. Once the sulfur-based self-immolative mechanism had been vindicated, attention was turned to substituting the diethyl handles for groups that have much greater utility and relevancy to an SMDC precursor. Both di-bromo azide- and alkyne PEG PDs were synthesised, with two thioaryl moieties being successfully installed onto both to form two SMDC precursors with azide and alkyne functionalities. These SMDC precursors' alkyne and azide groups could be utilised for click-based or cycloaddition installation of a targeting ligand or fluorophore; its PEG functionality could serve to aid with water solubility to combat the hydrophobic nature of targeting ligands, cytotoxic drugs or fluorophores; and the aromatic thiol groups for incorporation of drugs and fluorophores that could be detached in a self-immolative manner when the SMDC is taken up into a tumour cell. The successful installation of

three distinct groups on the PD core pays homage to its versatile and modular nature as a platform for the construction of a system which is a viable precursor to a full SMDC.

## 5.1 Outlook

Given the aforementioned success of PDs in the construction and cell-killing ability of ADCs, it is pertinent to outline the future work to be conducted on SMDC precursors **83** and **84** that could enable its use in a complete SMDC targeted towards a particular cancer type.

### 5.1.1 Extension of the aryl moieties of SMDC precursors **83** and **84**

Though the presence of 4-methylbenzenethiol groups on SMDC precursors **83** and **84** is sufficient to show that non-protein thiol attachment to di-bromo PEG alkyne and azide PDs is viable and high-yielding, the next logical step in the advancement of **83** and **84** would involve the derivatisation of the thioaryl portion's methyl functionality in order to incorporate the novel sulfur-based self-immolative linker developed in this work. This could yield PDs **85** and **86** (Figure 47).

Assuming these structures remain water-soluble, which is likely considering they would now possess both carboxylic acid and PEG functionalities, the next step would constitute their incubation with GluSH **19** under the previously tested conditions to confirm that these larger, more complex structures still undergo the desired substitution by this highly abundant intracellular thiol.

A further challenge regarding the thiol reactive centres would be the synthesis of analogues of **83** and **84**, but which instead of having either two identical aromatic thiols substitute the bromine positions, have two different aromatic thiols on the same PD core, such as a thiophenol moiety and a 4-methylbenzenethiol group. As the bromine centres are fairly reactive, it is conceivable that simply adding 1 eq. of each in a stepwise fashion may not yield the desired product in an appreciable yield, and thus conditions such as diluting the reaction, cooling, adding < 1 eq. of each thiol etc. may all need to be investigated. If this were to be achieved then the PD platform's use as a

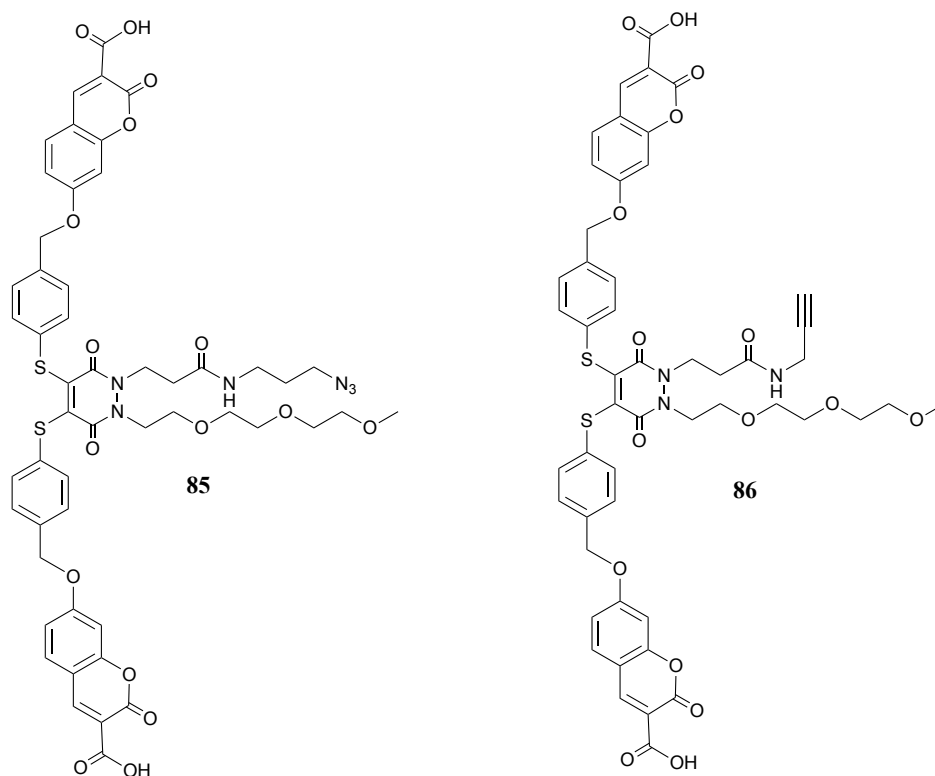
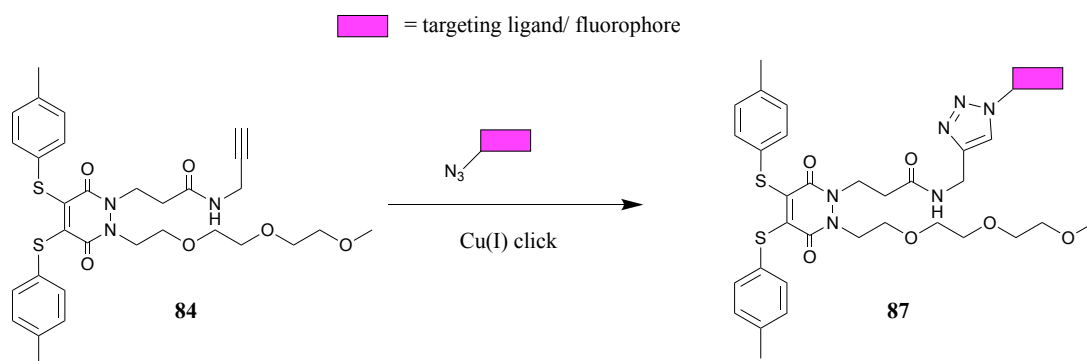


Figure 47. Structures of **85** and **86**, where the 4-methylbenzenethiol moieties have been extended to include the previously developed water-soluble fluorophore attached to the PD *via* a self-immolative linker.

flexible and modular core for an SMDC precursor would be further vindicated by virtue of being able to install four different groups on the same PD structure. This feat, if achieved, could allow further work to be done on installing two different aromatic thiols which could be derivatised independently, a useful asset for the potential installation of two different drugs or fluorophores on the adjacent thiol centres of the PD core.

### 5.1.2 Derivatisation of SMDC precursors' azide and alkyne groups

The presence of the azide and alkyne functionalities on PDs **83** and **84** respectively allows the potential for “click” reactions to take place on these handles for the purpose of installing targeting ligands or fluorophores onto the SMDC precursor construct (Scheme 48). Reaction of bis-thioaryl PEG alkyne PD **84** with an azide targeting ligand/fluorophore in a click, Cu(I)-catalysed process could afford 1,4-triazole PD **87**.



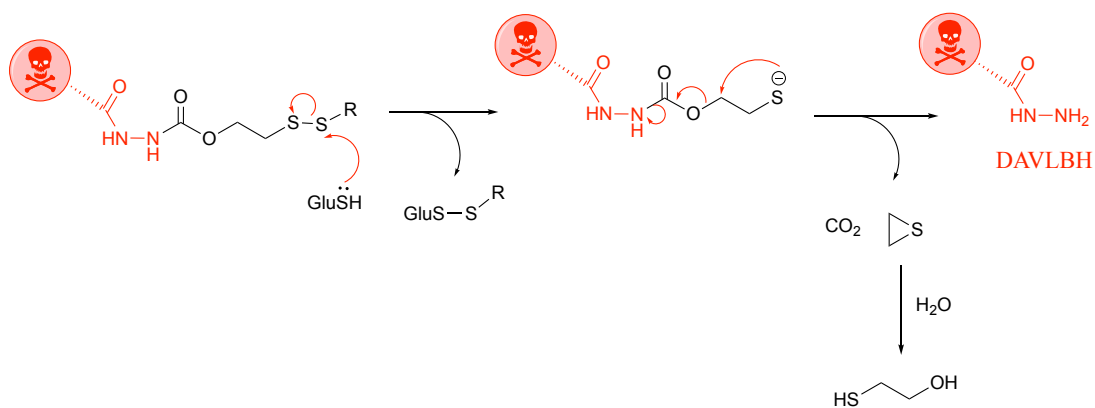
Scheme 48. Proposed reaction of bis-thioaryl PEG alkyne PD **84** with an azide targeting ligand/fluorophore to afford 1,4-triazole PD **87**.

The same could be done with bis-thioaryl PEG azide PD **83**, but this time having the targeting ligand/fluorophore linked to an alkyne functionality. It is also worth considering the installation of a strained alkyne to the PD construct, which can undergo “click” reactions without the need for copper.

The ideal end goal of such a project would be to construct a full SMDC which incorporated self-immolatively releasable drugs on the PD core’s thiol reactive centres, a targeting ligand conjugated to the platform *via* either an alkyne or azide, and a PEG chain on the remaining *N*-handle, the length and structure of which could be extended or modified to offset any potential hydrophobicity exerted by either the drug or targeting ligand, or both. Such a construct would then need to be submitted to the previously tested intracellular conditions, as well having its stability in human serum conditions evaluated. It is hoped that the SDMC precursors developed in this work provide a useful framework from which the described SMDC could be developed.

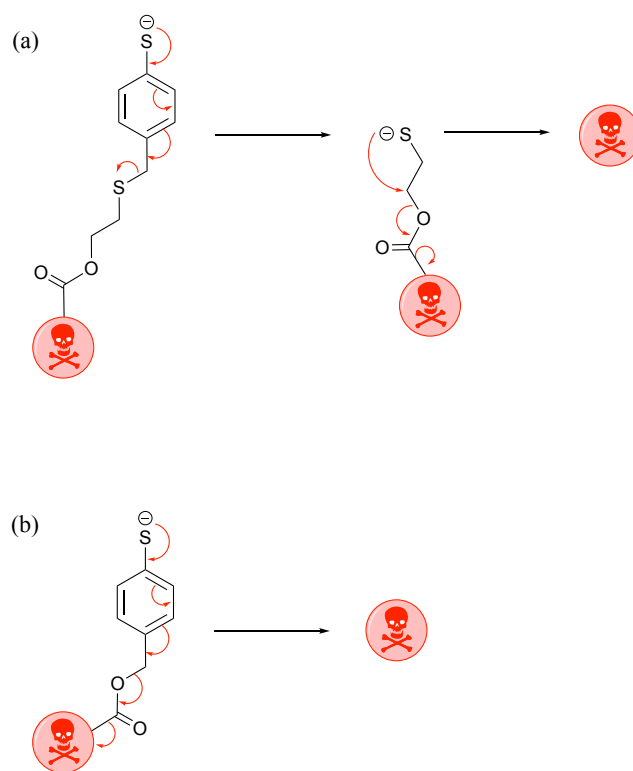
### 5.1.3 Aryl-alkyl self-immolative linkers

Though the work in this thesis has focussed exclusively on a thioaryl-based self-immolative linker to release an aromatic molecule, future work could centre on incorporating a releasable alkyl moiety. Inspiration could be taken from the release mechanism of vintafolide (Scheme 49). Vintafolide’s disulfide bond can be attacked by intracellular GluSH to form a thiolate. This thiolate can then expel the drug DAVLBH in a 1,2-elimination pathway by forming carbon dioxide and ethylene sulfide, and water present inside the cell can ring open the latter to produce 2-mercaptoethan-1-ol.



Scheme 49. Self-immolative, 1,2-elimination release mechanism of vintafolide.<sup>45</sup>

As disulfides are known to be cleaved in the bloodstream<sup>45,149</sup> it may be best to begin by designing an aryl-alkyl releasable linker that lacks this component. It is conceivable that the above structure may be readily incorporated into the structure developed in this work (Scheme 50).



Scheme 50. Possible aryl-alkyl self-immolative designs, with (a) based on a ring-closing mechanism and (b) centred on initial CO<sub>2</sub> release.

Pathway (a) of the above scheme is a direct incorporation of vintafolide's release strategy into the thioaryl self-immolative linker developed in this thesis. It may be relatively easy to synthesise; it can be envisaged that the brominated PD 32 could have



its bromines substituted by the drug thiol in an S<sub>N</sub>2 reaction. However, it remains to be seen whether the thiolate involved in the 1,2-elimination would be stabilised enough to form in the first place.

Pathway (b) is designed to proceed *via* the proven oxygen-based self-immolative linkage to release CO<sub>2</sub> and the relevant drug or fluorophore. However, this construct may be challenging to synthesise. Either way, it is plausible that a viable aryl-alkyl self-immolative linker on the PD construct could be developed, which would only improve the scope of this platform further by allowing both aromatic- and alkyl-based substituents to be attached to the aromatic thiols of the PD core.

# Experimental

## General Experimental

All reagents were purchased from Sigma Aldrich, Alfa Aesar, Thermo Fisher and Acros. Compounds and solvents were used as received. Petrol refers to petroleum ether (40–60 °C). All reactions were monitored by thin-layer chromatography (TLC) on pre-coated SIL G/UV254 silica gel plates (254  $\mu\text{m}$ ) purchased from VWR. Detection was by UV (254 nm and 365 nm) or chemical stain ( $\text{KMnO}_4$ ). The term *in vacuo* refers to solvent removal using Büchi rotary evaporation between 15–60 °C, at approximately 10 mmHg. Flash column chromatography was carried out with pre-coated FlashPure flash cartridges on a Biotage Isolera Spektra One flash chromatography system.  $^1\text{H}$  NMR spectra were obtained at 400, 600 or 700 MHz and  $^{13}\text{C}$  NMR spectra were obtained at 150 MHz on Bruker NMR instrument Avance III 400, Bruker NMR instrument Avance III 600 or Bruker NMR instrument Avance Neo 700. All samples were run at the default number of scans and at 21 °C. Chemical shifts ( $\delta$ ) for  $^1\text{H}$  NMR and  $^{13}\text{C}$  NMR are quoted relative to residual signals of the solvent on a parts per million (ppm) scale. Coupling constants ( $J$  values) are reported in Hertz (Hz) and are reported as  $J_{\text{H-H}}$  couplings. The multiplicity of each signal is indicated as s-singlet, d-doublet, t-triplet, q-quartet and m-multiplet (*i.e.* complex peak obtained due to overlap). App. implies apparent. Infrared spectra were obtained on a Perkin Elmer Spectrum 100 FTIR Spectrometer operating in ATR mode with frequencies given in reciprocal centimetres ( $\text{cm}^{-1}$ ). Optical rotations were determined from an average of five measurements at 21 °C using a 1 mL, 1 dm cell and were measured using a Perkin-Elmer 343 polarimeter.  $[\alpha]_{\text{D}}$  values are reported in  $10^{-1} \text{ deg cm}^2 \text{ g}^{-1}$ ,  $c$  is concentration (g/100 mL). Mass spectra were obtained for synthetic products, from the UCL mass spectroscopy service on either a Thermo Finnigan MAT900Xp (EI and CI) or Waters LCT Premier XE (ES) mass spectrometer. Melting points and decomposition temperatures (d.t.) were measured with a Gallenkamp apparatus and are uncorrected. All bioconjugation reactions were carried out in duplicate.

## **Bioconjugation General Remarks**

Conjugation experiments were carried out in standard polypropylene Eppendorf® safe-lock tubes (2.0 mL) at atmospheric pressure. All buffer solutions were prepared with doubly deionised water and filter-sterilised. Phosphate-buffered saline (PBS) was 10 mM phosphates, 137 mM NaCl and 2.7 mM KCl at pH 7.4. Ultrafiltration was carried out in Amicon® Ultra-4 Centrifugal Filter Units with a molecular weight cut-off (MWCO) of 5 kDa or in Vivaspin® 500 centrifugal concentrators (5 kDa MWCO). Centrifugation was carried out on an Eppendorf 5415R fixed angle rotor centrifuge operating at 14000 rcf at 21 °C or in an Eppendorf 5810 swing-bucket rotor centrifuge operating at 3220 rcf at 21 °C. FPLC system (GE Healthcare), equilibrated in PBS. Detection was by absorption at 280 nm.

## **Protein LC-MS for Figures S10–S18**

After the 4 h incubations, the samples were diluted to 3  $\mu$ M (0.2 mg/mL) in ammonium acetate buffer (20 mM, pH 7.4) and submitted to the UCL Chemistry Mass Spectrometry Facility at the Chemistry Department, UCL for analysis of unmodified protein on the Agilent 6510 QTOF LC-MS system (Agilent, UK). 10  $\mu$ L of each sample was injected onto a PLRP-S, 1000A, 8  $\mu$ M, 150 mm  $\times$  2.1 mm column, which was maintained at 60 °C. The separation was achieved using mobile phase A (95% H<sub>2</sub>O, 5% MeCN, 0.1% formic acid) and B (95% MeCN, 5% H<sub>2</sub>O, 0.1% formic acid) using a gradient elution. Agilent 6510 QTOF mass spectrometer was operated in a positive polarity mode, coupled with an ESI ion source. The ion source parameters were set up with a VCap of 3500 V, a gas temperature at 350 °C, a dry gas flow rate at 10 L/min and a nebulizer of 30 psig. MS TOF was acquired under conditions of a fragmentor at 350 V, a skimmer at 65 V and an acquisition rate at 0.5 spectra/s in a profile mode, within a scan range between 40,000 and 100,000  $m/z$  in profile mode. The raw data was converted to zero charge mass spectra using maximum entropy deconvolution algorithm over the *ca.* region 18.5–22.8 min with MassHunter software (version B.07.00).

## **Small Molecule LC-MS for Figures S19–S68, S75, S76 and S84–S86**

After 0.05, 1, 2, 4 and 24 h incubations, the samples were analysed on a Waters Acquity uPLC connected to Waters Acquity Single Quad Detector (SQD) and a photodiode array. Flow rate was set at 0.600 mL/min. LC-MS was performed on a ThermoScientific MSQ Plus connected to an Accela 1250 pump and Accela UV–Vis detector, with 10  $\mu$ L of each sample being injected onto an Acquity UPLC BEH C18 (50  $\times$  21 mm) maintained at 50 °C. The separation was achieved using mobile phase A (H<sub>2</sub>O, 0.1% formic acid) and B (MeCN, 0.1% formic acid) using a gradient elution. Mobile phase: 95:5 A:B; gradient over 5 minutes to 5:95 A:B. MS mode ES+; scan range: m/z 100–1000; scan time: 0.25 s. The electrospray source of the MS was operated with a capillary voltage of 3.5 kV and a cone voltage of 20 V were employed. All deconvoluted mass spectra were produced using the software provided by the manufacturer.

## **UV–Vis Spectroscopy**

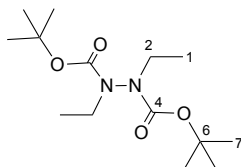
UV–Vis spectroscopy was used to determine the maximum UV absorption of a given reaction mixture. Measurements were obtained using a Varian Cary 100 Bio UV–Visible spectrophotometer operating at 21 °C. Sample buffer was used as a blank for baseline correction.

## **Fluorescence Emission Spectroscopy**

Fluorescence emission spectroscopy was used to determine the maximum fluorescence emission of a given reaction mixture. Measurements were obtained using a Varian Cary Eclipse Fluorescence spectrophotometer operating at 21 °C. Sample buffer was used as a blank for baseline correction.

## Experimental for Chapter 2

### Di-*tert*-butyl 1,2-diethylhydrazine-1,2-dicarboxylate **3**<sup>139</sup>



To a solution of di-*tert*-butyl hydrazine-1,2-dicarboxylate **1** (3.10 g, 13.4 mmol) and bromoethane **2** (2.34 mL, 31.4 mmol) in DMF (60 mL) was added cesium carbonate (17.4 g, 47.4 mmol), and the reaction mixture was stirred at 21 °C for 21 h. Following this, the reaction mixture was diluted with water (60 mL) and extracted with EtOAc (3 × 35 mL). The organic extracts were combined and subsequently washed with sat. aq. LiCl solution (35 mL). The organic phase was then dried over MgSO<sub>4</sub>, concentrated *in vacuo* and the crude residue was purified by flash column chromatography (0–20% EtOAc/Pet.). The appropriate fractions were then combined and concentrated *in vacuo* to afford di-*tert*-butyl 1,2-diethylhydrazine-1,2-dicarboxylate (3.70 g, 12.8 mmol, 96%) as a colourless oil. <sup>1</sup>H NMR (600 MHz, CDCl<sub>3</sub>, rotamers) δ 3.54–3.38 (m, 4H, H-2), 1.50–1.43 (m, 18H, H-7), 1.18–1.14 (m, 6H, H-1); <sup>13</sup>C NMR (150 MHz, CDCl<sub>3</sub>, rotamers) δ 155.8 (C-4), 155.1 (C-4), 154.9 (C-4), 80.7 (C-6), 80.6 (C-6), 80.5 (C-6), 46.4 (C-2), 44.4 (C-2), 28.4 (C-7), 28.1 (C-7), 13.6 (C-1), 13.1 (C-1), 13.0 (C-1); IR (thin film) 2976, 1703 cm<sup>-1</sup>.

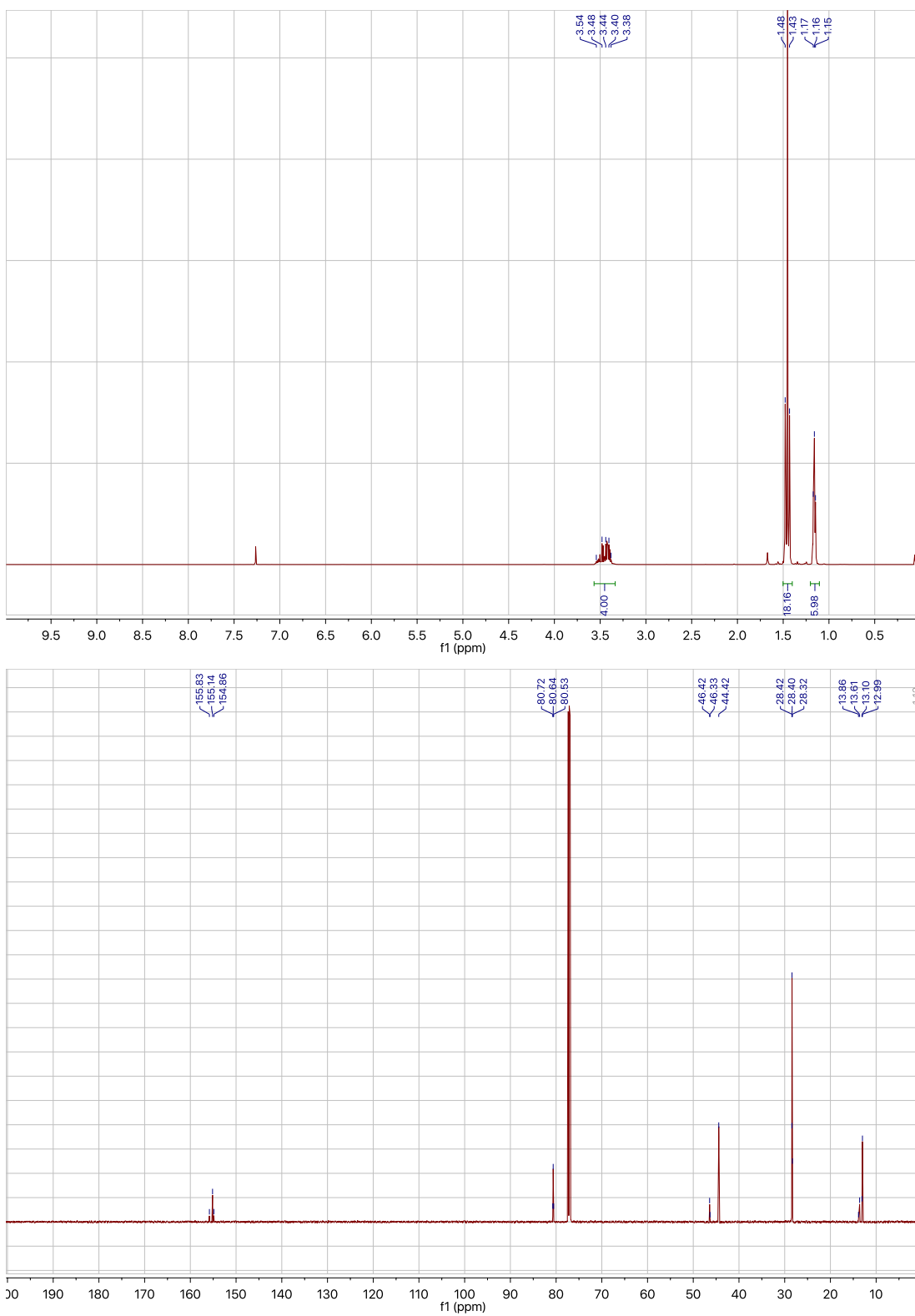
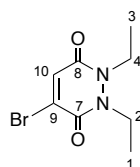
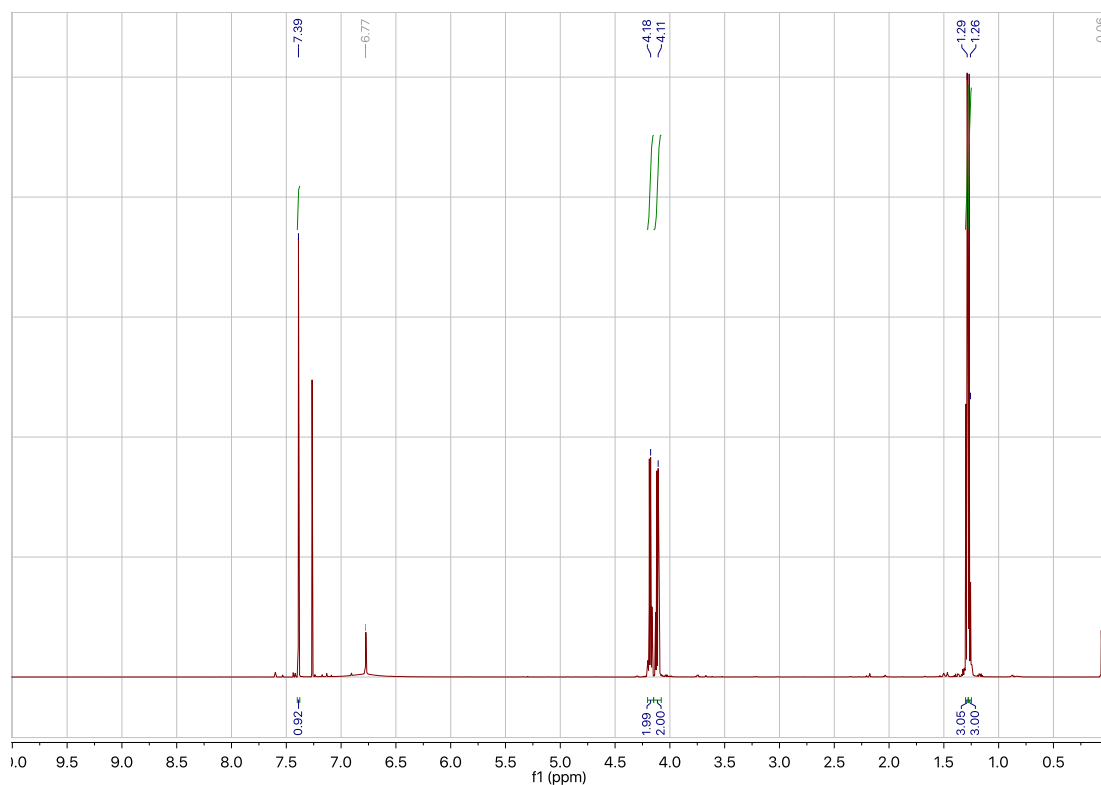


Figure S1.  $^1\text{H}$  and  $^{13}\text{C}$ NMR data for di-*tert*-butyl 1,2-diethylhydrazine-1,2-dicarboxylate **3**.

## 4-Bromo-1,2-diethyl-1,2-dihydropyridazine-3,6-dione **5**<sup>103</sup>



To a solution of bromomaleic anhydride **4** (0.16 mL, 1.7 mmol) in AcOH (5 mL) was added di-*tert*-butyl 1,2-diethylhydrazine-1,2-dicarboxylate **3** (0.50 g, 1.7 mmol), and the reaction mixture was stirred under reflux for 17 h. Following this, the reaction mixture was concentrated *in vacuo* with toluene co-evaporation (3 × 20 mL, as an azeotrope). The crude residue was purified by flash column chromatography (15–85% EtOAc/Pet.). The appropriate fractions were then combined and concentrated *in vacuo* to afford 4-bromo-1,2-diethyl-1,2-dihydropyridazine-3,6-dione (0.40 g, 1.6 mmol, 94%) as a brown solid. m.p 73–76 °C; <sup>1</sup>H NMR (600 MHz, CDCl<sub>3</sub>) δ 7.39 (s, 1H, H-10), 4.18 (q, *J* = 7.1 Hz, 2H, H-2), 4.11 (q, *J* = 7.1 Hz, 2H, H-4), 1.29 (t, *J* = 7.1 Hz, 3H, H-1), 1.26 (t, *J* = 7.1 Hz, 3H, H-3); <sup>13</sup>C NMR (150 MHz, CDCl<sub>3</sub>) δ 156.4 (C-7), 154.3 (C-8), 135.9 (C-10), 134.0 (C-9), 42.1 (C-2), 41.0 (C-4), 13.3 (C-1), 13.2 (C-3); IR (solid) 3047, 2982, 1712, 1615, 1591 cm<sup>-1</sup>.



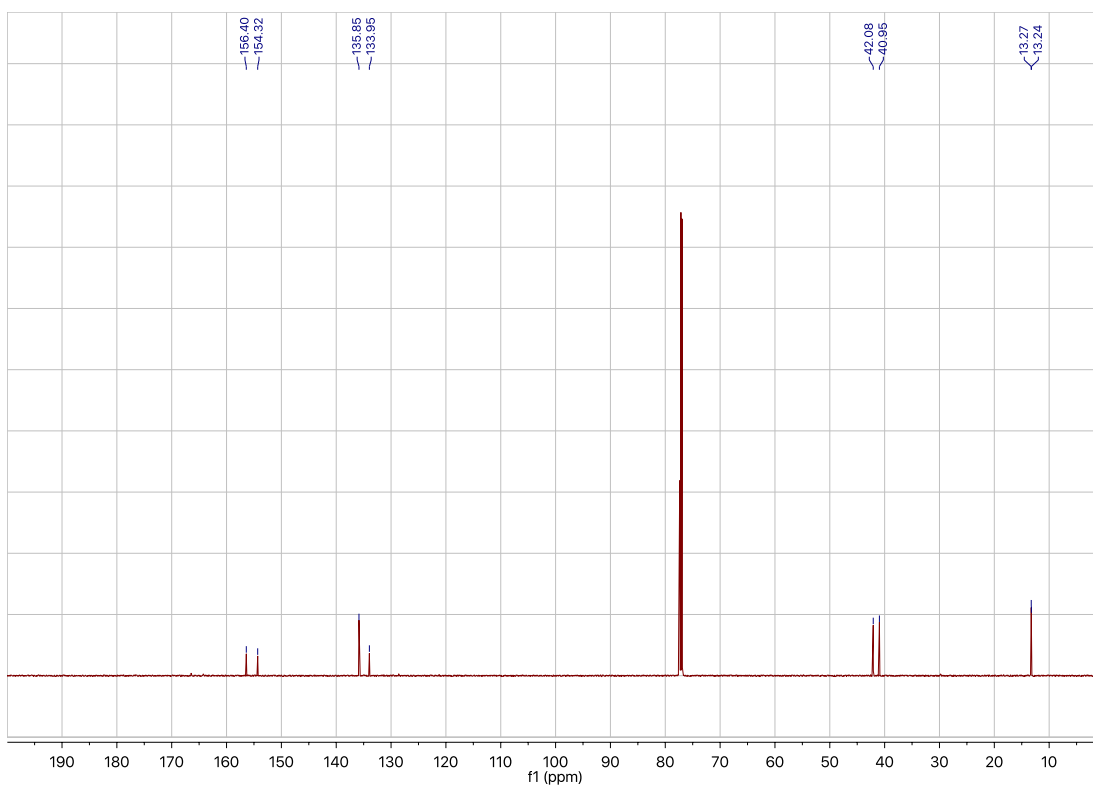
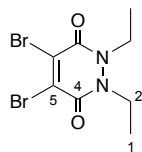


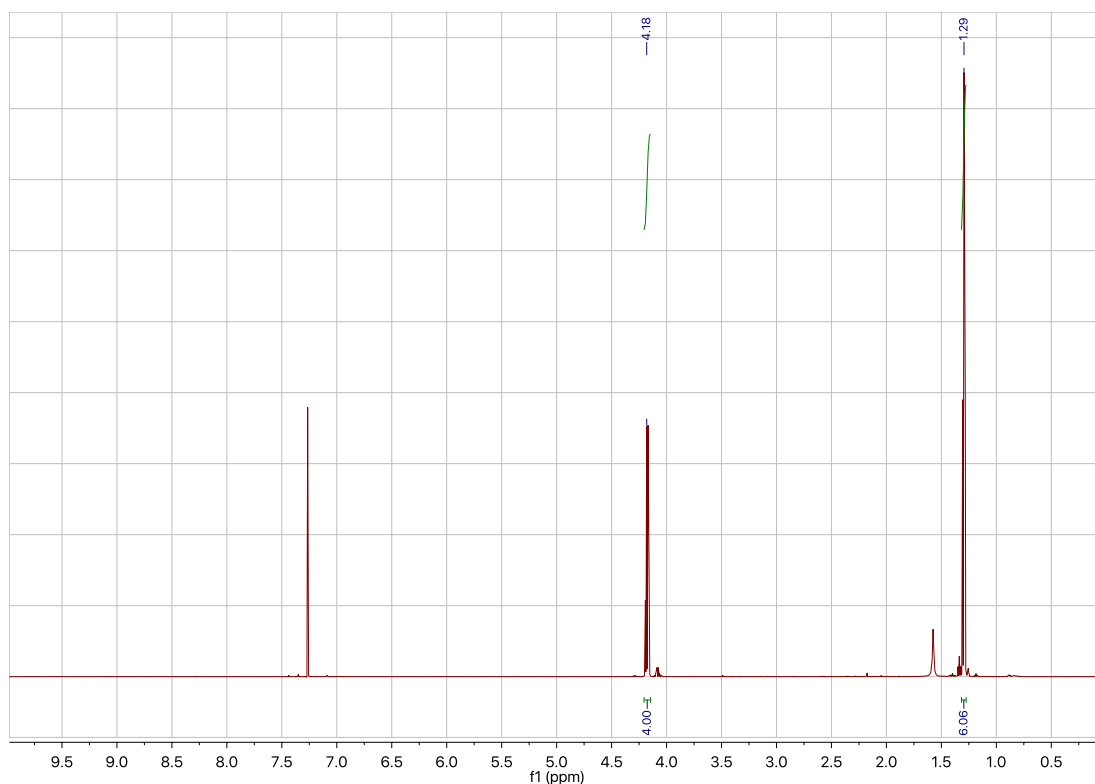
Figure S2.  $^1\text{H}$  and  $^{13}\text{C}$  NMR data for 4-bromo-1,2-diethyl-1,2-dihydropyridazine-3,6-dione **5**.



## 4,5-Dibromo-1,2-diethyl-1,2-dihydropyridazine-3,6-dione **8**<sup>139</sup>



To a solution of dibromomaleic acid **9** (1.27 g, 4.64 mmol) in AcOH (6 mL) was added di-*tert*-butyl 1,2-diethylhydrazine-1,2-dicarboxylate **3** (1.10 g, 3.81 mmol), and the reaction mixture was stirred under reflux for 20 h. Following this, the reaction mixture was concentrated *in vacuo* with toluene co-evaporation ( $3 \times 20$  mL, as an azeotrope). The crude residue was purified by flash column chromatography (15–60% EtOAc/Pet.). The appropriate fractions were then combined and concentrated *in vacuo* to afford 4,5-dibromo-1,2-diethyl-1,2-dihydropyridazine-3,6-dione (1.00 g, 3.07 mmol, 81%) as an orange solid. m.p. 115–117 °C;  $^1\text{H}$  NMR (600 MHz,  $\text{CDCl}_3$ )  $\delta$  4.18 (q,  $J = 7.1$  Hz, 4H, H-2), 1.29 (t,  $J = 7.1$  Hz, 6H, H-1);  $^{13}\text{C}$  NMR (150 MHz,  $\text{CDCl}_3$ )  $\delta$  153.3 (C-4), 136.1 (C-5), 42.5 (C-2), 13.2 (C-1); IR (solid) 2978, 2937, 1655, 1567  $\text{cm}^{-1}$ .



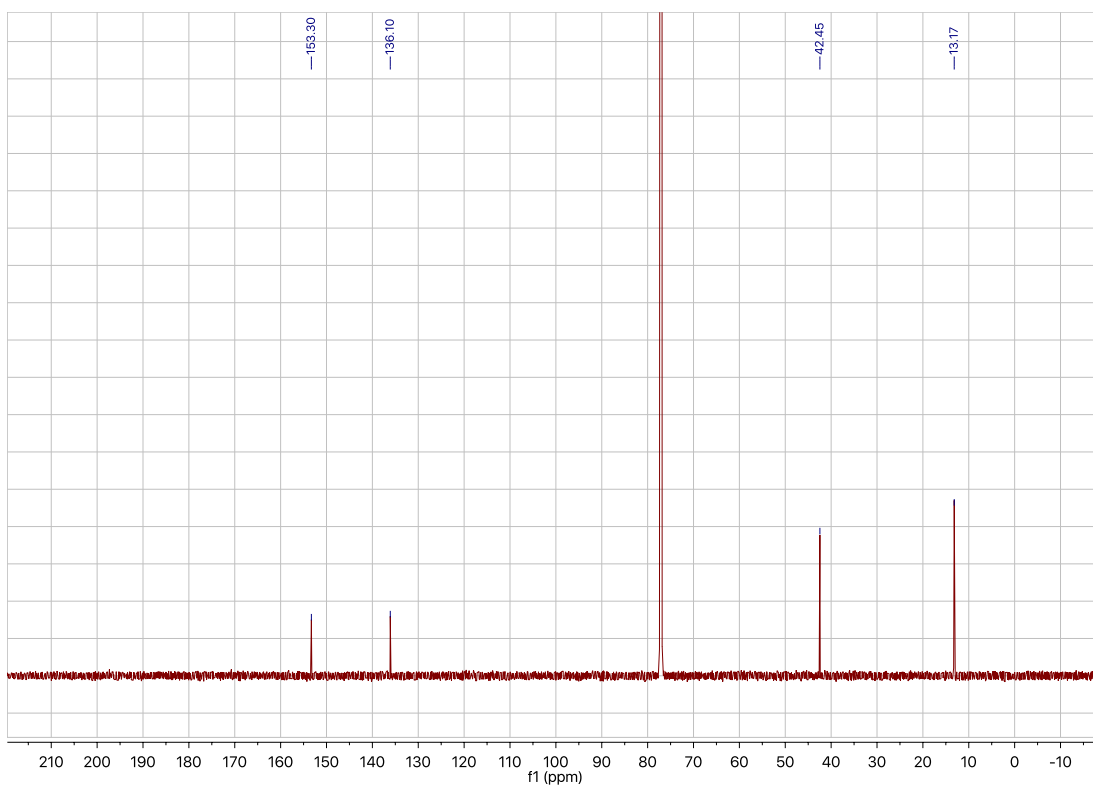
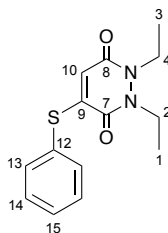


Figure S3.  $^1\text{H}$  and  $^{13}\text{C}$  NMR data for 4,5-dibromo-1,2-diethyl-1,2-dihydropyridazine-3,6-dione **8**.

## 1,2-Diethyl-4-(phenylthio)-1,2-dihydropyridazine-3,6-dione **11**



To a solution of thiophenol **10** (0.05 mL, 0.5 mmol) and triethylamine (0.18 mL, 1.3 mmol) in CH<sub>2</sub>Cl<sub>2</sub> (6 mL) at 21 °C, was added a solution of 4-bromo-1,2-diethyl-1,2-dihydropyridazine-3,6-dione **5** (0.11 g, 0.45 mmol) in CH<sub>2</sub>Cl<sub>2</sub> (6 mL), and the reaction mixture was stirred for 10 mins. Following this, the reaction mixture was diluted with CH<sub>2</sub>Cl<sub>2</sub> (20 mL) and washed with water (3 × 15 mL) and brine (15 mL). The organic phase was dried over MgSO<sub>4</sub>, concentrated *in vacuo* and the crude residue was purified by flash column chromatography (15–85% EtOAc/Pet.). The appropriate fractions were then combined and concentrated *in vacuo* to afford 1,2-diethyl-4-(phenylthio)-1,2-dihydropyridazine-3,6-dione (0.11 g, 0.40 mmol, 89%) as a green solid. m.p. 104–105 °C; <sup>1</sup>H NMR (600 MHz, CDCl<sub>3</sub>) δ 7.53–7.46 (m, 5H, H-13, H-14, H-15), 5.96 (s, 1H, H-10), 4.17 (q, *J* = 7.0 Hz, 2H, H-2), 4.07 (q, *J* = 7.0 Hz, 2H, H-4), 1.29 (t, *J* = 7.0 Hz, 3H, H-1), 1.21 (t, *J* = 7.0 Hz, 3H, H-3); <sup>13</sup>C NMR (150 MHz, CDCl<sub>3</sub>) δ 157.3 (C-7), 155.7 (C-8), 151.9 (C-9), 135.8 (C-12), 130.7 (C-13), 130.5 (C-14), 127.5 (C-15), 123.0 (C-10), 40.8 (C-2), 40.1 (C-4), 13.2 (C-1), 13.2 (C-3); IR (solid) 2967, 2926, 2854, 1654, 1616, 1573 cm<sup>-1</sup>; LRMS (ES+) 277 (100, [M+H]<sup>+</sup>); HRMS (ES+) calcd for C<sub>14</sub>H<sub>17</sub>N<sub>2</sub>O<sub>2</sub>S [M+H]<sup>+</sup> 277.1011, observed 277.1011.

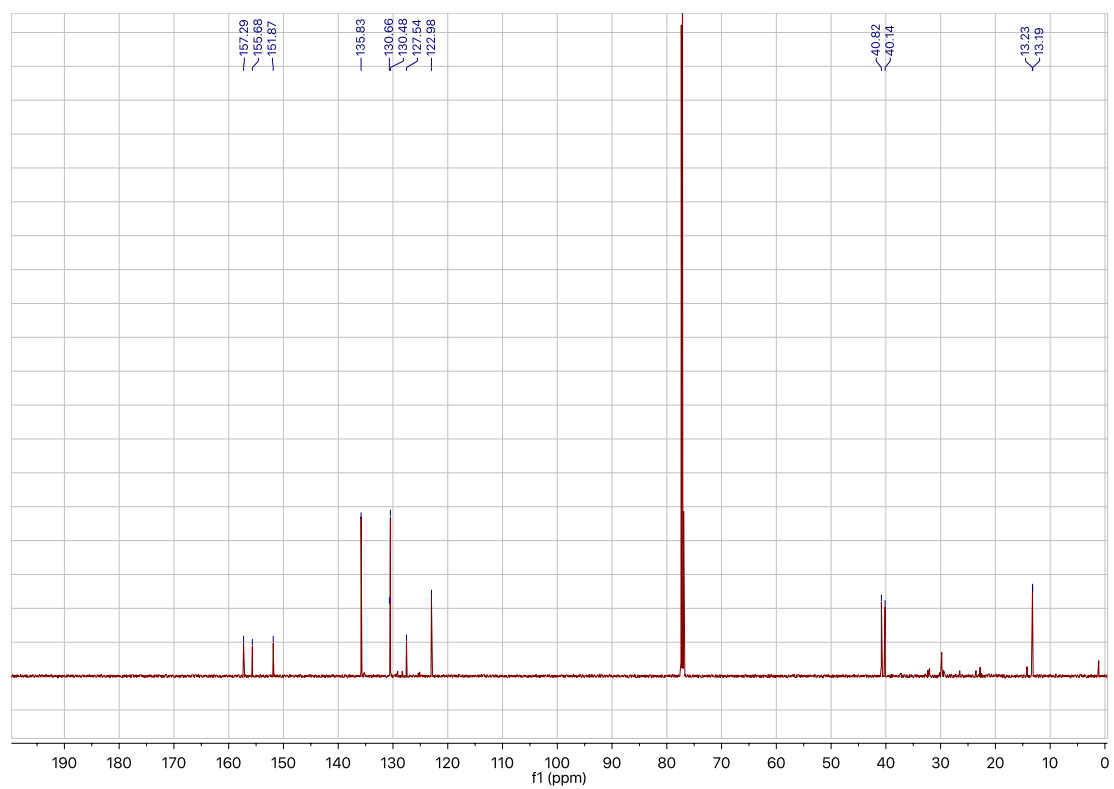
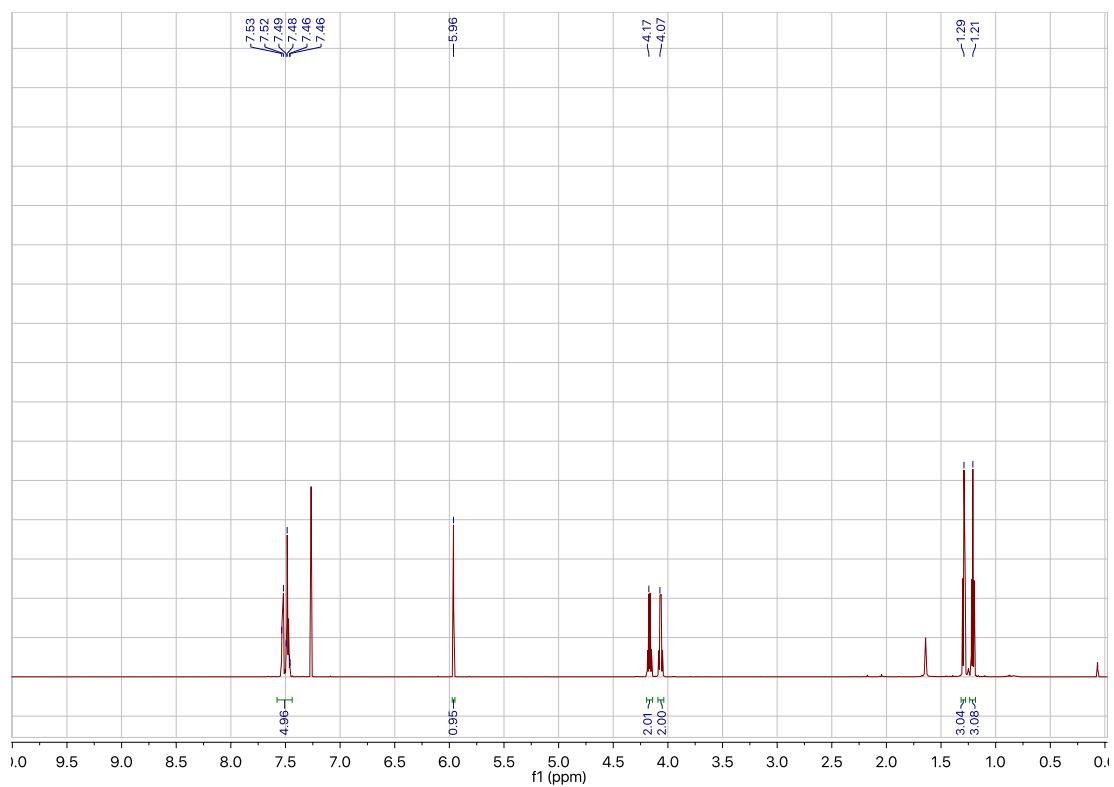
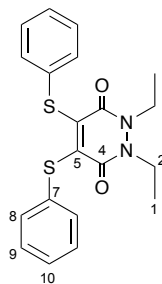


Figure S4.  $^1\text{H}$  and  $^{13}\text{C}$  NMR data for 1,2-diethyl-4-(phenylthio)-1,2-dihydropyridazine-3,6-dione **11**.

## 1,2-Diethyl-4,5-bis(phenylthio)-1,2-dihydropyridazine-3,6-dione **12**



To a solution of thiophenol **10** (0.10 mL, 0.97 mmol) and triethylamine (0.39 mL, 2.8 mmol) in CH<sub>2</sub>Cl<sub>2</sub> (6 mL) at 21 °C, was added a solution of 4,5-dibromo-1,2-diethyl-1,2-dihydropyridazine-3,6-dione **8** (0.10 g, 0.31 mmol) in CH<sub>2</sub>Cl<sub>2</sub> (6 mL), and the reaction mixture was stirred for 10 mins. Following this, the reaction mixture was diluted with CH<sub>2</sub>Cl<sub>2</sub> (20 mL) and washed with water (3 × 15 mL) and brine (15 mL). The organic phase was dried over MgSO<sub>4</sub>, concentrated *in vacuo* and the crude residue was purified by flash column chromatography (15–80% EtOAc/Pet.). The appropriate fractions were combined to afford 1,2-diethyl-4,5-bis(phenylthio)-1,2-dihydropyridazine-3,6-dione (0.09g, 0.23 mmol, 76%) as a yellow solid. m.p. 126–130 °C; <sup>1</sup>H NMR (600 MHz, CDCl<sub>3</sub>) δ 7.28–7.25 (m, 7H, H-8, H-9, H-10), 7.22–7.20 (m, 3H, H-8, H-9, H-10), 4.05 (q, *J* = 7.1 Hz, 4H, H-2), 1.23 (t, *J* = 7.1 Hz, 6H, H-1); <sup>13</sup>C NMR (150 MHz, CDCl<sub>3</sub>) δ 156.0 (C-4), 141.9 (C-5), 132.6 (C-7), 131.0 (C-8), 129.1 (C-9), 127.9 (C-10), 41.2 (C-2), 12.8 (C-1); IR (solid) 3058, 2967, 2928, 1657, 1574 cm<sup>-1</sup>; LRMS (ES+) 385 (100, [M+H]<sup>+</sup>); HRMS (ES+) calcd for C<sub>20</sub>H<sub>21</sub>N<sub>2</sub>O<sub>2</sub>S<sub>2</sub> [M+H]<sup>+</sup> 385.1039, observed 385.1040.

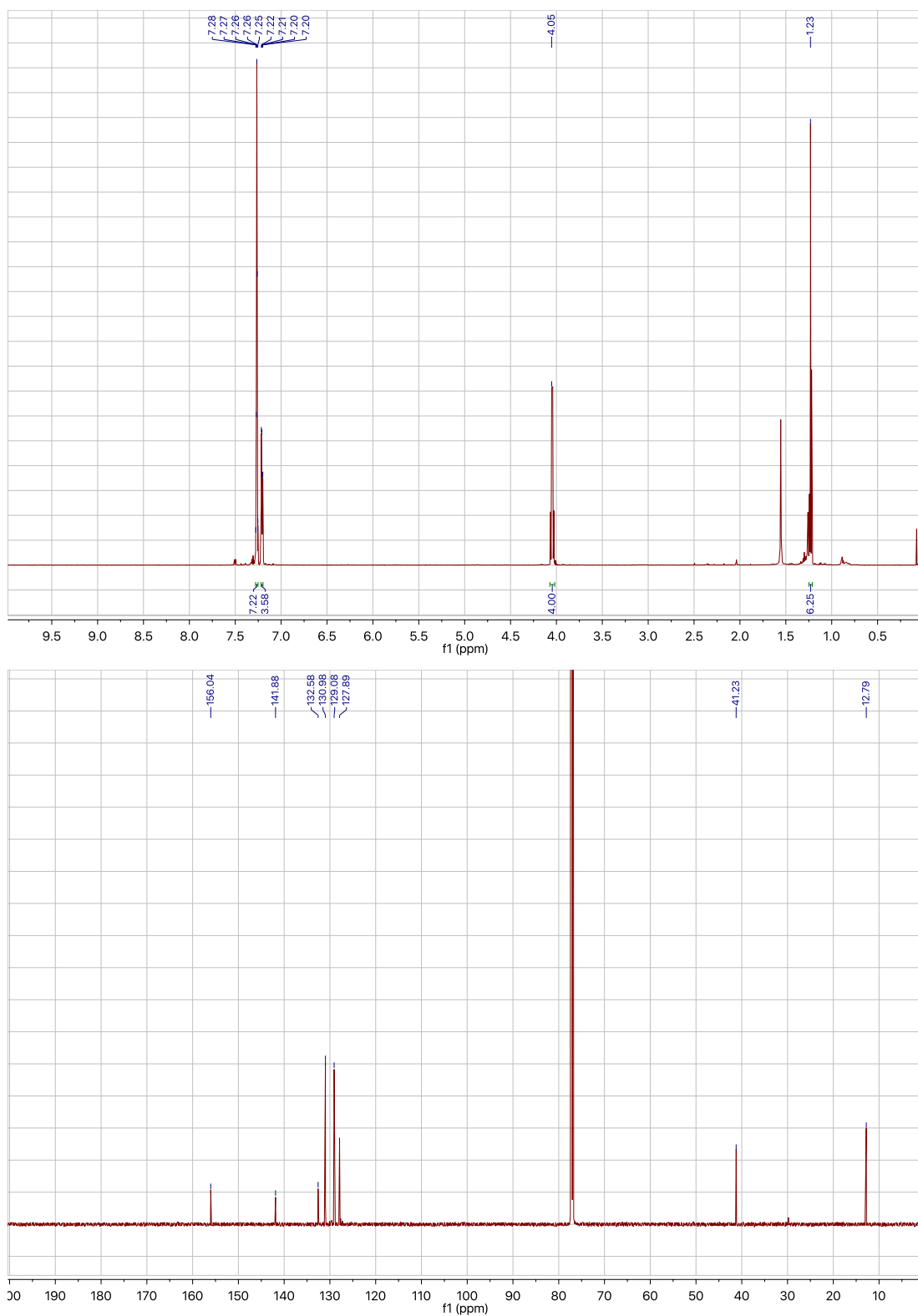
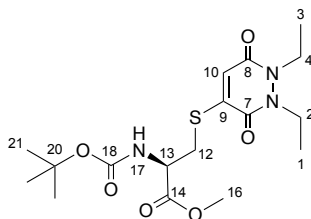


Figure S5. <sup>1</sup>H and <sup>13</sup>C NMR data for 1,2-diethyl-4,5-bis(phenylthio)-1,2-dihydropyridazine-3,6-dione **12**.

**Methyl *N*-(*tert*-butoxycarbonyl)-*S*-(1,2-diethyl-3,6-dioxo-1,2,3,6-tetrahydropyridazin-4-yl)cysteinate **14****



To a solution of *N*-(*tert*-butoxycarbonyl)-L-cysteine methyl ester **13** (0.24 g, 1.0 mmol) and triethylamine (0.40 mL, 2.9 mmol) in CH<sub>2</sub>Cl<sub>2</sub> (8 mL) at 21 °C, was added a solution of 4-bromo-1,2-diethyl-1,2-dihydropyridazine-3,6-dione **5** (0.24 g, 0.97 mmol) in CH<sub>2</sub>Cl<sub>2</sub> (8 mL), and the reaction mixture was stirred for 10 mins. Following this, the reaction mixture was diluted with CH<sub>2</sub>Cl<sub>2</sub> (20 mL) and washed with water (3 × 15 mL) and brine (15 mL). The organic phase was dried over MgSO<sub>4</sub>, concentrated *in vacuo* and the crude residue was purified by flash column chromatography (20–85% EtOAc/Pet.). The appropriate fractions were then combined and concentrated *in vacuo* to afford methyl *N*-(*tert*-butoxycarbonyl)-*S*-(1,2-diethyl-3,6-dioxo-1,2,3,6-tetrahydropyridazin-4-yl)cysteinate (0.31 g, 0.77 mmol, 80%) as a white solid.  $[\alpha]_D^{20.0} +3.0$  (*c* 1, CHCl<sub>3</sub>); m.p. 86–90 °C; <sup>1</sup>H NMR (600 MHz, CDCl<sub>3</sub>) δ 6.56 (s, 1H, H-10), 5.37 (d, *J* = 7.6 Hz, 1H, H-17), 4.68–4.65 (m, 1H, H-13), 4.17–4.07 (m, 4H, H-2, H-4), 3.79 (s, 3H, H-16), 3.31 (dd, *J* = 13.2, 5.0 Hz, 1H, H-12), 3.20 (dd, *J* = 13.2, 5.0 Hz, 1H, H-12), 1.44 (s, 9H, H-21), 1.26 (t, *J* = 7.1 Hz, 3H, H-1), 1.22 (t, *J* = 7.1 Hz, 3H, H-3); <sup>13</sup>C NMR (150 MHz, CDCl<sub>3</sub>) δ 170.5 (C-14), 156.9 (C-7), 155.6 (C-8), 155.1 (C-18), 148.7 (C-9), 122.6 (C-10), 80.7 (C-20), 53.1 (C-16), 52.2 (C-13), 40.9 (C-2), 40.2 (C-4), 33.0 (C-12), 28.4 (C-21), 13.2 (C-1), 13.1 (C-3); IR (solid) 2979, 1746, 1709, 1615 cm<sup>-1</sup>; LRMS (ES+) 402 (100, [M+H]<sup>+</sup>); HRMS (ES+) calcd for C<sub>17</sub>H<sub>28</sub>N<sub>3</sub>O<sub>6</sub>S [M+H]<sup>+</sup> 402.1693, observed 402.1694.

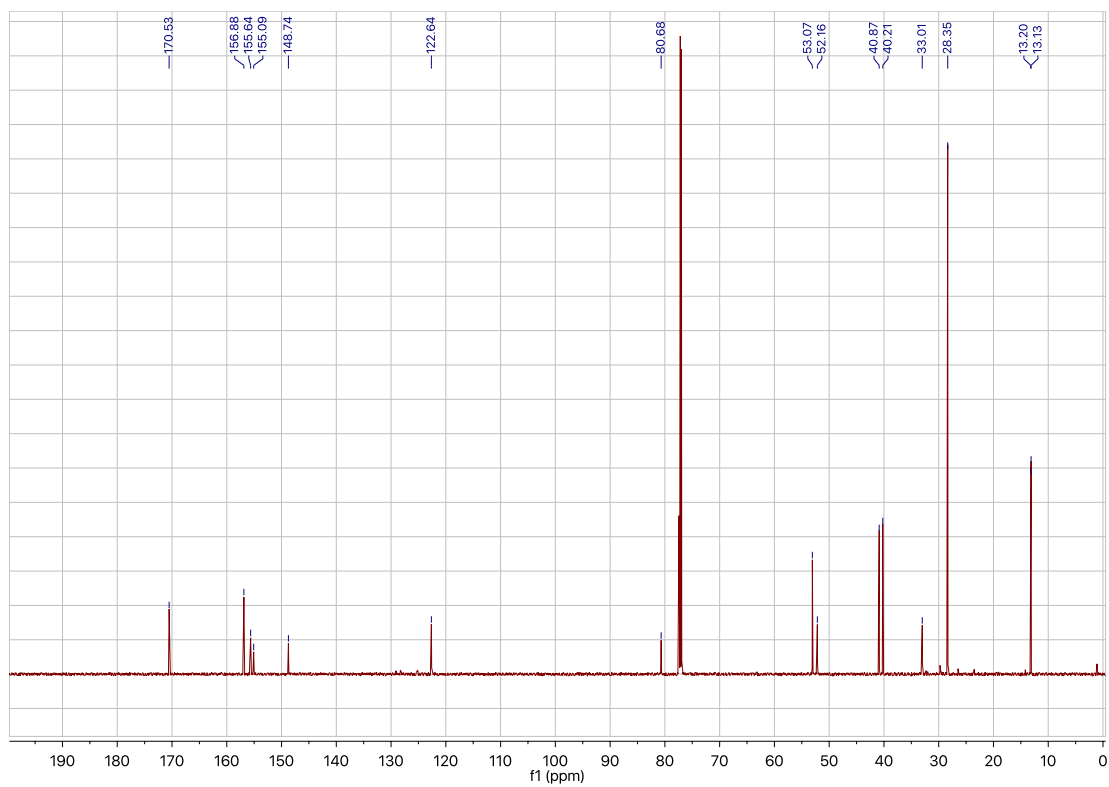
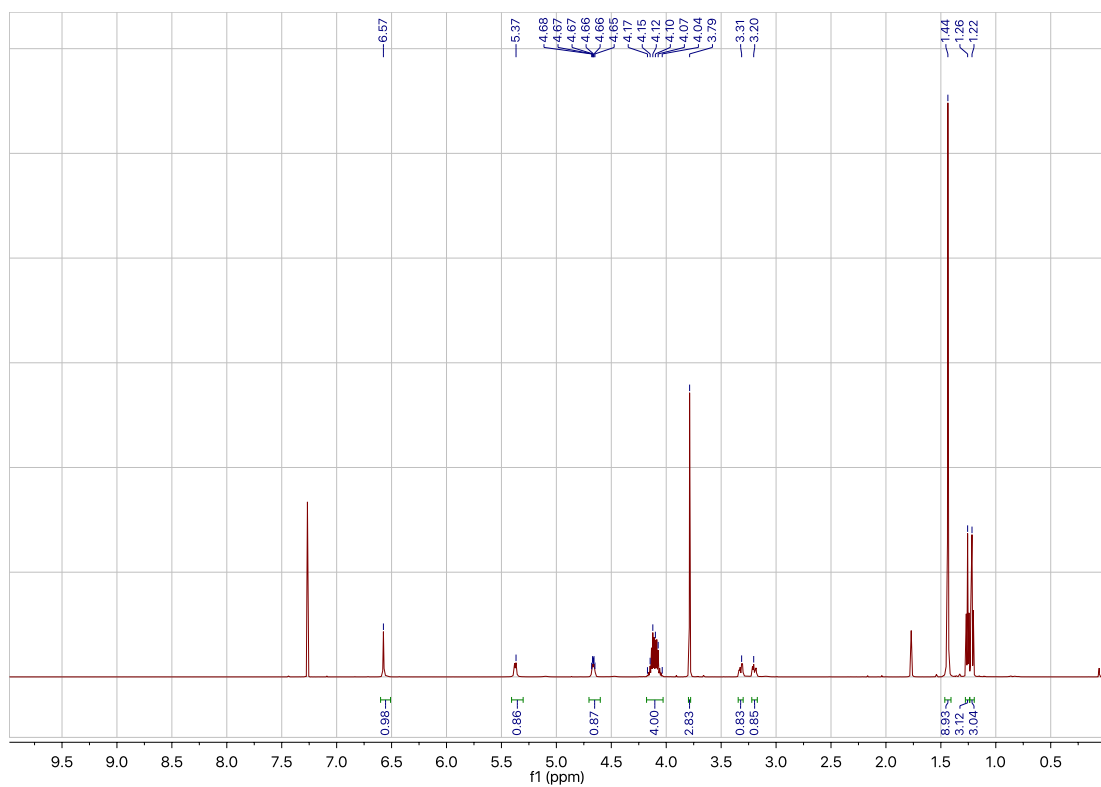
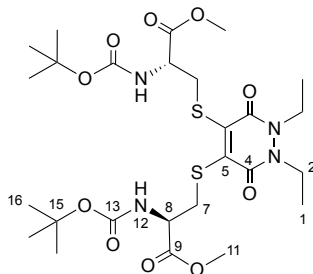


Figure S6. <sup>1</sup>H and <sup>13</sup>C NMR data for methyl *N*-(*tert*-butoxycarbonyl)-*S*-(1,2-diethyl-3,6-dioxo-1,2,3,6-tetrahydropyridazin-4-yl)cysteinate **14**.



**Dimethyl 3,3'-((1,2-diethyl-3,6-dioxo-1,2,3,6-tetrahydropyridazine-4,5-diyl)bis(sulfanediyl))bis(2-((*tert*-butoxycarbonyl)amino)propanoate)**  
**15**



To a solution of 4,5-dibromo-1,2-diethyl-1,2-dihydropyridazine-3,6-dione **8** (0.13 g, 0.40 mmol) and *N*-(*tert*-butoxycarbonyl)-L-cysteine methyl ester **13** (0.47 g, 2.0 mmol) in CH<sub>2</sub>Cl<sub>2</sub> (10 mL) was added triethylamine (0.07 mL, 0.5 mmol), and the reaction mixture was stirred at 21 °C for 65 h. Following this, the reaction mixture was diluted with CH<sub>2</sub>Cl<sub>2</sub> (20 mL) and washed with water (3 × 20 mL) and brine (15 mL). The organic phase was then dried over MgSO<sub>4</sub>, concentrated *in vacuo* and the crude residue was purified by flash column chromatography (15–60% EtOAc/Pet.). The appropriate fractions were then combined and concentrated *in vacuo* to afford dimethyl 3,3'-((1,2-diethyl-3,6-dioxo-1,2,3,6-tetrahydropyridazine-4,5-diyl)bis(sulfanediyl))bis(2-((*tert*-butoxycarbonyl)amino)propanoate) (0.15 g, 0.24 mmol, 59%) as a yellow oil.  $[\alpha]_D^{20.0} +60.6$  (*c* 1, CHCl<sub>3</sub>); <sup>1</sup>H NMR (600 MHz, CDCl<sub>3</sub>) δ 5.76 (d, *J* = 7.8 Hz, 2H, H-12), 4.55–4.53 (m, 2H, H-8), 4.09–3.98 (m, 4H, H-2), 3.74–3.68 (m, 3H, H-7), 3.68 (s, 6H, H-11), 3.65–3.60 (m, 1H, H-7) 1.38 (s, 18H, H-16), 1.21 (t, *J* = 7.2 Hz, 6H, H-1); <sup>13</sup>C NMR (150 MHz, CDCl<sub>3</sub>) δ 171.2 (C-9), 155.3 (C-4), 155.3 (C-13), 141.9 (C-5), 80.1 (C-15), 53.9 (C-8), 52.6 (C-11), 41.3 (C-2), 35.7 (C-7), 28.4 (C-16), 13.0 (C-1); IR (thin film) 2978, 1707, 1617 cm<sup>-1</sup>; LRMS (ES+) 635 (100, [M+H]<sup>+</sup>); HRMS (ES+) calcd for C<sub>26</sub>H<sub>43</sub>N<sub>4</sub>O<sub>10</sub>S<sub>2</sub> [M+H]<sup>+</sup> 635.2415, observed 635.2411.

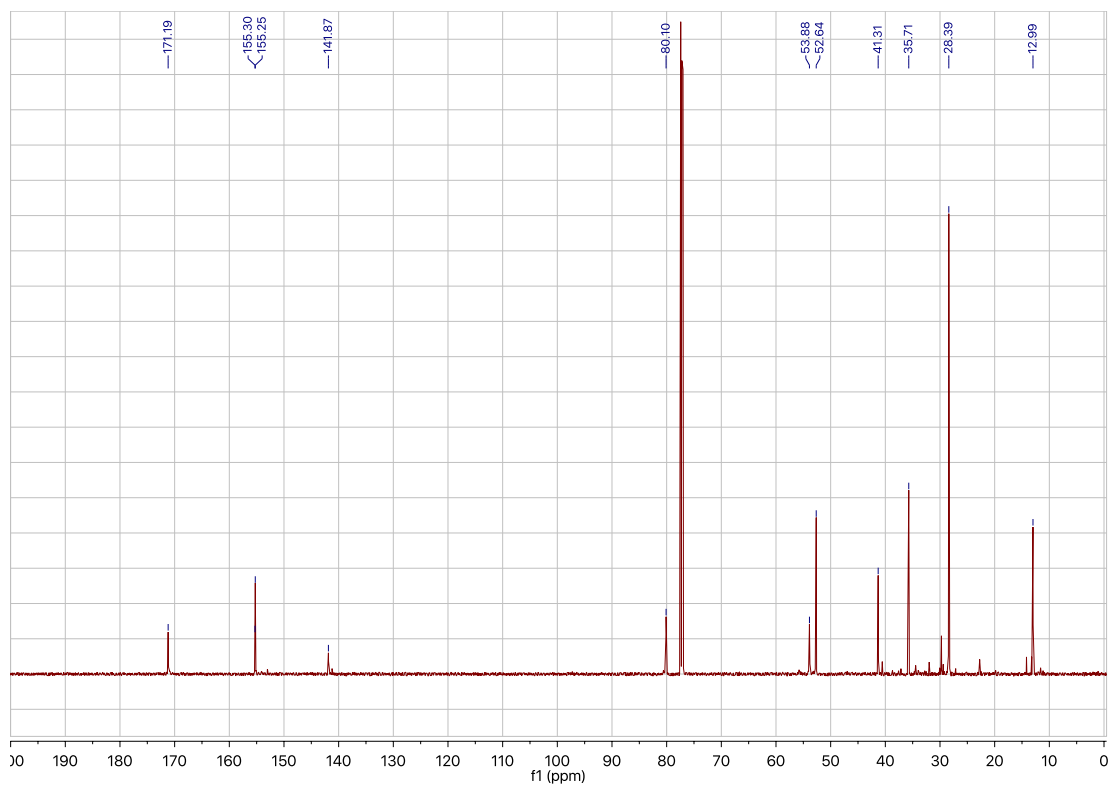
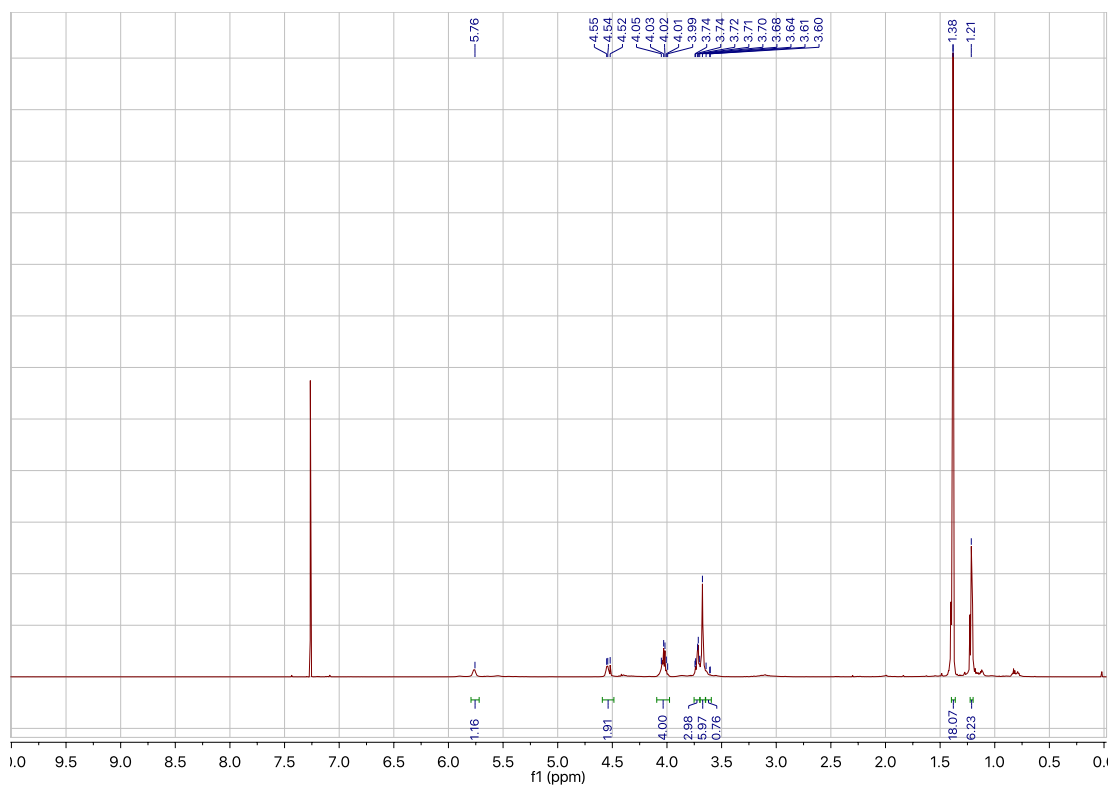
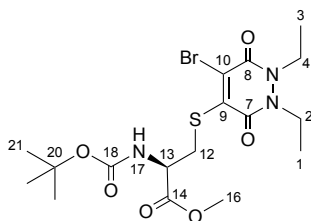


Figure S7.  $^1\text{H}$  and  $^{13}\text{C}$  NMR data for dimethyl 3,3'-((1,2-diethyl-3,6-dioxo-1,2,3,6-tetrahydropyridazine-4,5-diyl)bis(sulfanediyl))bis(2-((*tert*-butoxycarbonyl)amino)propanoate) **15**.

**Methyl *S*-(5-bromo-1,2-diethyl-3,6-dioxo-1,2,3,6-tetrahydropyridazin-4-yl)-*N*-(*tert*-butoxycarbonyl)cysteinate **16****



To a solution of 4,5-dibromo-1,2-diethyl-1,2-dihydropyridazine-3,6-dione **8** (0.20 g, 0.61 mmol) in CH<sub>2</sub>Cl<sub>2</sub> (6 mL) at 21 °C, was added dropwise over 10 mins a solution of *N*-(*tert*-butoxycarbonyl)-L-cysteine methyl ester **13** (0.14 g, 0.59 mmol) and triethylamine (0.13 mL, 0.93 mmol) in CH<sub>2</sub>Cl<sub>2</sub> (6 mL). Following this, the reaction mixture was diluted with CH<sub>2</sub>Cl<sub>2</sub> (12 mL) and washed with water (3 × 15 mL) and brine (15 mL). The organic phase was dried over MgSO<sub>4</sub>, concentrated *in vacuo* and the crude residue was purified by flash column chromatography (0–30% EtOAc/CHCl<sub>3</sub>). The appropriate fractions were then combined and concentrated *in vacuo* to afford methyl *S*-(5-bromo-1,2-diethyl-3,6-dioxo-1,2,3,6-tetrahydropyridazin-4-yl)-*N*-(*tert*-butoxycarbonyl)cysteinate (0.17 g, 0.35 mmol, 60%) as a yellow oil.  $[\alpha]_D^{20.0} +17.7$  (*c* 1, CHCl<sub>3</sub>); <sup>1</sup>H NMR (600 MHz, CDCl<sub>3</sub>) δ 5.42 (d, *J* = 8.1 Hz, 1H, H-17), 4.63–4.59 (m, 1H, H-13), 4.22–4.03 (m, 4H, H-2, H-4), 3.85–3.82 (m, 1H, H-12), 3.75 (d, *J* = 7.0 Hz, 1H, H-12), 3.73 (s, 3H, H-16), 1.42 (s, 9H, H-21), 1.30–1.25 (m, 6H, H-1, H-3); <sup>13</sup>C NMR (150 MHz, CDCl<sub>3</sub>) δ 171.1 (C-14), 155.2 (C-7/C-8/C-18), 154.6 (C-7/C-8/C-18), 153.7 (C-7/C-8/C-18), 145.3 (C-9), 130.9 (C-10), 80.4 (C-20), 53.9 (C-13), 52.8 (C-16), 42.2 (C-2), 41.1 (C-4), 35.9 (C-12), 28.4 (C-21), 13.2 (C-1), 12.9 (C-3); IR (thin film) 2977, 2934, 1743, 1708, 1622 cm<sup>-1</sup>; LRMS (ES+) 482 (100, [M<sup>81</sup>Br+H]<sup>+</sup>), 480 (96, [M<sup>79</sup>Br+H]<sup>+</sup>); HRMS (ES+) calcd for C<sub>17</sub>H<sub>27</sub>N<sub>3</sub>O<sub>6</sub>SBr [M<sup>81</sup>Br+H]<sup>+</sup> 482.0779, observed 482.0770.

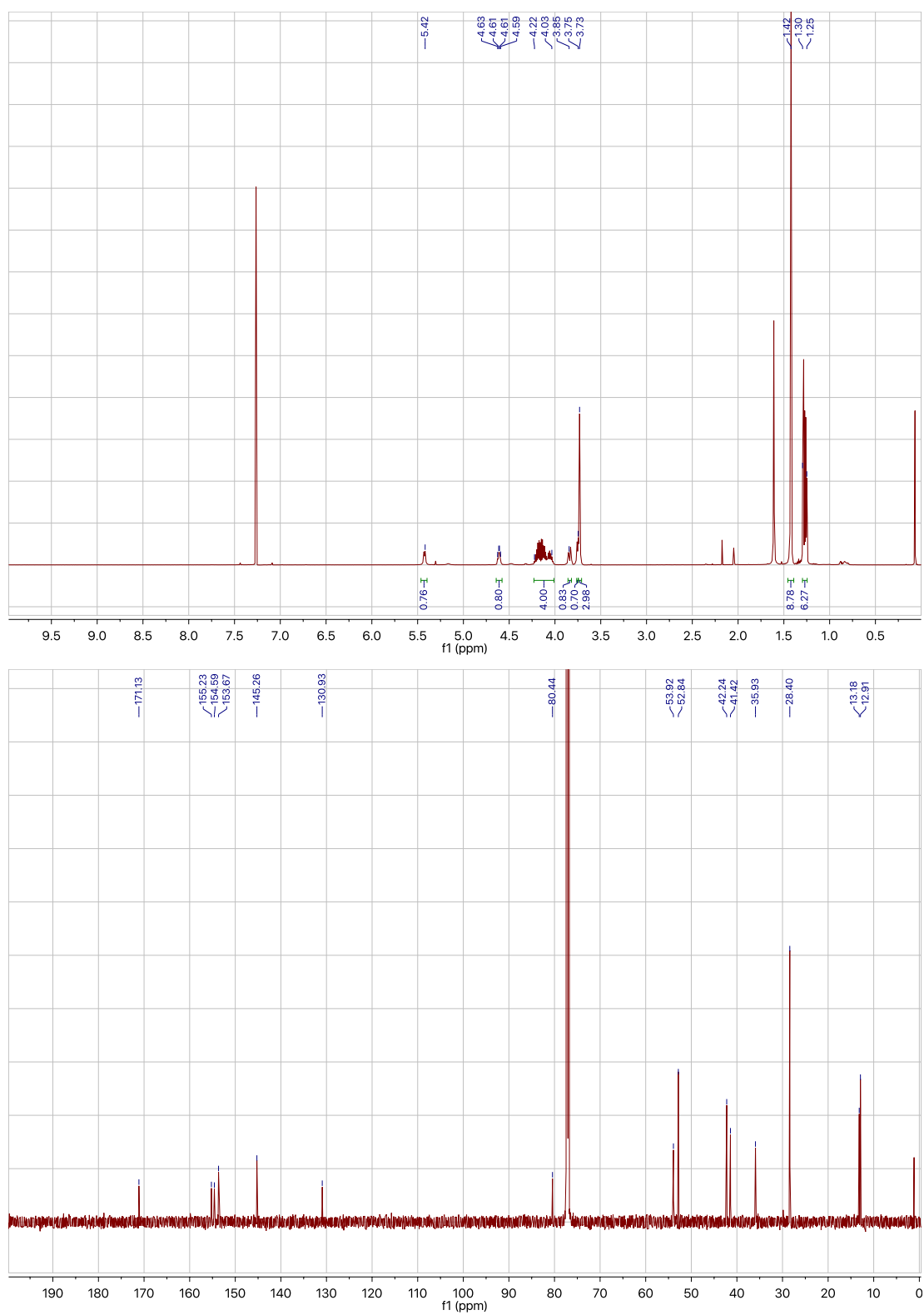
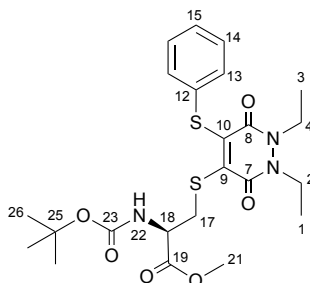


Figure S8.  $^1\text{H}$  and  $^{13}\text{C}$  NMR spectra for methyl *S*-(5-bromo-1,2-diethyl-3,6-dioxo-1,2,3,6-tetrahydropyridazin-4-yl)-*N*-(*tert*-butoxycarbonyl)cysteinate **16**.

**Methyl *N*-(*tert*-butoxycarbonyl)-*S*-(1,2-diethyl-3,6-dioxo-5-(phenylthio)-1,2,3,6-tetrahydropyridazin-4-yl)cysteinate **17****



To a solution of methyl *S*-(5-bromo-1,2-diethyl-3,6-dioxo-1,2,3,6-tetrahydropyridazin-4-yl)-*N*-(*tert*-butoxycarbonyl)cysteinate **16** (0.45 g, 0.94 mmol) in CH<sub>2</sub>Cl<sub>2</sub> (8 mL) at 21 °C, was added a solution of thiophenol **10** (0.10 mL, 0.98 mmol) and triethylamine (0.20 mL, 1.4 mmol) in CH<sub>2</sub>Cl<sub>2</sub> (8 mL) and the reaction was stirred for 10 mins. Following this, the reaction mixture was diluted with CH<sub>2</sub>Cl<sub>2</sub> (16 mL) and washed with water (3 × 15 mL) and brine (15 mL). The organic phase was dried over MgSO<sub>4</sub>, concentrated *in vacuo* and the crude residue was purified by flash column chromatography (0–40% EtOAc/CHCl<sub>3</sub>). The appropriate fractions were then combined and concentrated *in vacuo* to afford methyl *N*-(*tert*-butoxycarbonyl)-*S*-(1,2-diethyl-3,6-dioxo-5-(phenylthio)-1,2,3,6-tetrahydropyridazin-4-yl)cysteinate (0.24 g, 0.47 mmol, 50%) as a yellow oil. [ $\alpha$ ]<sub>D</sub><sup>20.0</sup> +26.9 (*c* 1, CHCl<sub>3</sub>); <sup>1</sup>H NMR (600 MHz, CDCl<sub>3</sub>)  $\delta$  7.37–7.27 (m, 5H, H-13, H-14, H-15), 5.48 (d, *J* = 8.1 Hz, 1H, H-22), 4.52 (m, 1H, H-18), 4.15–3.98 (m, 4H, H-2, H-4), 3.70 (s, 3H, H-21), 3.68 (d, *J* = 6.3 Hz, 1H, H-17), 3.58 (dd, *J* = 14.0, 6.3 Hz, 1H, H-17), 1.41 (s, 9H, H-26), 1.27 (t, *J* = 7.1 Hz, 3H, H-1/H-3), 1.22 (t, *J* = 7.1 Hz, 3H, H-1/H-3); <sup>13</sup>C NMR (150 MHz, CDCl<sub>3</sub>)  $\delta$  171.3 (C-19), 155.8 (C-7/C-8/C-23), 155.3 (C-7/C-8/C-23), 155.3 (C-7/C-8/C-23), 142.6 (C-9), 142.1 (C-10), 132.8 (C-12), 131.1 (C-13), 129.3 (C-14), 128.0 (C-15), 80.3 (C-25), 53.8 (C-18), 52.7 (C-21), 41.3 (C-2/C-4), 41.3 (C-2/C-4), 35.7 (C-17), 28.4 (C-26), 13.0 (C-1/C-3), 12.9 (C-1/C-3); IR (thin film) 2975, 2932, 1743, 1708, 1614 cm<sup>-1</sup>; LRMS (ES<sup>+</sup>) 510 (100, [M+H]<sup>+</sup>); HRMS (ES<sup>+</sup>) calcd for C<sub>23</sub>H<sub>32</sub>N<sub>3</sub>O<sub>6</sub>S<sub>2</sub> [M+H]<sup>+</sup> 510.1727, observed 510.1718.

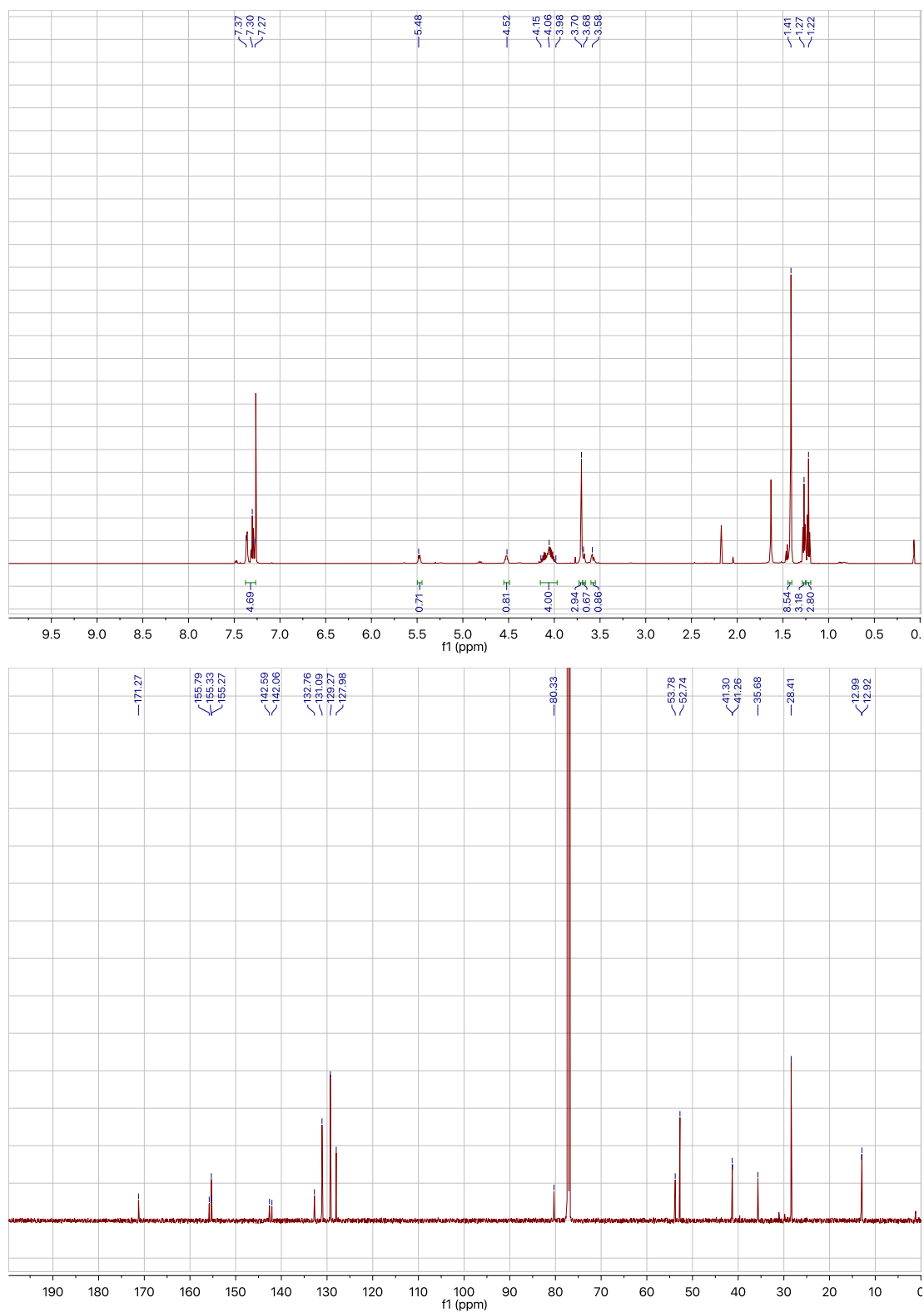
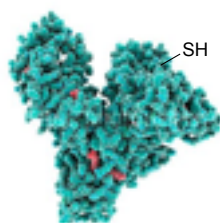


Figure S9.  $^1\text{H}$  and  $^{13}\text{C}$  NMR spectra for methyl *N*-(*tert*-butoxycarbonyl)-*S*-(1,2-diethyl-3,6-dioxo-5-(phenylthio)-1,2,3,6-tetrahydropyridazin-4-yl)cysteinate **17**.

# Incubations involving human serum albumin, maleimide 18 and pyridazinediones 5, 8, 11, 12, 14, 15 and 17

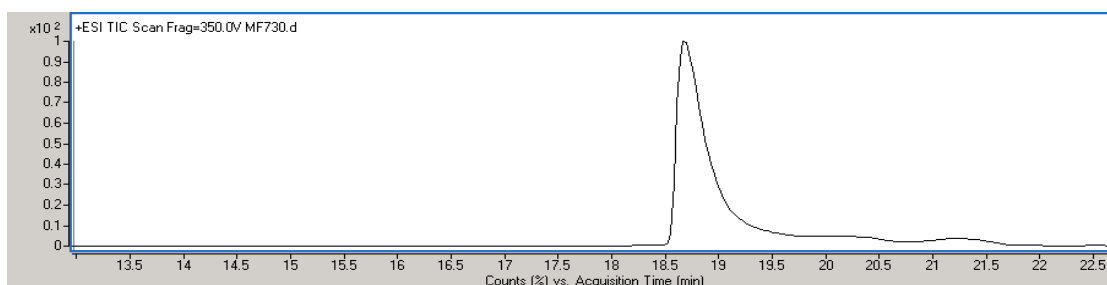
## Human serum albumin control

Human serum albumin (20  $\mu$ L, 3.8 mg/mL, 57  $\mu$ M) in PBS (10 mM phosphate, 137 mM NaCl, 2.7 mM KCl, pH 7.4) was incubated at 37  $^{\circ}$ C for 4 h. The PBS was exchanged with ammonium acetate buffer (20 mM, pH 7.4) by repeated diafiltration ( $\times$  3) into VivaSpin sample concentrators (GE Healthcare, 10,000 MWCO). The sample was then analysed by LC-MS. Expected mass: 66,439 Da. Observed mass: 66,438 Da.

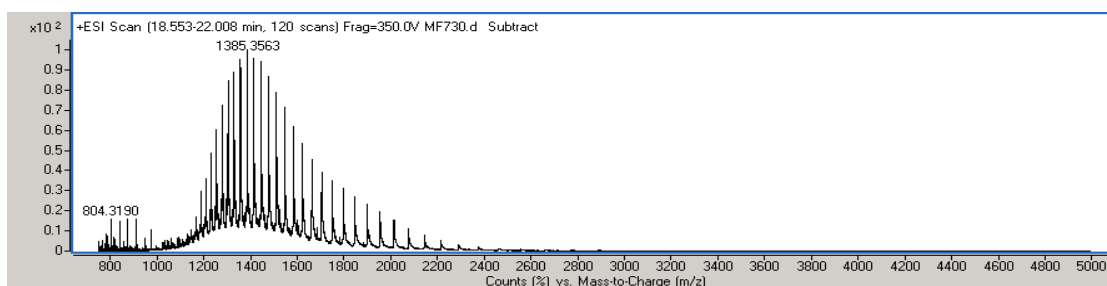


pH 7.4, 37  $^{\circ}$ C, 4 h

(a)



(b)



(c)

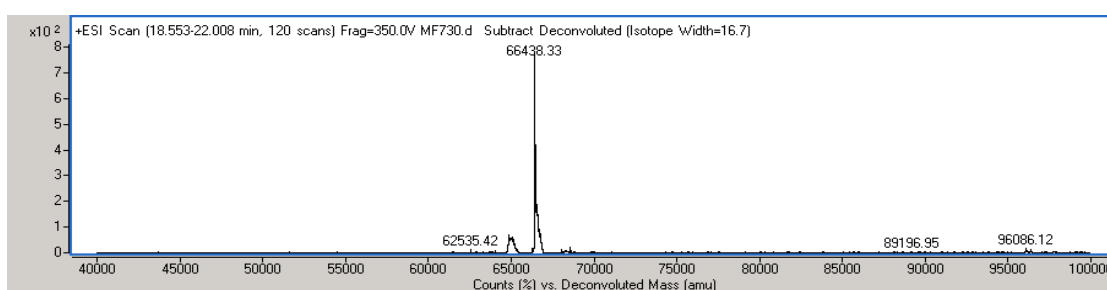
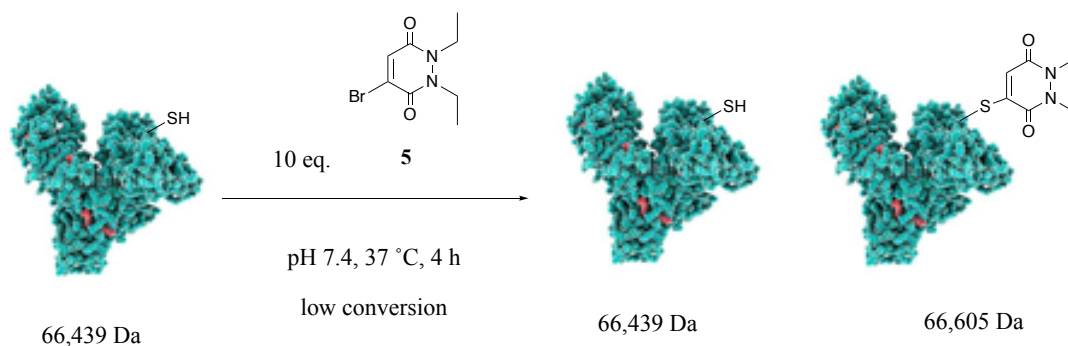


Figure S10. (a) TIC, (b) non-deconvoluted and (c) deconvoluted MS data for untreated human serum albumin used in the incubations with pyridazinediones **5**, **8**, **11**, **12**, **14**, **15**, **17** and maleimide **18**.

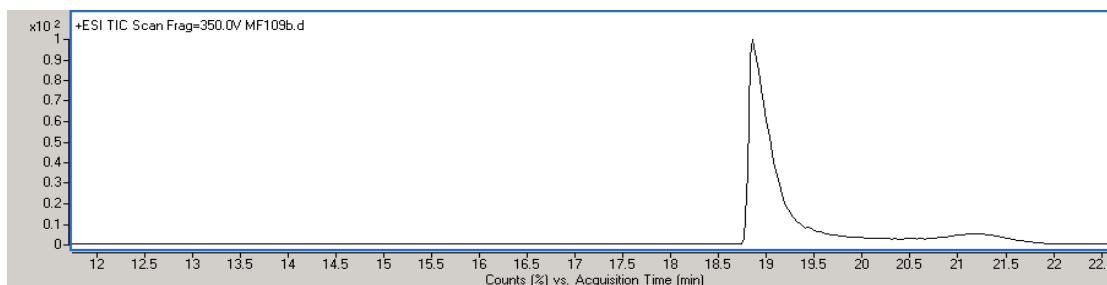


## Incubation of human serum albumin with mono-bromo PD 5 (10 eq.)

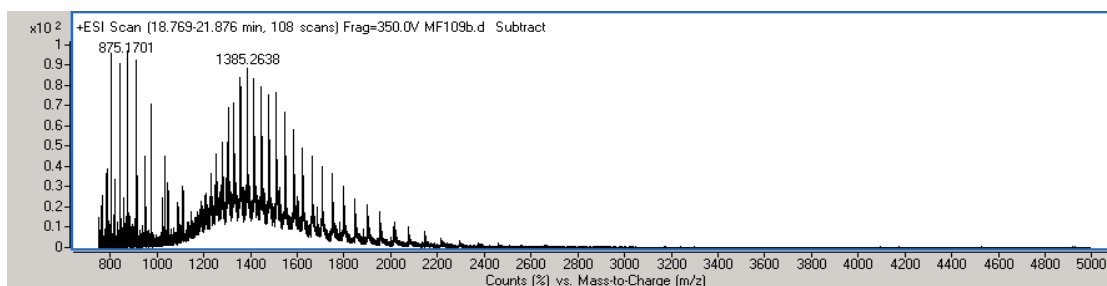


Pyridazinedione **5** (1.1  $\mu\text{L}$ , 10 mM in MeCN, 10 eq.) was added to human serum albumin (20  $\mu\text{L}$ , 3.8 mg/mL, 57  $\mu\text{M}$ ) in PBS (10 mM phosphate, 137 mM NaCl, 2.7 mM KCl, pH 7.4). The mixture was incubated at 37 °C for 4 h. Excess reagents were then removed by repeated diafiltration ( $\times 3$ ) into ammonium acetate buffer (20 mM, pH 7.4) using VivaSpin sample concentrators (GE Healthcare, 10,000 MWCO). The sample was then analysed by LC-MS. Expected mass: 66,605 Da. Observed masses: 66,606 and 66,440 Da.

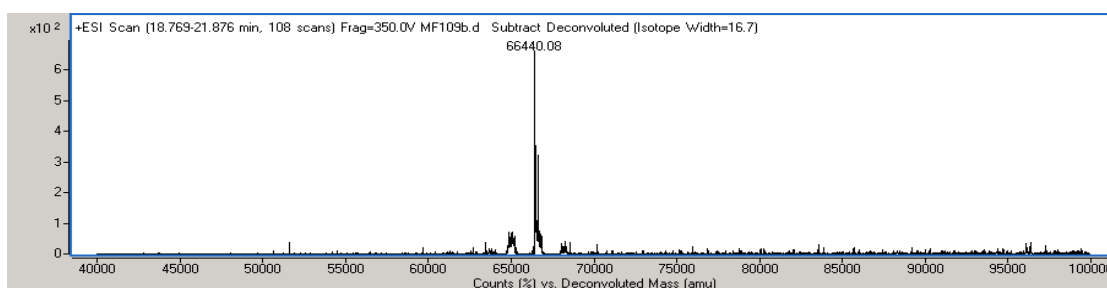
(a)



(b)



(c)



(d)

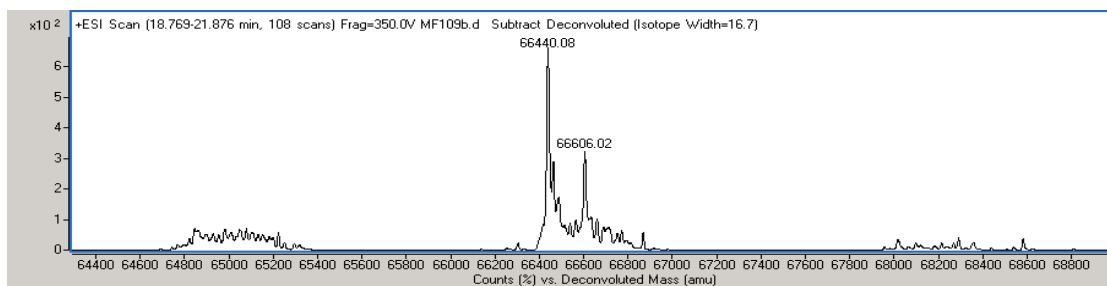
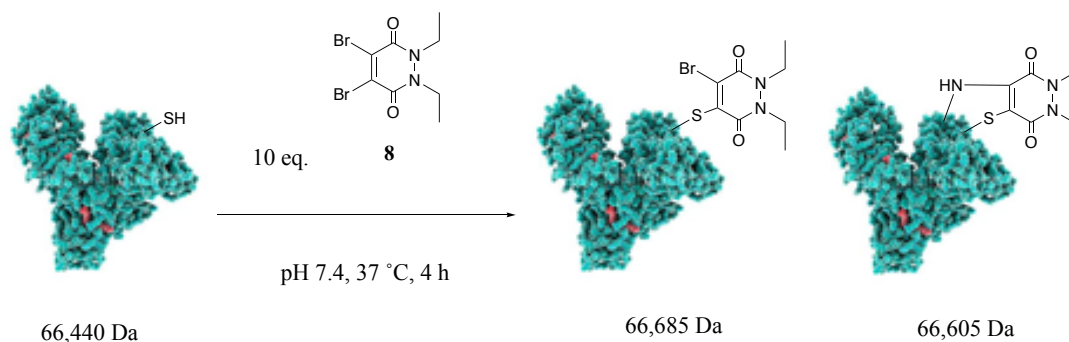


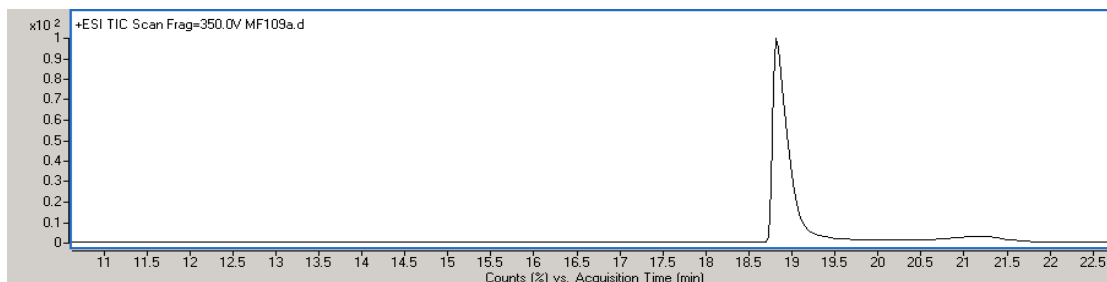
Figure S11. (a) TIC, (b) non-deconvoluted, (c) deconvoluted and (d) zoomed in of deconvolution MS data for human serum albumin incubated with pyridazinedione **5** (10 eq.).

## Incubation of human serum albumin with mono-bromo PD **8** (10 eq.)

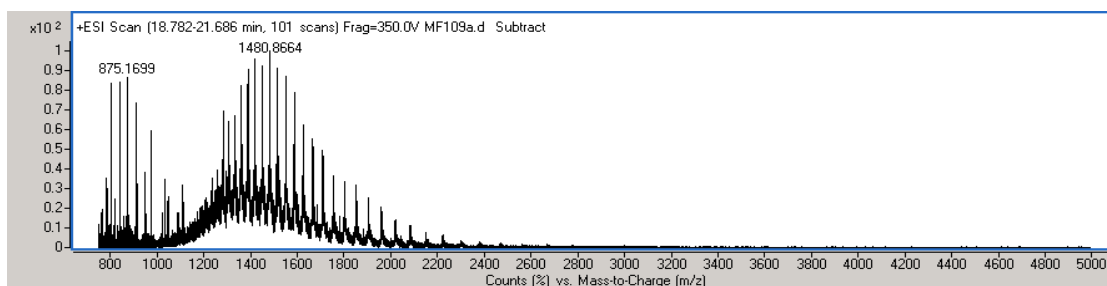


Pyridazinedione **8** (1.1  $\mu\text{L}$ , 10 mM in MeCN, 10 eq.) was added to human serum albumin (20  $\mu\text{L}$ , 3.8 mg/mL, 57  $\mu\text{M}$ ) in PBS (10 mM phosphate, 137 mM NaCl, 2.7 mM KCl, pH 7.4). The mixture was incubated at 37  $^{\circ}\text{C}$  for 4 h. Excess reagents were then removed by repeated diafiltration ( $\times 3$ ) into ammonium acetate buffer (20 mM, pH 7.4) using VivaSpin sample concentrators (GE Healthcare, 10,000 MWCO). The sample was then analysed by LC-MS. Expected mass: 66,685 Da. Observed masses: 66,685 and 66,605 Da.

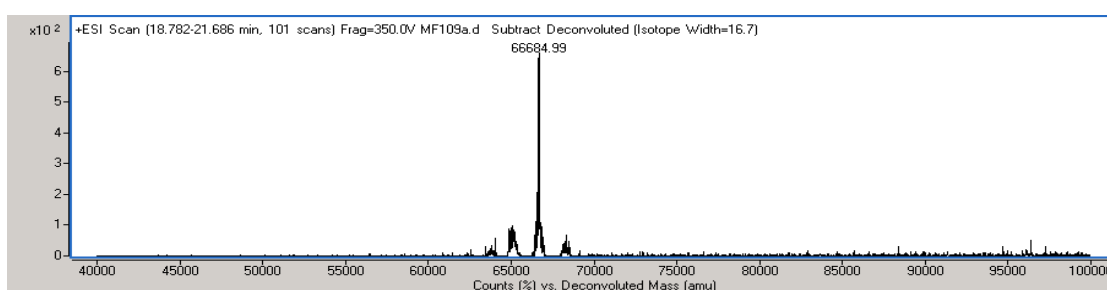
(a)



(b)



(c)



(d)

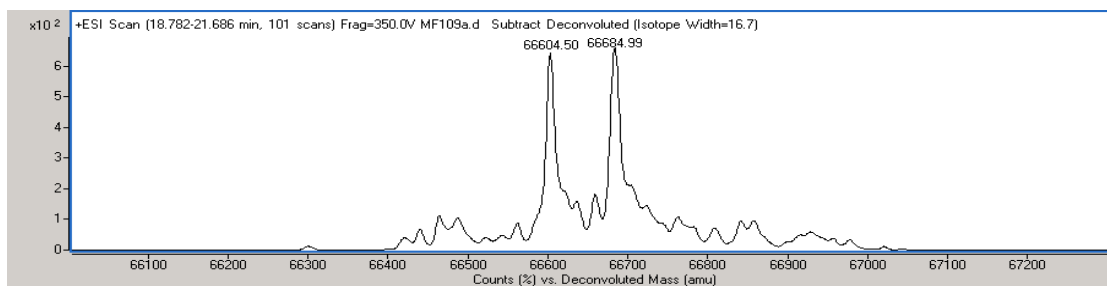
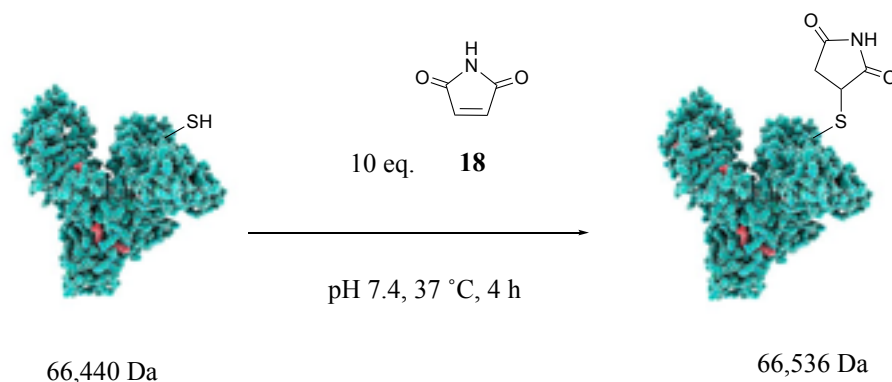


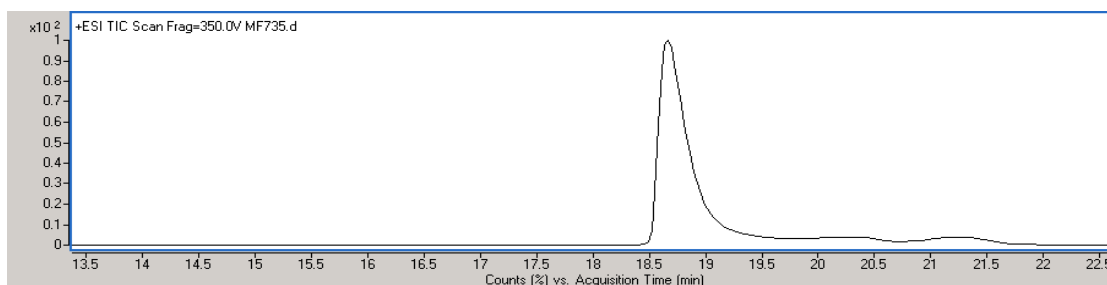
Figure S12. (a) TIC, (b) non-deconvoluted, (c) deconvoluted and (d) zoomed in of deconvolution MS data for human serum albumin incubated with pyridazinedione **8** (10 eq.).

## Incubation of human serum albumin with maleimide **18** (10 eq.)

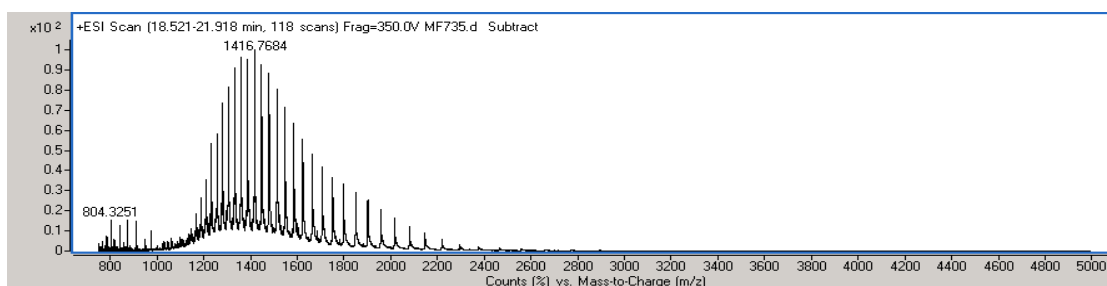


Maleimide **18** (1.1  $\mu$ L, 10 mM in MeCN, 10 eq.) was added to human serum albumin (20  $\mu$ L, 3.8 mg/mL, 57  $\mu$ M) in PBS (10 mM phosphate, 137 mM NaCl, 2.7 mM KCl, pH 7.4). The reaction was incubated at 37  $^{\circ}$ C for 4 h. Excess reagents were then removed by repeated diafiltration ( $\times$  3) into ammonium acetate buffer (20 mM, pH 7.4) using VivaSpin sample concentrators (GE Healthcare, 10,000 MWCO). The sample was then analysed by LC-MS. Expected mass: 66,536 Da. Observed mass: 66,536 Da.

(a)



(b)



(c)

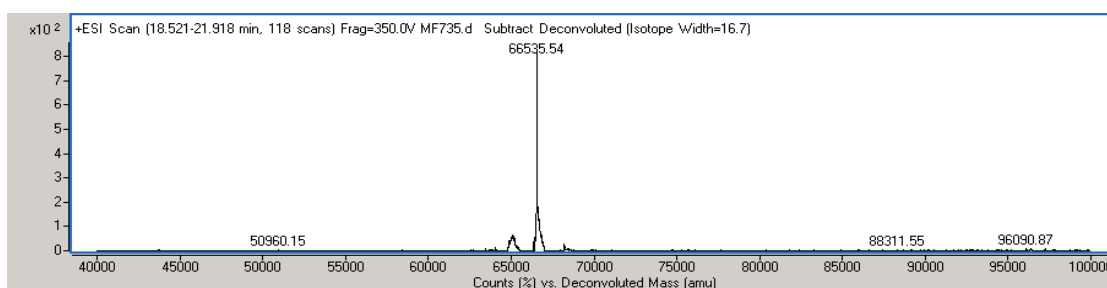
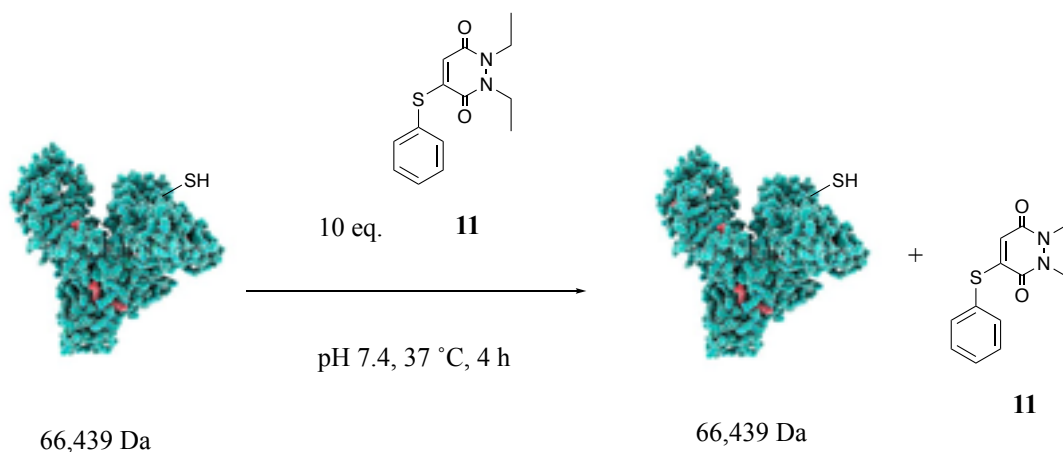


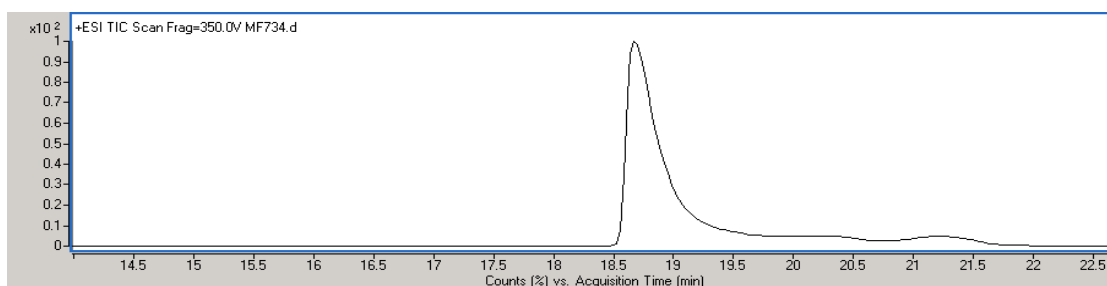
Figure S13. (a) TIC, (b) non-deconvoluted and (c) deconvoluted MS data for human serum albumin reacted with maleimide **18** (10 eq.).

## Incubation of human serum albumin with pyridazinedione **11** (10 eq.)

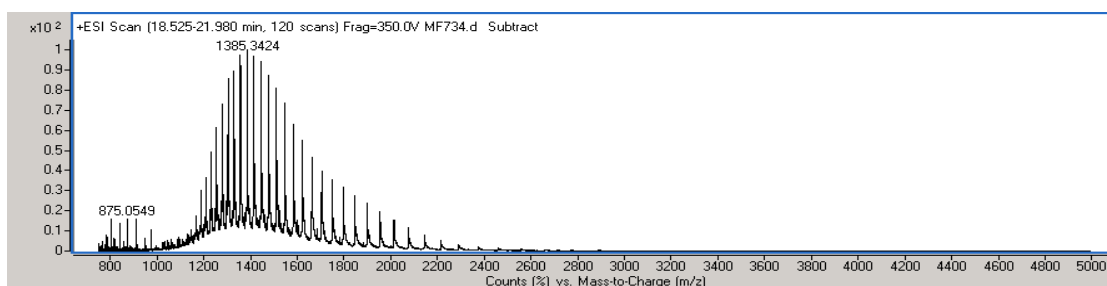


Pyridazinedione **11** (1.1  $\mu\text{L}$ , 10 mM in MeCN, 10 eq.) was added to human serum albumin (20  $\mu\text{L}$ , 3.8 mg/mL, 57  $\mu\text{M}$ ) in PBS (10 mM phosphate, 137 mM NaCl, 2.7 mM KCl, pH 7.4). The mixture was incubated at 37 °C for 4 h. Excess reagents were then removed by repeated diafiltration ( $\times 3$ ) into ammonium acetate buffer (20 mM, pH 7.4) using VivaSpin sample concentrators (GE Healthcare, 10,000 MWCO). The sample was then analysed by LC-MS. Expected mass: 66,438 Da. Observed mass: 66,439 Da.

(a)



(b)



(c)

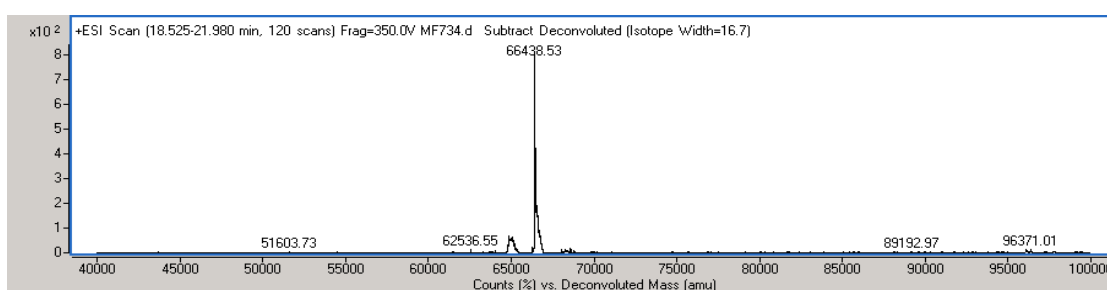
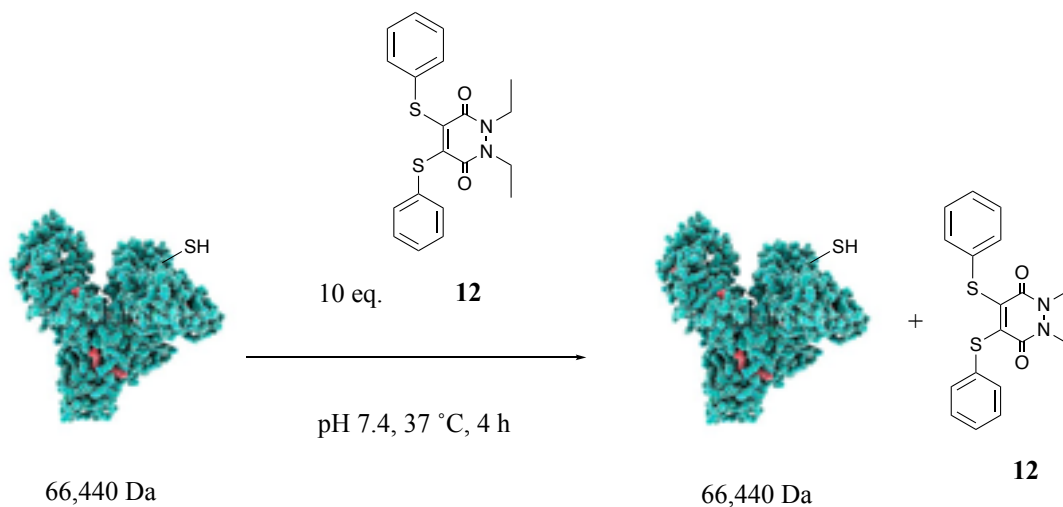


Figure S14. TIC, (b) non-deconvoluted and (c) deconvoluted MS data for human serum albumin incubated with pyridazinedione **11** (10 eq.).

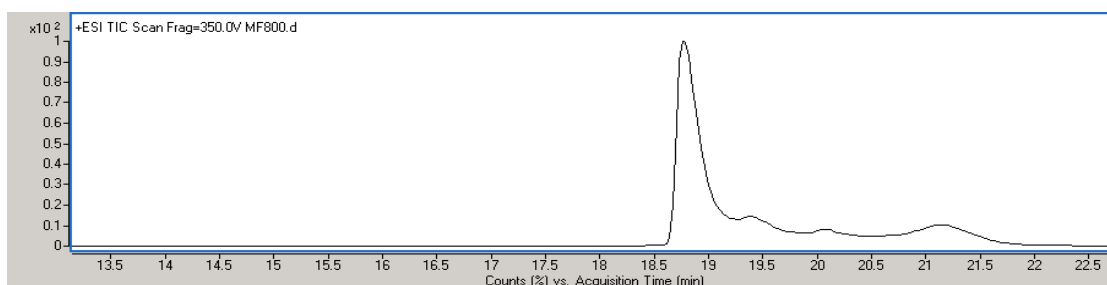


## Incubation of human serum albumin with pyridazinedione **12** (10 eq.)

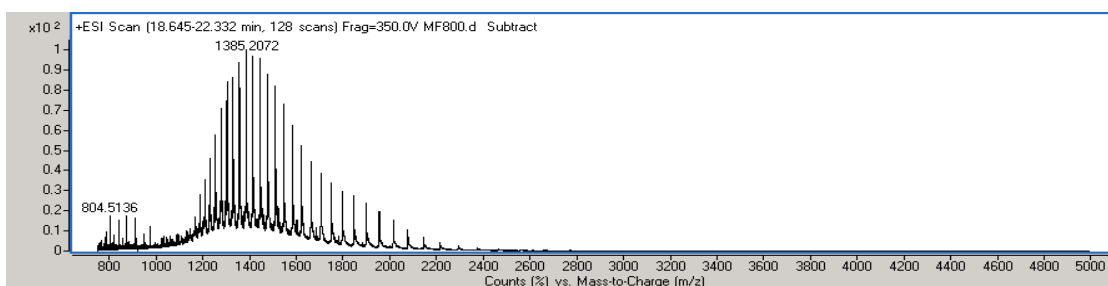


Pyridazinedione **12** (1.1  $\mu\text{L}$ , 10 mM in MeCN, 10 eq.) was added to human serum albumin (20  $\mu\text{L}$ , 3.8 mg/mL, 57  $\mu\text{M}$ ) in PBS (10 mM phosphate, 137 mM NaCl, 2.7 mM KCl, pH 7.4). The mixture was incubated at 37 °C for 4 h. Excess reagents were then removed by repeated diafiltration ( $\times 3$ ) into ammonium acetate buffer (20 mM, pH 7.4) using VivaSpin sample concentrators (GE Healthcare, 10,000 MWCO). The sample was then analysed by LC-MS. Expected mass: 66,438 Da. Observed mass: 66,440 Da.

(a)



(b)



(c)

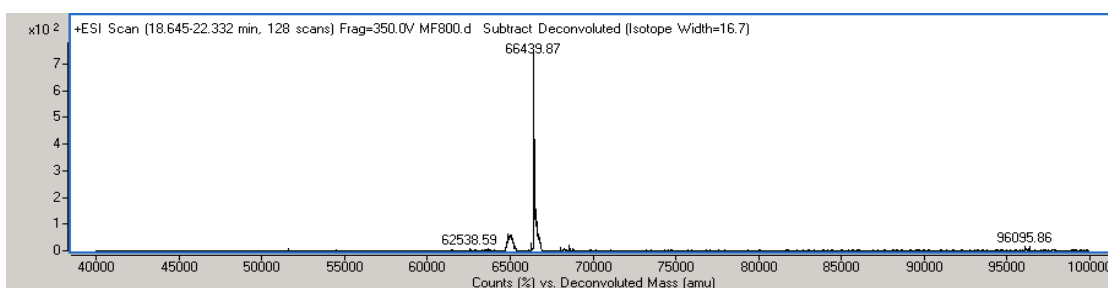
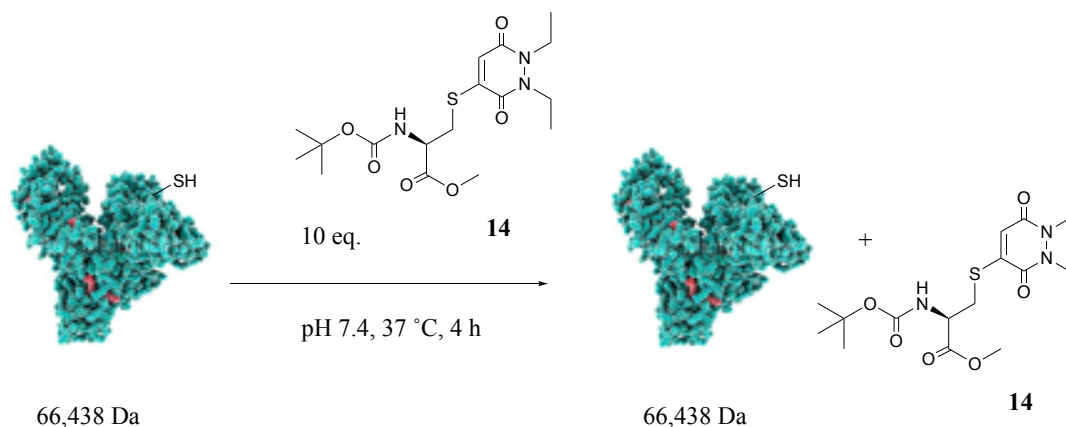


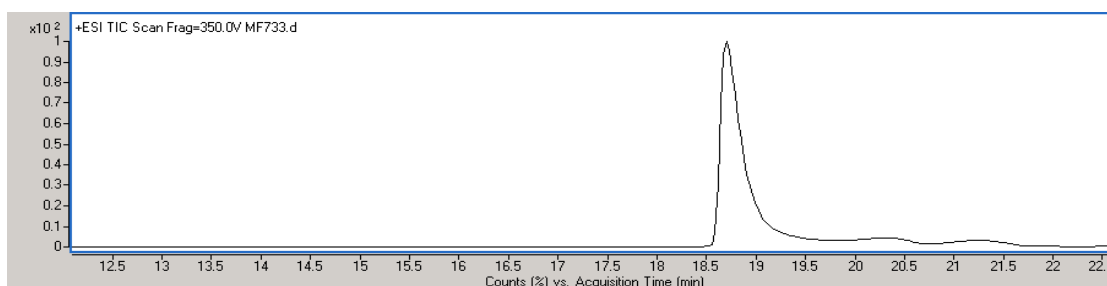
Figure S15. (a) TIC, (b) non-deconvoluted and (c) deconvoluted MS data for human serum albumin incubated with pyridazinedione **12** (10 eq.).

## Incubation of human serum albumin with pyridazinedione **14** (10 eq.)

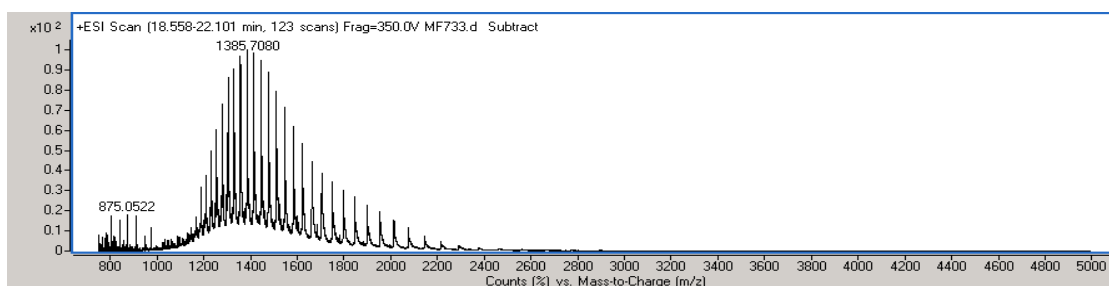


Pyridazinedione **14** (1.1  $\mu\text{L}$ , 10 mM in MeCN, 10 eq.) was added to human serum albumin (20  $\mu\text{L}$ , 3.8 mg/mL, 57  $\mu\text{M}$ ) in PBS (10 mM phosphate, 137 mM NaCl, 2.7 mM KCl, pH 7.4). The mixture was incubated at 37 °C for 4 h. Excess reagents were then removed by repeated diafiltration ( $\times 3$ ) into ammonium acetate buffer (20 mM, pH 7.4) using VivaSpin sample concentrators (GE Healthcare, 10,000 MWCO). The sample was then analysed by LC-MS. Expected mass: 66,438 Da. Observed mass: 66,438 Da.

(a)



(b)



(c)

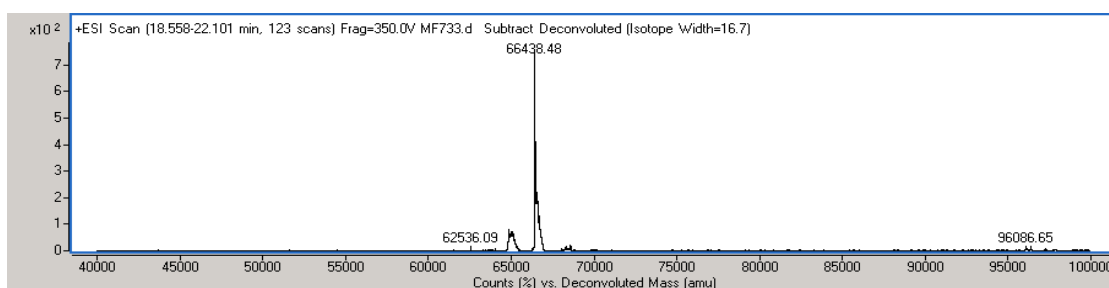
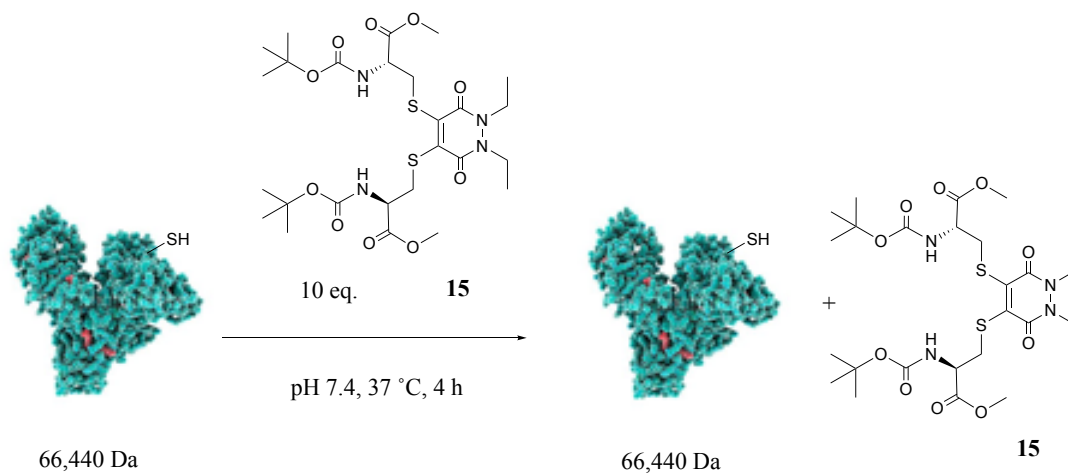


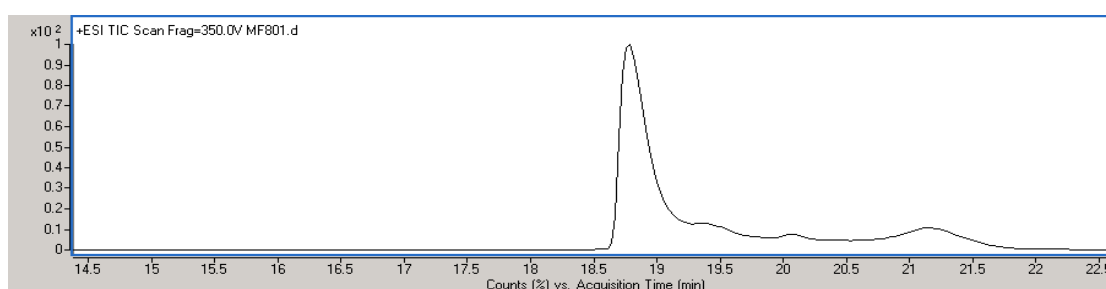
Figure S16. (a) TIC, (b) non-deconvoluted and (c) deconvoluted MS data for human serum albumin incubated with pyridazinedione **14** (10 eq.).

## Incubation of human serum albumin with pyridazinedione **15** (10 eq.)

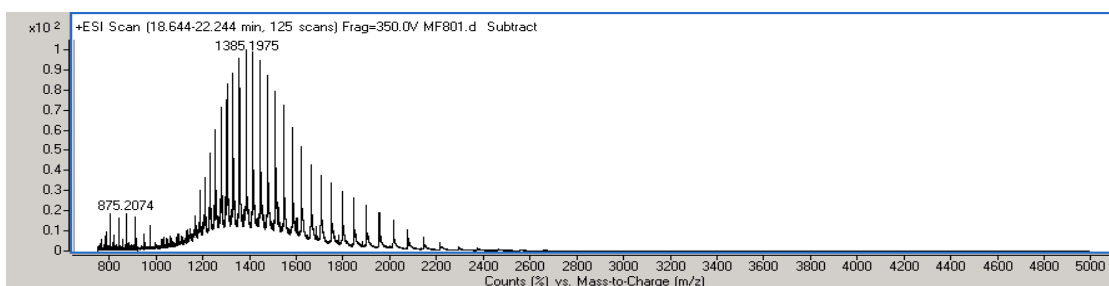


Pyridazinedione **15** (1.1  $\mu\text{L}$ , 10 mM in MeCN, 10 eq.) was added to human serum albumin (20  $\mu\text{L}$ , 3.8 mg/mL, 57  $\mu\text{M}$ ) in PBS (10 mM phosphate, 137 mM NaCl, 2.7 mM KCl, pH 7.4). The mixture was incubated at 37  $^{\circ}\text{C}$  for 4 h. Excess reagents were then removed by repeated diafiltration ( $\times 3$ ) into ammonium acetate buffer (20 mM, pH 7.4) using VivaSpin sample concentrators (GE Healthcare, 10,000 MWCO). The sample was then analysed by LC-MS. Expected mass: 66,438 Da. Observed mass: 66,440 Da.

(a)



(b)



(c)

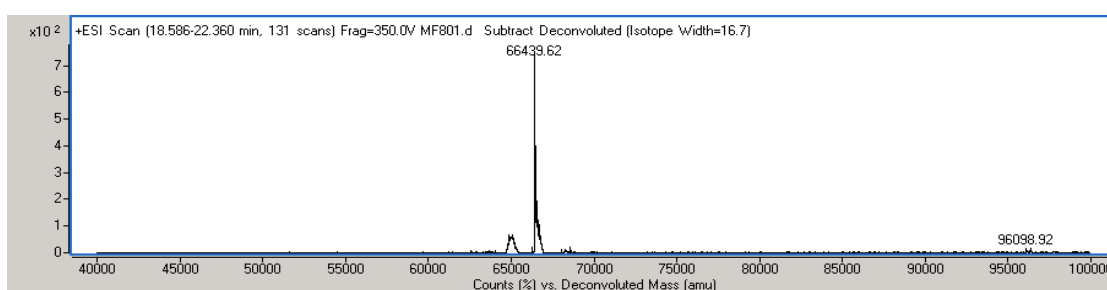
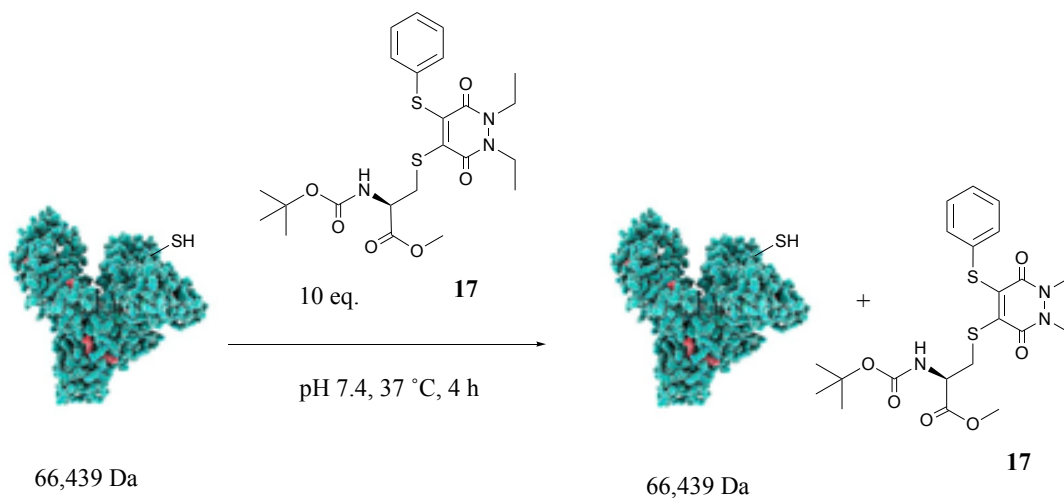


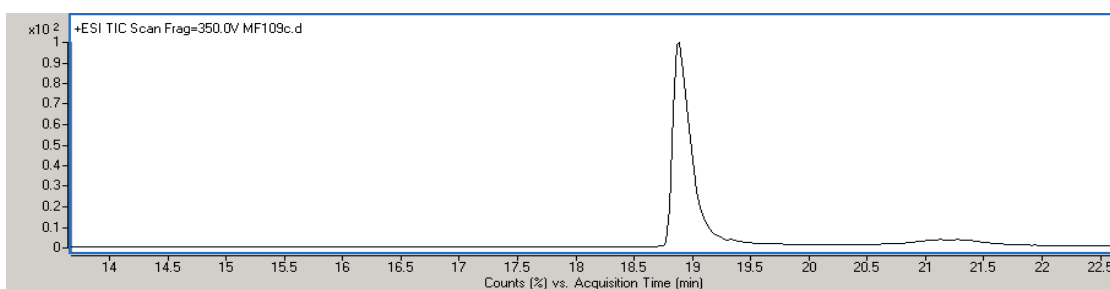
Figure S17. (a) TIC, (b) non-deconvoluted and (c) deconvoluted MS data for human serum albumin incubated with pyridazinedione **15** (10 eq.).

## Incubation of human serum albumin with pyridazinedione **17** (10 eq.)

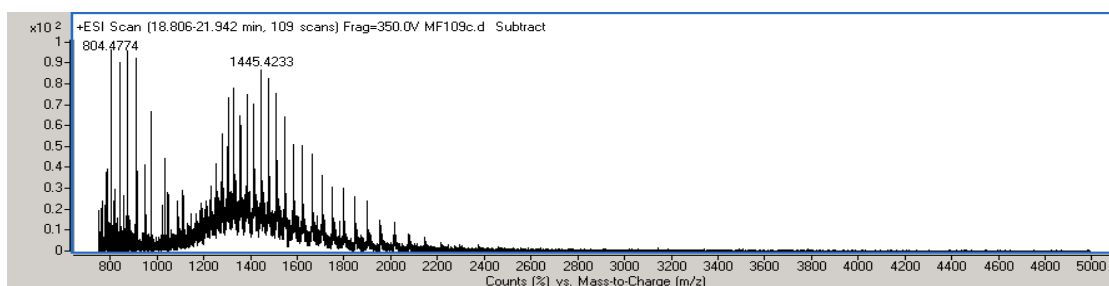


Pyridazinedione **17** (1.1  $\mu\text{L}$ , 10 mM in MeCN, 10 eq.) was added to human serum albumin (20  $\mu\text{L}$ , 3.8 mg/mL, 57  $\mu\text{M}$ ) in PBS (10 mM phosphate, 137 mM NaCl, 2.7 mM KCl, pH 7.4). The mixture was incubated at 37 °C for 4 h. Excess reagents were then removed by repeated diafiltration ( $\times 3$ ) into ammonium acetate buffer (20 mM, pH 7.4) using VivaSpin sample concentrators (GE Healthcare, 10,000 MWCO). The sample was then analysed by LC-MS. Expected mass: 66,438 Da. Observed mass: 66,439 Da.

(a)



(b)



(c)

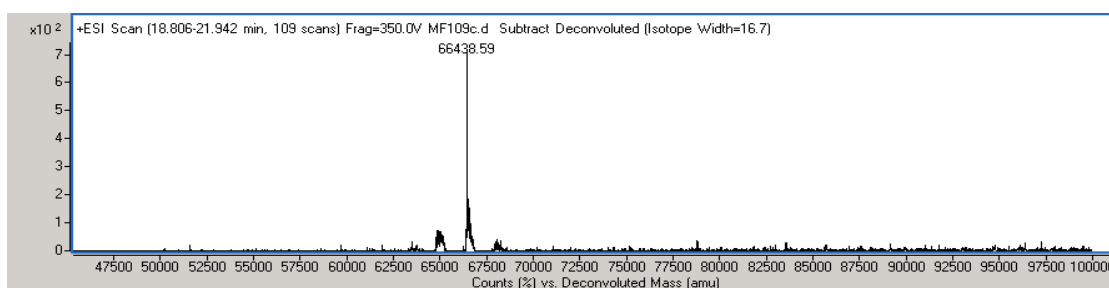
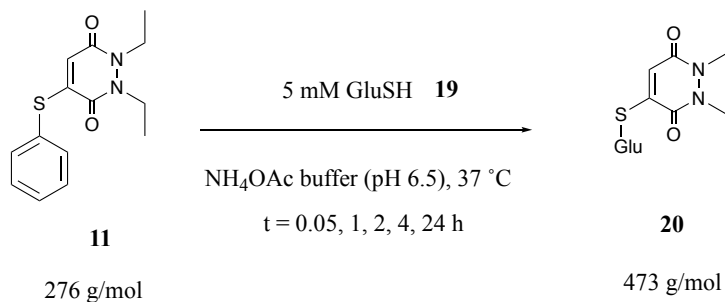


Figure S18. (a) TIC, (b) non-deconvoluted and (c) deconvoluted MS data for human serum albumin incubated with pyridazinedione **17** (10 eq.).



# Incubations involving GluSH and pyridazinediones 11, 12, 14, 15 and 17 at pH 6.5

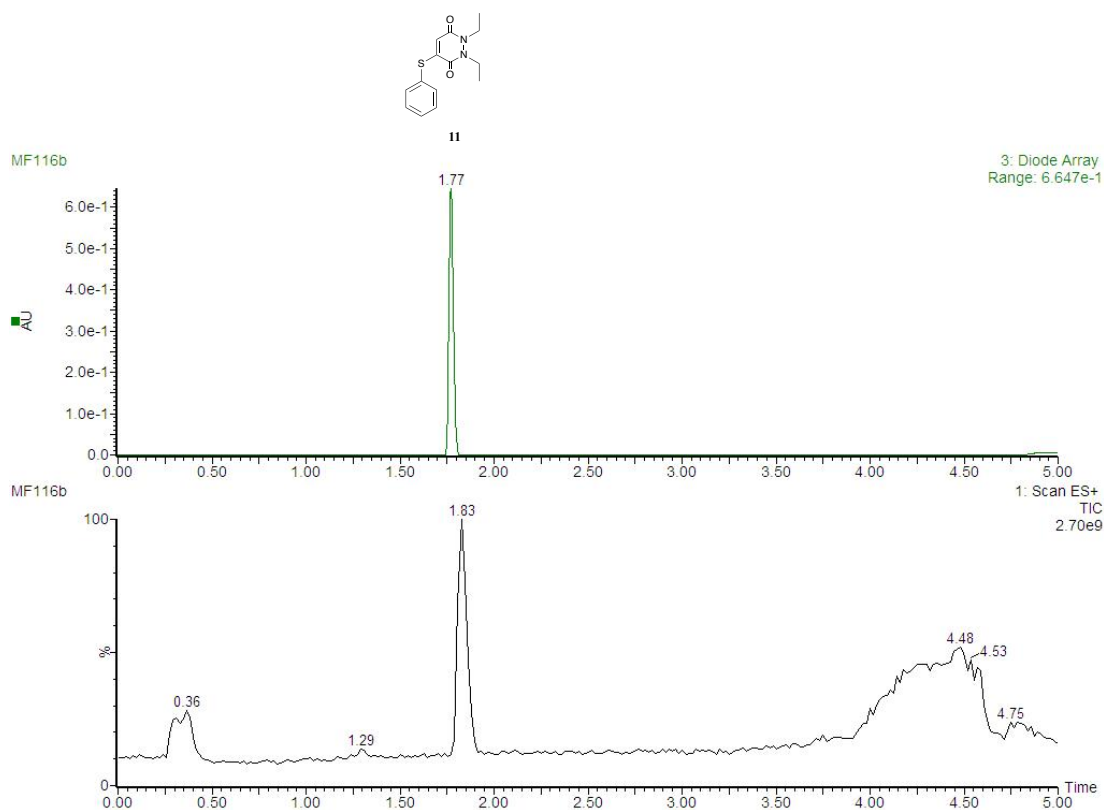
## Incubation of pyridazinedione 11 with GluSH (10 eq.)



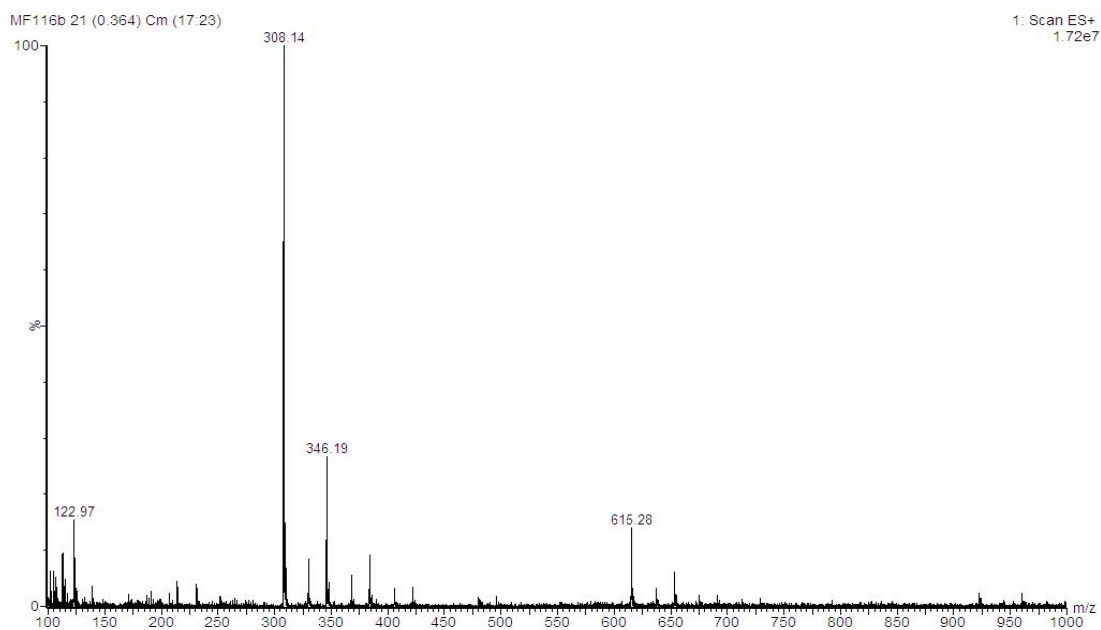
Pyridazinedione **11** (10  $\mu\text{L}$ , 10 mM in MeCN, 1 eq.) was added to GluSH **19** (190  $\mu\text{L}$ , 5.3 mM, 10 eq.) in ammonium acetate buffer (50 mM, pH 6.5). The mixture was incubated at 37  $^\circ\text{C}$  for 24 h. The samples were analysed by LC-MS at  $t = 0.05, 1, 2, 4$  and 24 h.

### LC-MS data for $t = 0.05 \text{ h}$

(a)



(b)



(c)

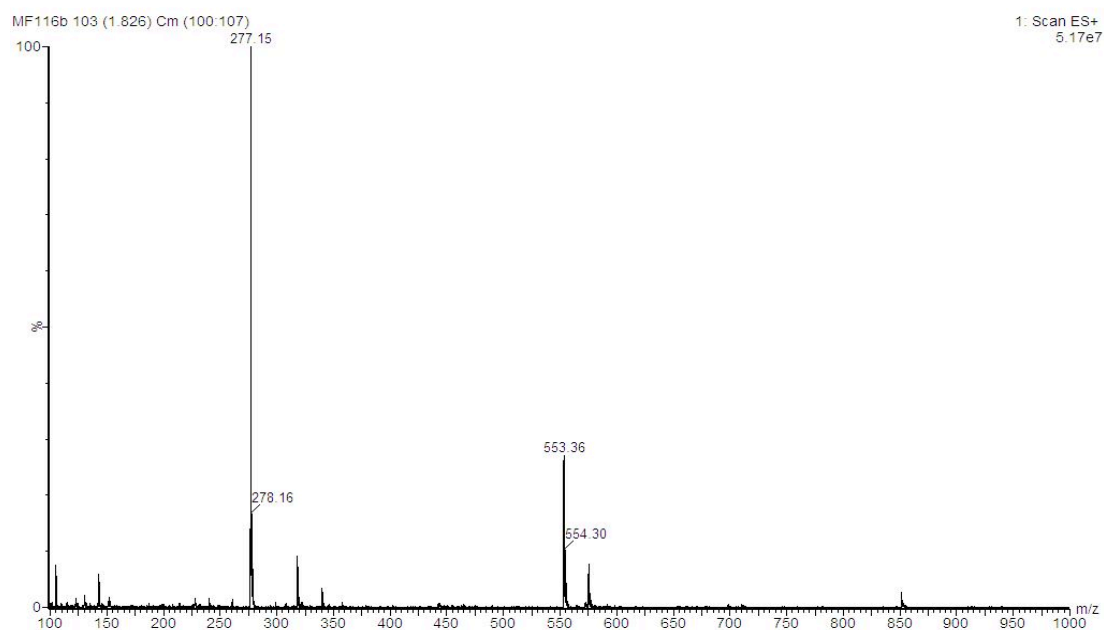
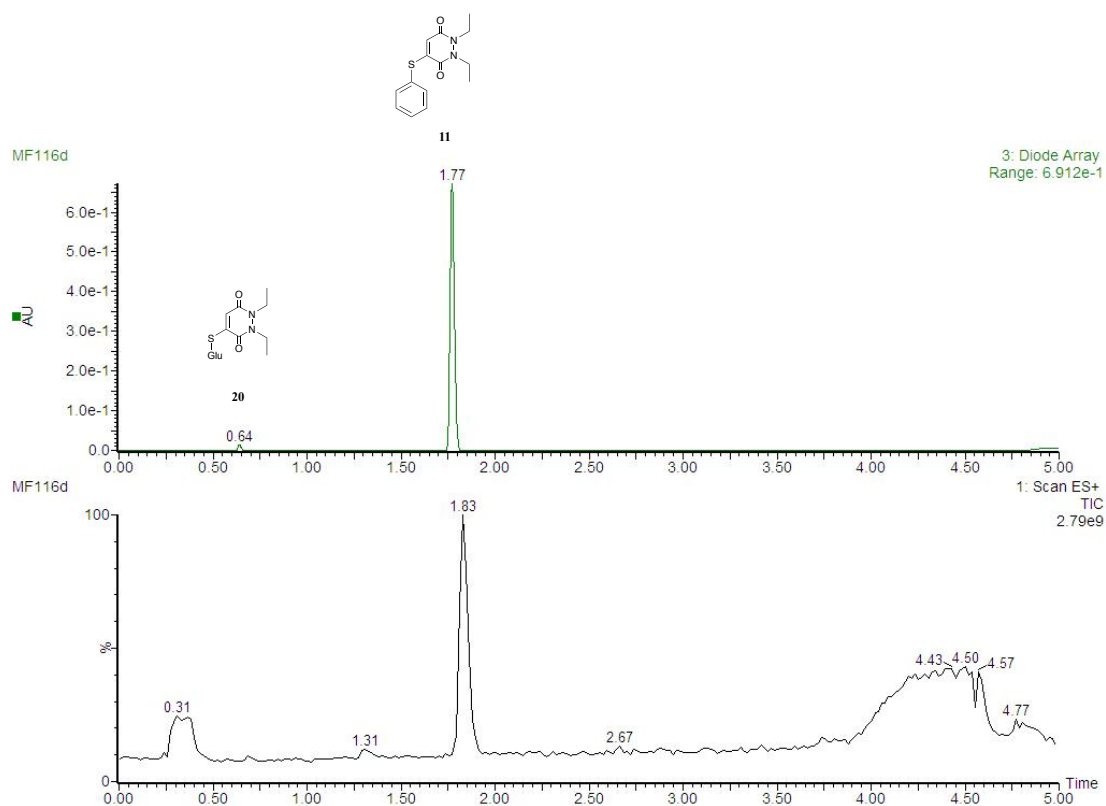


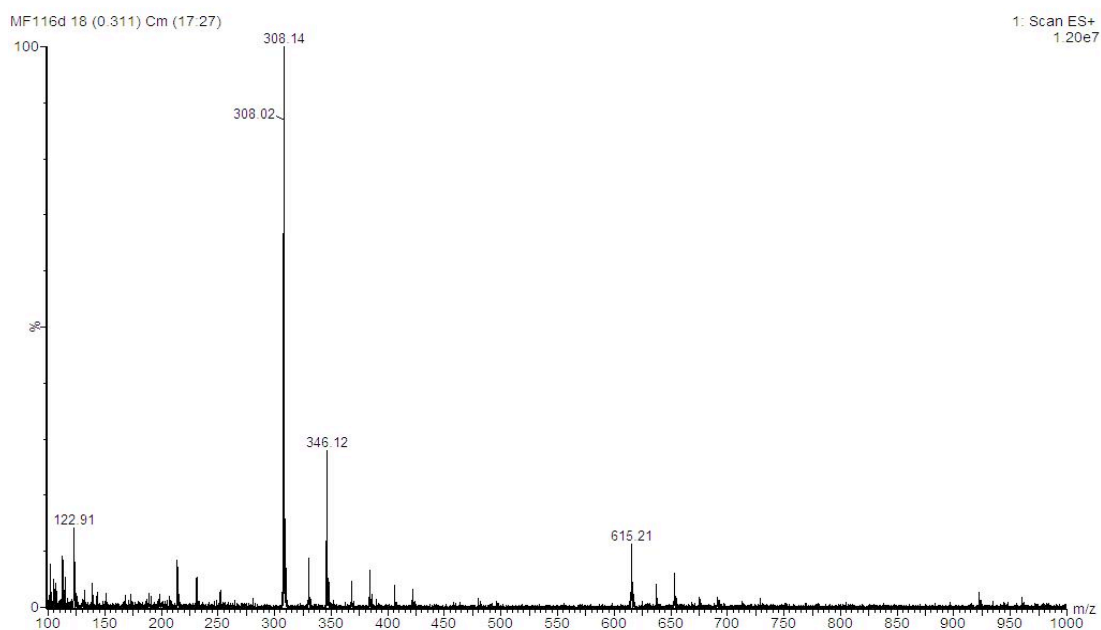
Figure S19. (a) TIC and UV trace at  $t = 0.05$  h, (b) MS data at 0.36 mins in the TIC and (c) MS data at 1.77 mins in the UV for PD 11 incubated with GluSH 19 (10 eq.) at pH 6.5.

# LC-MS data for t = 1 h

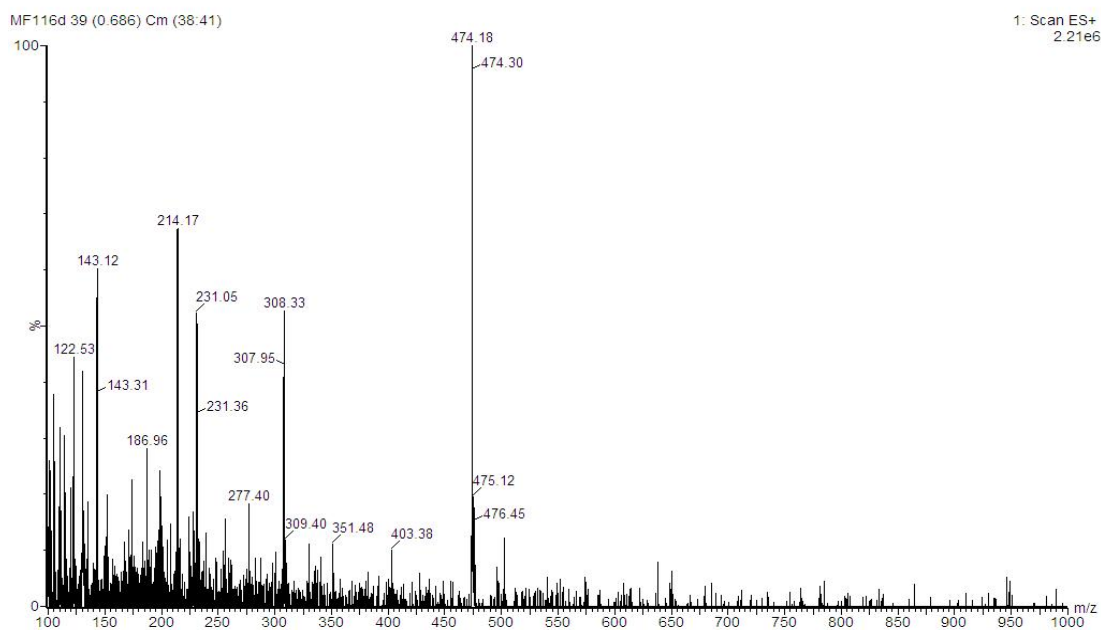
(a)



(b)



(c)



(d)

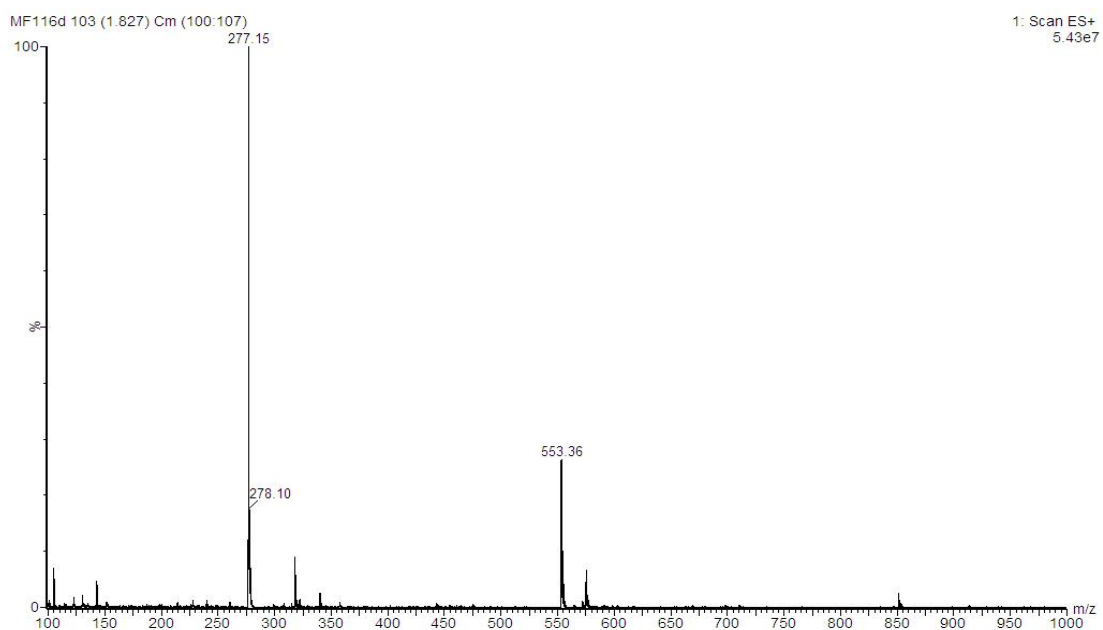
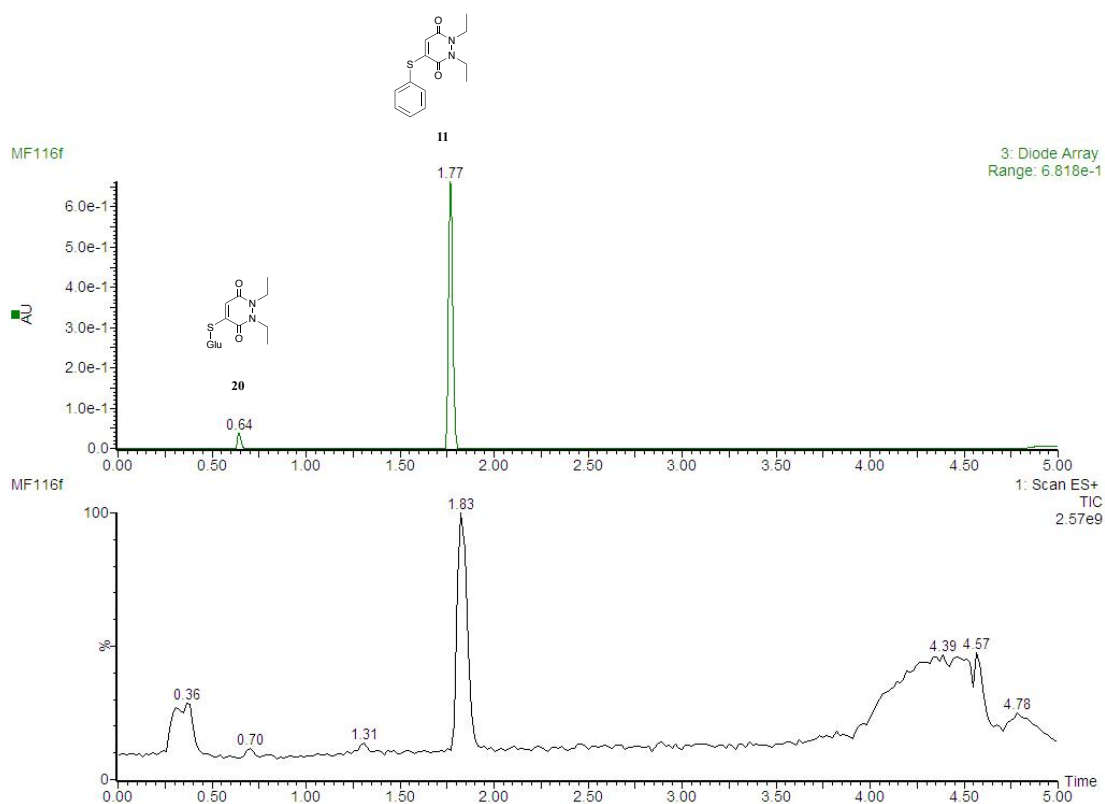


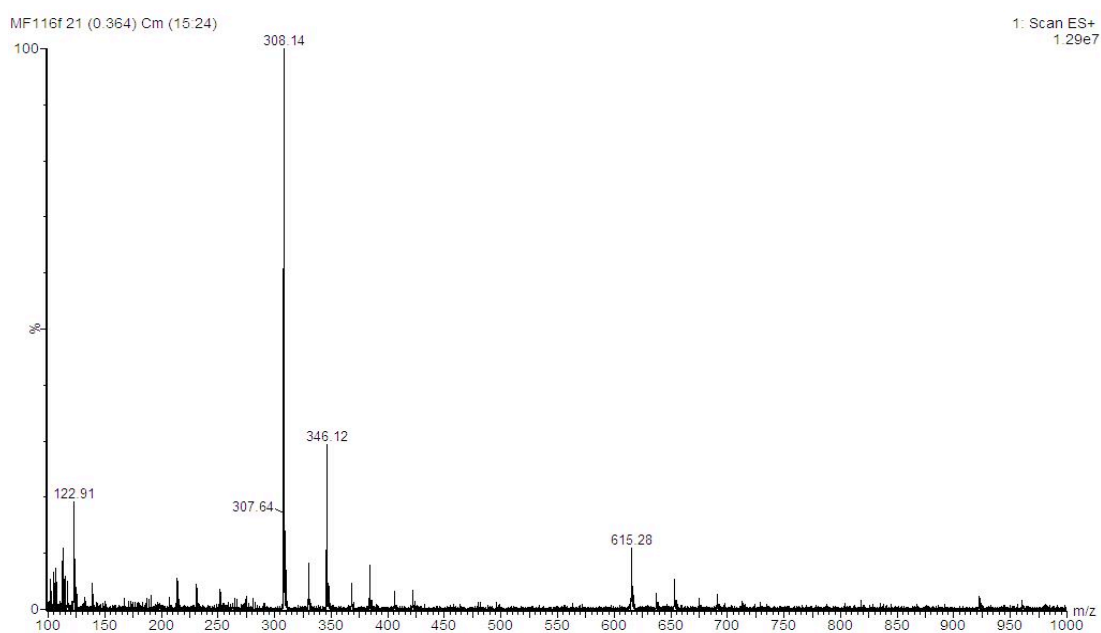
Figure S20. (a) TIC and UV trace at  $t = 1$  h, (b) MS data at 0.31 mins in the TIC, (c) MS data at 0.64 mins in the UV and (d) at 1.77 mins in the UV for PD **11** incubated with GluSH **19** (10 eq.) at pH 6.5.

# LC-MS data for t = 2 h

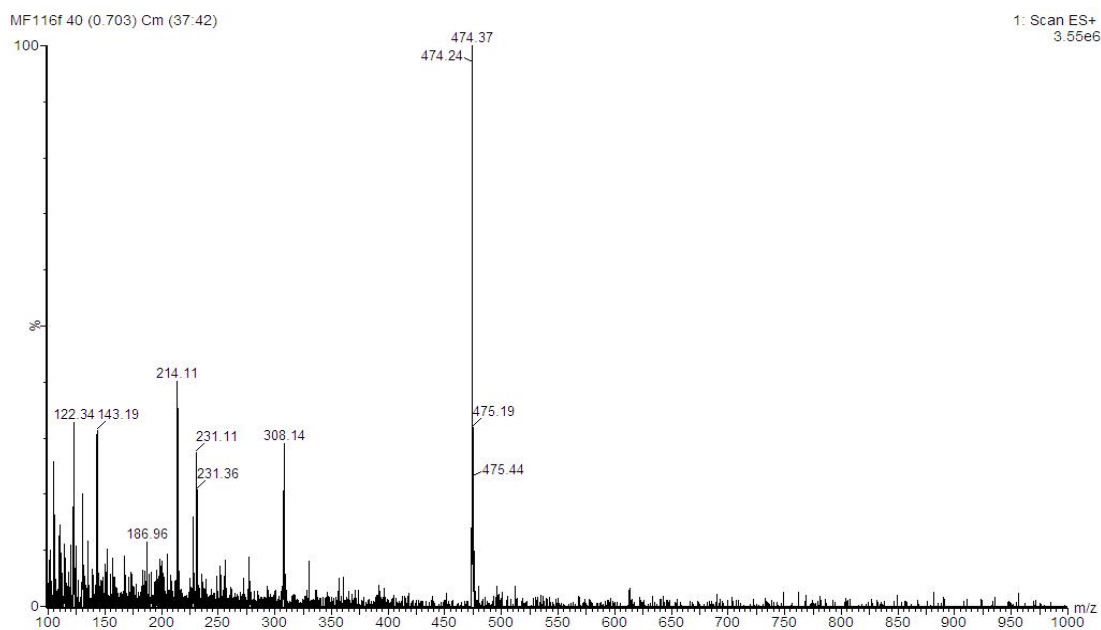
(a)



(b)



(c)



(d)

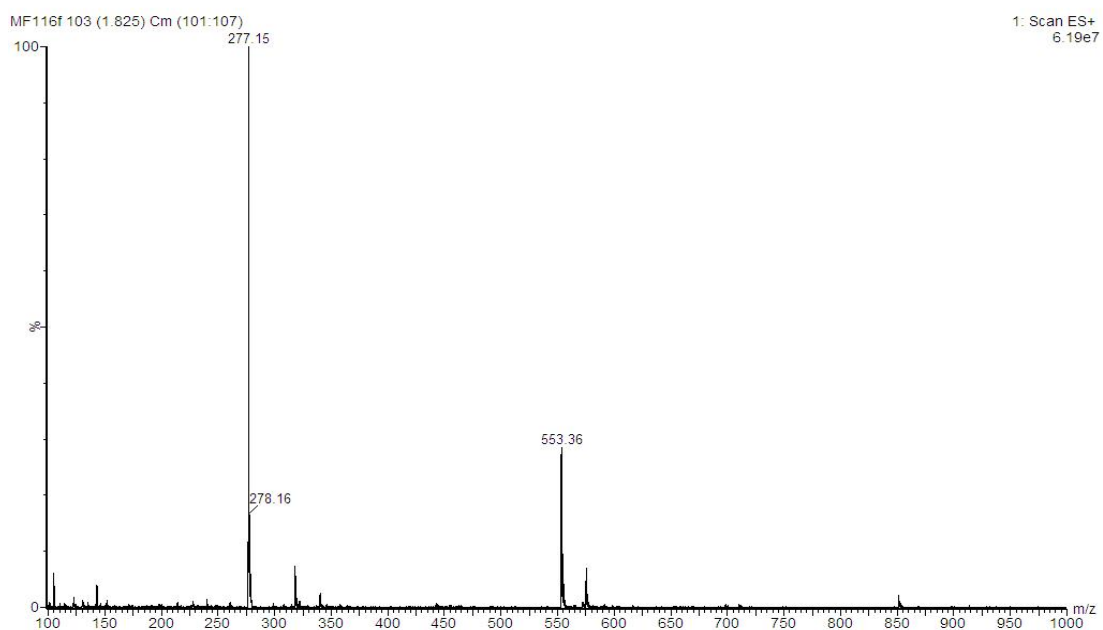
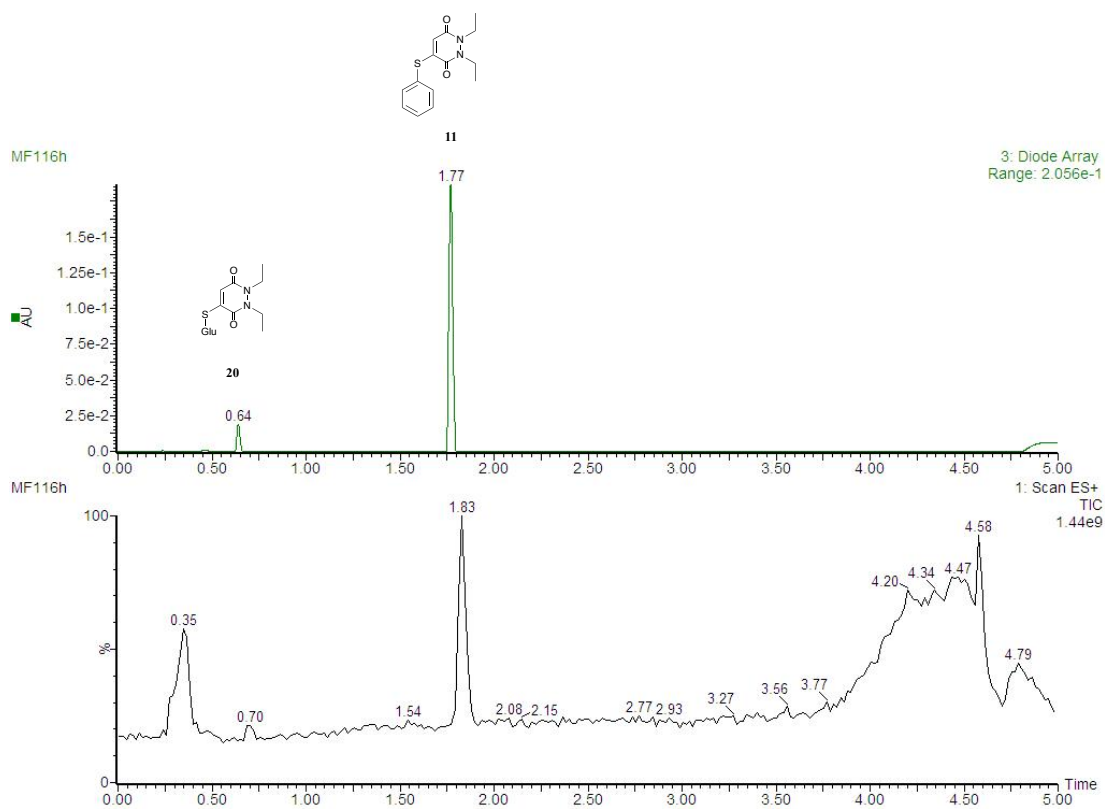


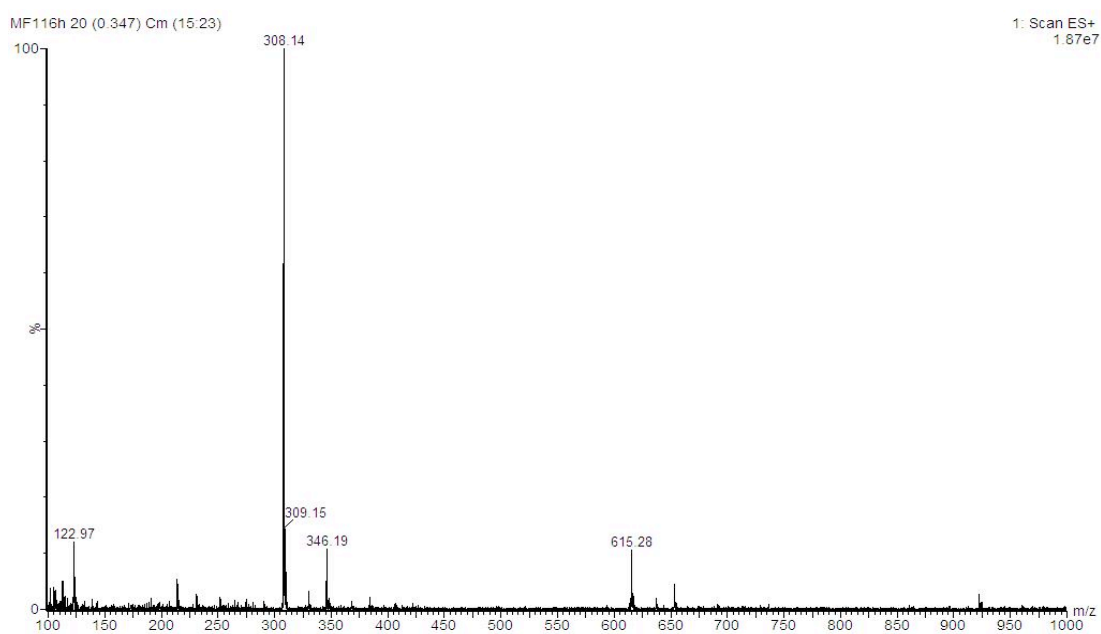
Figure S21. (a) TIC and UV trace at  $t = 2$  h, (b) MS data at 0.36 mins in the TIC, (c) MS data at 0.64 mins in the UV and (d) at 1.77 mins in the UV for PD **11** incubated with GluSH **19** (10 eq.) at pH 6.5.

# LC-MS data for t = 4 h

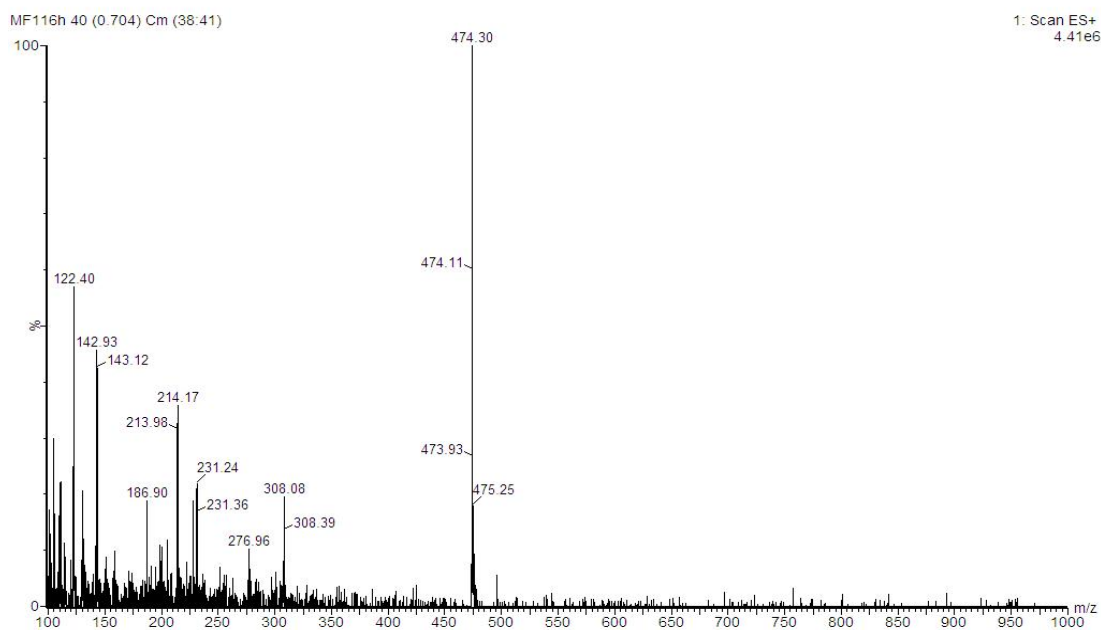
(a)



(b)



(c)



(d)

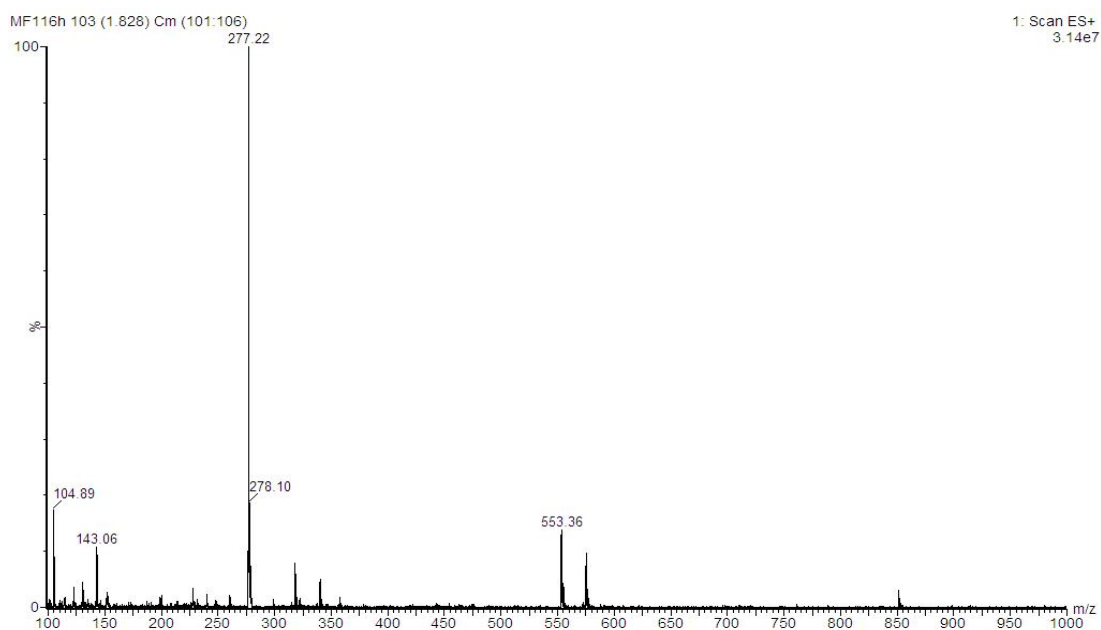
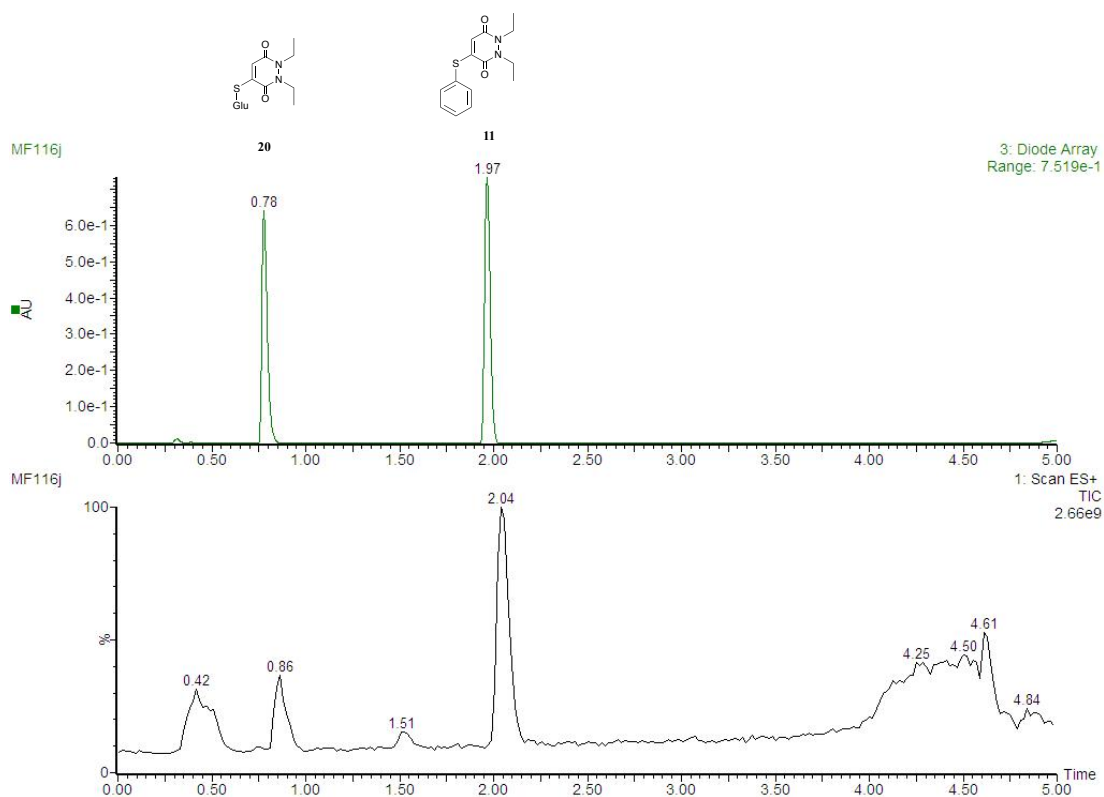


Figure S22. (a) TIC and UV trace at  $t = 4$  h, (b) MS data at 0.35 mins in the TIC, (c) MS data at 0.64 mins in the UV and (d) at 1.77 mins in the UV for PD 11 incubated with GluSH 19 (10 eq.) at pH 6.5.

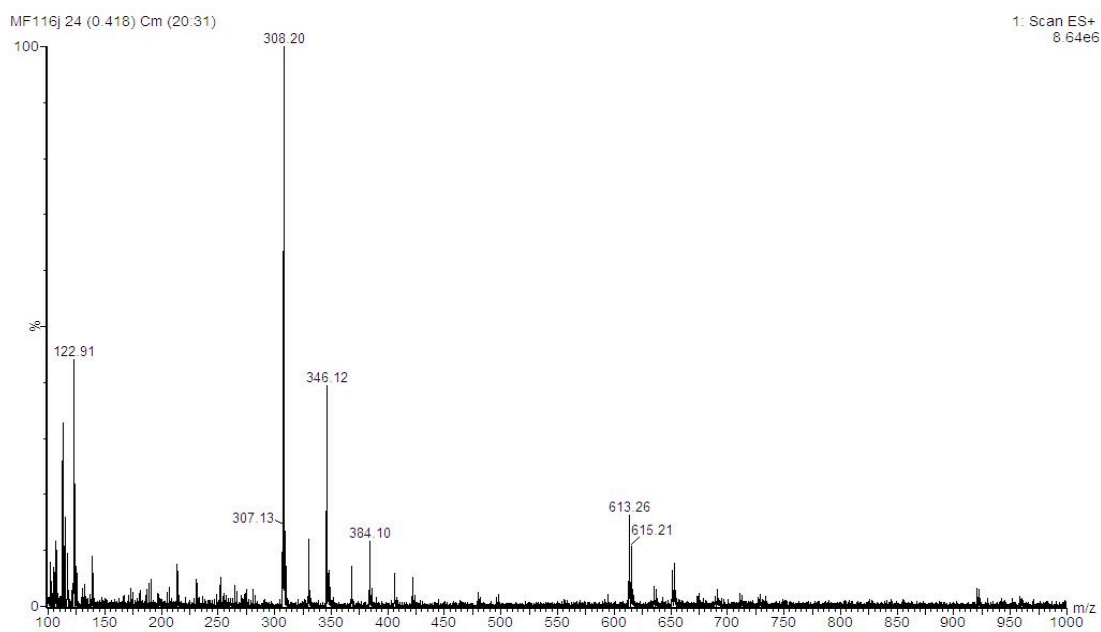


# LC-MS data for t = 24 h

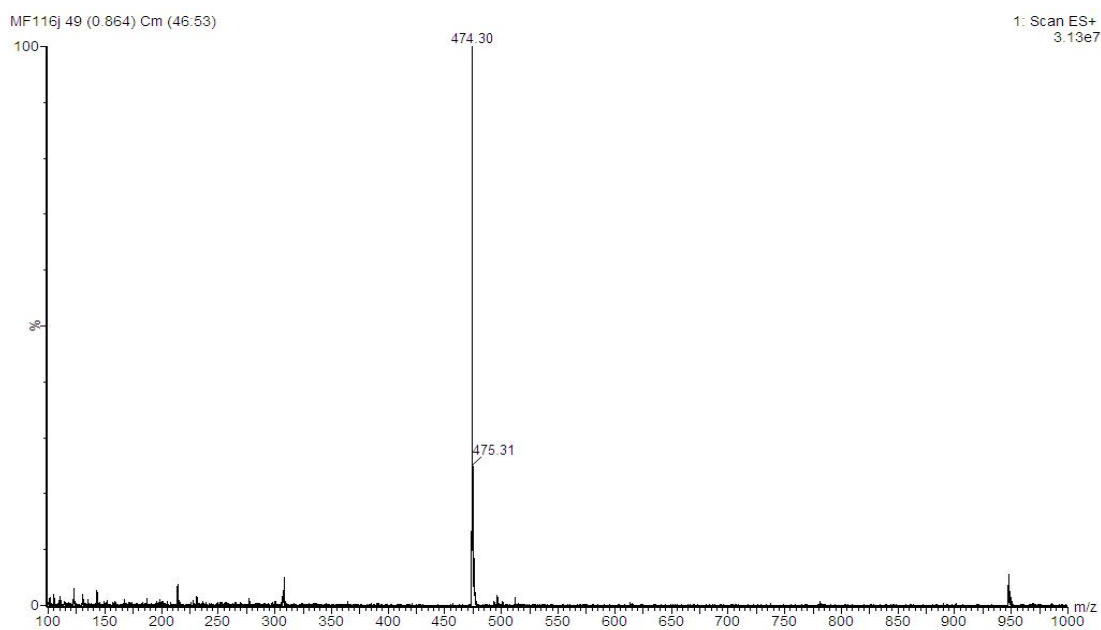
(a)



(b)



(c)



(d)

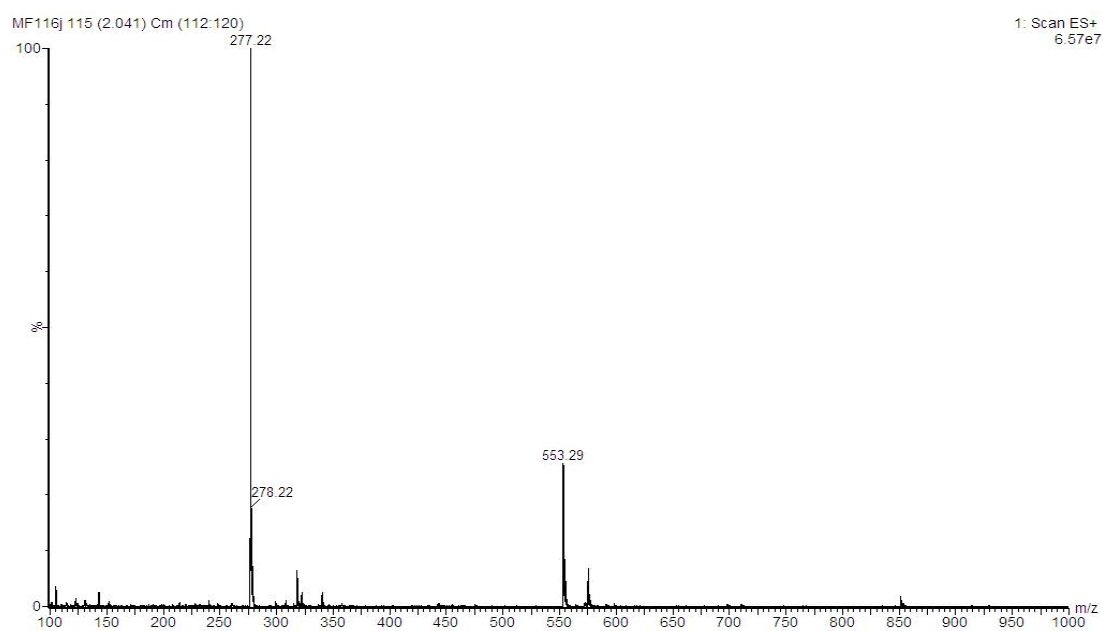
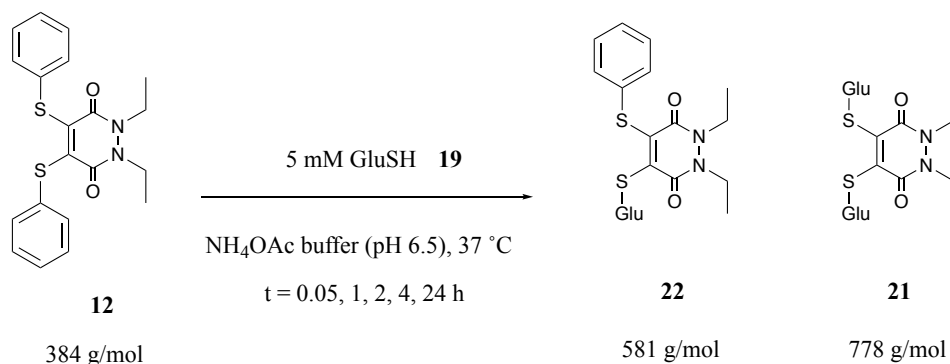


Figure S23. (a) TIC and UV trace at  $t = 24$  h, (b) MS data at 0.42 mins in the TIC, (c) MS data at 0.78 mins in the UV and (d) at 1.97 mins in the UV for PD **11** incubated with GluSH **19** (10 eq.) at pH 6.5.

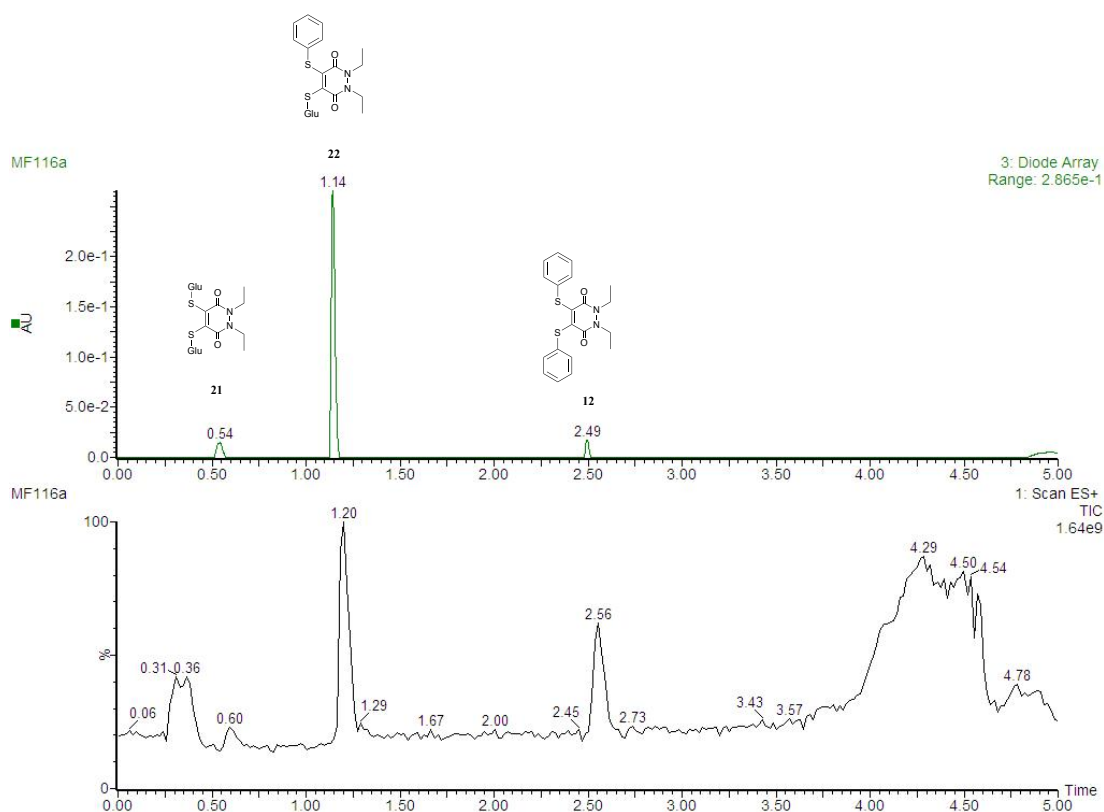
## Incubation of pyridazinedione **12** with GluSH (**10 eq.**)



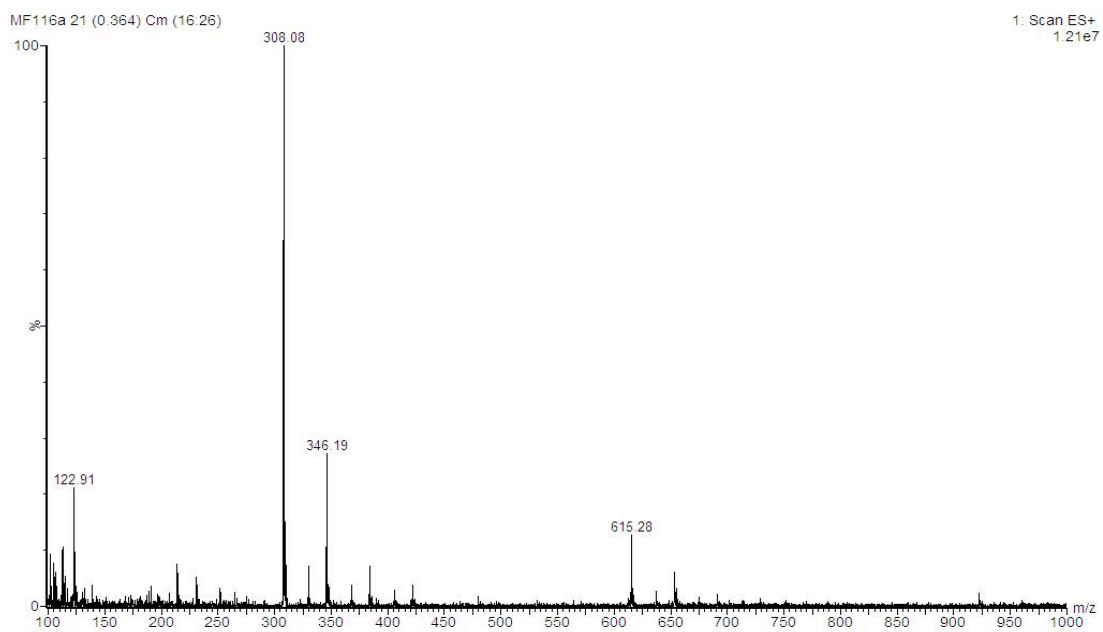
Pyridazinedione **12** (10  $\mu$ L, 10 mM in MeCN, 1 eq.) was added to GluSH **19** (190  $\mu$ L, 5.3 mM, 10 eq.) in ammonium acetate buffer (50 mM, pH 6.5). The mixture was incubated at 37 °C for 24 h. The samples were analysed by LC-MS at  $t = 0.05, 1, 2, 4$  and 24 h.

### LC-MS data for $t = 0.05$ h

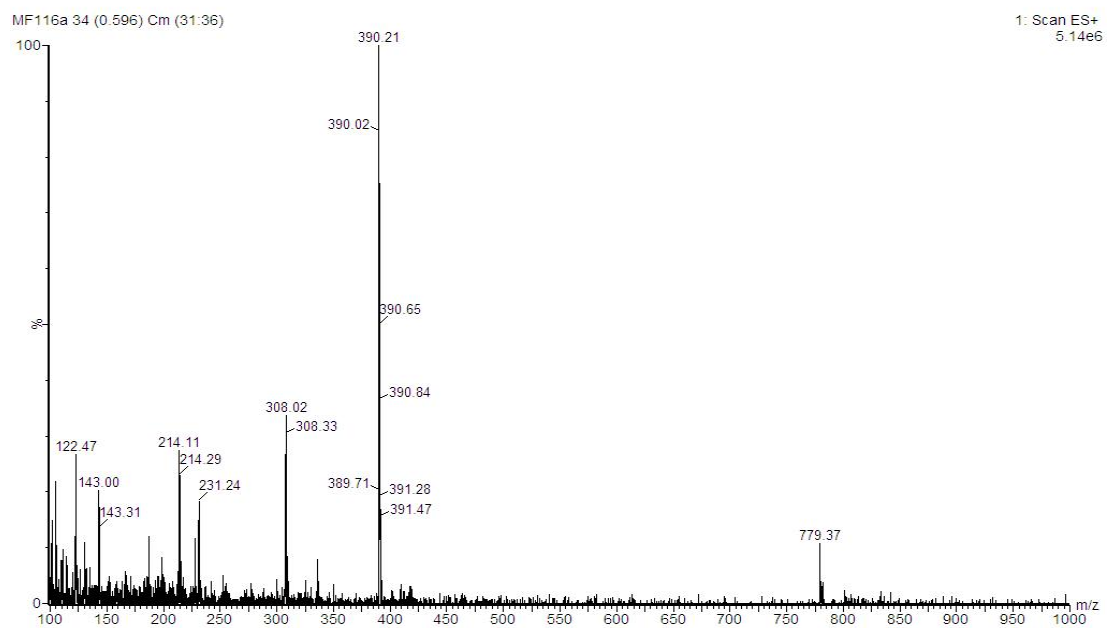
(a)



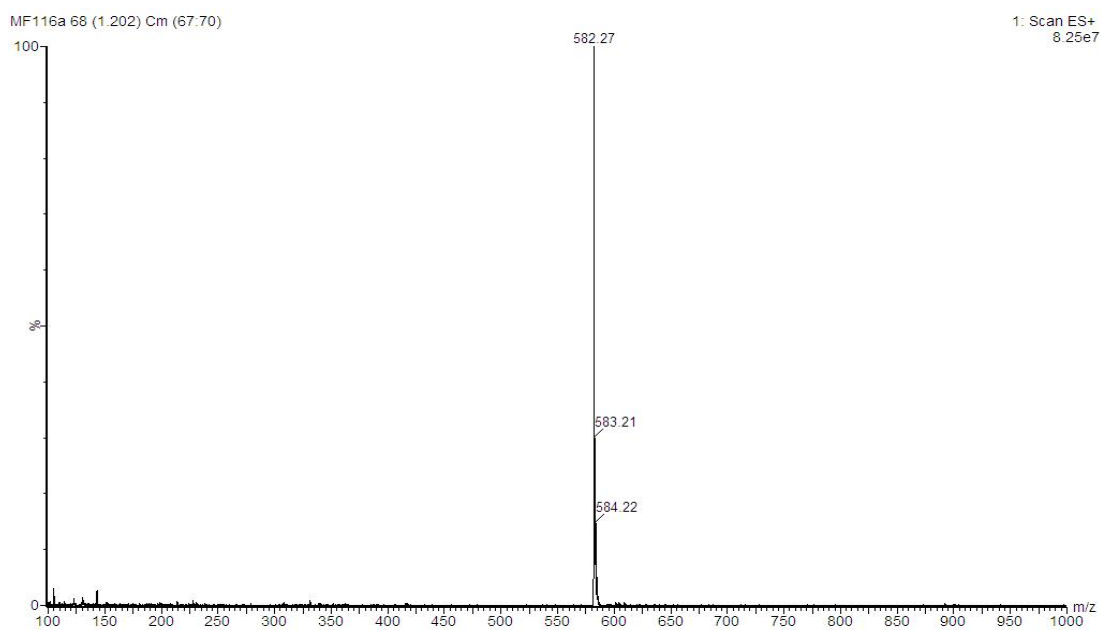
(b)



(c)



(d)



(e)

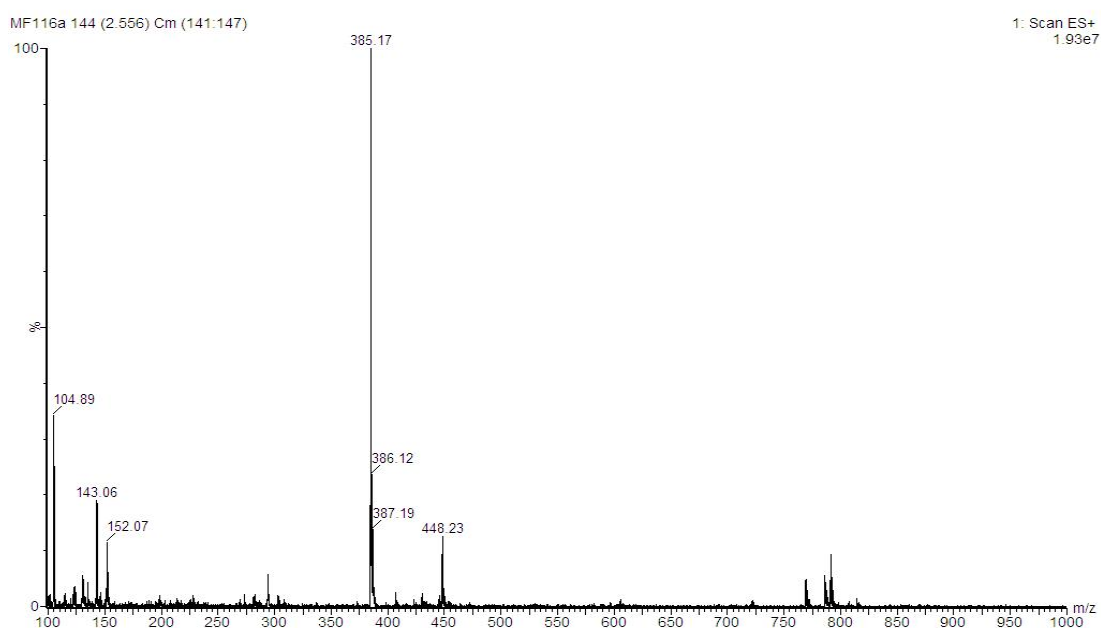
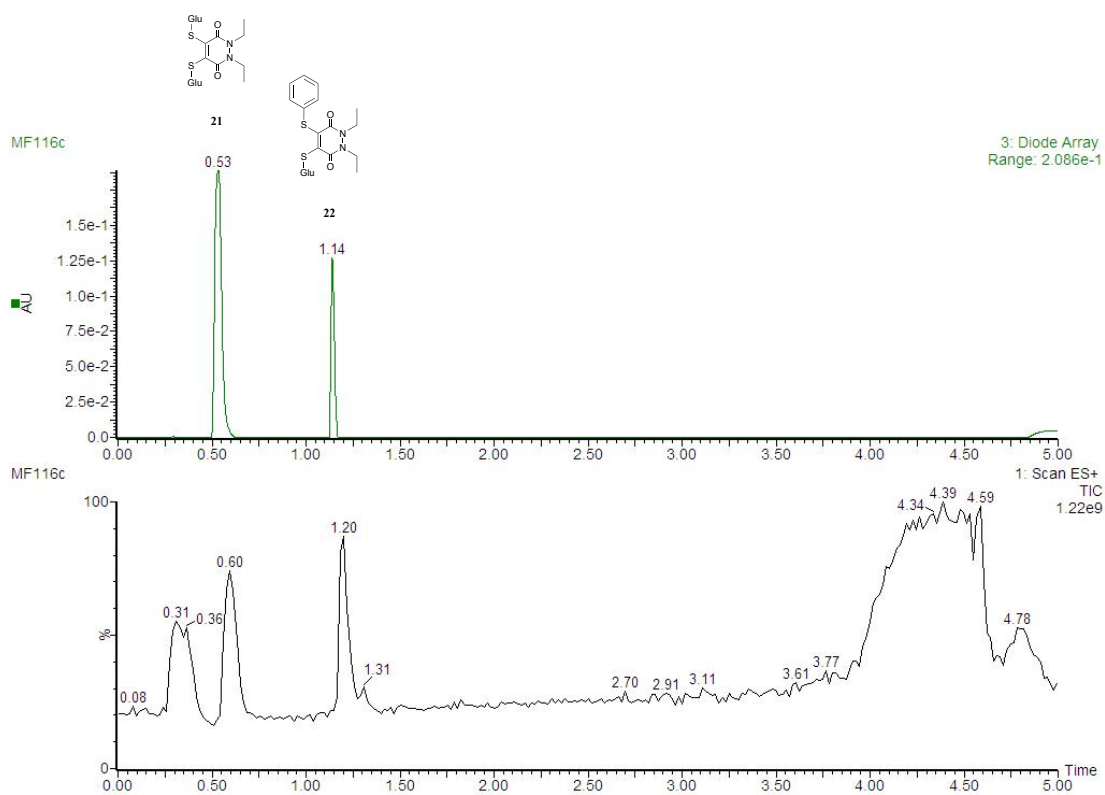


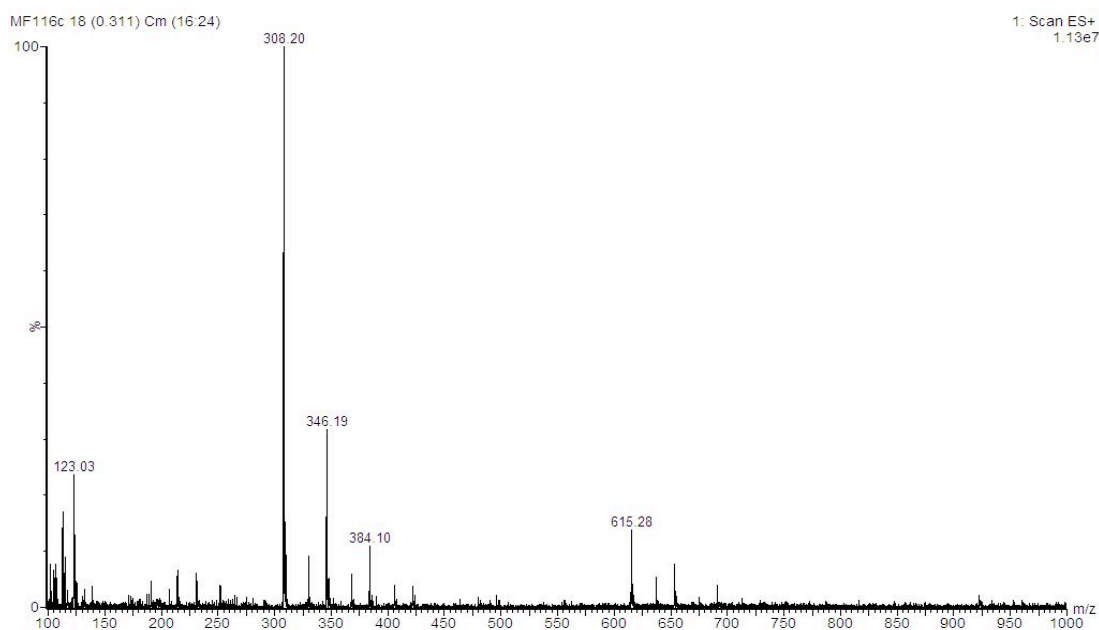
Figure S24. (a) TIC and UV trace at  $t = 0.05$  h, (b) MS data at 0.36 mins in the TIC, (c) MS data at 0.54 mins in the UV, (d) at 1.14 mins in the UV and (e) at 2.49 mins in the UV for PD **12** incubated with GluSH **19** (10 eq.) at pH 6.5.

# LC-MS data for t = 1 h

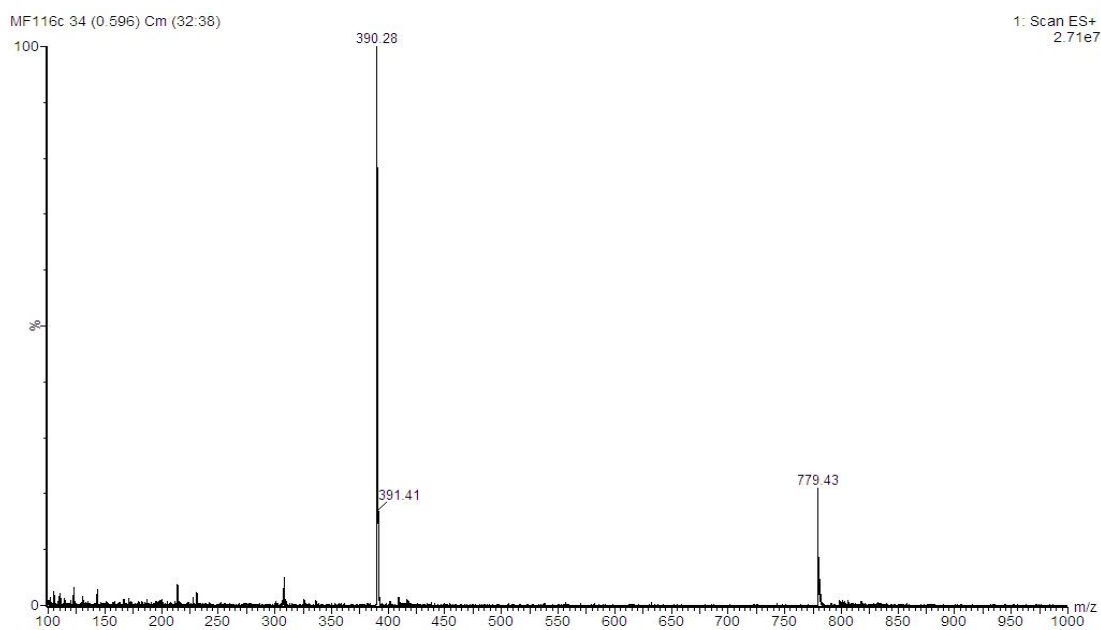
(a)



(b)



(c)



(d)

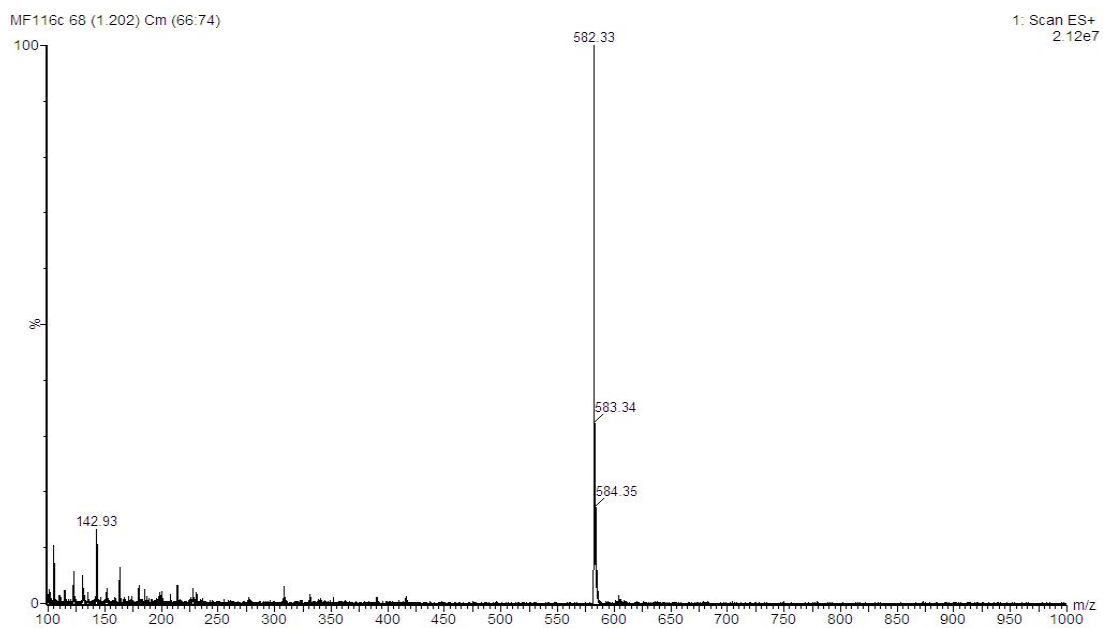
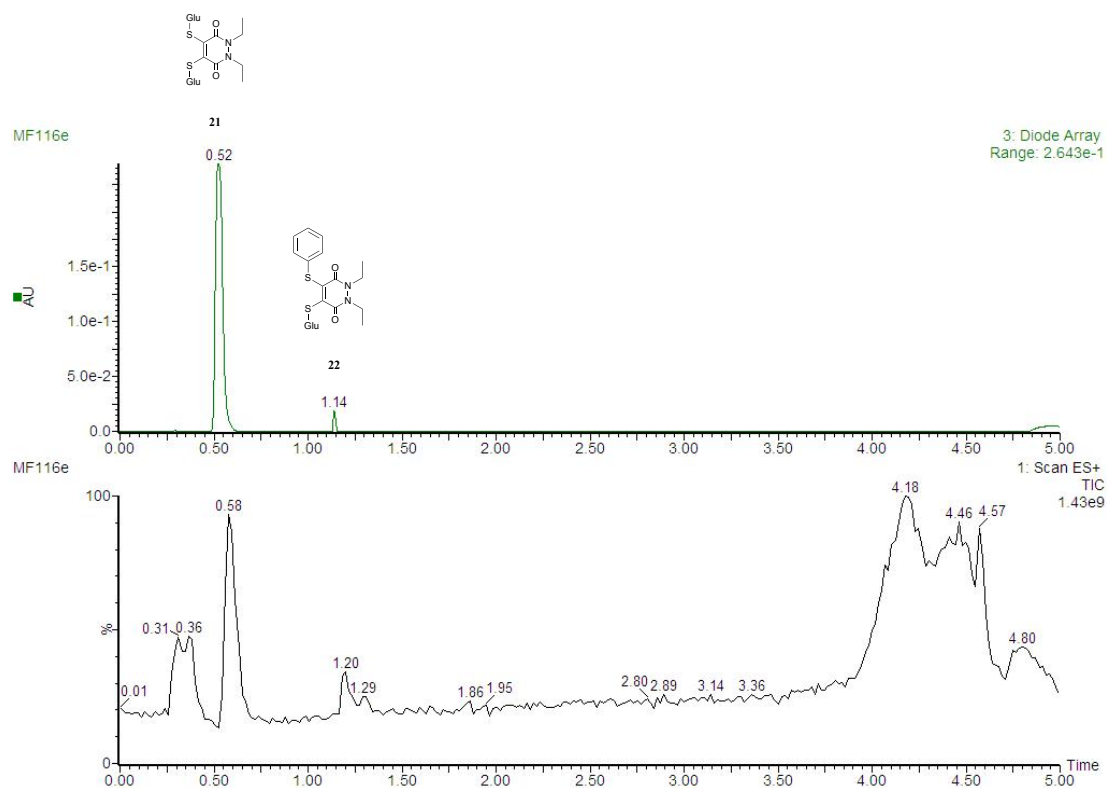


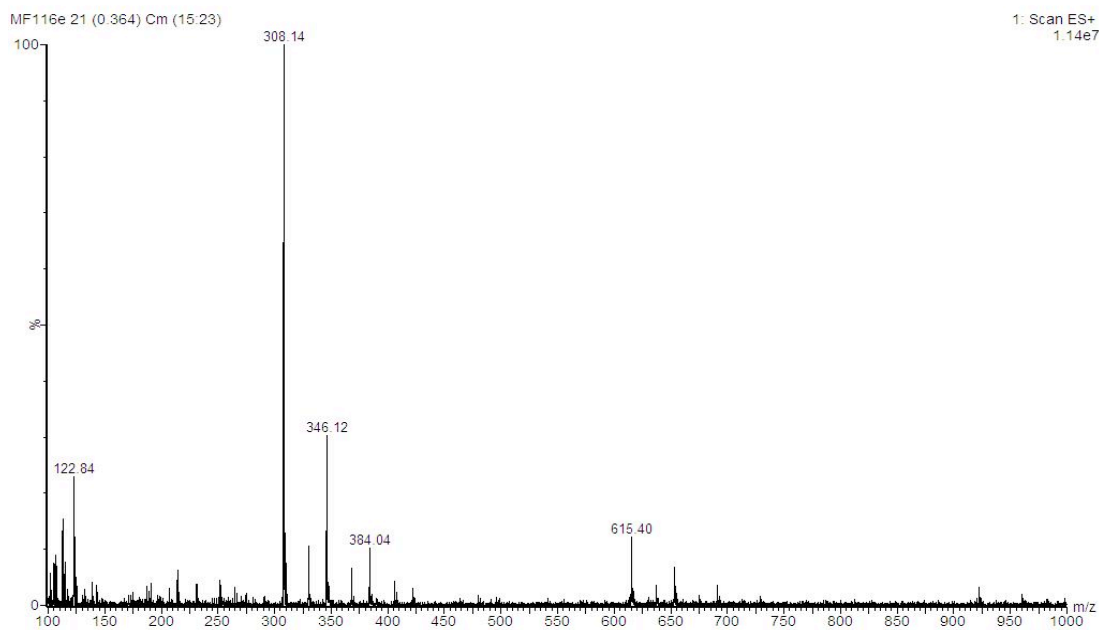
Figure S25. (a) TIC and UV trace at  $t = 1$  h, (b) MS data at 0.36 mins in the TIC, (c) MS data at 0.53 mins in the UV and (d) at 1.14 mins in the UV for PD **12** incubated with GluSH **19** (10 eq.) at pH 6.5.

# LC-MS data for t = 2 h

(a)

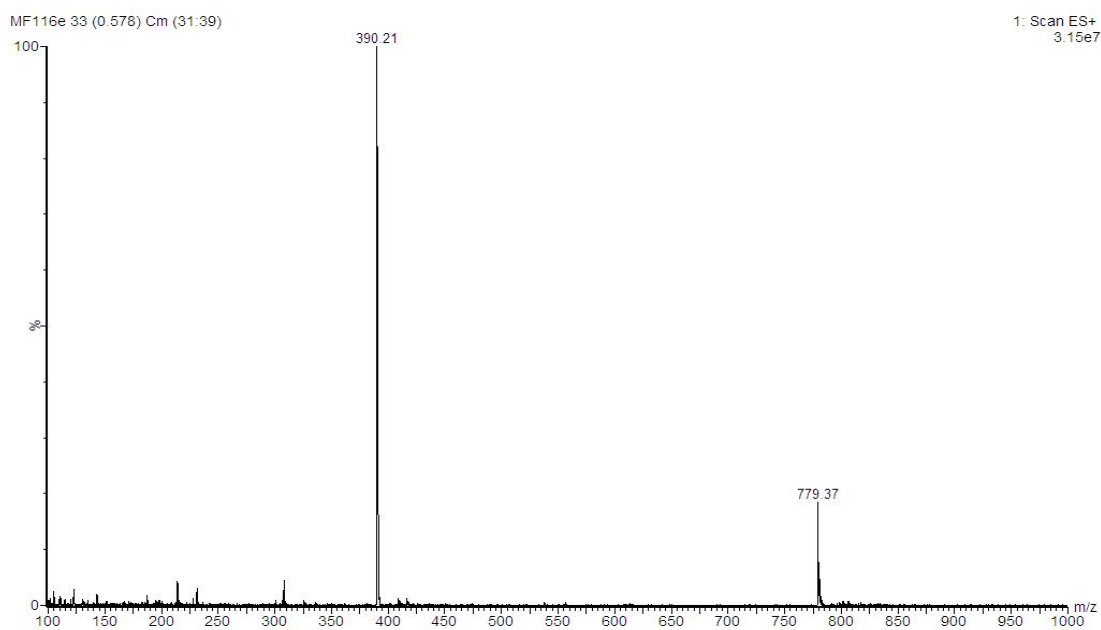


(b)





(c)



(d)

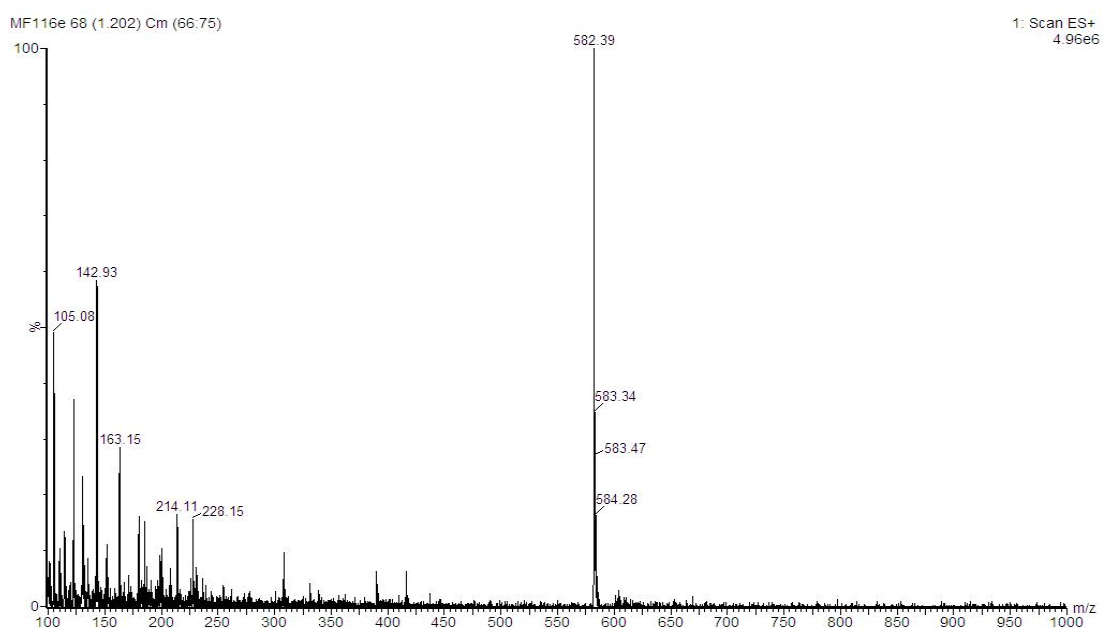
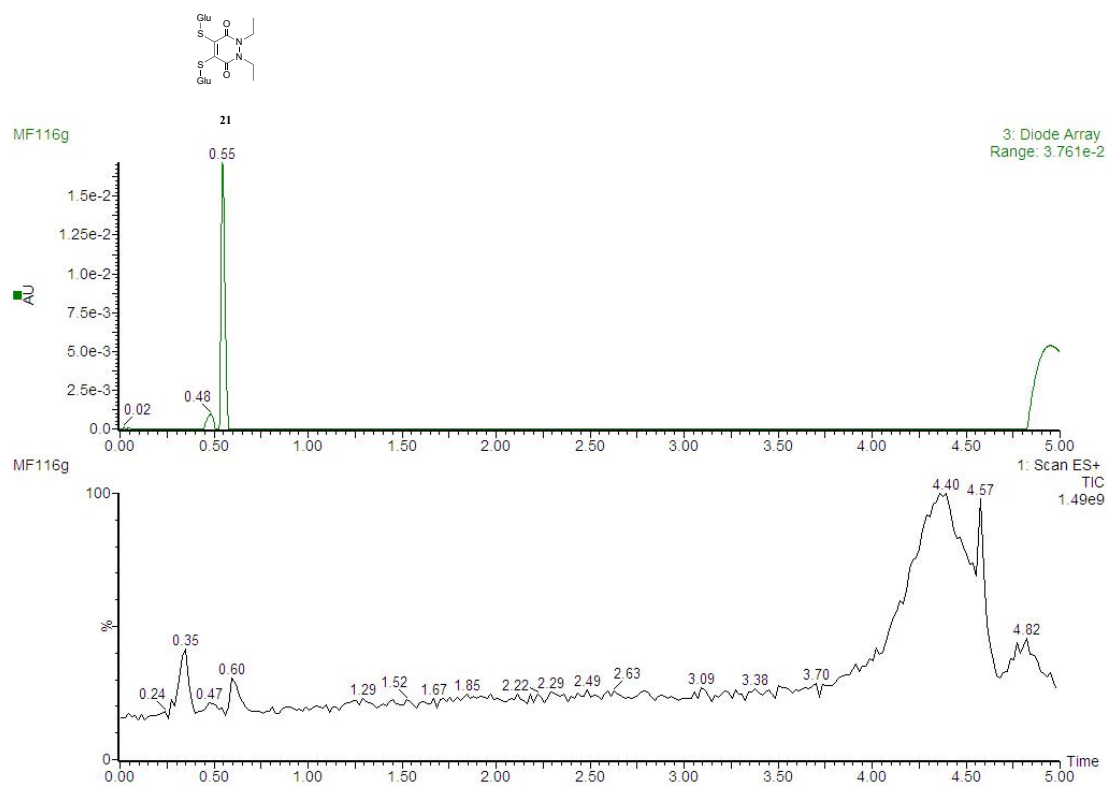


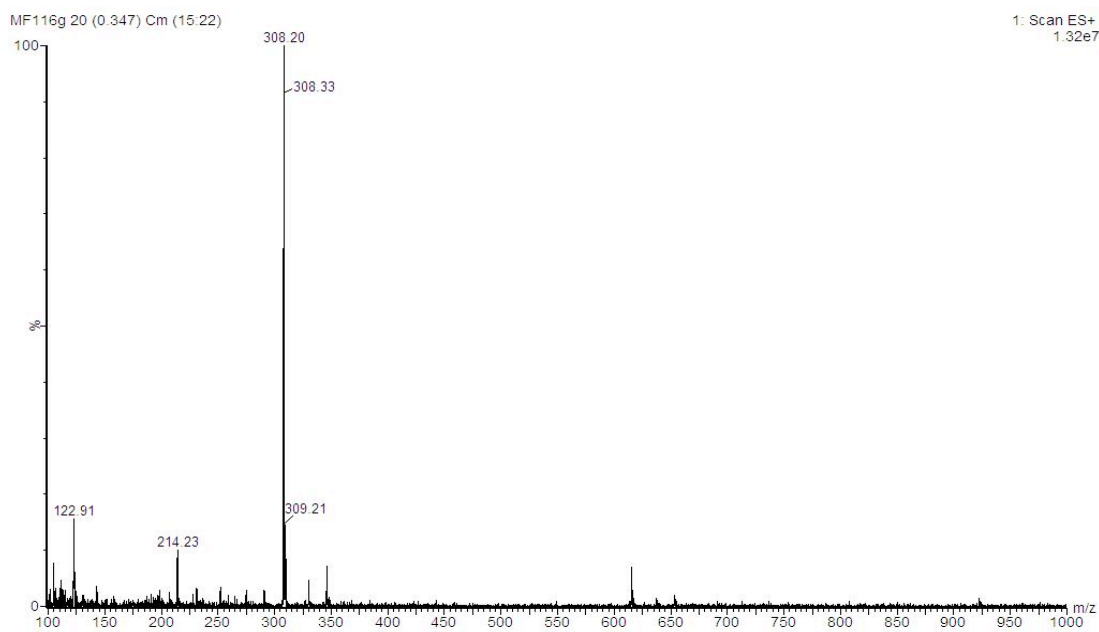
Figure S26. (a) TIC and UV trace at  $t = 2$  h, (b) MS data at 0.36 mins in the TIC, (c) MS data at 0.52 mins in the UV and (d) at 1.14 mins in the UV for PD **12** incubated with GluSH **19** (10 eq.) at pH 6.5.

# LC-MS data for t = 4 h

(a)



(b)



(c)

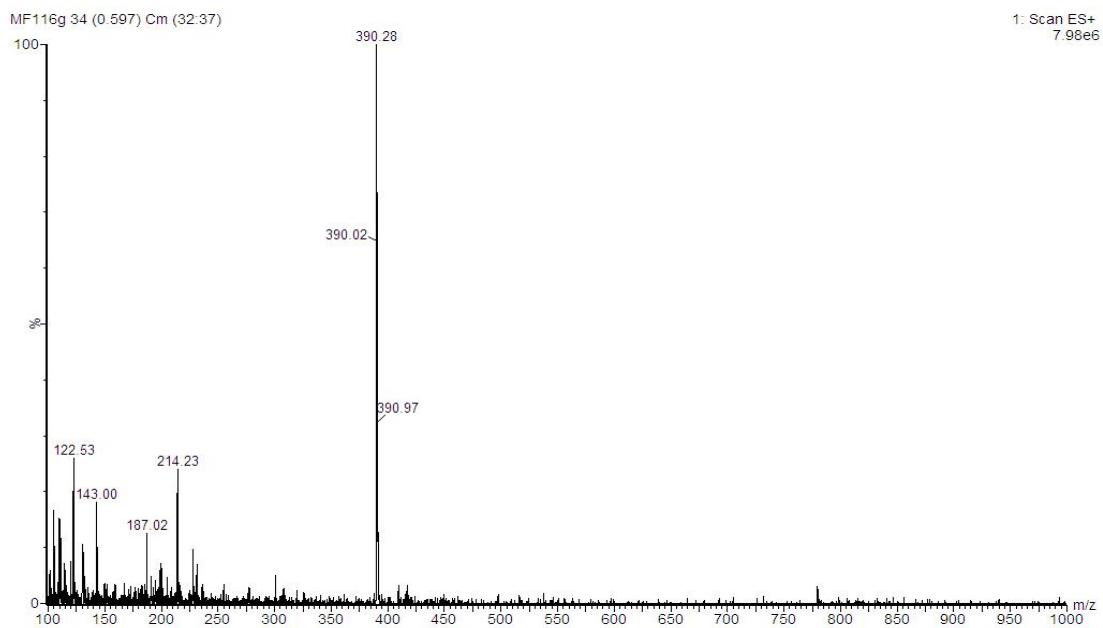
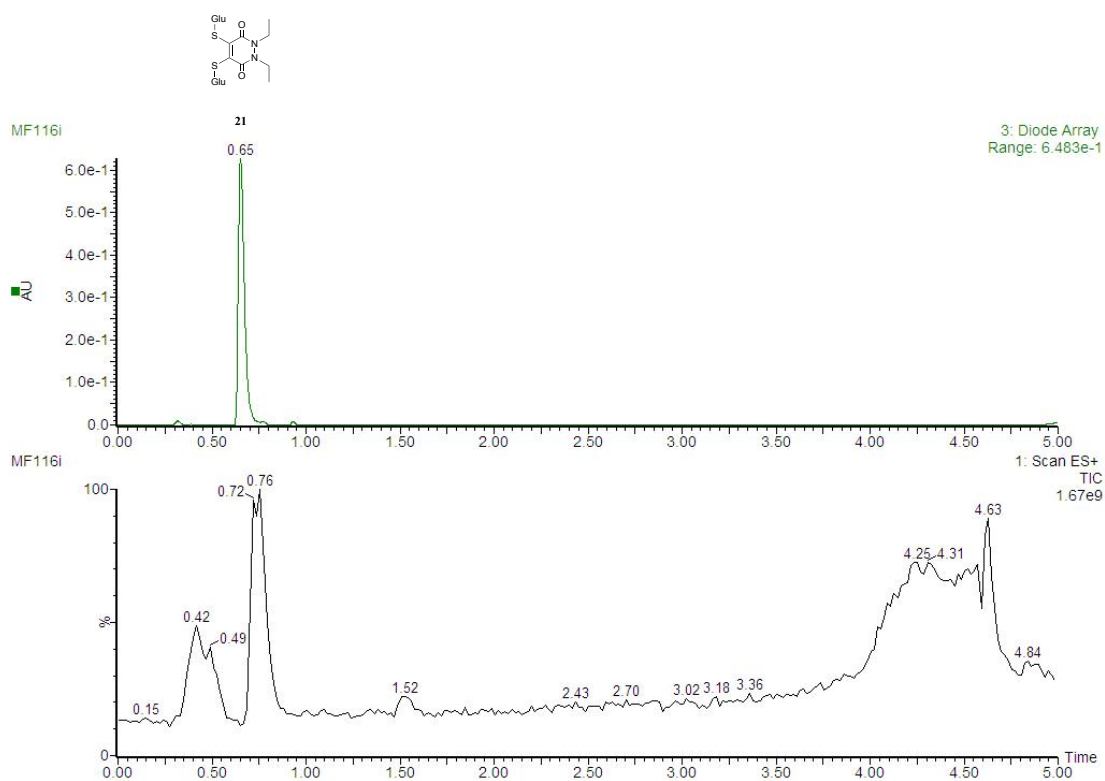


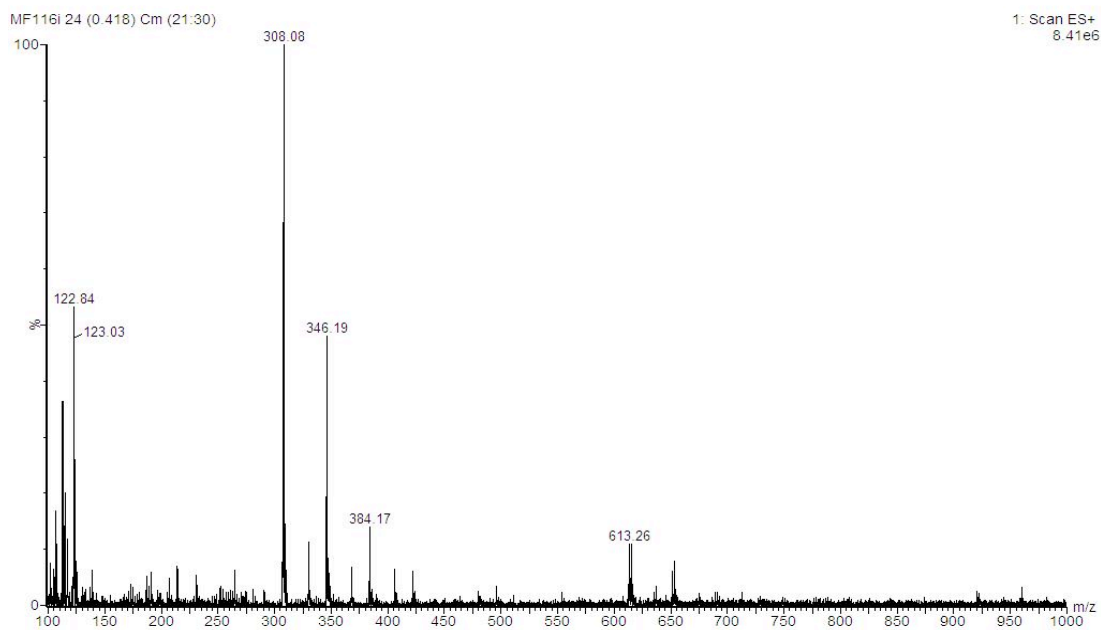
Figure S27. (a) TIC and UV trace at  $t = 4$  h, (b) MS data at 0.35 mins in the TIC and (c) MS data at 0.55 mins in the UV for PD 12 incubated with GluSH 19 (10 eq.) at pH 6.5.

# LC-MS data for t = 24 h

(a)



(b)



(c)

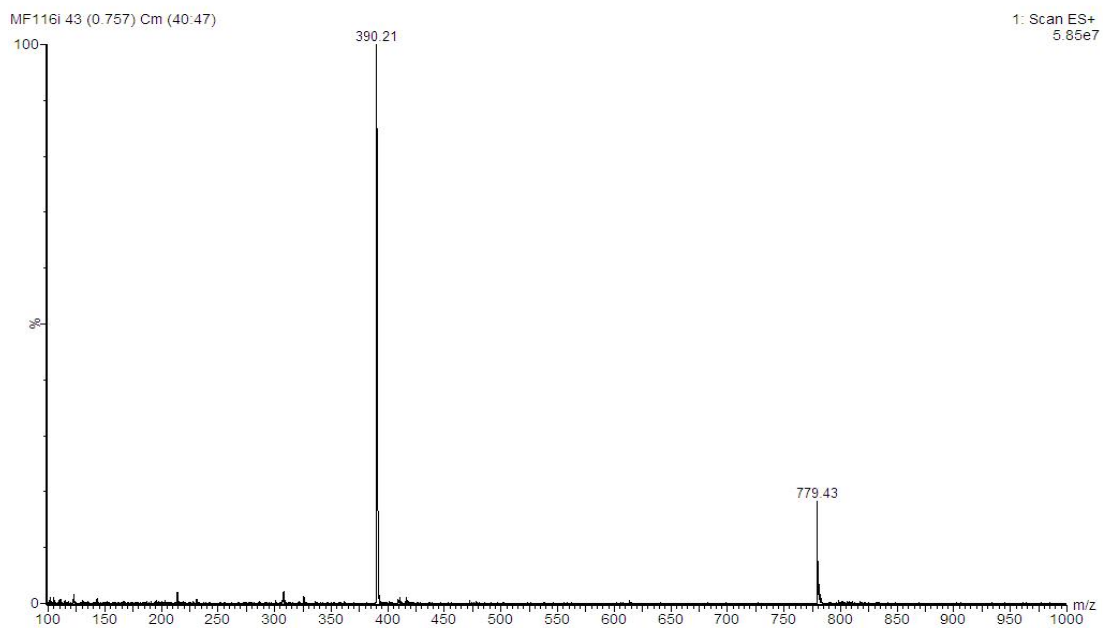
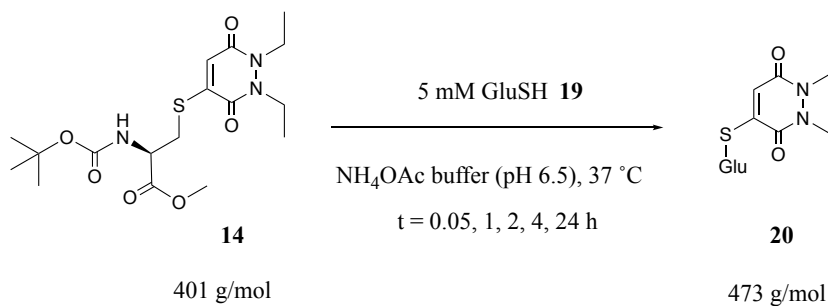


Figure S28. (a) TIC and UV trace at  $t = 24$  h, (b) MS data at 0.42 mins in the TIC and (c) MS data at 0.65 mins in the UV for PD **12** incubated with GluSH **19** (10 eq.) at pH 6.5.

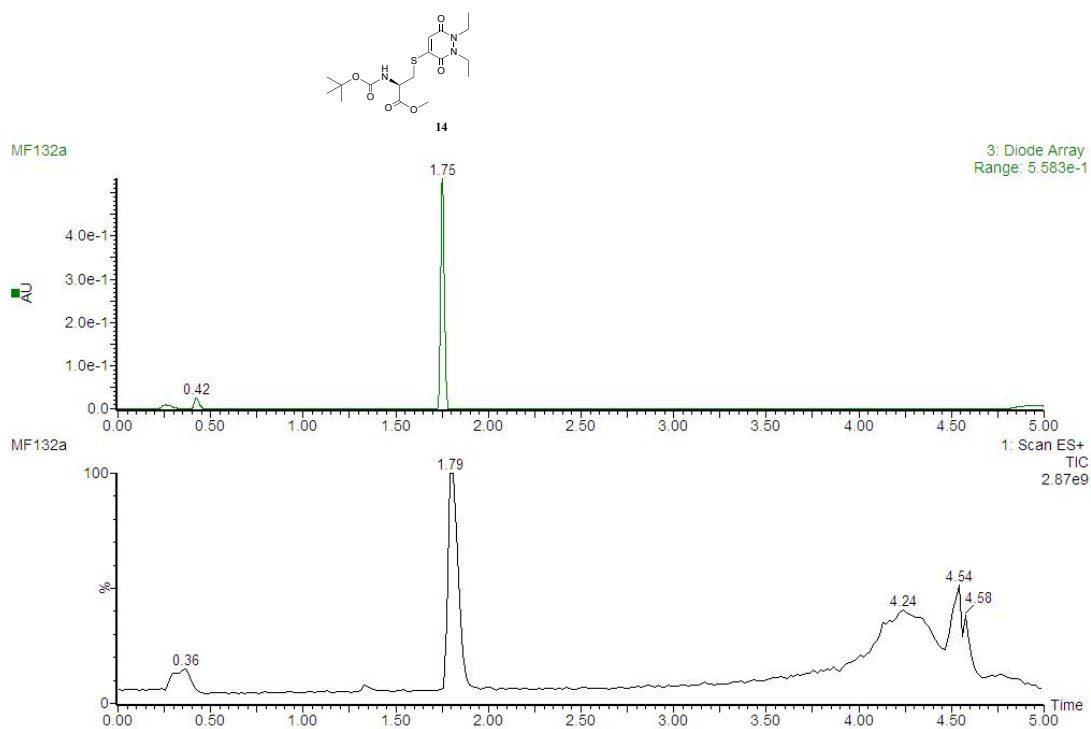
## Incubation of pyridazinedione **14** with GluSH (**10 eq.**)



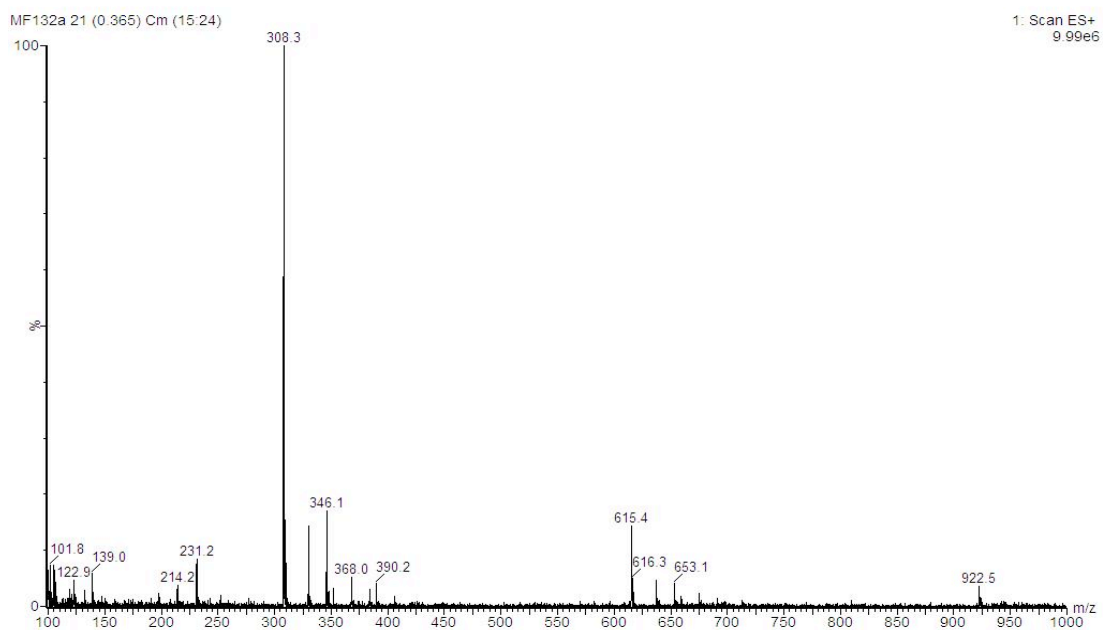
Pyridazinedione **14** (10  $\mu\text{L}$ , 10 mM in MeCN, 1 eq.) was added to GluSH **19** (190  $\mu\text{L}$ , 5.3 mM, 10 eq.) in ammonium acetate buffer (50 mM, pH 6.5). The mixture was incubated at 37  $^\circ\text{C}$  for 24 h. The samples were analysed by LC-MS at  $t = 0.05, 1, 2, 4$  and 24 h.

### LC-MS data for $t = 0.05 \text{ h}$

(a)



(b)



(c)

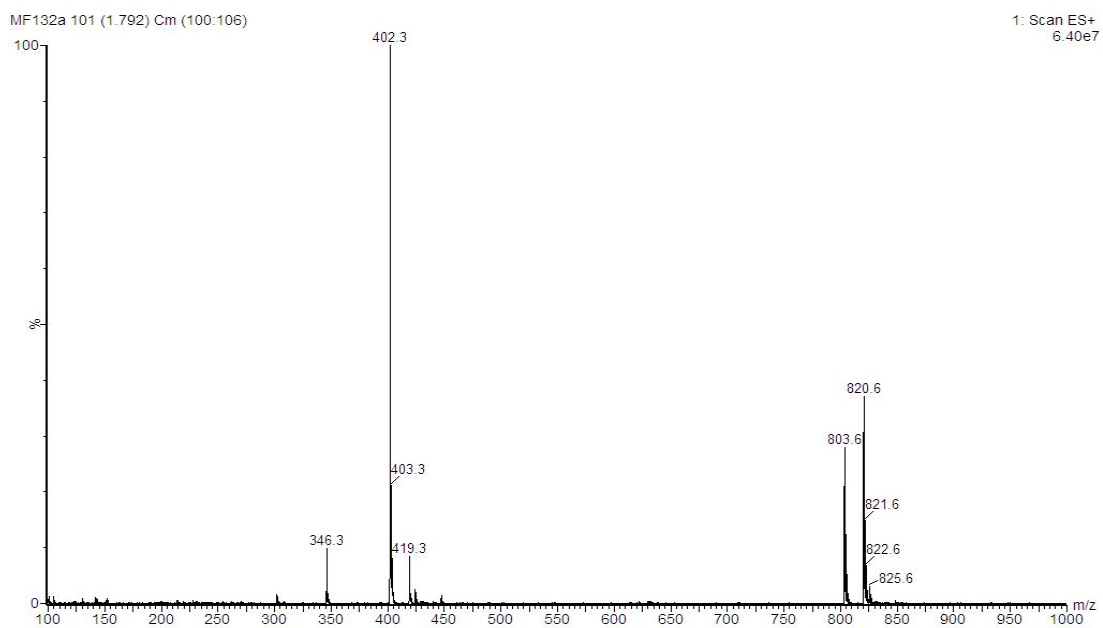
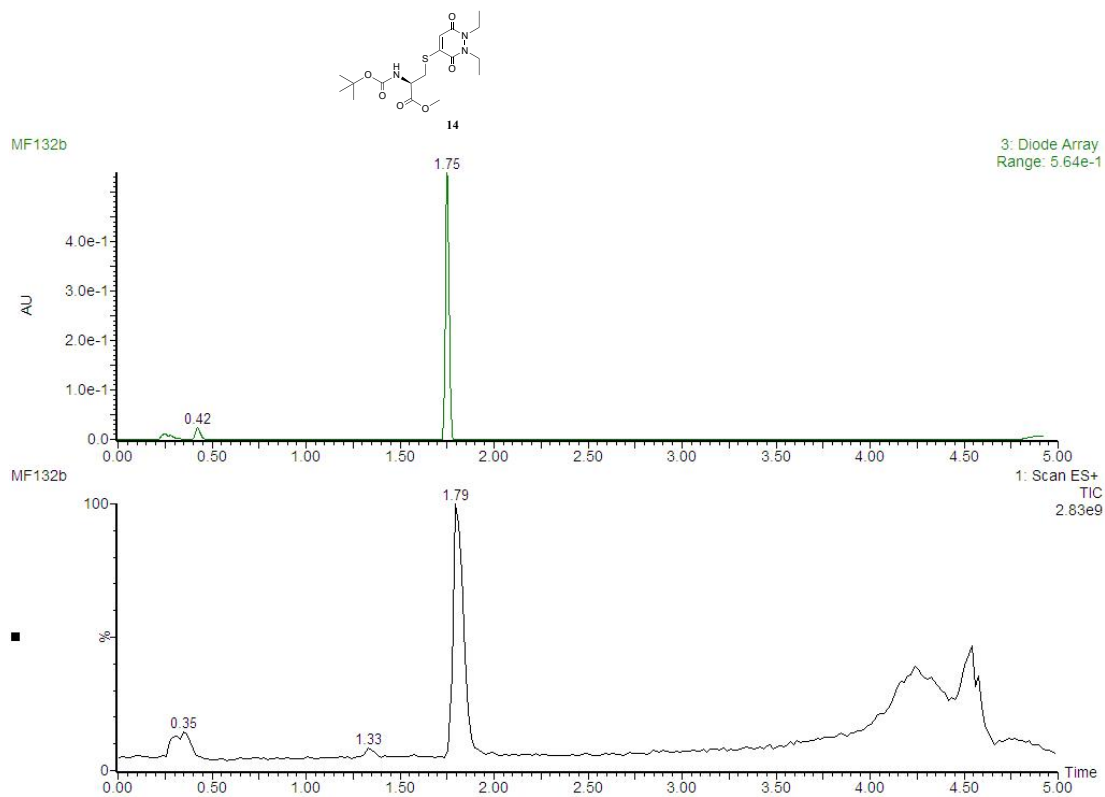


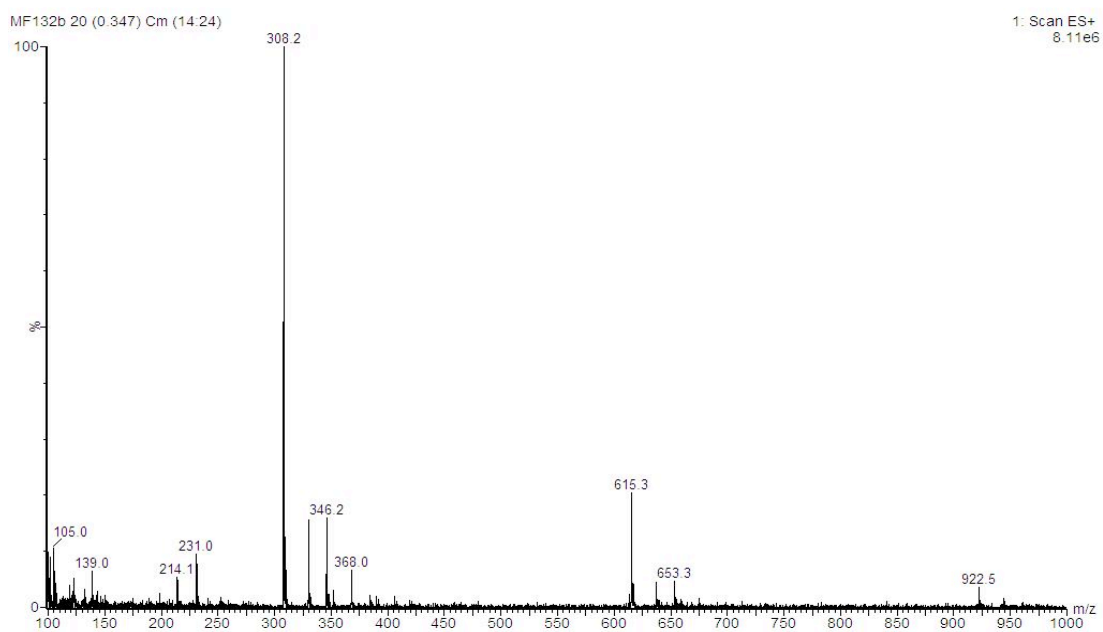
Figure S29. (a) TIC and UV trace at  $t = 0.05$  h, (b) MS data at 0.42 mins in the UV and (c) MS data at 1.75 mins in the UV for PD **14** incubated with GluSH **19** (10 eq.) at pH 6.5.

# LC-MS data for t = 1 h

(a)



(b)





(c)

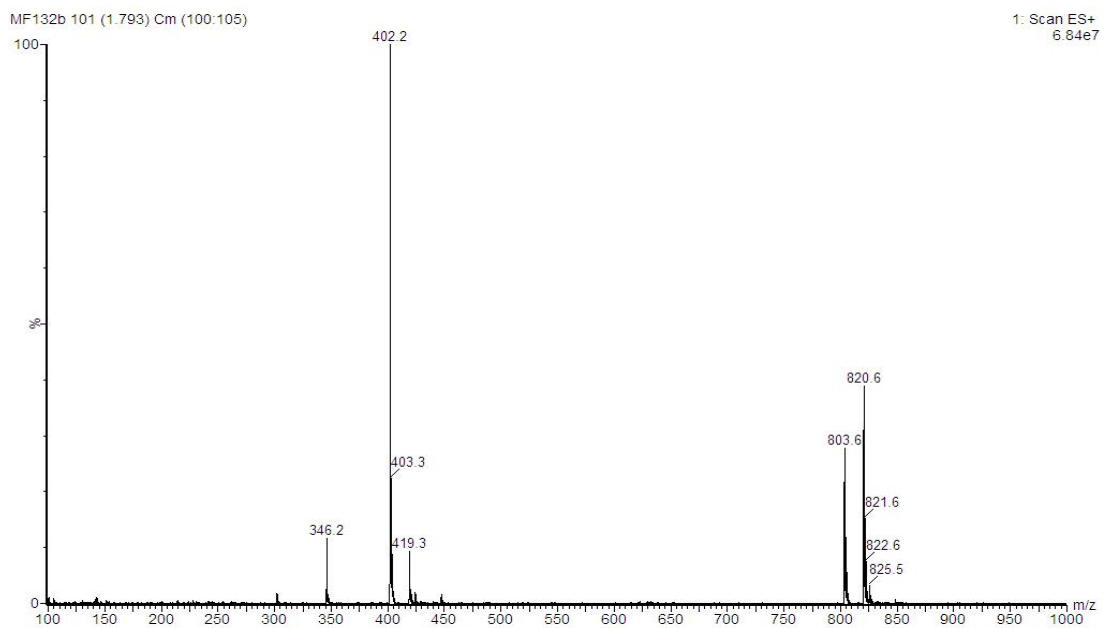
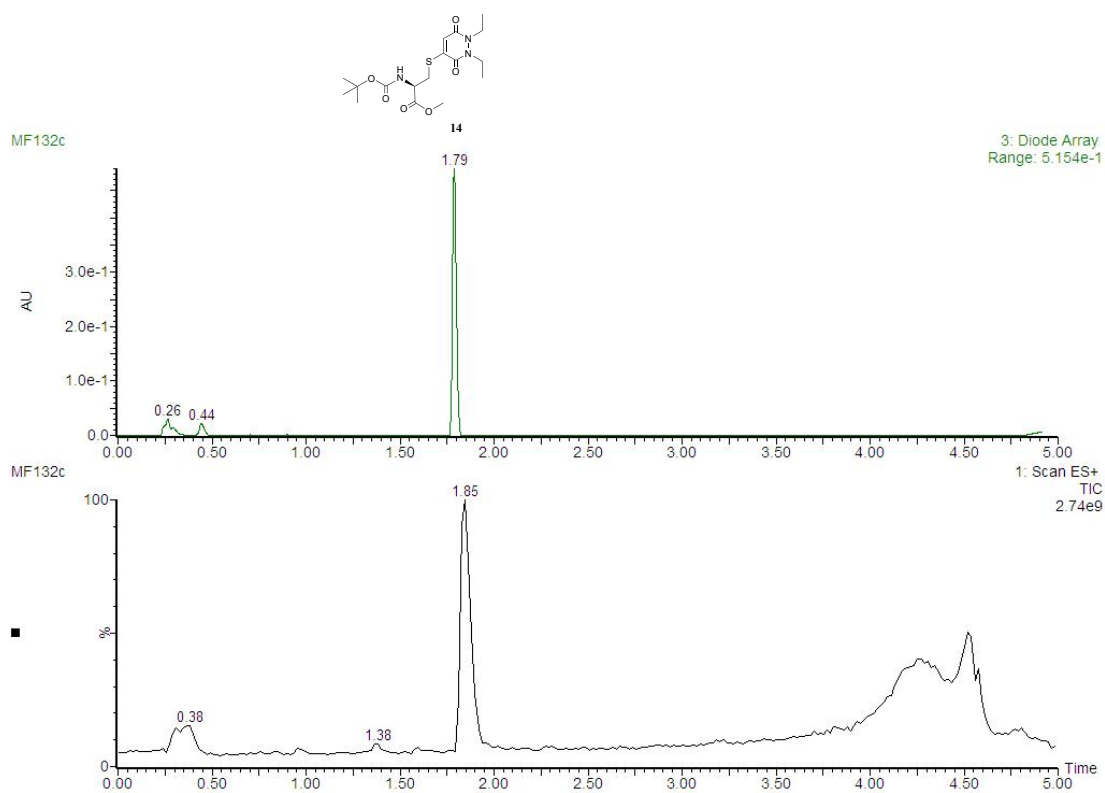


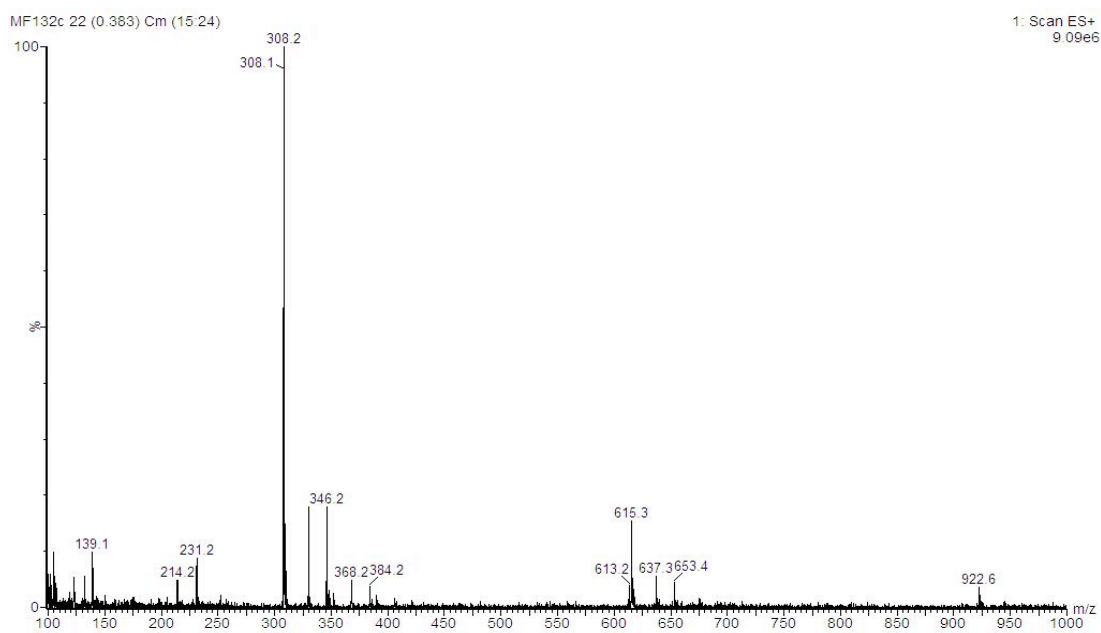
Figure S30. (a) TIC and UV trace at  $t = 1$  h, (b) MS data at 0.42 mins in the UV and (c) MS data at 1.75 mins in the UV for PD 14 incubated with GluSH 19 (10 eq.) at pH 6.5.

# LC-MS data for t = 2 h

(a)



(b)



(c)

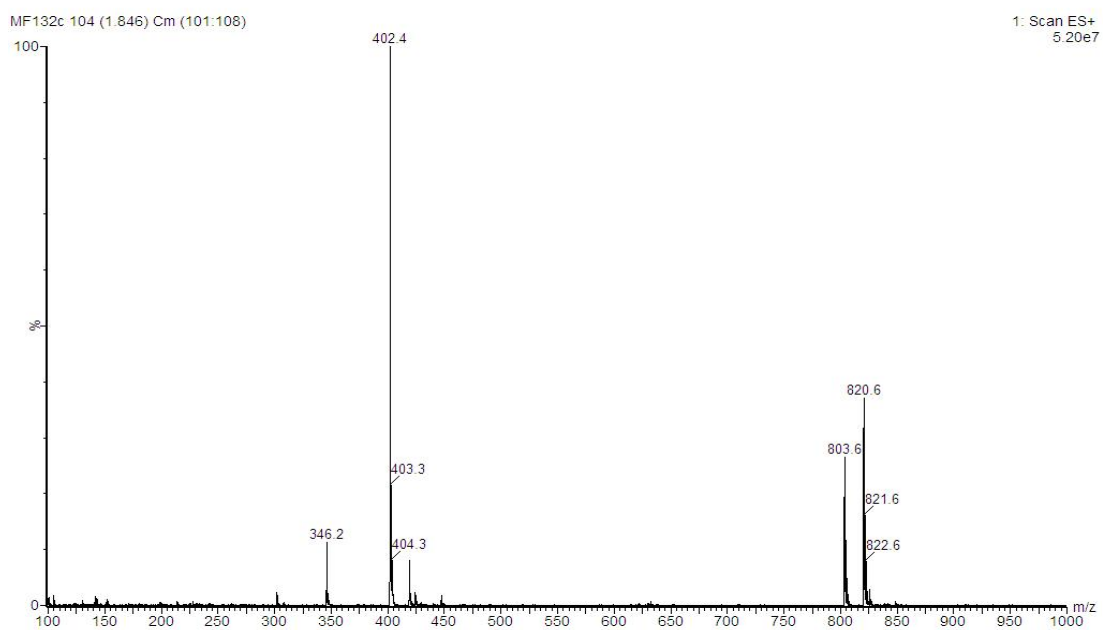
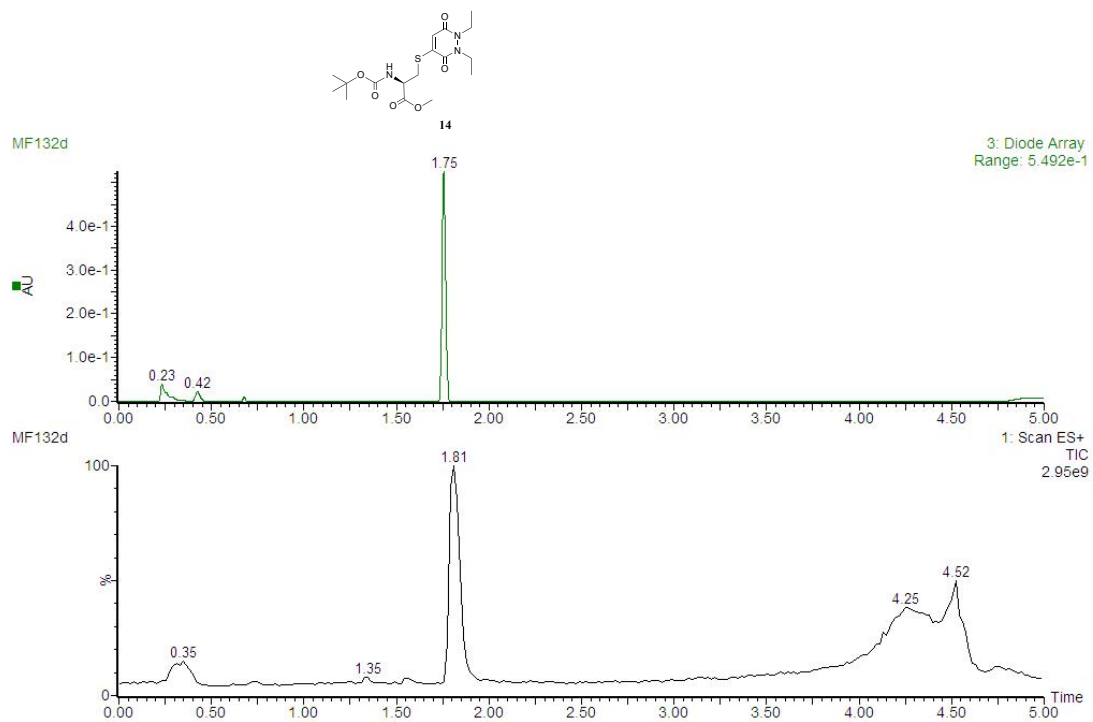


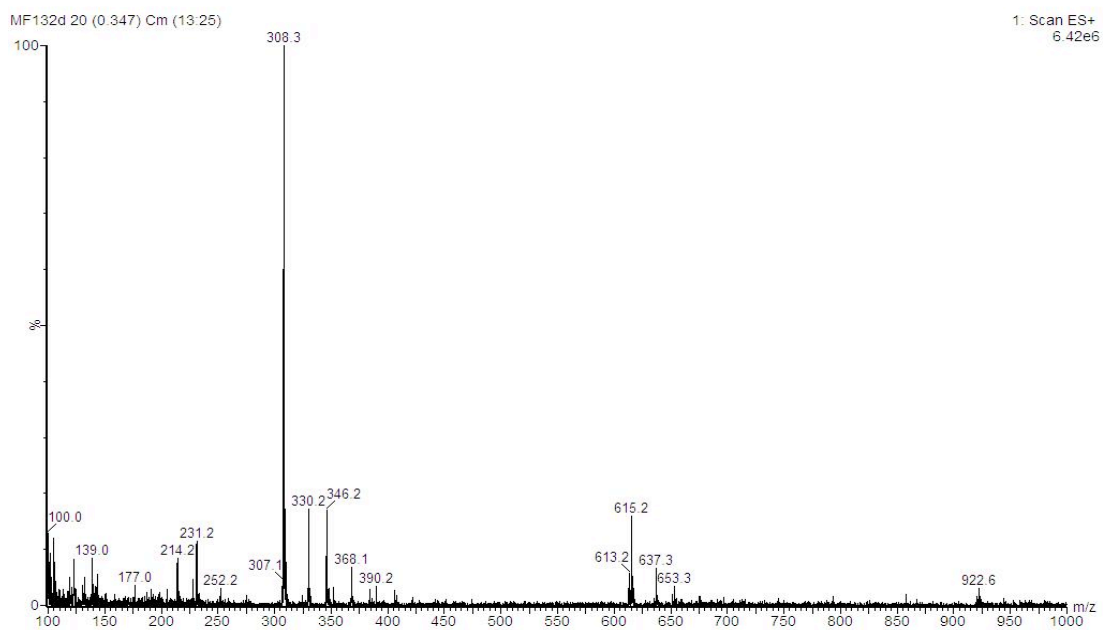
Figure S31. (a) TIC and UV trace at  $t = 2$  h, (b) MS data at 0.26–0.44 mins in the UV and (c) MS data at 1.79 mins in the UV for PD 14 incubated with GluSH 19 (10 eq.) at pH 6.5.

# LC-MS data for t = 4 h

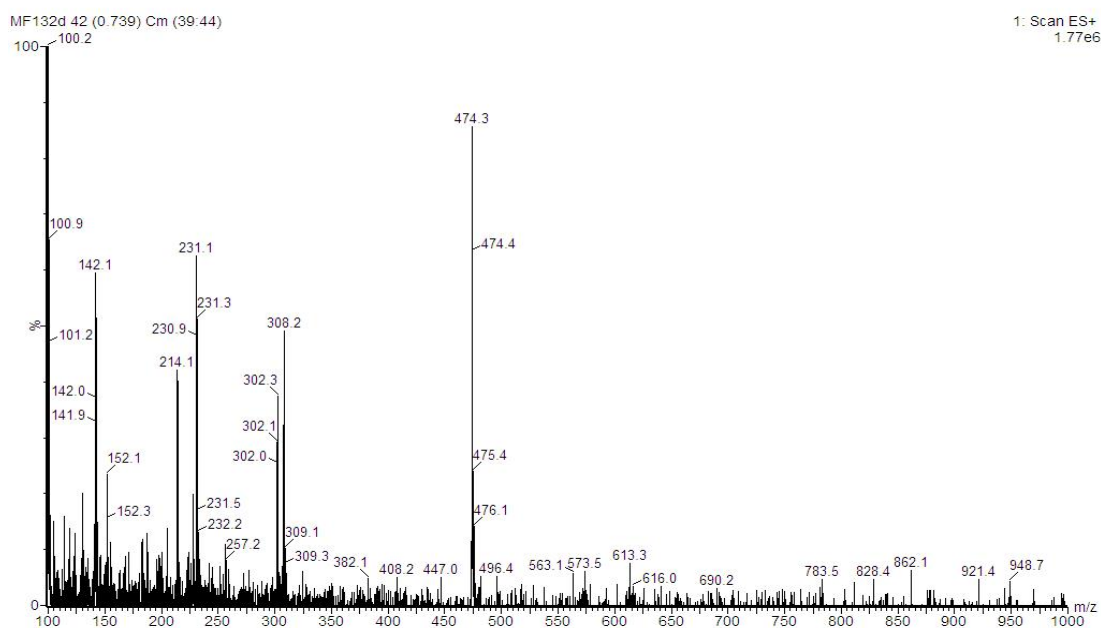
(a)



(b)



(c)



(d)

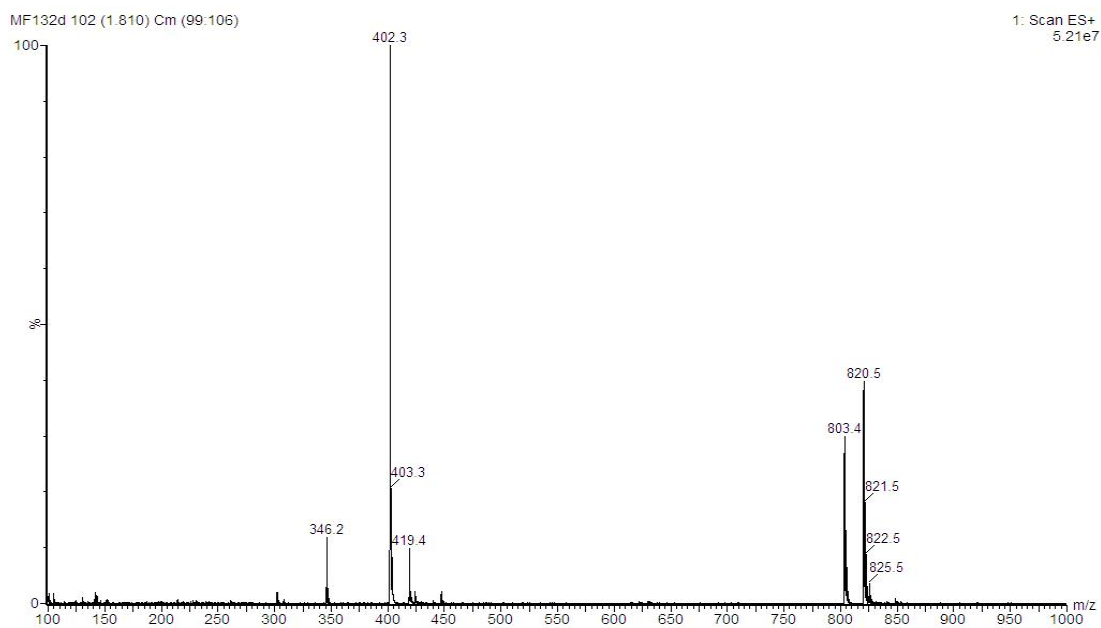
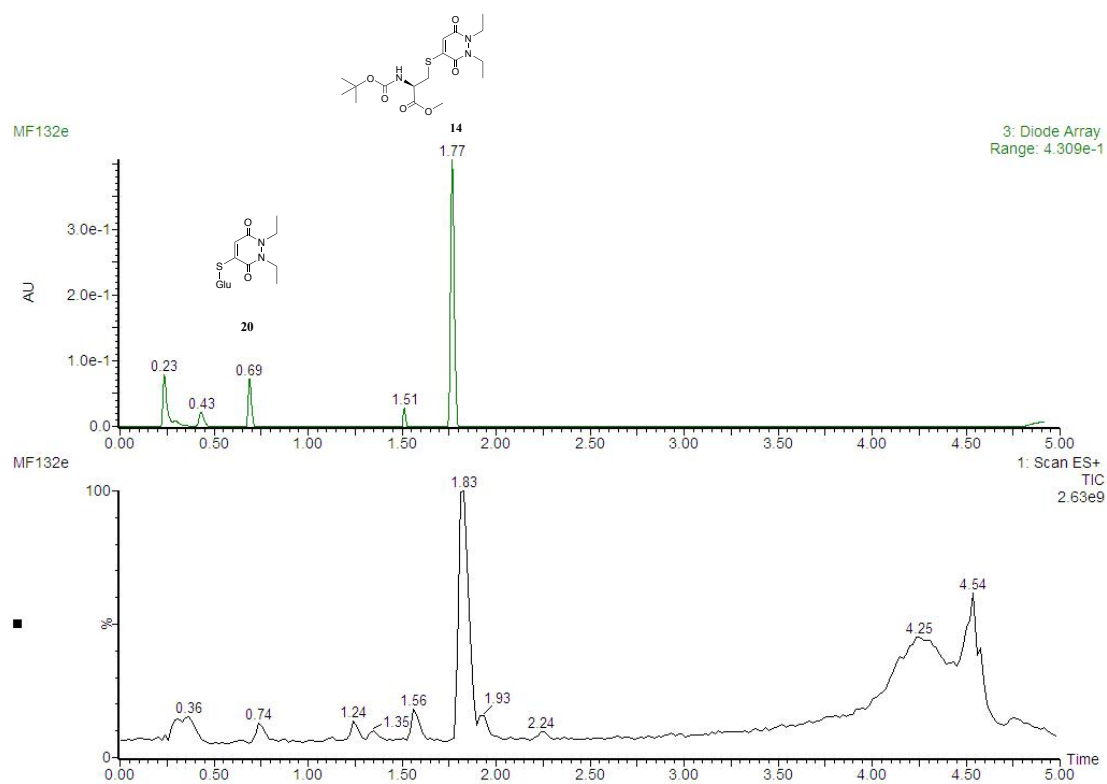


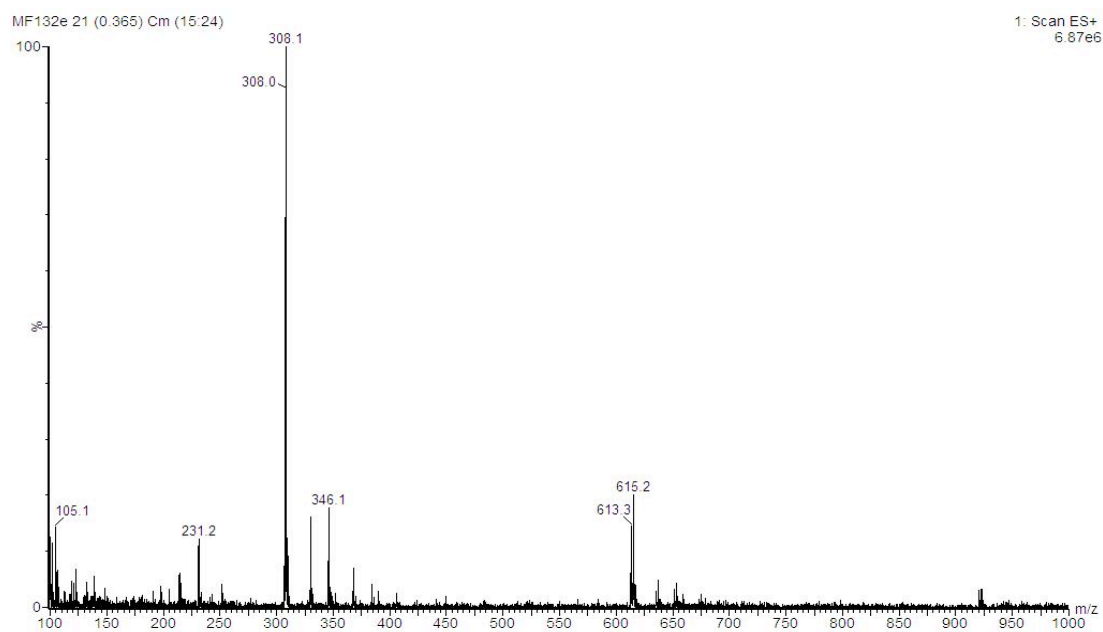
Figure S32. (a) TIC and UV trace at  $t = 4$  h, (b) MS data at 0.26–0.42 mins in the UV, (c) MS data at 0.68 mins in the UV and (d) at 1.75 mins in the UV for PD **14** incubated with GluSH **19** (10 eq.) at pH 6.5.

# LC-MS data for t = 24 h

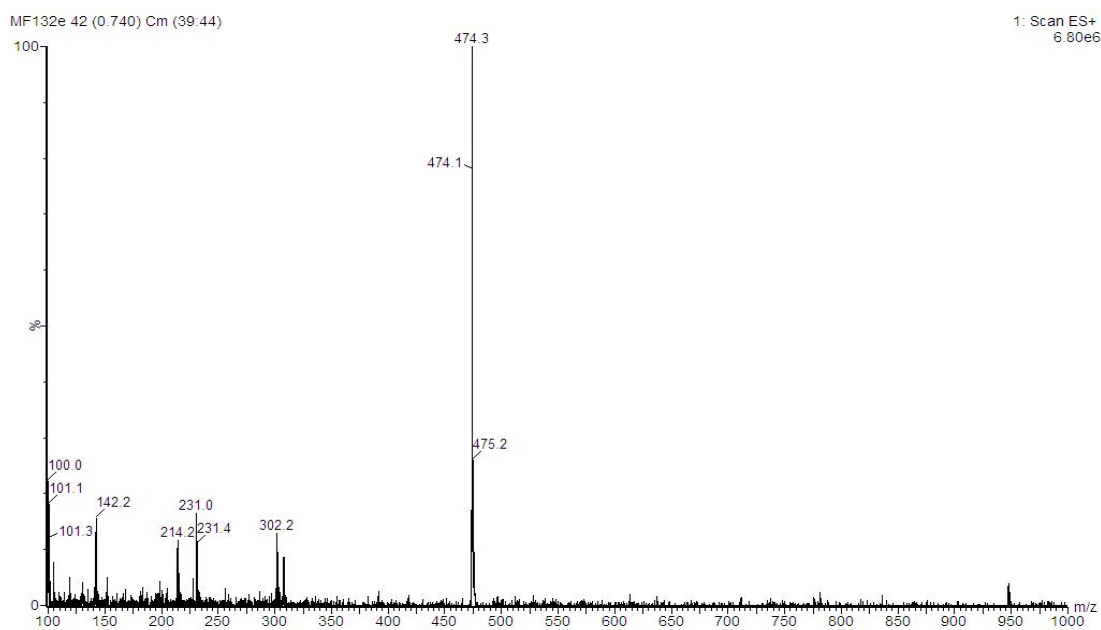
(a)



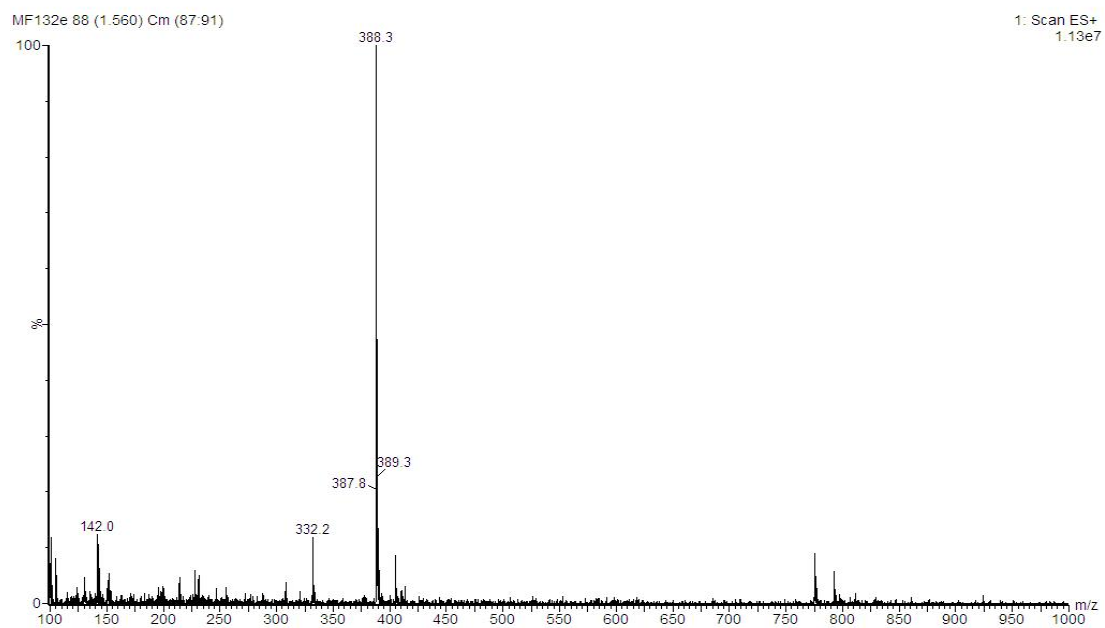
(b)



(c)



(d)



(e)

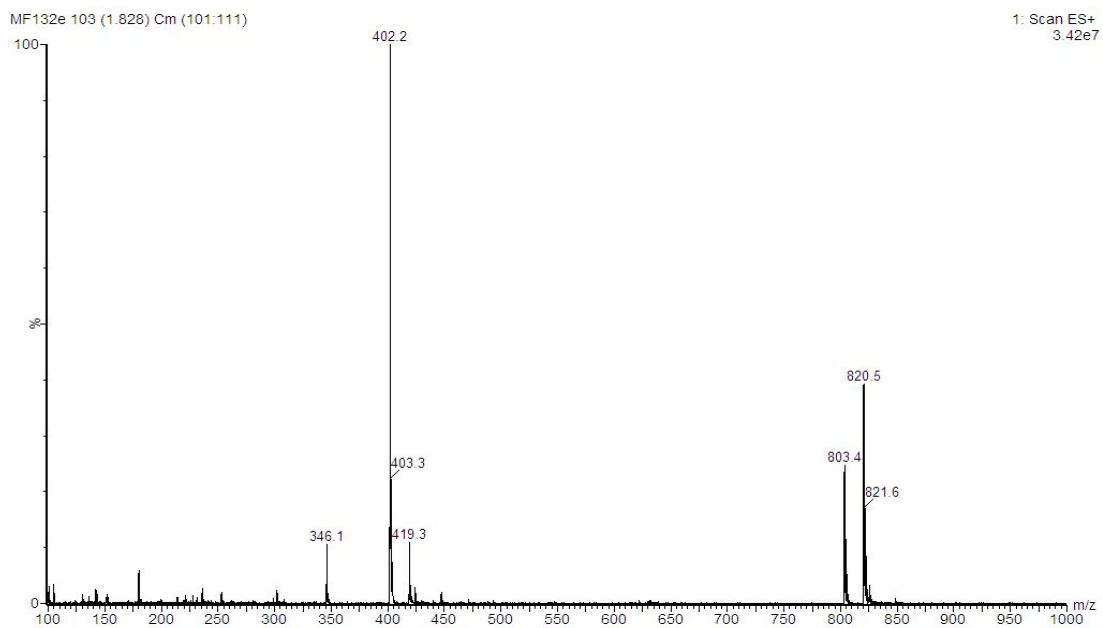
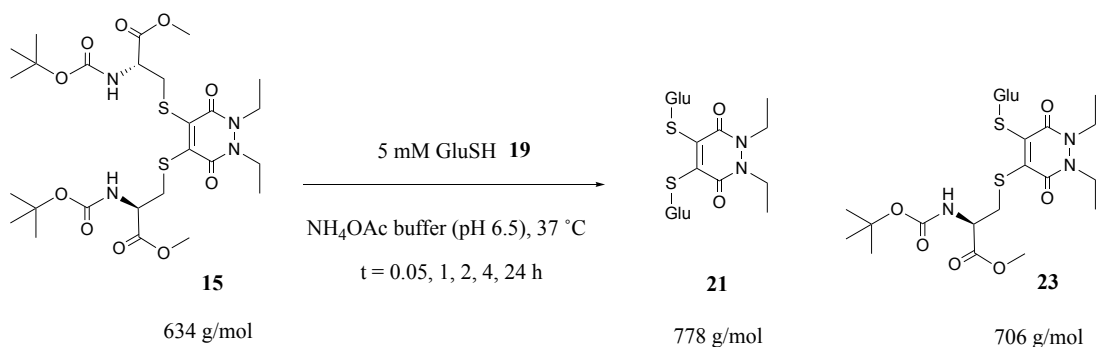


Figure S33. (a) TIC and UV trace at  $t = 24$  h, (b) MS data at 0.26–0.43 mins in the UV, (c) MS data at 0.69 mins in the UV, (d) at 1.51 mins in the UV and (e) at 1.77 mins in the UV for PD **14** incubated with GluSH **19** (10 eq.) at pH 6.5.



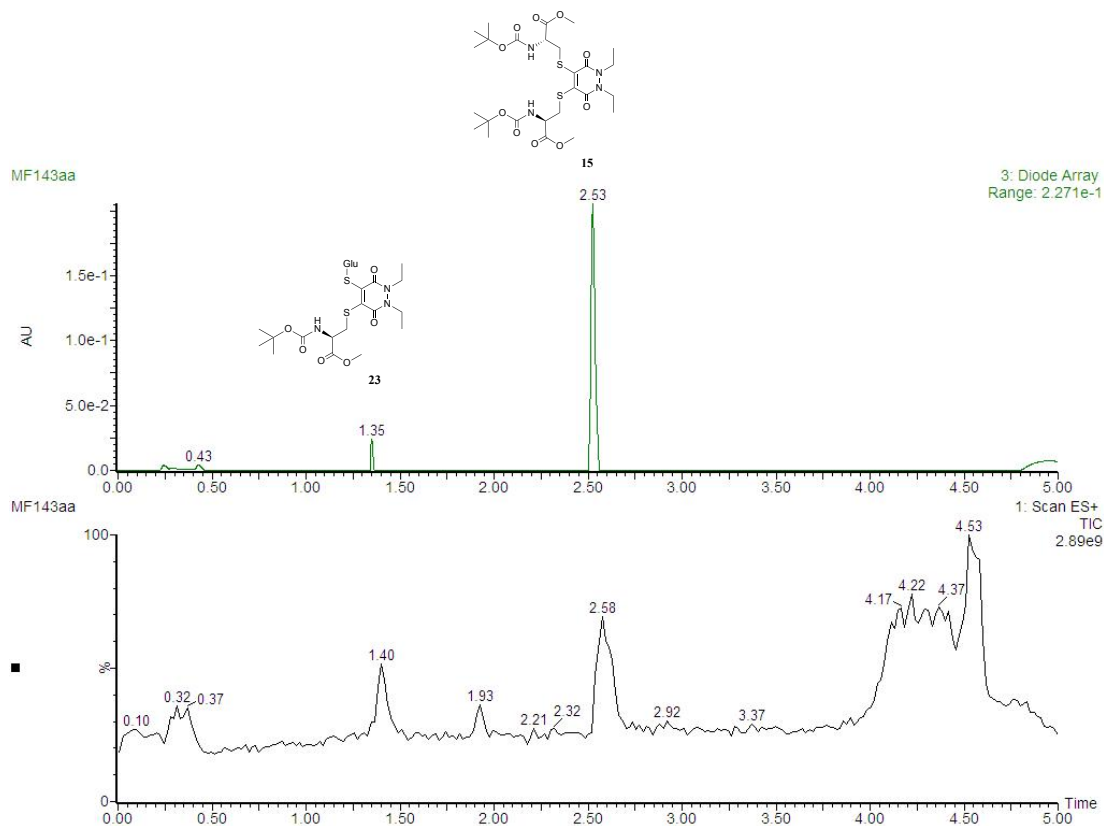
## Incubation of pyridazinedione **15** with GluSH (**10 eq.**)



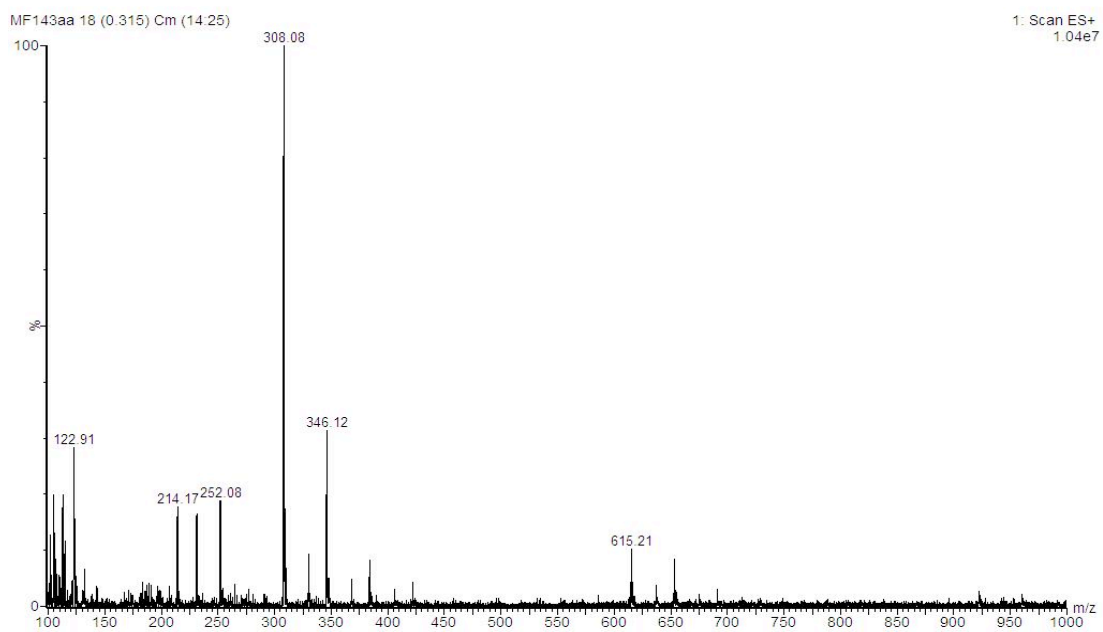
Pyridazinedione **15** (10  $\mu\text{L}$ , 10 mM in MeCN, 1 eq.) was added to GluSH **19** (190  $\mu\text{L}$ , 5.3 mM, 10 eq.) in ammonium acetate buffer (50 mM, pH 6.5). The mixture was incubated at 37 °C for 24 h. The samples were analysed by LC-MS at t = 0.05, 1, 2, 4 and 24 h.

### LC-MS data for t = 0.05 h

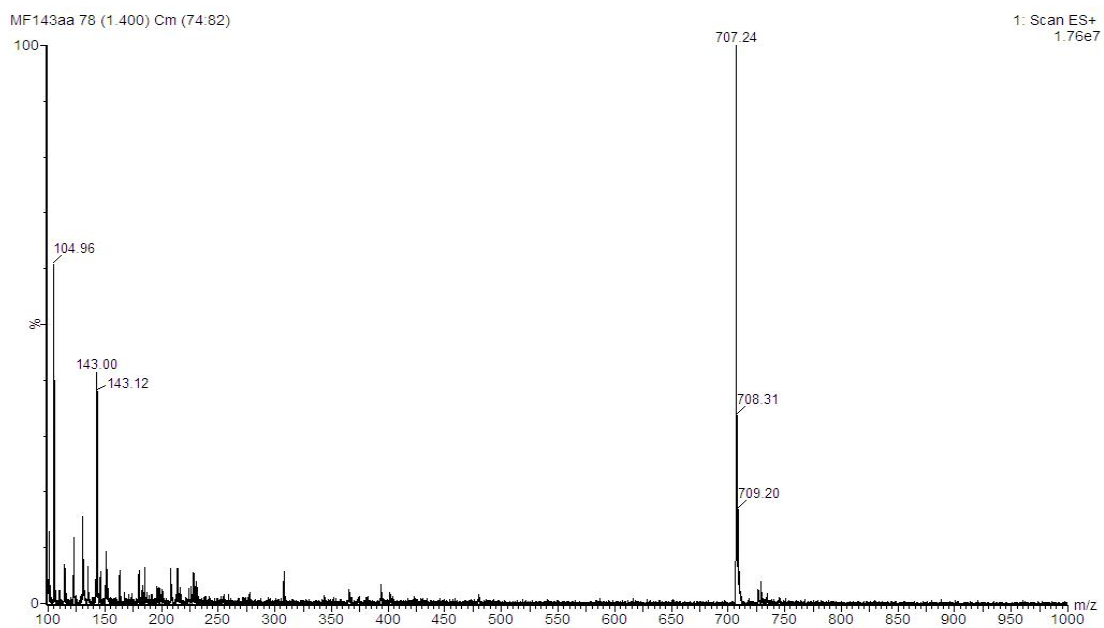
(a)



(b)



(c)



(d)

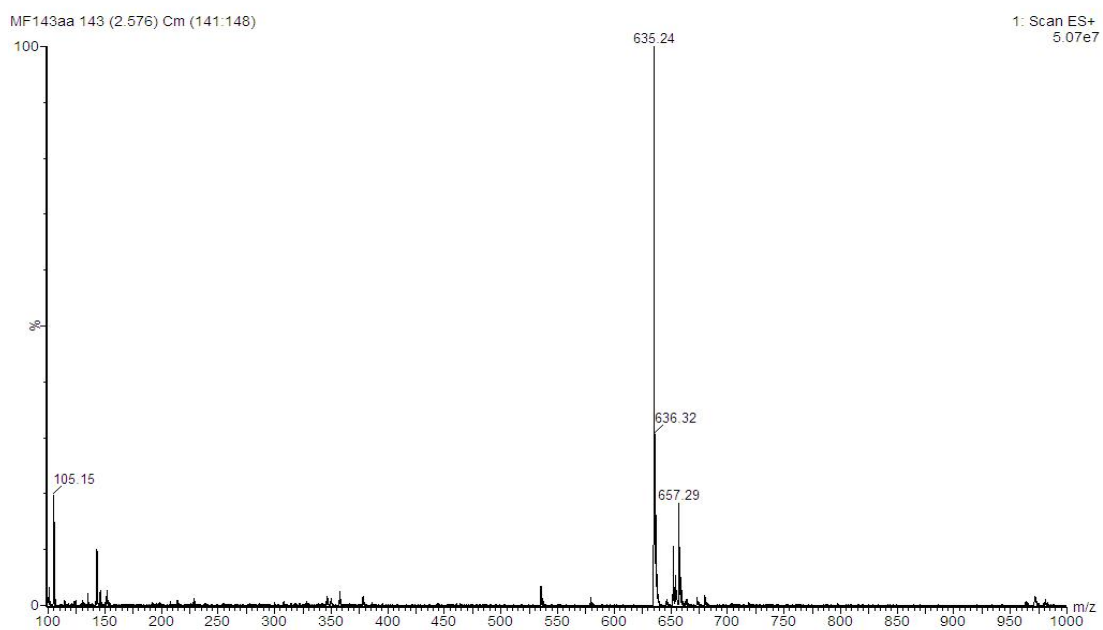
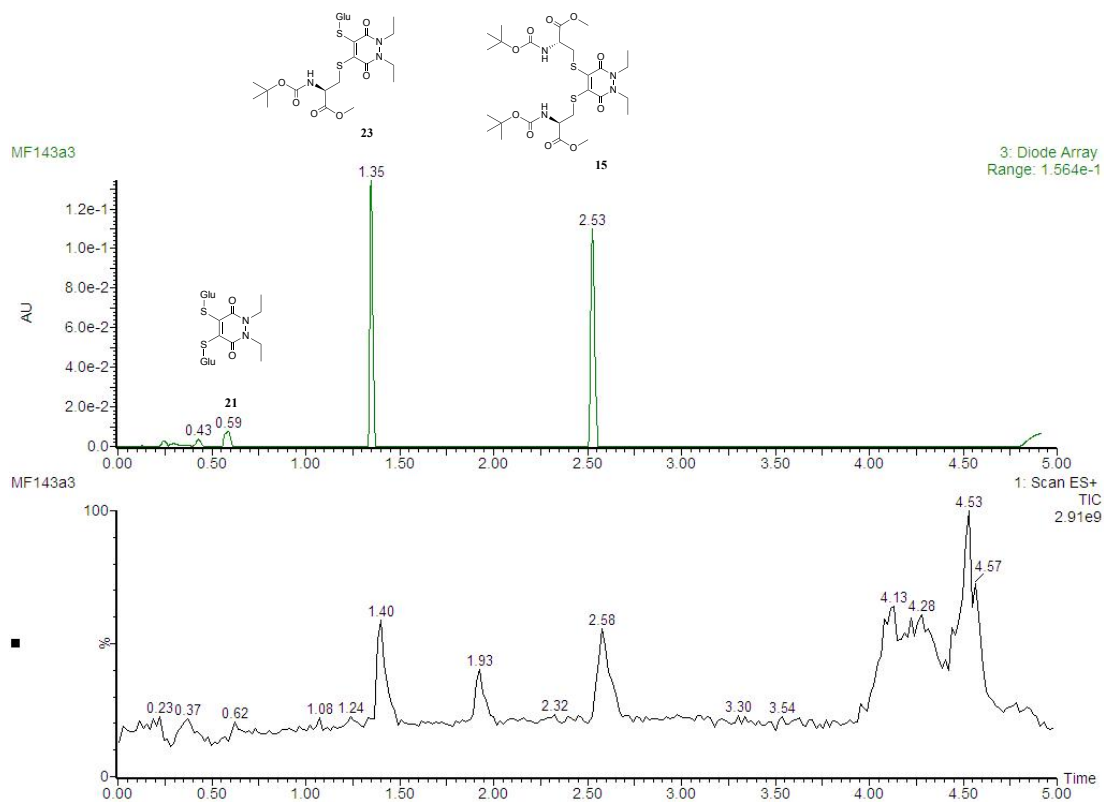


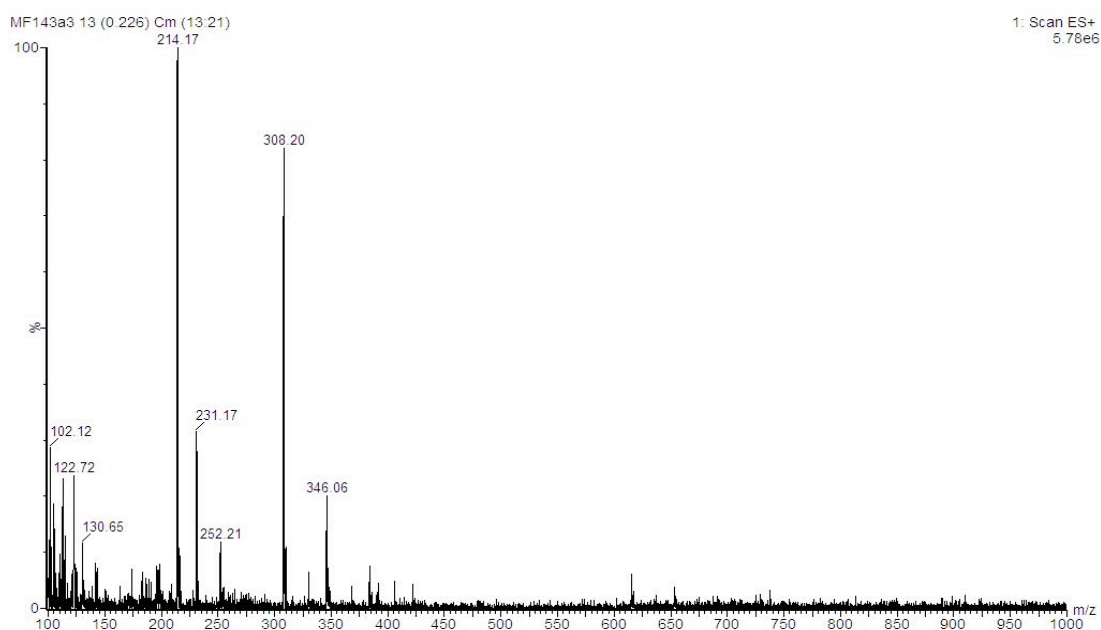
Figure S34. (a) TIC and UV trace at  $t = 0.05$  h, (b) MS data at 0.43 mins in the TIC, (c) MS data at 1.35 mins in the UV and (d) at 2.53 mins in the UV for PD **15** incubated with GluSH **19** (10 eq.) at pH 6.5.

# LC-MS data for t = 1 h

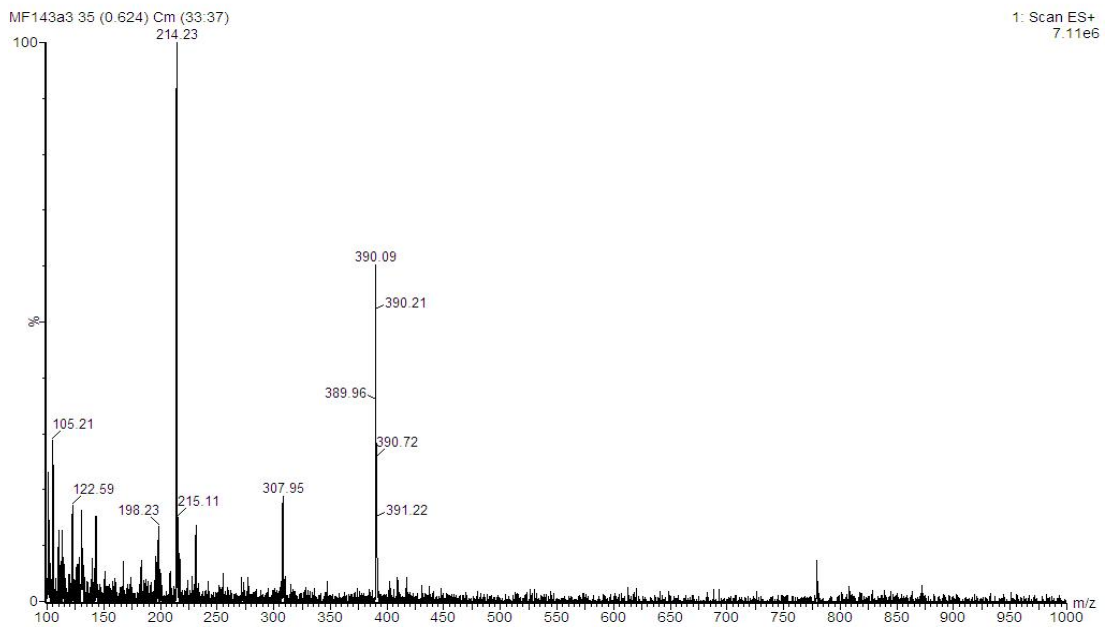
(a)



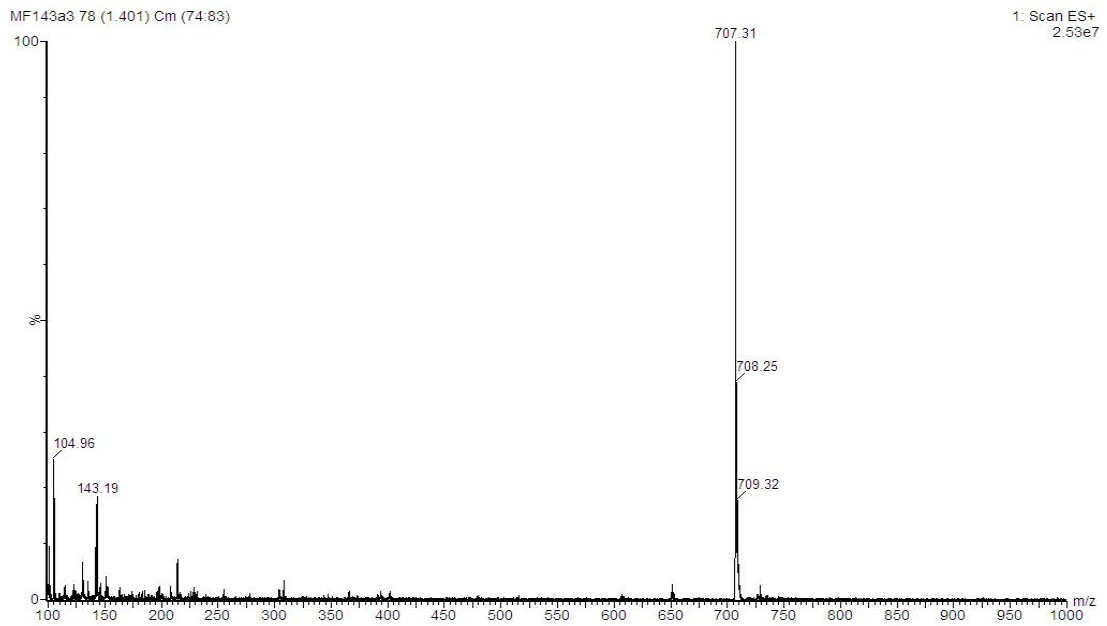
(b)



(c)



(d)



(e)

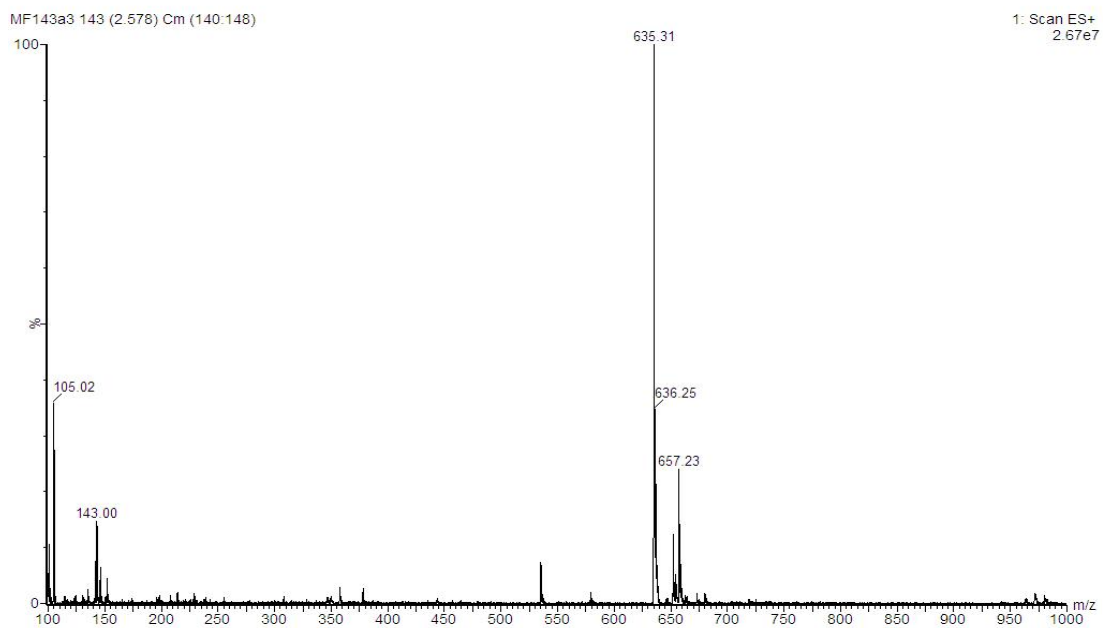
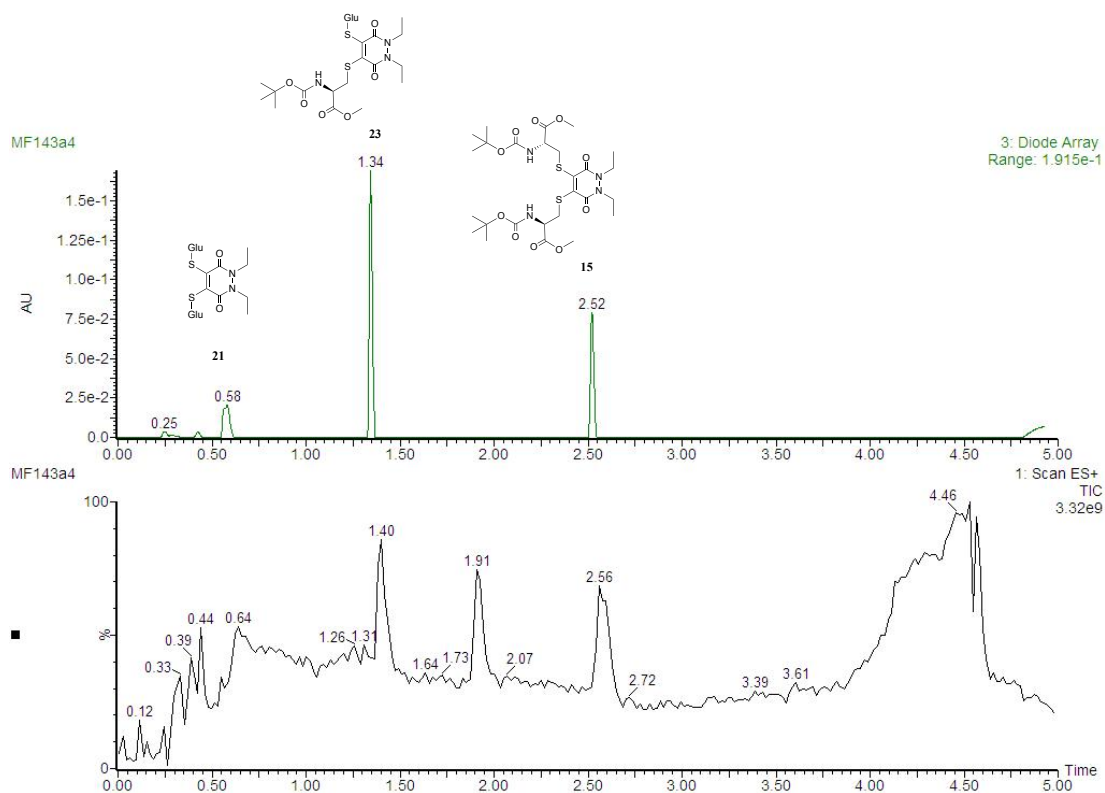


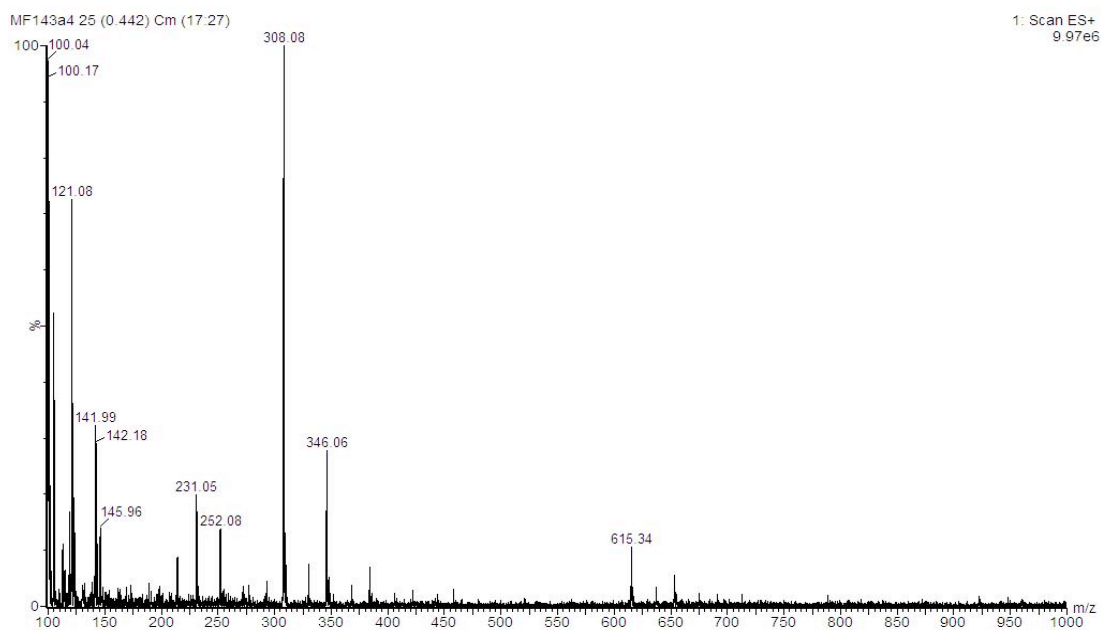
Figure S35. (a) TIC and UV trace at  $t = 1$  h, (b) MS data at 0.43 mins in the TIC, (c) MS data at 0.59 mins in the UV, (d) at 1.35 mins in the UV and (e) at 2.53 mins in the UV for PD **15** incubated with GluSH **19** (10 eq.) at pH 6.5.

# LC-MS data for t = 2 h

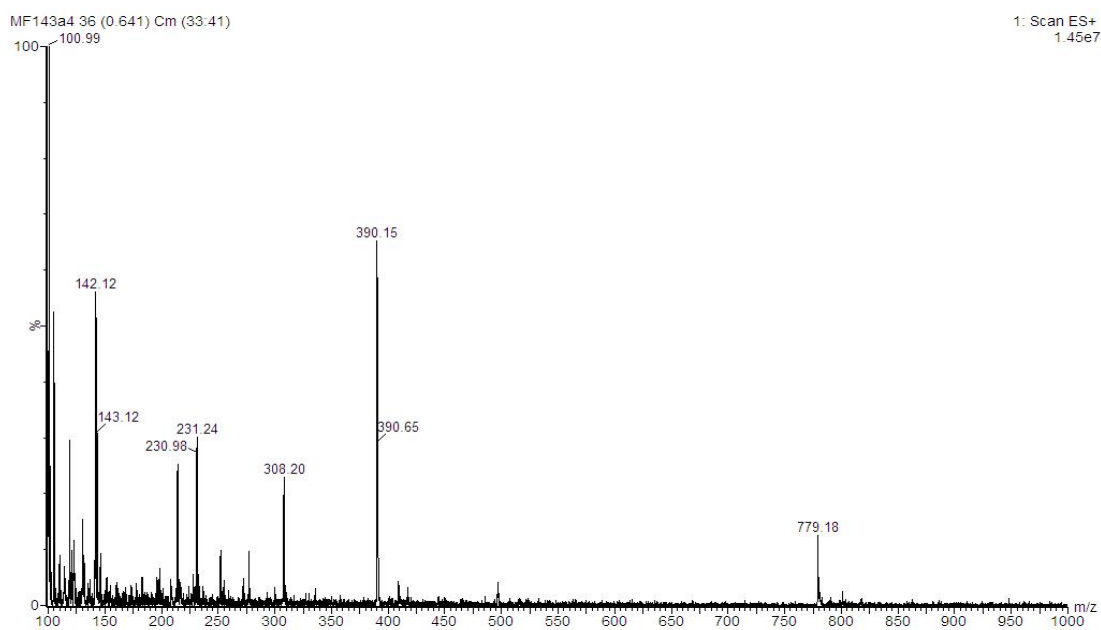
(a)



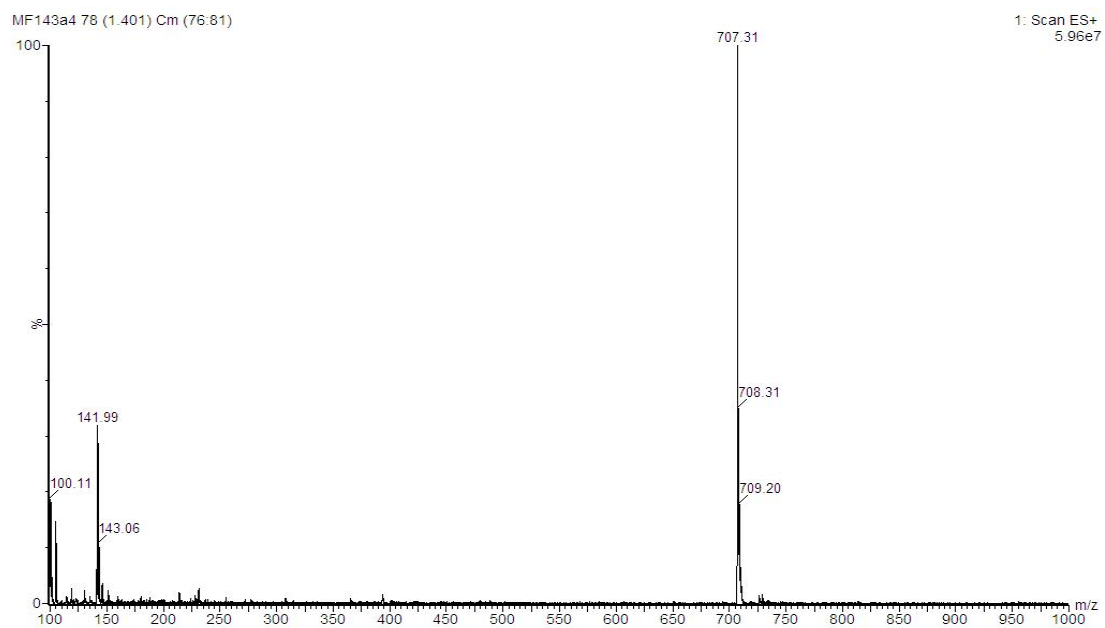
(b)



(c)



(d)





(e)

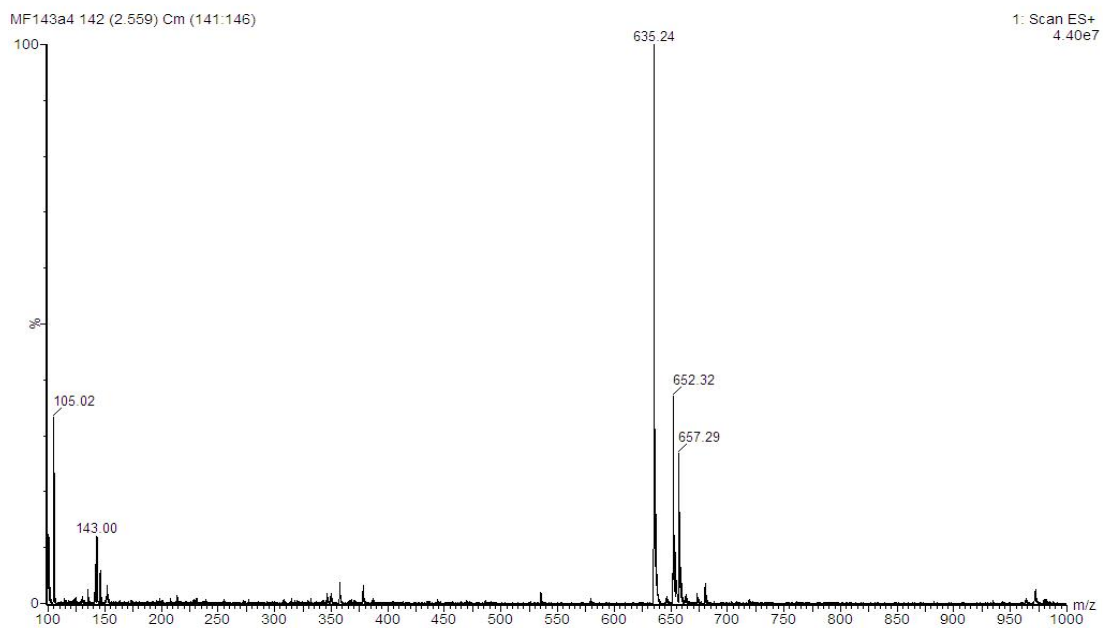
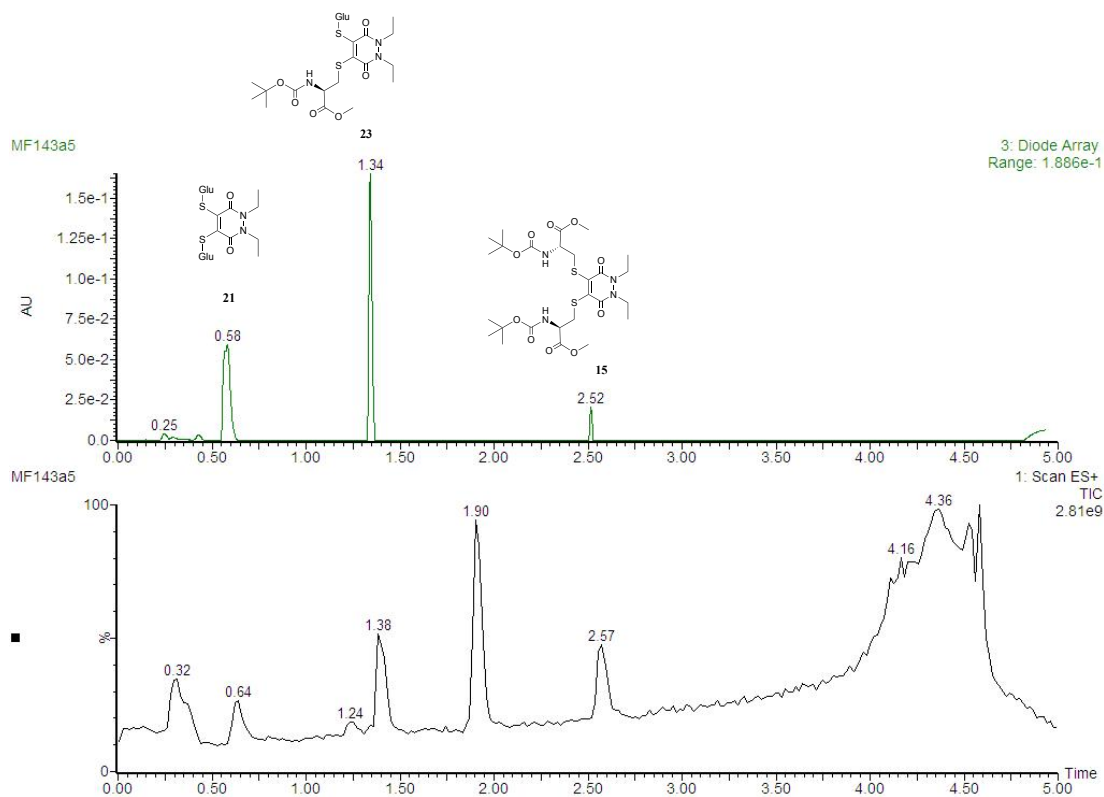


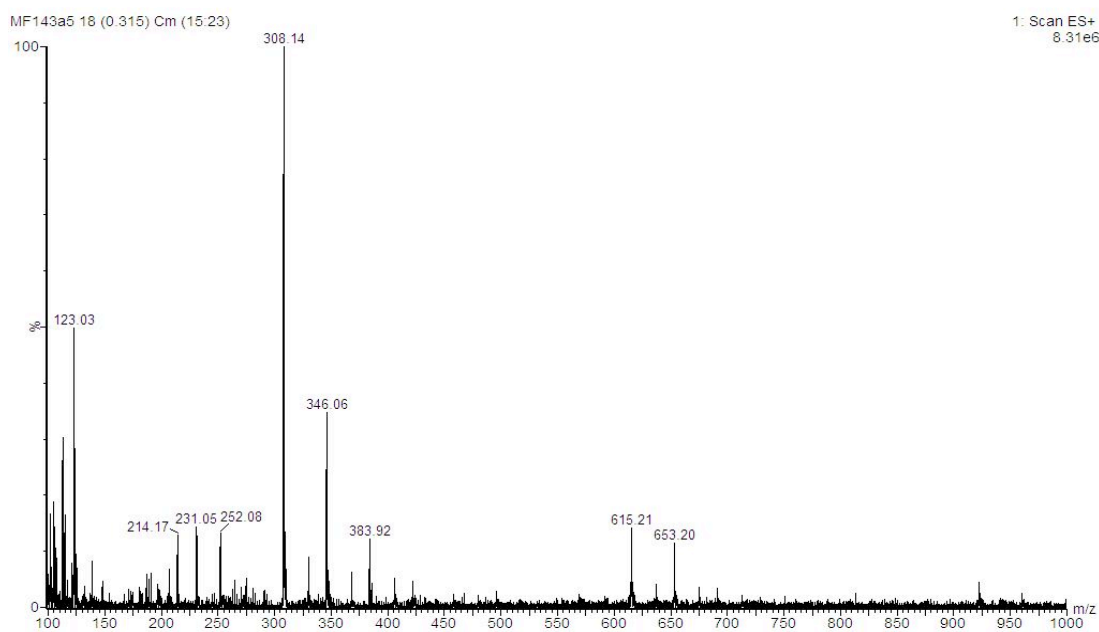
Figure S36. (a) TIC and UV trace at  $t = 2$  h, (b) MS data at 0.25–0.44 mins in the UV, (c) MS data at 0.58 mins in the UV, (d) at 1.34 mins in the UV and (e) at 2.52 mins in the UV for PD **15** incubated with GluSH **19** (10 eq.) at pH 6.5.

# LC-MS data for t = 4 h

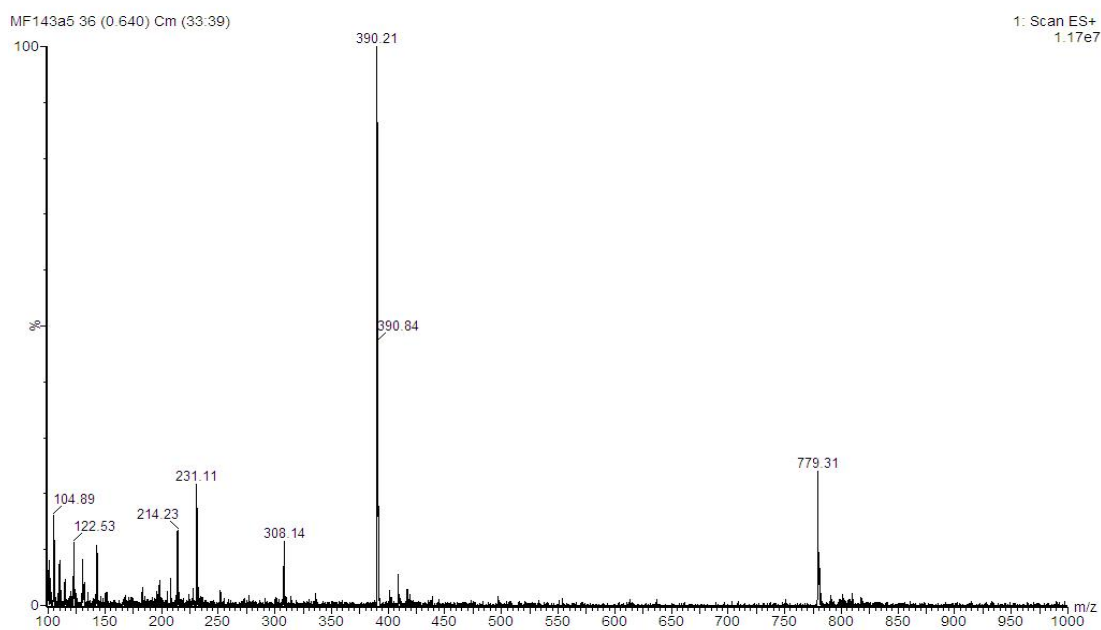
(a)



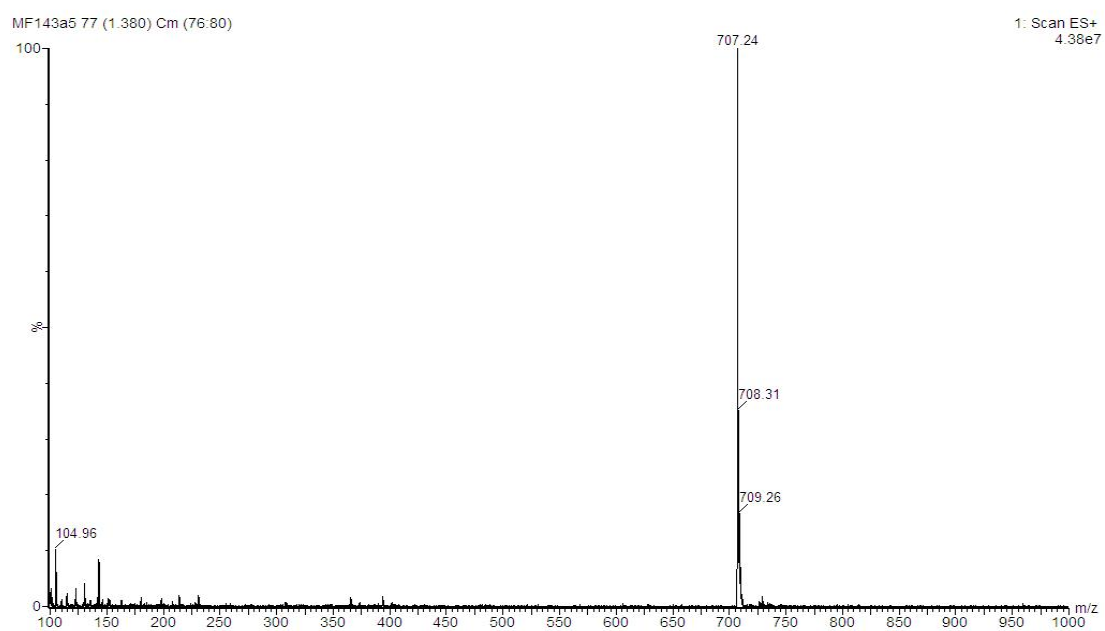
(b)



(c)



(d)



(e)

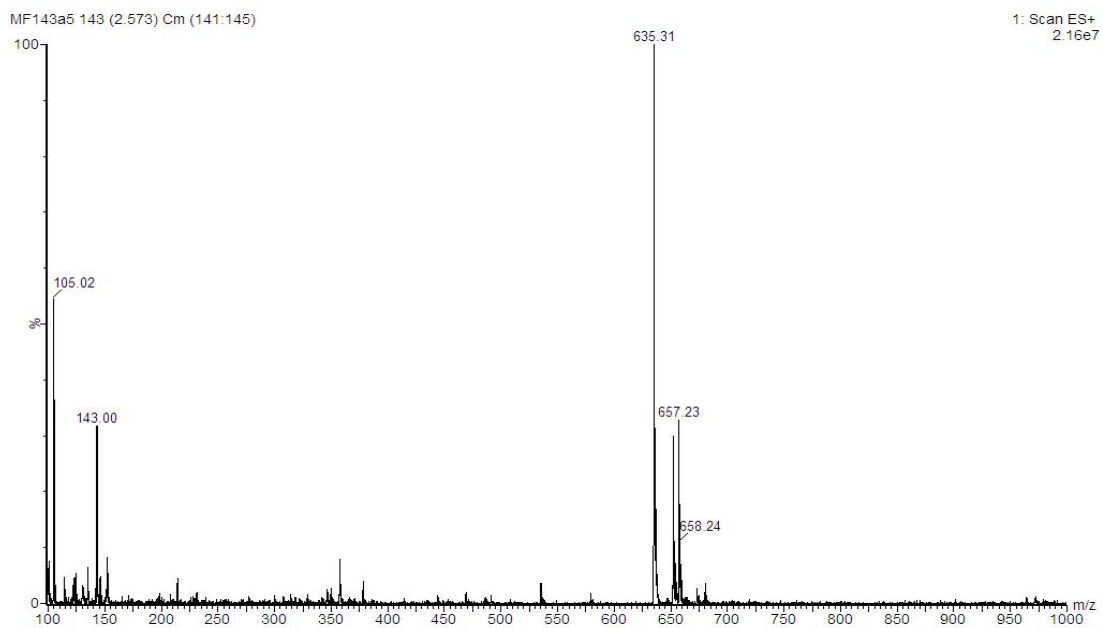
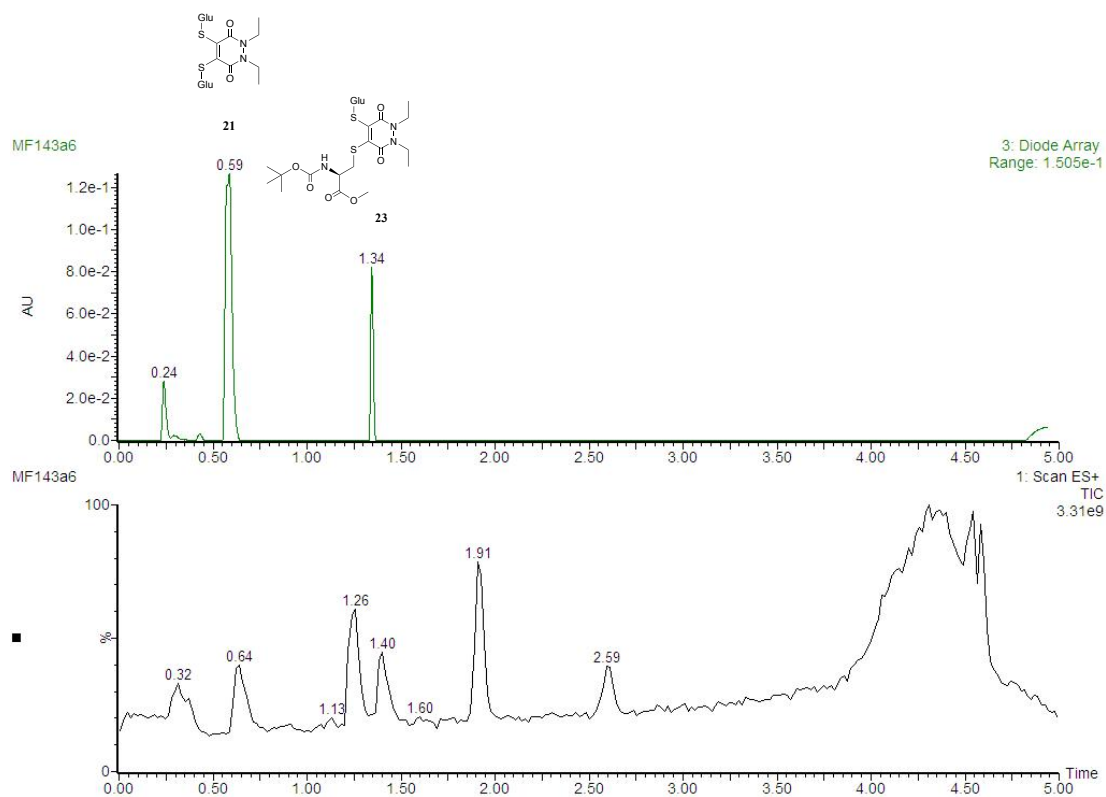


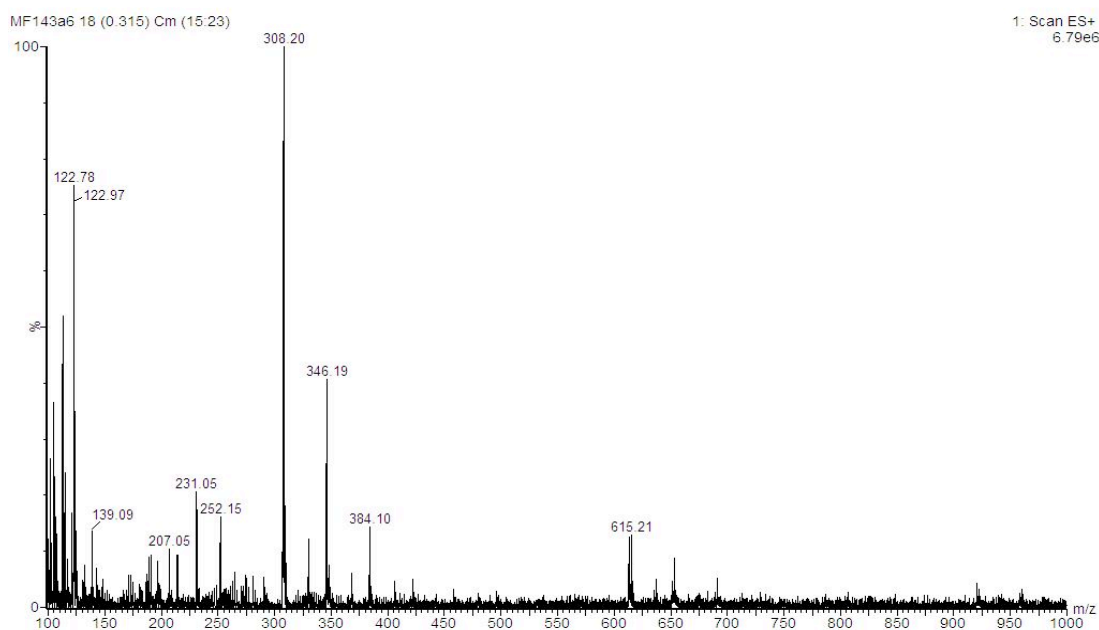
Figure S37. (a) TIC and UV trace at  $t = 4$  h, (b) MS data at 0.25–0.44 mins in the UV, (c) MS data at 0.58 mins in the UV, (d) at 1.34 mins in the UV and (e) at 2.52 mins in the UV for PD **15** incubated with GluSH **19** (10 eq.) at pH 6.5.

# LC-MS data for t = 24 h

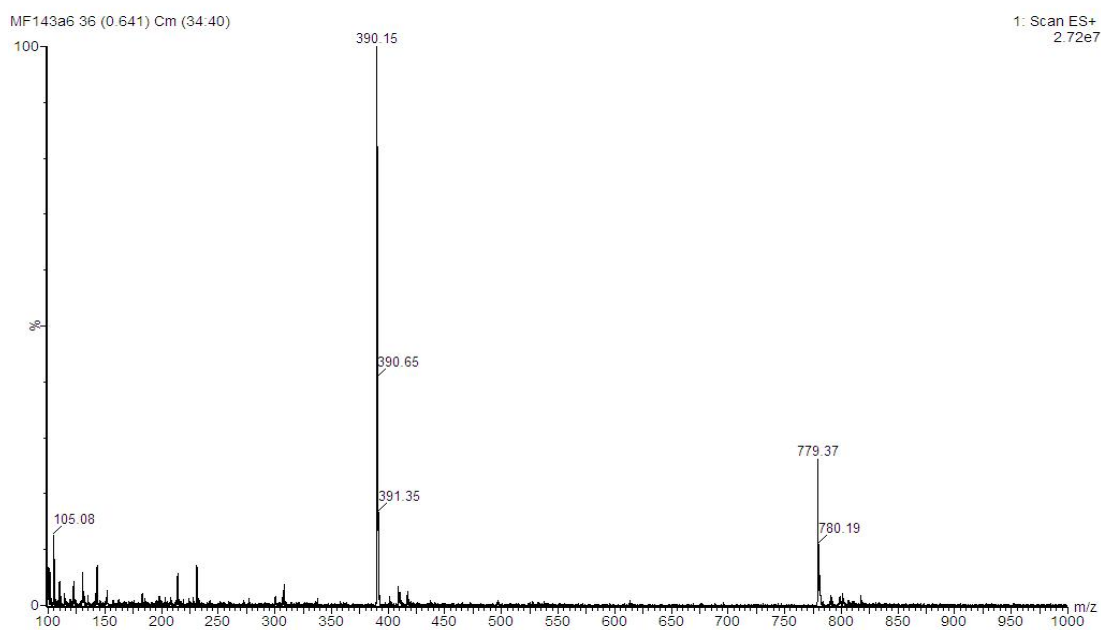
(a)



(b)



(c)



(d)

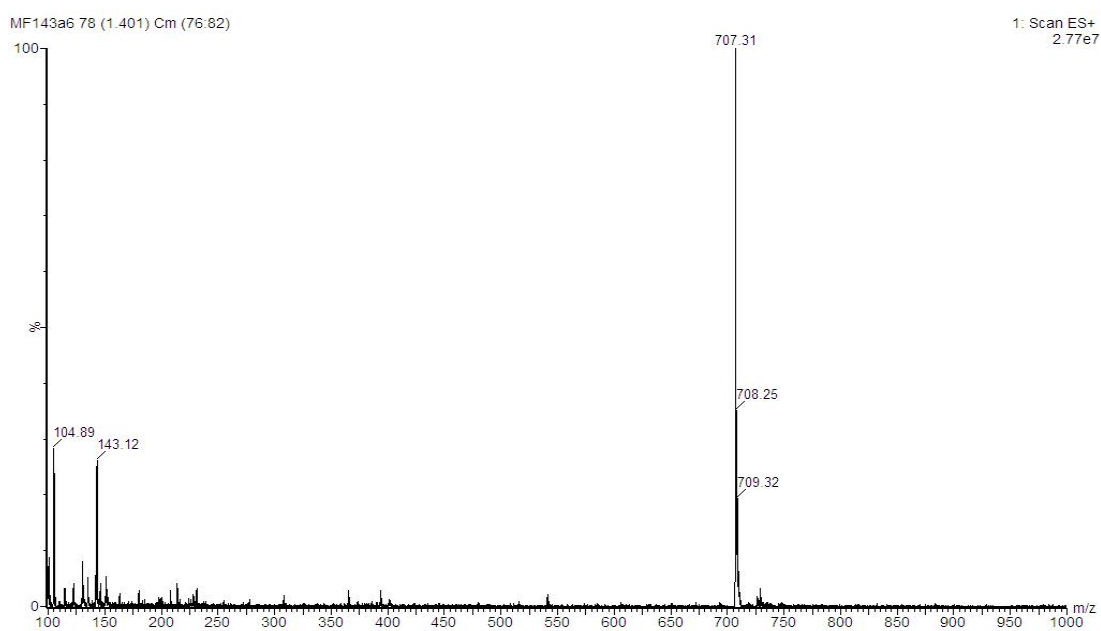
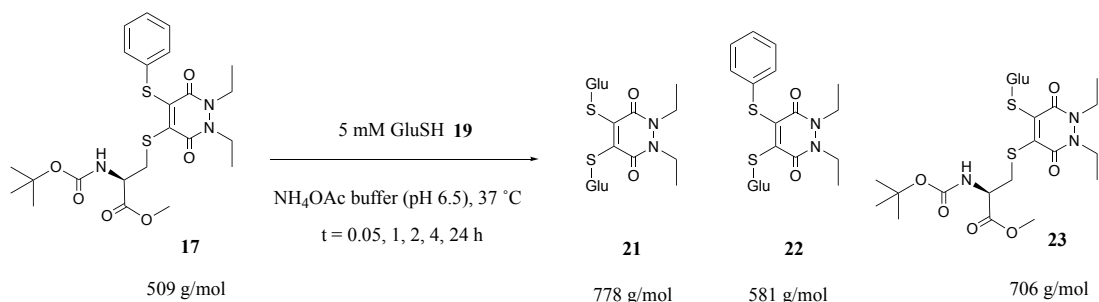


Figure S38. (a) TIC and UV trace at  $t = 24$  h, (b) MS data at 0.24–0.44 mins in the UV, (c) MS data at 0.59 mins in the UV and (d) at 1.34 mins in the UV for PD **15** incubated with GluSH **19** (10 eq.) at pH 6.5.

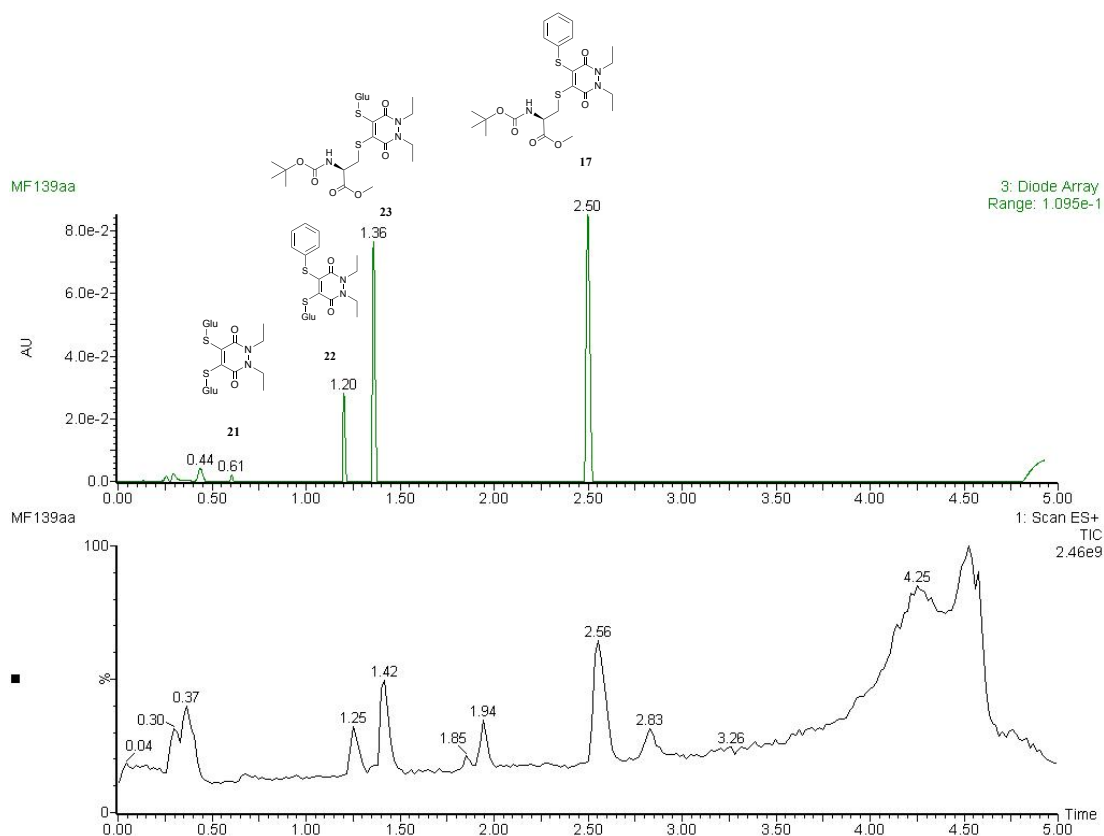
## Incubation of pyridazinedione **17** with GluSH (**10 eq.**)



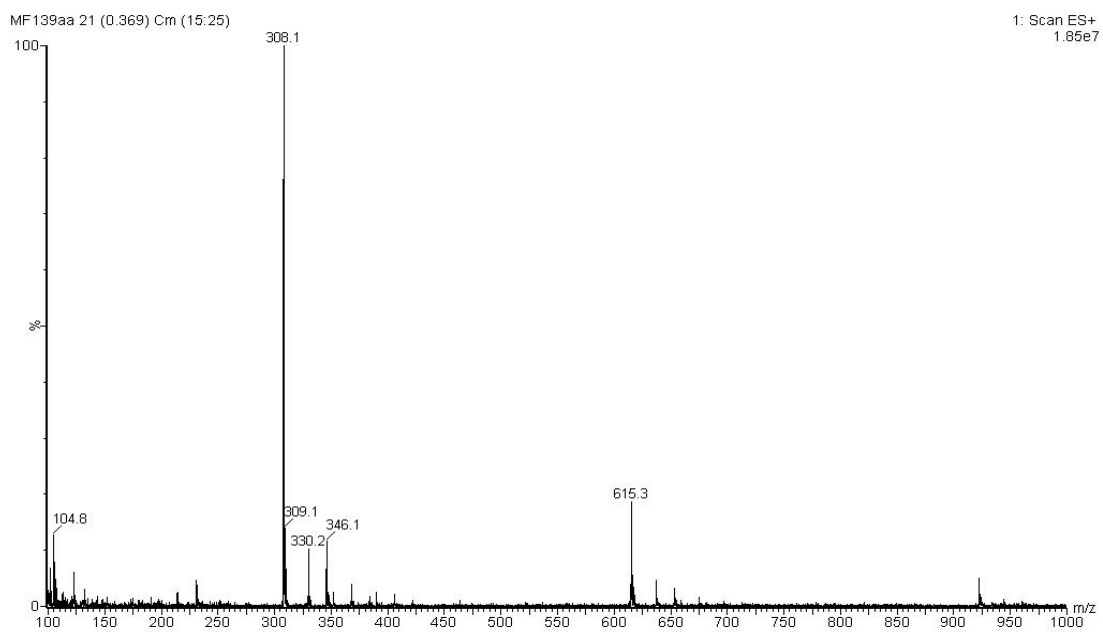
Pyridazinedione **17** (10  $\mu$ L, 10 mM in MeCN, 1 eq.) was added to GluSH **19** (190  $\mu$ L, 5.3 mM, 10 eq.) in ammonium acetate buffer (50 mM, pH 6.5). The mixture was incubated at 37 °C for 24 h. The samples were analysed by LC-MS at t = 0.05, 1, 2, 4 and 24 h.

### LC-MS data for t = 0.05 h

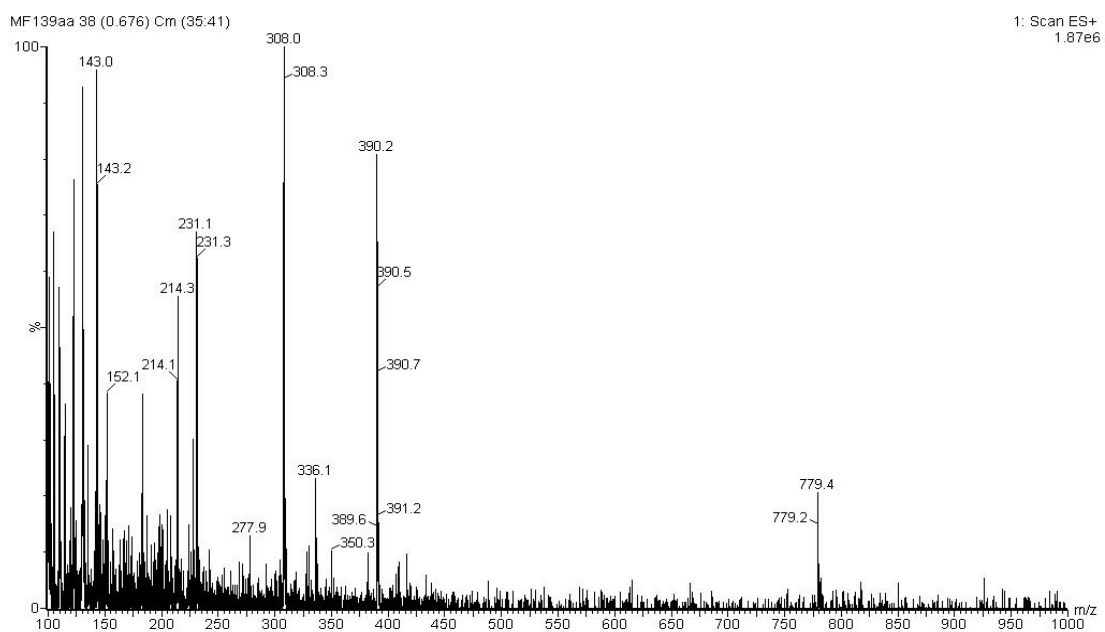
(a)



(b)

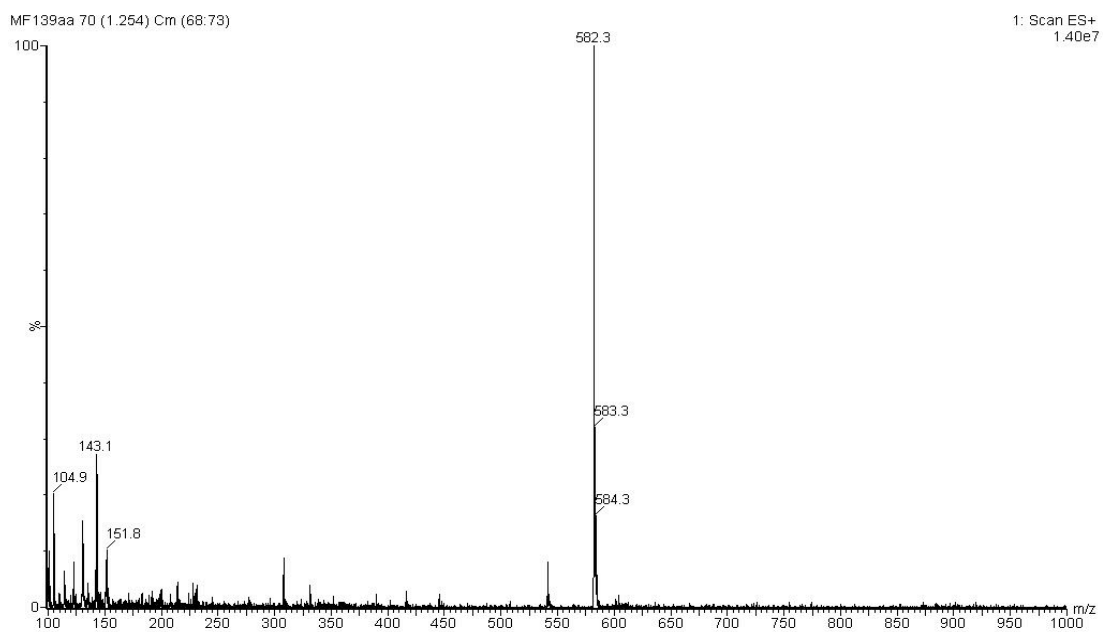


(c)

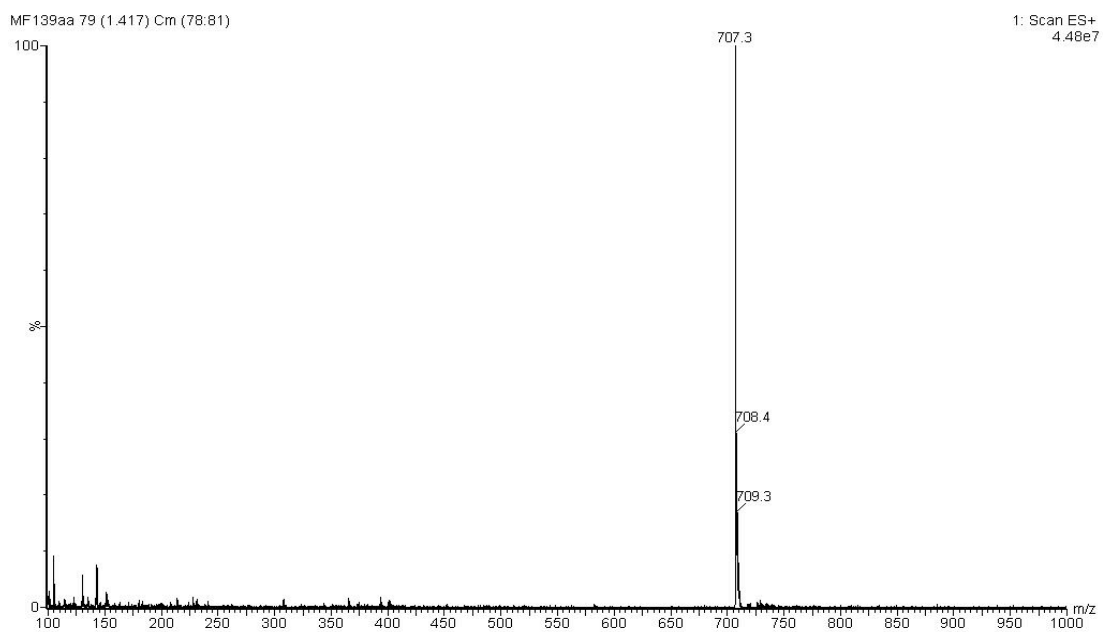




(d)



(e)



(f)

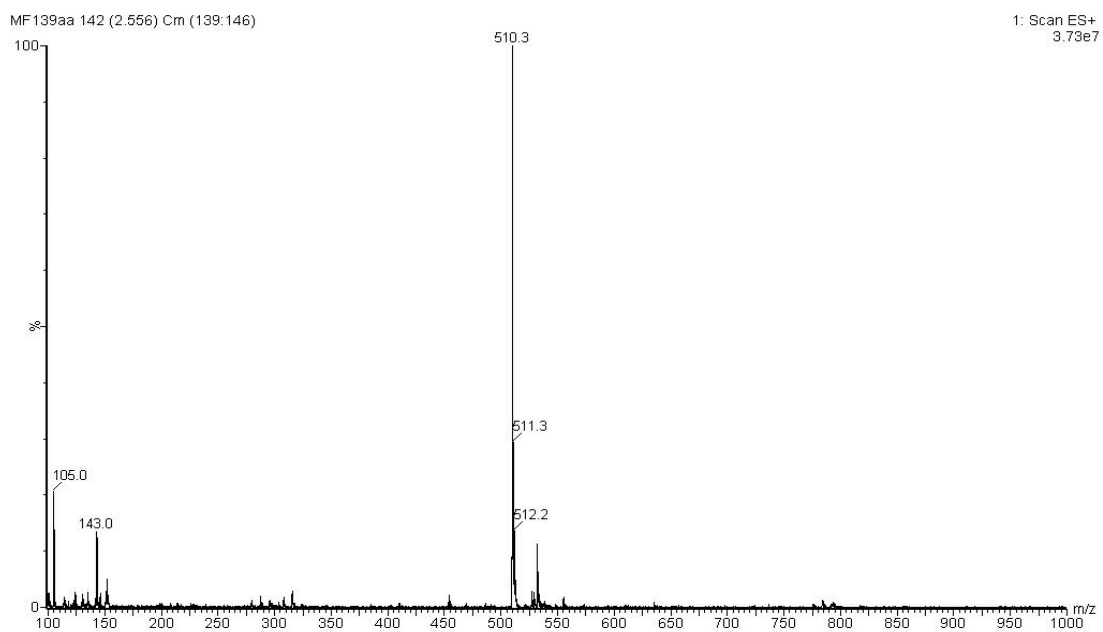
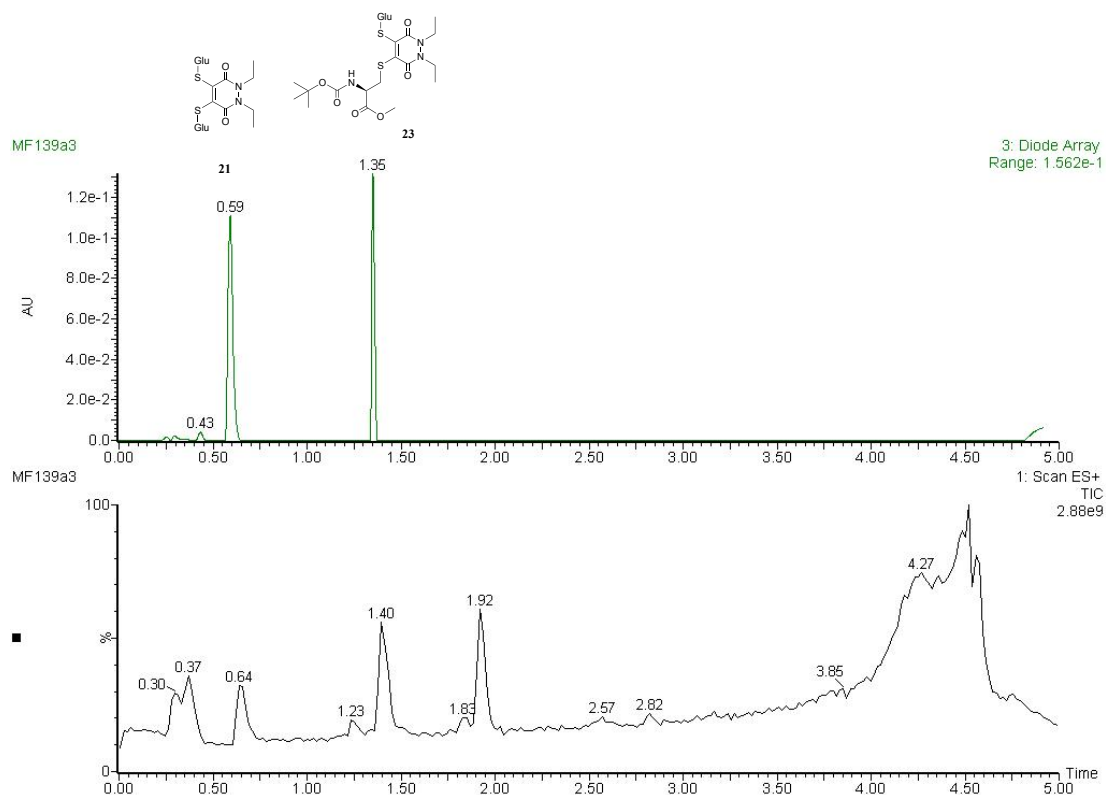


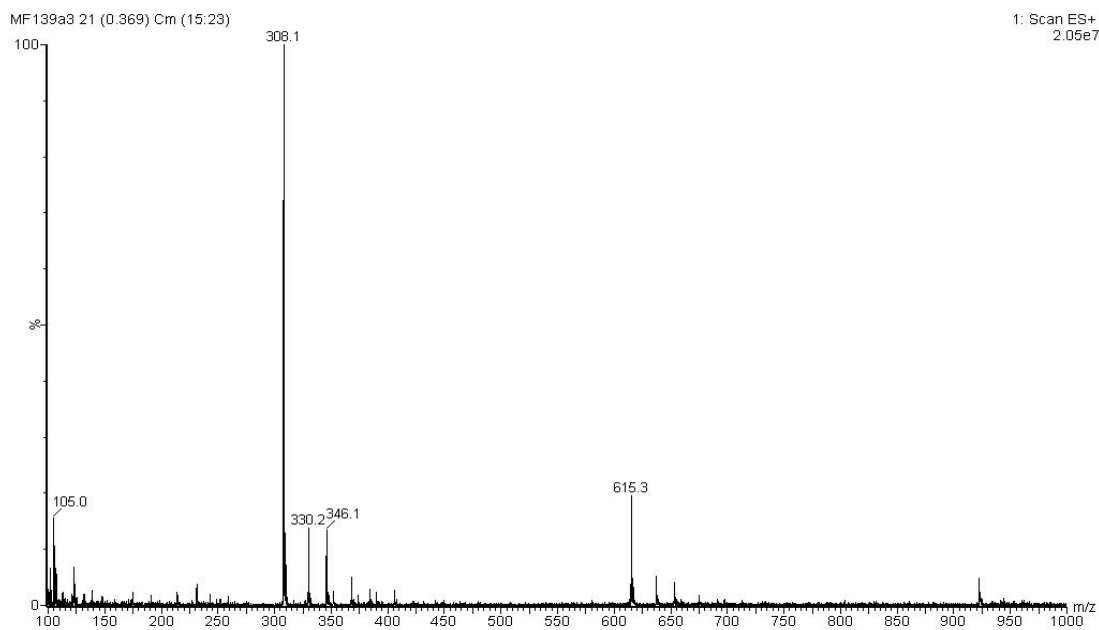
Figure S39. (a) TIC and UV trace at  $t = 0.05$  h, (b) MS data at 0.24–0.44 mins in the UV, (c) MS data at 0.61 mins in the UV, (d) at 1.20 mins in the UV, (e) at 1.36 mins in the UV and (f) at 2.50 mins in the UV for PD **17** incubated with GluSH **19** (10 eq.) at pH 6.5.

# LC-MS data for t = 1 h

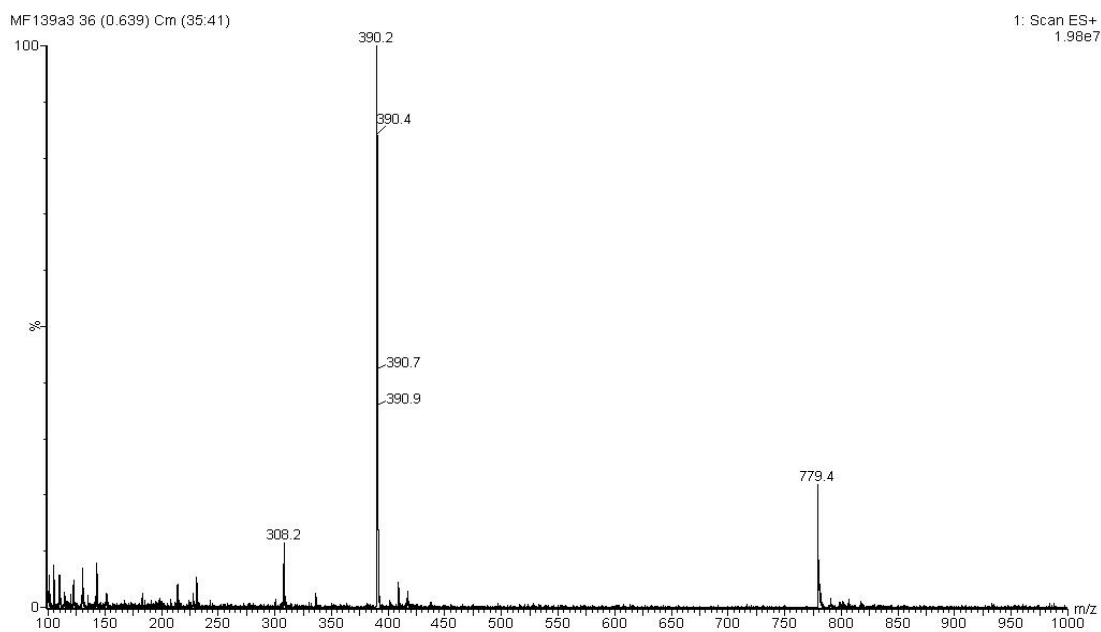
(a)



(b)



(c)



(d)

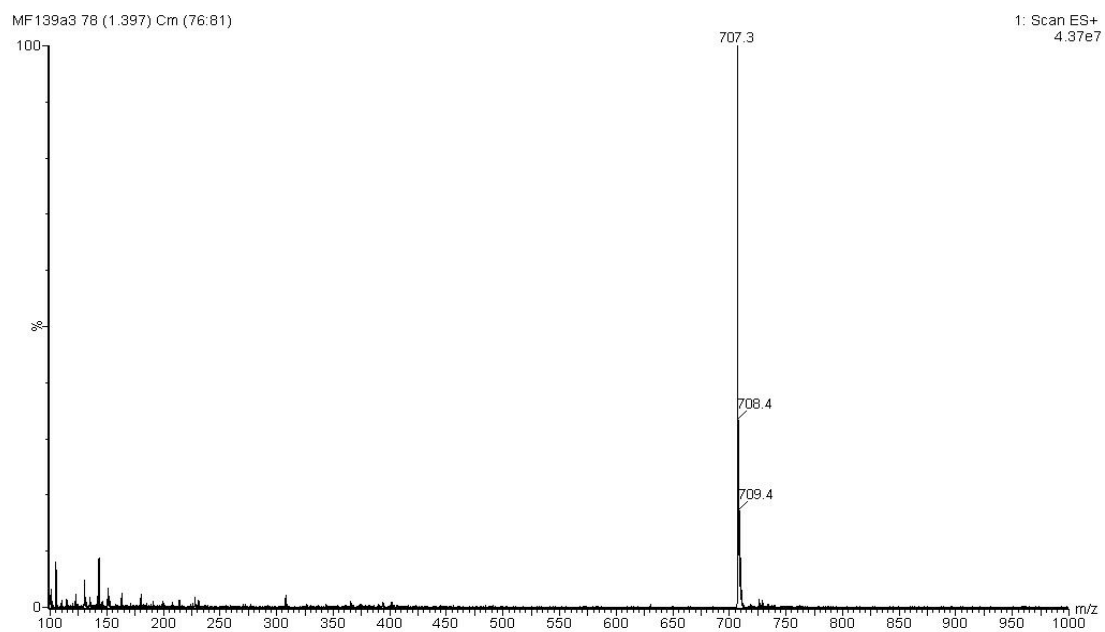
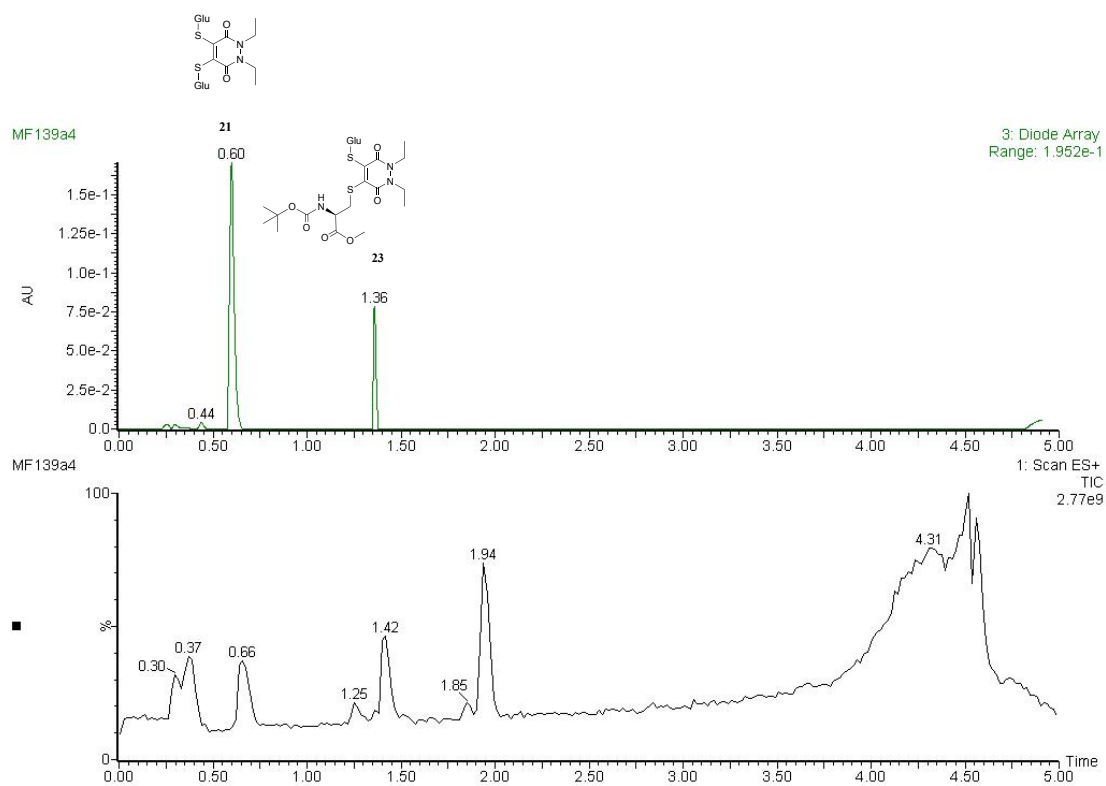


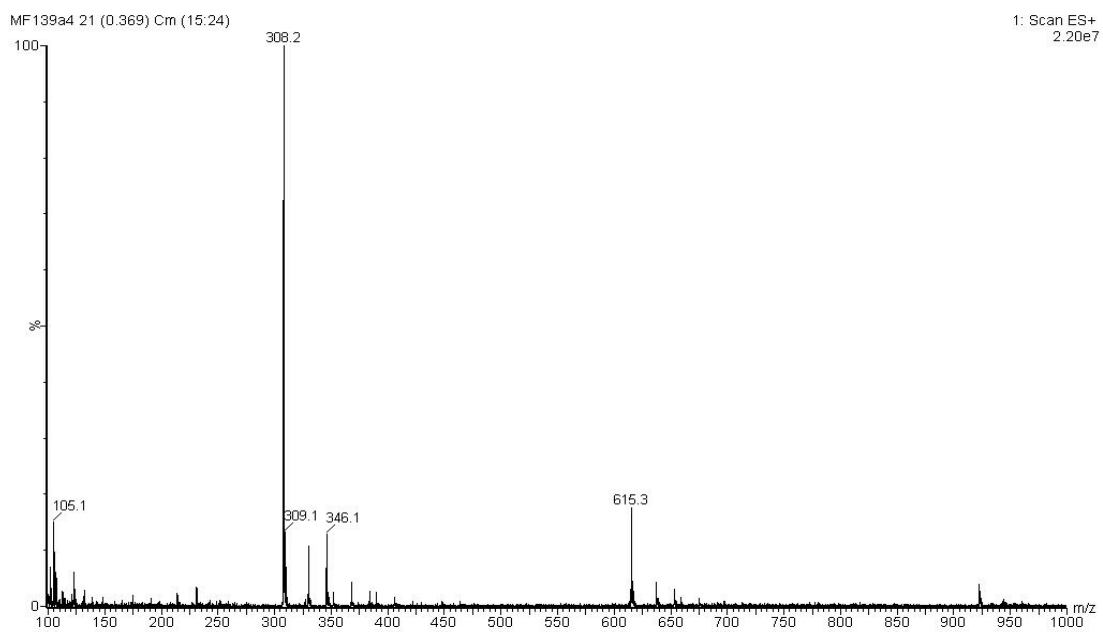
Figure S40. (a) TIC and UV trace at  $t = 1$  h, (b) MS data at 0.24–0.43 mins in the UV, (c) MS data at 0.59 mins in the UV and (d) at 1.35 mins in the UV for PD **17** incubated with GluSH **19** (10 eq.) at pH 6.5.

# LC-MS data for t = 2 h

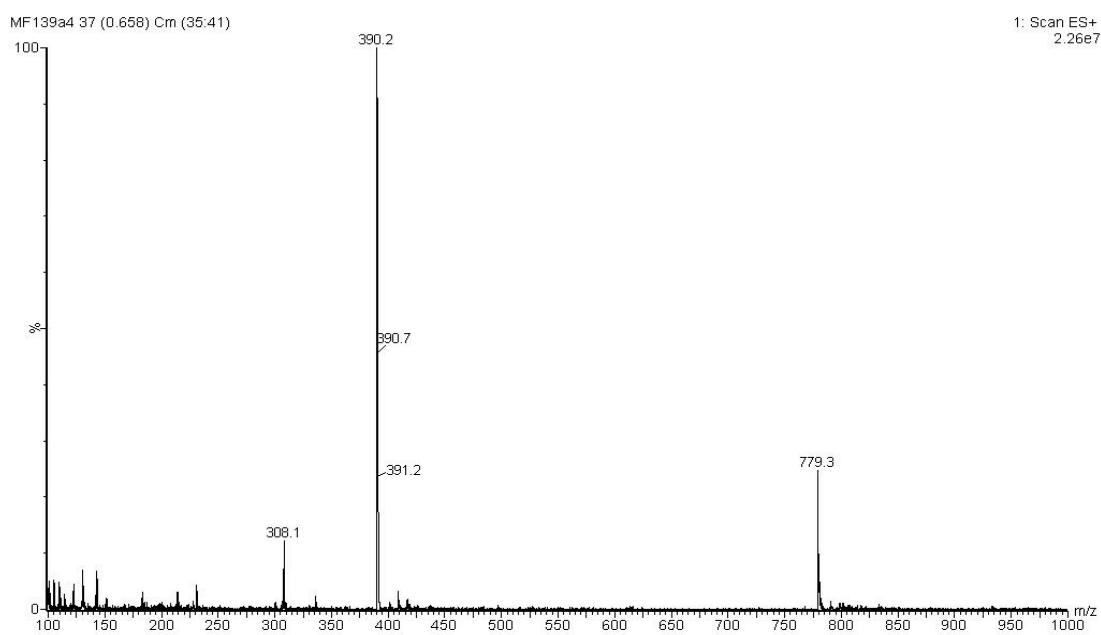
(a)



(b)



(c)



(d)

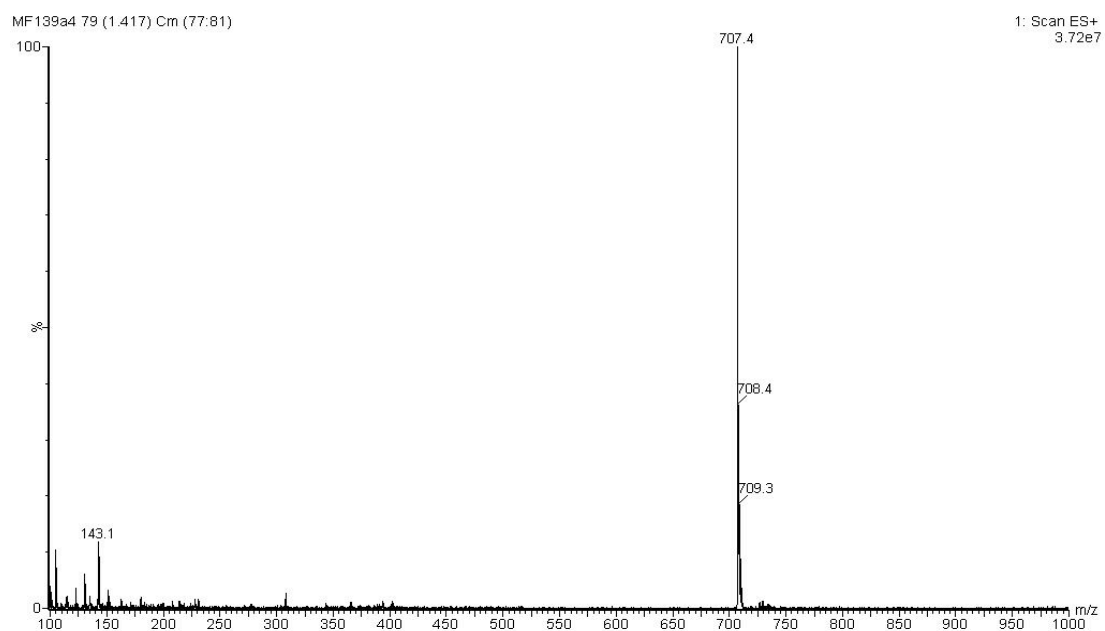
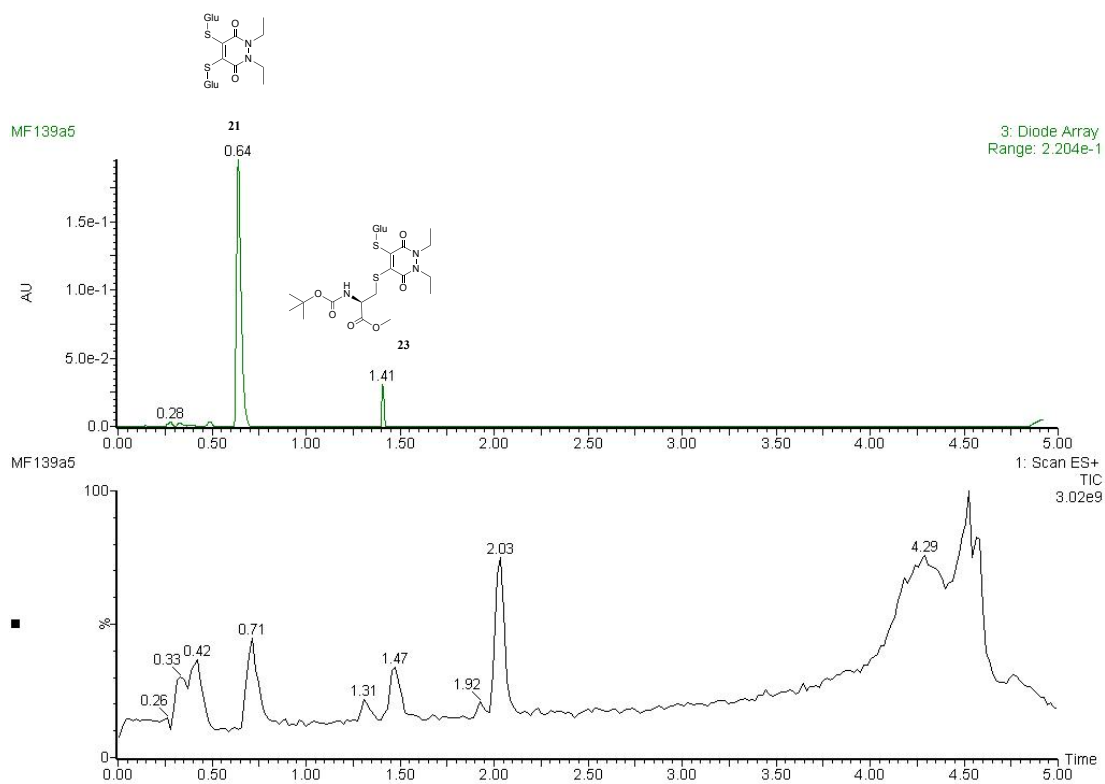


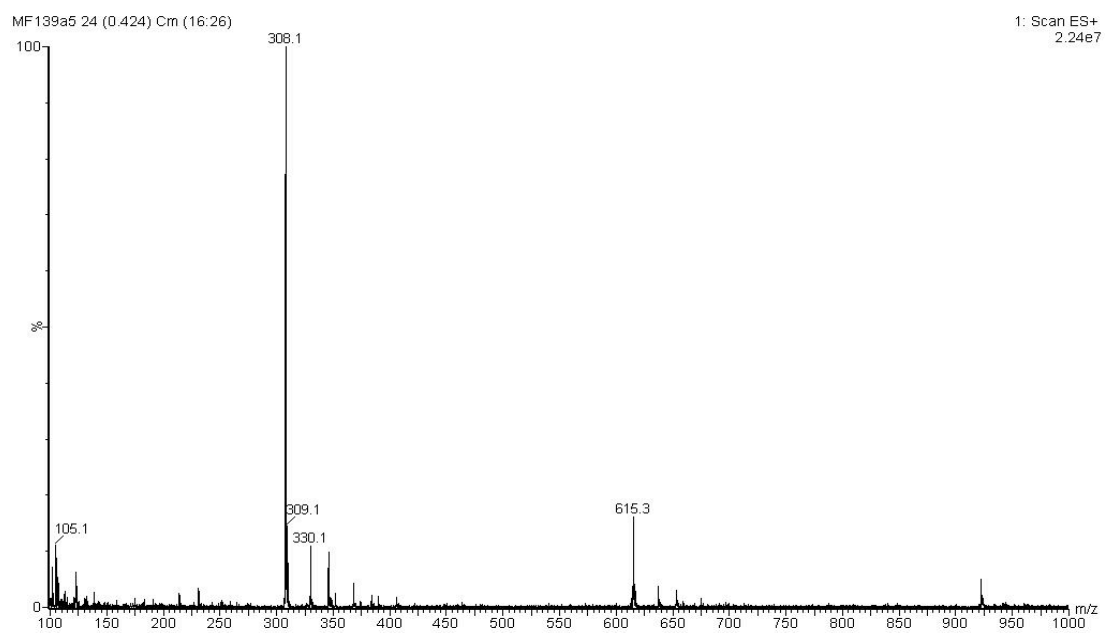
Figure S41. (a) TIC and UV trace at  $t = 2$  h, (b) MS data at 0.24–0.44 mins in the UV, (c) MS data at 0.60 mins in the UV and (d) at 1.36 mins in the UV for PD 17 incubated with GluSH 19 (10 eq.) at pH 6.5.

# LC-MS data for t = 4 h

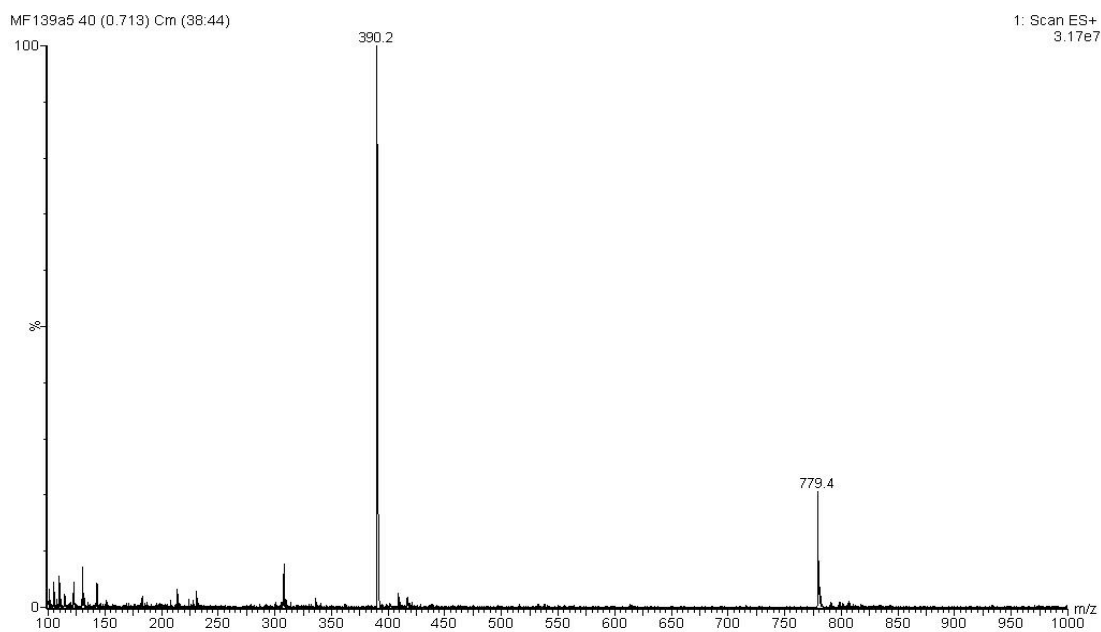
(a)



(b)



(c)



(d)

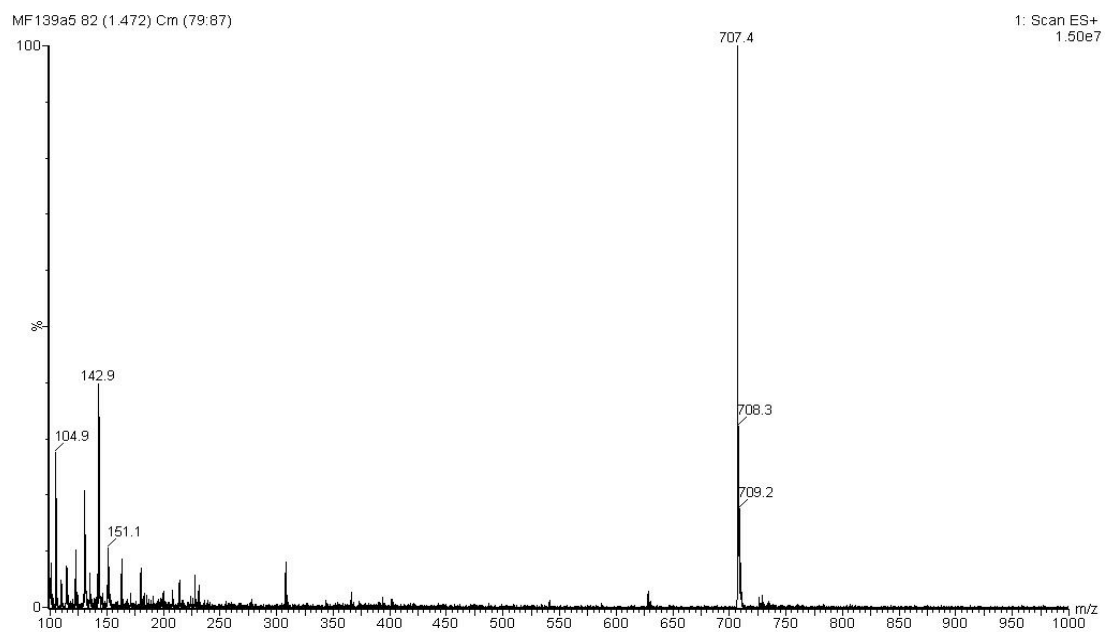
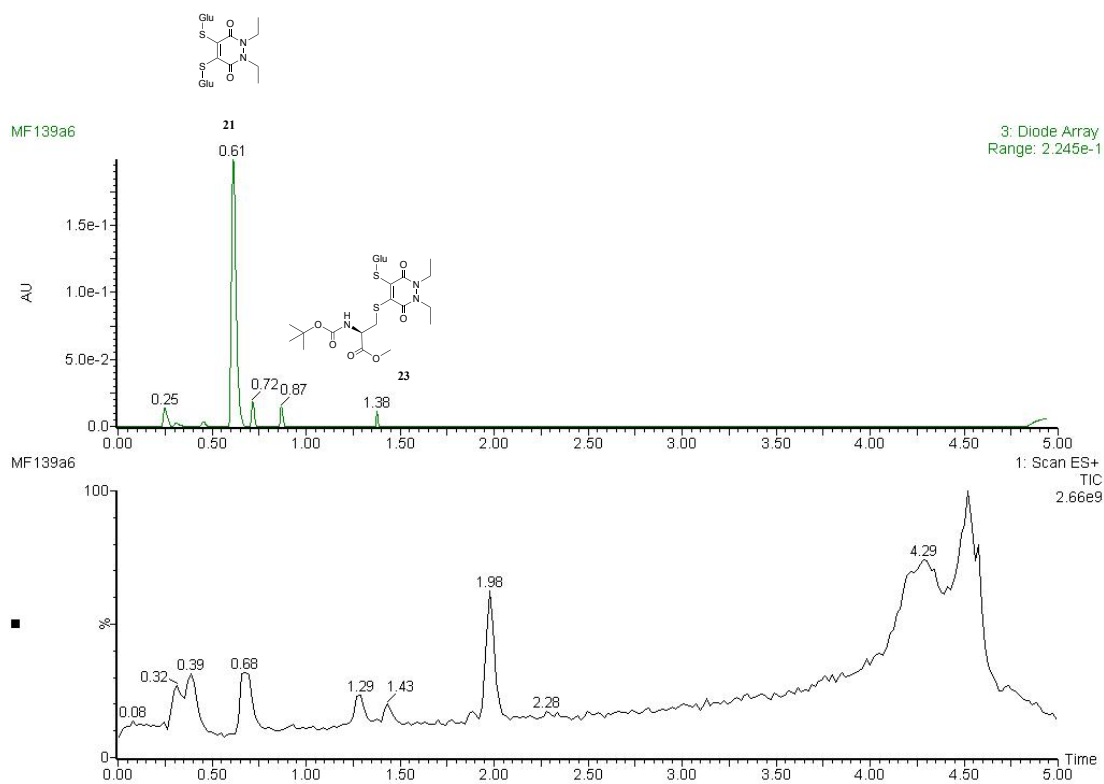


Figure S42. (a) TIC and UV trace at  $t = 4$  h, (b) MS data at 0.28–0.44 mins in the UV, (c) MS data at 0.64 mins in the UV and (d) at 1.41 mins in the UV for PD **17** incubated with GluSH **19** (10 eq.) at pH 6.5.

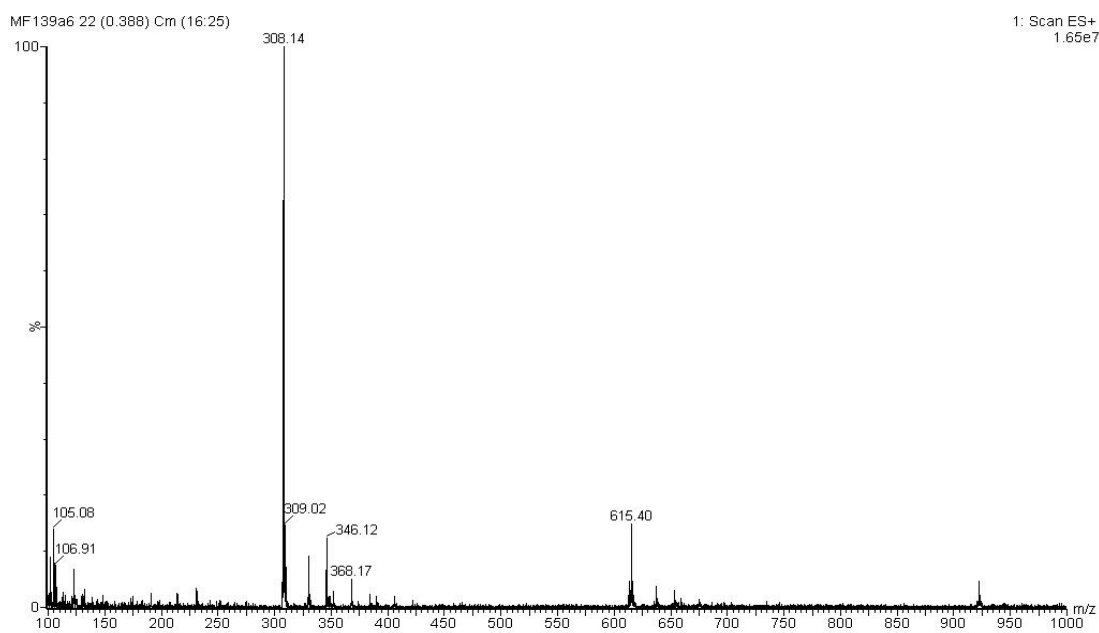


# LC-MS data for t = 24 h

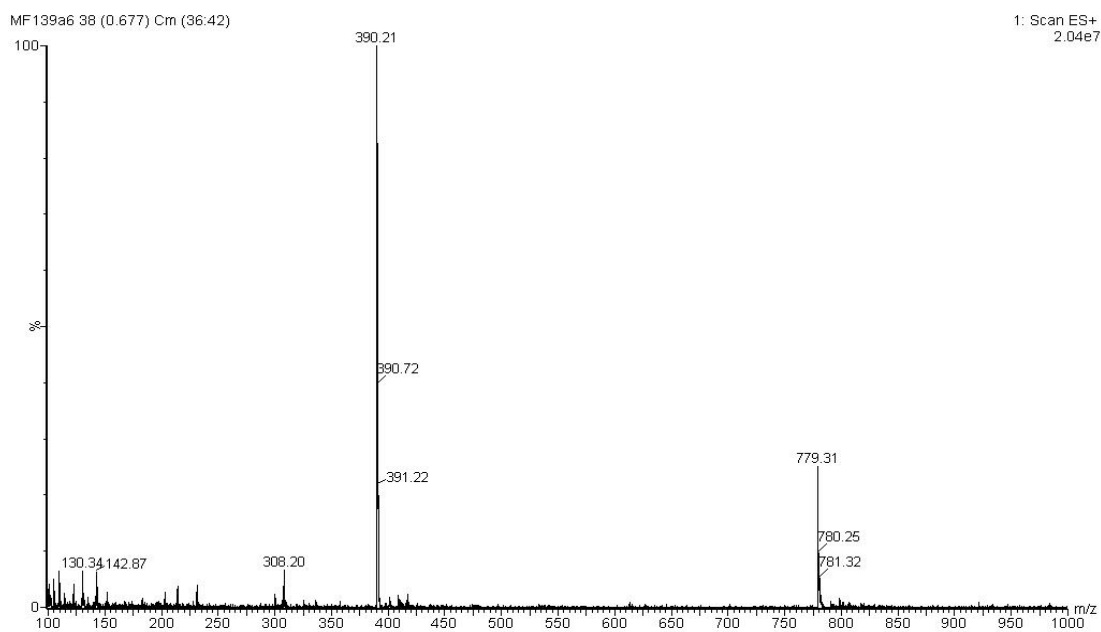
(a)



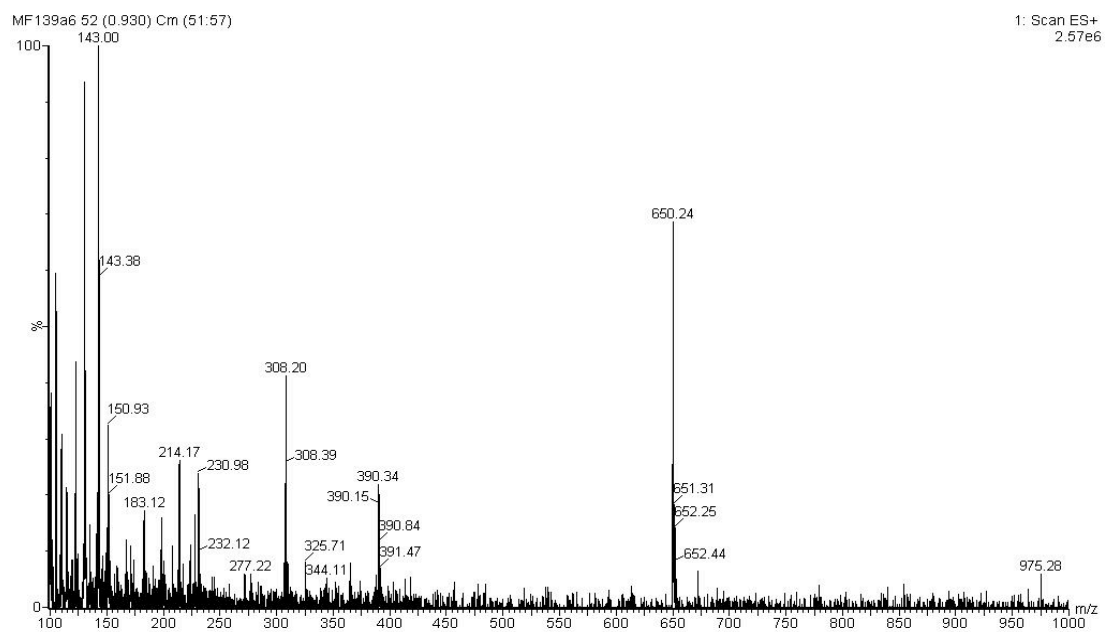
(b)



(c)



(d)



(e)

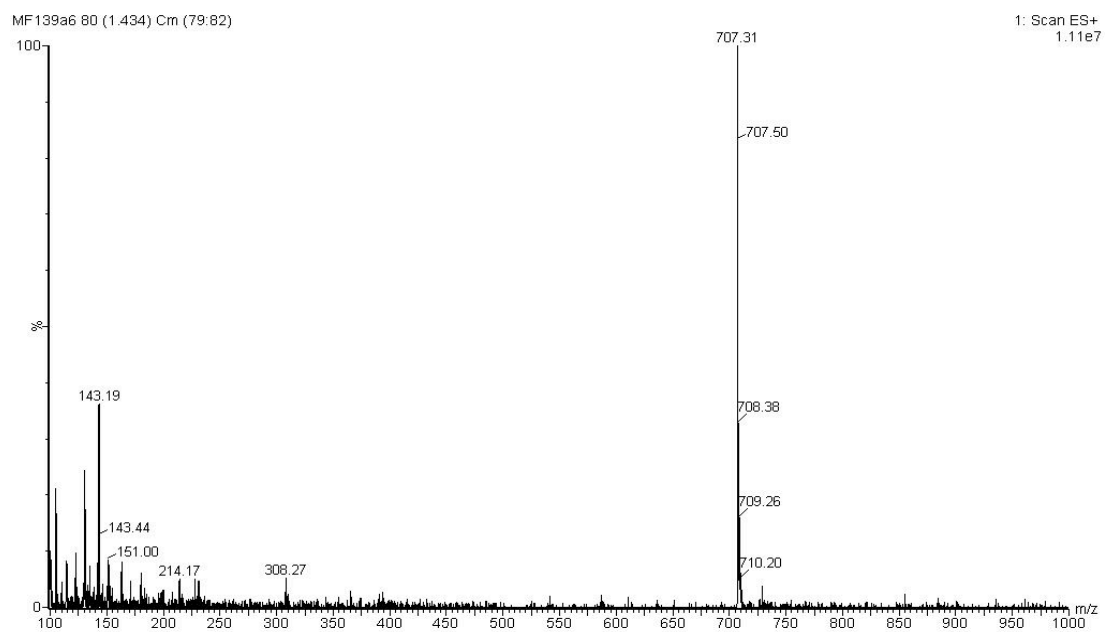
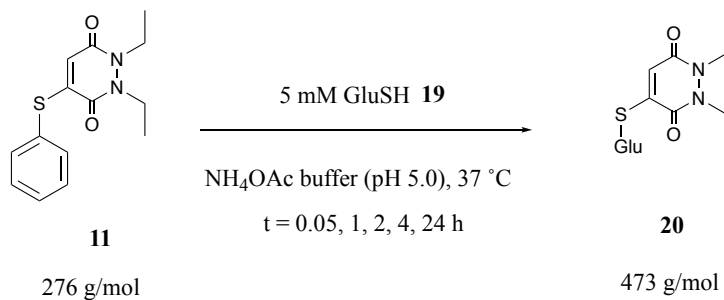


Figure S43. (a) TIC and UV trace at  $t = 24$  h, (b) MS data at 0.25–0.44 mins in the UV, (c) MS data at 0.61–0.72 mins in the UV, (d) at 0.87 mins in the UV and (e) at 1.38 mins in the UV for PD **17** incubated with GluSH **19** (10 eq.) at pH 6.5.

# Incubations involving GluSH and pyridazinediones 11, 12, 14, 15 and 17 at pH 5.0

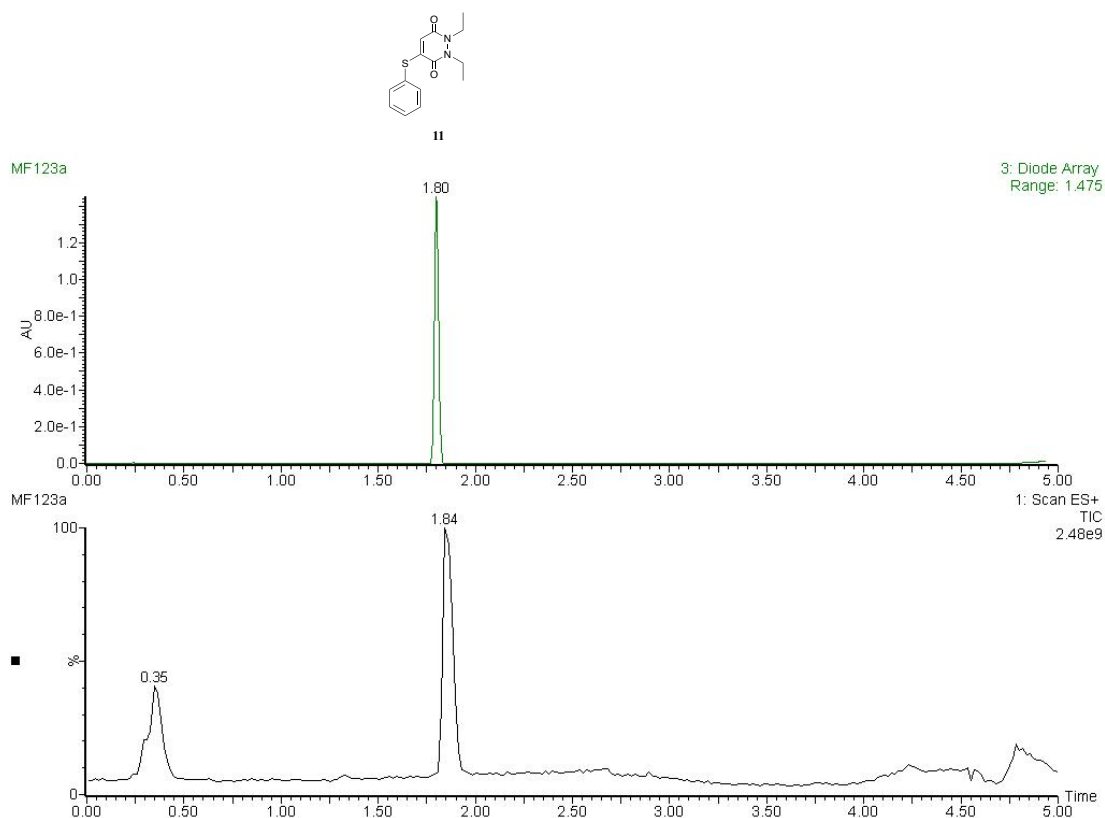
## Incubation of pyridazinedione 11 with GluSH (10 eq.)



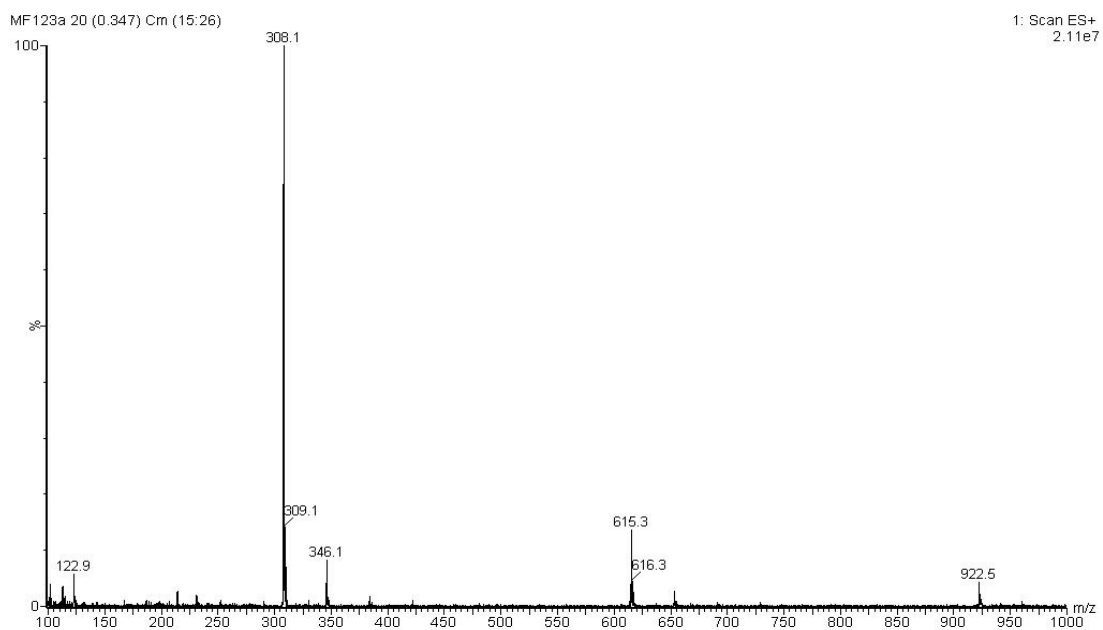
Pyridazinedione **11** (10  $\mu\text{L}$ , 10 mM in MeCN, 1 eq.) was added to GluSH **19** (190  $\mu\text{L}$ , 5.3 mM, 10 eq.) in ammonium acetate buffer (50 mM, pH 5.0). The mixture was incubated at 37  $^\circ\text{C}$  for 24 h. The samples were analysed by LC-MS at  $t = 0.05, 1, 2, 4$  and 24 h.

### LC-MS data for $t = 0.05 \text{ h}$

(a)



(b)



(c)

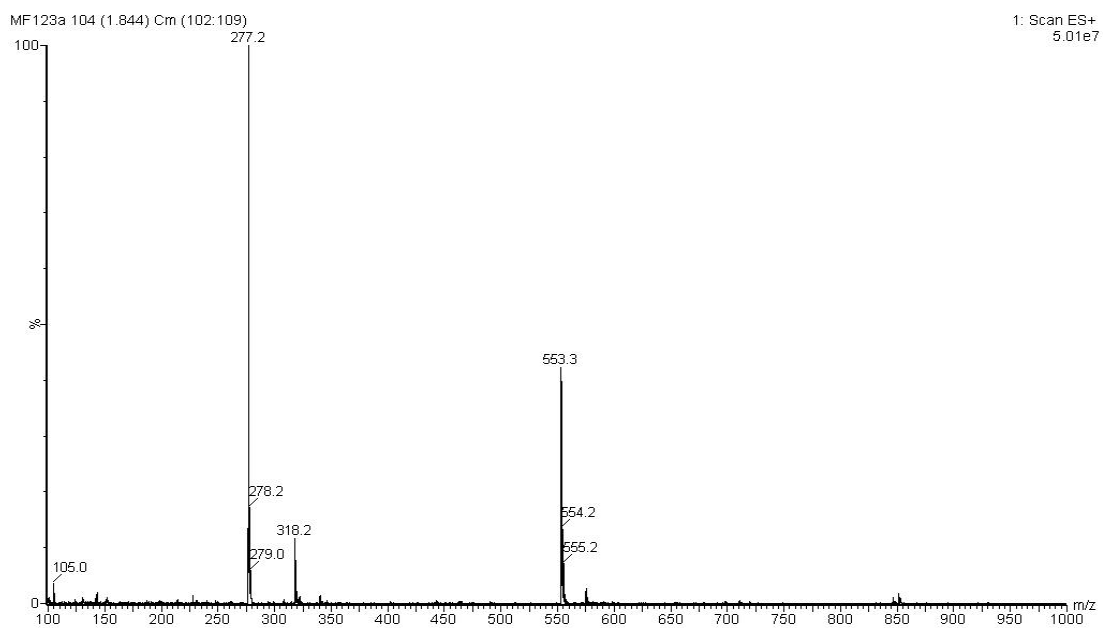
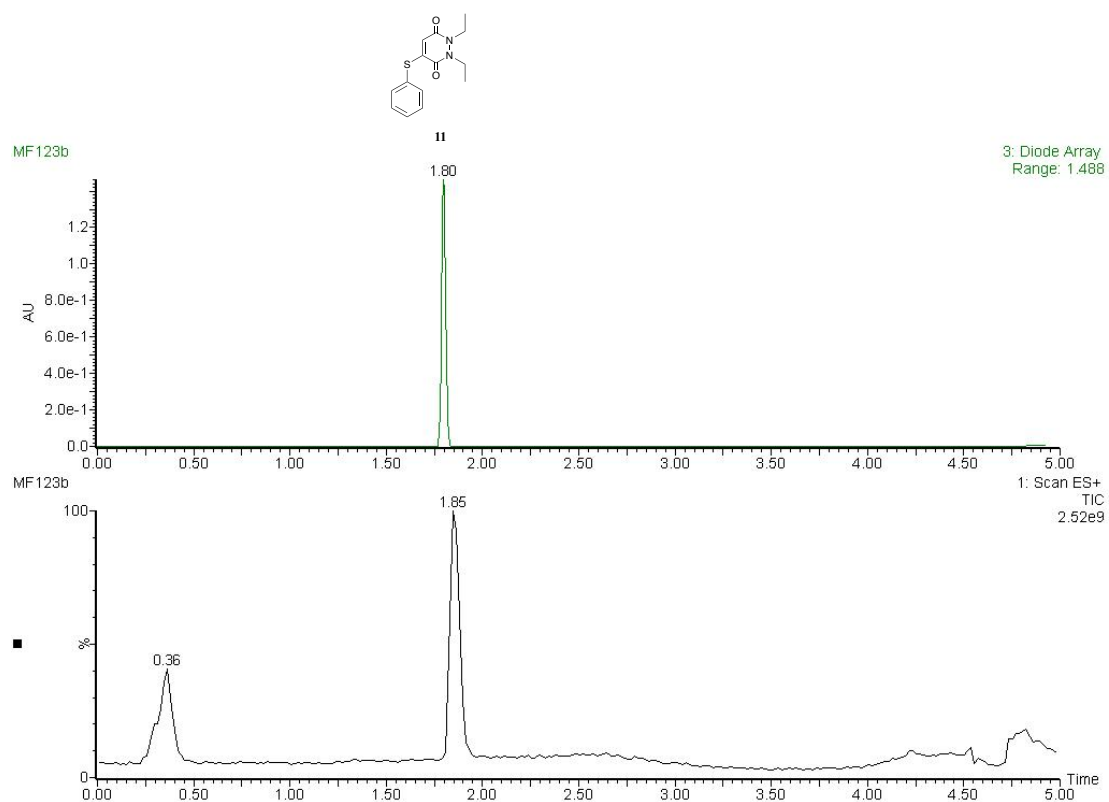


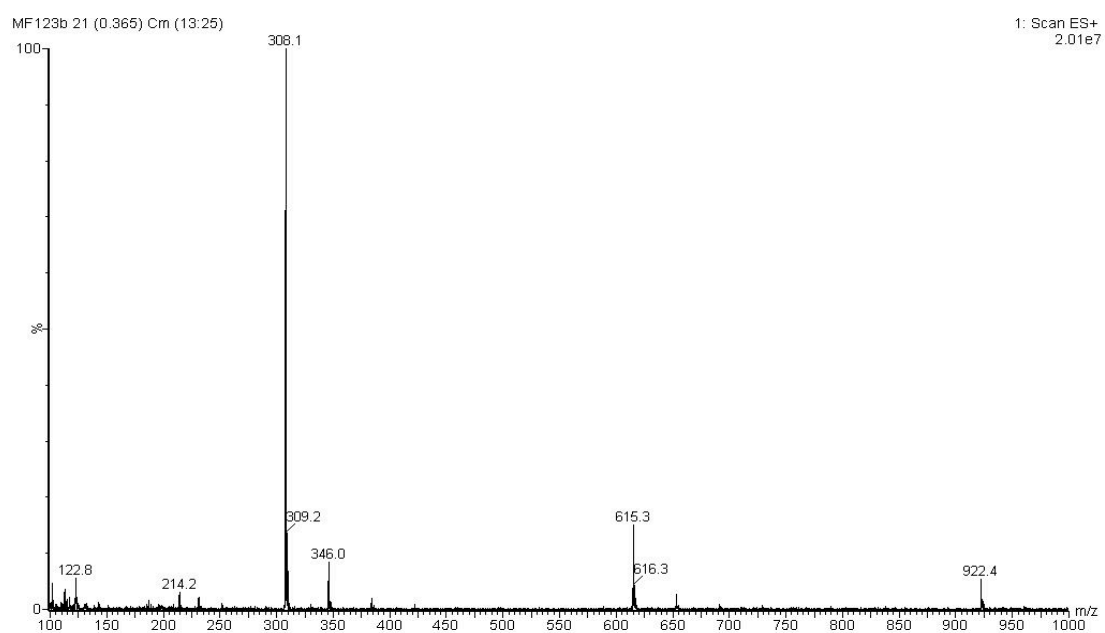
Figure S44. (a) TIC and UV trace at  $t = 0.05$  h, (b) MS data at 0.35 mins in the TIC and (c) MS data at 1.80 mins in the UV for PD **11** incubated with GluSH **19** (10 eq.) at pH 5.0.

# LC-MS data for t = 1 h

(a)



(b)



(c)

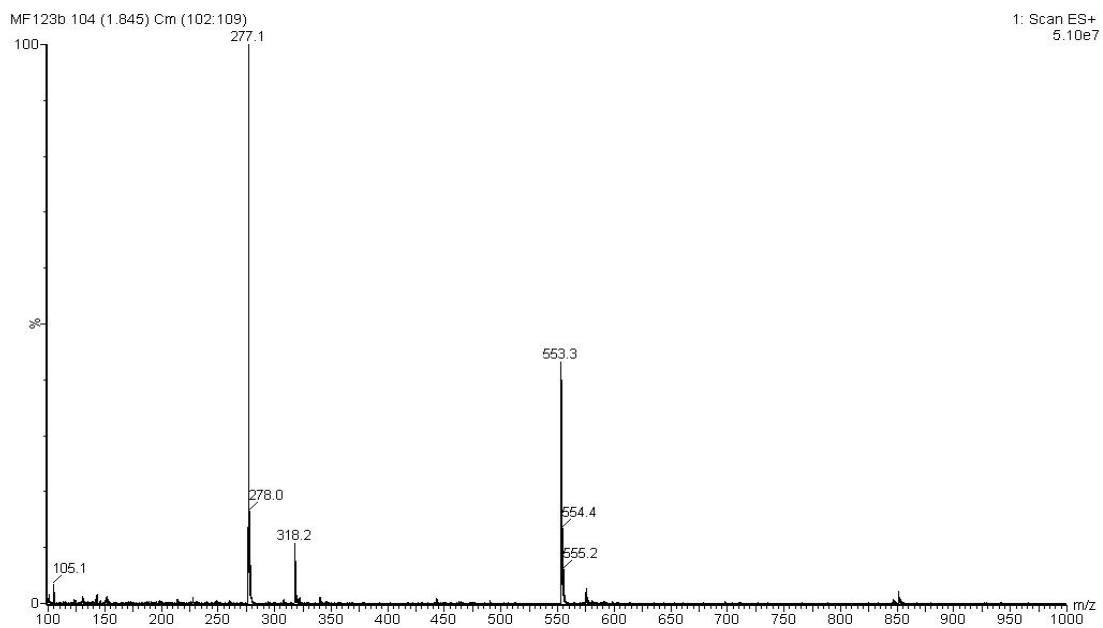
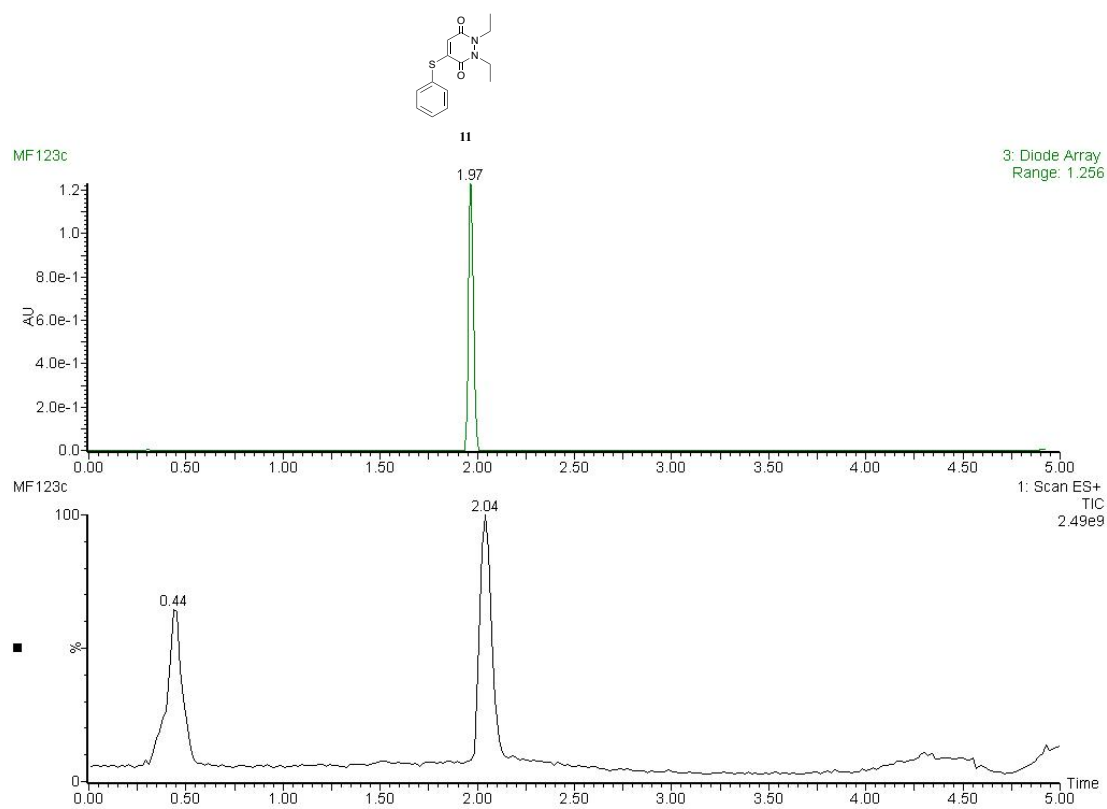


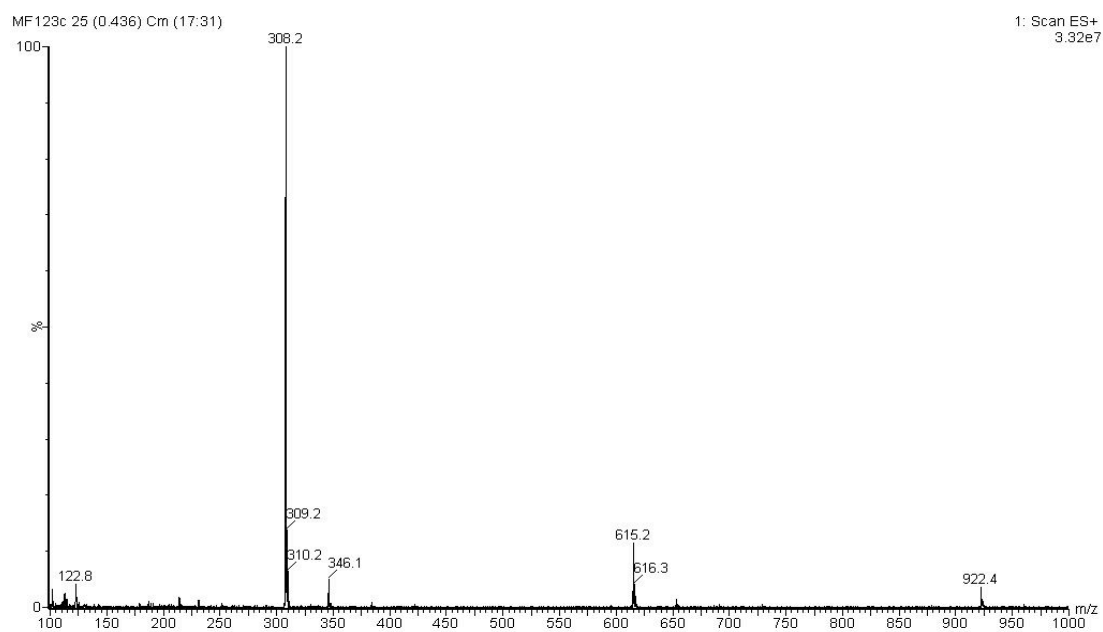
Figure S45. (a) TIC and UV trace at  $t = 1$  h, (b) MS data at 0.36 mins in the TIC and (c) MS data at 1.80 mins in the UV for PD **11** incubated with GluSH **19** (10 eq.) at pH 5.0.

# LC-MS data for t = 2 h

(a)



(b)





(c)

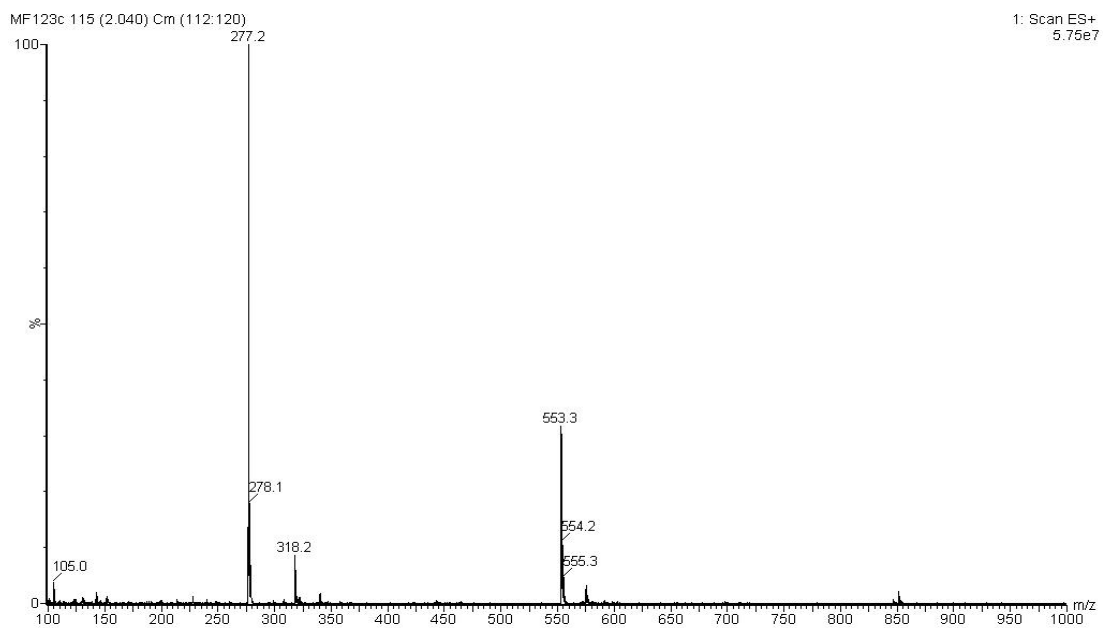
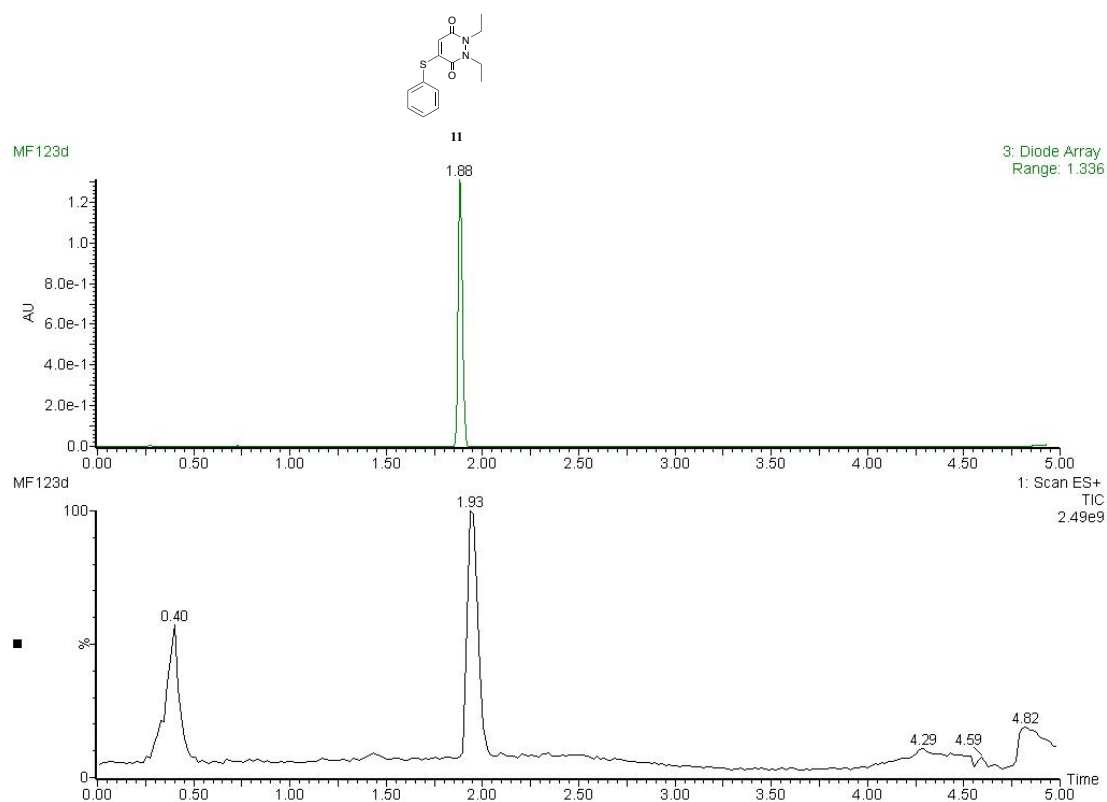


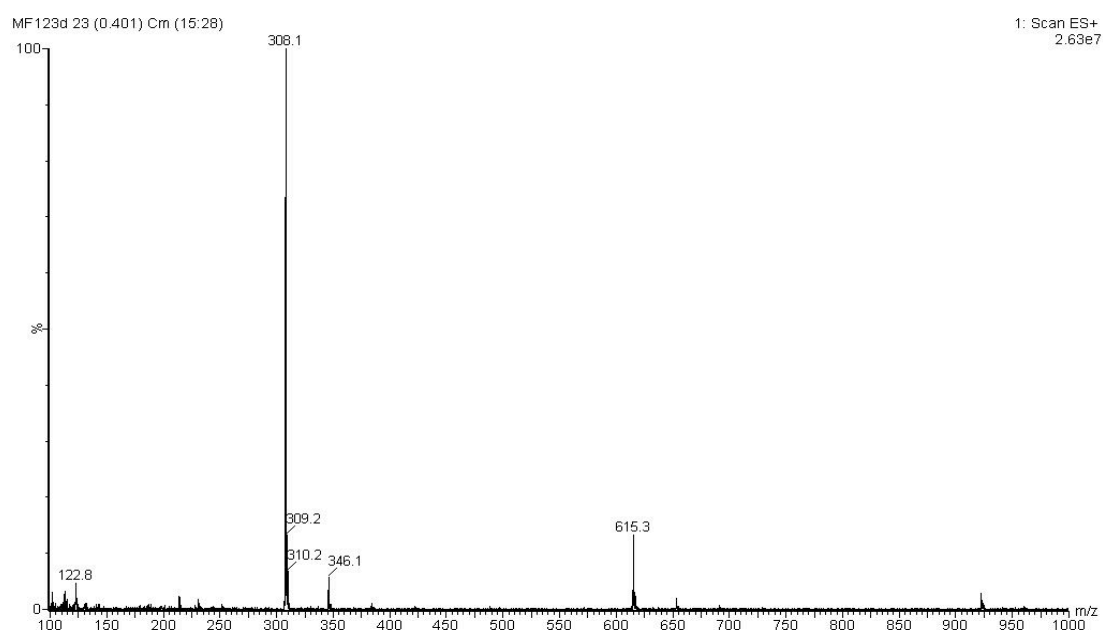
Figure S46. (a) TIC and UV trace at  $t = 2$  h, (b) MS data at 0.44 mins in the TIC and (c) MS data at 1.97 mins in the UV for PD **11** incubated with GluSH **19** (10 eq.) at pH 5.0.

# LC-MS data for t = 4 h

(a)



(b)



(c)

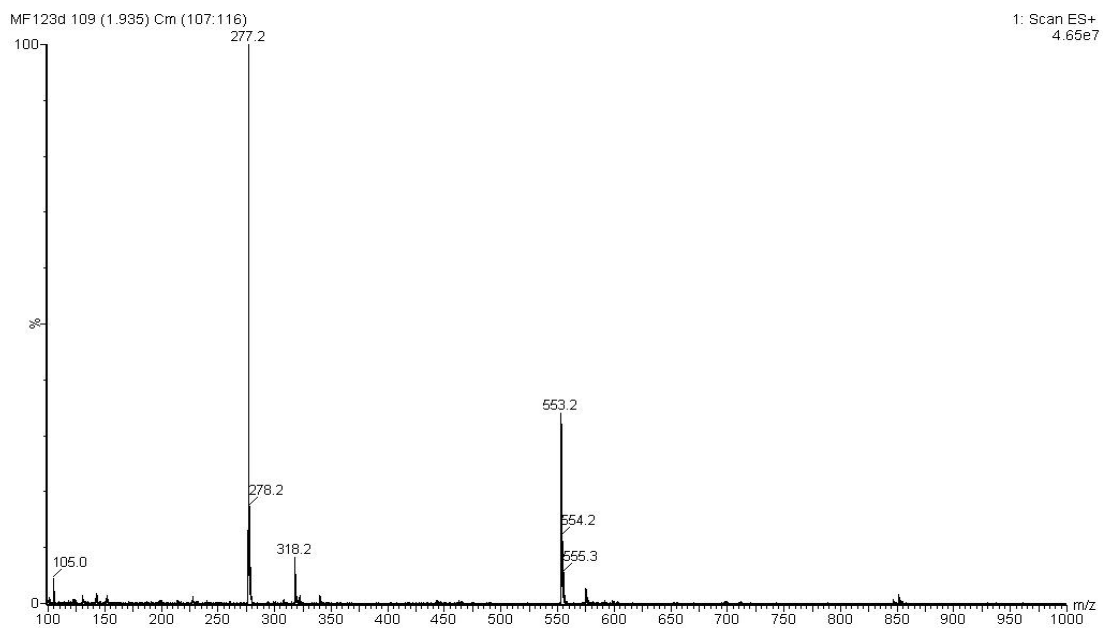
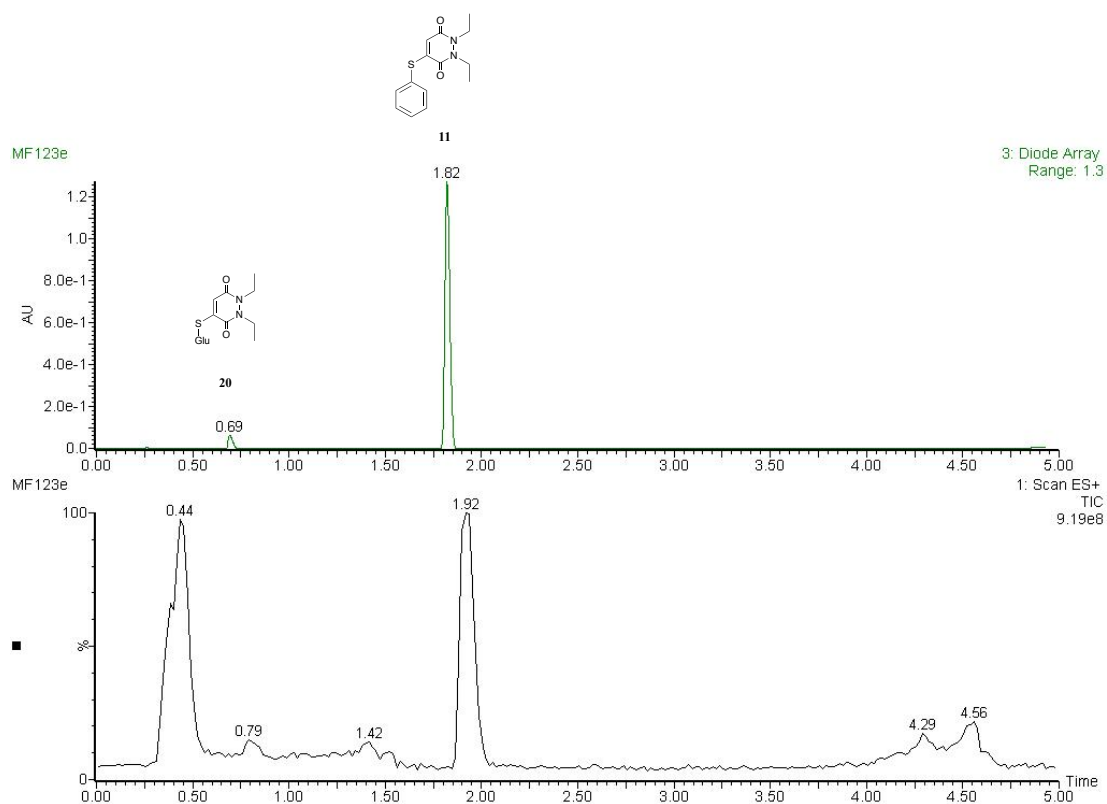


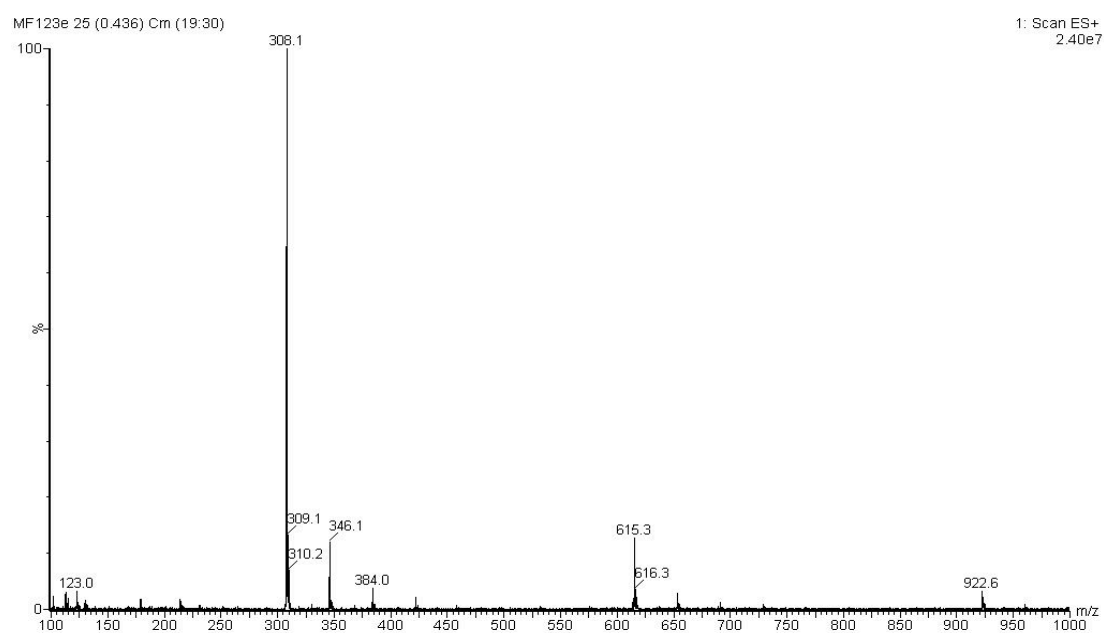
Figure S47. (a) TIC and UV trace at  $t = 4$  h, (b) MS data at 0.40 mins in the TIC and (c) MS data at 1.88 mins in the UV for PD 11 incubated with GluSH 19 (10 eq.) at pH 5.0.

# LC-MS data for t = 24 h

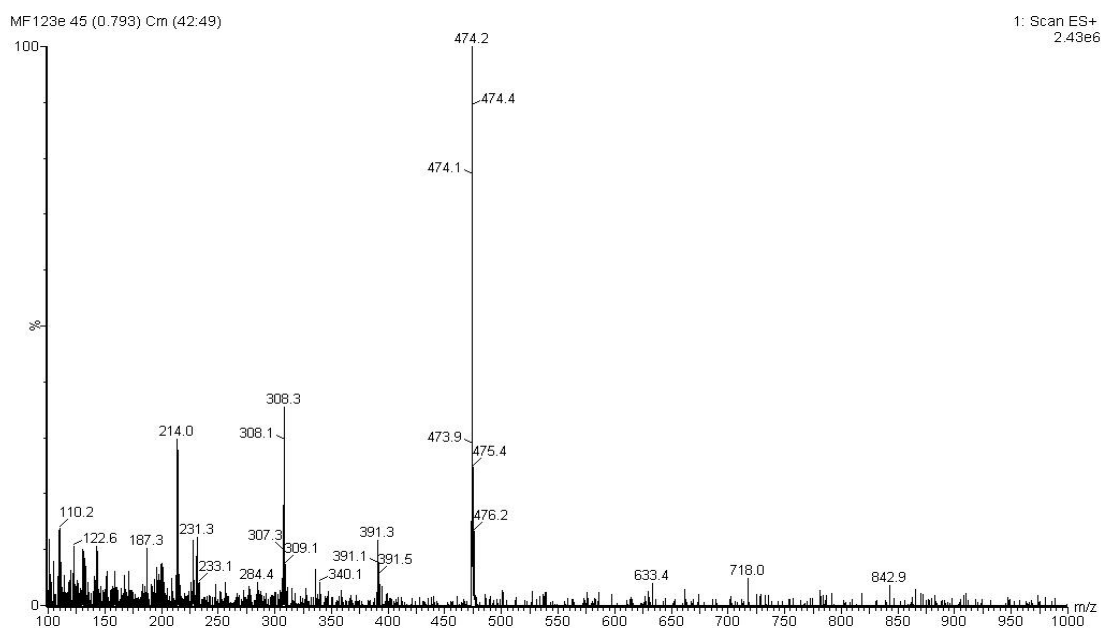
(a)



(b)



(c)



(d)

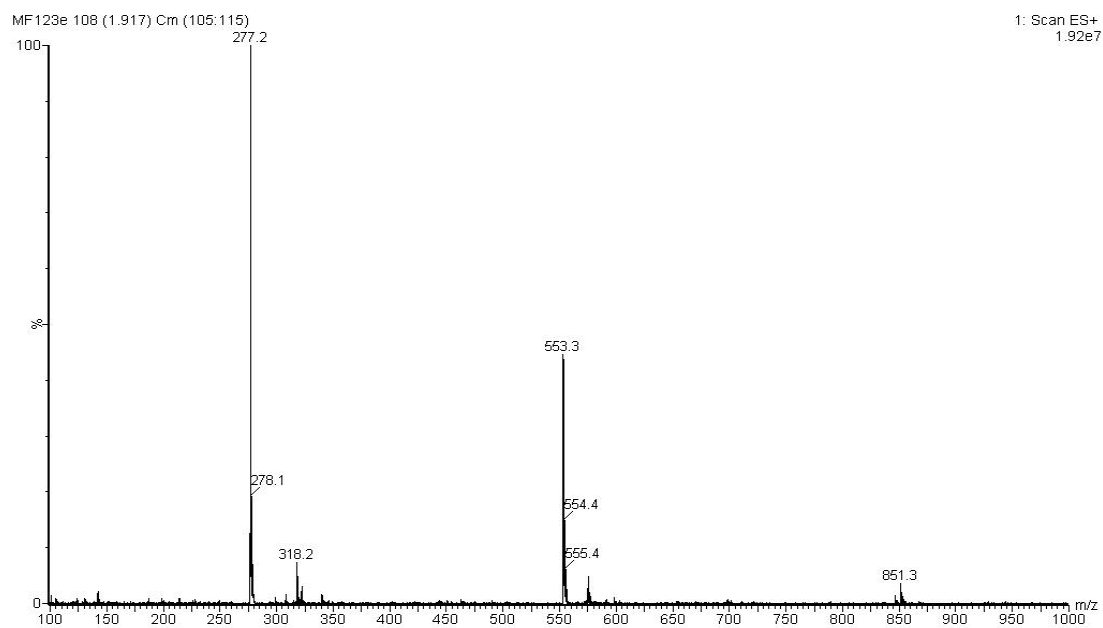
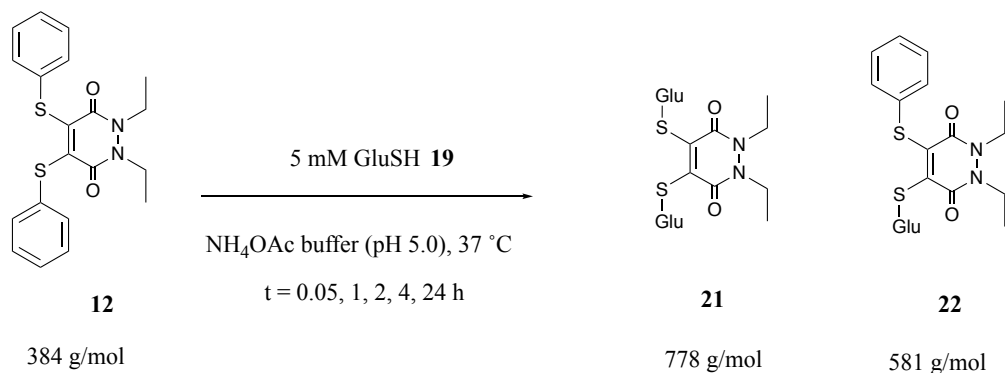


Figure S48. (a) TIC and UV trace at  $t = 24$  h, (b) MS data at 0.44 mins in the TIC, (c) MS data at 0.69 mins in the UV and (d) at 1.82 mins in the UV for PD **11** incubated with GluSH **19** (10 eq.) at pH 5.0.

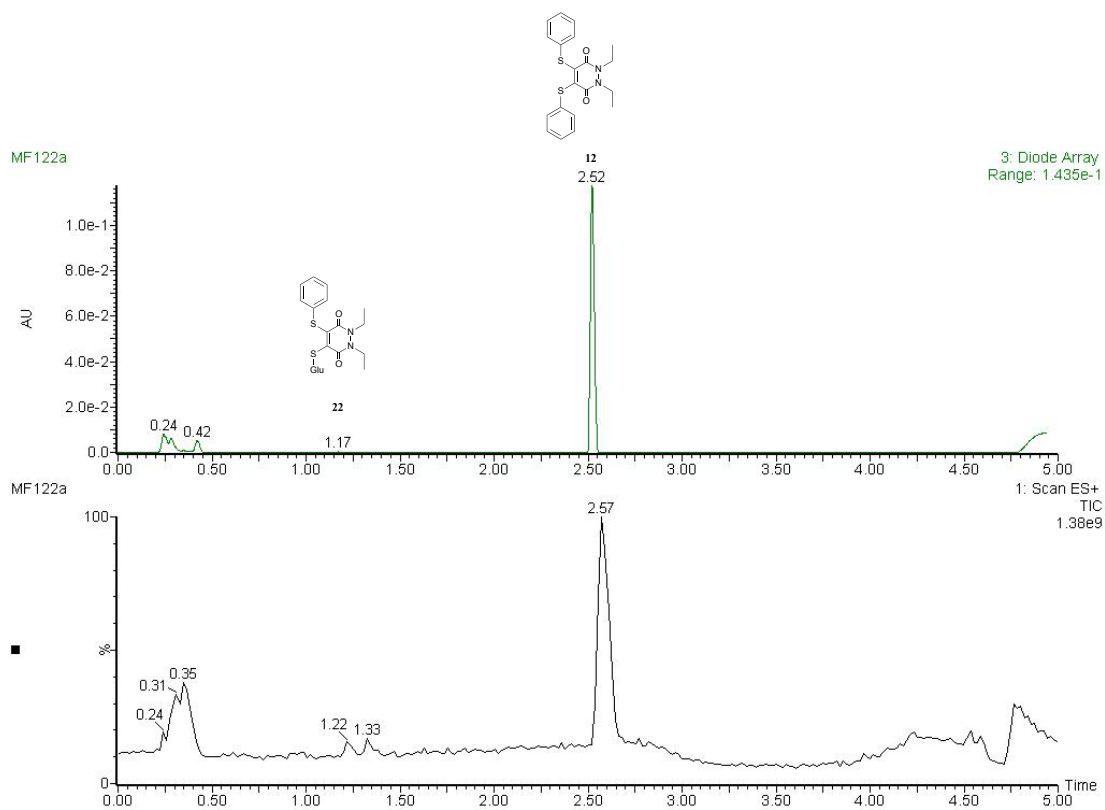
## Incubation of pyridazinedione **12** with GluSH (**10 eq.**)



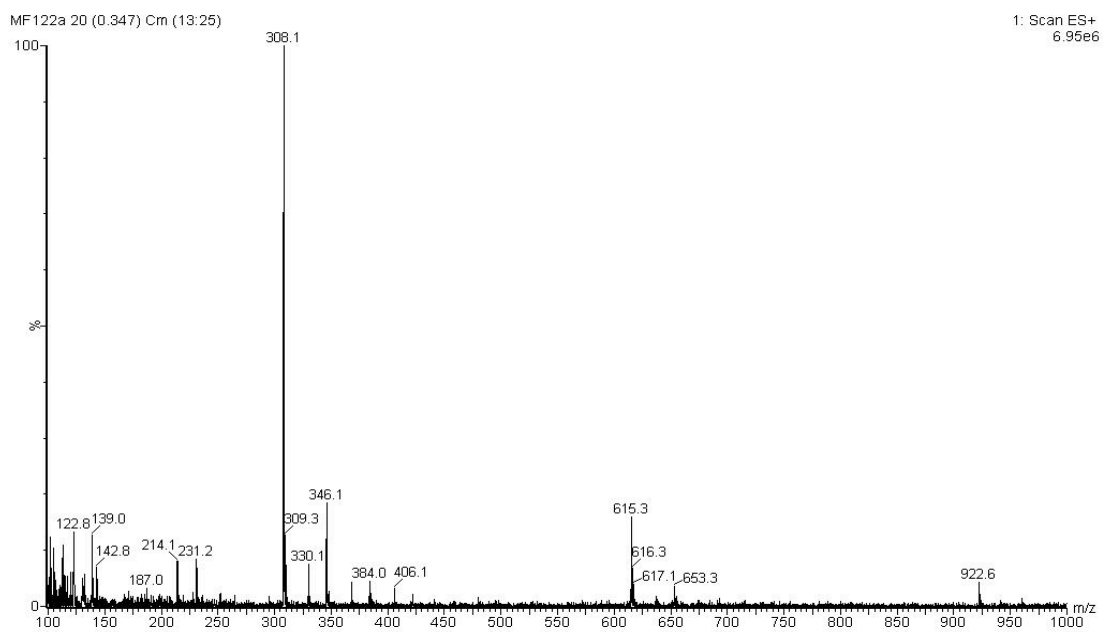
Pyridazinedione **12** (10  $\mu\text{L}$ , 10 mM in MeCN, 1 eq.) was added to GluSH **19** (190  $\mu\text{L}$ , 5.3 mM, 10 eq.) in ammonium acetate buffer (50 mM, pH 5.0). The mixture was incubated at 37  $^\circ\text{C}$  for 24 h. The samples were analysed by LC-MS at  $t = 0.05, 1, 2, 4$  and 24 h.

### LC-MS data for $t = 0.05 \text{ h}$

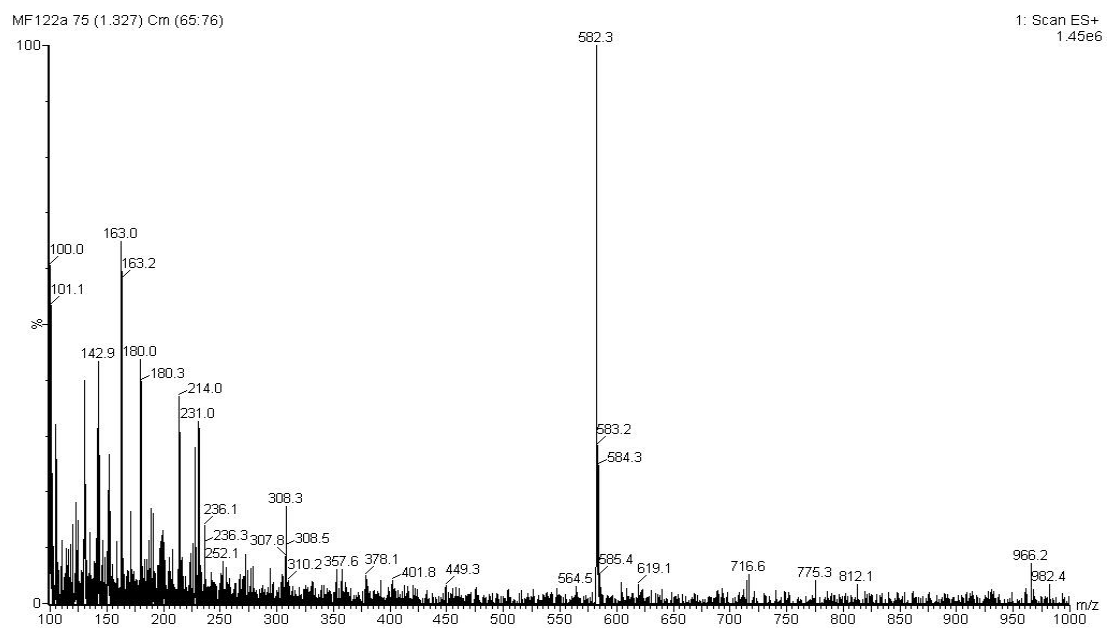
(a)



(b)



(c)



(d)

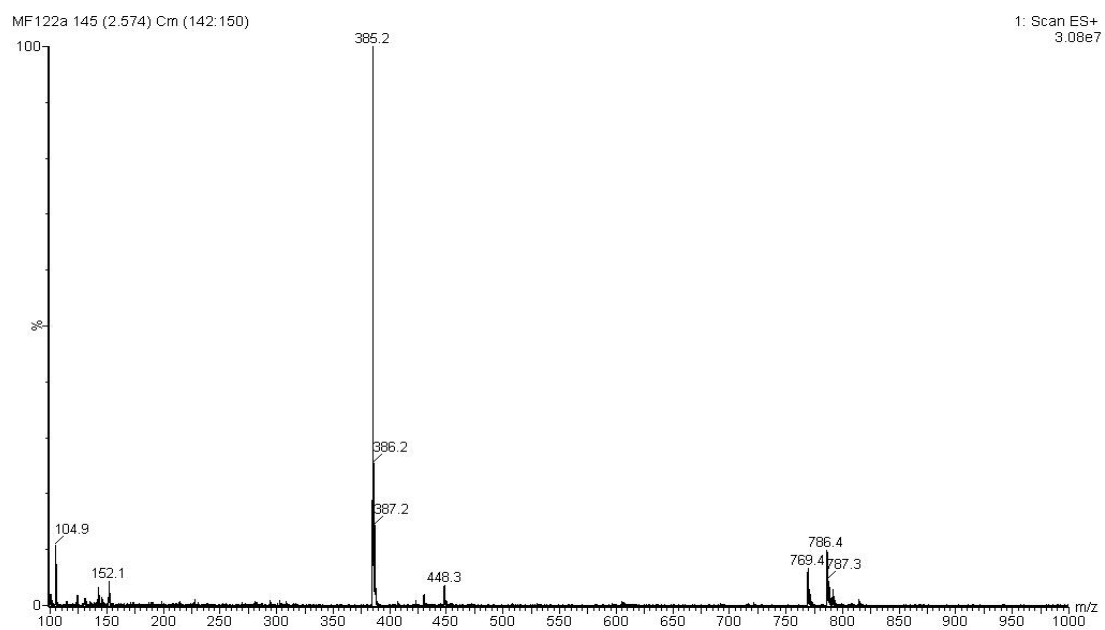
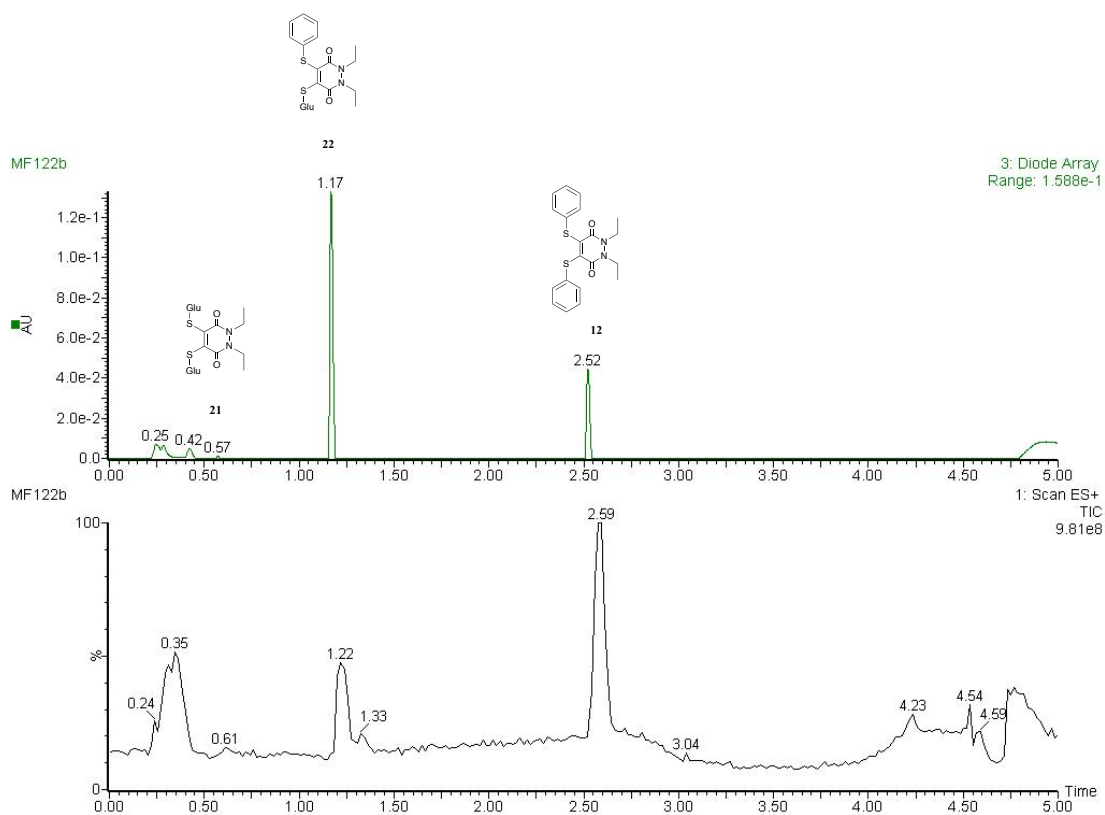


Figure S49. (a) TIC and UV trace at  $t = 0.05$  h, (b) MS data at 0.24–0.42 mins in the UV, (c) MS data at 1.17 mins in the UV and (d) at 2.52 mins in the UV for PD 12 incubated with GluSH 19 (10 eq.) at pH 5.0.

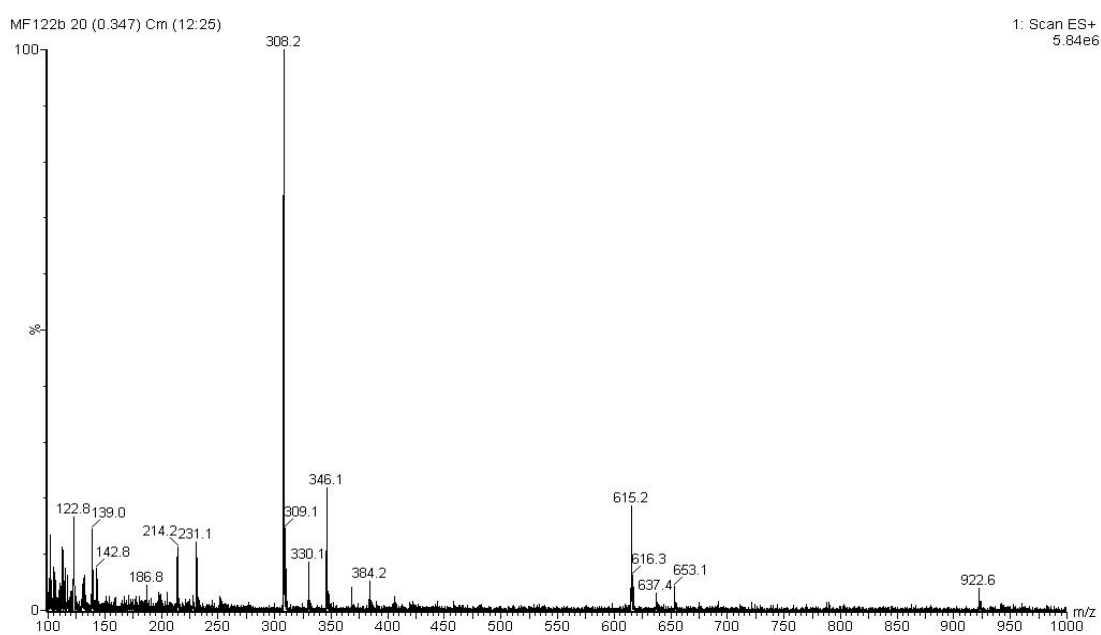


# LC-MS data for t = 1 h

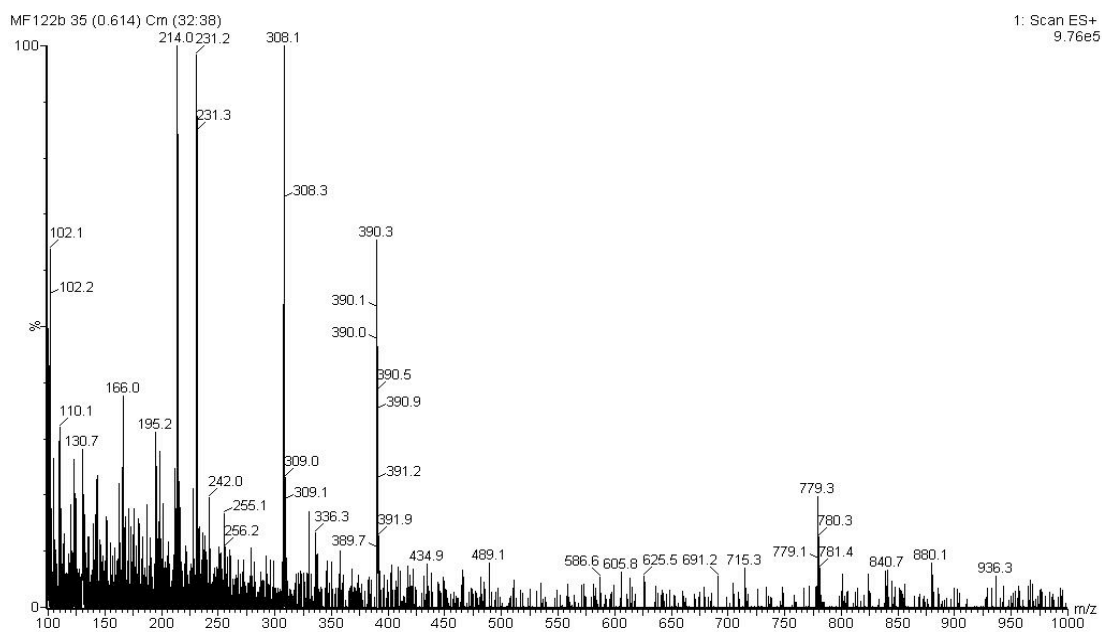
(a)



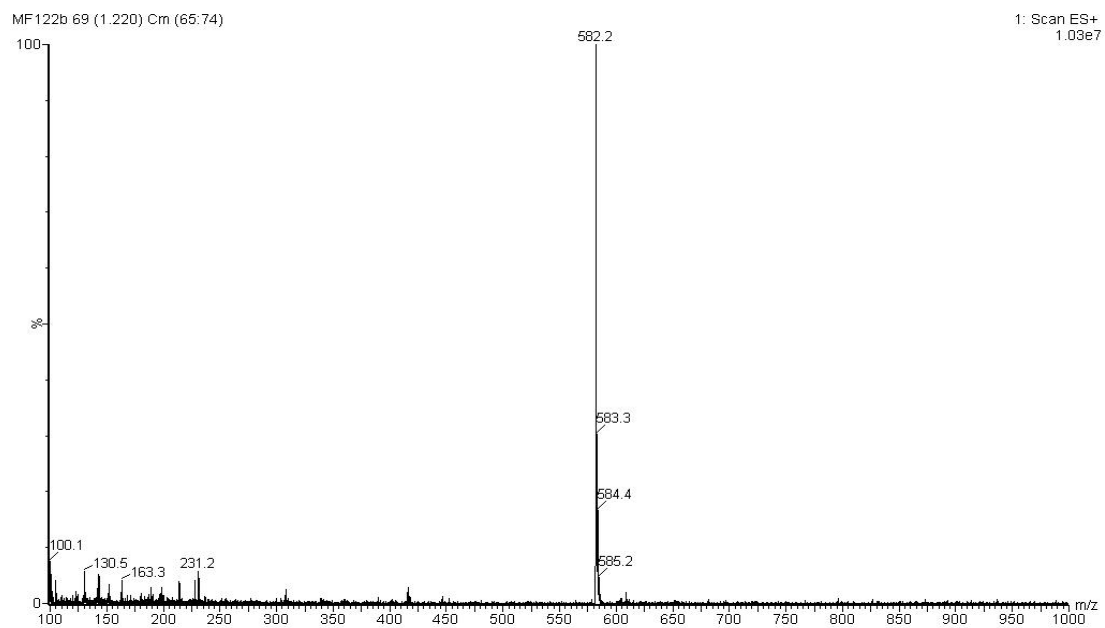
(b)



(c)



(d)



(e)

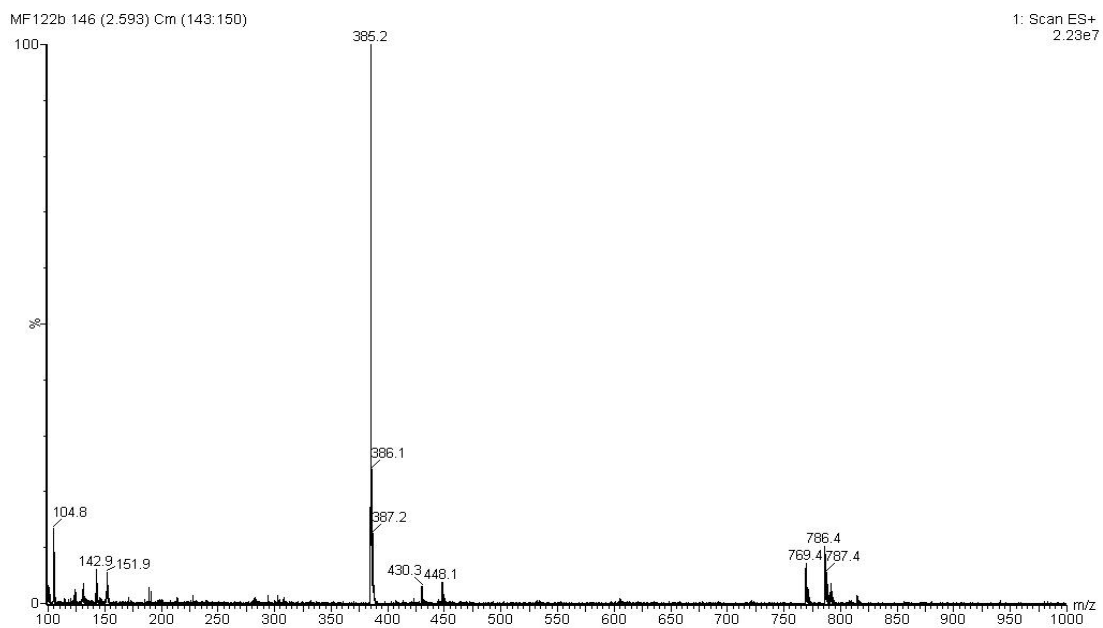
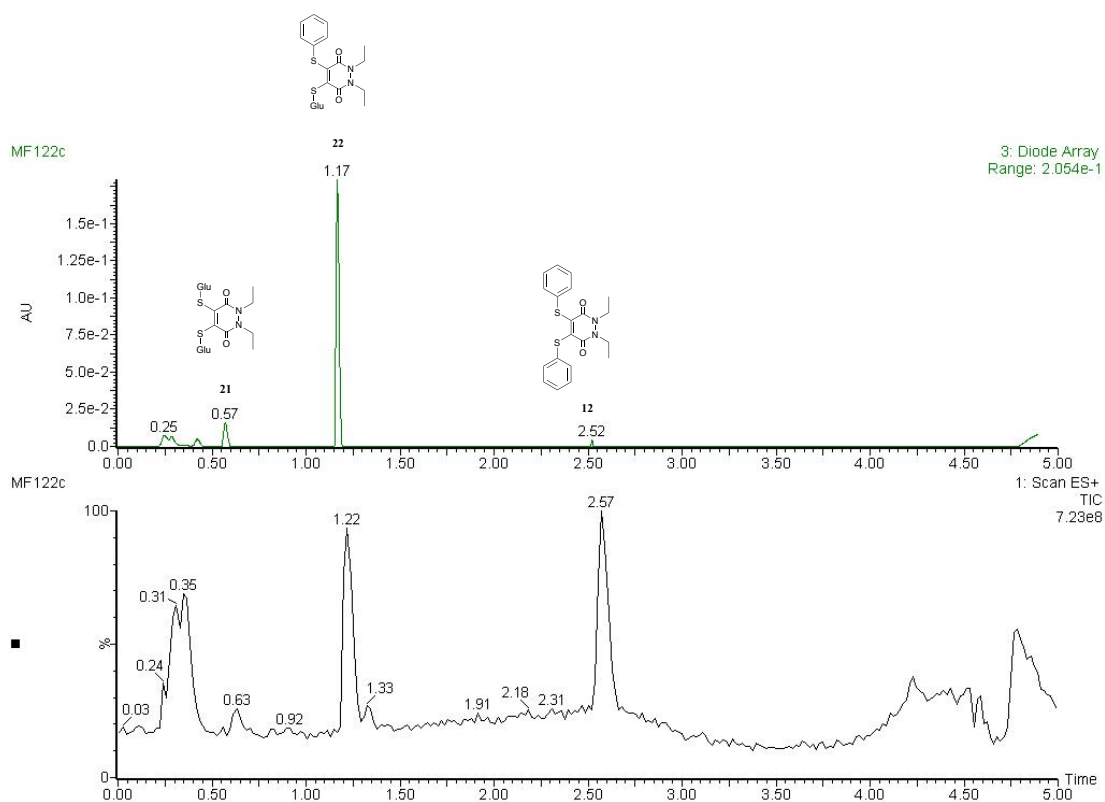


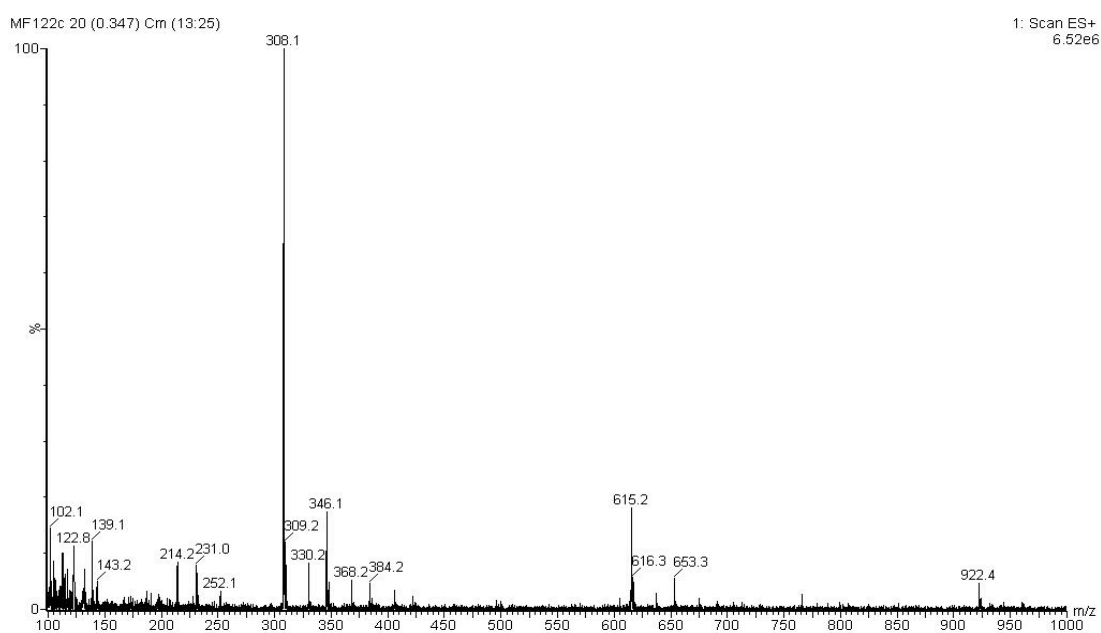
Figure S50. (a) TIC and UV trace at  $t = 1$  h, (b) MS data at 0.25–0.42 mins in the UV, (c) MS data at 0.57 mins in the UV, (d) at 1.17 mins in the UV and (e) at 2.52 mins in the UV for PD **12** incubated with GluSH **19** (10 eq.) at pH 5.0.

# LC-MS data for t = 2 h

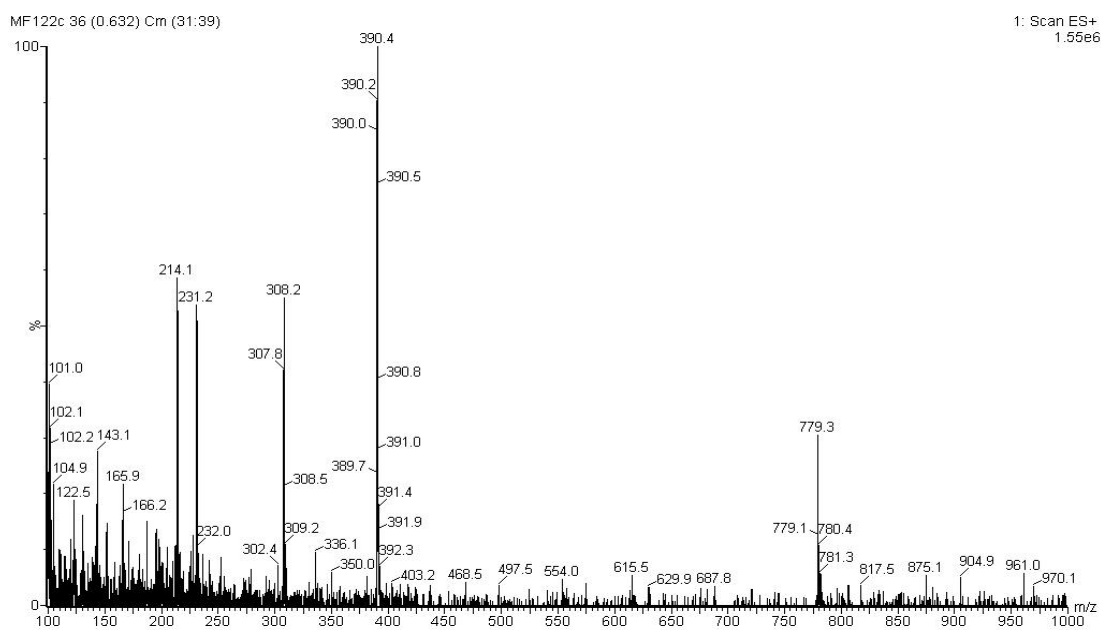
(a)



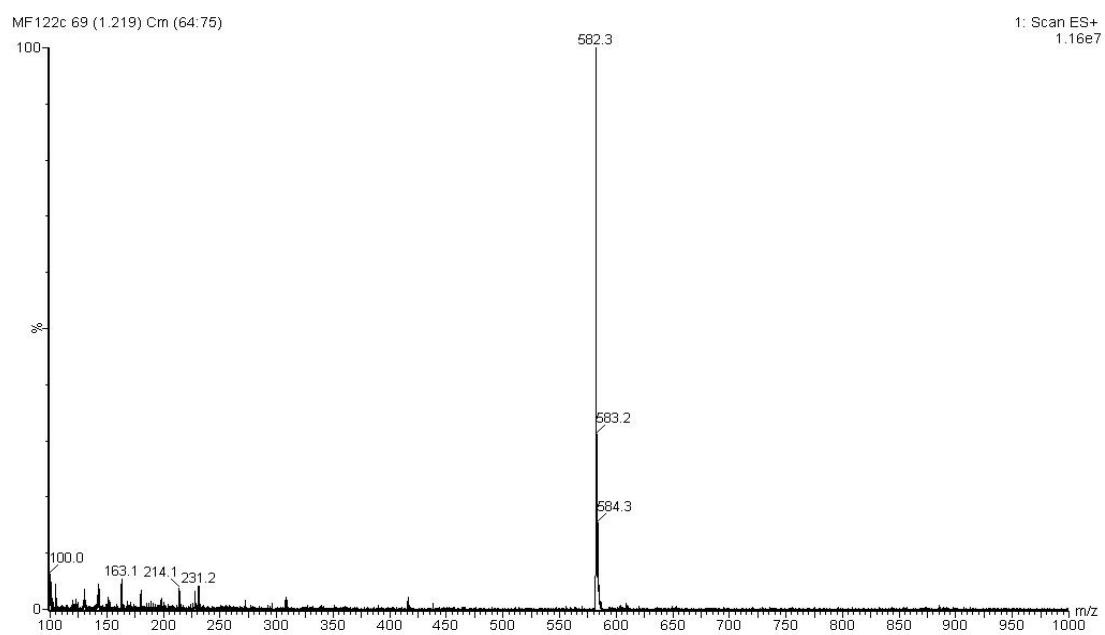
(b)



(c)



(d)



(e)

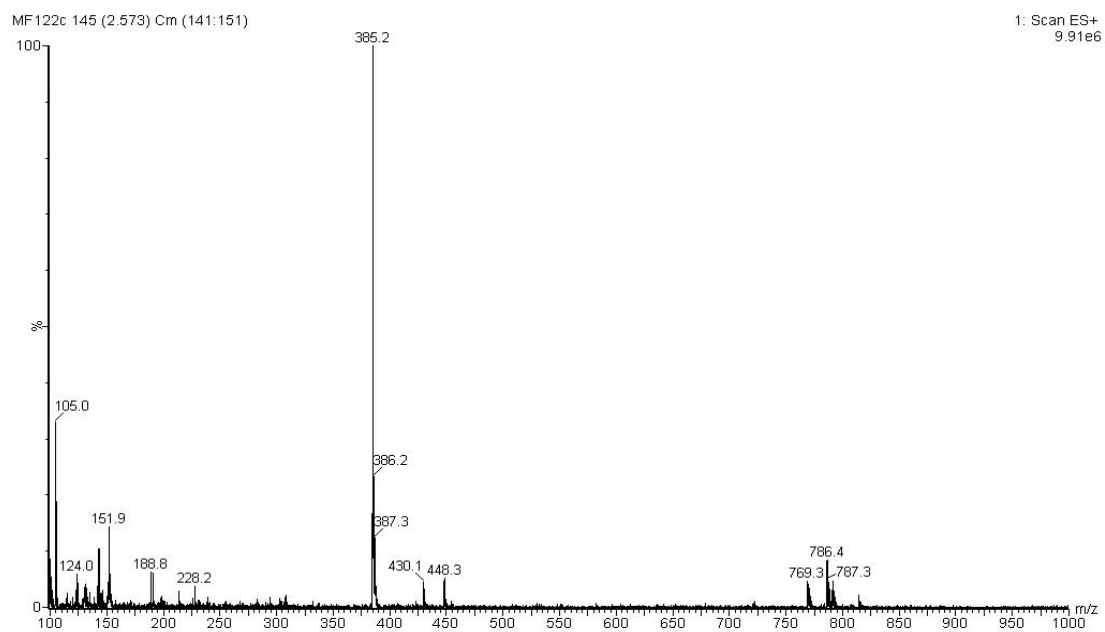
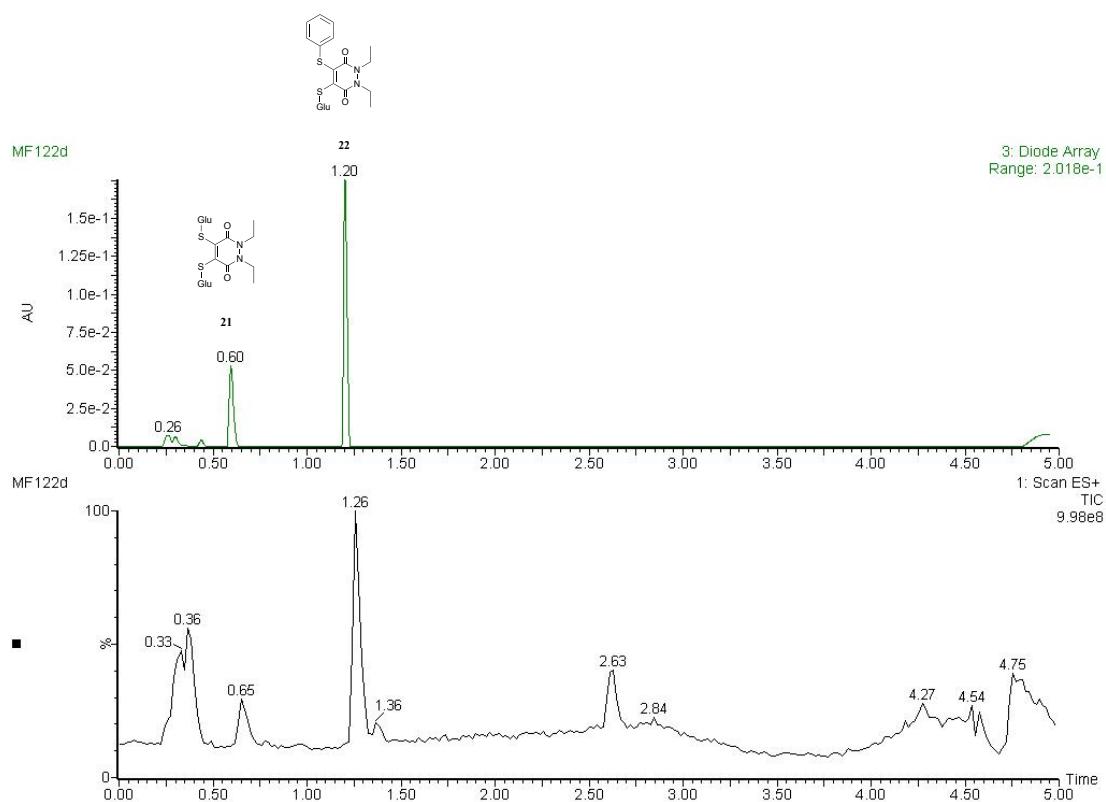


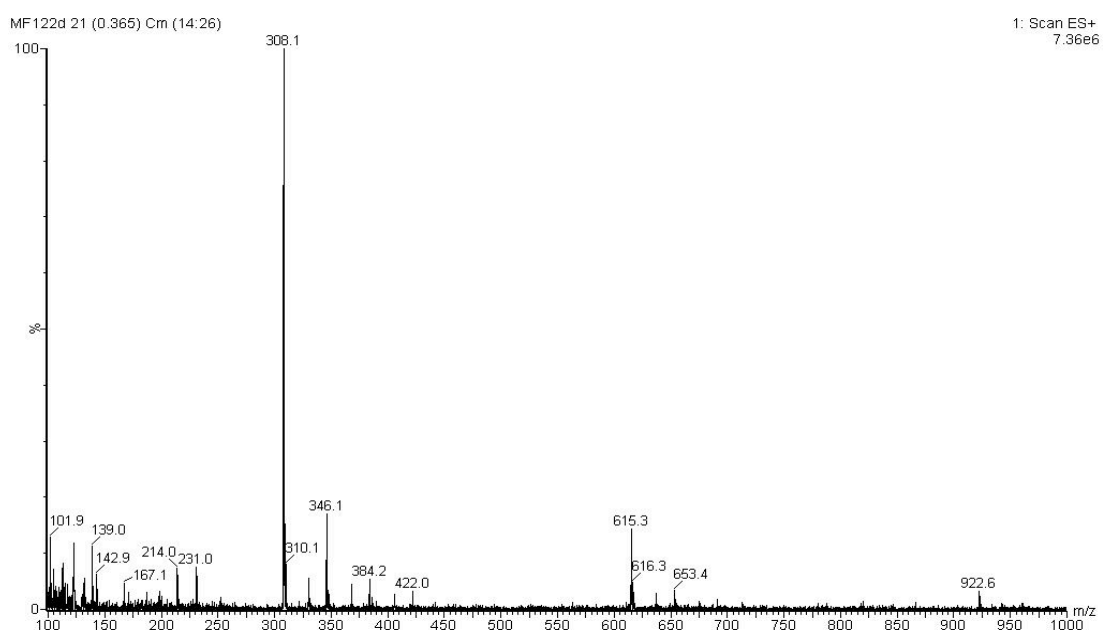
Figure S51. (a) TIC and UV trace at  $t = 2$  h, (b) MS data at 0.25–0.42 mins in the UV, (c) MS data at 0.57 mins in the UV, (d) at 1.17 mins in the UV and (e) at 2.52 mins in the UV for PD **12** incubated with GluSH **19** (10 eq.) at pH 5.0.

# LC-MS data for t = 4 h

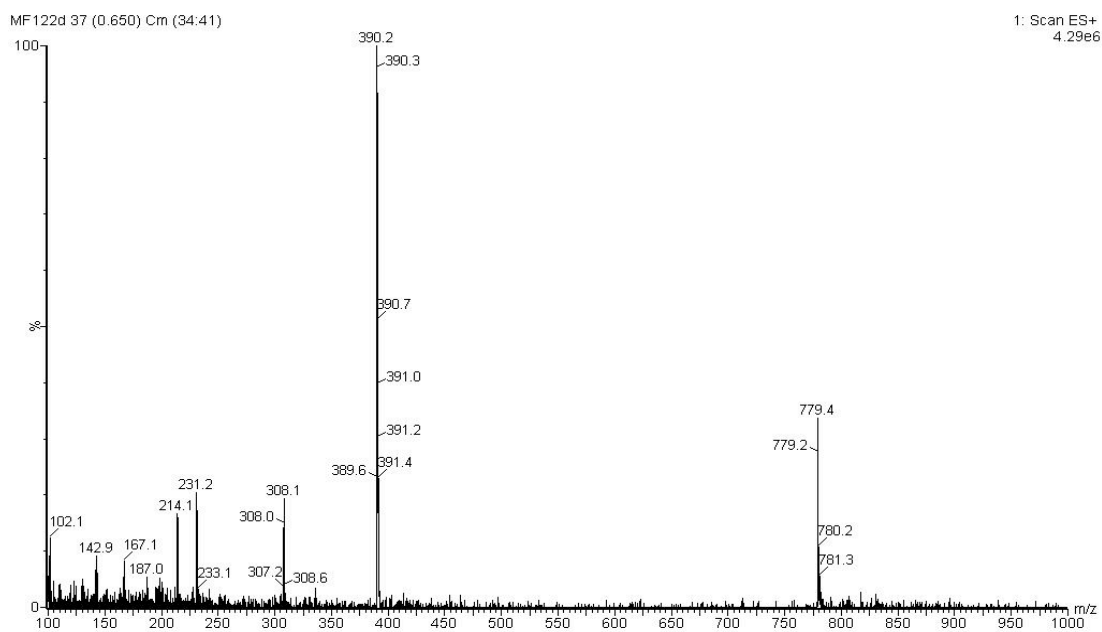
(a)



(b)



(c)



(d)

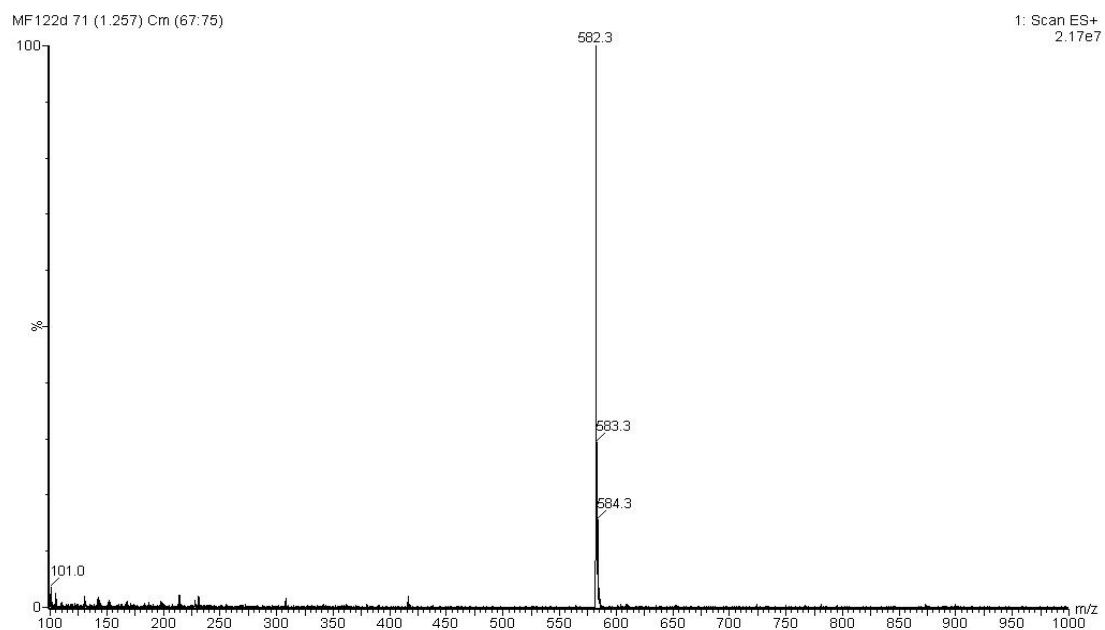
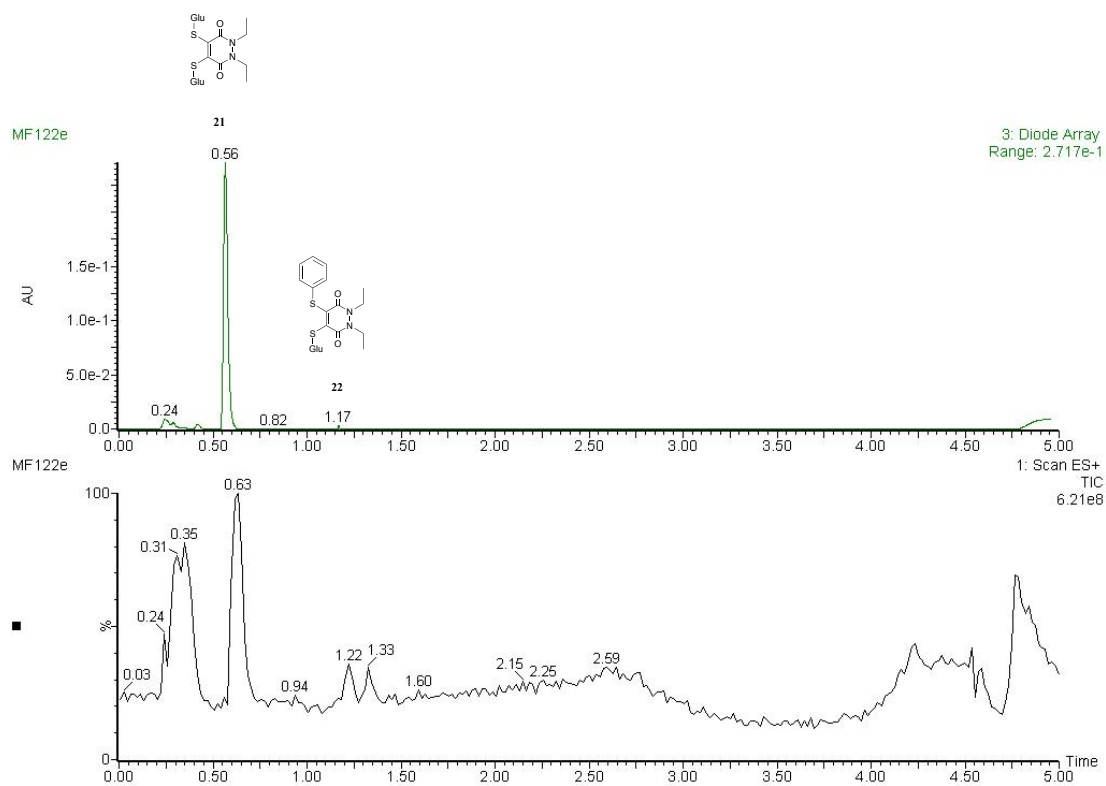


Figure S52. (a) TIC and UV trace at  $t = 4$  h, (b) MS data at 0.26–0.42 mins in the UV, (c) MS data at 0.60 mins in the UV and (d) at 1.20 mins in the UV for PD **12** incubated with GluSH **19** (10 eq.) at pH 5.0.

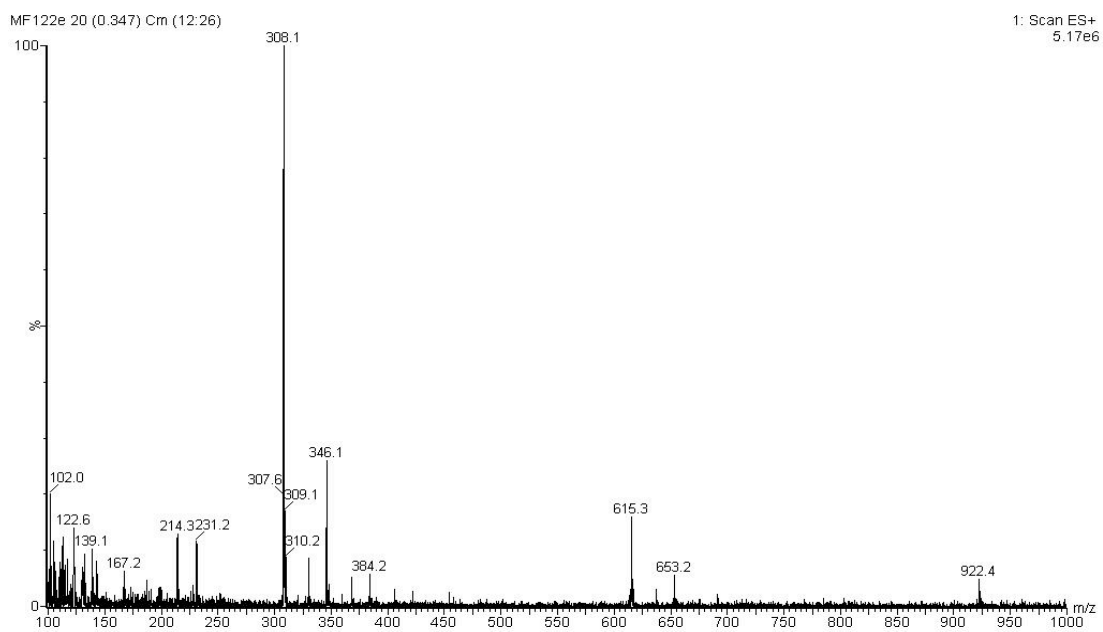


# LC-MS data for t = 24 h

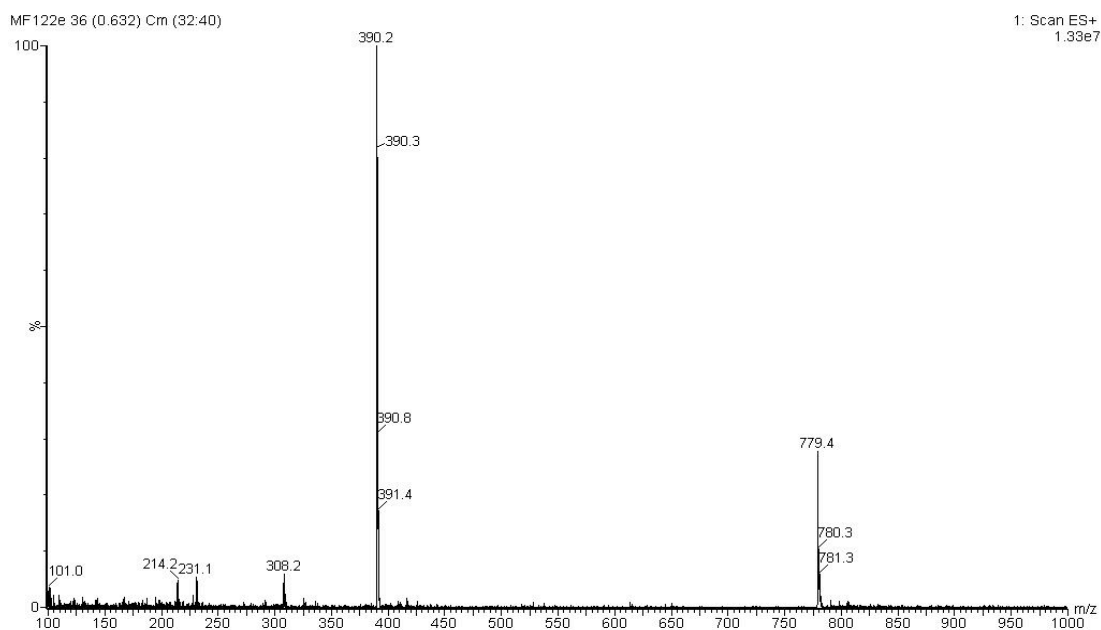
(a)



(b)



(c)



(d)

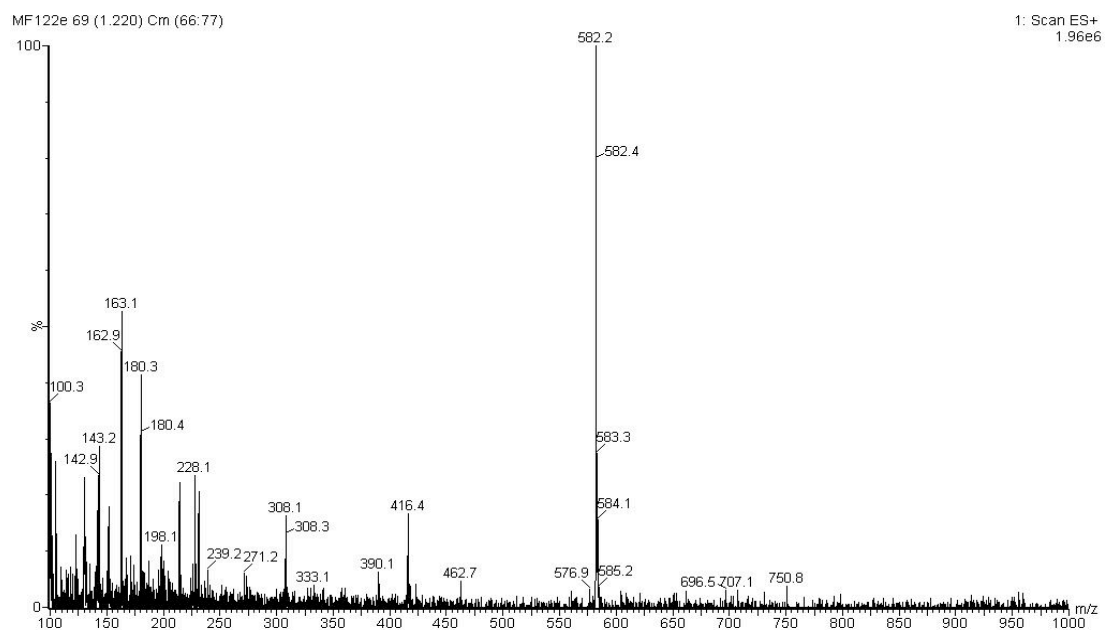
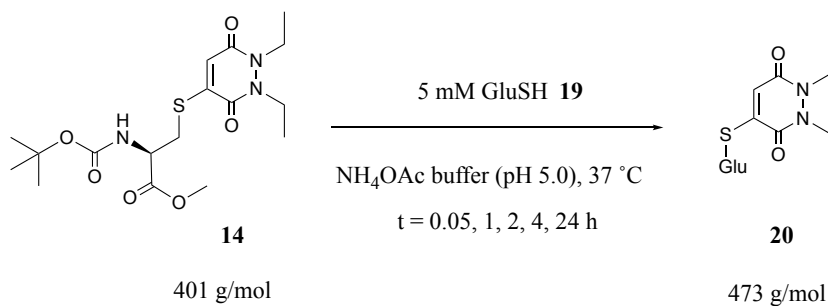


Figure S53. (a) TIC and UV trace at  $t = 24$  h, (b) MS data at 0.24–0.42 mins in the UV, (c) MS data at 0.56 mins in the UV and (d) at 1.17 mins in the UV for PD 12 incubated with GluSH 19 (10 eq.) at pH 5.0.

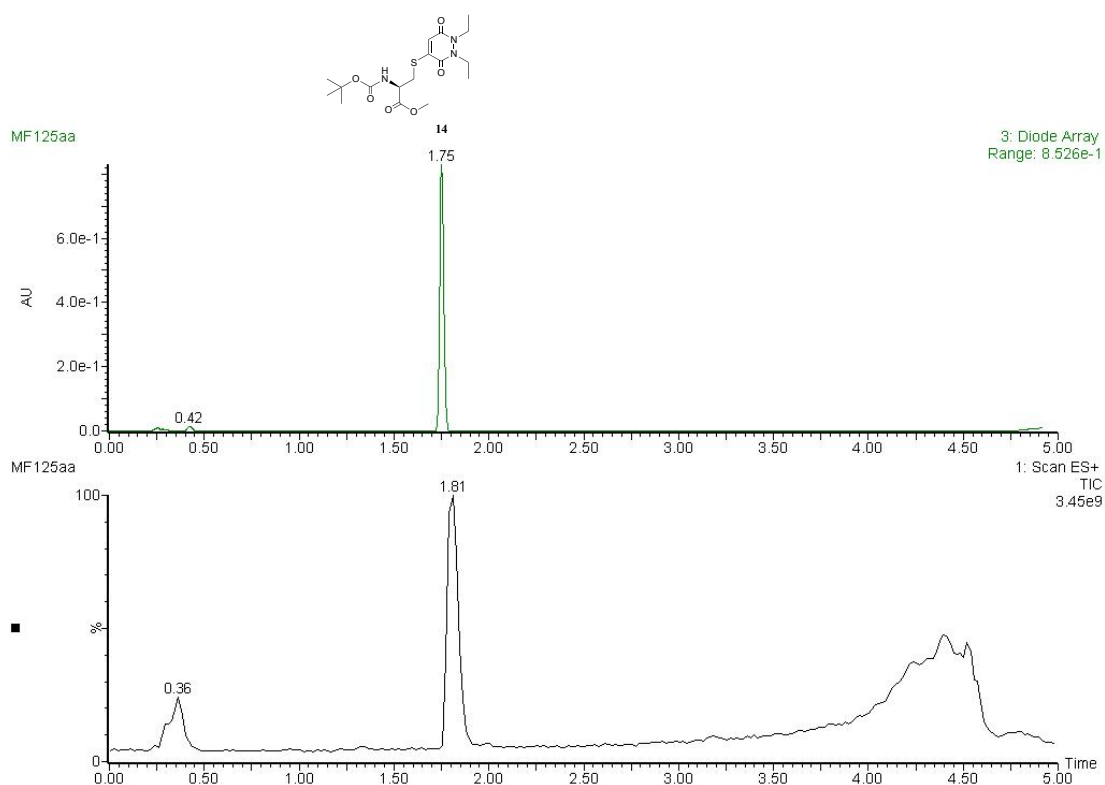
## Incubation of pyridazinedione **14** with GluSH (**10 eq.**)



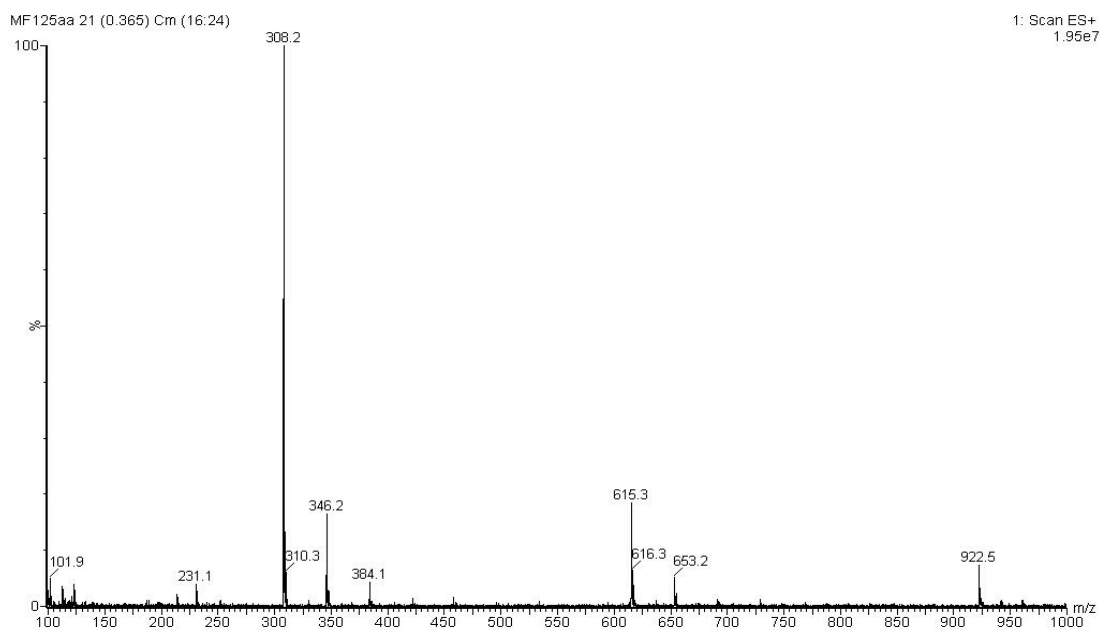
Pyridazinedione **14** (10  $\mu\text{L}$ , 10 mM in MeCN, 1 eq.) was added to GluSH **19** (190  $\mu\text{L}$ , 5.3 mM, 10 eq.) in ammonium acetate buffer (50 mM, pH 5.0). The mixture was incubated at 37  $^\circ\text{C}$  for 24 h. The samples were analysed by LC-MS at  $t = 0.05, 1, 2, 4$  and 24 h.

### LC-MS data for $t = 0.05 \text{ h}$

(a)



(b)



(c)

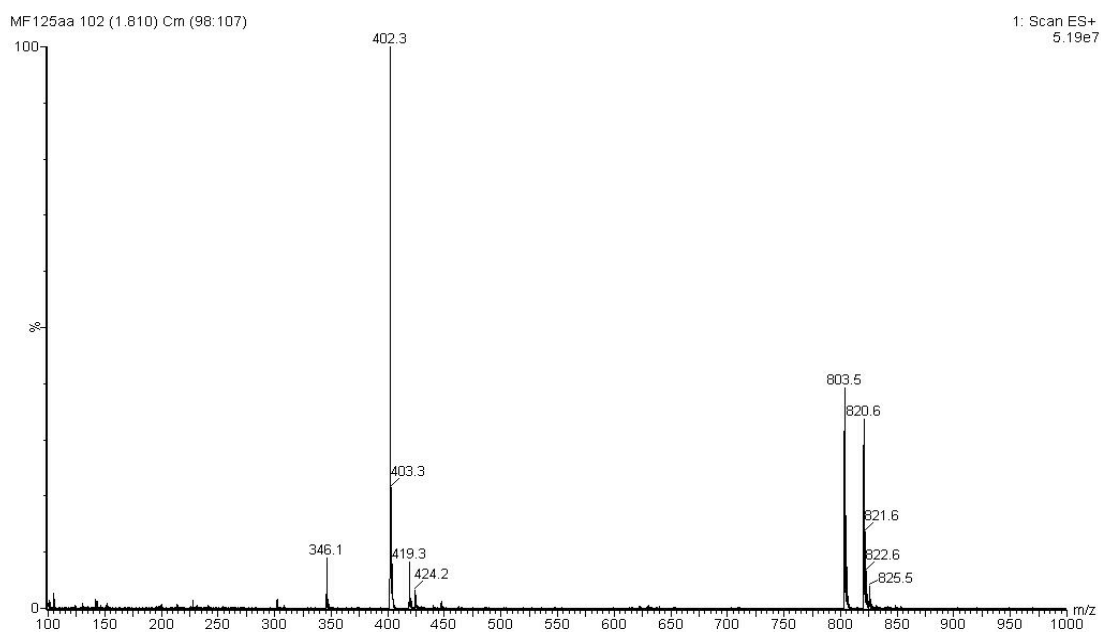
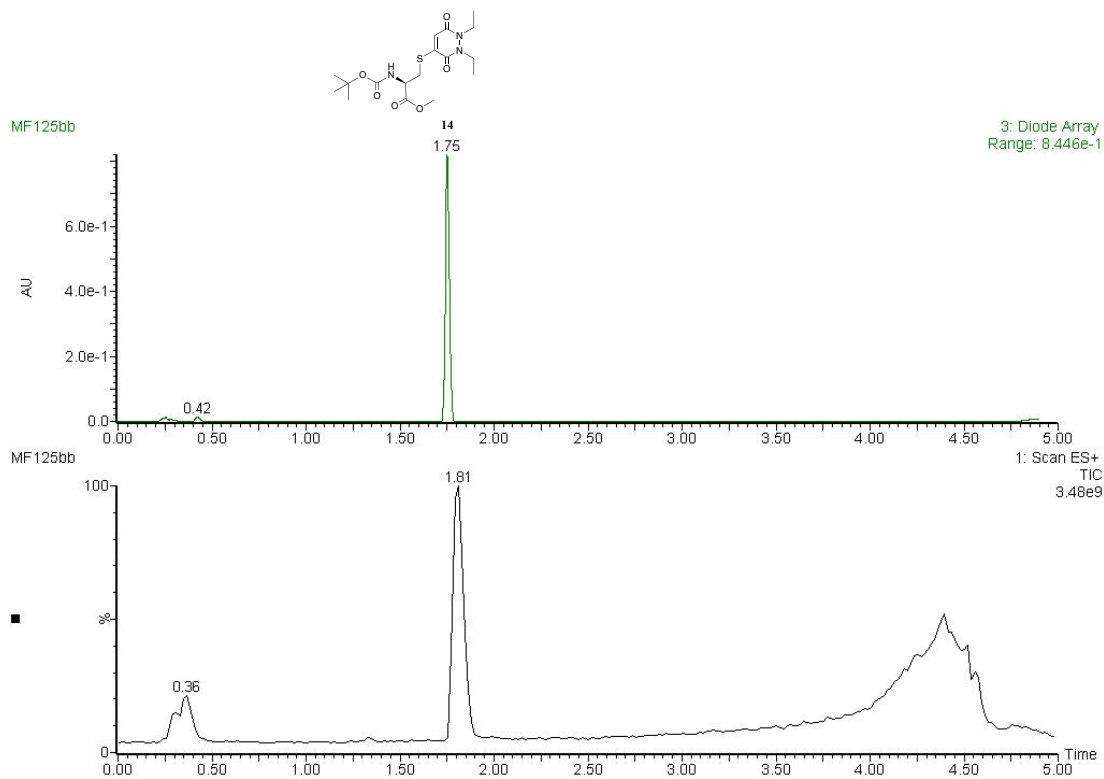


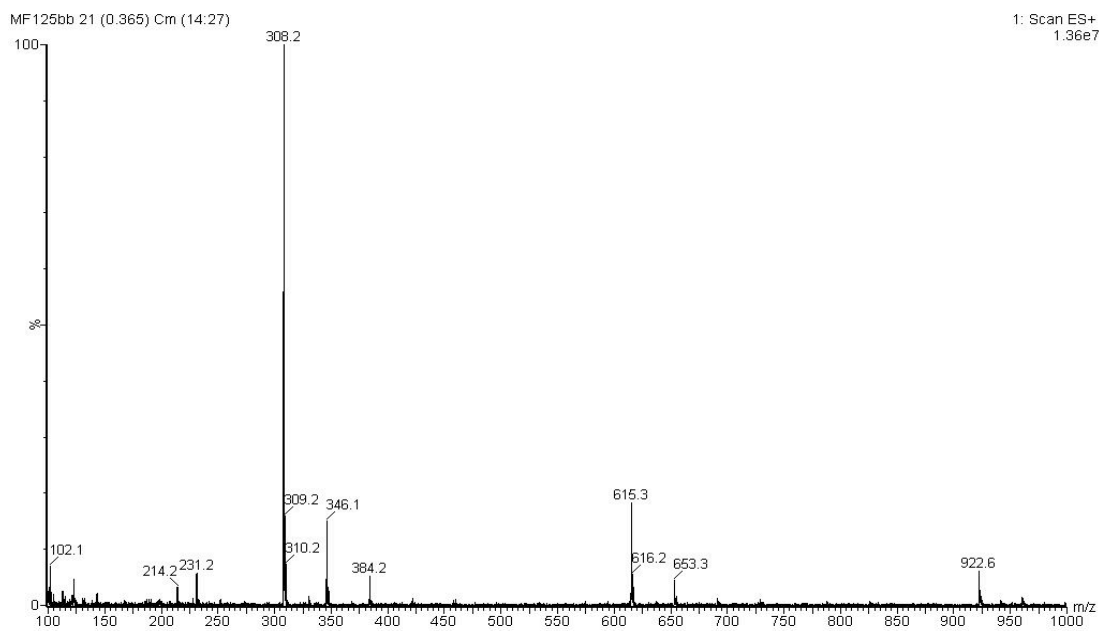
Figure S54. (a) TIC and UV trace at  $t = 0.05$  h, (b) MS data at 0.24–0.42 mins in the UV, and (c) MS data at 1.75 mins in the UV for PD 14 incubated with GluSH 19 (10 eq.) at pH 5.0.

# LC-MS data for t = 1 h

(a)



(b)



(c)

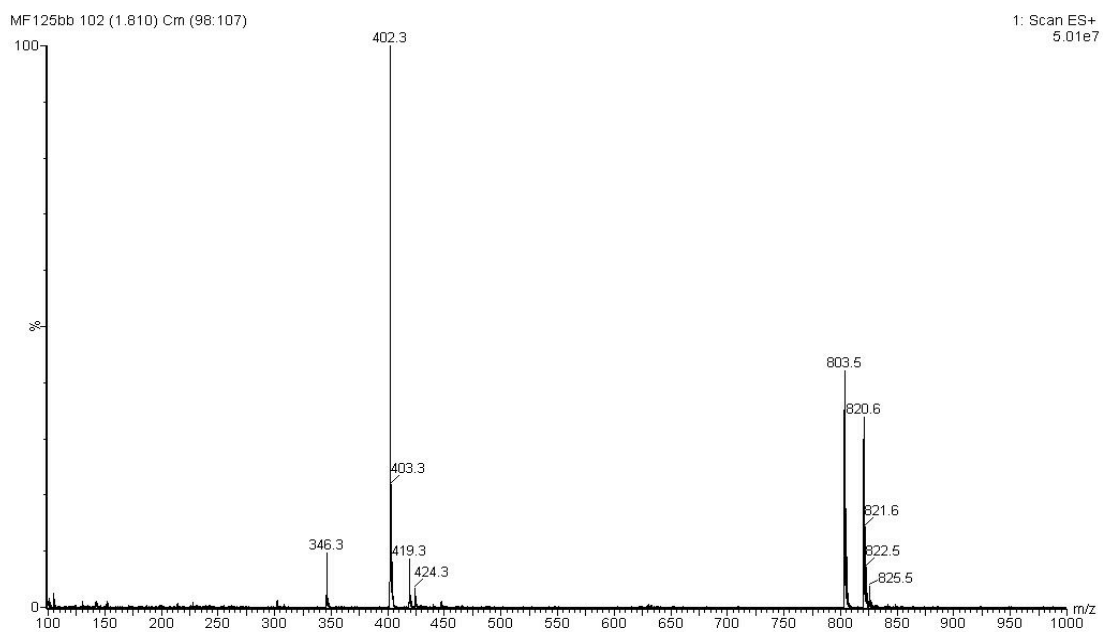
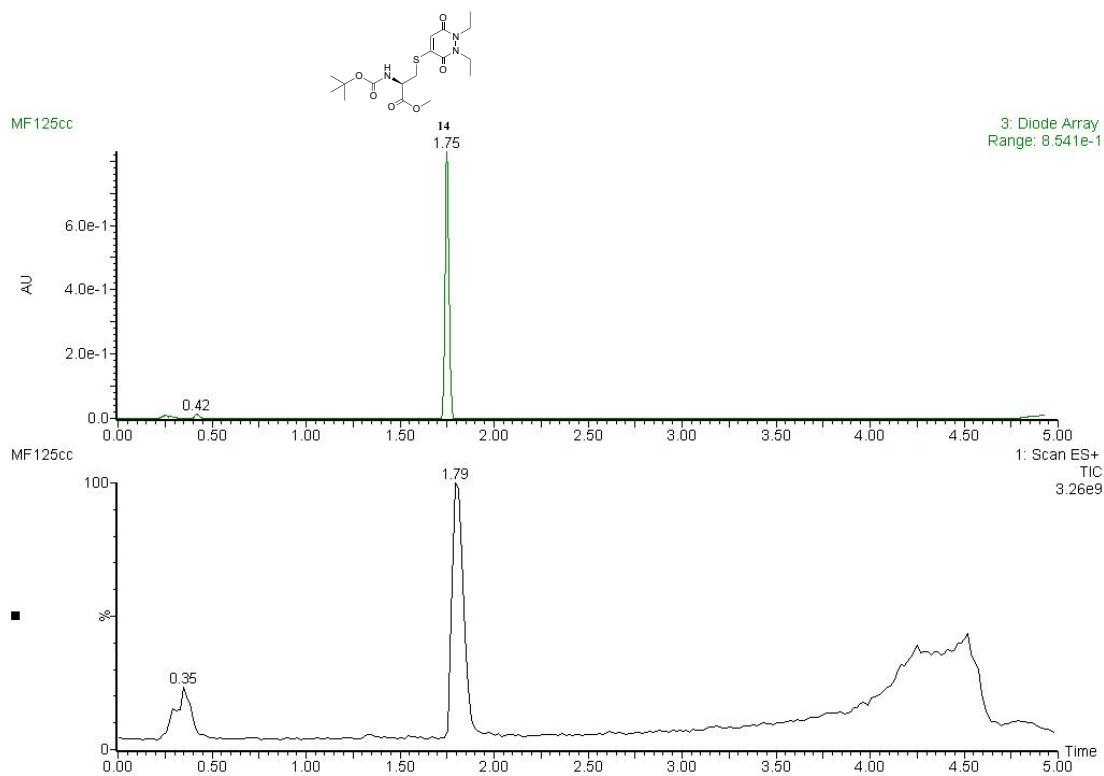


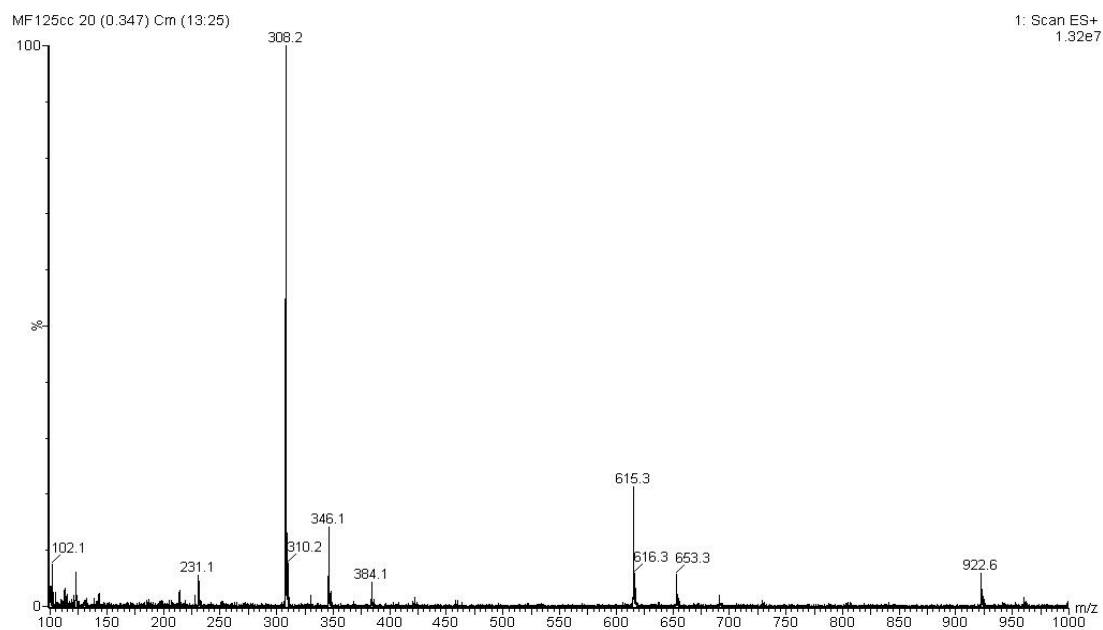
Figure S55. (a) TIC and UV trace at  $t = 1$  h, (b) MS data at 0.24–0.42 mins in the UV, and (c) MS data at 1.75 mins in the UV for PD **14** incubated with GluSH **19** (10 eq.) at pH 5.0.

# LC-MS data for t = 2 h

(a)



(b)



(c)

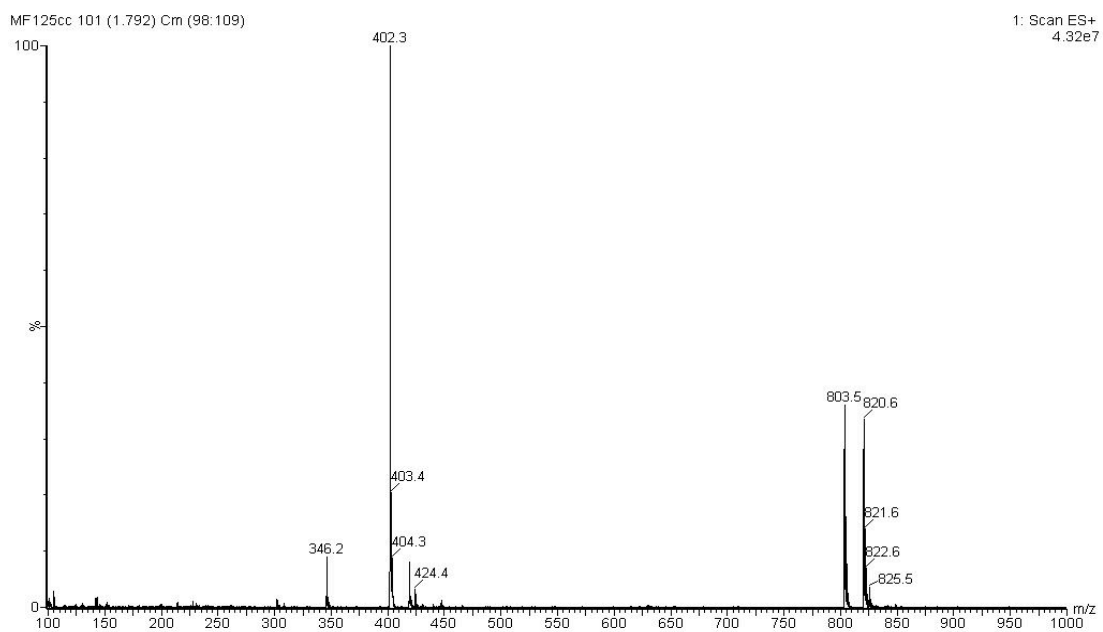
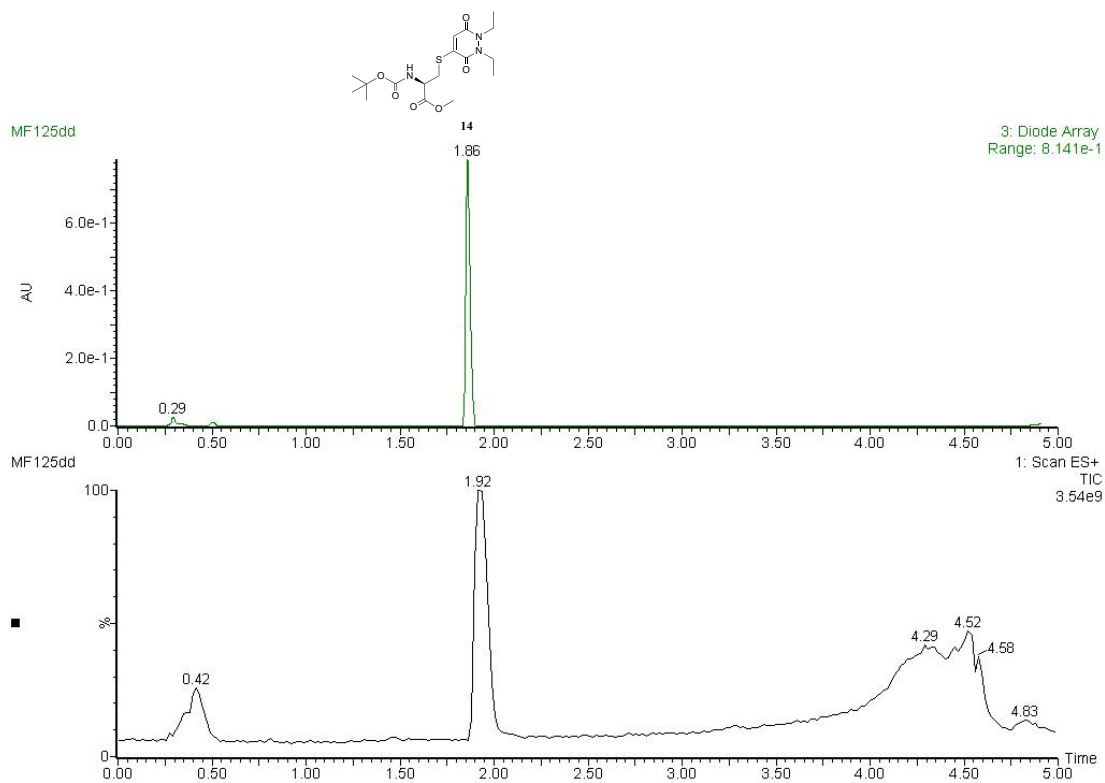


Figure S56. (a) TIC and UV trace at  $t = 2$  h, (b) MS data at 0.24–0.42 mins in the UV, and (c) MS data at 1.75 mins in the UV for PD **14** incubated with GluSH **19** (10 eq.) at pH 5.0.

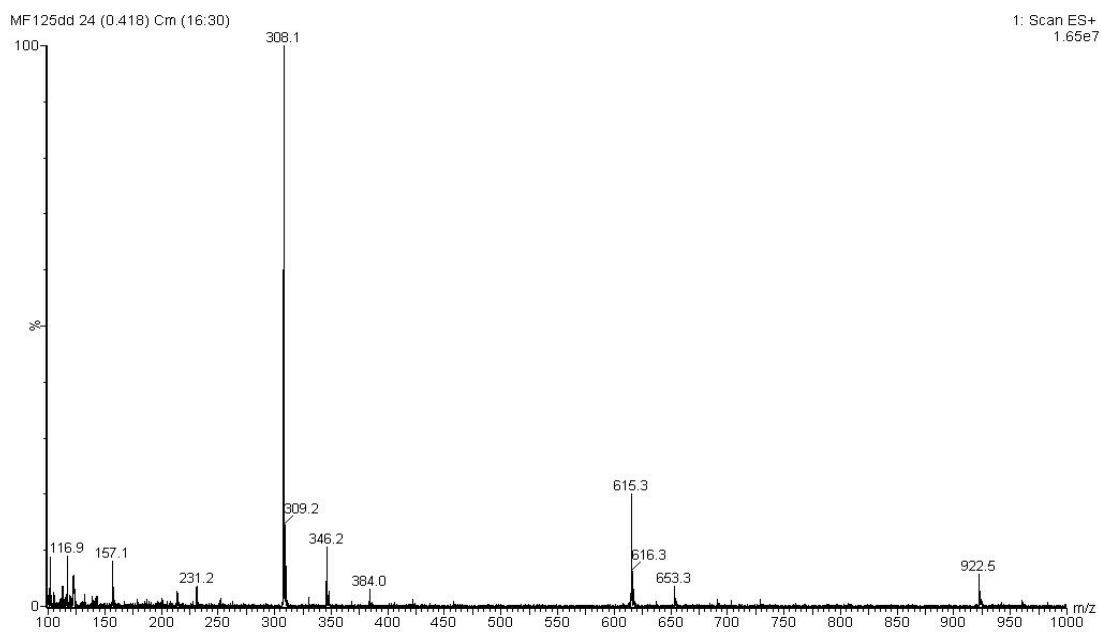


# LC-MS data for t = 4 h

(a)



(b)



(c)

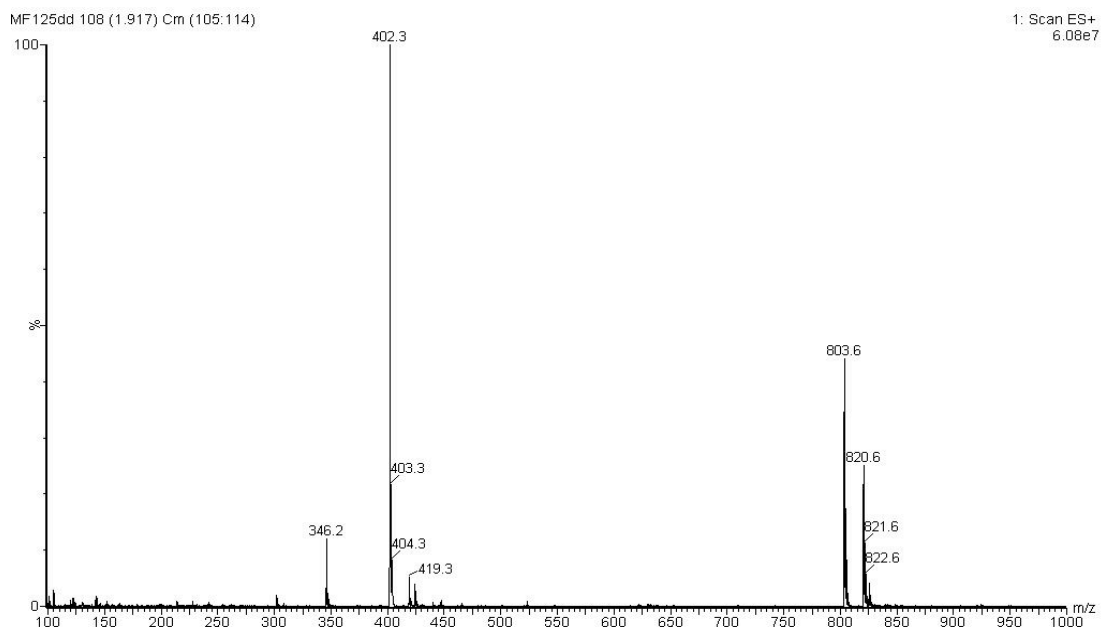
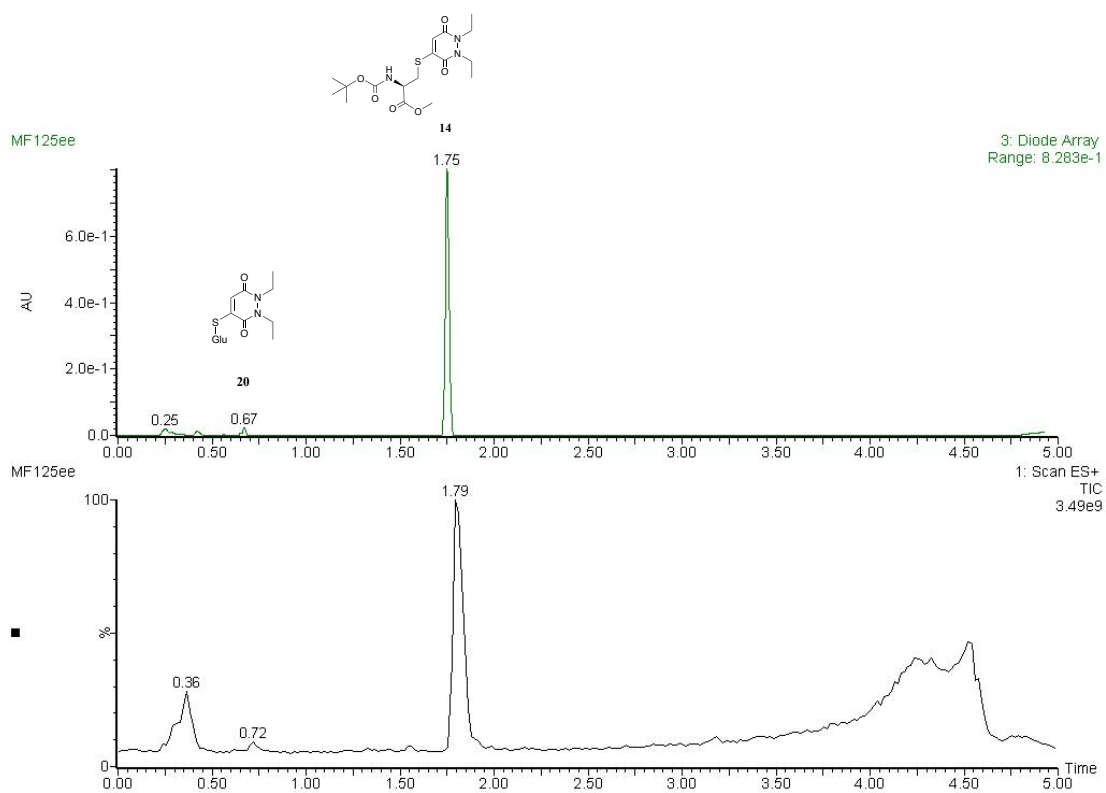


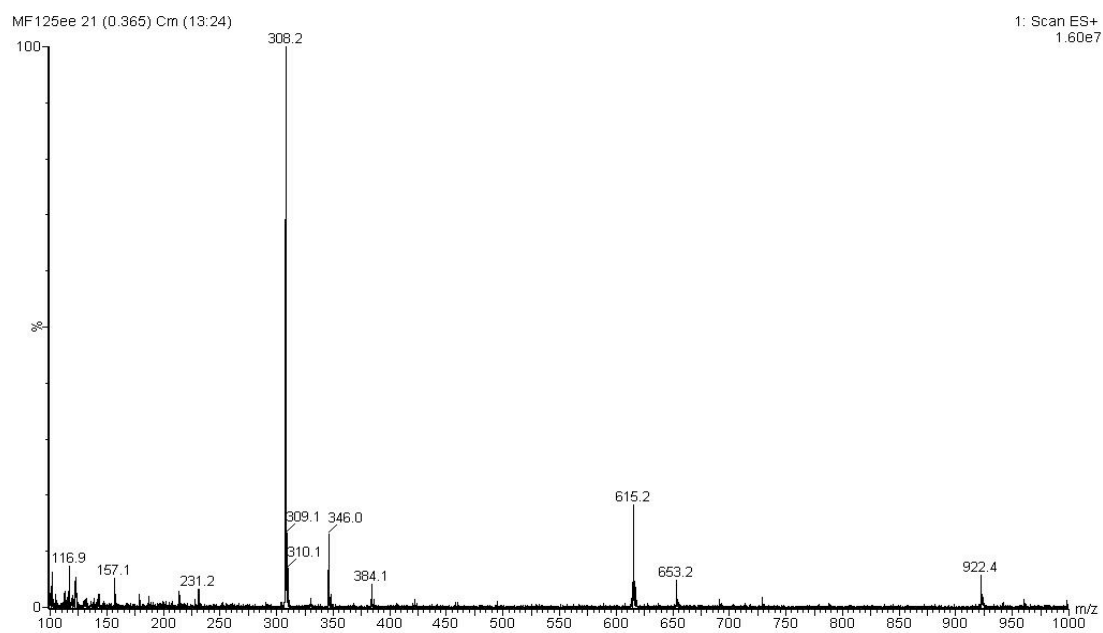
Figure S57. (a) TIC and UV trace at  $t = 4$  h, (b) MS data at 0.29–0.42 mins in the UV and (c) MS data at 1.86 mins in the UV for PD 14 incubated with GluSH 19 (10 eq.) at pH 5.0.

# LC-MS data for t = 24 h

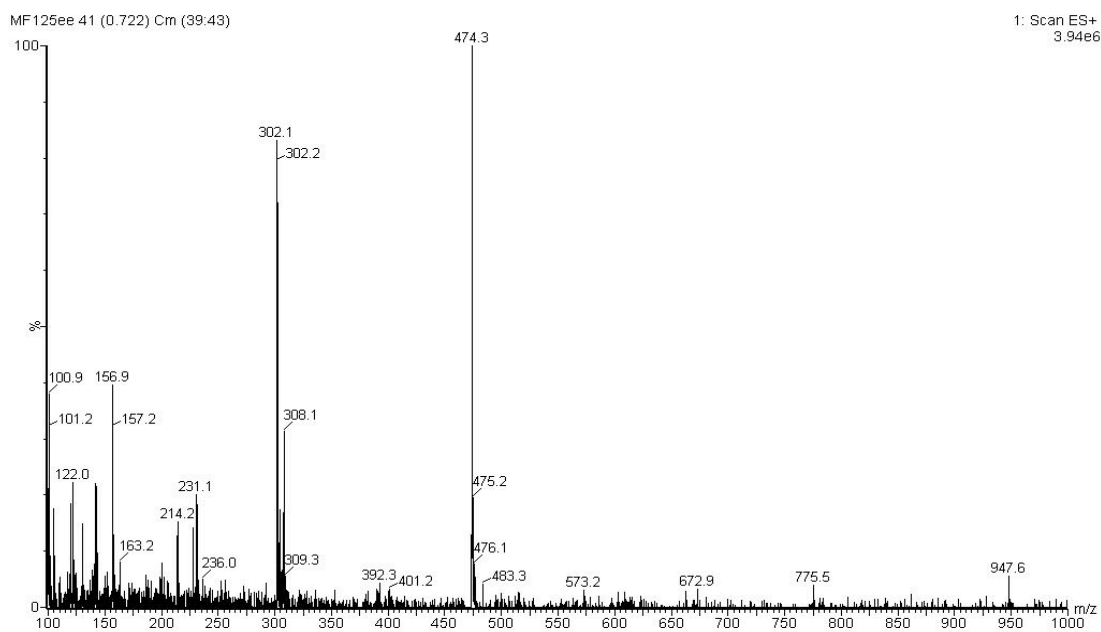
(a)



(b)



(c)



(d)

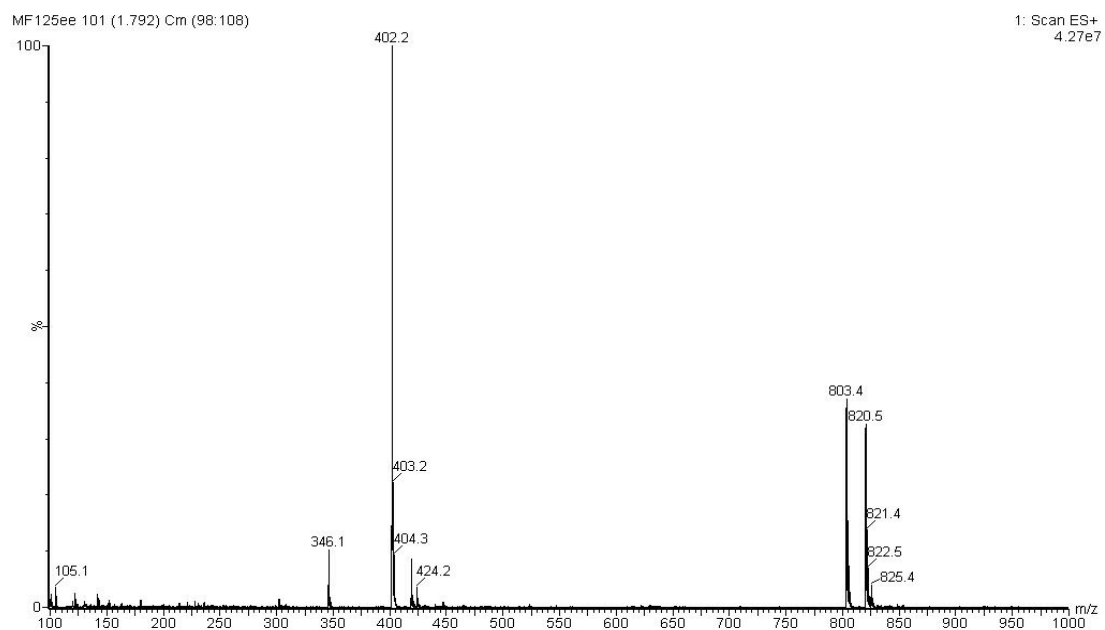
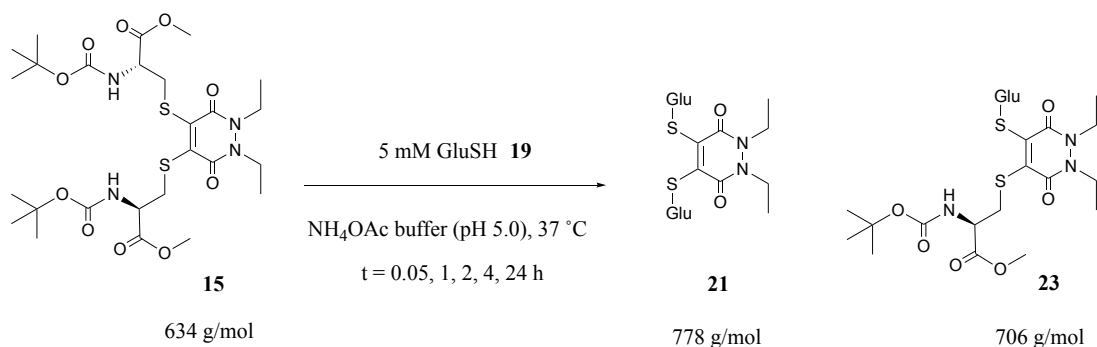


Figure S58. (a) TIC and UV trace at  $t = 24$  h, (b) MS data at 0.25–0.42 mins in the UV, (c) MS data at 0.67 mins in the UV and (d) at 1.75 mins in the UV for PD 14 incubated with GluSH 19 (10 eq.) at pH 5.0.

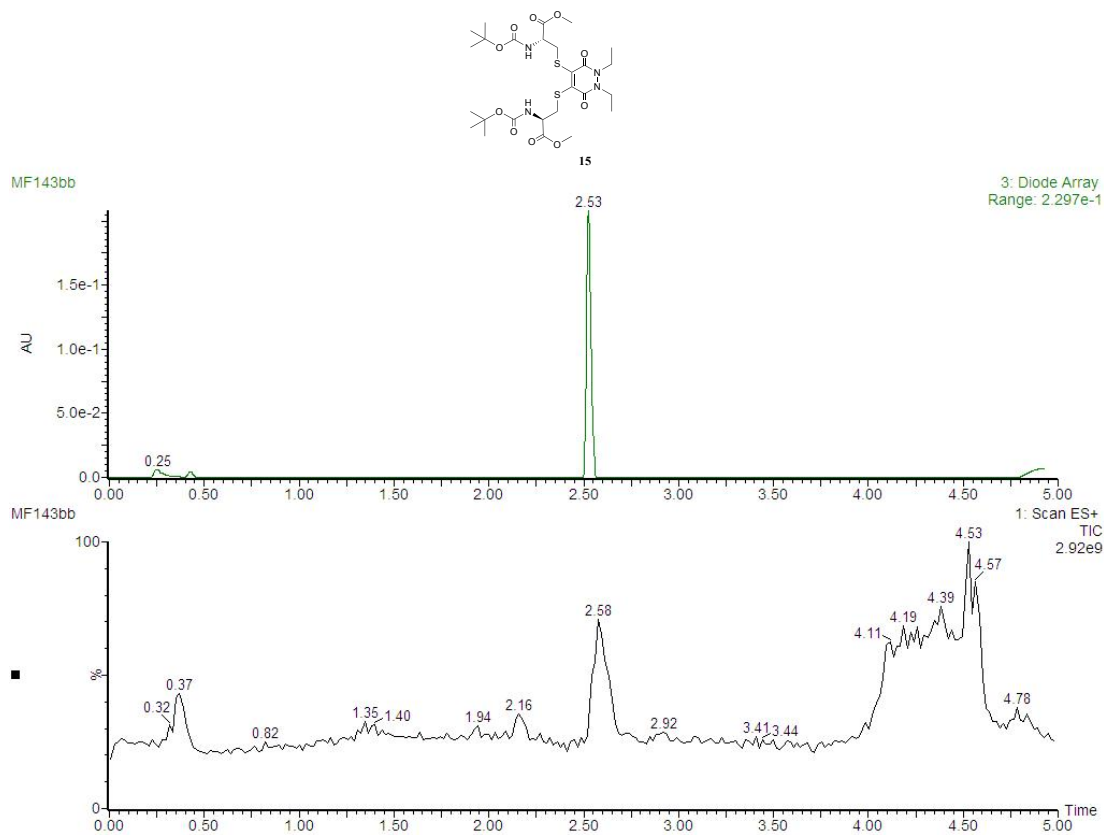
## Incubation of pyridazinedione **15** with GluSH (**10 eq.**)



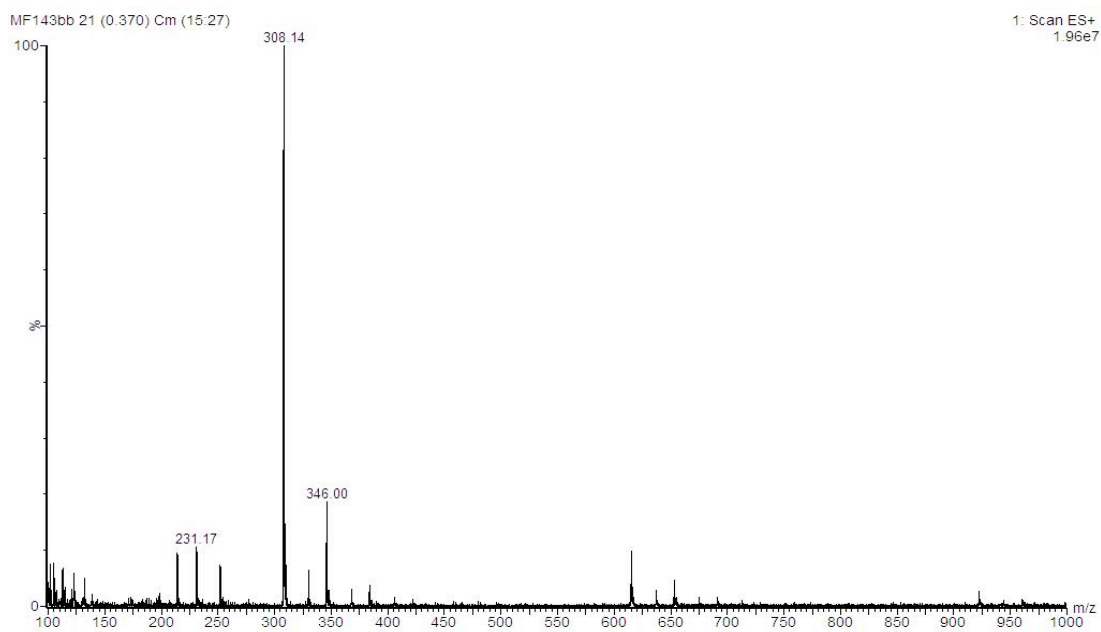
Pyridazinedione **15** (10  $\mu$ L, 10 mM in MeCN, 1 eq.) was added to GluSH **19** (190  $\mu$ L, 5.3 mM, 10 eq.) in ammonium acetate buffer (50 mM, pH 5.0). The mixture was incubated at 37 °C for 24 h. The samples were analysed by LC-MS at t = 0.05, 1, 2, 4 and 24 h.

### LC-MS data for t = 0.05 h

(a)



(b)



(c)

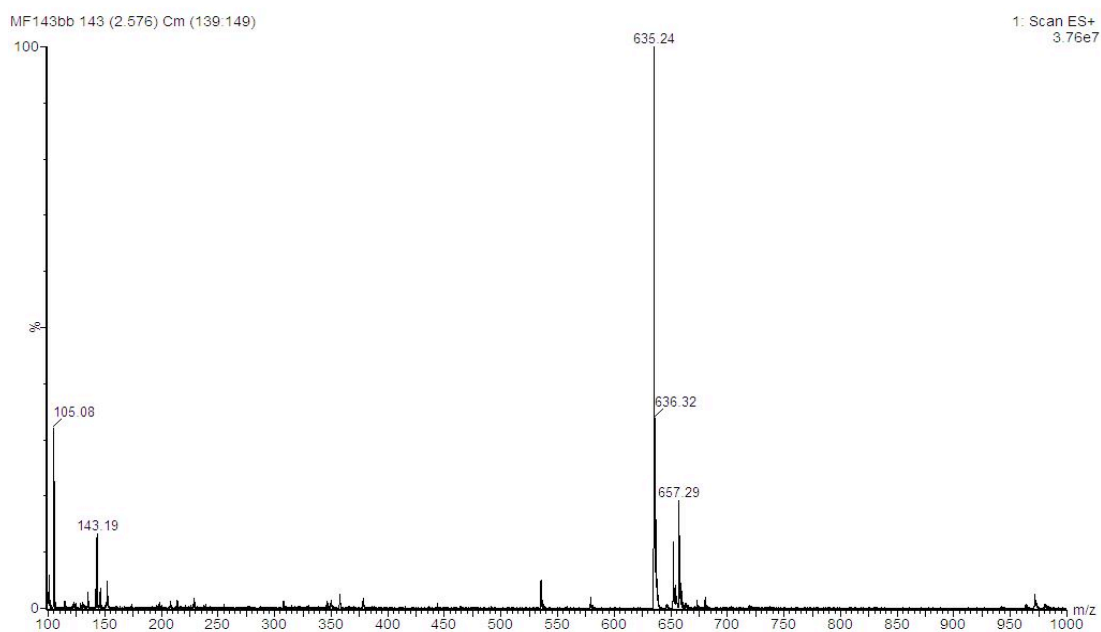
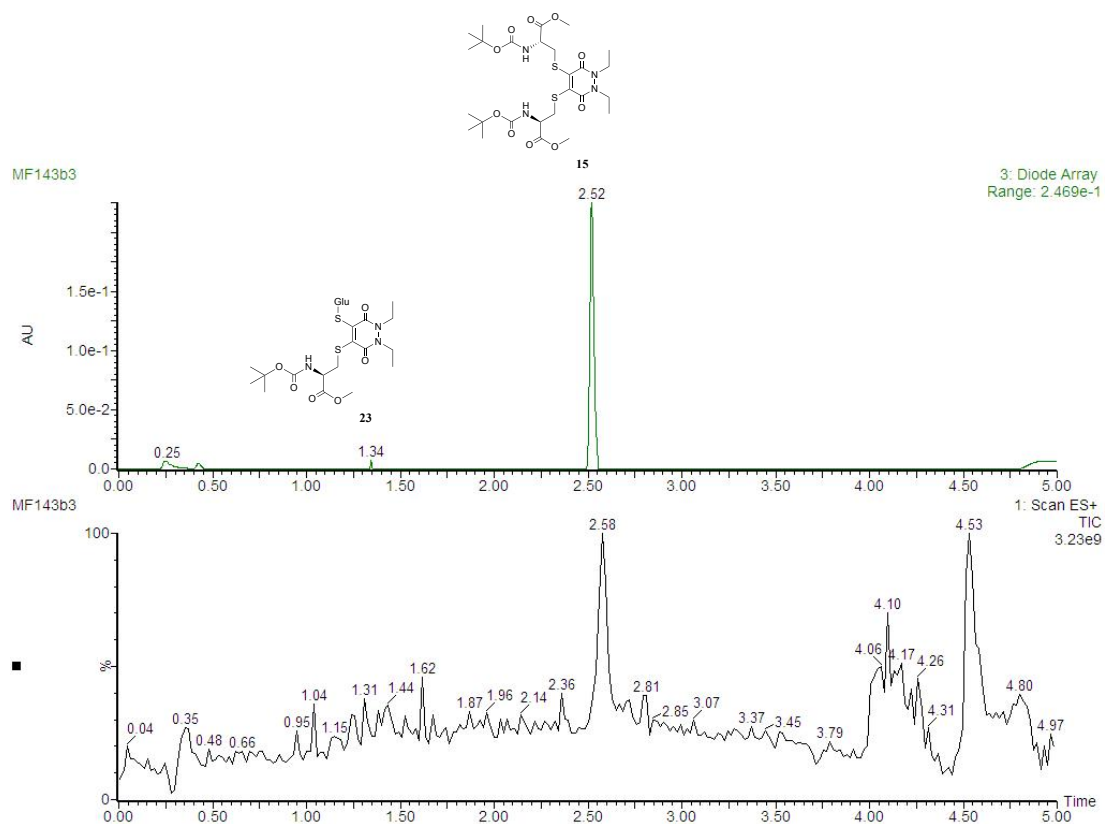


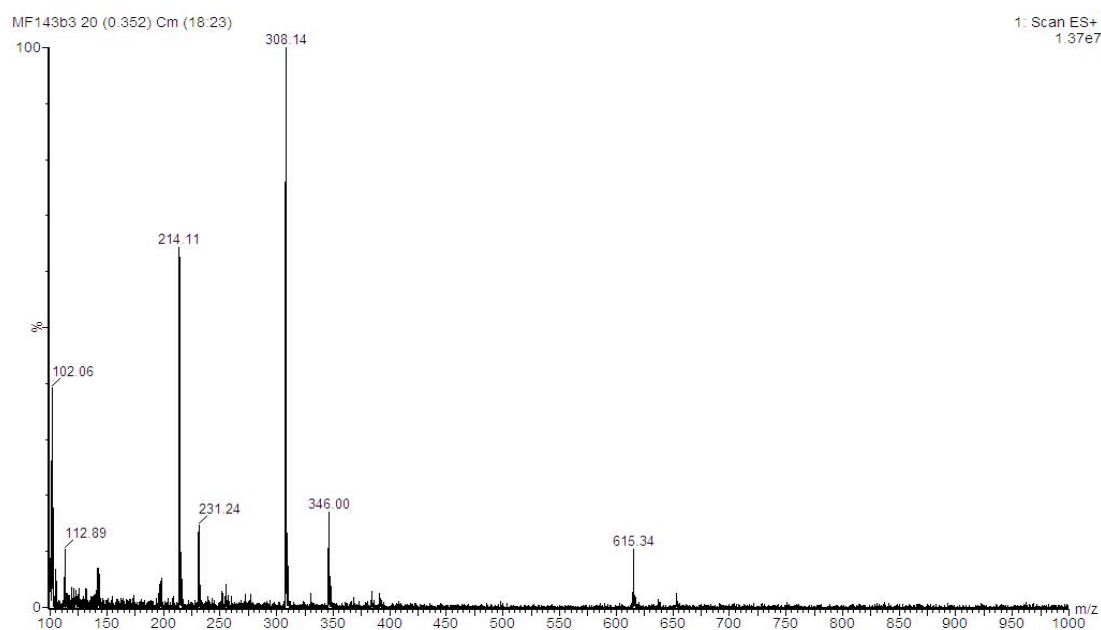
Figure S59. (a) TIC and UV trace at  $t = 0.05$  h, (b) MS data at 0.25–0.42 mins in the UV and (c) MS data at 2.53 mins in the UV for PD 15 incubated with GluSH 19 (10 eq.) at pH 5.0.

# LC-MS data for t = 1 h

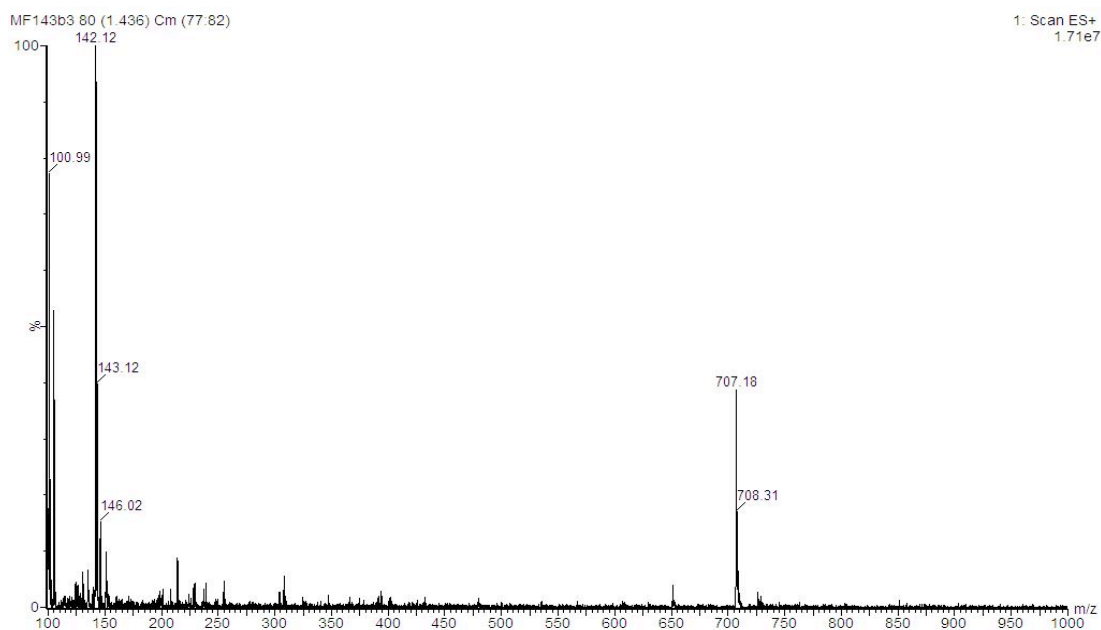
(a)



(b)



(c)



(d)

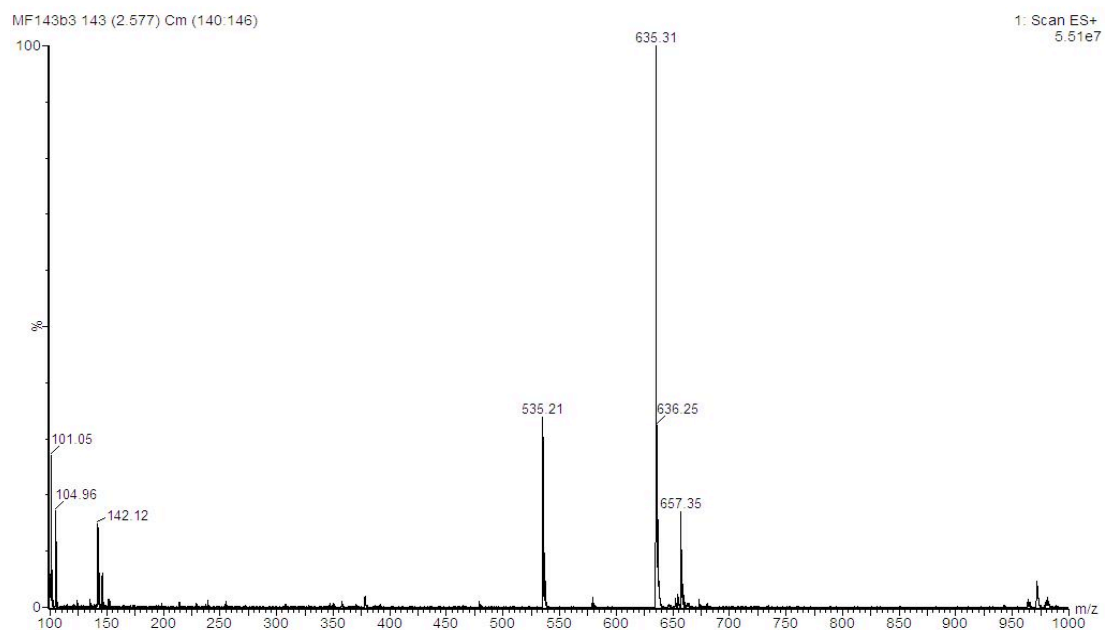
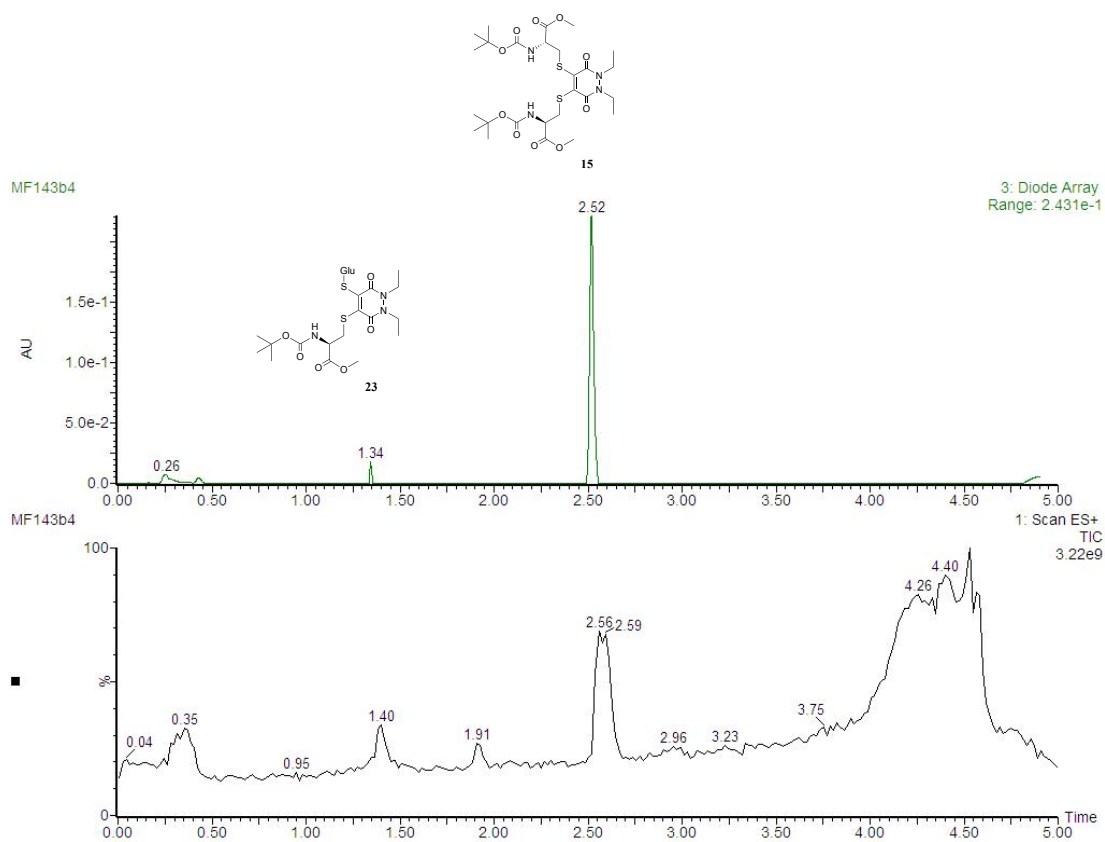


Figure S60. (a) TIC and UV trace at  $t = 1$  h, (b) MS data at 0.25–0.42 mins in the UV, (c) MS data at 1.34 mins in the UV and (d) at 2.52 mins in the UV for PD **15** incubated with GluSH **19** (10 eq.) at pH 5.0.

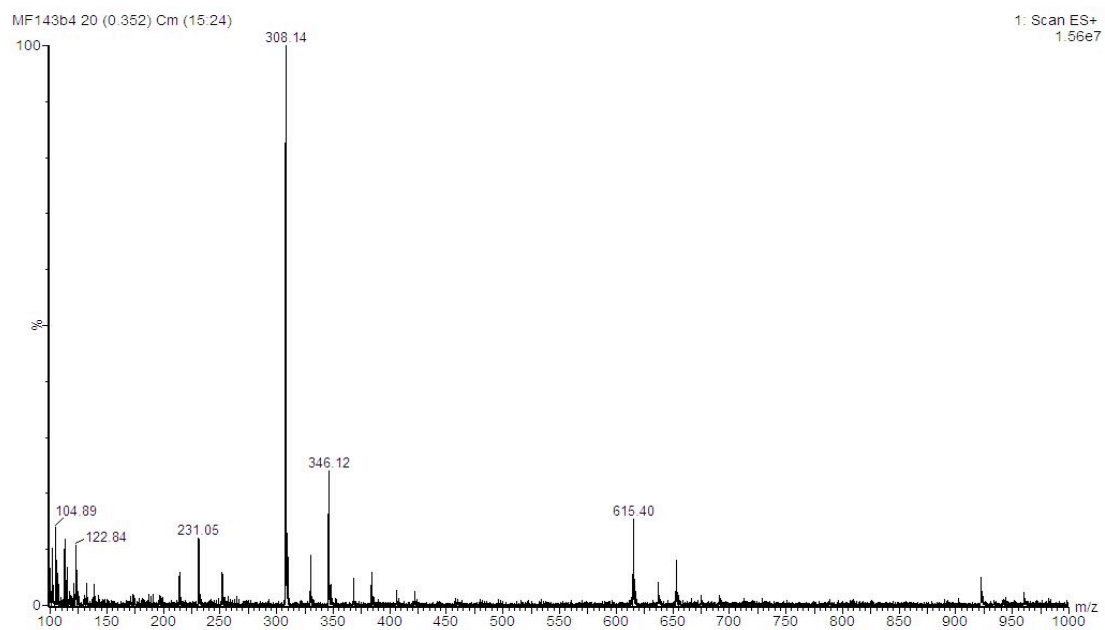


# LC-MS data for t = 2 h

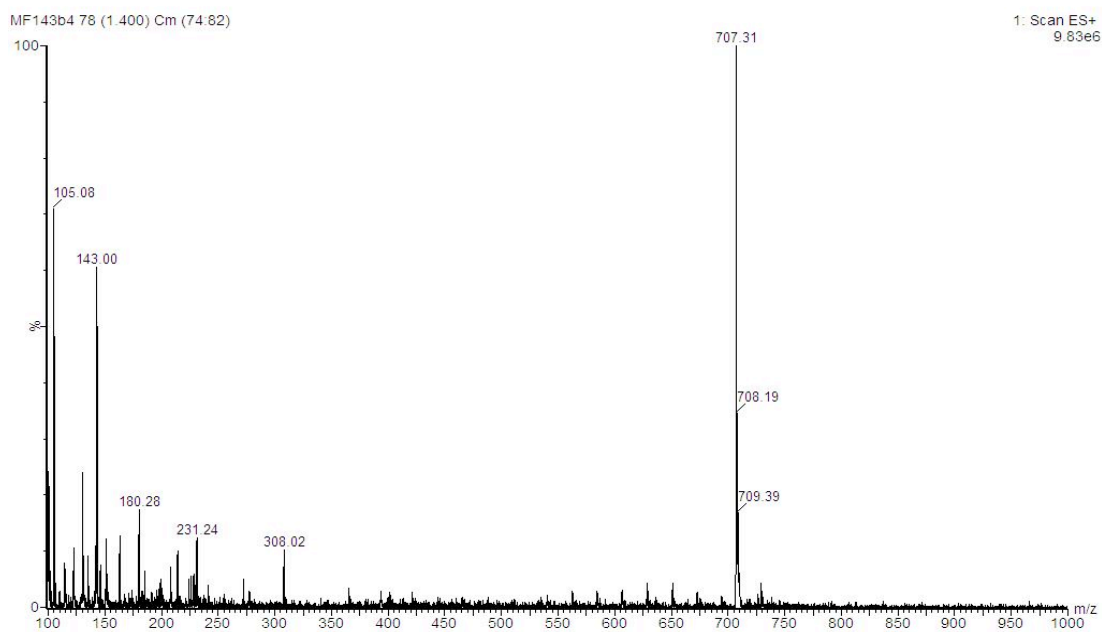
(a)



(b)



(c)



(d)

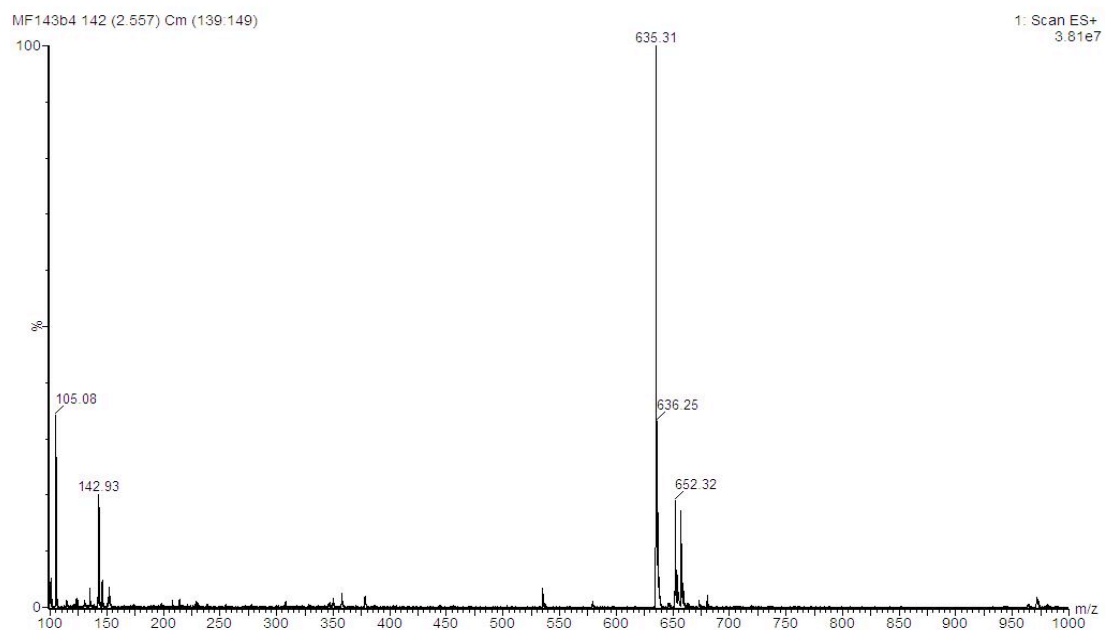
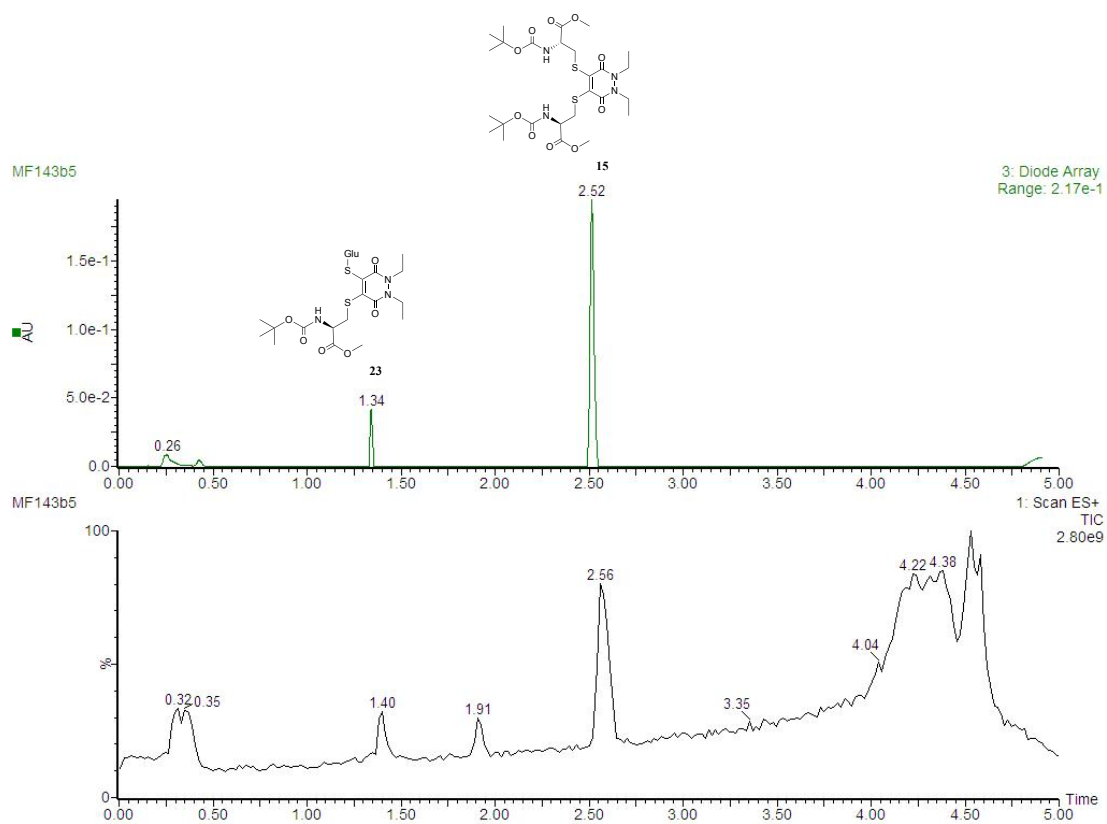


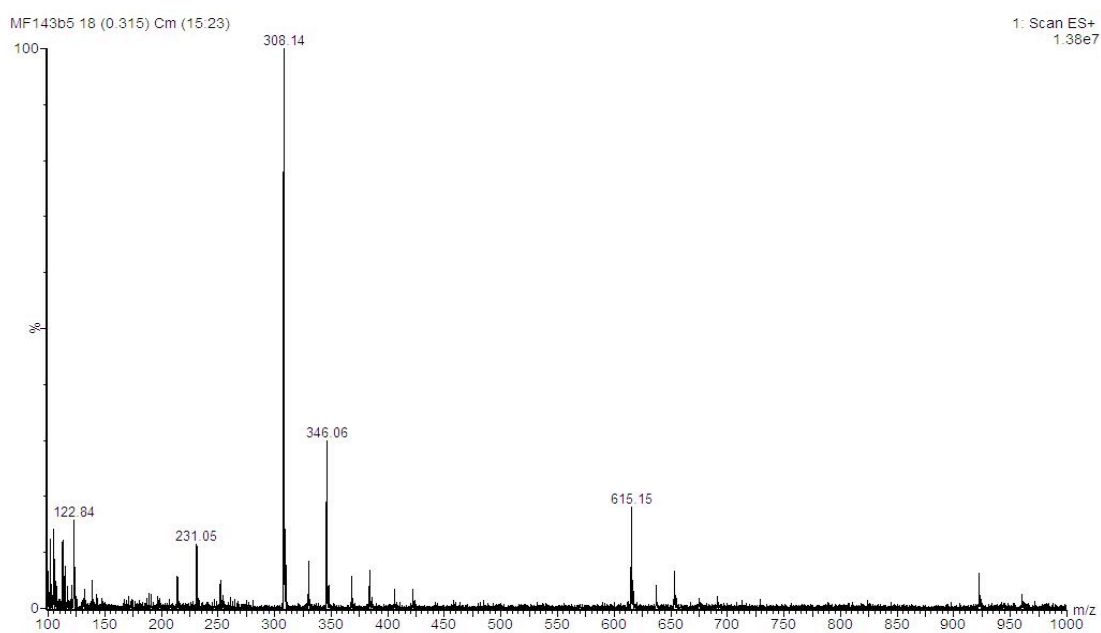
Figure S61. (a) TIC and UV trace at  $t = 2$  h, (b) MS data at 0.26–0.42 mins in the UV, (c) MS data at 1.34 mins in the UV and (d) at 2.52 mins in the UV for PD **15** incubated with GluSH **19** (10 eq.) at pH 5.0.

# LC-MS data for t = 4 h

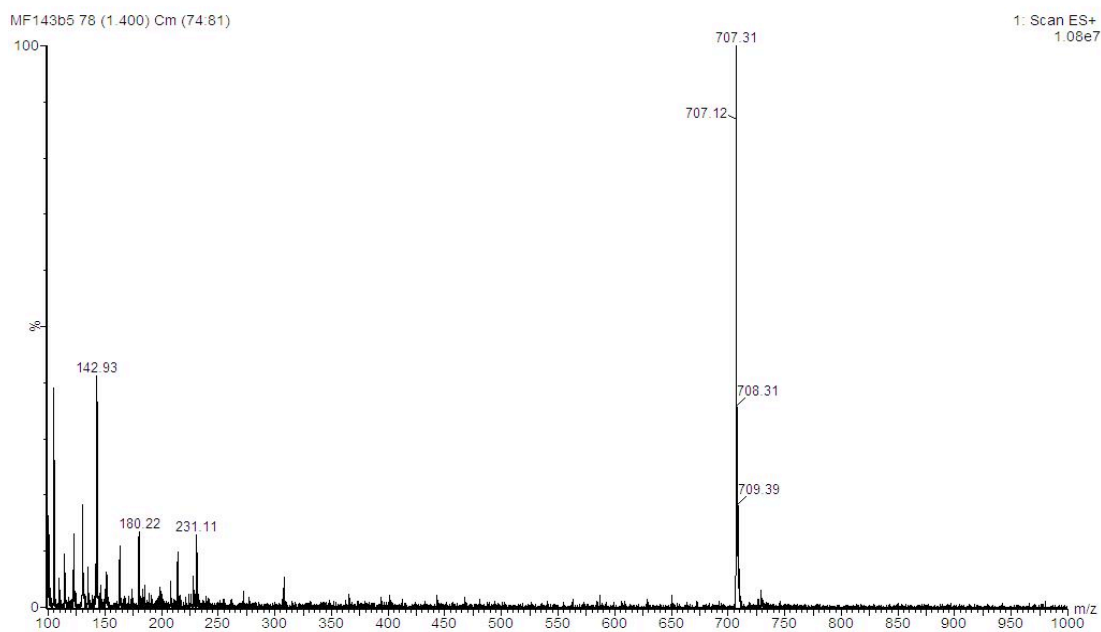
(a)



(b)



(c)



(d)

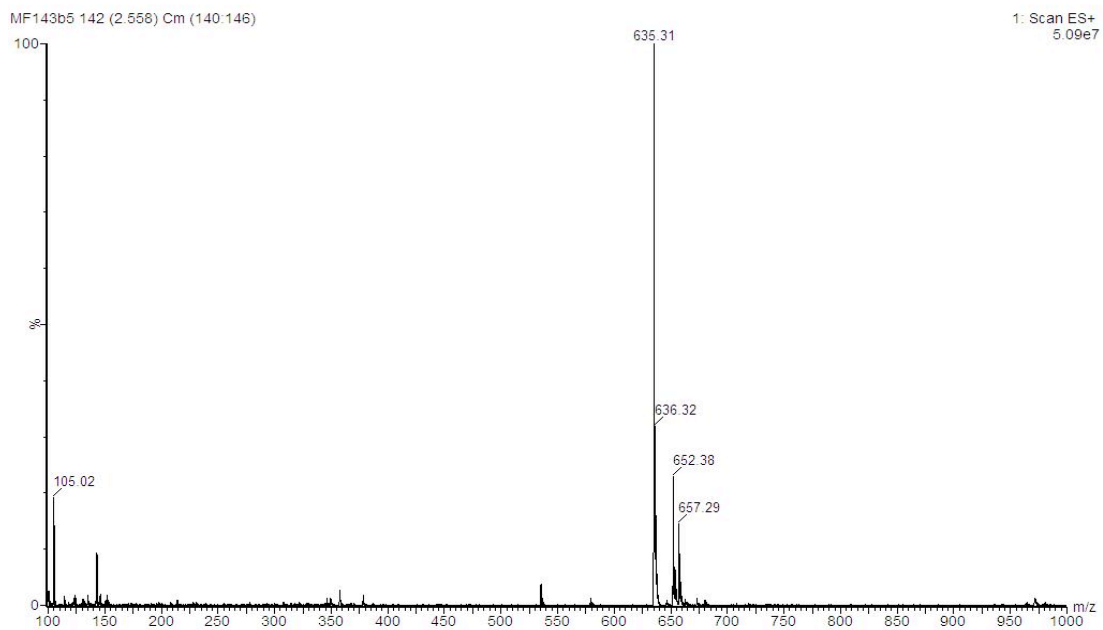
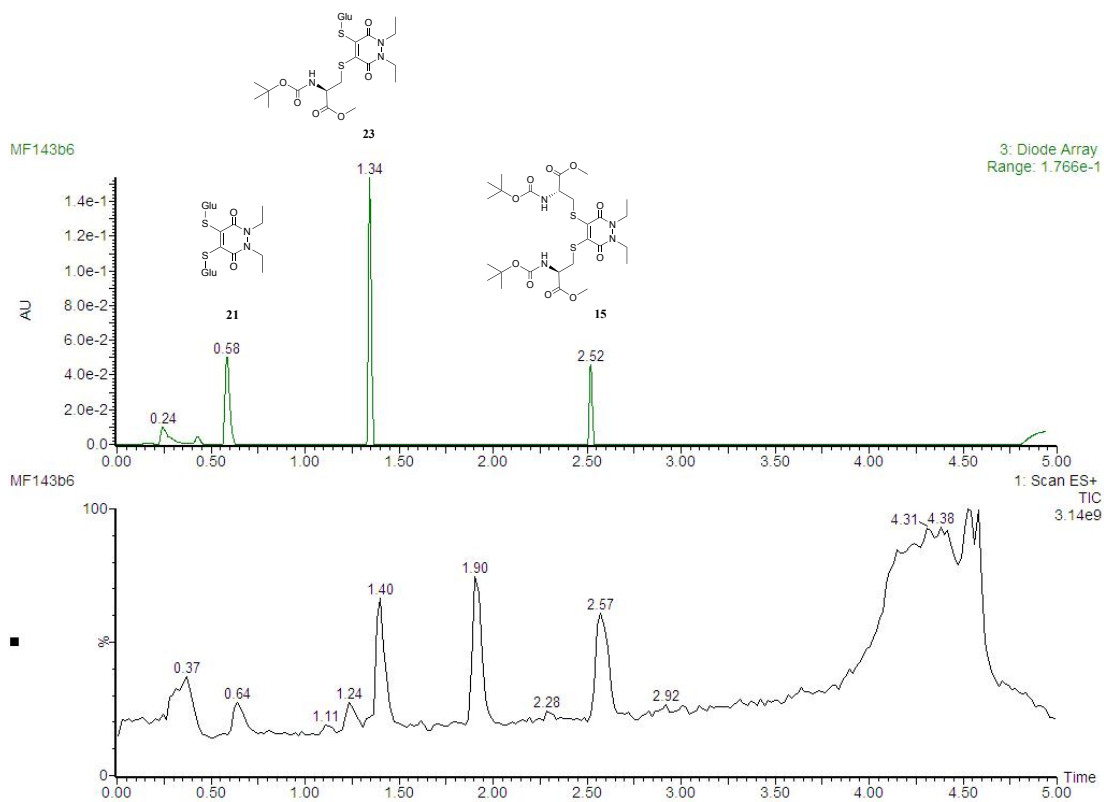


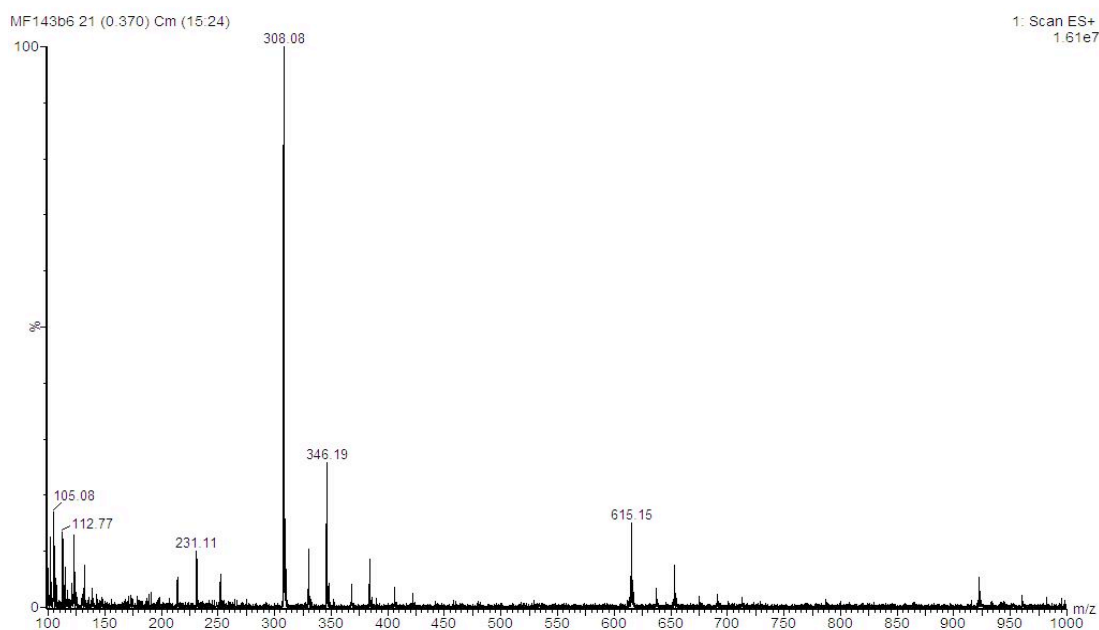
Figure S62. (a) TIC and UV trace at  $t = 4$  h, (b) MS data at 0.26–0.42 mins in the UV, (c) MS data at 1.34 mins in the UV and (d) at 2.52 mins in the UV for PD **15** incubated with GluSH **19** (10 eq.) at pH 5.0.

# LC-MS data for t = 24 h

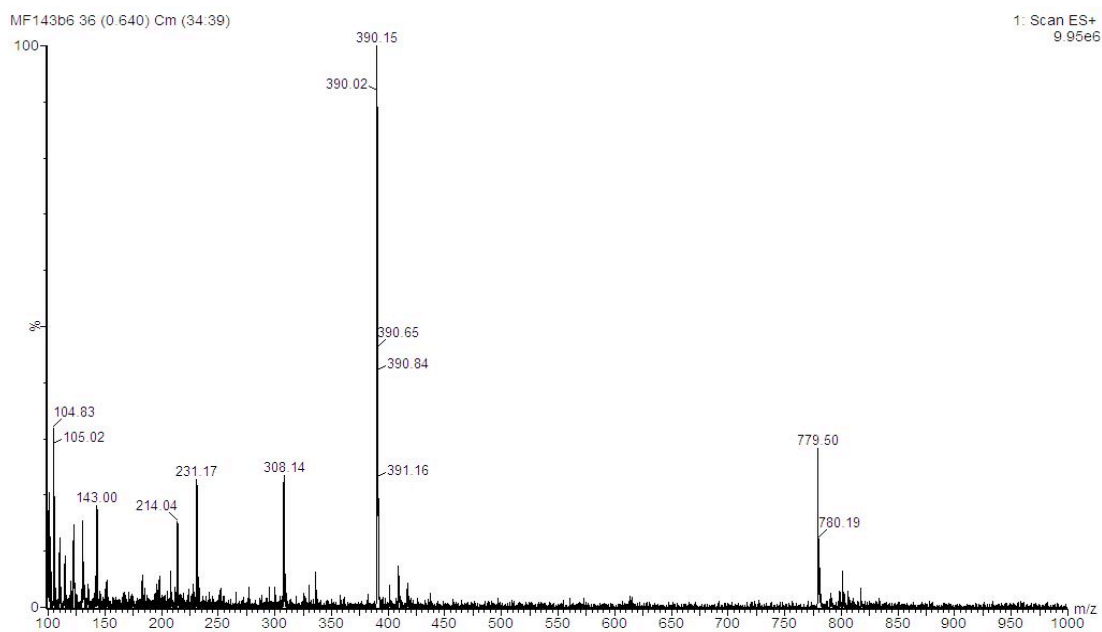
(a)



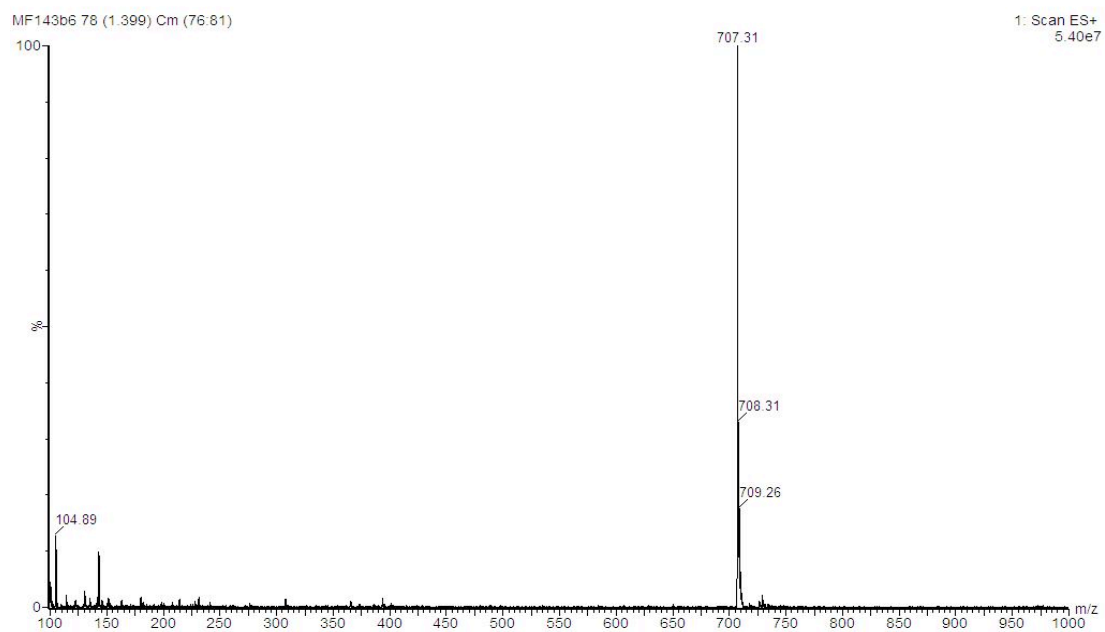
(b)



(c)



(d)



(e)

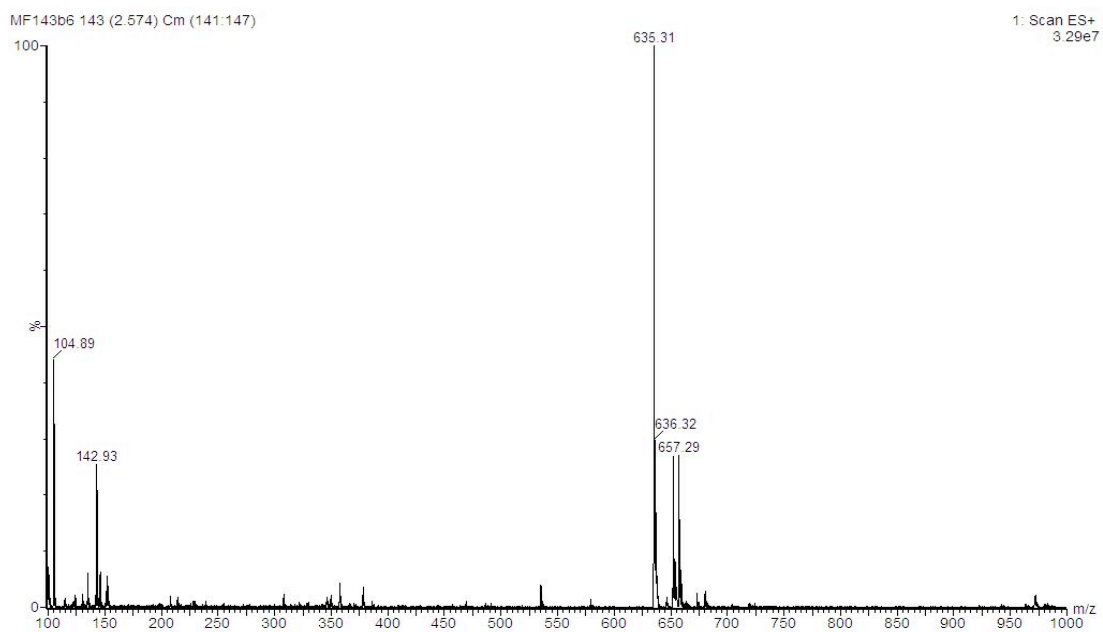
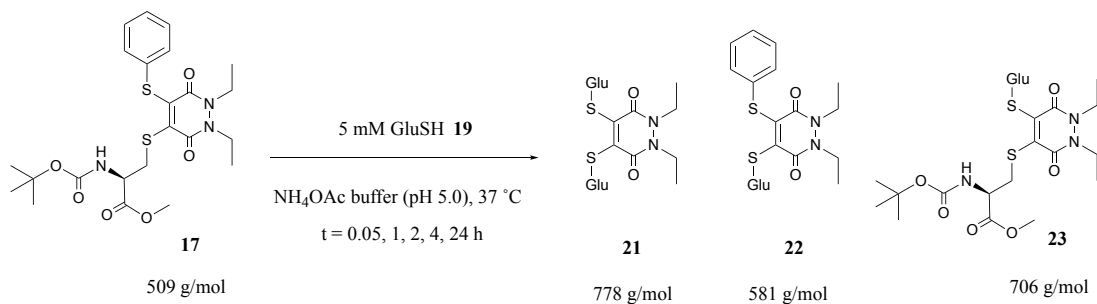


Figure S63. (a) TIC and UV trace at  $t = 24$  h, (b) MS data at 0.24–0.42 mins in the UV, (c) MS data at 0.58 mins in the UV, (d) at 1.34 mins in the UV and (e) at 2.52 mins in the UV for PD **15** incubated with GluSH **19** (10 eq.) at pH 5.0.

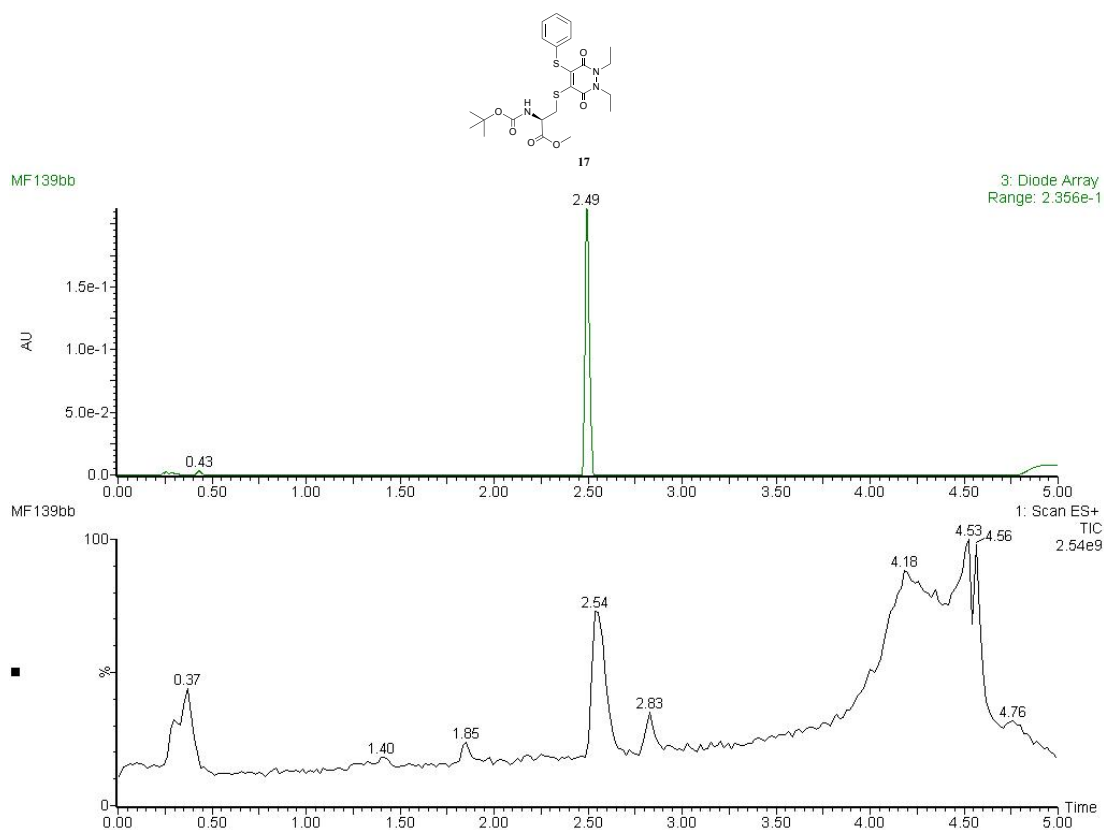
## Incubation of pyridazinedione **17** with GluSH (**10 eq.**)



Pyridazinedione **17** (10  $\mu\text{L}$ , 10 mM in MeCN, 1 eq.) was added to GluSH **19** (190  $\mu\text{L}$ , 5.3 mM, 10 eq.) in ammonium acetate buffer (50 mM, pH 5.0). The mixture was incubated at 37 °C for 24 h. The samples were analysed by LC-MS at  $t = 0.05, 1, 2, 4$  and 24 h.

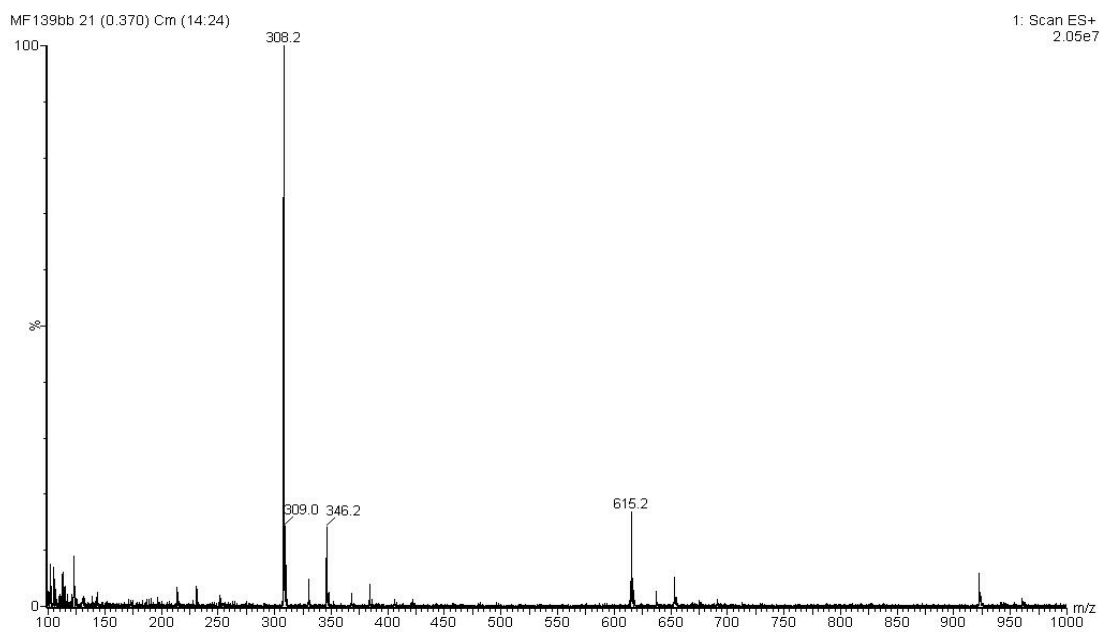
### LC-MS data for $t = 0.05$ h

(a)





(b)



(c)

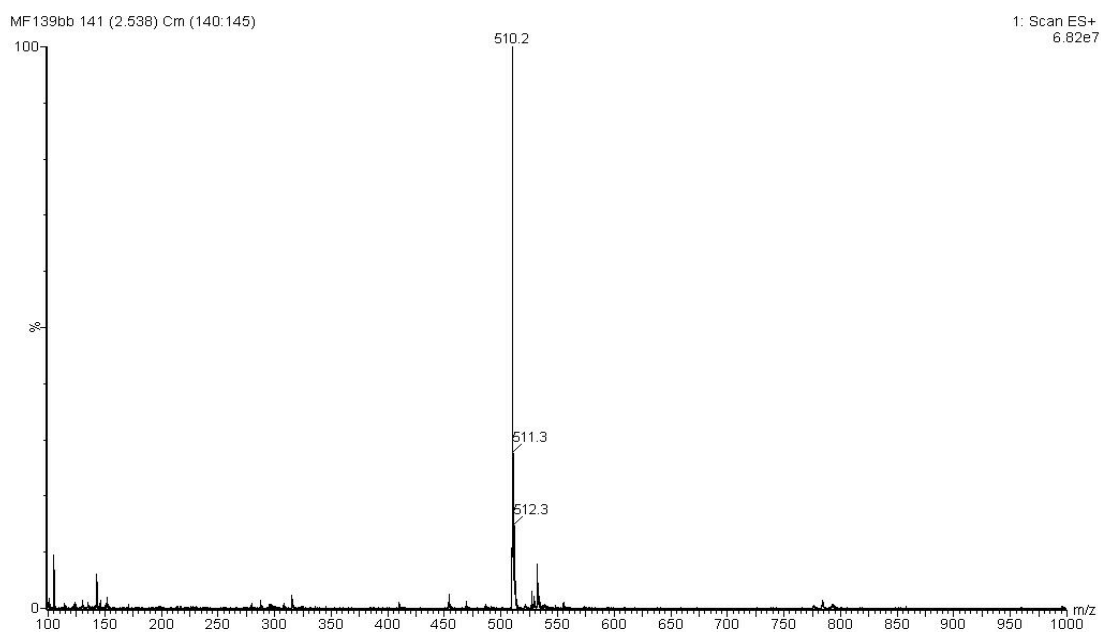
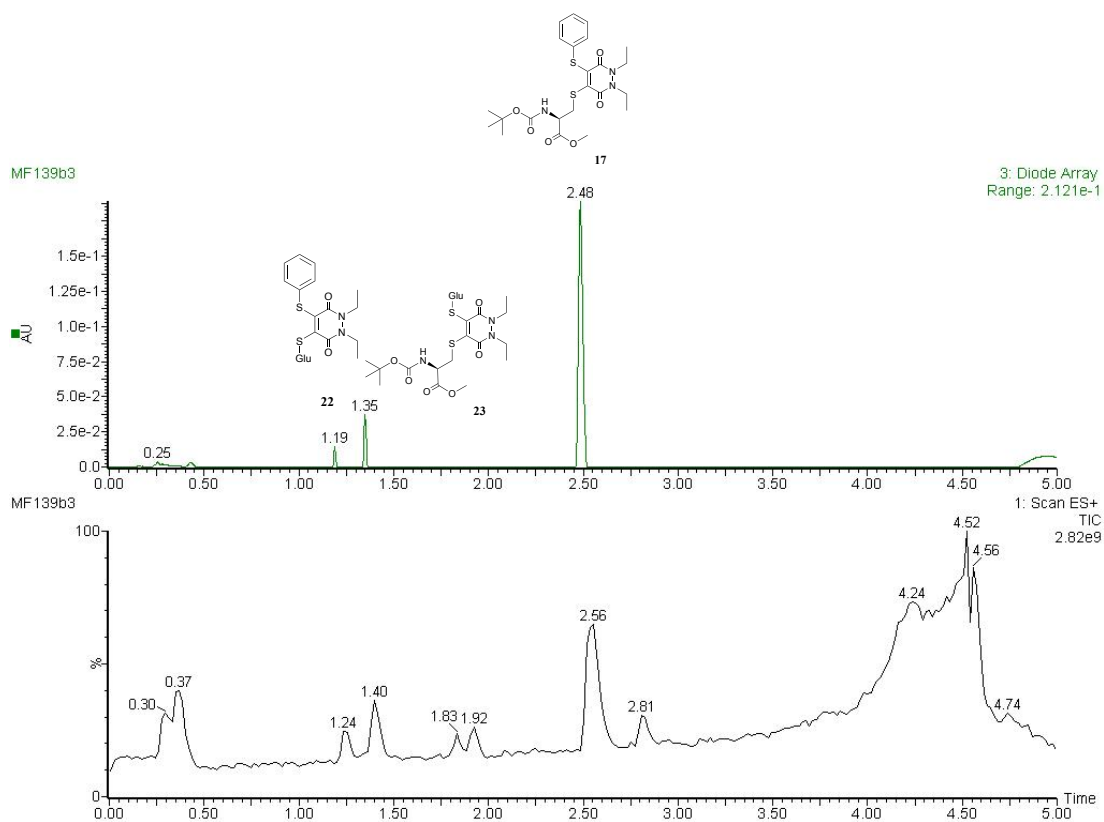


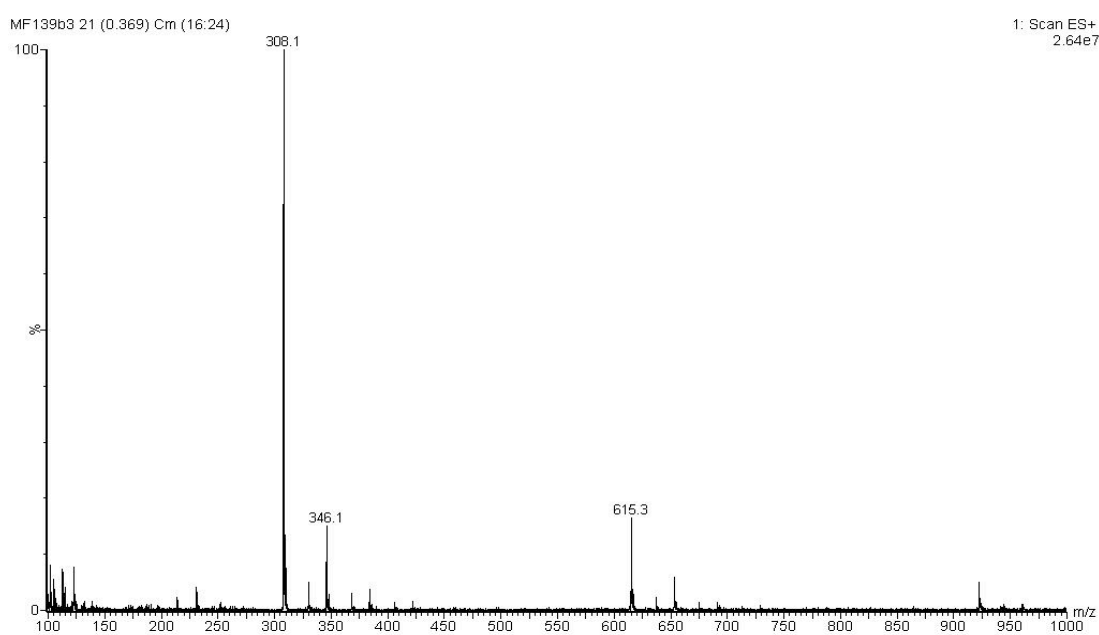
Figure S64. (a) TIC and UV trace at  $t = 0.05$  h, (b) MS data at 0.24–0.43 mins in the UV and (c) MS data at 2.49 mins in the UV for PD 17 incubated with GluSH 19 (10 eq.) at pH 5.0.

# LC-MS data for t = 1 h

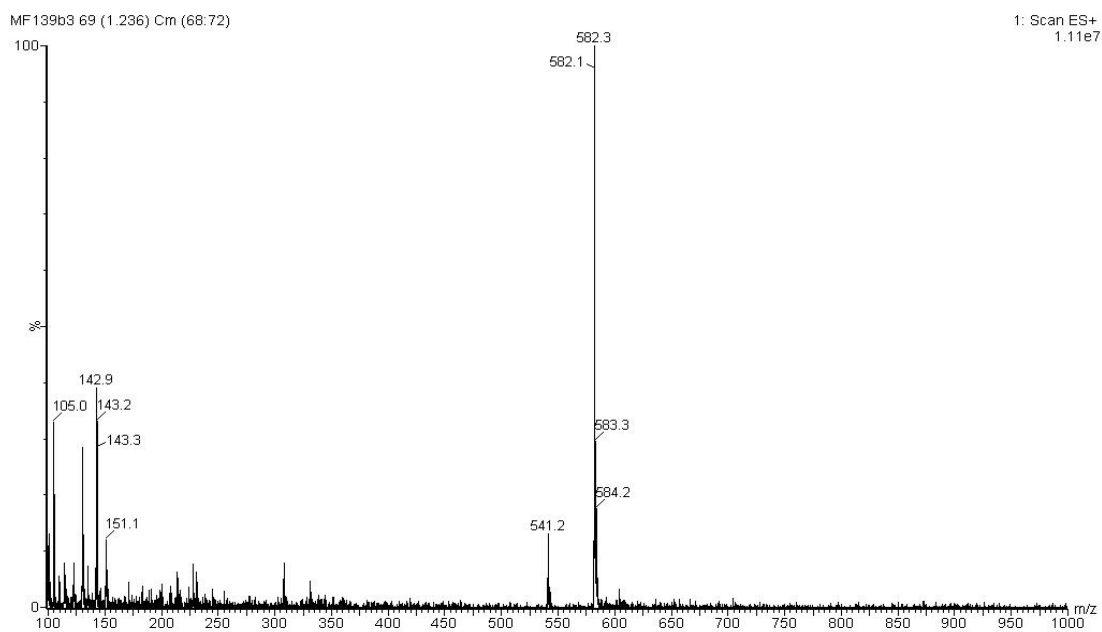
(a)



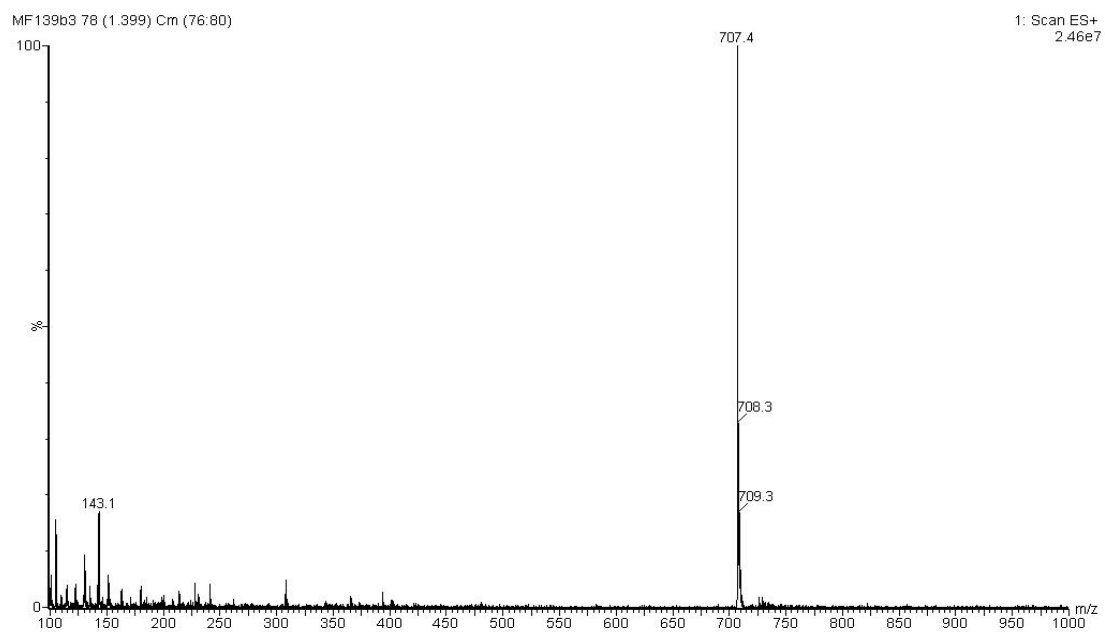
(b)



(c)



(d)



(e)

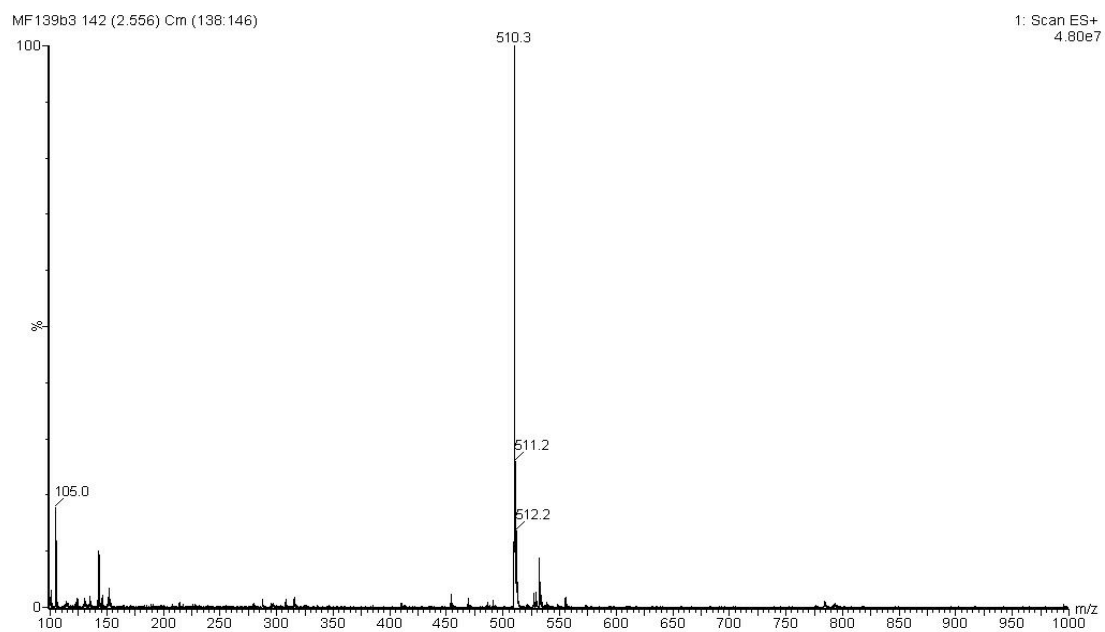
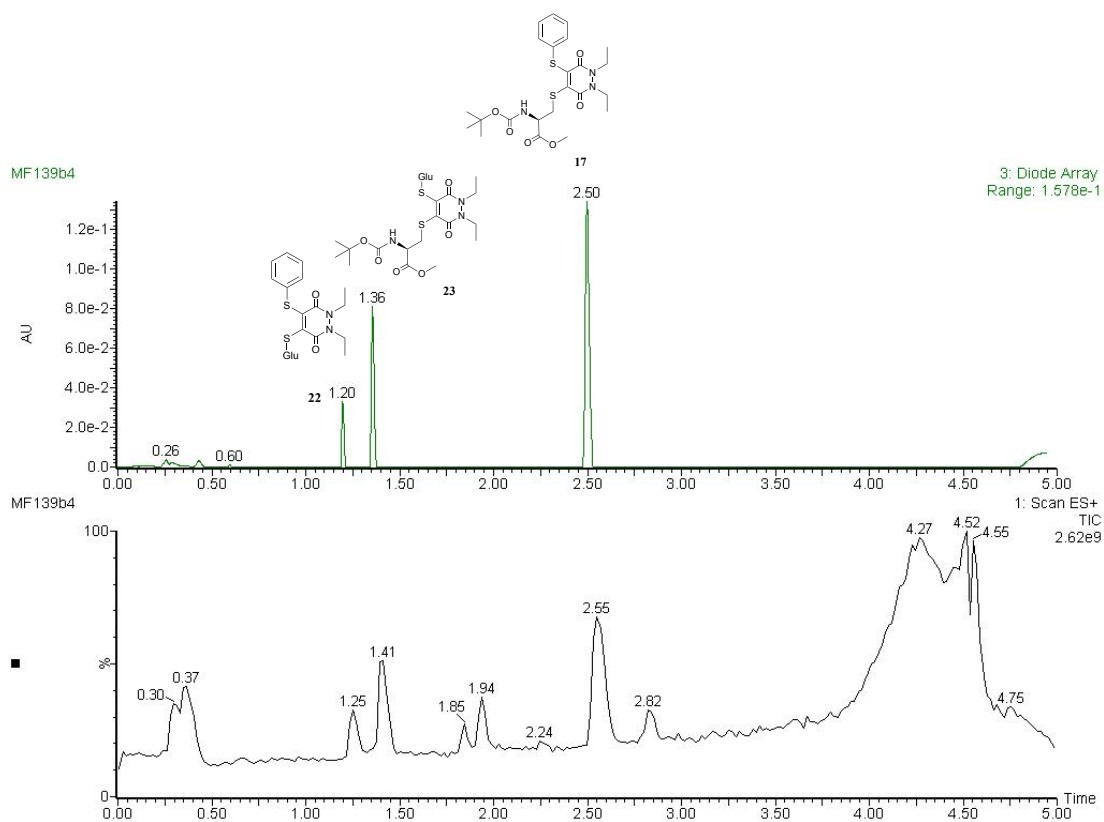


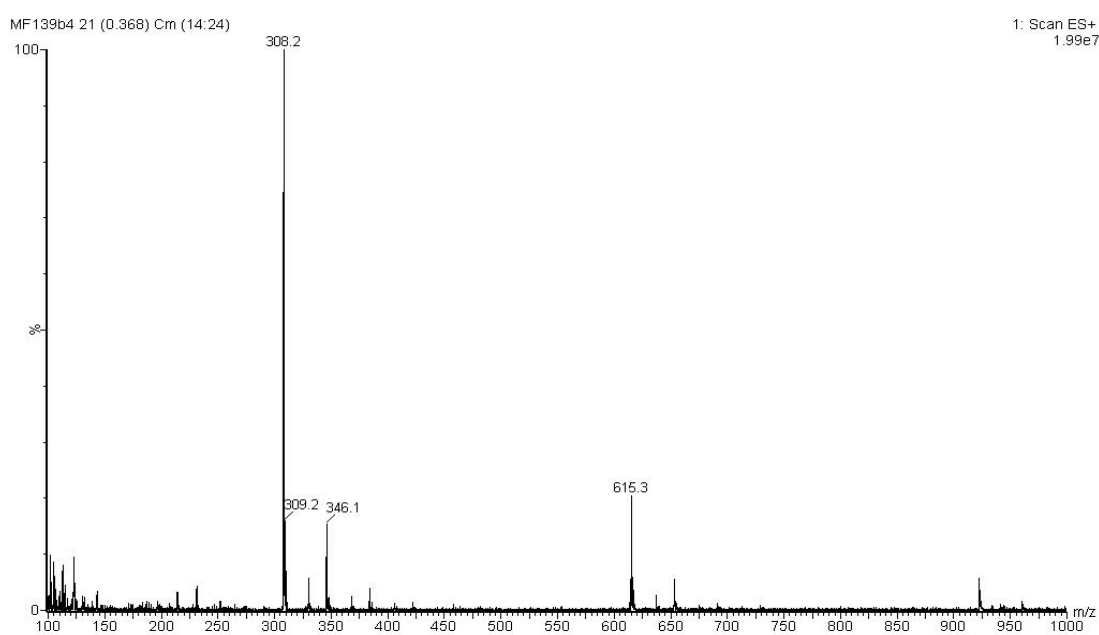
Figure S65. (a) TIC and UV trace at  $t = 1$  h, (b) MS data at 0.25–0.43 mins in the UV, (c) MS data at 1.19 mins in the UV, (d) at 1.35 mins in the UV and (e) at 2.48 mins in the UV for PD **17** incubated with GluSH **19** (10 eq.) at pH 5.0.

# LC-MS data for t = 2 h

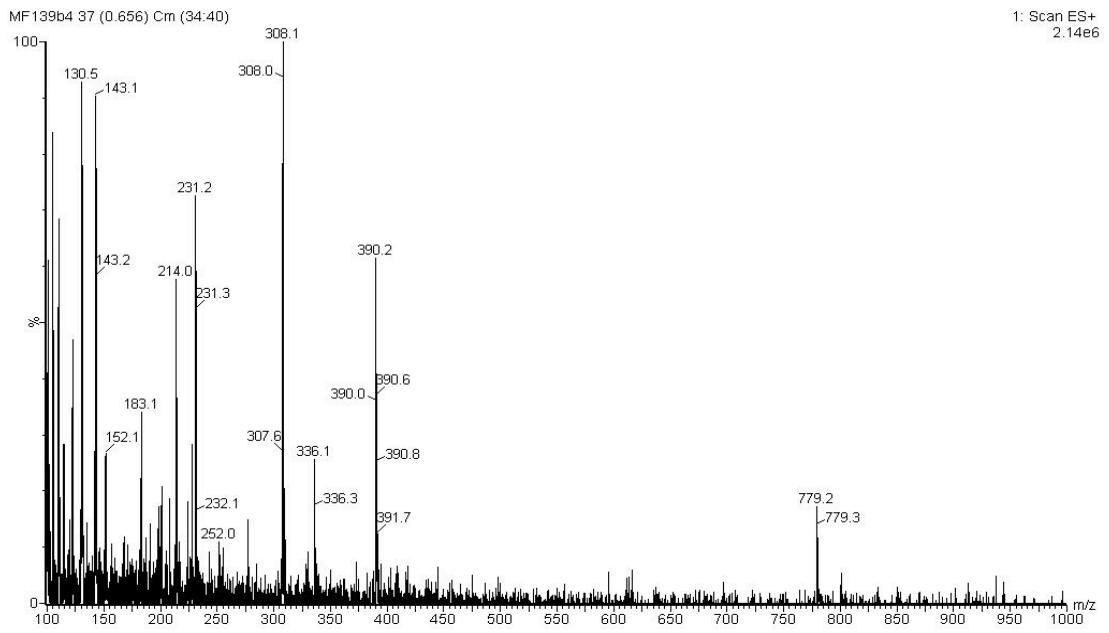
(a)



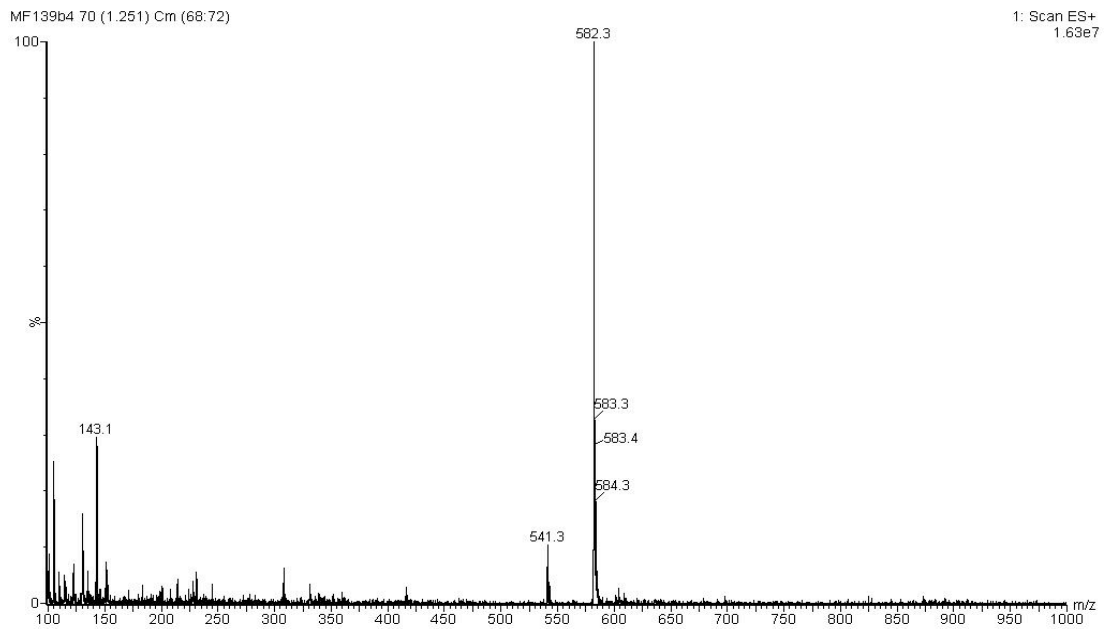
(b)



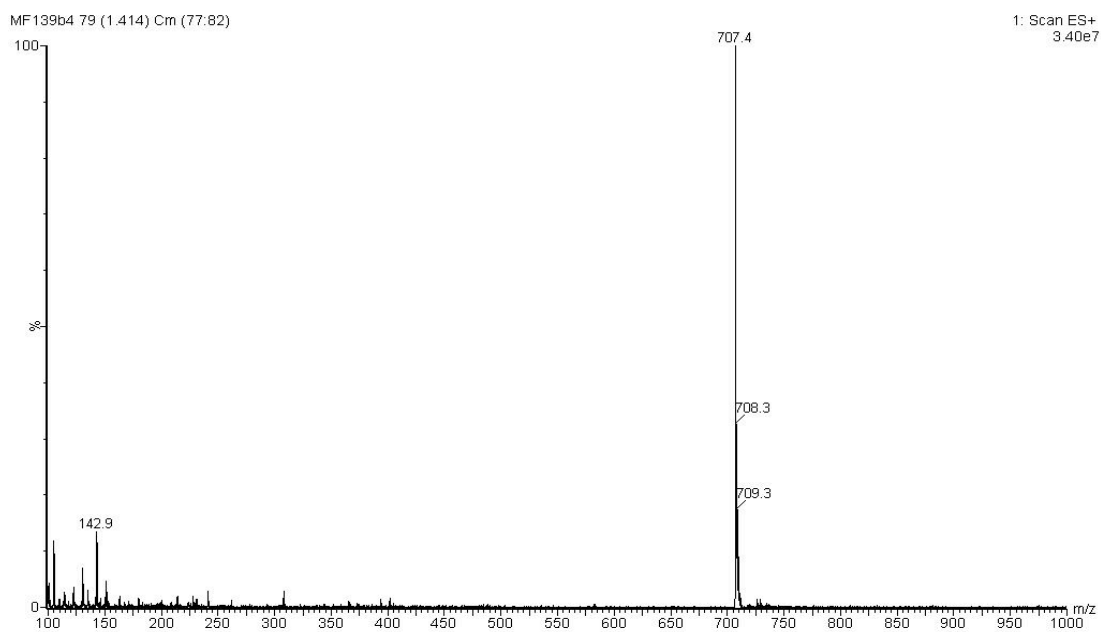
(c)



(d)



(e)



(f)

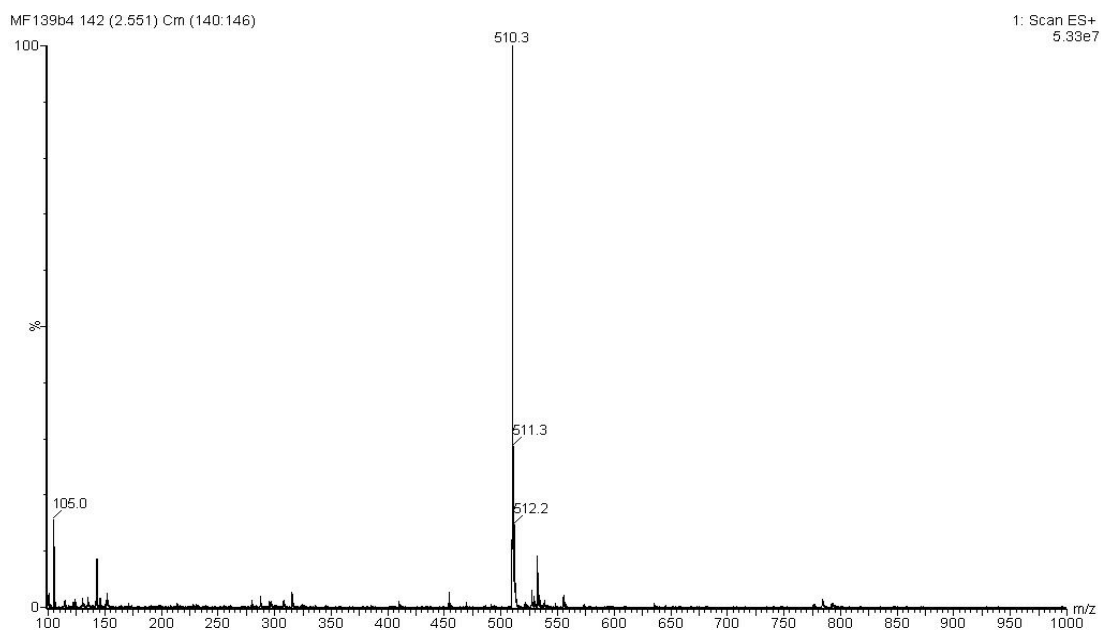
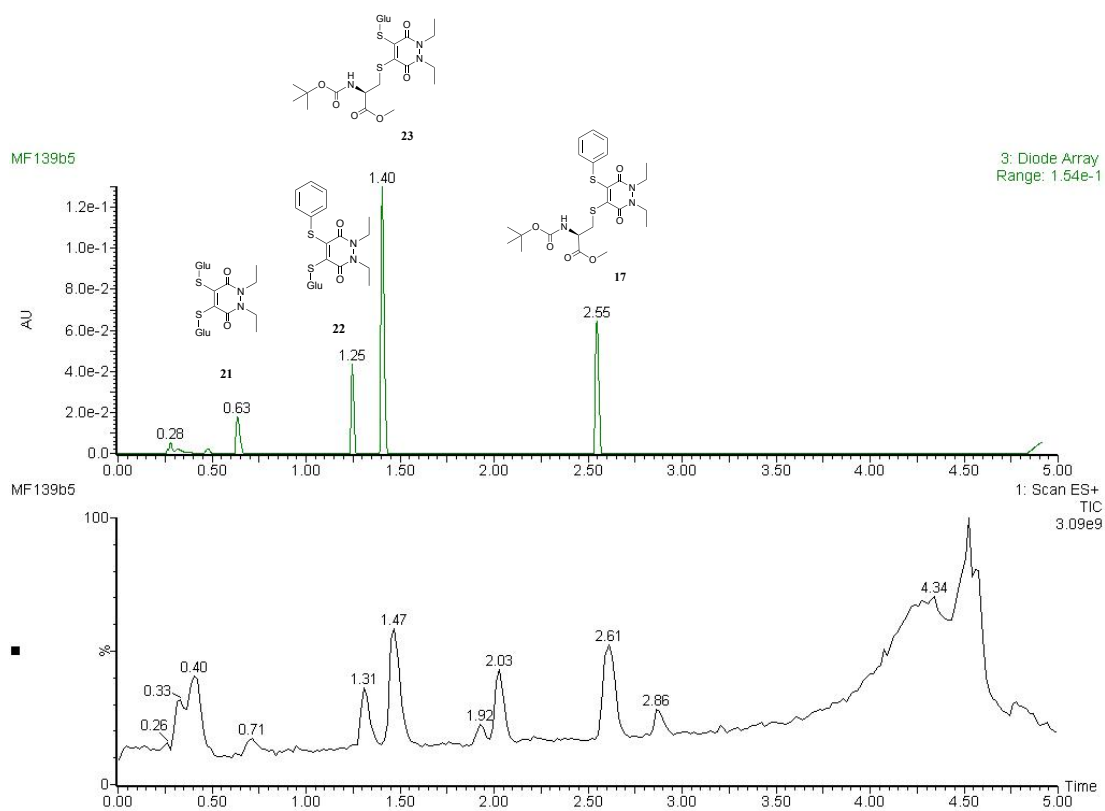


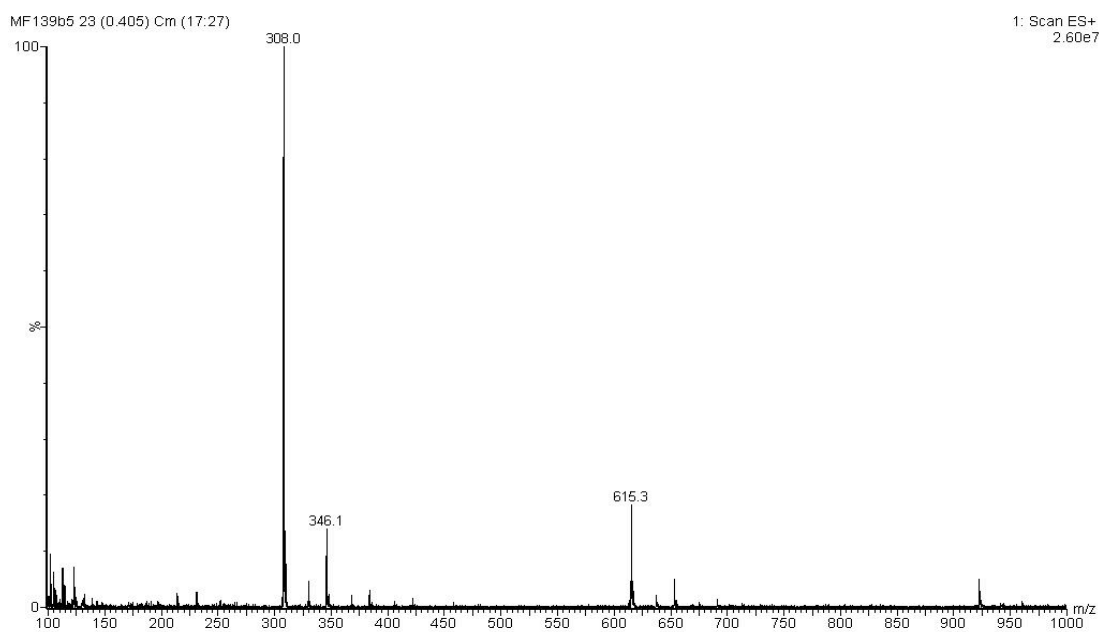
Figure S66. (a) TIC and UV trace at  $t = 2$  h, (b) MS data at 0.26–0.43 mins in the UV, (c) MS data at 0.60 mins in the UV, (d) at 1.20 mins in the UV, (e) at 1.36 mins in the UV and (f) at 2.50 mins in the UV for PD **17** incubated with GluSH **19** (10 eq.) at pH 5.0.

# LC-MS data for t = 4 h

(a)

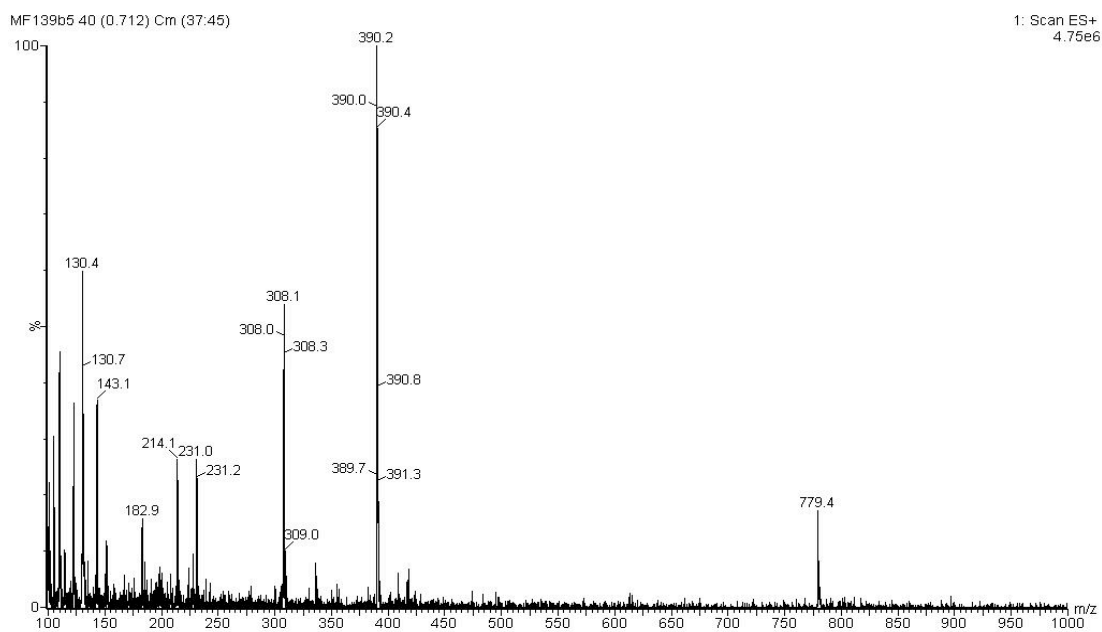


(b)

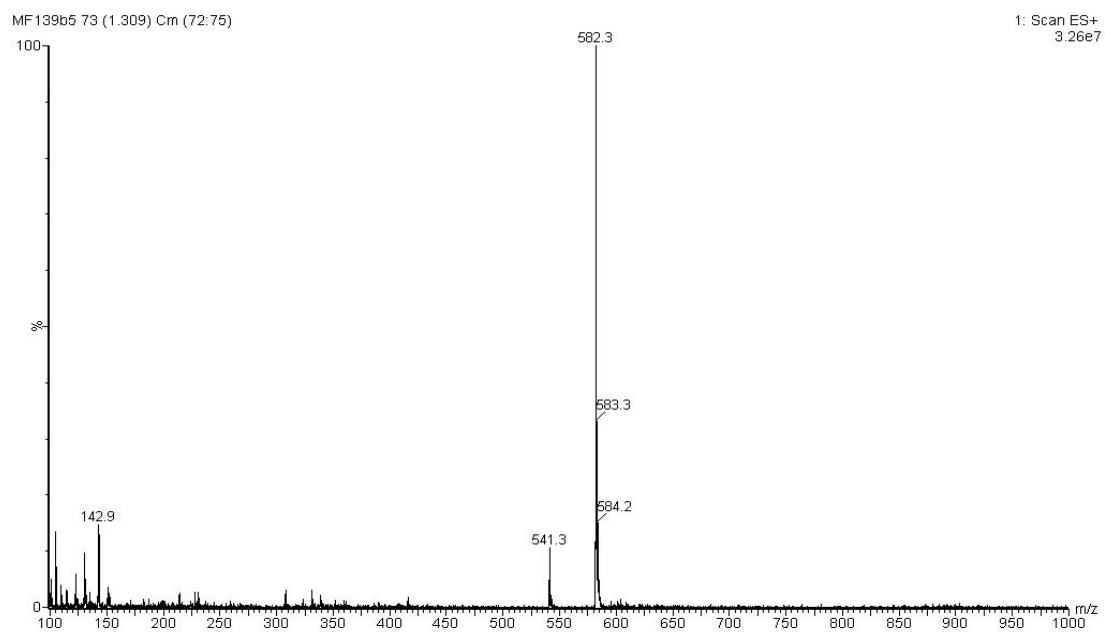




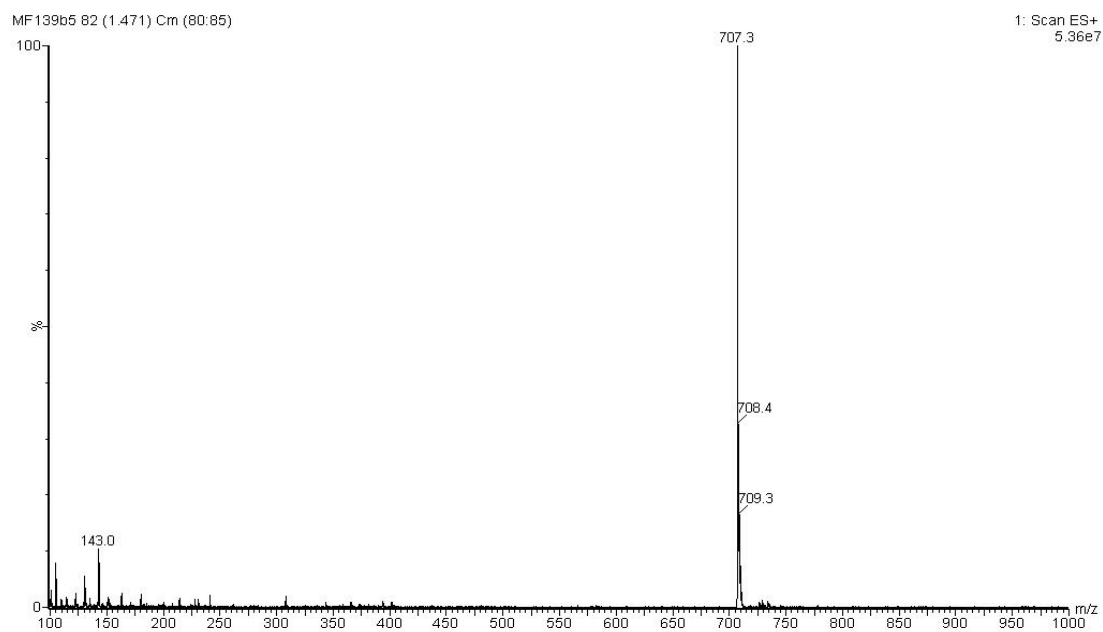
(c)



(d)



(e)



(f)

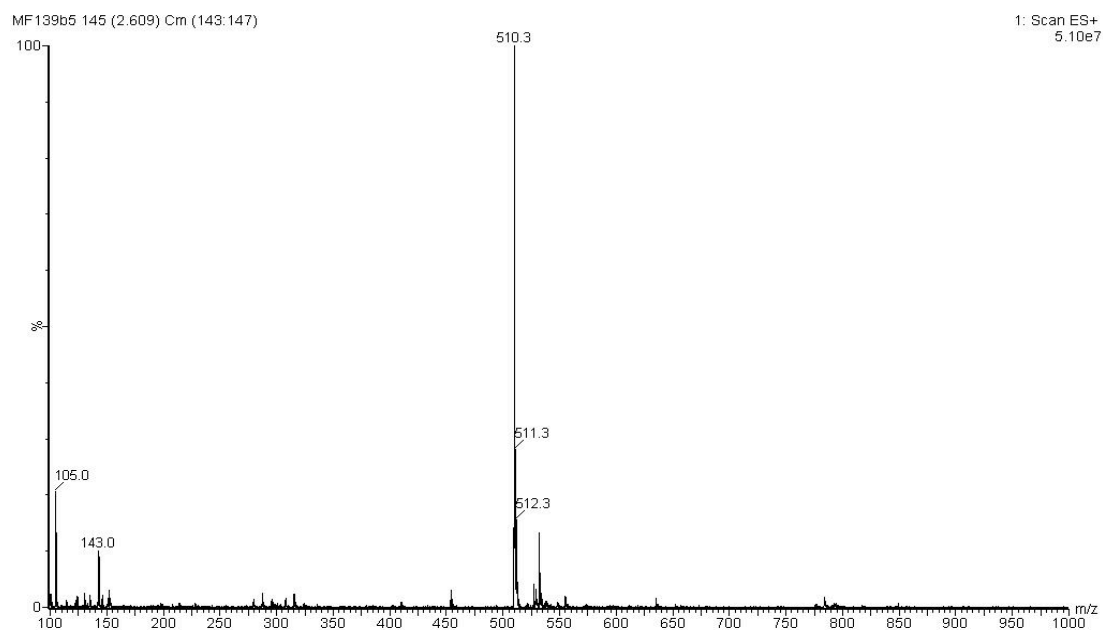
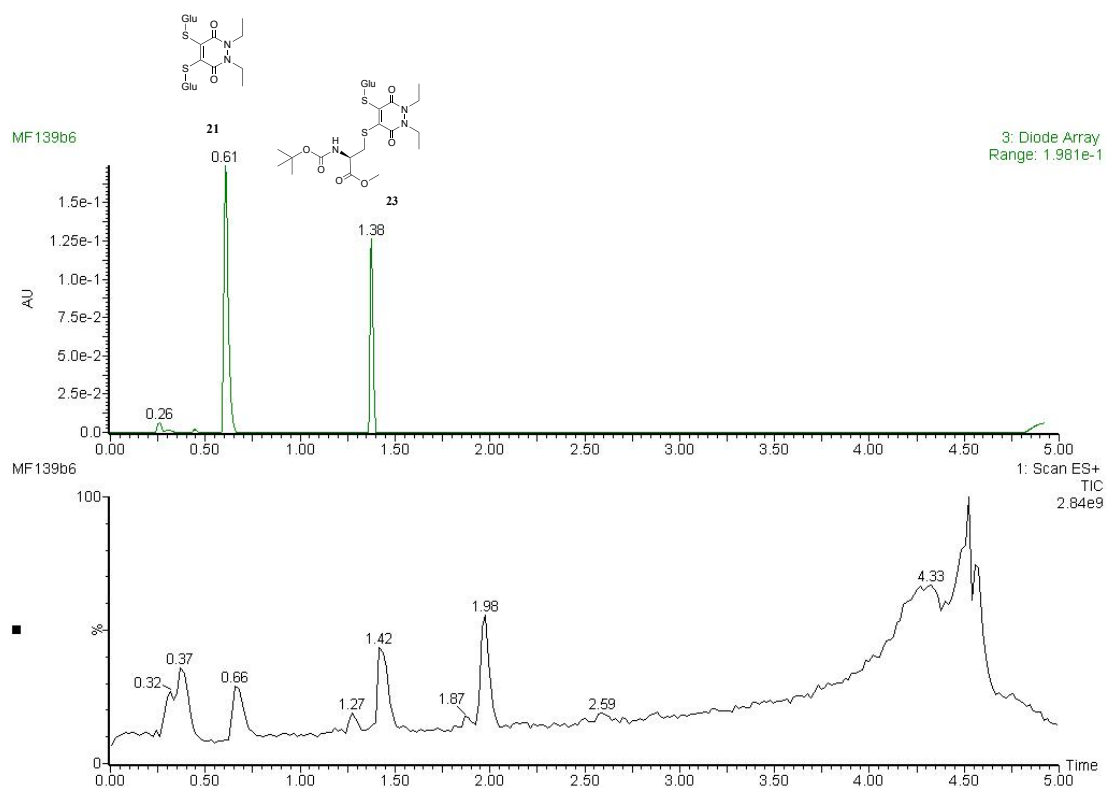


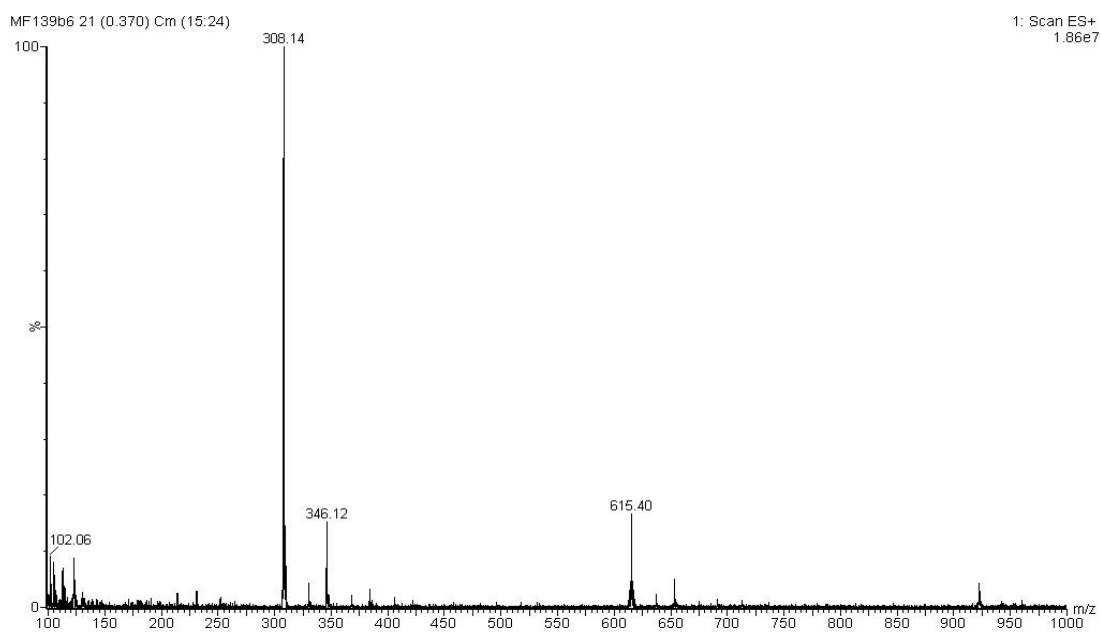
Figure S67. (a) TIC and UV trace at  $t = 4$  h, (b) MS data at 0.28–0.43 mins in the UV, (c) MS data at 0.63 mins in the UV, (d) at 1.25 mins in the UV, (e) at 1.40 mins in the UV and (f) at 2.55 mins in the UV for PD **17** incubated with GluSH **19** (10 eq.) at pH 5.0.

# LC-MS data for t = 24 h

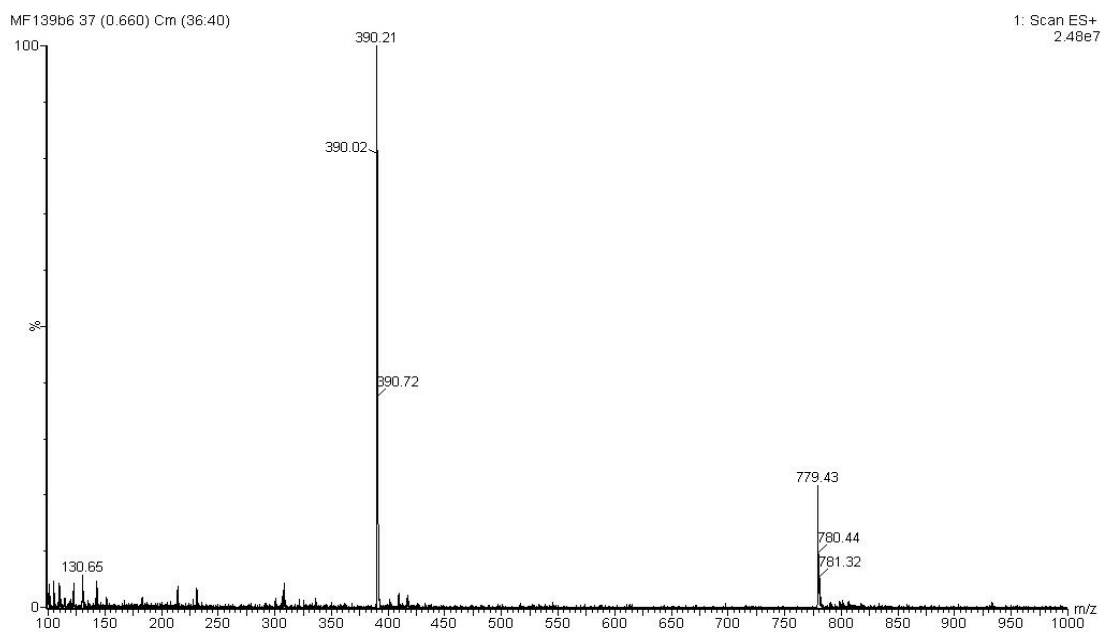
(a)



(b)



(c)



(d)

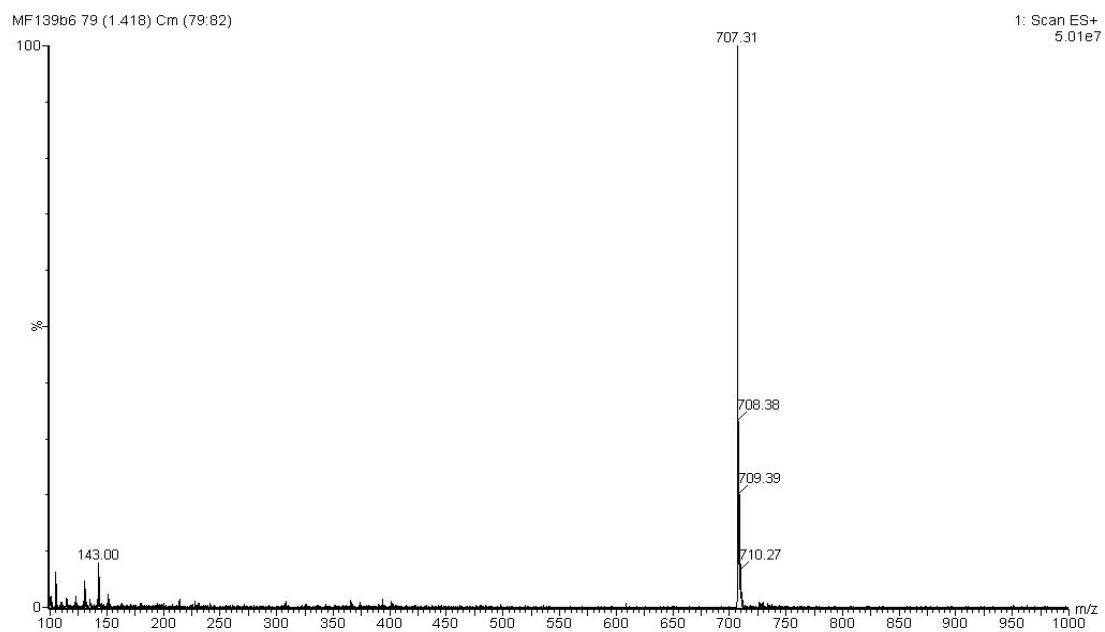
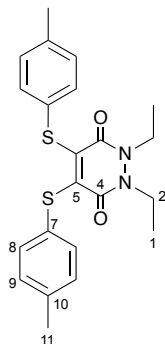


Figure S68. (a) TIC and UV trace at  $t = 24$  h, (b) MS data at 0.26–0.43 mins in the UV, (c) MS data at 0.61 mins in the UV and (d) at 1.38 mins in the UV for PD 17 incubated with GluSH 19 (10 eq.) at pH 5.0.

## Experimental for Chapter 3

### 1,2-Diethyl-4,5-bis(*p*-tolylthio)-1,2-dihydropyridazine-3,6-dione **33**



To a solution of 4,5-dibromo-1,2-diethyl-1,2-dihydropyridazine-3,6-dione **8** (1.63 g, 5.00 mmol) in  $\text{CH}_2\text{Cl}_2$  (10 mL) at 21 °C, was added a solution of 4-methylbenzenethiol **36** (1.55 g, 12.5 mmol) and triethylamine (2.27 mL, 16.3 mmol) in  $\text{CH}_2\text{Cl}_2$  (10 mL), and the reaction mixture was stirred for 10 mins. Following this, the reaction mixture was diluted with  $\text{CH}_2\text{Cl}_2$  (20 mL) and washed with water ( $3 \times 30$  mL) and brine (30 mL). The organic phase was dried over  $\text{MgSO}_4$ , concentrated *in vacuo* and the crude residue was purified by flash column chromatography (10–60% EtOAc/Pet.). The appropriate fractions were then combined and concentrated *in vacuo* to afford 1,2-diethyl-4,5-bis(*p*-tolylthio)-1,2-dihydropyridazine-3,6-dione (1.85 g, 4.49 mmol, 90%) as a yellow solid. m.p. 114–116 °C;  $^1\text{H}$  NMR (600 MHz,  $\text{CDCl}_3$ )  $\delta$  7.15 (d,  $J = 8.2$  Hz, 4H, H-8), 7.09 (d,  $J = 8.2$  Hz, 4H, H-9), 4.02 (q,  $J = 7.1$  Hz, 4H, H-2), 2.33 (s, 6H, H-11), 1.21 (t,  $J = 7.1$  Hz, 6H, H-1);  $^{13}\text{C}$  NMR (150 MHz,  $\text{CDCl}_3$ )  $\delta$  156.1 (C-4), 142.3 (C-5), 138.1 (C-10), 131.3 (C-8), 129.9 (C-9), 129.3 (C-7), 41.1 (C-2), 21.4 (C-11), 12.8 (C-1); IR (solid) 2980, 2956, 2923, 2868, 1617, 1567  $\text{cm}^{-1}$ ; LRMS (ES+) 413 (100,  $[\text{M}+\text{H}]^+$ ); HRMS (ES+) calcd for  $\text{C}_{22}\text{H}_{25}\text{N}_2\text{O}_2\text{S}_2$   $[\text{M}+\text{H}]^+$  413.1352, observed 413.1346.

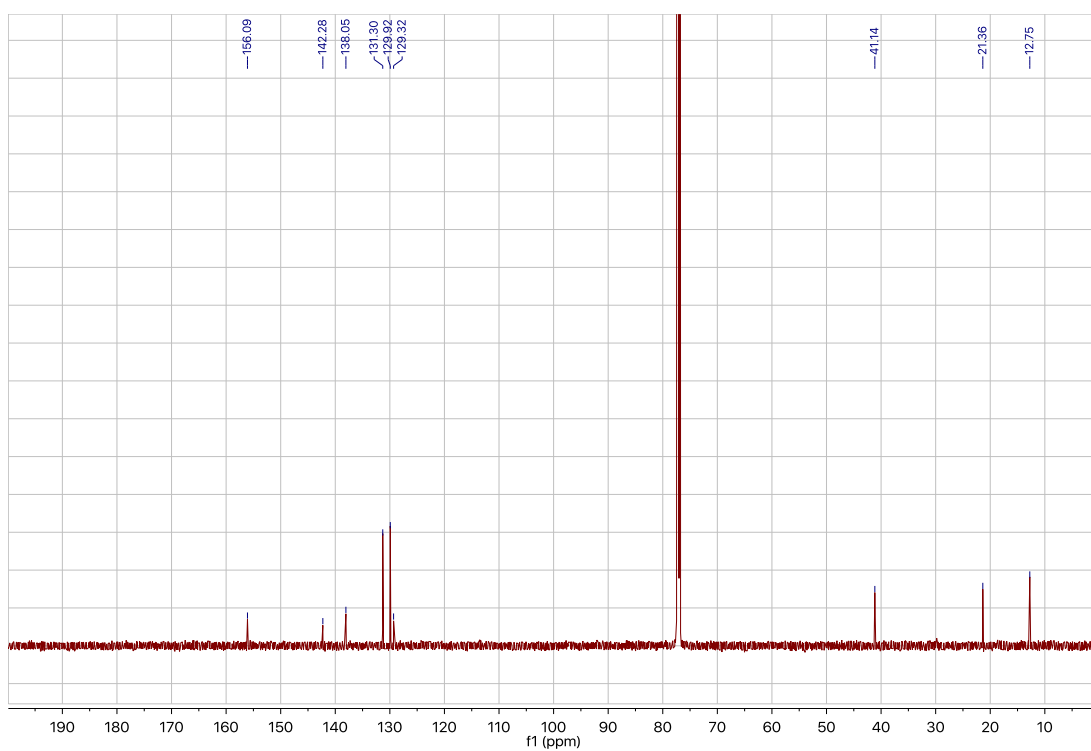
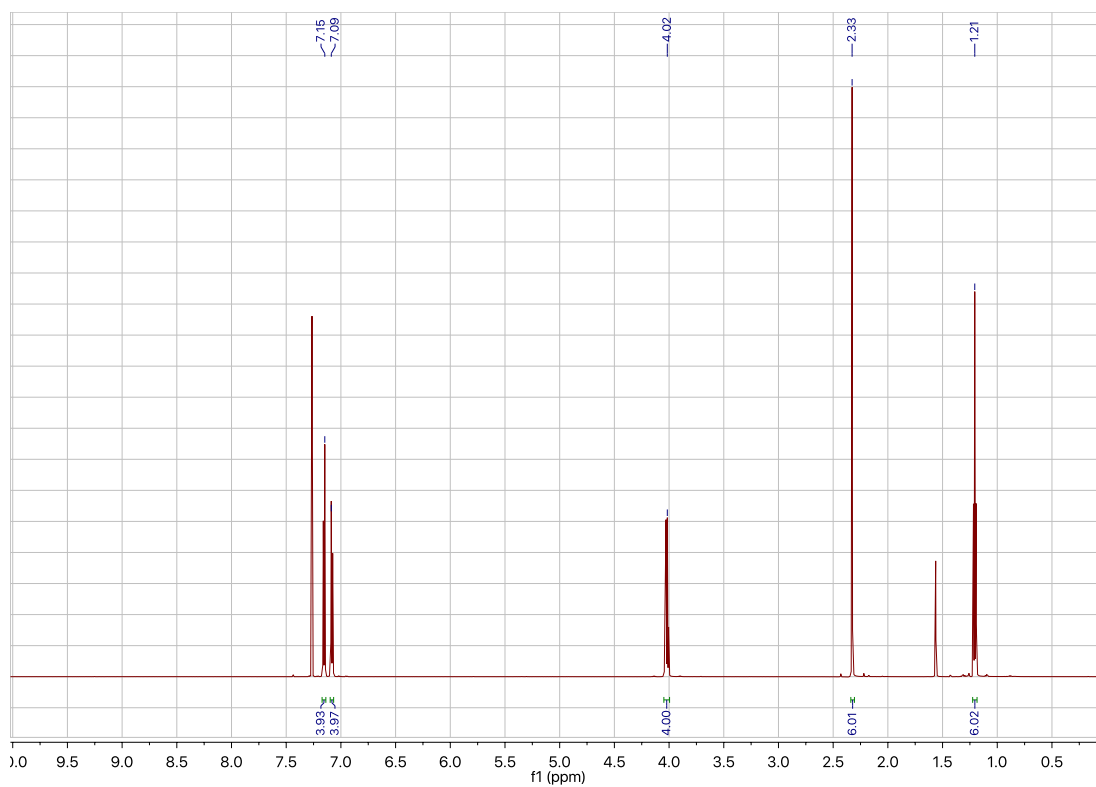
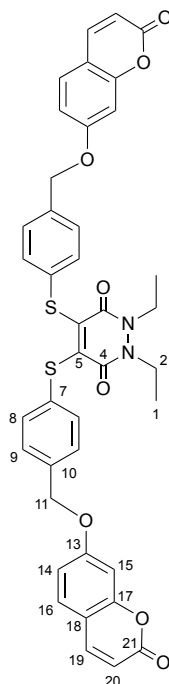


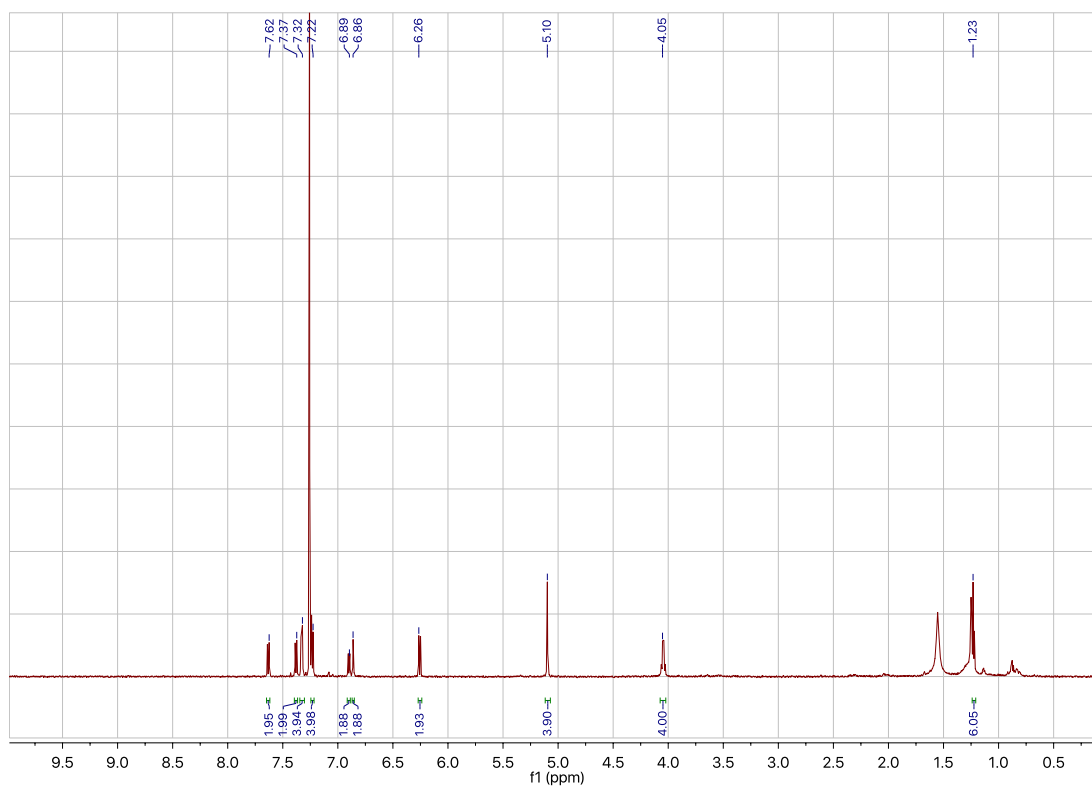
Figure S69.  $^1\text{H}$  and  $^{13}\text{C}$  NMR spectra for 1,2-diethyl-4,5-bis(*p*-tolylthio)-1,2-dihydropyridazine-3,6-dione **33**.

**1,2-Diethyl-4,5-bis((4-(((2-oxo-2*H*-chromen-7-yl)oxy)methyl)phenyl)thio)-1,2-dihydropyridazine-3,6-dione **29****



To a solution of 1,2-diethyl-4,5-bis(*p*-tolylthio)-1,2-dihydropyridazine-3,6-dione **33** (0.11 g, 0.27 mmol) in fluorobenzene (6 mL) was added NBS **34** (0.13 g, 0.73 mmol) and AIBN **35** (0.03 g, 0.2 mmol), and the reaction mixture was stirred under reflux for 7 h. Following this, the reaction mixture was diluted with EtOAc (20 mL) and washed with water (3 × 20 mL). The organic phase was dried over MgSO<sub>4</sub> and concentrated *in vacuo* to afford the crude 4,5-bis((4-(bromomethyl)phenyl)thio)-1,2-diethyl-1,2-dihydropyridazine-3,6-dione **32** (0.11 g total). The crude mixture was dissolved in dry THF (4 mL) along with cesium carbonate (0.22 g, 0.68 mmol) and umbelliferone **25** (0.08 g, 0.5 mmol), and the reaction mixture was stirred under reflux for 21 h. Following this, the reaction mixture was diluted with water (10 mL) and extracted with EtOAc (3 × 15 mL). The organic phase was dried over MgSO<sub>4</sub>, concentrated *in vacuo* and the crude residue was purified by preparative TLC (50% EtOAc/CHCl<sub>3</sub>) to afford 1,2-diethyl-4,5-bis((4-(((2-oxo-2*H*-chromen-7-yl)oxy)methyl)phenyl)thio)-1,2-dihydropyridazine-3,6-dione (0.02 g, 0.03 mmol, 9%) as a yellow solid. m.p. 179–183 °C; <sup>1</sup>H NMR (600 MHz, CDCl<sub>3</sub>) δ 7.62 (d, *J* = 9.5 Hz, 2H, H-19), 7.37 (d, *J* = 8.6 Hz, 2H, H-16), 7.32 (d, *J* = 8.2 Hz, 4H, H-8), 7.22 (d, *J* = 8.2 Hz, 4H, H-9), 6.89 (dd, *J* = 8.6, 2.5 Hz, 2H, H-14), 6.86 (d, *J* = 2.5 Hz, 2H, H-15), 6.26 (d, *J* = 9.5 Hz, 2H, H-20), 5.10 (s, 4H, H-11), 4.05 (q, *J* = 7.0 Hz, 4H, H-2), 1.23 (t, *J* = 7.0 Hz, 6H,

H-1);  $^{13}\text{C}$  NMR (150 MHz,  $\text{CDCl}_3$ )\*  $\delta$  161.8 (C-13), 161.2 (C-21), 156.0 (C-17), 155.8 (C-4), 143.5 (C-19), 141.9 (C-5), 135.7 (C-10), 132.7 (C-7), 131.3 (C-8), 129.0 (C-16), 128.2 (C-9), 113.5 (C-20), 113.3 (C-14), 113.0 (C-18), 102.1 (C-15), 70.0 (C-11), 41.4 (C-2), 12.9 (C-1); IR (solid) 2919, 2851, 1726, 1608  $\text{cm}^{-1}$ ; LRMS (ES+) 733 (100,  $[\text{M}+\text{H}]^+$ ); HRMS (ES+) calcd for  $\text{C}_{40}\text{H}_{33}\text{N}_2\text{O}_8\text{S}_2$   $[\text{M}+\text{H}]^+$  733.1678, observed 733.1674.





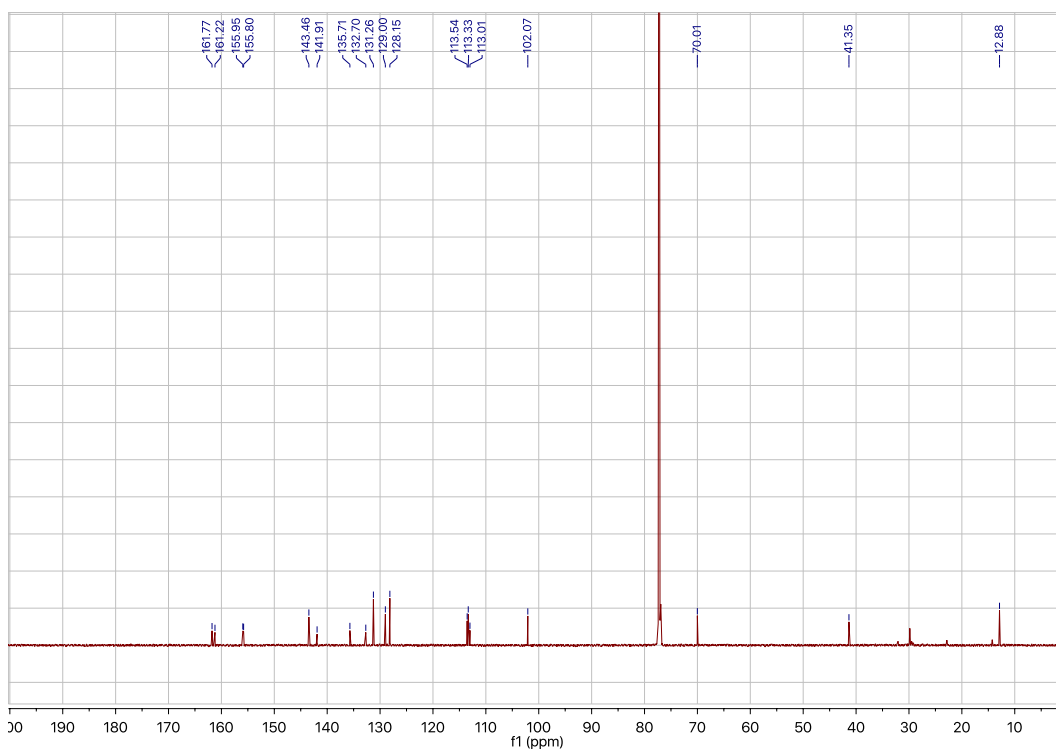
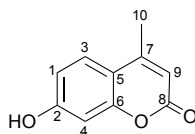
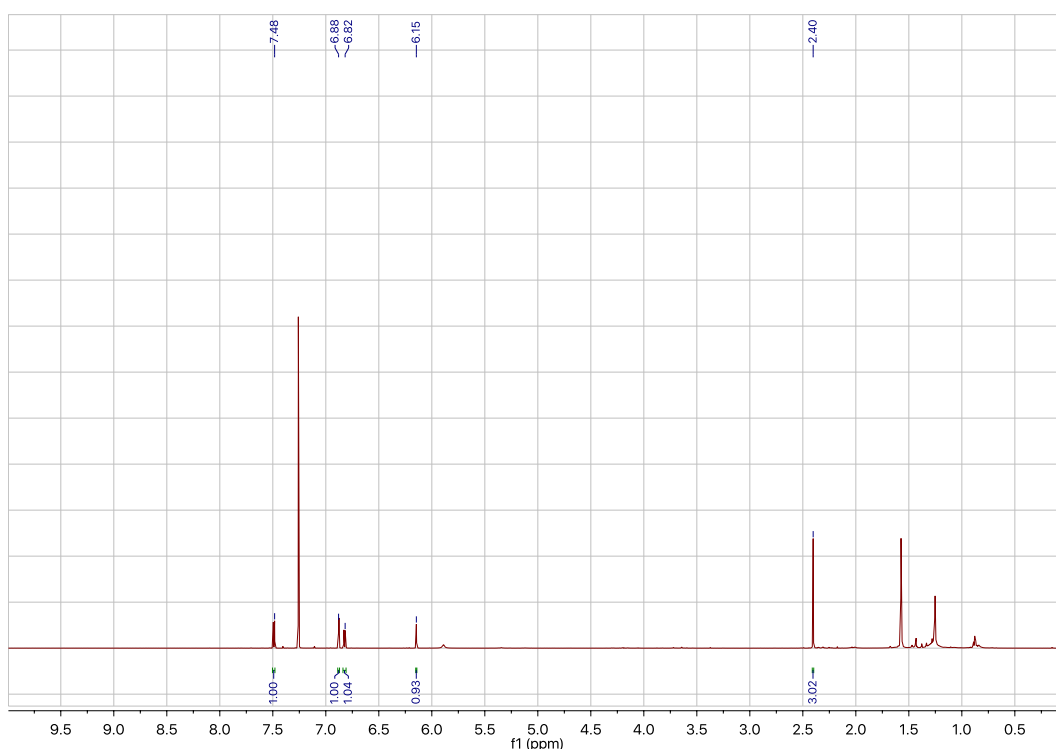


Figure S70.  $^1\text{H}$  and  $^{13}\text{C}$  NMR spectra for 1,2-diethyl-4,5-bis((4-(((2-oxo-2*H*-chromen-7-yl)oxy)methyl)phenyl)thio)-1,2-dihydropyridazine-3,6-dione **29**. \*29.8 (H grease), 1.15 (silicon grease).

## 7-Hydroxy-4-methyl-2*H*-chromen-2-one **40**<sup>150</sup>



A solution of 7-hydroxycoumarin-4-acetic acid **39** (0.21 g, 0.95 mmol) in dry THF (7 mL) was cooled to 0 °C and stirred for 10 mins. To this was added EDC·HCl (0.27 g, 1.4 mmol) and the resulting solution was stirred at 0 °C for a further 30 mins. After this time DMAP (0.17 g, 1.4 mmol) and *tert*-butanol **41** (0.90 mL, 9.4 mmol) were added to the solution which was then stirred at 21 °C for 24 h. Following this, the reaction mixture was diluted with EtOAc (10 mL) and washed with 0.5% citric acid (3 × 10 mL), distilled water (10 mL) and brine (10 mL). The organic phase was dried over MgSO<sub>4</sub>, concentrated *in vacuo* and the crude residue was purified by flash column chromatography (0–50% EtOAc/Pet.) to afford 7-hydroxy-4-methyl-2*H*-chromen-2-one (4 mg, 0.02 mmol, 2%) as a cream solid. m.p. 179–181 °C; <sup>1</sup>H NMR (700 MHz, CDCl<sub>3</sub>) δ 7.49 (d, *J* = 8.7 Hz, 1H, H-3), 6.88 (d, *J* = 2.5 Hz, 1H, H-4), 6.82 (dd, *J* = 8.7, 2.5 Hz, 1H, H-1), 6.15 (s, 1H, H-9), 2.41 (s, 3H, H-10); <sup>13</sup>C NMR (150 MHz, CDCl<sub>3</sub>) δ 162.0 (C-8), 159.7 (C-2), 155.2 (C-6), 153.3 (C-7), 126.1 (C-3), 113.8 (C-5), 113.2 (C-1), 111.8 (C-9), 103.5 (C-4), 18.9 (C-10); IR (solid) 3127, 2920, 2851, 1677, 1603, 1562 cm<sup>-1</sup>.



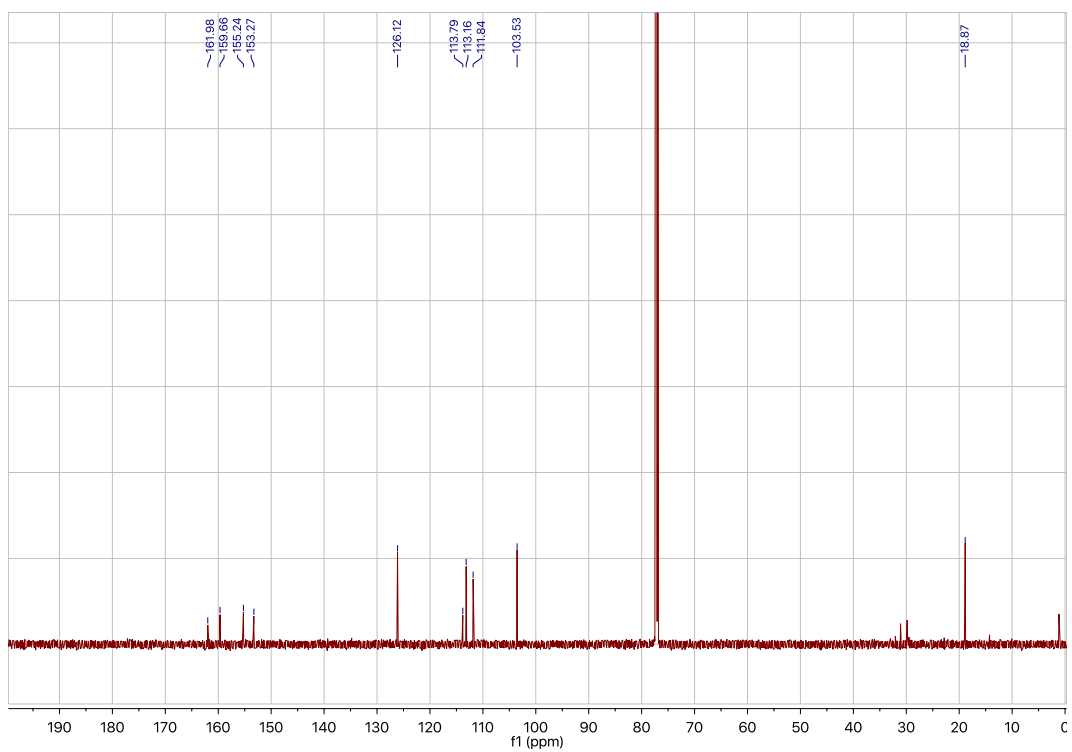
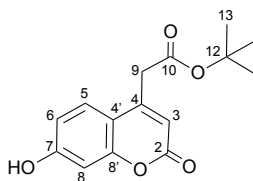


Figure S71.  $^1\text{H}$  and  $^{13}\text{C}$  NMR spectra for 7-hydroxy-4-methyl-2*H*-chromen-2-one **40**.

***Tert*-butyl 2-(7-hydroxy-2-oxo-2*H*-chromen-4-yl)acetate **42**<sup>137</sup>**



A solution of 7-hydroxycoumarin-4-acetic acid **39** (0.21 g, 0.95 mmol) in dry THF (7 mL) was cooled to 0 °C and stirred for 10 mins. To this was added EDC·HCl (0.24 g, 1.3 mmol) and the resulting solution was stirred at 0 °C for a further 30 mins. After this time DMAP (0.14 g, 1.15 mmol) and *tert*-butanol **41** (0.90 mL, 9.4 mmol) were added and the solution was stirred at 21 °C for 24 h. Following this, the reaction mixture was diluted with EtOAc (10 mL) and washed with 0.5% citric acid (3 × 10 mL), distilled water (10 mL) and brine (10 mL). The organic phase was dried over MgSO<sub>4</sub>, concentrated *in vacuo* and the crude residue was purified by preparative TLC (50% EtOAc/Toluene) to afford *tert*-butyl 2-(7-hydroxy-2-oxo-2*H*-chromen-4-yl)acetate (50 mg, 0.18 mmol, 19%) as a pale green solid. m.p. 150–153 °C; <sup>1</sup>H NMR (700 MHz, CDCl<sub>3</sub>) δ 7.46 (d, *J* = 8.5 Hz, 1H, H-5), 6.83 (dd, *J* = 8.5, 1.8 Hz, 2H, H-6, H-8), 6.20 (s, 1H, H-3), 3.65 (s, 2H, H-9), 1.44 (s, 9H, H-13); <sup>13</sup>C NMR (150 MHz, CDCl<sub>3</sub>) δ 168.4 (C-10), 161.7 (C-2), 160.2 (C-7), 155.5 (C-8'), 149.4 (C-4), 126.1 (C-5), 113.5 (C-6), 113.3 (C-3), 112.5 (C-4'), 103.7 (C-8), 82.8 (C-12), 39.8 (C-9), 28.1 (C-13); IR (solid) 3368, 3084, 2977, 2923, 2851, 2162, 2089, 1975, 1910, 1775, 1724, 1688, 1607 cm<sup>-1</sup>; LRMS (ES+) 277 (100, [M+H]<sup>+</sup>); HRMS (ES+) calcd for C<sub>15</sub>H<sub>17</sub>O<sub>5</sub> [M+H]<sup>+</sup> 277.1071, observed 277.1074.

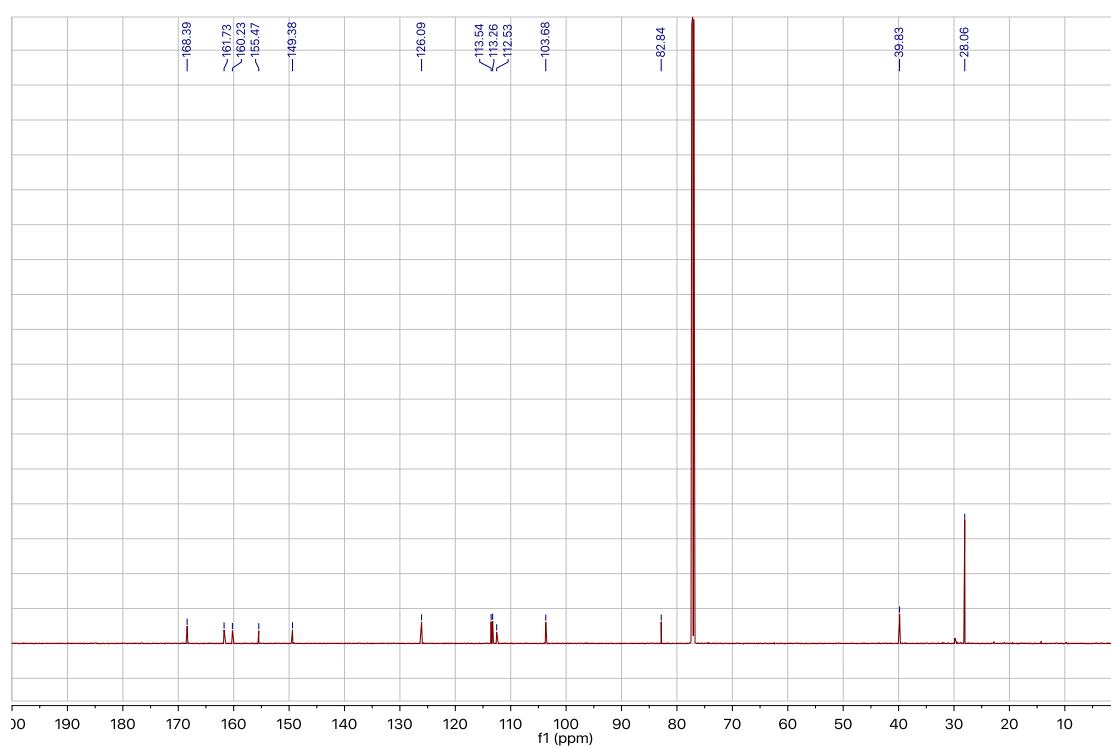
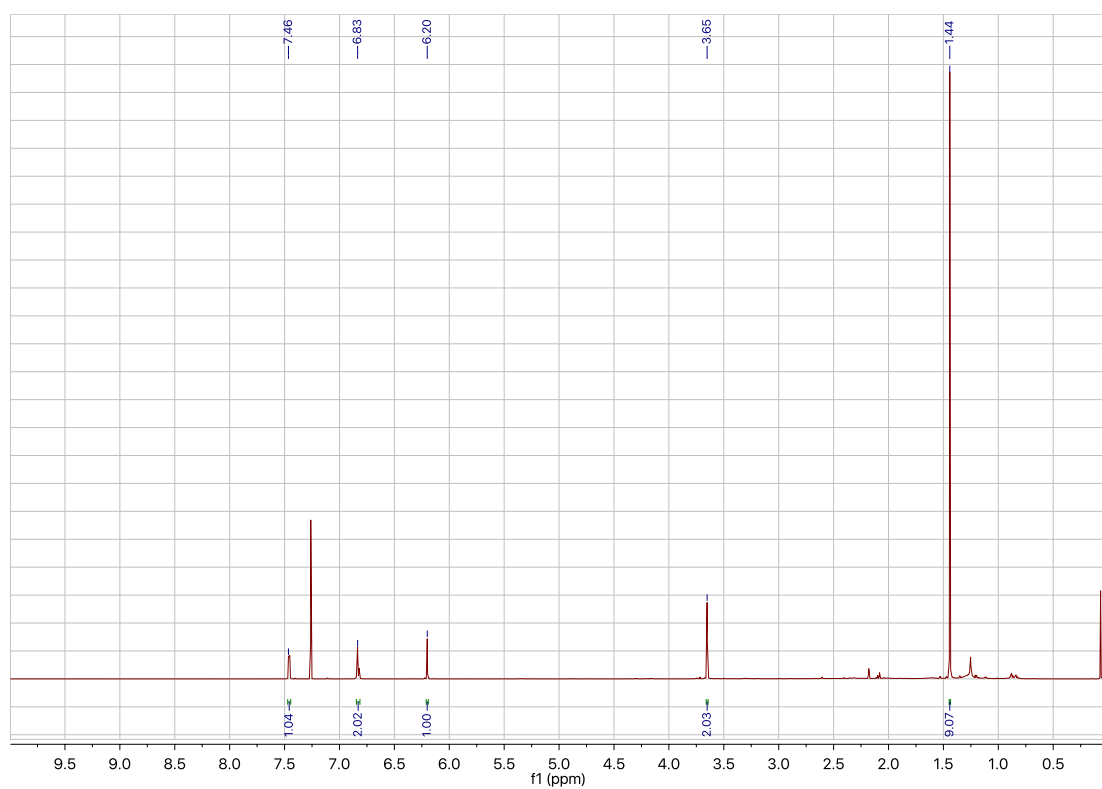
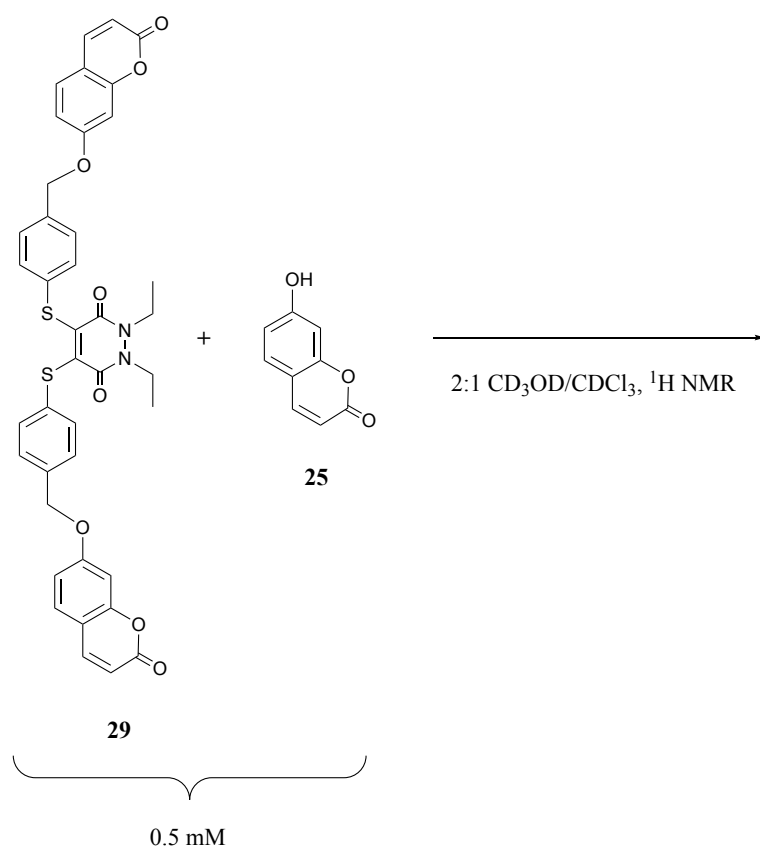


Figure S72.  $^1\text{H}$  and  $^{13}\text{C}$  NMR spectra for *tert*-butyl 2-(7-hydroxy-2-oxo-2*H*-chromen-4-yl)acetate **42**.

## <sup>1</sup>H NMR spectrum of a mixture of umbelliferone–PD **29** and umbelliferone **25**



Umbelliferone–PD **29** (70  $\mu$ L, 5 mM in 2:1 CD<sub>3</sub>OD/CDCl<sub>3</sub>, 1 eq.) was added to umbelliferone **25** (70  $\mu$ L, 5 mM in 2:1 CD<sub>3</sub>OD/CDCl<sub>3</sub>, 1 eq.) to form a mixed solution of umbelliferone–PD **29** and umbelliferone **25** (140  $\mu$ L, 2.5 mM in 2:1 CD<sub>3</sub>OD/CDCl<sub>3</sub>). This solution was diluted 5 times to afford a mixed solution of umbelliferone–PD **29** and umbelliferone **25** (650  $\mu$ L, 0.5 mM in 2:1 CD<sub>3</sub>OD/CDCl<sub>3</sub>) which was subsequently analysed by NMR (Figure S73). <sup>1</sup>H NMR (400 MHz, 2:1 CD<sub>3</sub>OD/CDCl<sub>3</sub>)  $\delta$  7.83 (d,  $J$  = 9.4 Hz, 1.82H), 7.79 (d,  $J$  = 9.4 Hz, 0.67H), 7.51 (d,  $J$  = 8.8 Hz, 1.92H), 7.40 (d,  $J$  = 2.2 Hz, 0.61H), 7.34 (d,  $J$  = 8.0 Hz, 3.98H), 7.15 (d,  $J$  = 8.3 Hz, 4.00H), 6.98 (m, 1.97H), 6.91 (d,  $J$  = 2.5 Hz, 1.95H), 6.79 (m, 0.64H), 6.72 (d,  $J$  = 2.5 Hz, 0.71H), 6.25 (d,  $J$  = 9.5 Hz, 2.02H), 6.18 (d,  $J$  = 9.5 Hz, 0.66H).

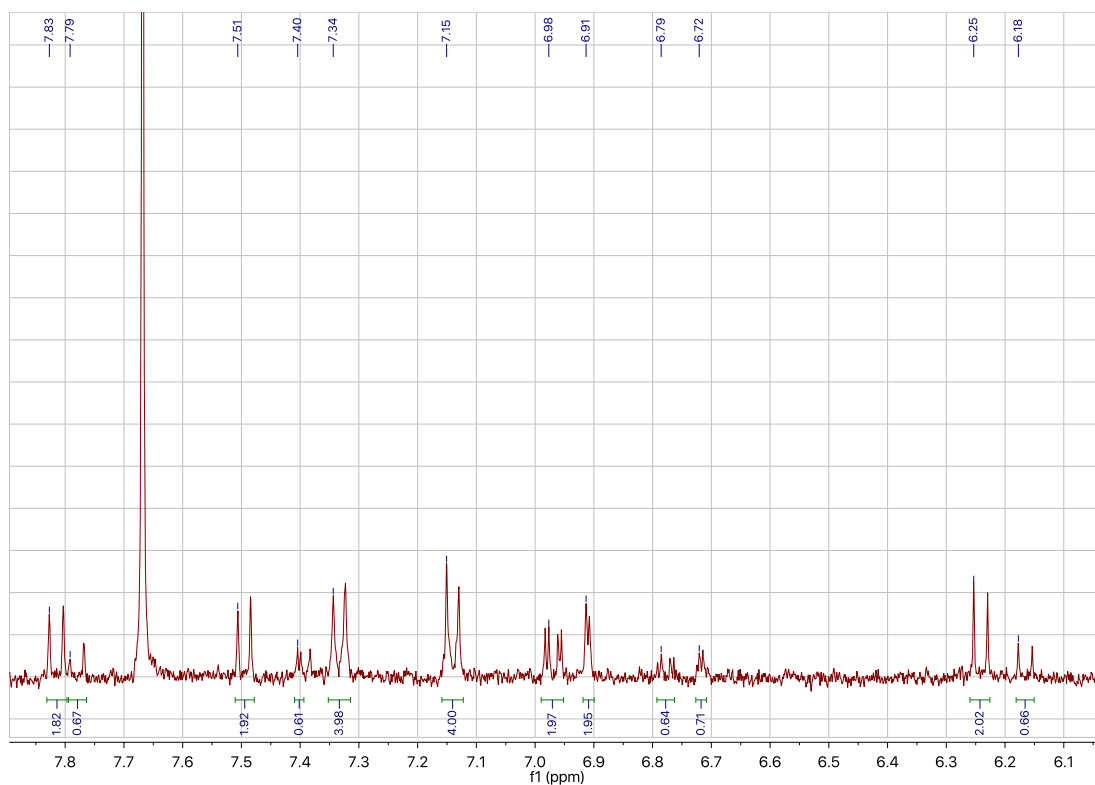
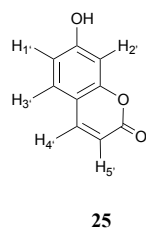
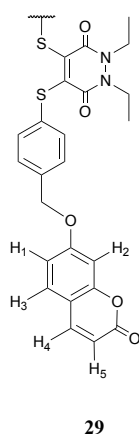


Figure S73. <sup>1</sup>H NMR spectrum of umbelliferone–PD **29** and umbelliferone **25** in 2:1 CD<sub>3</sub>OD/CDCl<sub>3</sub> where the ratio of both **29** and **25** was presumed to be 1:1.

Upon analysing this <sup>1</sup>H NMR spectrum it became clear, however, from the integration values that the two molecules were only near equimolar concentrations, most likely due to the balance error associated with weighing such small amounts of umbelliferone–PD **29**. As the umbelliferone moiety is the only common structural portion shared by both umbelliferone–PD **29** and umbelliferone **25**, it was necessary to only compare the integration values of the peaks arising from this moiety (from 7.83–6.18 ppm) in order to calculate the true ratio of these molecules in solution (Table S1).



Chemical shift and splitting of umbelliferone–PD <b>29</b> peak	Chemical shift and splitting of corresponding umbelliferone <b>25</b> peak	Original ratio of integration values <b>29:25</b>	True ratio of integration values <b>29:25</b>
7.83 ppm, d, H <sub>4</sub>	7.79 ppm, d, H <sub>4</sub> '	1.82:0.67	0.91:0.67 = <b>1.4:1</b>
7.51 ppm, d, H <sub>3</sub>	7.40 ppm, d, H <sub>3</sub> '	1.92:0.61	0.96:0.61 = <b>1.6:1</b>
6.98 ppm, m, H <sub>1</sub>	6.79 ppm, m, H <sub>1</sub> '	1.97:0.64	0.99:0.64 = <b>1.5:1</b>
6.91 ppm, d, H <sub>2</sub>	6.72 ppm, d, H <sub>2</sub> '	1.95:0.71	0.98:0.71 = <b>1.4:1</b>
6.25 ppm, d, H <sub>5</sub>	6.18 ppm, d, H <sub>5</sub> '	2.02:0.66	1.01:0.66 = <b>1.5:1</b>

Table S1. Chemical shifts, splittings of umbelliferone–PD **29** and umbelliferone **25** in addition to the original and true integration value ratios.

As umbelliferone–PD **29** contains two umbelliferone moieties, halving the integrations of the former's peaks was required in order to obtain the true ratio of the two species. The two doublets at 7.34 ppm and 7.15 ppm could be ignored as they comprise the thiophenol moiety aromatic protons umbelliferone–PD **29**, and these have no equivalent peaks on umbelliferone **25**. An average of the ratios shown in red was then taken to obtain the result that in this solution, umbelliferone–PD **29** and umbelliferone



**25** were at a ratio of 1.5:1. This same NMR solution was then analysed on the Waters LC-MS (C18 column) in order to compare the UV area ratios (Figure S74).

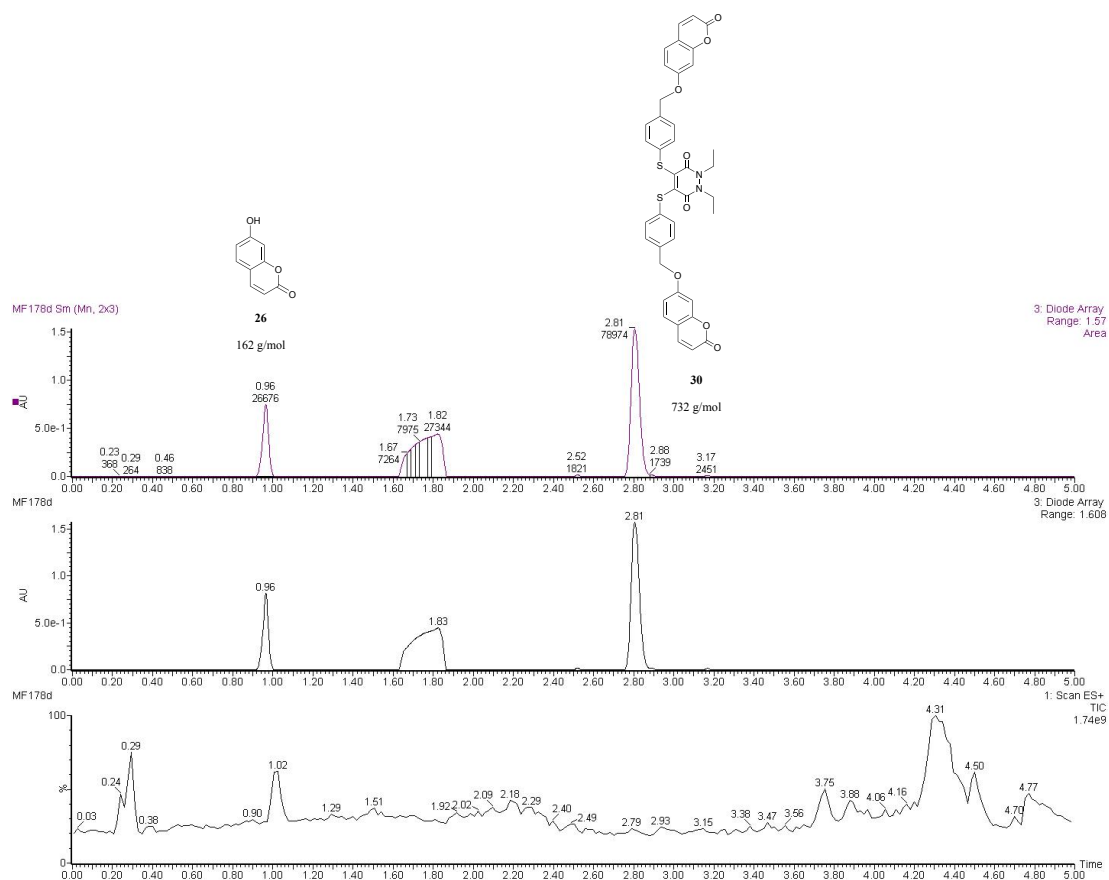
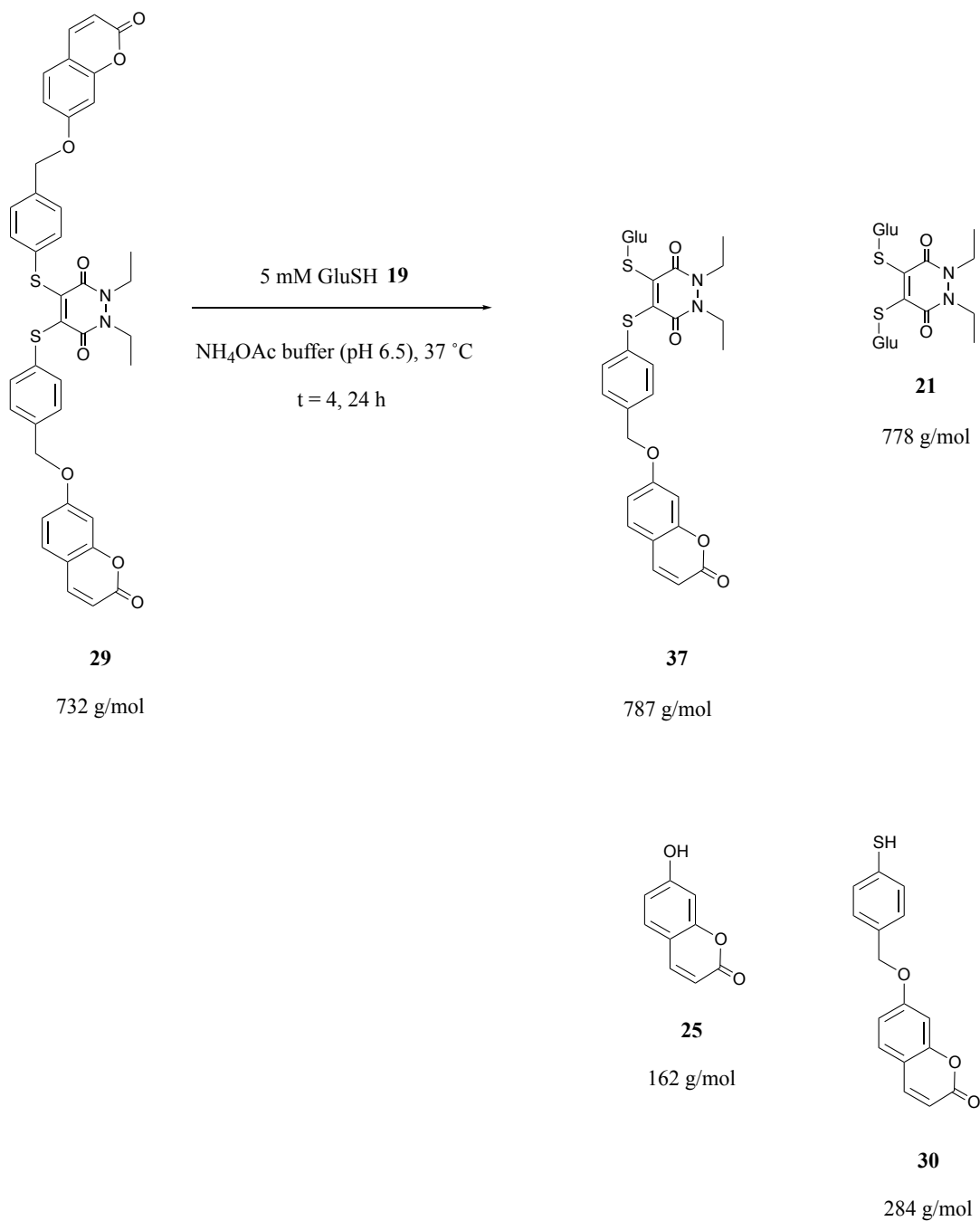


Figure S74. TIC, UV trace and area of UV trace peaks of 1.5:1 solution of umbelliferone–PD **29** and umbelliferone **25** in 2:1 CD<sub>3</sub>OD/CDCl<sub>3</sub>.

As can be seen from the UV trace peaks, umbelliferone **25** has a retention time of 0.96 mins whereas umbelliferone–PD **29** comes off the column at 2.81 mins (an unrelated impurity was observed at 1.83 mins); the UV area ratio of **29:25** is 78,974:26,676. Adjusting this area to take into account the previously calculated ratio of **29:25** in this solution of 1.5:1 yields a true UV area ratio of 52,649:26,676 which simplifies to a ratio of *ca.* 2:1. Therefore if a solution of umbelliferone–PD **29** and umbelliferone **25** were analysed on the LC-MS where the ratio of the two molecules were exactly 1:1, the UV peak area of the former would be approximately twice as great as that of the latter's.

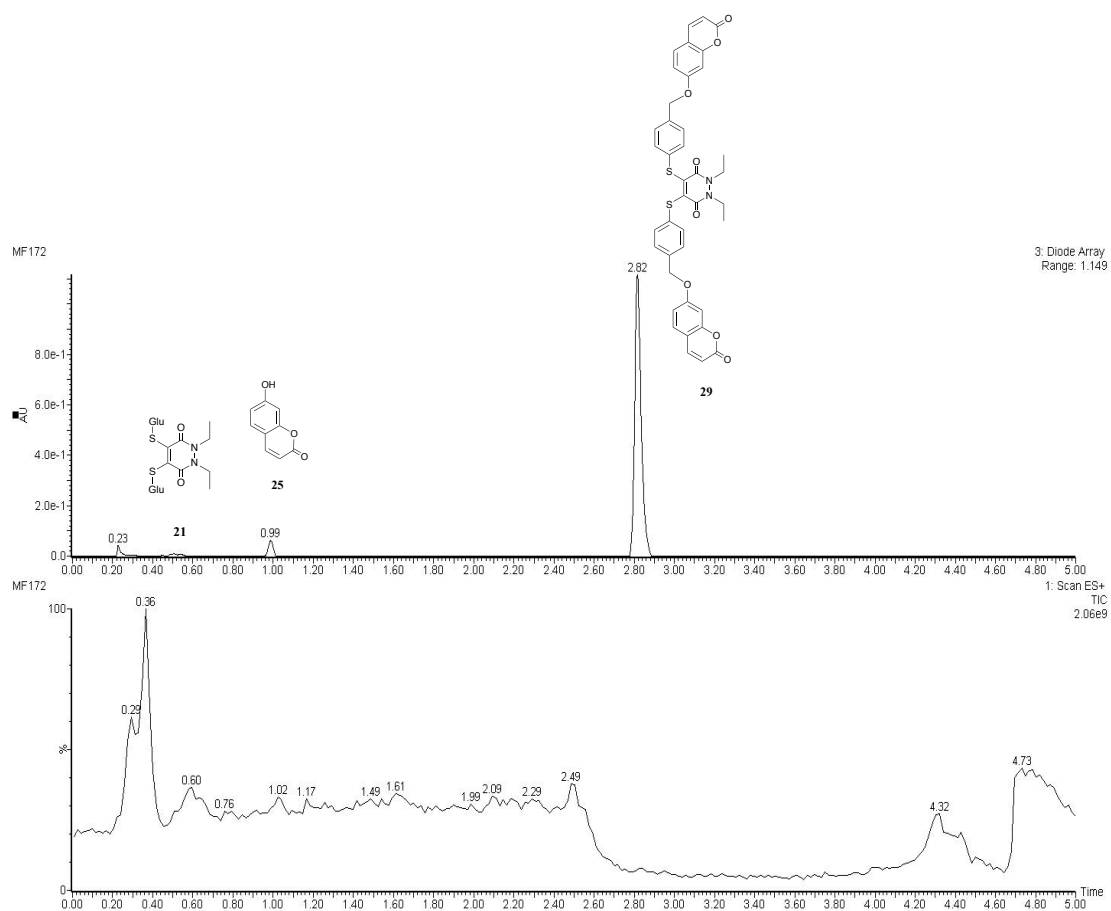
## Incubation of umbelliferone–PD 29 with GluSH (10 eq.)



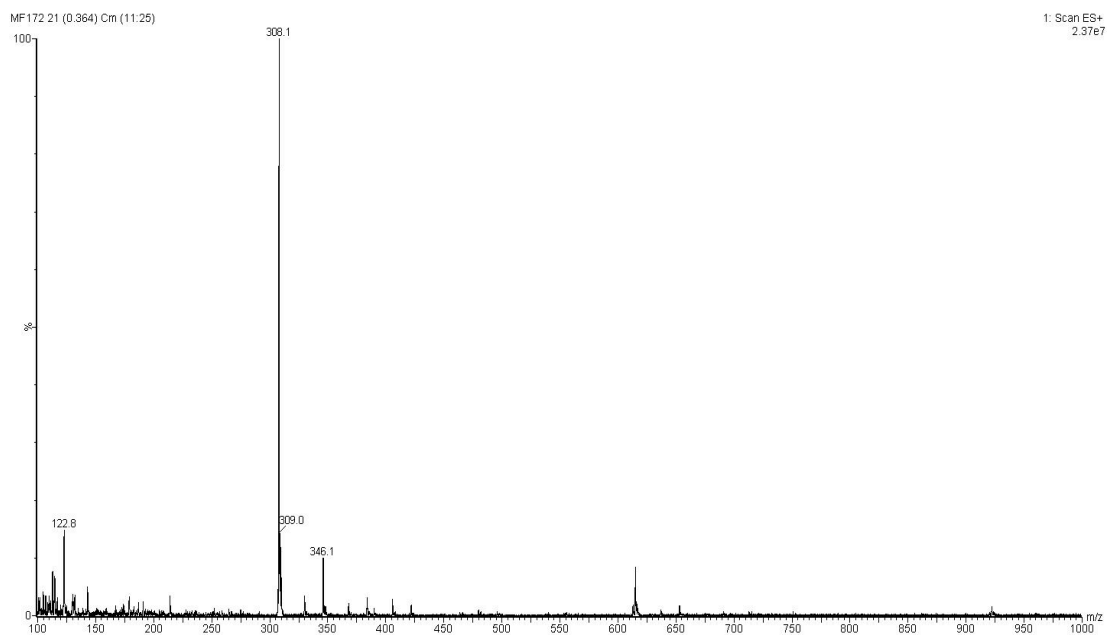
Pyridazinedione **29** (10  $\mu$ L, 10 mM in THF, 1 eq.) was added to GluSH **19** (190  $\mu$ L, 5.3 mM, 10 eq.) in ammonium acetate buffer (50 mM, pH 6.5). The mixture was incubated at 37 °C for 24 h. The samples were analysed by LC-MS at t = 4 and 24 h.

# LC-MS data for t = 4 h

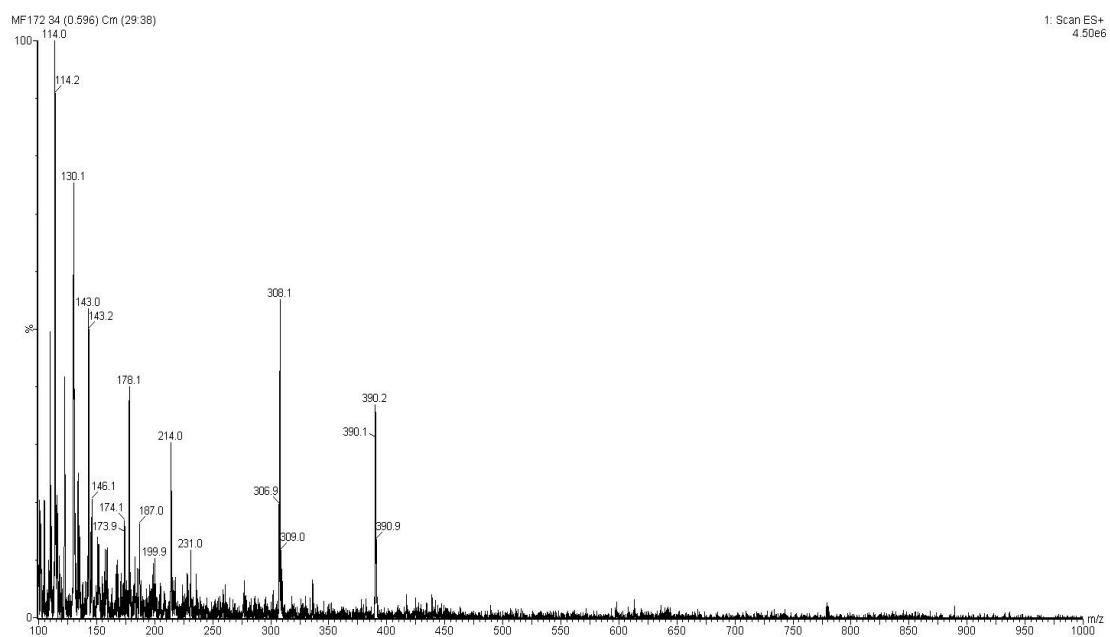
(a)



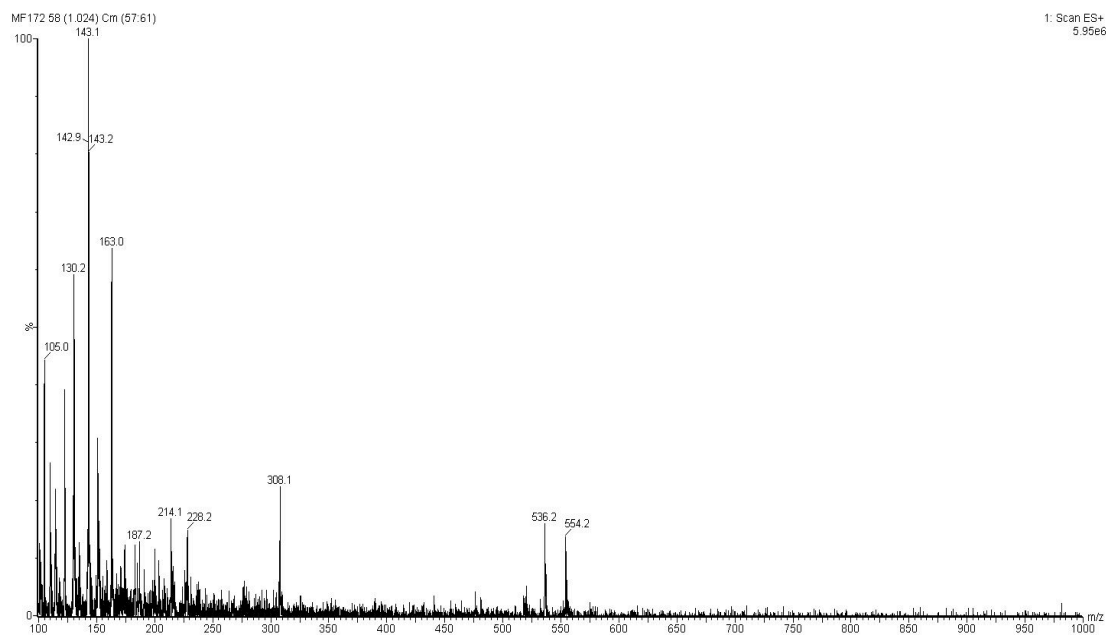
(b)



(c)



(d)



(e)

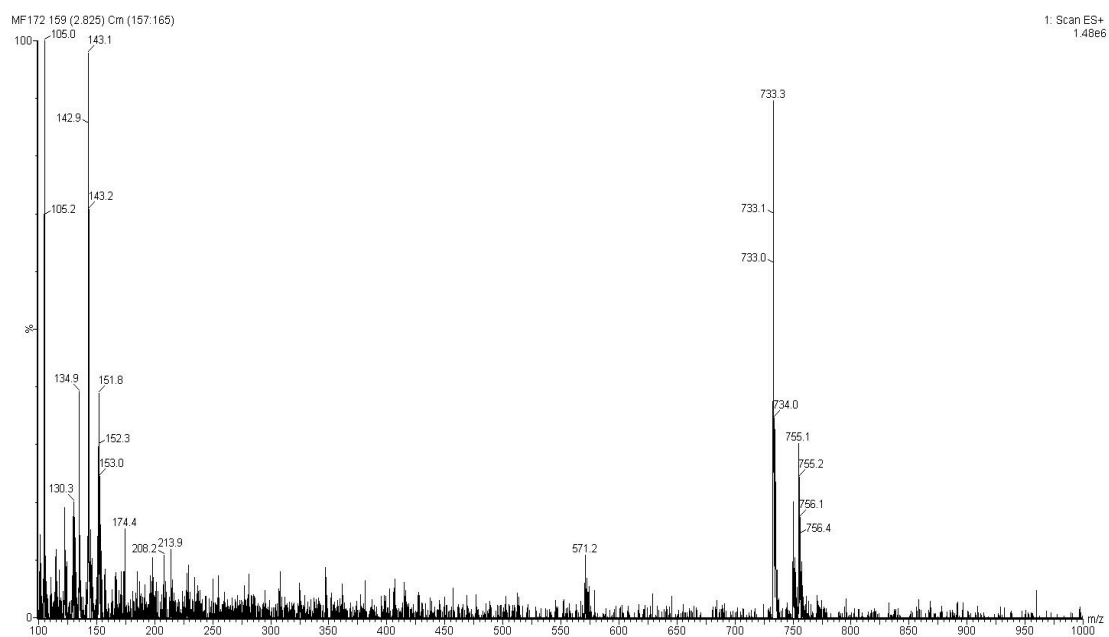
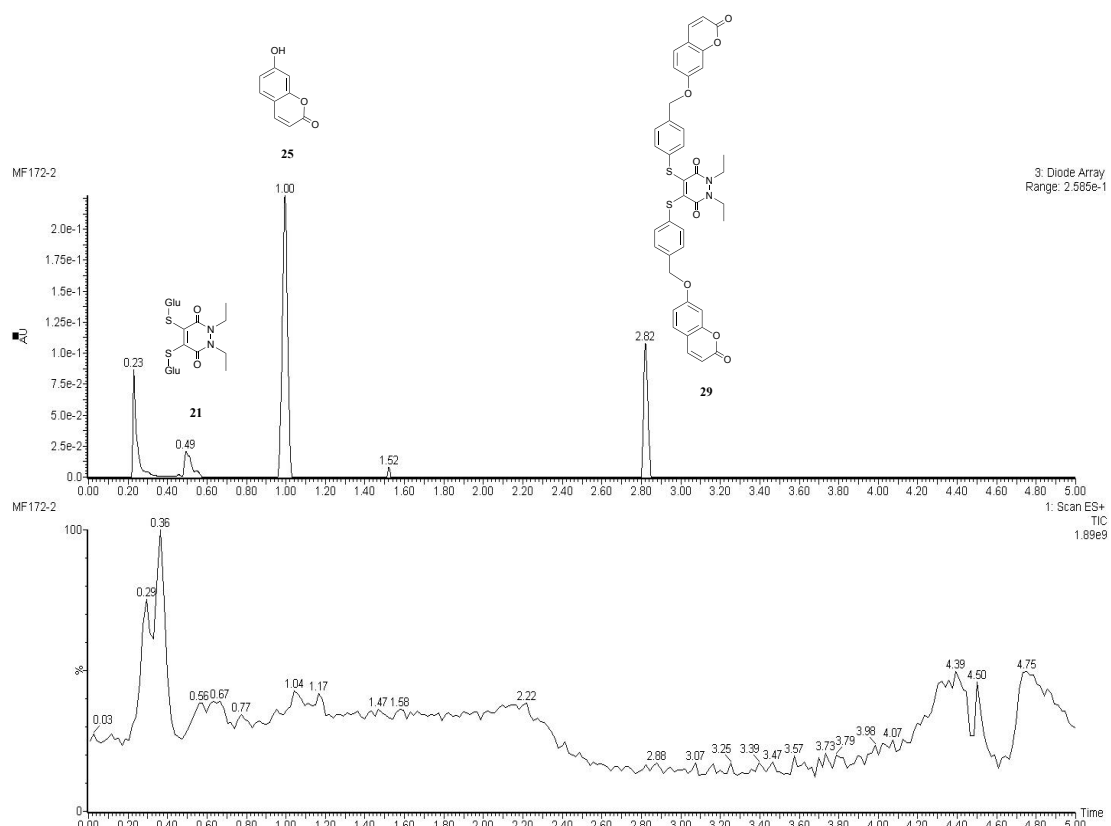


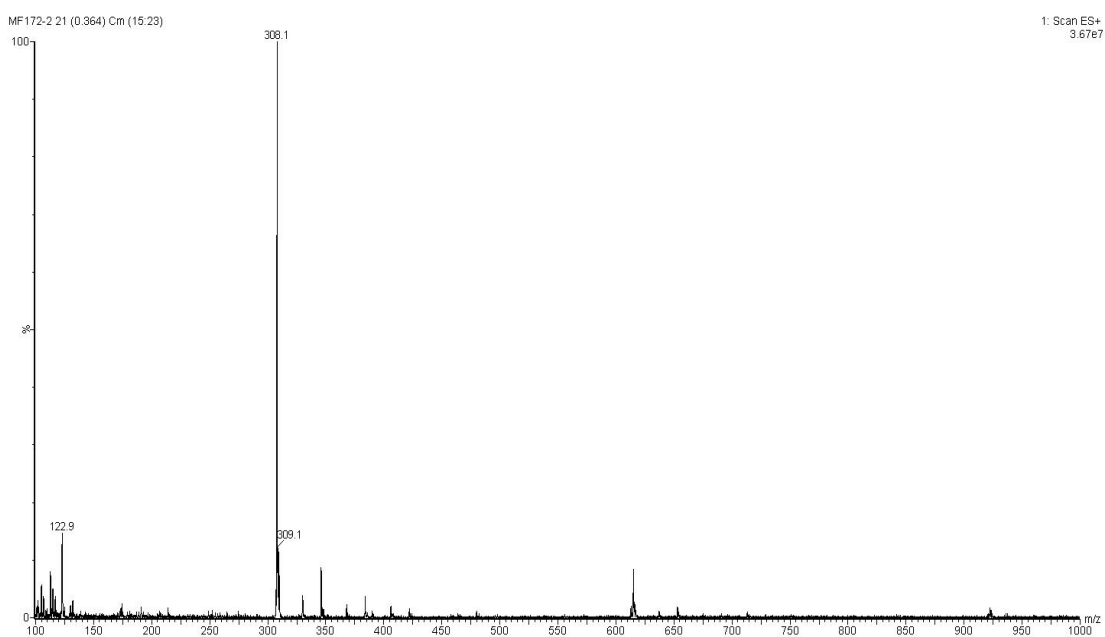
Figure S75. (a) TIC and UV trace at  $t = 4$  h, (b) MS data at 0.23 mins in the UV, (c) at 0.50 mins in the UV, (d) at 0.99 mins in the UV and (e) at 2.82 mins in the UV for PD **29** incubated with GluSH **19** (10 eq.) at pH 6.5.

# LC-MS data for t = 24 h

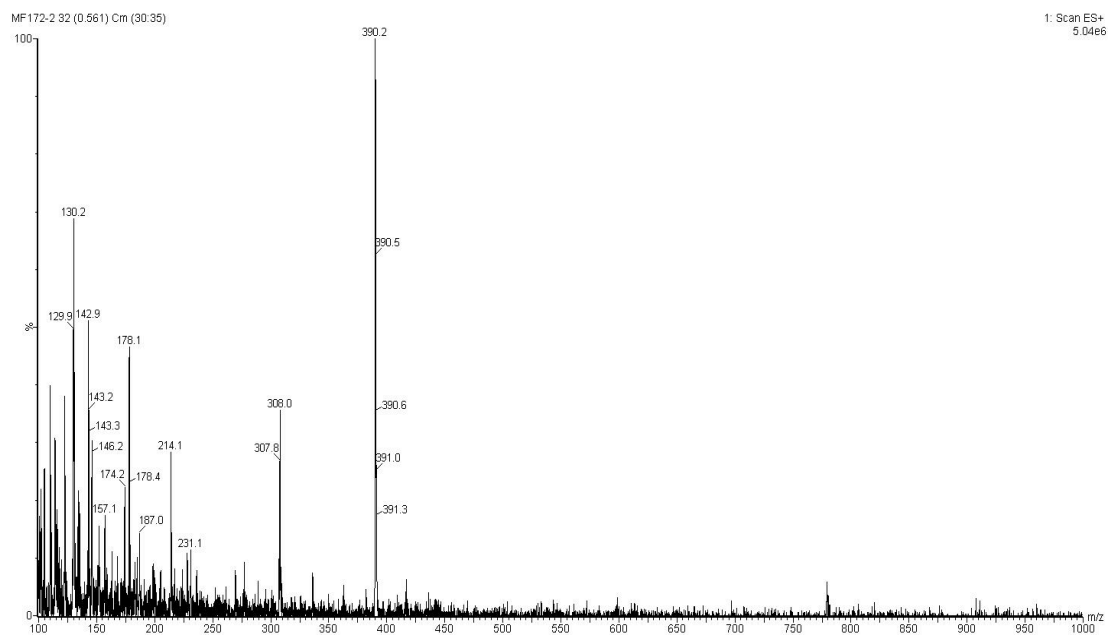
(a)



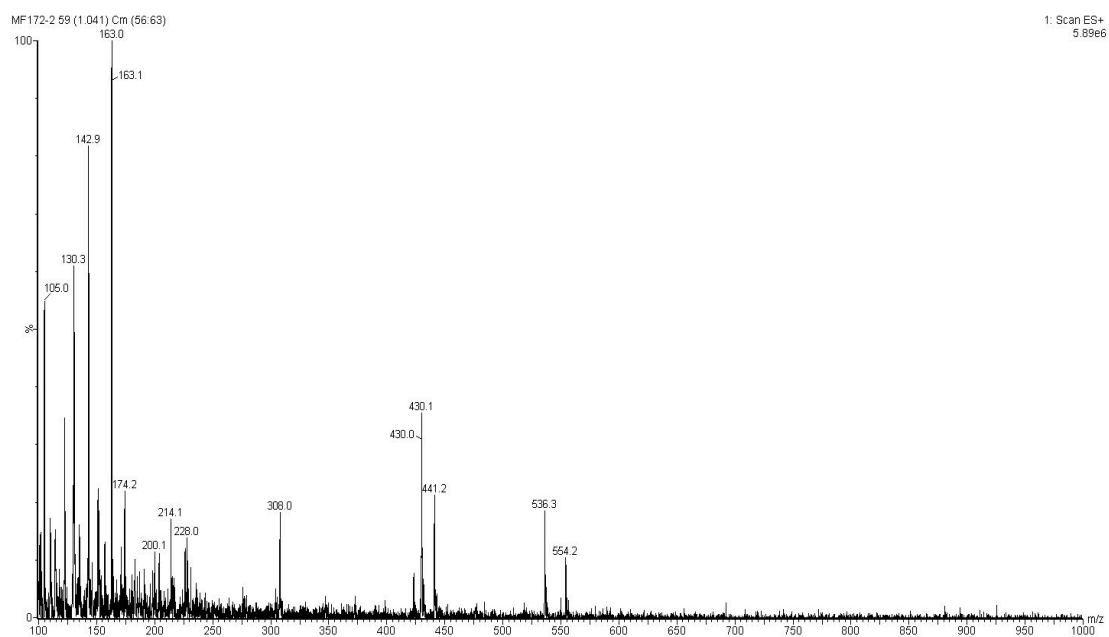
(b)



(c)



(d)



(e)

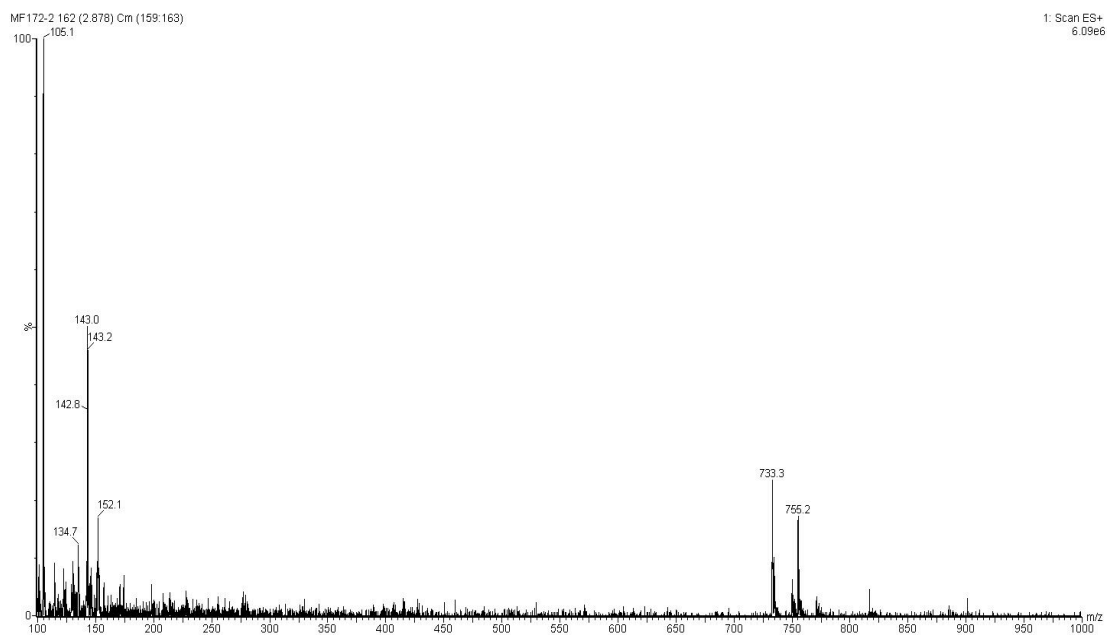
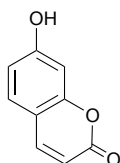


Figure S76. (a) TIC and UV trace at  $t = 24$  h, (b) MS data at 0.23 mins in the UV, (c) at 0.50 mins in the UV, (d) at 1.00 mins in the UV and (e) at 2.82 mins in the UV for PD **29** incubated with GluSH **19** (10 eq.) at pH 6.5.



## UV absorption and fluorescence emission spectroscopy of umbelliferone and umbelliferone–PD (10 eq.) at pH 6.5

### UV absorption of umbelliferone



**25**

A solution of umbelliferone **25** (170  $\mu\text{L}$ , 1 mM in THF) was scanned in the 200–800 nm range using a UV–Vis spectrophotometer in order to obtain the maximum UV absorption for umbelliferone **25**.

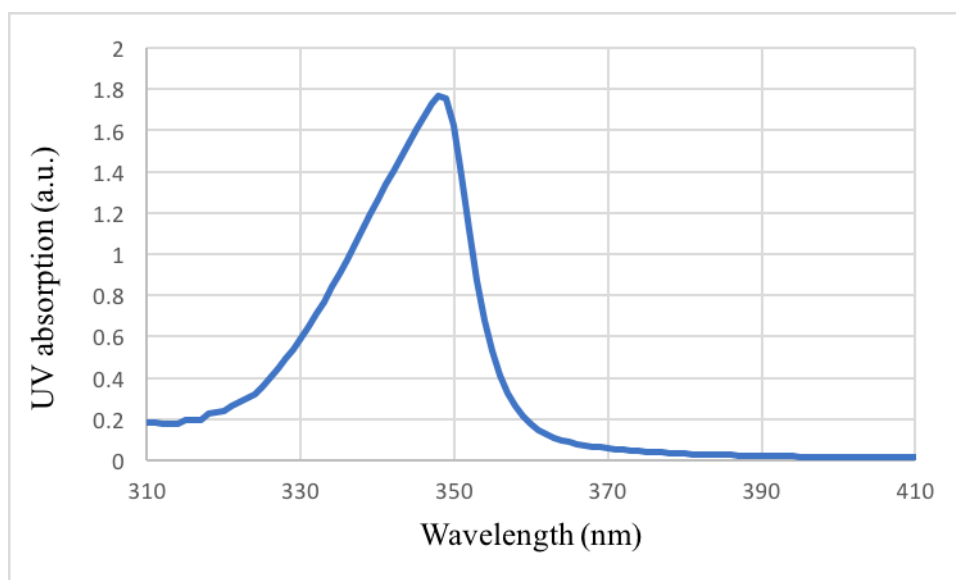
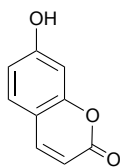


Figure S77. UV absorbance spectrum of umbelliferone **25** in THF. When scanned in the 200–800 nm range, the maximum UV absorption for umbelliferone **25** occurred at 348 nm, and  $\epsilon_{348} = 1770 \text{ M}^{-1} \text{ cm}^{-1}$ .

## Fluorescence emission of umbelliferone



**25**

A solution of umbelliferone **25** (170  $\mu$ L, 1 mM in THF) was excited at 348 nm using a fluorescence spectrophotometer in order to obtain the maximum fluorescence emission for umbelliferone **25**.

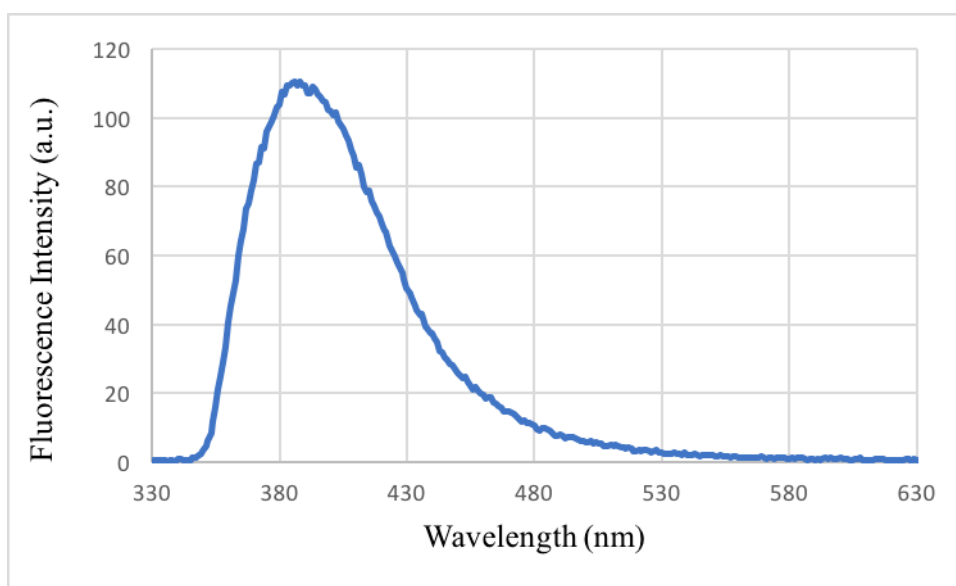
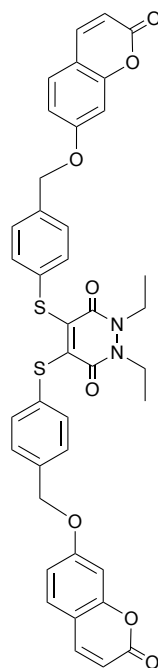


Figure S78. Fluorescence emission spectrum of umbelliferone **25** in THF. When excited at 348 nm, the maximum fluorescence emission for umbelliferone **25** occurred at 388 nm with a maximum intensity of 111 a.u.

## UV absorption of umbelliferone–PD



**29**

A solution of umbelliferone–PD **29** (170  $\mu$ L, 1 mM in THF) was scanned in the 200–800 nm range using a UV–Vis spectrophotometer in order to obtain the maximum UV absorption for umbelliferone–PD **29**.

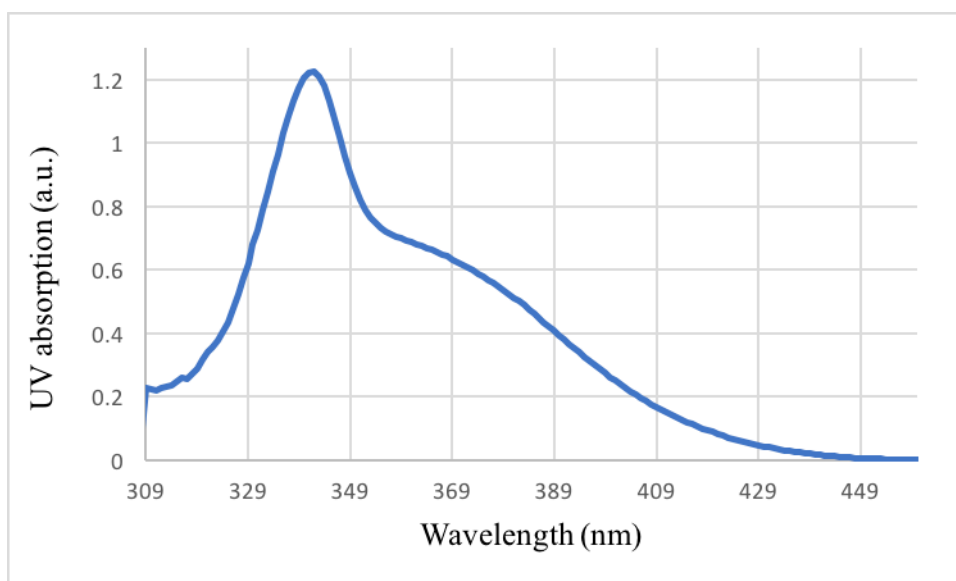
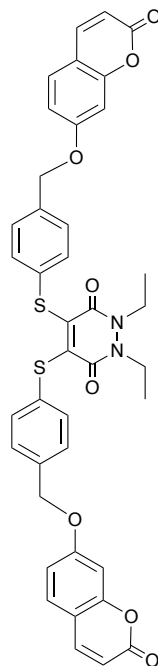


Figure S79. UV absorbance spectrum of umbelliferone-PD **29** in THF. When scanned in the 200–800 nm range, the maximum UV absorption for umbelliferone-PD **29** occurred at 342 nm, and  $\epsilon_{342} = 1230 \text{ M}^{-1}\text{cm}^{-1}$ .

## Fluorescence emission of umbelliferone



**29**

A solution of umbelliferone–PD **29** (170  $\mu$ L, 1 mM in THF) was excited at 342 nm using a fluorescence spectrophotometer in order to obtain the maximum fluorescence emission for umbelliferone–PD **29**.

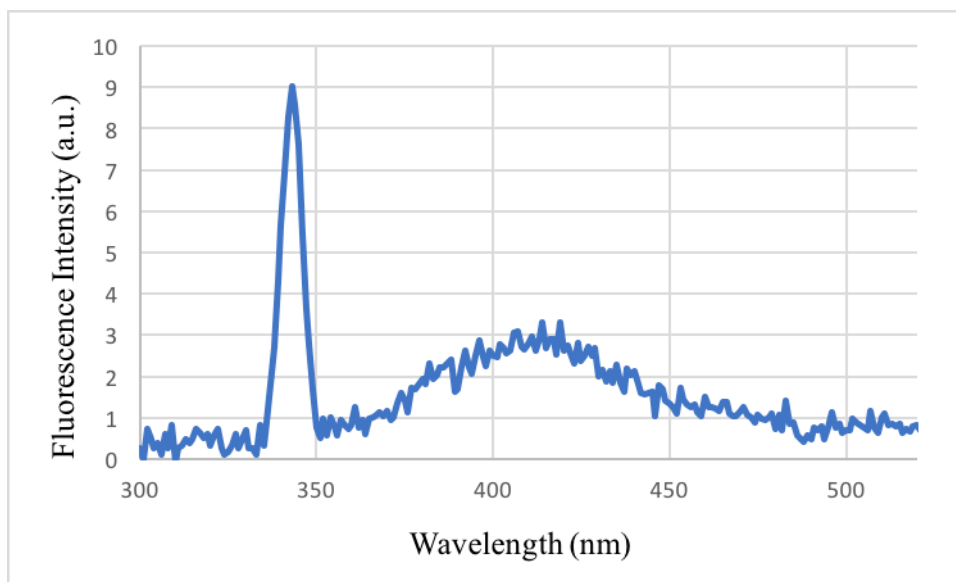
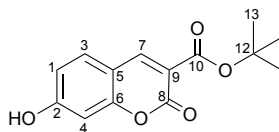


Figure S80. Fluorescence emission spectrum of umbelliferone–PD **29** in THF. When excited at 342 nm, the maximum fluorescence emission of umbelliferone–PD **29** occurred at 344 nm with a maximum intensity of 9 a.u.

***Tert*-butyl 7-hydroxy-2-oxo-2*H*-chromene-3-carboxylate 48<sup>151</sup>**



To a solution of di-*tert*-butyl malonate **47** (0.69 g, 3.2 mmol) and potassium carbonate (1.11 g, 8.03 mmol) in DMF (16 mL), was added 2,4-dihydroxybenzaldehyde **46** (0.22 g, 1.6 mmol), and the reaction mixture was stirred at 80 °C for 19 h. Following this, the reaction mixture was diluted with water (16 mL), 0.1 M citric acid (16 mL), and extracted with EtOAc (3 × 40 mL). The organic extracts were combined and subsequently washed with sat. aq. LiCl solution (40 mL). The organic phase was dried over MgSO<sub>4</sub>, concentrated *in vacuo* and the crude residue was purified by flash column chromatography (10–60% EtOAc/Pet.). The appropriate fractions were then combined and concentrated *in vacuo* to afford *tert*-butyl 7-hydroxy-2-oxo-2*H*-chromene-3-carboxylate (0.05 g, 0.2 mmol, 12%) as a beige solid. m.p. 249–251 °C; <sup>1</sup>H NMR (700 MHz, CDCl<sub>3</sub>) δ 8.39 (s, 1H, H-7), 7.47 (d, *J* = 8.5 Hz, 1H, H-3), 6.91 (d, *J* = 2.2 Hz, 1H, H-4), 6.87 (dd, *J* = 8.5, 2.2 Hz, 1H, H-1), 1.59 (s, 9H, H-13); <sup>13</sup>C NMR (150 MHz, CDCl<sub>3</sub>) δ 162.5 (C-10), 162.3 (C-2), 158.0 (C-8), 157.3 (C-6), 148.5 (C-7), 131.2 (C-3), 115.1 (C-9) 114.3 (C-1), 111.8 (C-5), 103.2 (C-4), 82.6 (C-12), 28.3 (C-13); IR (solid) 3314, 2920, 2851, 1743, 1615, 1558 cm<sup>-1</sup>.

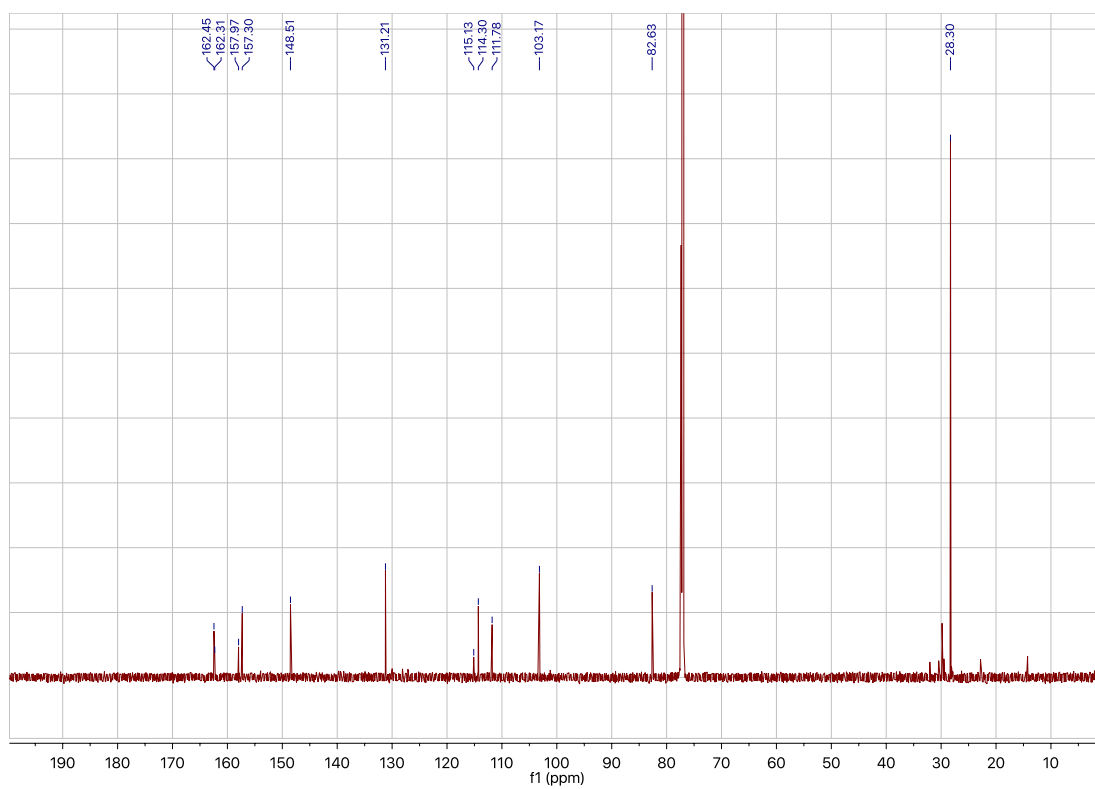
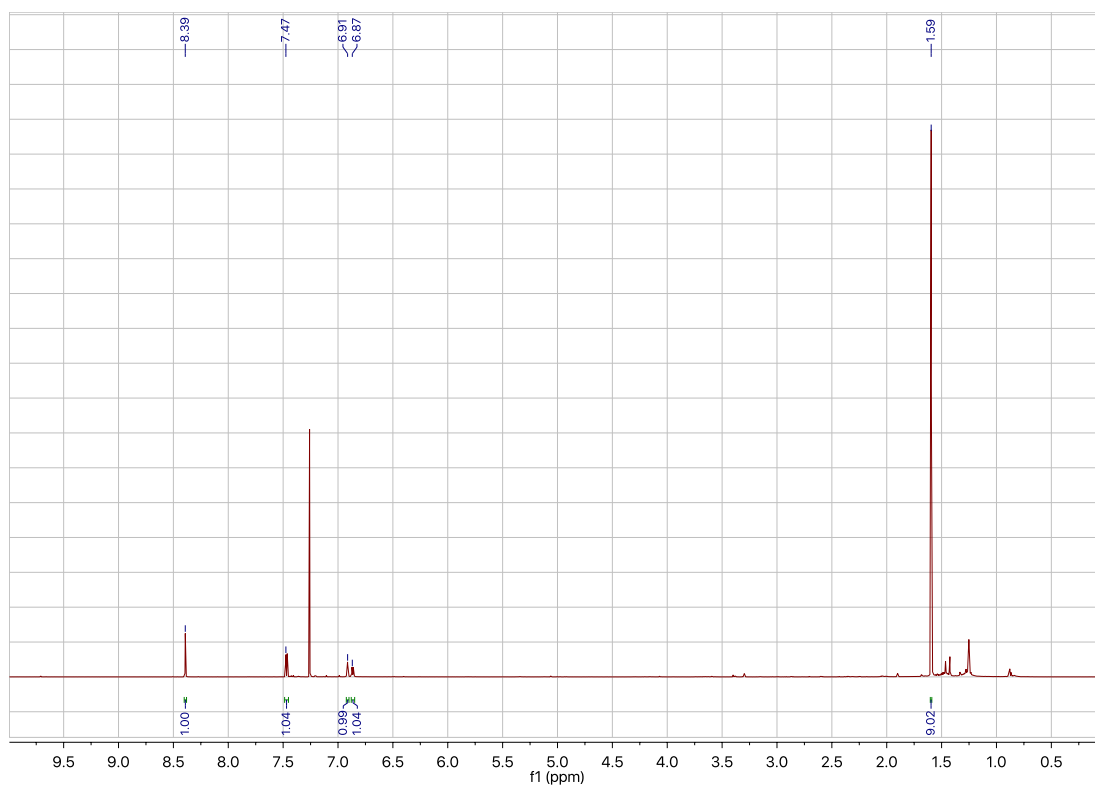
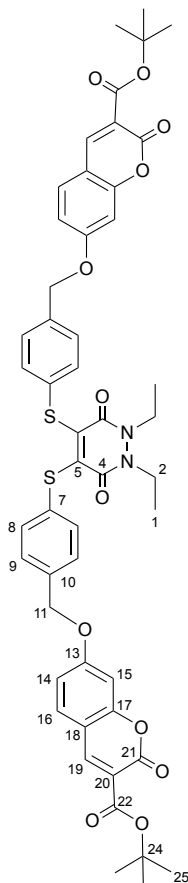


Figure S81.  $^1\text{H}$  and  $^{13}\text{C}$  NMR spectra for *tert*-butyl 7-hydroxy-2-oxo-2*H*-chromene-3-carboxylate **48**.

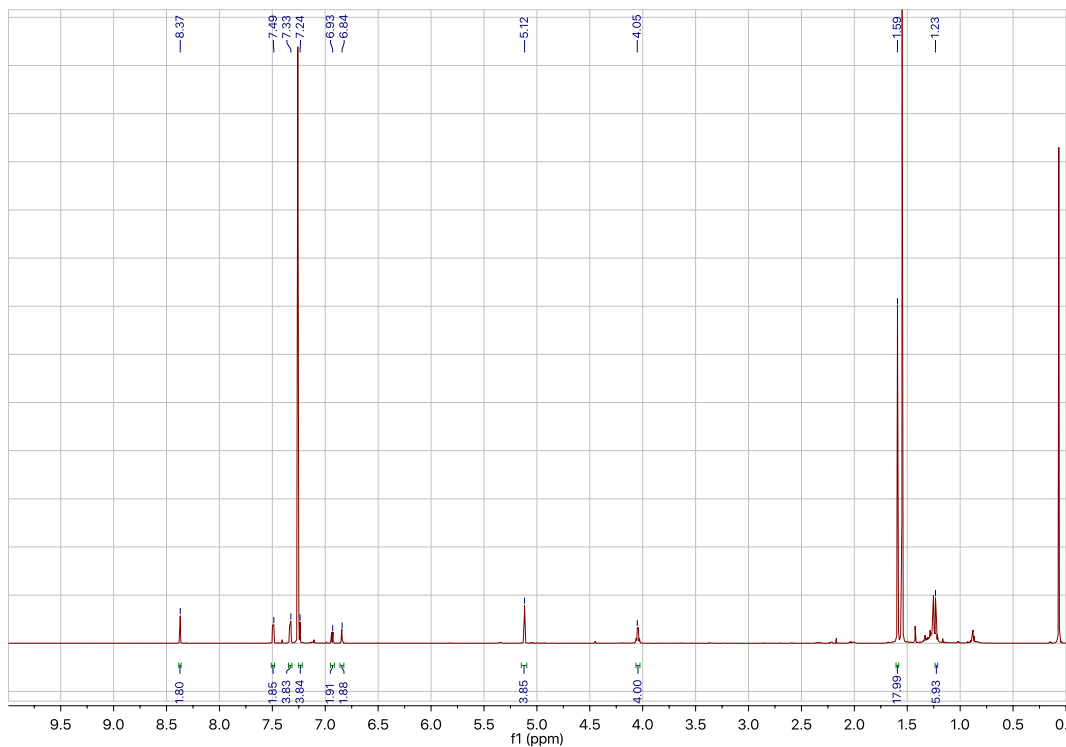
**Di-*tert*-butyl 7,7'-((((1,2-diethyl-3,6-dioxo-1,2,3,6-tetrahydropyridazine-4,5-diyl)bis(sulfanediyl))bis(4,1-phenylene))bis(methylene))bis(oxy))bis(2-oxo-2*H*-chromene-3-carboxylate) 49**



To a solution of 1,2-diethyl-4,5-bis(*p*-tolylthio)-1,2-dihydropyridazine-3,6-dione **33** (0.10 g, 0.24 mmol) in fluorobenzene (7 mL) was added NBS **34** (0.09 g, 0.5 mmol) and AIBN **35** (0.02 g, 0.1 mmol), and the reaction mixture was stirred at 60 °C for 21 h. Following this, the reaction mixture was diluted with fluorobenzene (7 mL) and washed with water (3 × 6 mL) and brine (7 mL). The organic phase was dried over MgSO<sub>4</sub> and concentrated *in vacuo* to afford the crude 4,5-bis((4-(bromomethyl)phenyl)thio)-1,2-diethyl-1,2-dihydropyridazine-3,6-dione **32** (0.11 g total). The crude mixture (0.04 g) was dissolved in dry THF (3 mL) along with cesium carbonate (0.03 g, 0.09 mmol) and *tert*-butyl 7-hydroxy-2-oxo-2*H*-chromene-3-carboxylate **48** (0.02 g, 0.08 mmol), and the reaction mixture was stirred under reflux for 21 h. Following this, the reaction mixture was diluted with water (7 mL) and



extracted with EtOAc (3 × 8 mL). The organic extracts were combined and subsequently washed with brine (8 mL). The organic phase was dried over MgSO<sub>4</sub>, concentrated *in vacuo* and the crude residue was purified by flash column chromatography (20–80% EtOAc/Pet.). The appropriate fractions were then combined and concentrated *in vacuo* to afford di-*tert*-butyl 7,7'-((((1,2-diethyl-3,6-dioxo-1,2,3,6-tetrahydropyridazine-4,5-diyl)bis(sulfanediyl))bis(4,1-phenylene))bis(methylene))bis(oxy))bis(2-oxo-2*H*-chromene-3-carboxylate) (0.02 g, 0.02 mmol, 23%) as a yellow solid. m.p. 83–86 °C; <sup>1</sup>H NMR (700 MHz, CDCl<sub>3</sub>) δ 8.37 (s, 2H, H-19), 7.49 (d, *J* = 8.7 Hz, 2H, H-16), 7.33 (d, *J* = 8.4 Hz, 4H, H-9), 7.24 (d, *J* = 8.4 Hz, 4H, H-8), 6.93 (dd, *J* = 8.7, 2.4 Hz, 2H, H-14), 6.84 (d, *J* = 2.4 Hz, 2H, H-15), 5.12 (s, 4H, H-11), 4.05 (q, *J* = 7.0 Hz, 4H, H-2), 1.59 (s, 18H, H-25), 1.23 (t, *J* = 7.0 Hz, 6H, H-1); <sup>13</sup>C NMR (150 MHz, CDCl<sub>3</sub>)\* δ 163.7 (C-13), 162.3 (C-22), 157.4 (C-21), 157.3 (C-17), 155.7 (C-4), 148.0 (C-19), 141.9 (C-5), 135.3 (C-10), 132.9 (C-7), 131.3 (C-8), 130.7 (C-16), 128.2 (C-9), 116.0 (C-20), 114.1 (C-14), 112.1 (C-18), 101.5 (C-15), 82.6 (C-24), 70.2 (C-11), 41.4 (C-2), 28.3 (C-25), 12.9 (C-1); IR (solid) 2924, 2854, 1748, 1606 cm<sup>-1</sup>; LRMS (ES<sup>+</sup>) 933 (100, [M+H]<sup>+</sup>); HRMS (ES<sup>+</sup>) calcd for C<sub>50</sub>H<sub>49</sub>N<sub>2</sub>O<sub>12</sub>S<sub>2</sub> [M+H]<sup>+</sup> 933.2727, observed 933.2778.



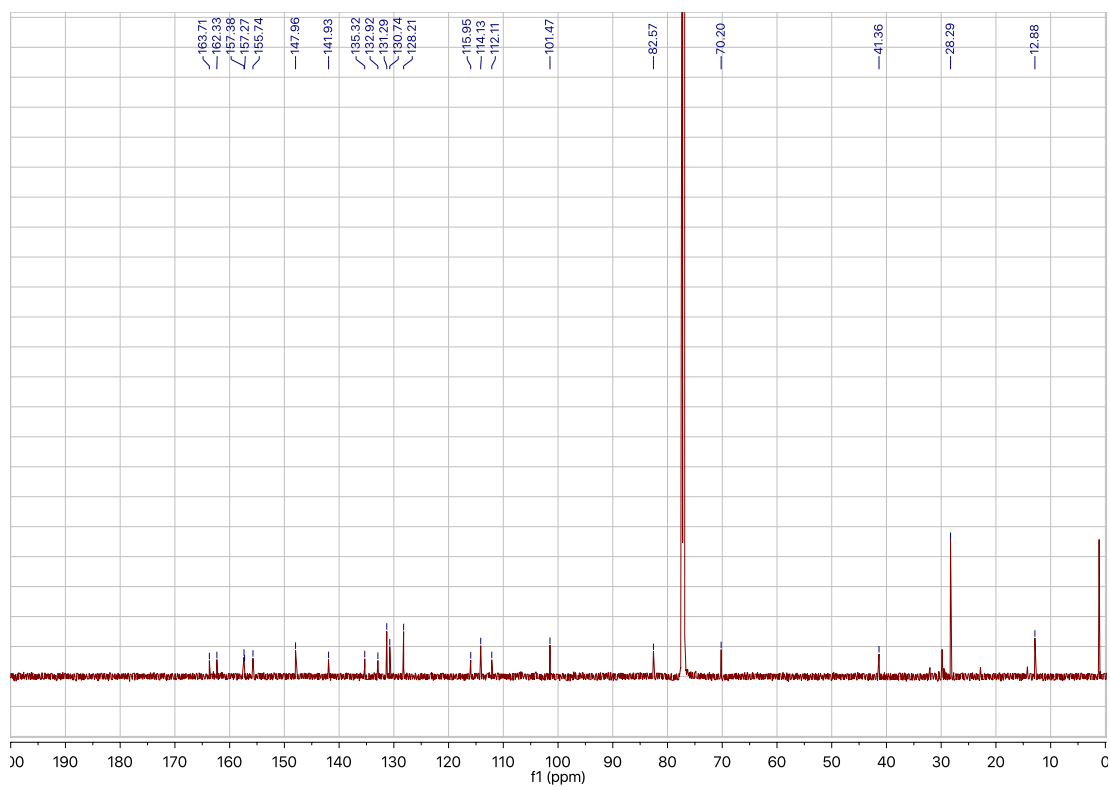
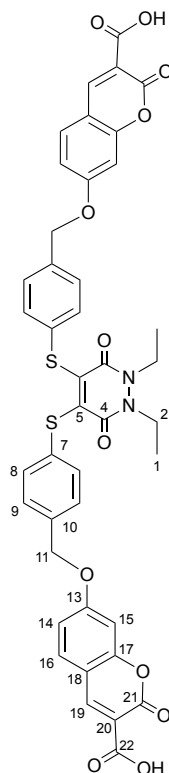


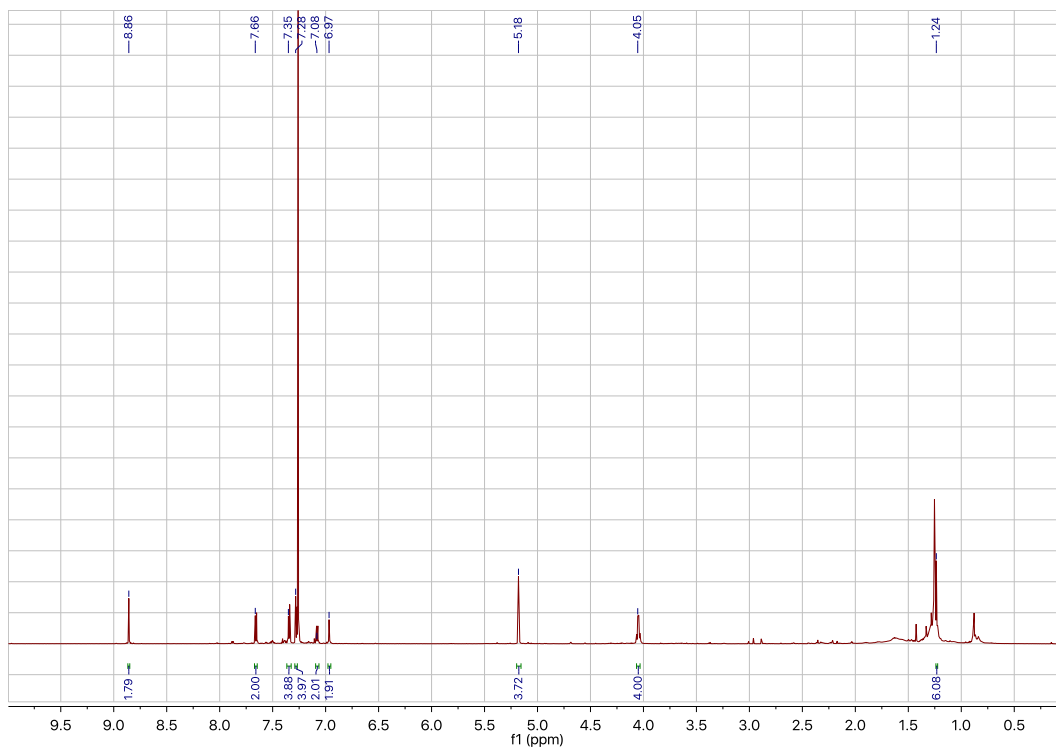
Figure S82.  $^1\text{H}$  and  $^{13}\text{C}$  NMR spectra for di-*tert*-butyl 7,7'-((((1,2-diethyl-3,6-dioxo-1,2,3,6-tetrahydropyridazine-4,5-diyl)bis(sulfanediy))bis(4,1-phenylene))bis(methylene))bis(oxy))bis(2-oxo-2*H*-chromene-3-carboxylate) **49**. \*29.8 (H grease), 1.15 (silicon grease).

**7,7'-((((1,2-Diethyl-3,6-dioxo-1,2,3,6-tetrahydropyridazine-4,5-diyl)bis(sulfanediyl))bis(4,1-phenylene))bis(methylene))bis(oxy))bis(2-oxo-2*H*-chromene-3-carboxylic acid) 45**



Di-*tert*-butyl 7,7'-((((1,2-diethyl-3,6-dioxo-1,2,3,6-tetrahydropyridazine-4,5-diyl)bis(sulfanediyl))bis(4,1-phenylene))bis(methylene))bis(oxy))bis(2-oxo-2*H*-chromene-3-carboxylate) **49** (11 mg, 0.010 mmol) was dissolved in TFA (0.25 mL) and CH<sub>2</sub>Cl<sub>2</sub> (0.75 mL), and stirred at 21 °C for 4 h. Following this, the reaction mixture was concentrated *in vacuo* with toluene co-evaporation (3 × 20 mL, as an azeotrope) to afford 7,7'-((((1,2-diethyl-3,6-dioxo-1,2,3,6-tetrahydropyridazine-4,5-diyl)bis(sulfanediyl))bis(4,1-phenylene))bis(methylene))bis(oxy))bis(2-oxo-2*H*-chromene-3-carboxylic acid) (10 mg, 0.010 mmol, quant.) as a yellow solid. d.t. 195–198 °C; <sup>1</sup>H NMR (700 MHz, CDCl<sub>3</sub>) δ 8.86 (s, 2H, H-19), 7.66 (d, *J* = 8.8 Hz, 2H, H-16), 7.35 (d, *J* = 8.5 Hz, 4H, H-9), 7.28 (d, *J* = 8.5 Hz, 4H, H-8), 7.08 (dd, *J* = 8.8, 2.4 Hz, 2H, H-14), 6.97 (d, *J* = 2.4 Hz, 2H, H-15), 5.18 (s, 4H, H-11), 4.05 (q, *J* = 7.0 Hz, 4H, H-2), 1.24 (t, *J* = 7.0 Hz, 6H, H-1); <sup>13</sup>C NMR (150 MHz, CDCl<sub>3</sub>) δ 165.1 (C-13), 164.6 (C-22), 163.1 (C-21), 157.0 (C-17), 155.7 (C-4), 151.3 (C-19), 142.1

(C-5), 134.8 (C-10), 133.4 (C-7), 131.9 (C-16), 131.4 (C-8), 128.2 (C-9), 115.8 (C-14), 112.7 (C-18), 111.4 (C-20), 102.0 (C-15), 70.6 (C-11), 41.4 (C-2), 12.9 (C-1); IR (solid) 3056, 2926, 2853, 1787, 1717, 1596  $\text{cm}^{-1}$ ; LRMS (ES+) 821 (100,  $[\text{M}+\text{H}]^+$ ); HRMS (ES+) calcd for  $\text{C}_{42}\text{H}_{33}\text{N}_2\text{O}_{12}\text{S}_2$   $[\text{M}+\text{H}]^+$  821.1450, observed 821.1475.



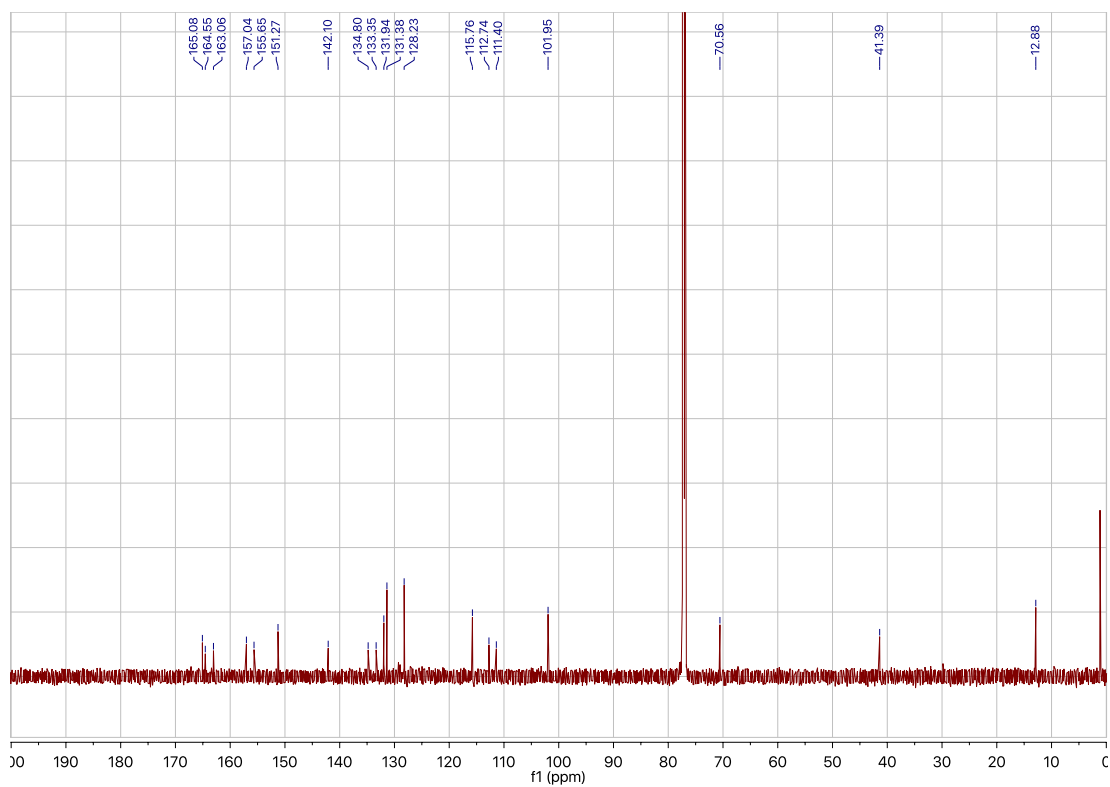
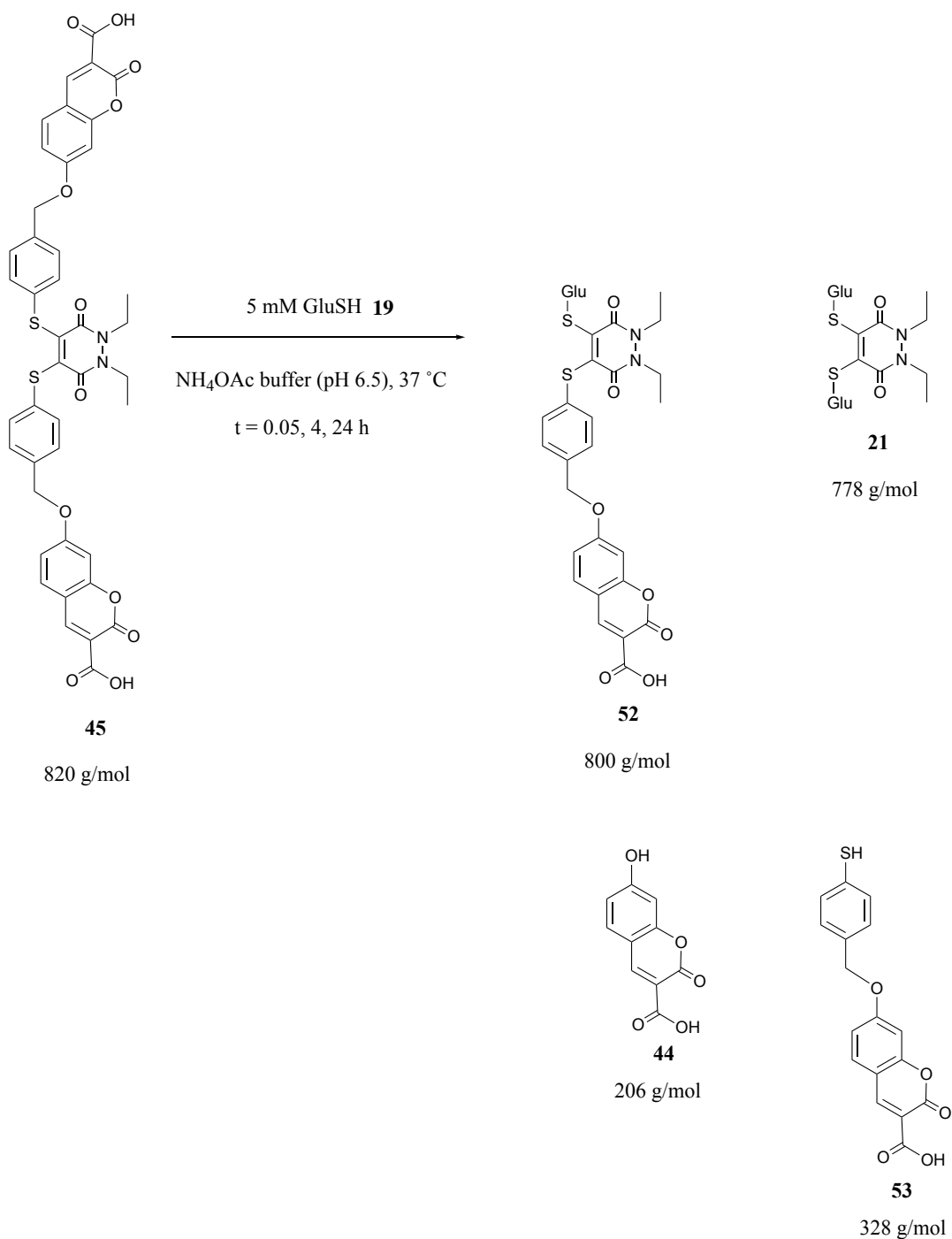


Figure S83.  $^1\text{H}$  and  $^{13}\text{C}$  NMR spectra for 7,7'-((((1,2-diethyl-3,6-dioxo-1,2,3,6-tetrahydropyridazine-4,5-diyl)bis(sulfanediy))bis(4,1-phenylene))bis(methylene))bis(oxy))bis(2-oxo-2*H*-chromene-3-carboxylic acid) **45**.

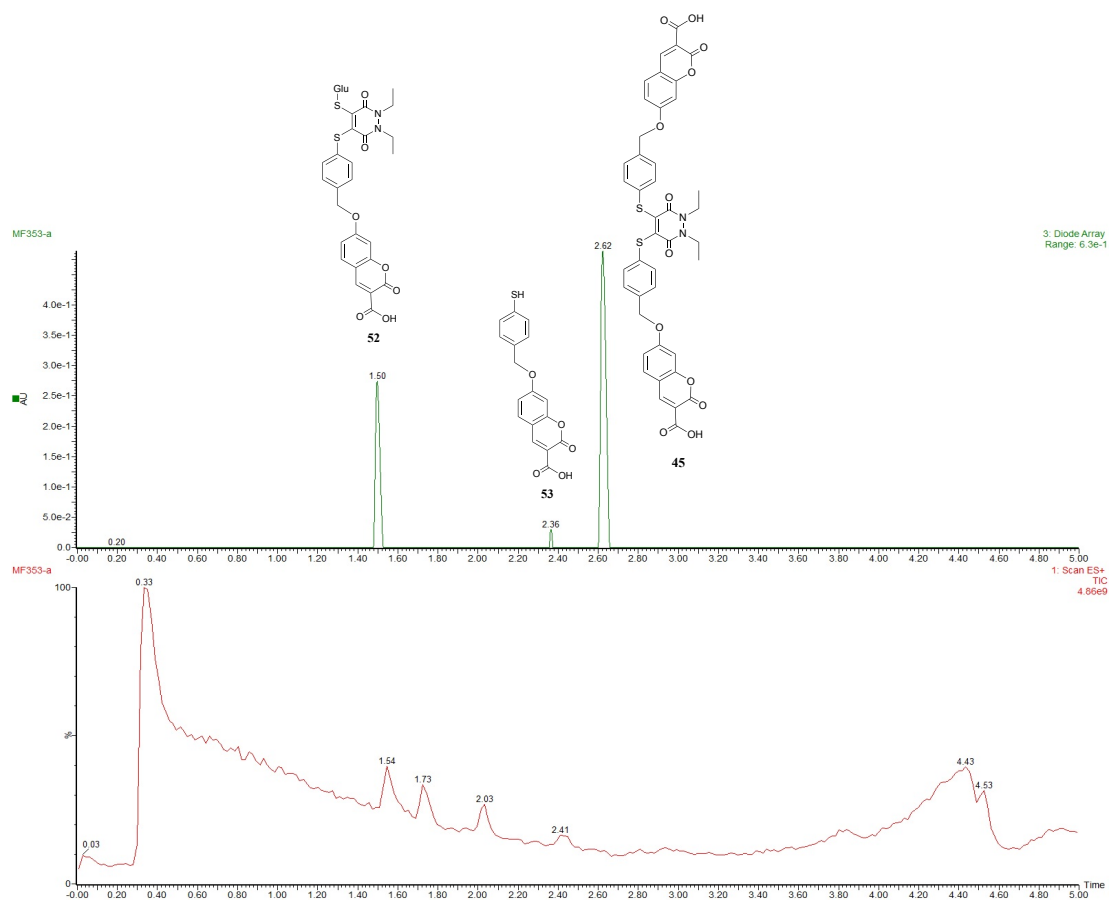
## Incubation of carboxylic acid umbelliferone–PD 45 with GluSH (10 eq.) at pH 6.5



PD 45 (15  $\mu$ L, 10 mM in DMSO, 1 eq.) was added to GluSH 19 (285  $\mu$ L, 5.3 mM, 10 eq.) in ammonium acetate buffer (50 mM, pH 6.5). The mixture was incubated at 37 °C for 24 h. The samples were analysed by LC-MS at t = 0.05, 4 and 24 h.

# LC-MS data for t = 0.05 h

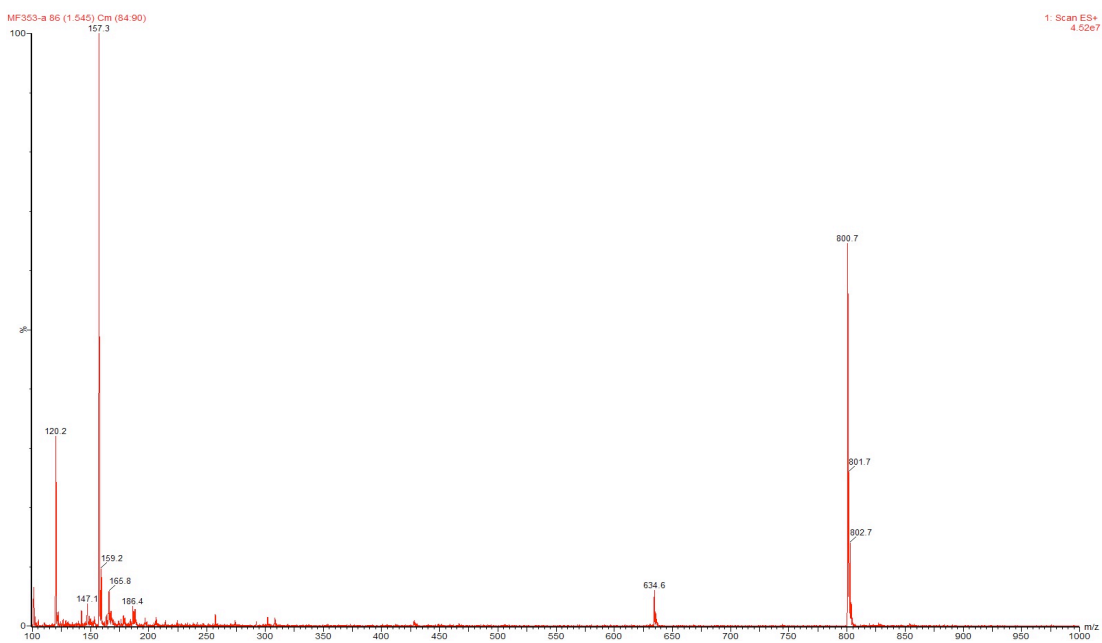
(a)



(b)

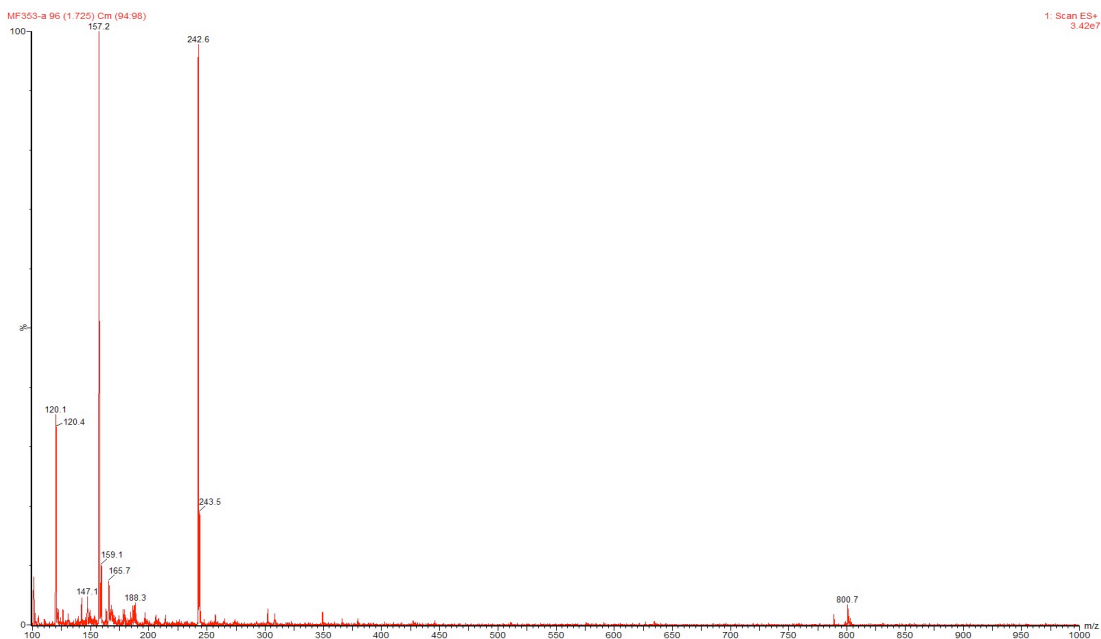


(c)

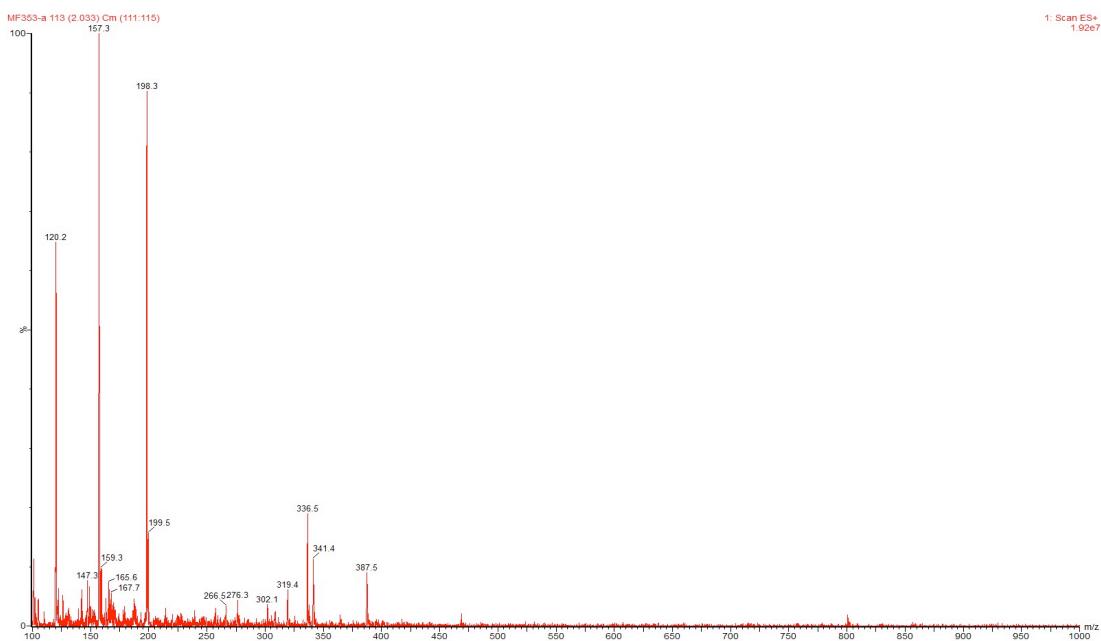




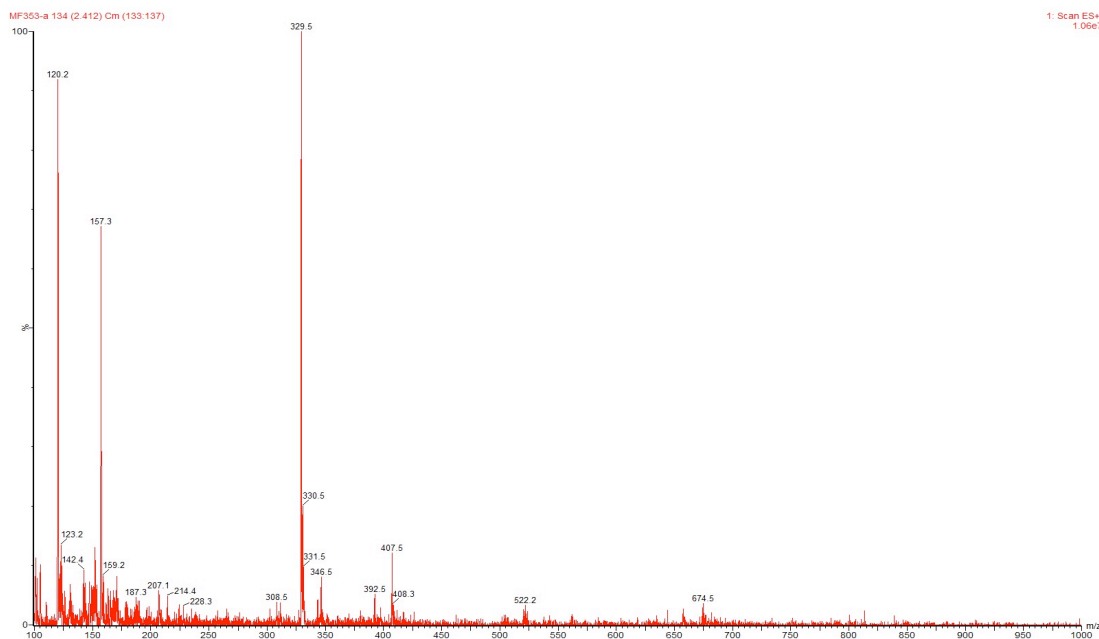
(d)



(e)



(f)



(g)

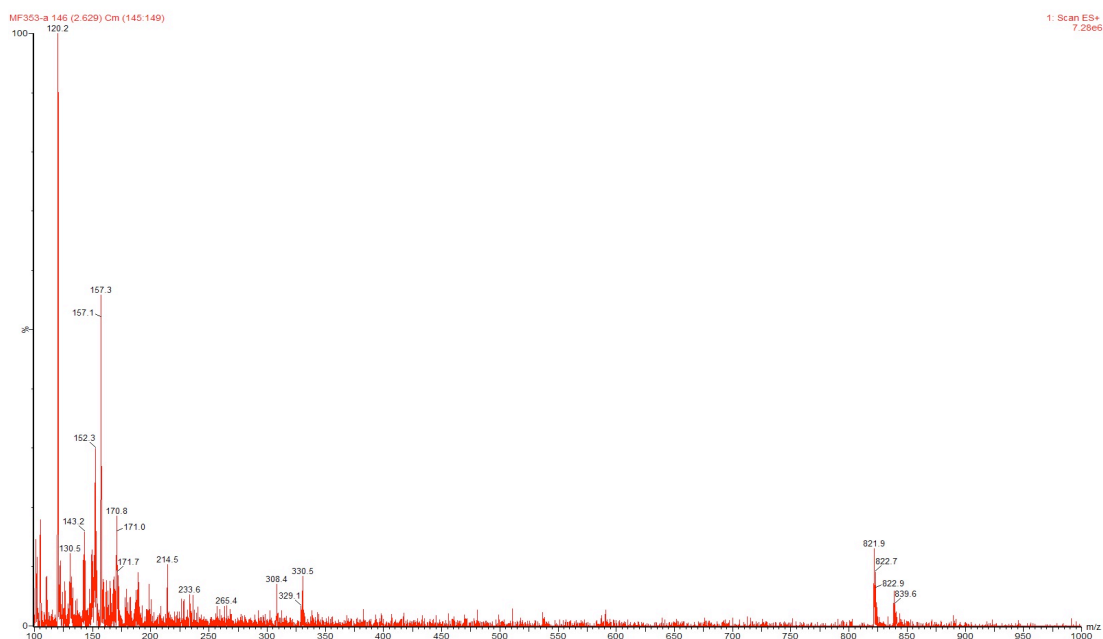
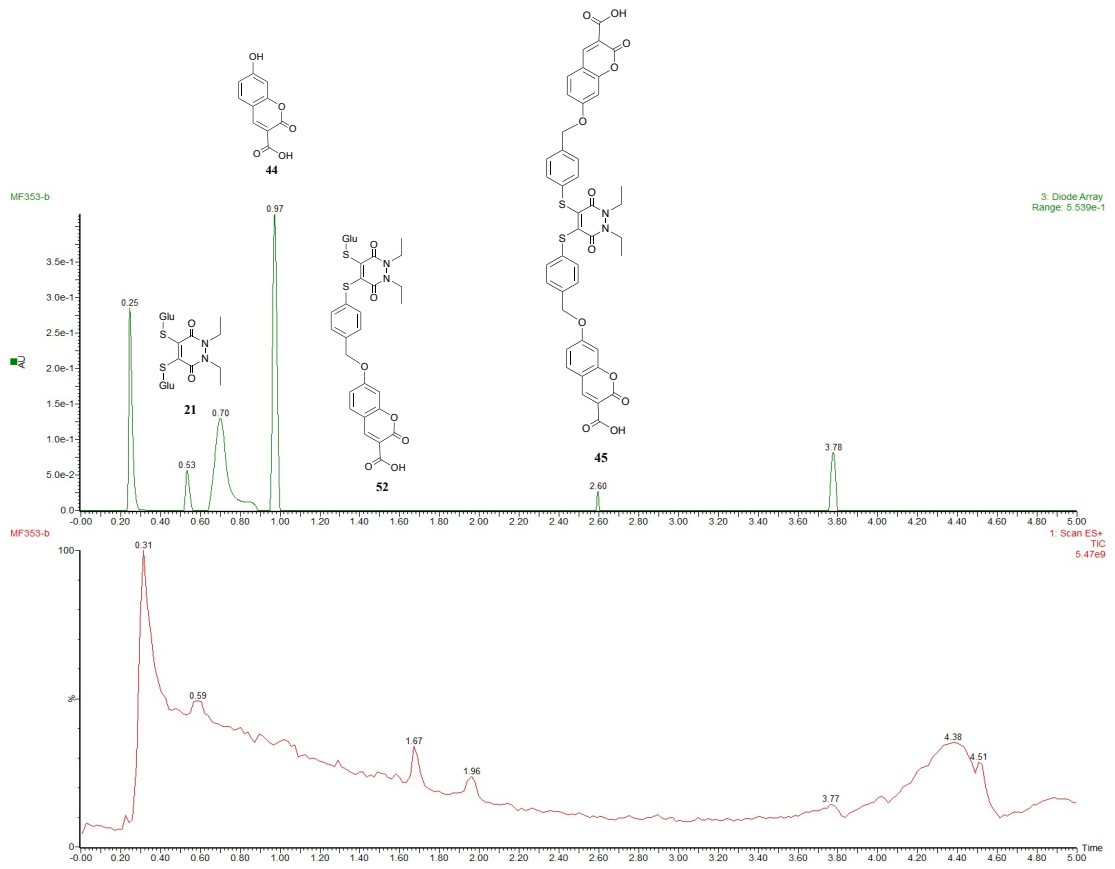


Figure S84. (a) TIC and UV trace at  $t = 0.05$  h, (b) MS data at 0.32 mins in the UV, (c) at 1.50 mins in the UV, (d) at 1.73 mins in the TIC, (e) at 2.03 mins in the TIC, (f) at 2.36 mins in the UV and (g) at 2.52 mins in the UV for PD **45** incubated with GluSH **19** (10 eq.) at pH 6.5. Please note that peaks at 1.73 and 2.03 mins in the TIC are minor impurities on the column that could not be removed; they are consistently present.

# LC-MS data for t = 4 h

(a)



(b)



(c)



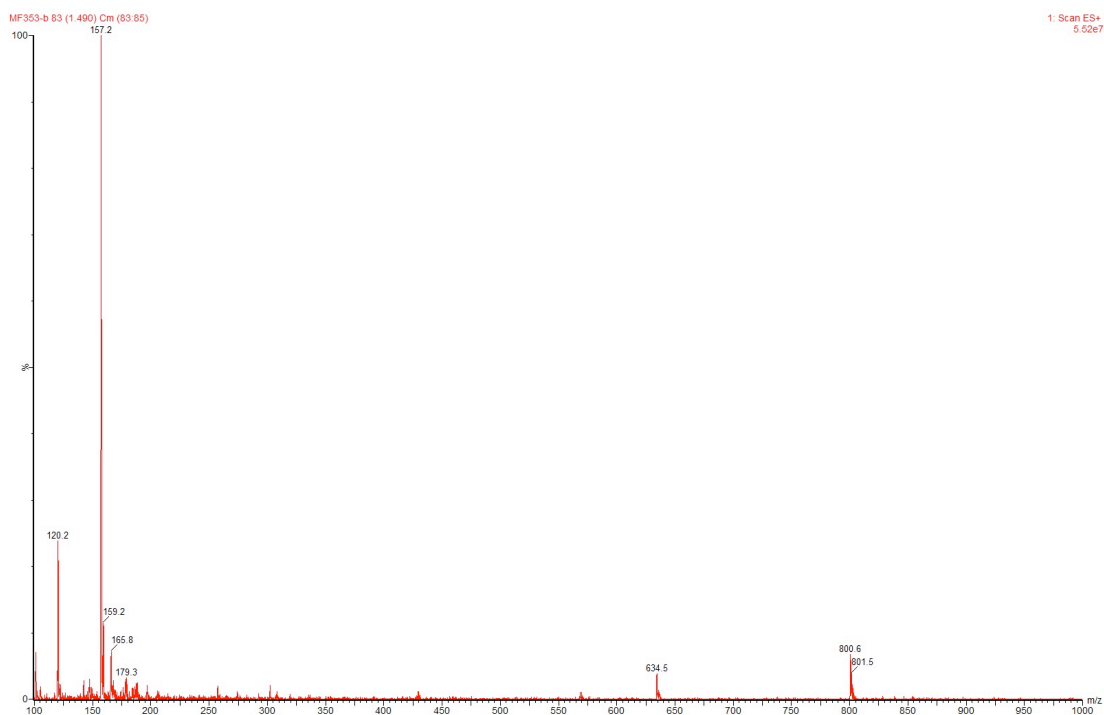
(d)



(e)



(f)



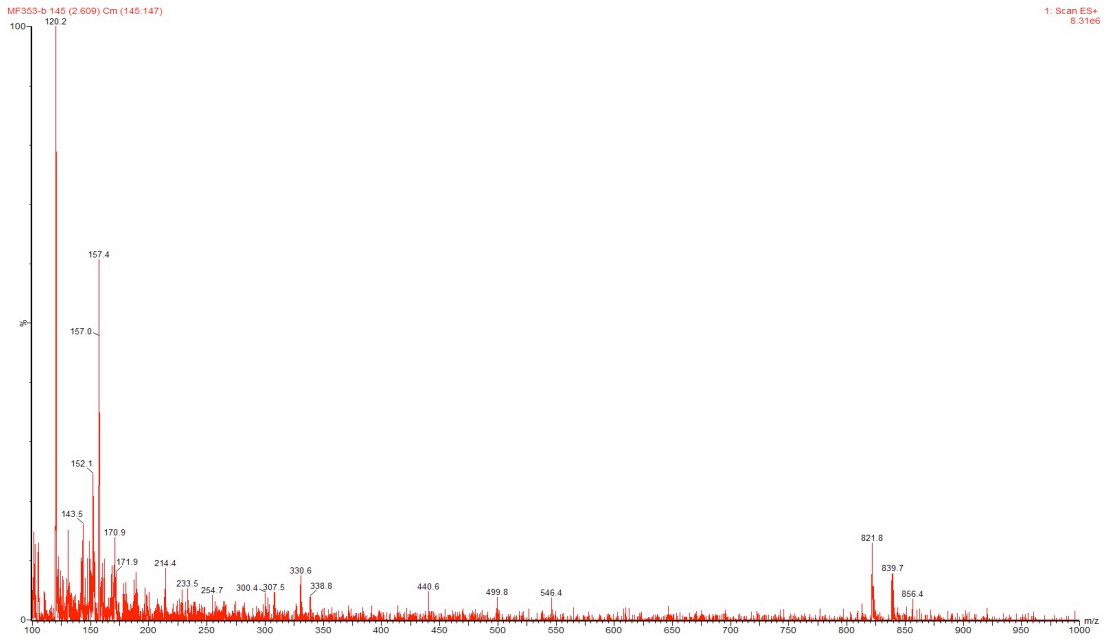
(g)



(h)



(i)



(j)

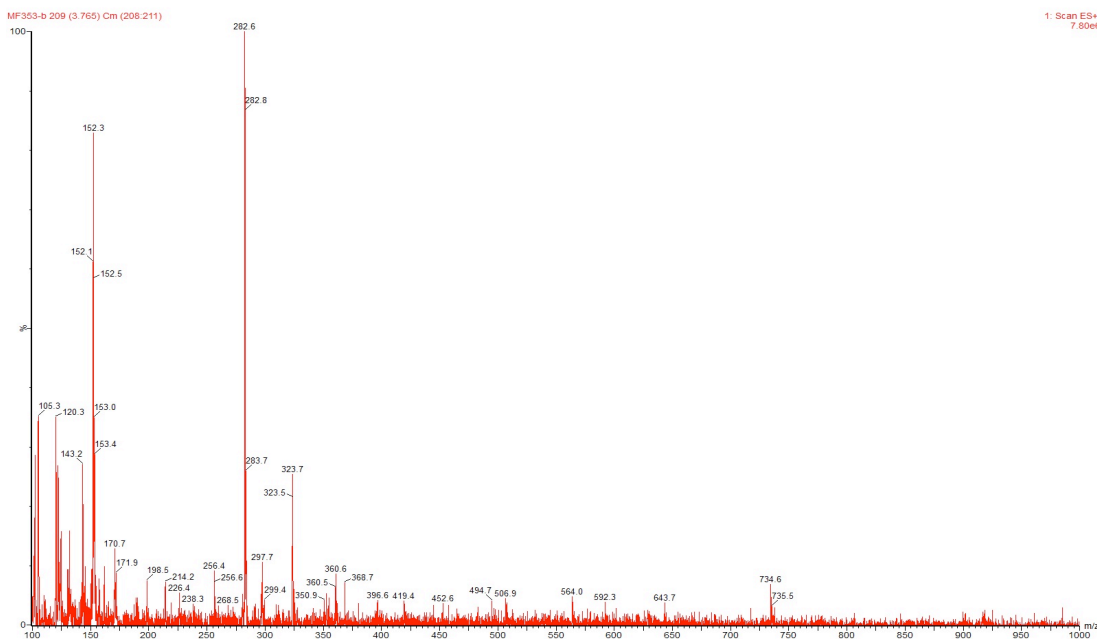
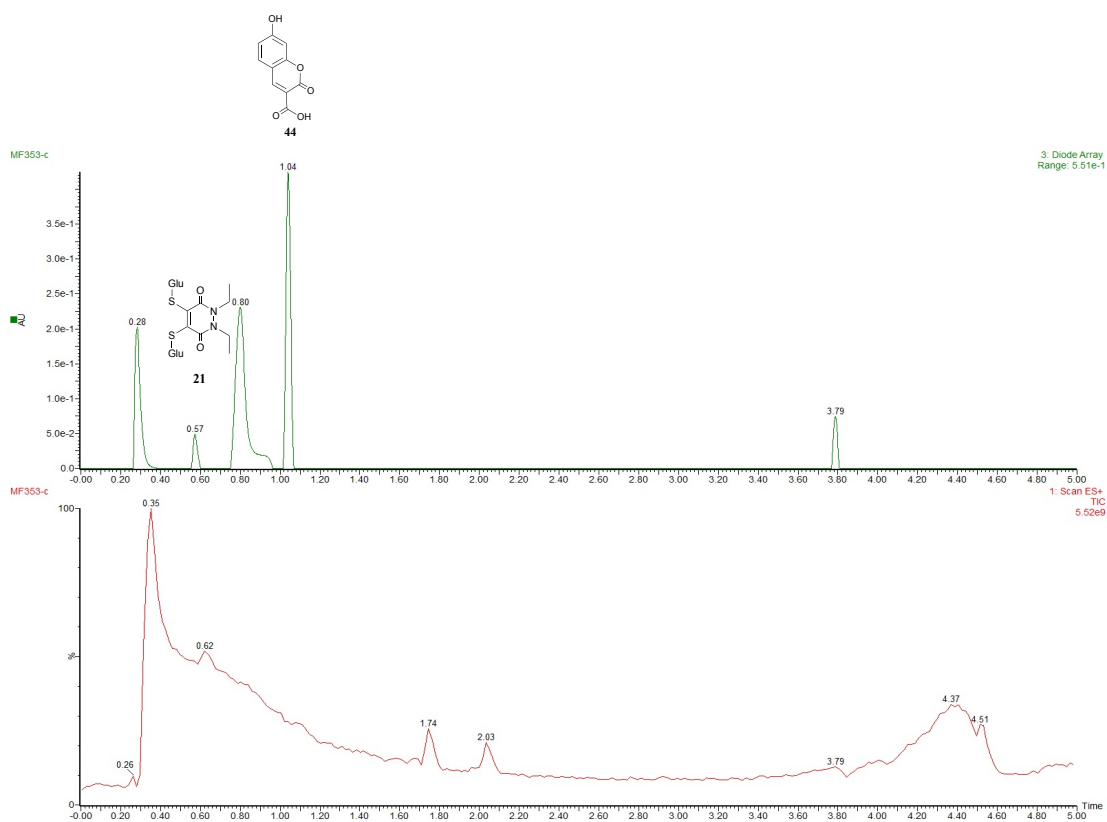


Figure S85. (a) TIC and UV trace at  $t = 4$  h, (b) MS data at 0.25 mins in the UV, (c) at 0.53 mins in the UV, (d) at 0.70 mins in the UV, (e) at 0.97 mins in the UV, (f) at 1.49 mins in the TIC, (g) at 1.67 mins in the TIC, (h) at 1.96 mins in the TIC, (i) at 2.60 mins in the UV and (j) at 3.78 mins in the UV for PD **45** incubated with GluSH **19** (10 eq.) at pH 6.5. Please note that peaks at 1.67 and 1.96 mins in the TIC, and at 3.78 mins in the UV are minor impurities on the column that could not be removed; they are consistently present.



# LC-MS data for t = 24 h

(a)



(b)



(c)



(d)



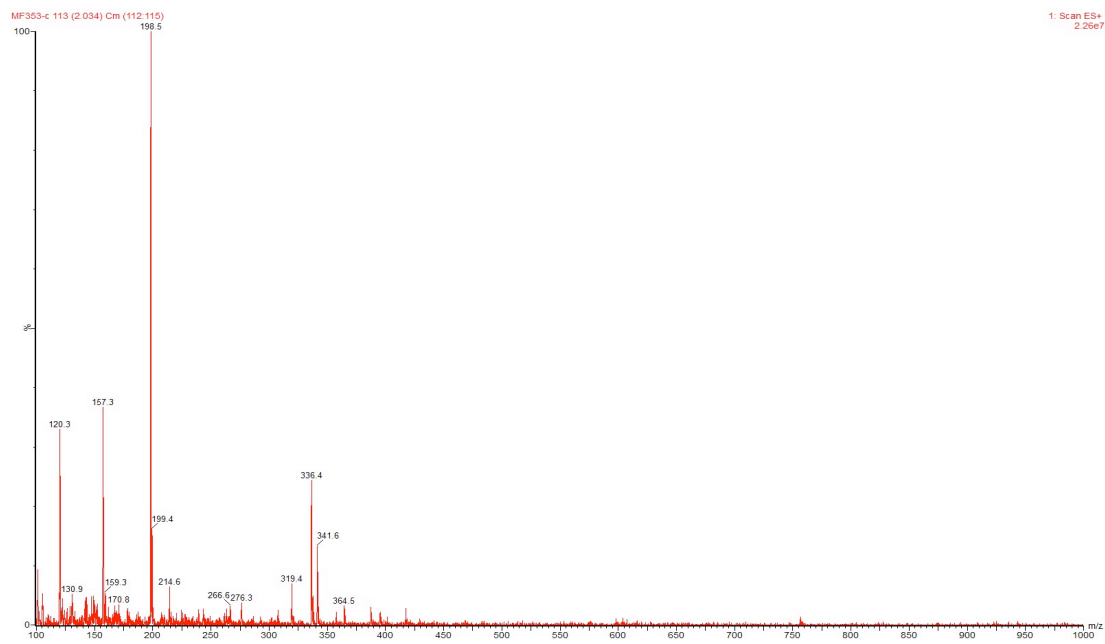
(e)



(f)



(g)



(h)

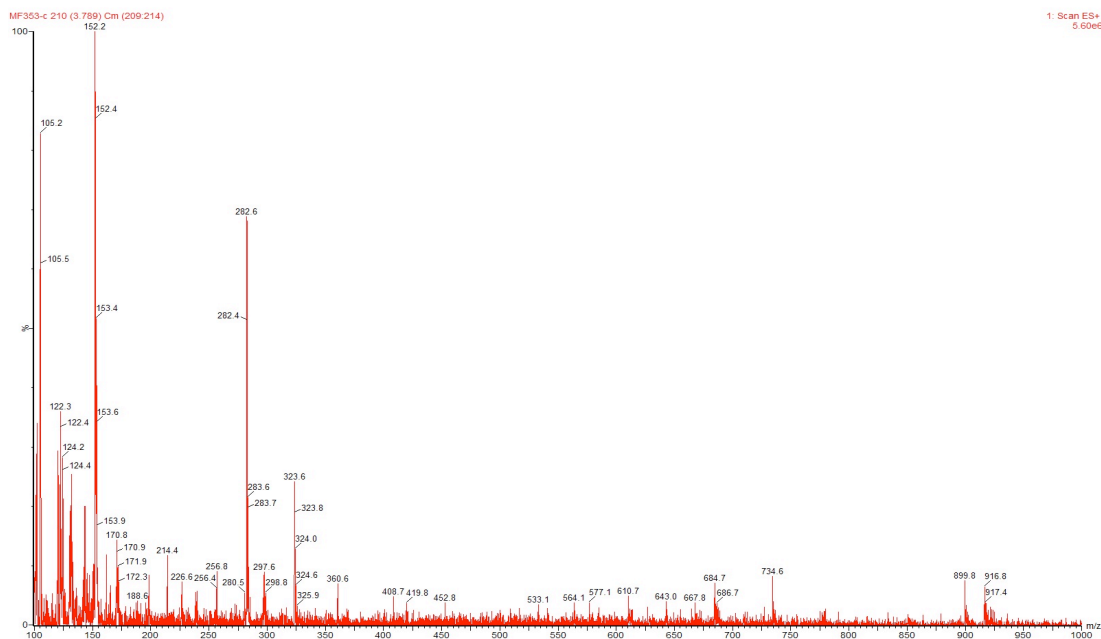
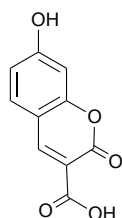


Figure S86. (a) TIC and UV trace at  $t = 24$  h, (b) MS data at 0.28 mins in the UV, (c) at 0.57 mins in the UV, (d) at 0.80 mins in the UV, (e) at 1.04 mins in the UV, (f) at 1.74 mins in the TIC, (g) at 2.03 mins in the TIC and (h) at 3.79 mins in the TIC for PD 45 incubated with GluSH 19 (10 eq.) at pH 6.5. Please note that peaks at 1.74 and 2.03 mins in the TIC, and at 3.79 mins in the UV are minor impurities on the column that could not be removed; they are consistently present.

## UV absorption and fluorescence emission spectroscopy of the reaction between carboxylic acid umbelliferone–PD and GluSH (10 eq.) at pH 6.5

### UV absorption of 7-hydroxy-2-oxo-2*H*-chromene-3-carboxylic acid



44

7-Hydroxy-2-oxo-2*H*-chromene-3-carboxylic acid **44** (100  $\mu$ L, 10 mM in DMSO) was added to ammonium acetate buffer (1900  $\mu$ L, 50 mM, pH 6.5). The solution was then scanned in the 200–800 nm range using a UV–Vis spectrophotometer in order to obtain the maximum UV absorption for 7-hydroxy-2-oxo-2*H*-chromene-3-carboxylic acid **44** in the DMSO/buffer mixture.

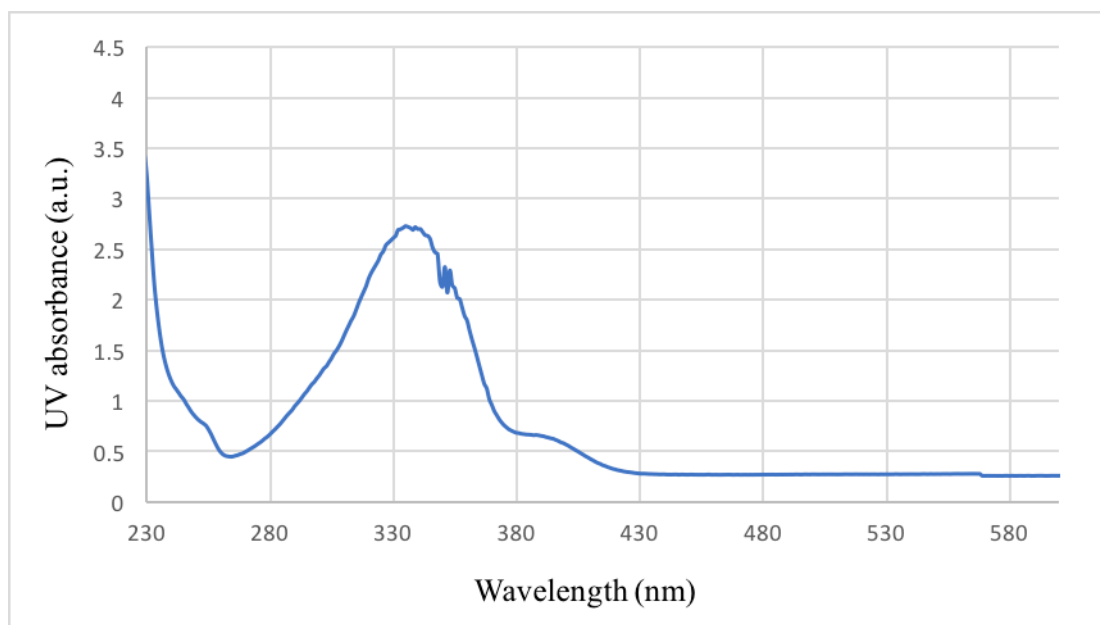
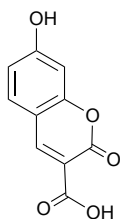


Figure S87. UV absorbance spectrum of 7-hydroxy-2-oxo-2*H*-chromene-3-carboxylic acid **44** in a 5:95 mixture of DMSO/ $\text{NH}_4\text{OAc}$  buffer (50 mM, pH 6.5). When scanned in the 200–800 nm range, the maximum UV absorption for 7-hydroxy-2-oxo-2*H*-chromene-3-carboxylic acid **44** occurred at 335 nm and  $\epsilon_{335} = 5462 \text{ M}^{-1}\text{cm}^{-1}$ .

## Fluorescence emission of 7-hydroxy-2-oxo-2*H*-chromene-3-carboxylic acid



**44**

7-Hydroxy-2-oxo-2*H*-chromene-3-carboxylic acid **44** (100  $\mu$ L, 10 mM in DMSO) was added to ammonium acetate buffer (1900  $\mu$ L, 50 mM, pH 6.5). The solution was then excited at 335 nm using a fluorescence spectrophotometer in order to obtain the maximum fluorescence emission for 7-hydroxy-2-oxo-2*H*-chromene-3-carboxylic acid **44** in the DMSO/buffer mixture.

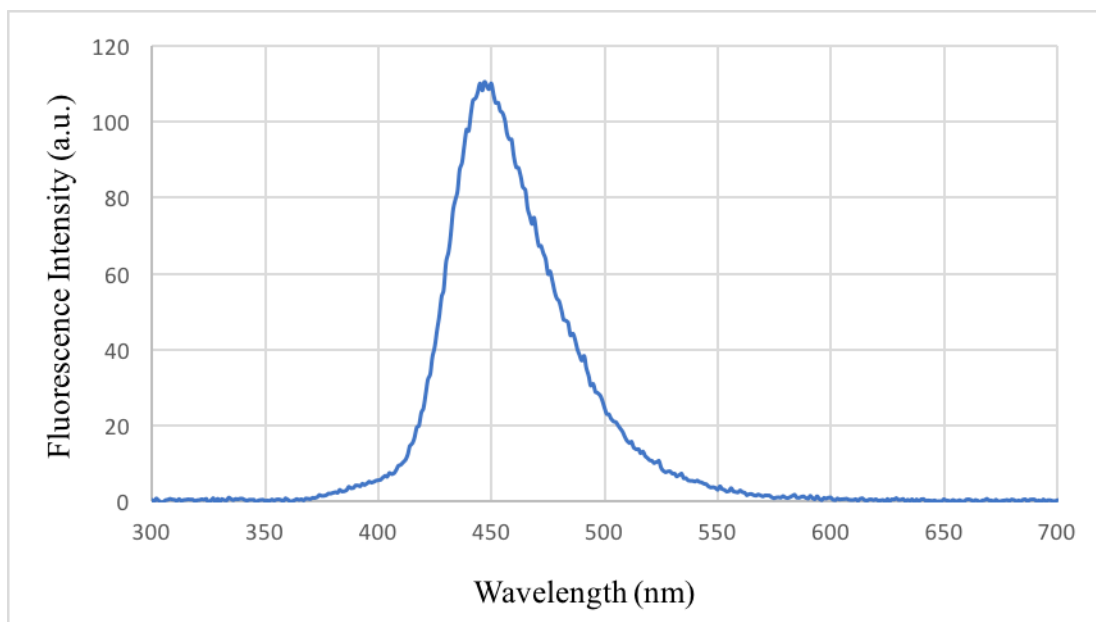
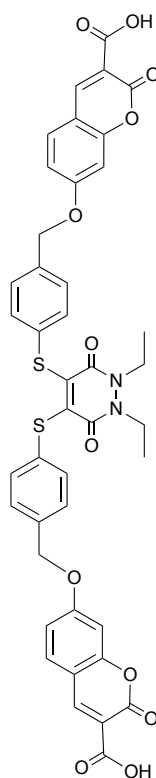


Figure **S88**. Fluorescence emission spectrum of 7-hydroxy-2-oxo-2*H*-chromene-3-carboxylic acid **44** in a 5:95 mixture of DMSO/ $\text{NH}_4\text{OAc}$  buffer (50 mM, pH 6.5). When excited at 335 nm, the maximum fluorescence emission for 7-hydroxy-2-oxo-2*H*-chromene-3-carboxylic acid **44** occurred at 447 nm with a maximum intensity of 110.6 a.u.

## Fluorescence emission of carboxylic acid umbelliferone–PD



45

PD **45** (100  $\mu\text{L}$ , 10 mM in DMSO) was added to ammonium acetate buffer (1900  $\mu\text{L}$ , 50 mM, pH 6.5). The solution was then excited at 335 nm using a fluorescence spectrophotometer in order to obtain the maximum fluorescence emission for PD **45** in the DMSO/buffer mixture.



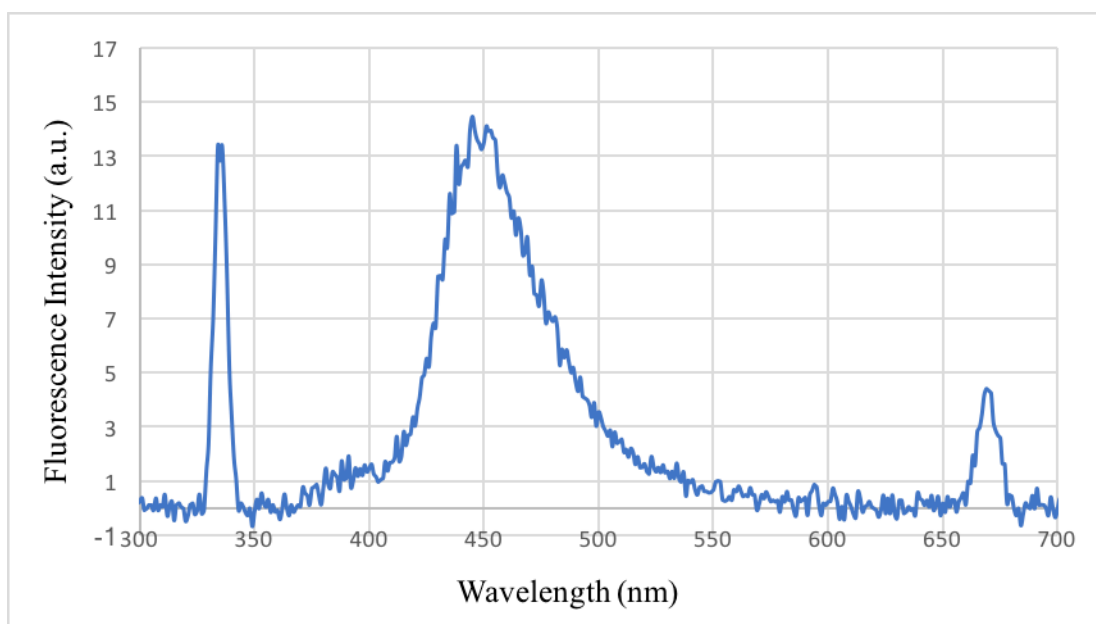
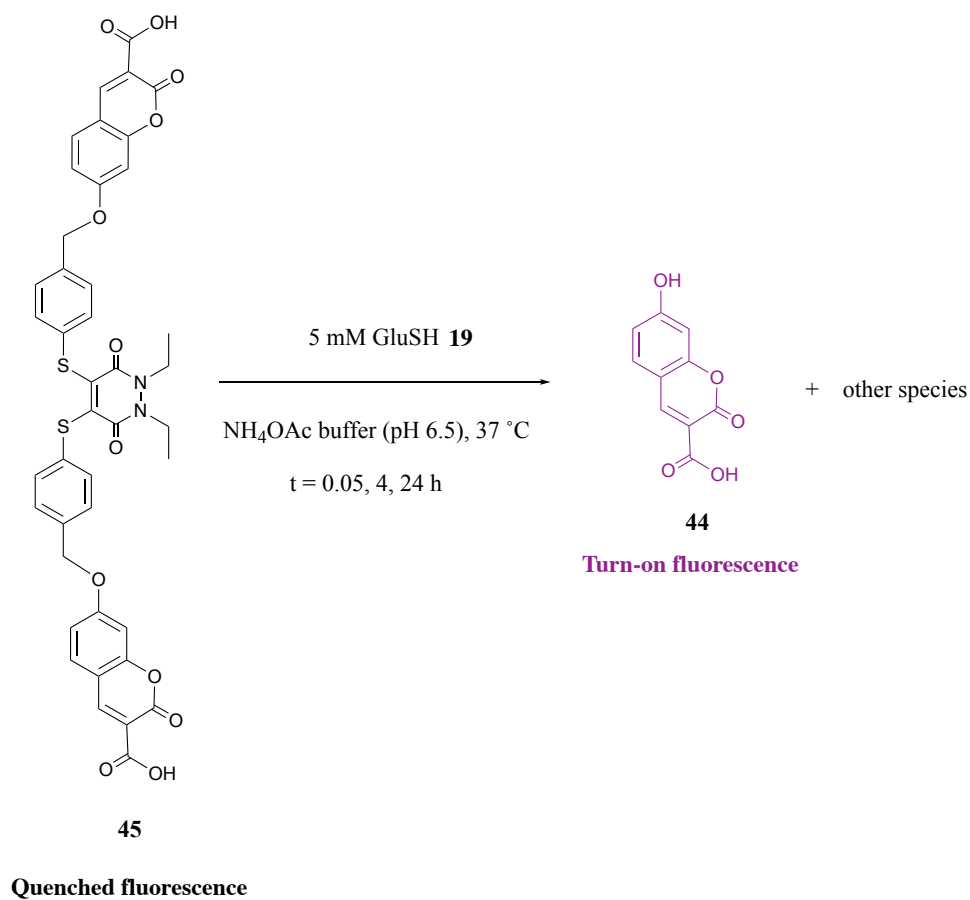


Figure S89. Fluorescence emission spectrum of PD **45** in a 5:95 mixture of DMSO/NH<sub>4</sub>OAc buffer (50 mM, pH 6.5). When excited at 335 nm, the maximum fluorescence emission for PD **45** occurred at 445 nm with a maximum intensity of 14.4 a.u.

## Fluorescence emission spectroscopy of the reaction between carboxylic acid umbelliferone–PD and GluSH (10 eq.) at pH 6.5



PD **45** (40  $\mu\text{L}$ , 10 mM in DMSO, 1 eq.) was added to GluSH **19** (760  $\mu\text{L}$ , 5.3 mM, 10 eq.) in ammonium acetate buffer (50 mM, pH 6.5). The mixture was incubated at 37 °C for 24 h. The reaction was excited at 335 nm at  $t = 0.05, 4$  and 24 h and the maximum fluorescence emission was recorded at each time point.

### Fluorescence emission at $t = 0.05$ h

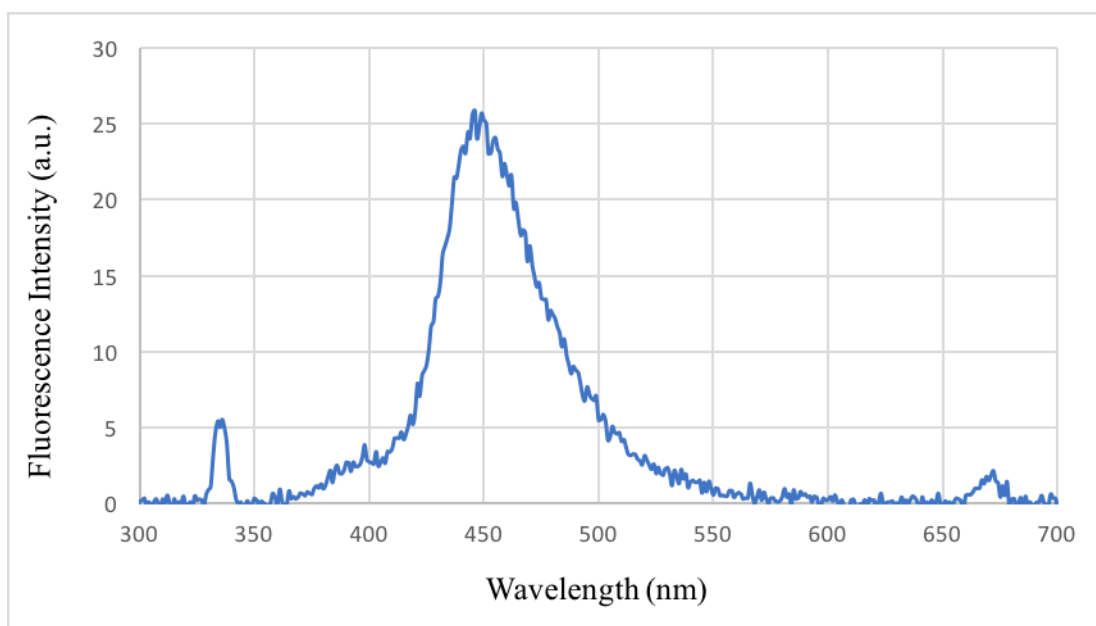


Figure S90. Fluorescence emission spectrum of the reaction between PD **45** and GluSH **19** to release 7-hydroxy-2-oxo-2*H*-chromene-3-carboxylic acid **44** at  $t = 0.05$  h. When excited at 335 nm, maximum fluorescence emission occurred at 446 nm with a maximum intensity of 25.8 a.u.

### Fluorescence emission at t = 4 h

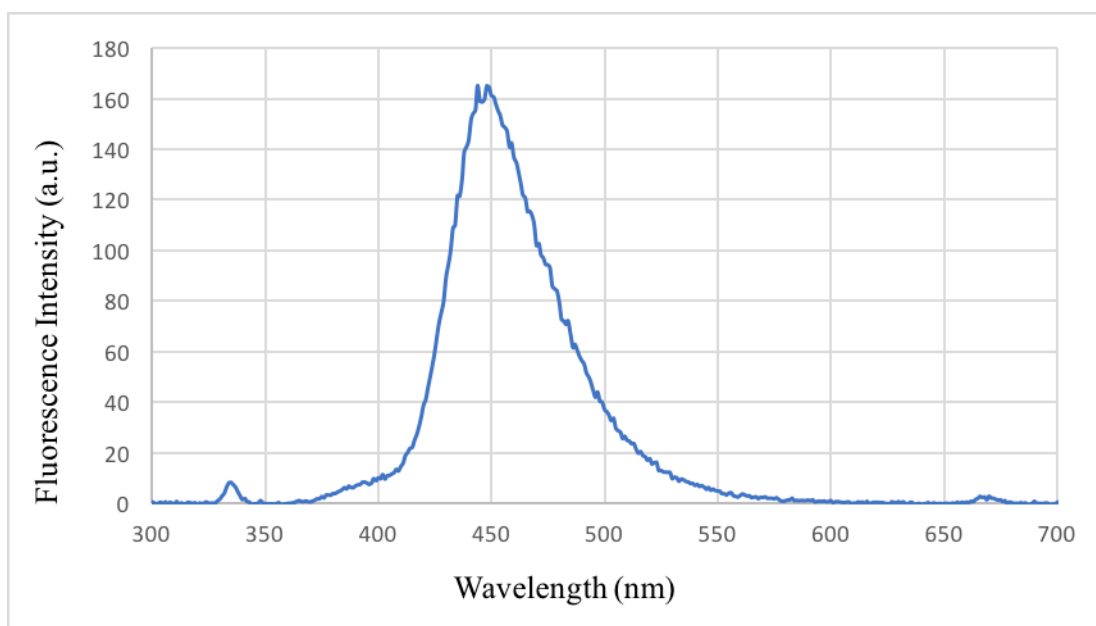


Figure S91. Fluorescence emission spectrum of the reaction between PD **45** and GluSH **19** to release 7-hydroxy-2-oxo-2*H*-chromene-3-carboxylic acid **44** at t = 4 h. When excited at 335 nm, maximum fluorescence emission occurred at 448 nm with a maximum intensity of 165.1 a.u.

### Fluorescence emission at t = 24 h

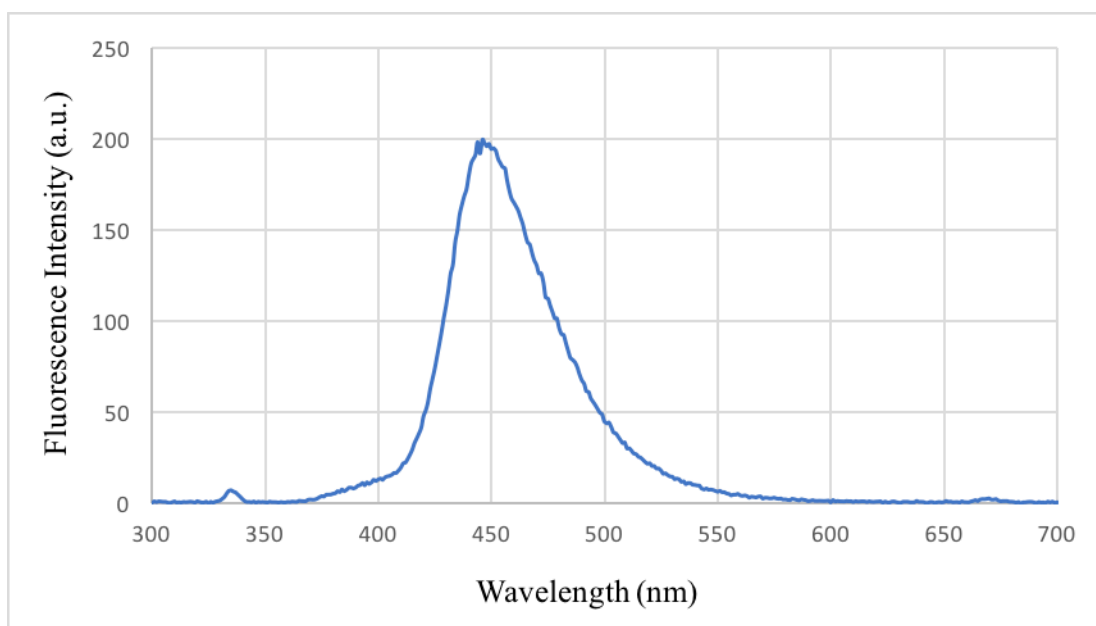
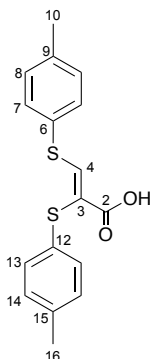


Figure S92. Fluorescence emission spectrum of the reaction between PD **45** and GluSH **19** to release 7-hydroxy-2-oxo-2*H*-chromene-3-carboxylic acid **44** at t = 24 h. When excited at 335 nm, maximum fluorescence emission occurred at 446 nm with a maximum intensity of 199.6 a.u.

## Experimental for Chapter 4

### (*Z*)-2,3-Bis(*p*-tolylthio)acrylic acid **62**



A solution of 4-methylbenzenethiol **36** (0.78 g, 6.3 mmol) and triethylamine (0.88 mL, 6.3 mmol) in THF (2 mL) was stirred at 21 °C for 5 mins. To this was added dibromomaleic acid **9** (0.86 g, 3.1 mmol) in THF (2 mL) and the resulting solution was stirred at 21 °C for 1 h. Following this, the reaction mixture was diluted with water (5 mL) and extracted with EtOAc (3 × 10 mL). The organic phase was dried over MgSO<sub>4</sub>, concentrated *in vacuo* and the crude residue was purified by preparative TLC (80% EtOAc/Pet. (0.25% AcOH)) to afford (*Z*)-2,3-bis(*p*-tolylthio)acrylic acid (0.02 g, 0.06 mmol, 2%) as a pink solid. No melting point able to be obtained. <sup>1</sup>H NMR (400 MHz, CDCl<sub>3</sub>) δ 8.30 (s, 1H, H-4), 7.22–6.87 (m, 8H, H-7, H-8, H-13, H-14), 2.38–2.13 (m, 6H, H-10, H-16); <sup>13</sup>C NMR (150 MHz, CDCl<sub>3</sub>) δ 166.3 (C-2), 161.0 (C-4), 139.4 (C-6, C-12), 136.9 (C-9, C-15), 131.6 (C-7/C-8/C-13/C-14), 130.1 (C-7/C-8/C-13/C-14), 129.4 (C-3), 128.9 (C-7/C-8/C-13/C-14); IR (solid) 3019, 2919, 2850, 1679, 1594 cm<sup>-1</sup>; LRMS (ES<sup>+</sup>) 299 (100, [M–OH]<sup>+</sup>), 316 (15, M<sup>+</sup>); HRMS (ES<sup>+</sup>) calcd for C<sub>17</sub>H<sub>16</sub>O<sub>2</sub>S<sub>2</sub> M<sup>+</sup> 316.0592, observed 316.0595.

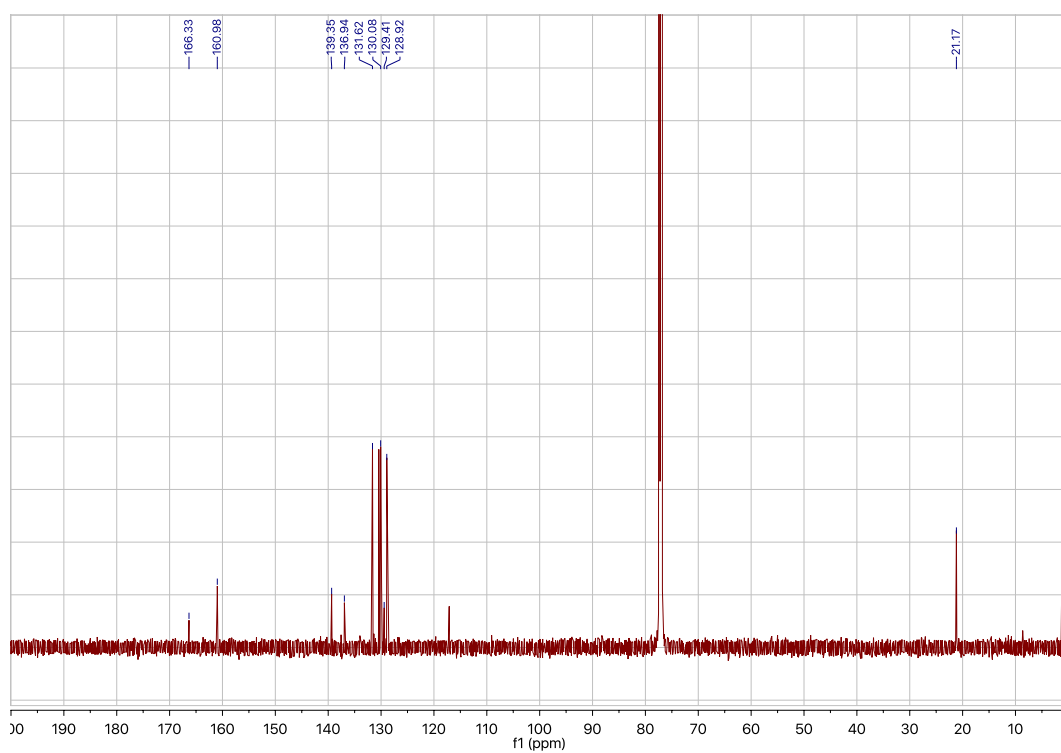
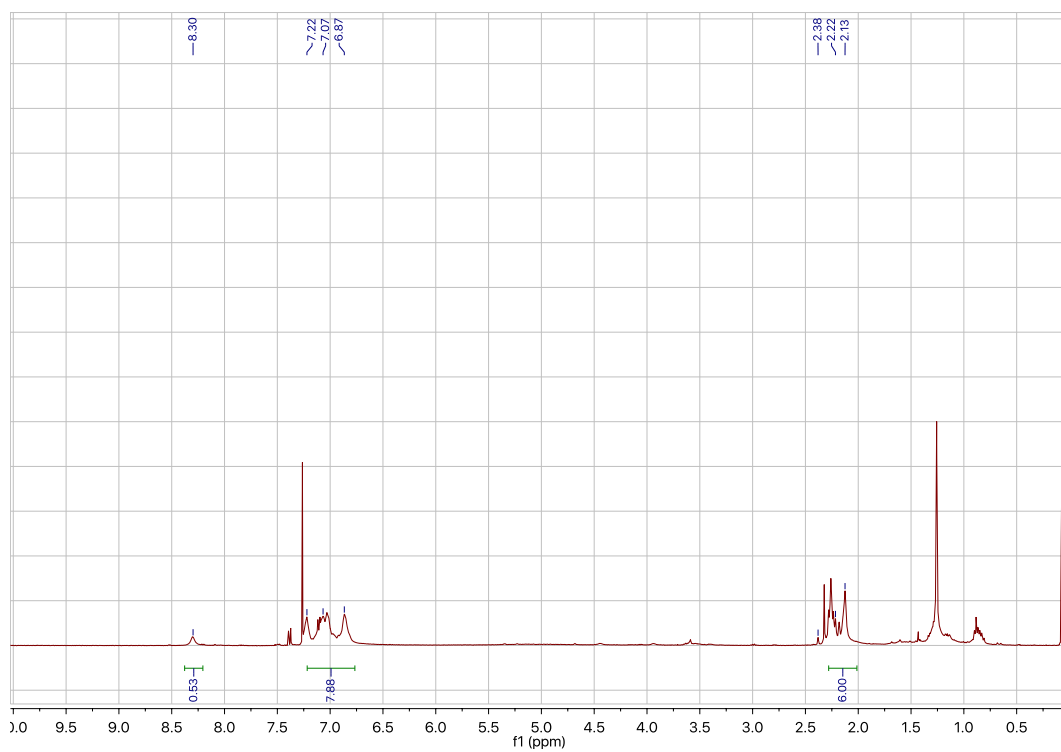
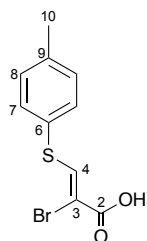


Figure S93. <sup>1</sup>H and <sup>13</sup>C NMR spectra for (Z)-2,3-bis(*p*-tolylthio)acrylic acid **62**.

### (Z)-2-Bromo-3-(p-tolylthio)acrylic acid **63**



A solution of 4-methylbenzenethiol **36** (0.78 g, 6.3 mmol) and triethylamine (0.88 mL, 6.3 mmol) in THF (2 mL) was stirred at 21 °C for 5 mins. To this was added dibromomaleic acid **9** (0.86 g, 3.1 mmol) in THF (2 mL) and the resulting solution was stirred at 21 °C for 1 h. Following this, the reaction mixture was diluted with water (5 mL) and extracted with EtOAc (3 × 10 mL). The organic phase was dried over MgSO<sub>4</sub>, concentrated *in vacuo* and the crude residue was purified by preparative TLC (80% EtOAc/Pet. (0.25% AcOH)) to afford what was tentatively assigned as (Z)-2-bromo-3-(p-tolylthio)acrylic acid (4 mg, 0.01 mmol, 0.4%) as a white-pink solid. No melting point able to be obtained; <sup>1</sup>H NMR (400 MHz, CDCl<sub>3</sub>) δ 8.25 (s, 1H, H-4), 7.33 (d, *J* = 7.7 Hz, 2H, H-7/H-8), 7.13 (d, *J* = 7.7 Hz, 2H, H-7/H-8), 2.34 (s, 3H, H-10); <sup>13</sup>C NMR (150 MHz, CDCl<sub>3</sub>, full carbon data could not be obtained) δ 131.5 (C-7/C-8), 130.4 (C-7/C-8), 21.2 (C-10); IR (solid) 2920, 1554, 1492 cm<sup>-1</sup>; LRMS (ES+) 275 (100, [M<sup>81</sup>Br+H]<sup>+</sup>), 273 (96, [M<sup>79</sup>Br+H]<sup>+</sup>); HRMS (ES+) calcd for C<sub>10</sub>H<sub>10</sub>O<sub>2</sub>SBr [M<sup>81</sup>Br+H]<sup>+</sup> 274.9564, observed 274.9557.



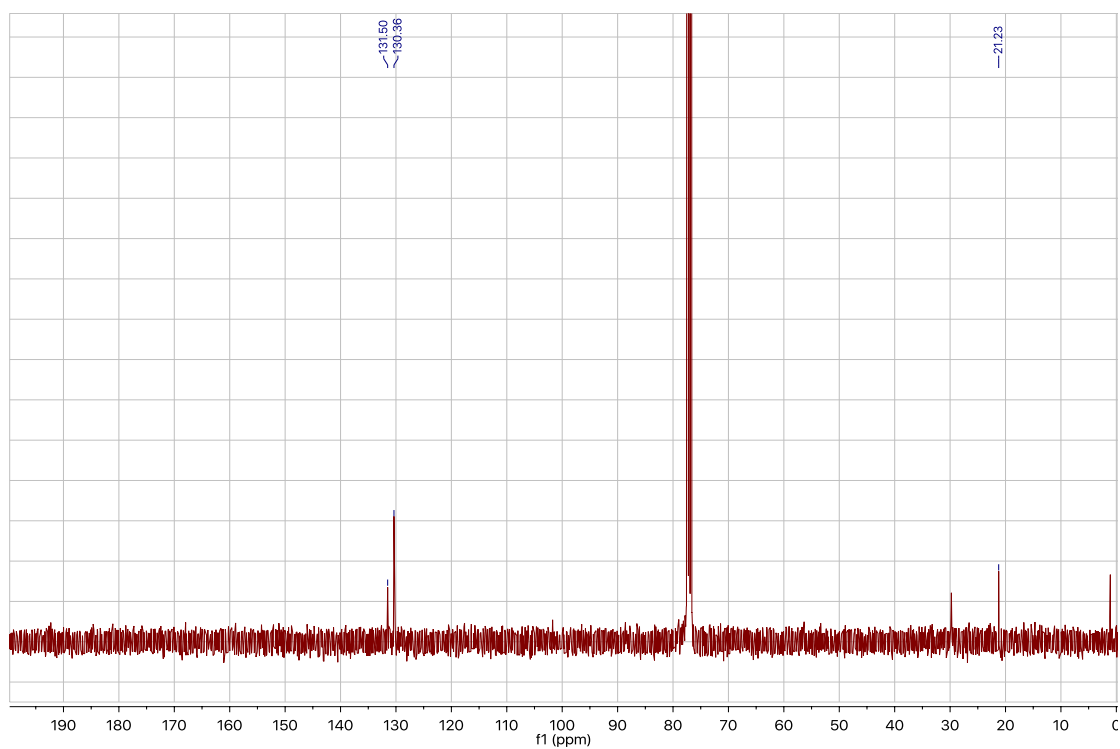
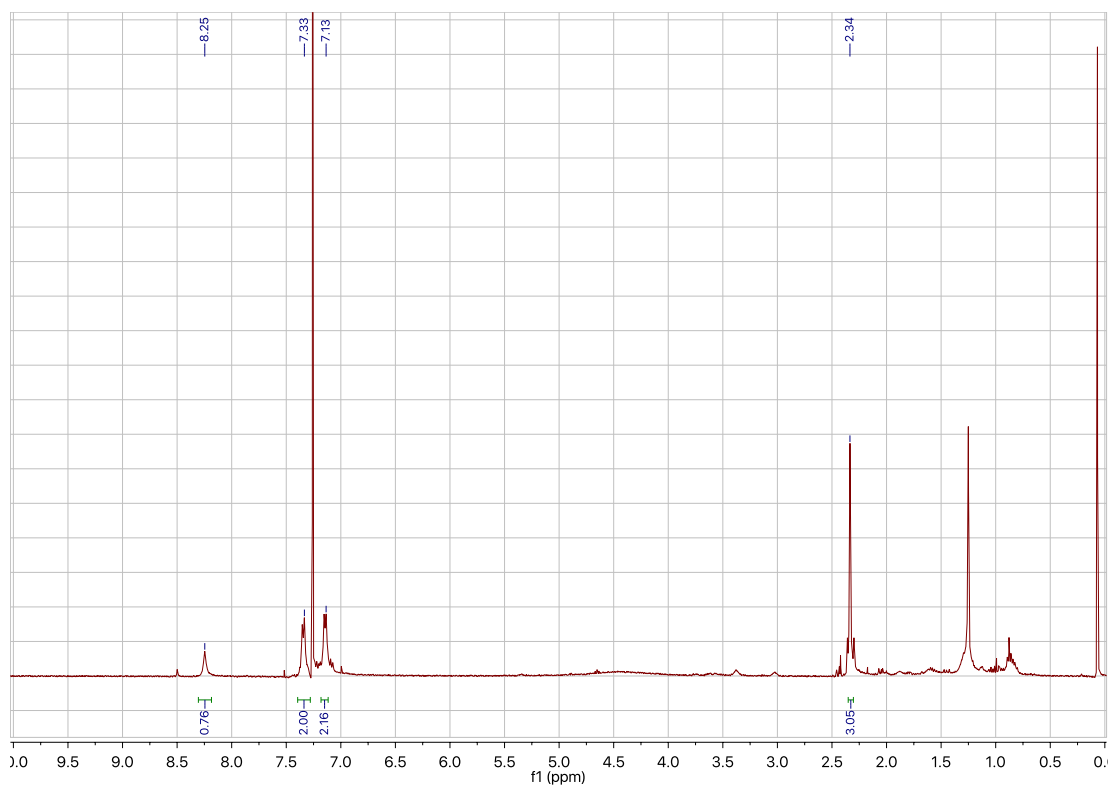
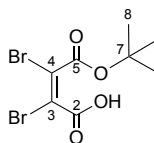
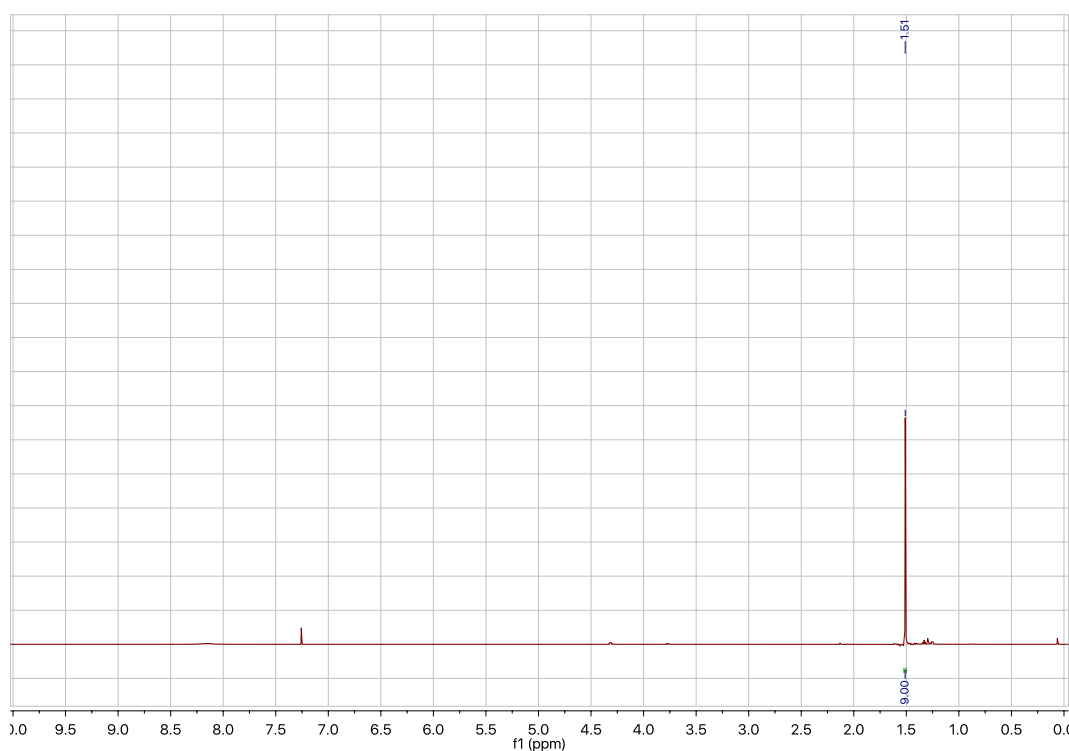


Figure S94. <sup>1</sup>H and <sup>13</sup>C NMR spectra for *Z*-2-bromo-3-(*p*-tolylthio)acrylic acid **63**.

## (Z)-2,3-Dibromo-4-(tert-butoxy)-4-oxobut-2-enoic acid **67**



Dibromomaleic acid **9** (1.16 g, 4.24 mmol) was dissolved in AcOH (10 mL) and stirred under reflux for 3 h. After this time, the AcOH was removed *in vacuo* and 1 M solution potassium *tert*-butoxide **65** in THF (5.51 mL, 5.51 mmol) was added and the resulting solution was stirred at 0 °C for 3 h. Following this, the reaction mixture was diluted with water (8 mL), EtOAc (8 mL) and the aqueous layer acidified with 1 M TFA until pH 2. The aqueous layer was then extracted with EtOAc (3 × 5 mL) and the resulting organic phase was dried over MgSO<sub>4</sub>, concentrated *in vacuo* and the crude residue was purified by flash column chromatography (0–10% MeOH/CH<sub>2</sub>Cl<sub>2</sub> (2% AcOH)) to afford (*Z*)-2,3-dibromo-4-(*tert*-butoxy)-4-oxobut-2-enoic acid (0.26 g, 0.79 mmol, 19%) as a brown solid. m.p. 72–75 °C; <sup>1</sup>H NMR (600 MHz, CDCl<sub>3</sub>) δ 1.51 (s, 9H, H-8); <sup>13</sup>C NMR (150 MHz, CDCl<sub>3</sub>) δ 166.5 (C-2), 161.1 (C-5), 130.4 (C-4), 121.6 (C-3), 85.6 (C-7), 27.7 (C-8); IR (solid) 2981, 2932, 2652, 2515, 1720, 1694 cm<sup>-1</sup>; LRMS (ES+) 329 (100, [M<sup>79</sup>Br+H]<sup>+</sup>); HRMS (ES+) calcd for C<sub>8</sub>H<sub>11</sub>O<sub>4</sub>Br<sub>2</sub> [M<sup>79</sup>Br+H]<sup>+</sup> 328.8848, observed 328.8846.



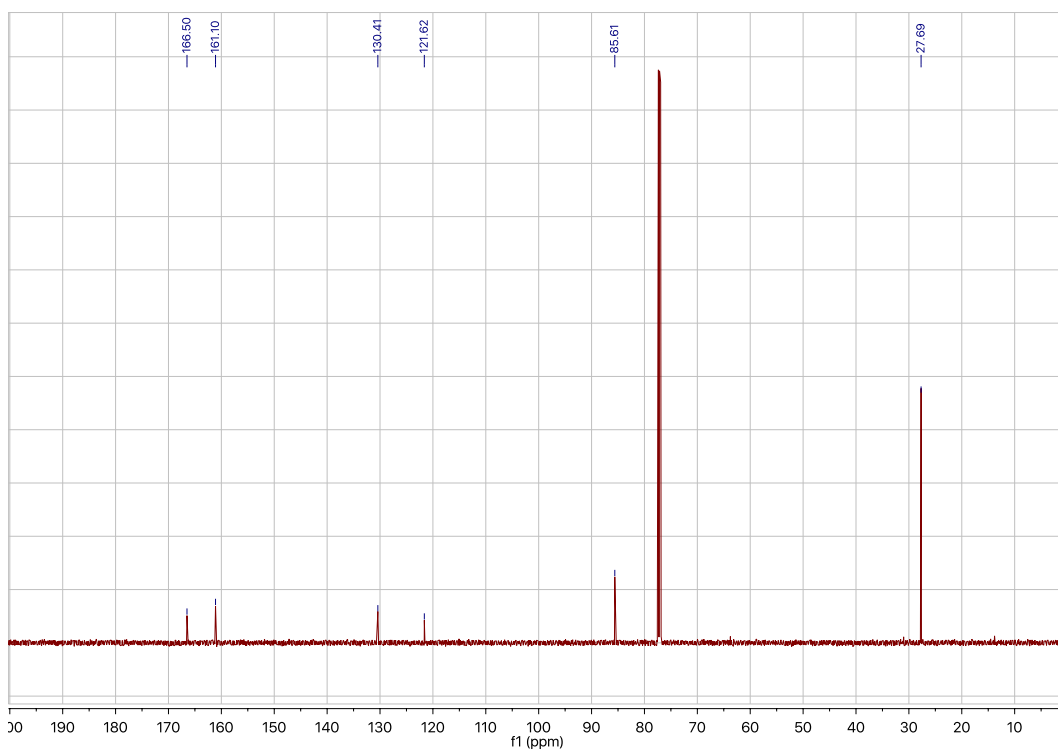
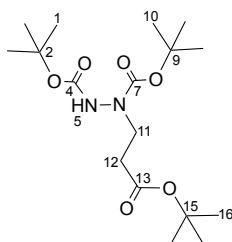


Figure S95.  $^1\text{H}$  and  $^{13}\text{C}$  NMR spectra for (*Z*)-2,3-dibromo-4-(*tert*-butoxy)-4-oxobut-2-enoic acid **67**.

## Di-*tert*-butyl 1-(3-(*tert*-butoxy)-3-oxopropyl)hydrazine-1,2-dicarboxylate **72**



To a solution of di-*tert*-butyl hydrazine-1,2-dicarboxylate **1** (1.22 g, 5.25 mmol) in EtOH (10 mL), was added fifteen drops of 2 M NaOH, and the reaction mixture was stirred at 21 °C for 10 mins. Following this, *tert*-butyl acrylate **57** (0.91 mL, 6.3 mmol) was added to the solution and the reaction mixture was stirred under reflux for 48 h. Following this, the reaction mixture was concentrated *in vacuo* and the crude residue was purified by flash column chromatography (0–20% EtOAc/Pet.). The appropriate fractions were then combined and concentrated *in vacuo* to afford di-*tert*-butyl 1-(3-(*tert*-butoxy)-3-oxopropyl)hydrazine-1,2-dicarboxylate (1.11 g, 3.08 mmol, 59%) as a colourless oil. <sup>1</sup>H NMR (700 MHz, CDCl<sub>3</sub>, rotamers) δ 6.39 (s, 0.70H, H-5), 6.08 (s, 0.20H, H-5), 3.71 (app. s, 2H, H-11), 2.52 (t, *J* = 6.6 Hz, 2H, H-12), 1.46–1.43 (m, 27H, H-1, H-10, H-16); <sup>13</sup>C NMR (150 MHz, CDCl<sub>3</sub>) δ 168.9 (C-13), 168.6 (C-13), 152.4 (C-4, C-7), 79.0 (C-2/C-9/C-15), 78.6 (C-2/C-9/C-15), 78.1 (C-2/C-9/C-15), 44.3 (C-11), 43.1 (C-11), 31.8 (C-12), 31.6 (C-12), 25.6 (C-1/C-10/C-16), 25.5 (C-1/C-10/C-16); IR (thin film) 2975, 2931, 1707 cm<sup>-1</sup>; LRMS (ES<sup>+</sup>) 361 (100, [M+H]<sup>+</sup>); HRMS (ES<sup>+</sup>) calcd for C<sub>17</sub>H<sub>33</sub>N<sub>2</sub>O<sub>6</sub> [M+H]<sup>+</sup> 361.2333, observed 361.2337.

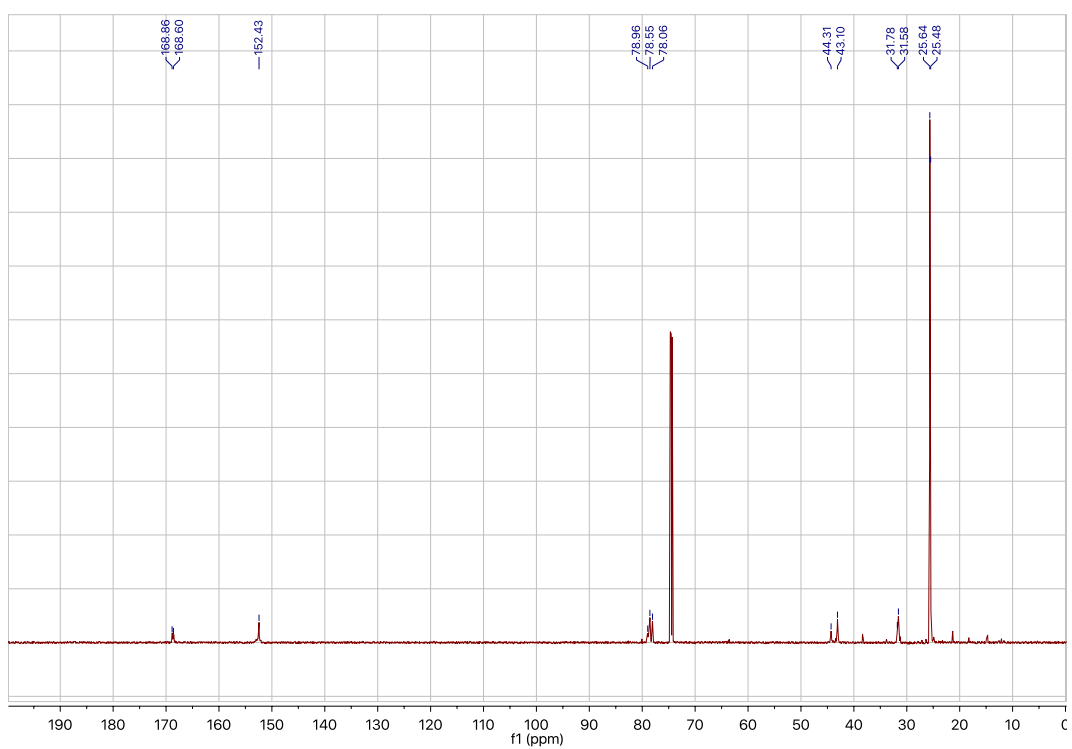
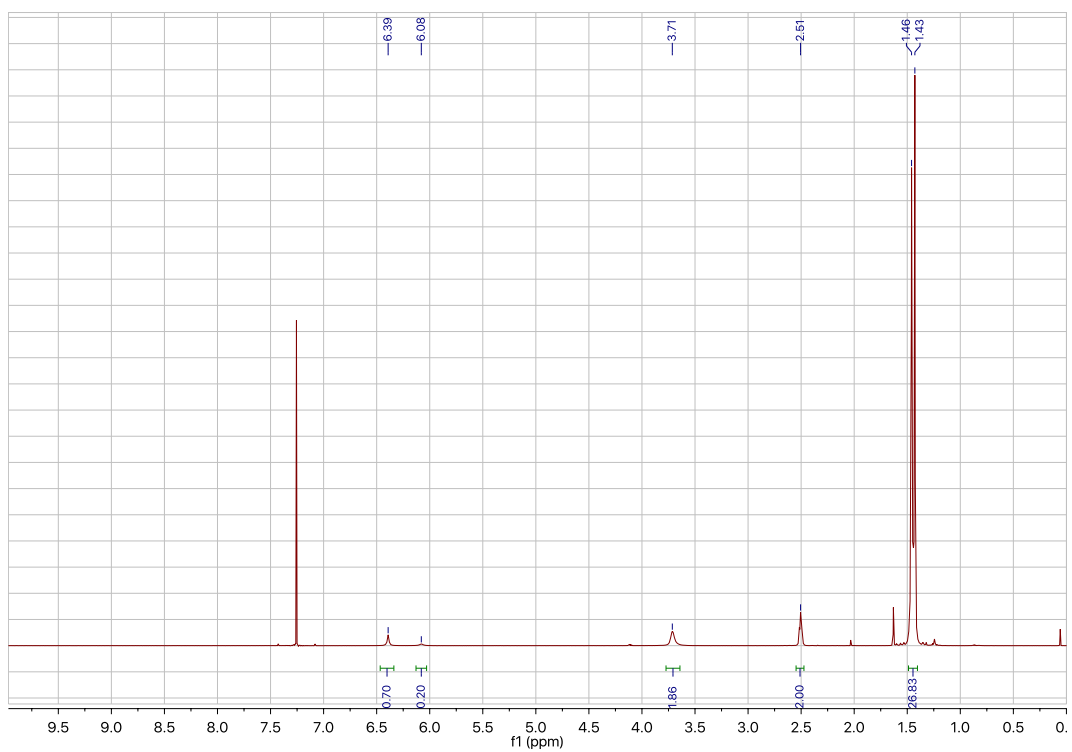
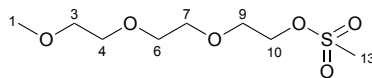


Figure S96.  $^1\text{H}$  and  $^{13}\text{C}$  NMR spectra for di-*tert*-butyl 1-(3-(*tert*-butoxy)-3-oxopropyl)hydrazine-1,2-dicarboxylate **72**.

## 2-(2-(2-Methoxyethoxy)ethoxy)ethyl methanesulfonate **74**<sup>152</sup>



To a solution of triethylene glycol monomethyl ether **58** (3.00 g, 18.3 mmol) and triethylamine (3.06 mL, 21.9 mmol) in dry THF (18 mL) at 0 °C, was added methanesulfonyl chloride **73** (1.70 mL, 22.0 mmol), and the reaction mixture was stirred at 0 °C for 2 h and then at 21 °C for 3 d. Following this, the reaction mixture was diluted with water (20 mL) and extracted with EtOAc (3 × 25 mL). The organic extracts were combined and subsequently washed with brine (25 mL). The organic phase was then dried over MgSO<sub>4</sub>, concentrated *in vacuo* and the crude residue was purified by flash column chromatography (20–80% EtOAc/Pet.). The appropriate fractions were then combined and concentrated *in vacuo* to afford 2-(2-(2-methoxyethoxy)ethoxy)ethyl methanesulfonate (4.41 g, 18.2 mmol, quant.) as a clear brown oil. <sup>1</sup>H NMR (400 MHz, CDCl<sub>3</sub>) δ 4.37–4.35 (m, 2H, H-10), 3.76–3.73 (m, 2H, H-9), 3.67–3.60 (m, 6H, H-4, H-6, H-7), 3.53–3.50 (m, 2H, H-3), 3.35 (s, 3H, H-1), 3.05 (s, 3H, H-13); <sup>13</sup>C NMR (150 MHz, CDCl<sub>3</sub>) δ 72.0 (C-3), 70.7 (C-4/C-6/C-7), 70.6 (C-4/C-6/C-7), 70.6 (C-4/C-6/C-7), 69.4 (C-10), 69.1 (C-9), 59.1 (C-1), 37.8 (C-13); IR (thin film) 2877, 1455, 1348 cm<sup>-1</sup>.

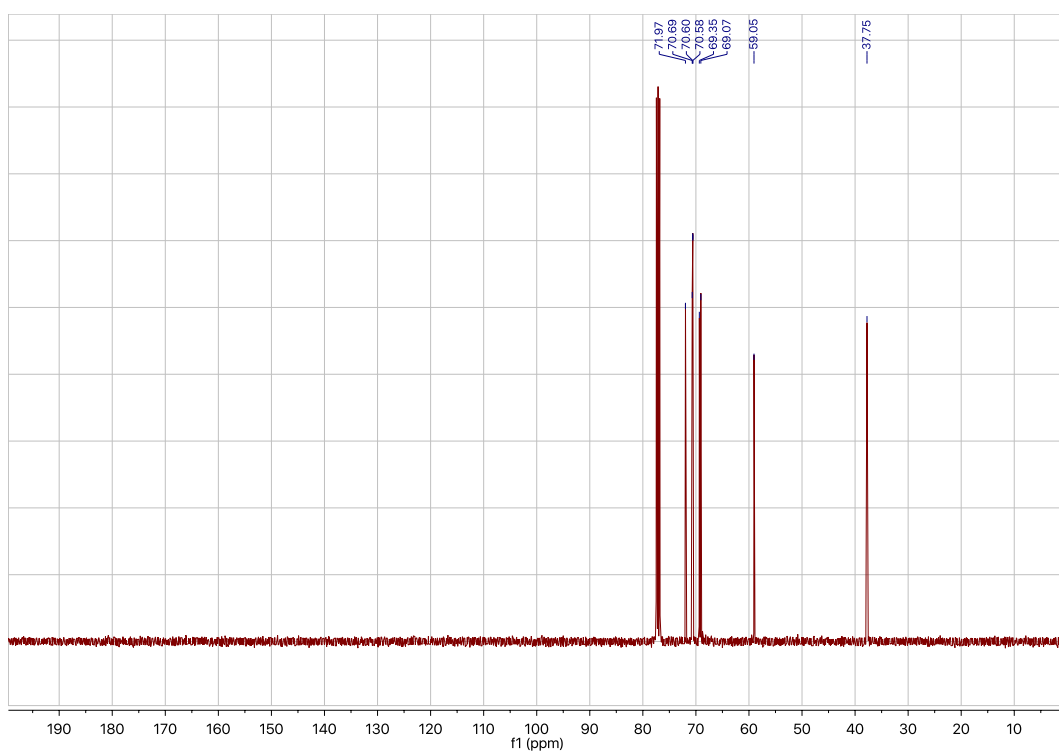
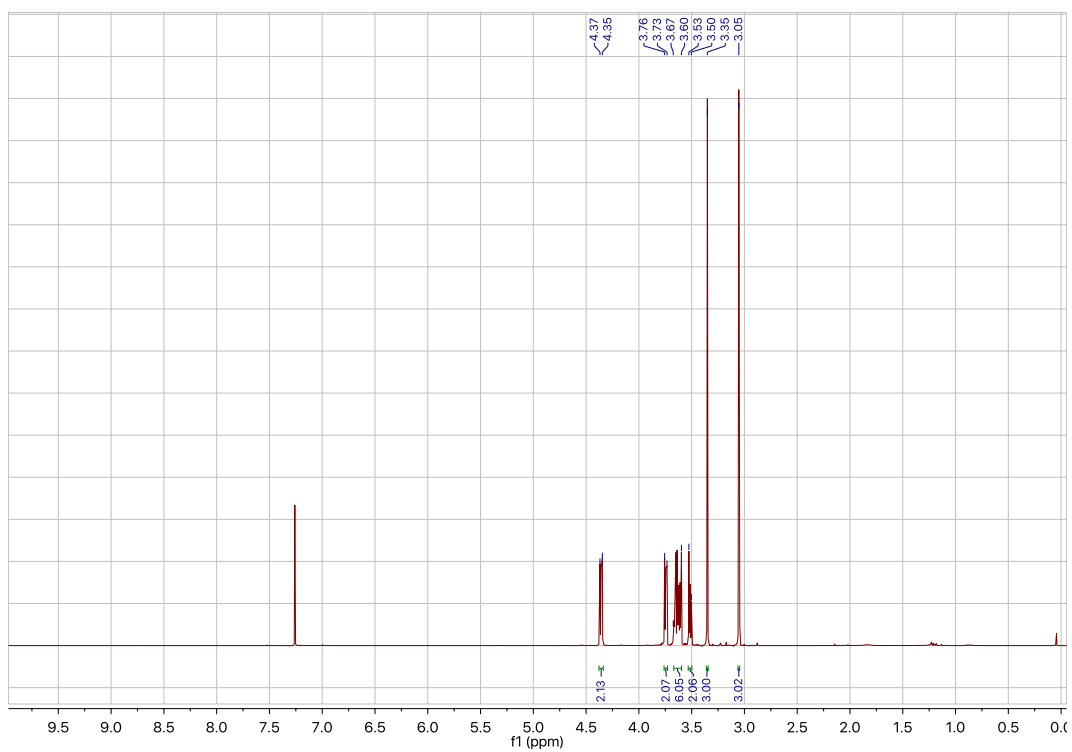
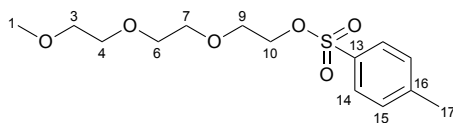


Figure S97.  $^1\text{H}$  and  $^{13}\text{C}$  NMR spectra for 2-(2-(2-methoxyethoxy)ethoxy)ethyl methanesulfonate **74**.

## 2-(2-(2-Methoxyethoxy)ethoxy)ethyl 4-methylbenzenesulfonate **76**<sup>153</sup>



To a solution of triethylene glycol monomethyl ether **58** (2.00 g, 12.2 mmol) and triethylamine (2.55 mL, 18.3 mmol) in dry THF (15 mL) at 21 °C, was added 4-methylbenzenesulfonyl chloride **75** (2.79 g, 14.6 mmol), and the reaction mixture was stirred for 21 h. Following this, the reaction mixture was diluted with water (15 mL) and extracted with EtOAc (3 × 15 mL). The organic extracts were combined and subsequently washed with brine (25 mL). The organic phase was then dried over MgSO<sub>4</sub>, concentrated *in vacuo* and the crude residue was purified by flash column chromatography (20–80% EtOAc/Pet.). The appropriate fractions were then combined and concentrated *in vacuo* to afford 2-(2-(2-methoxyethoxy)ethoxy)ethyl 4-methylbenzenesulfonate (3.74 g, 11.8 mmol, 96%) as a clear yellow oil. <sup>1</sup>H NMR (700 MHz, CDCl<sub>3</sub>) δ 7.76 (d, *J* = 8.3 Hz, 2H, H-14), 7.31 (d, *J* = 8.3 Hz, 2H, H-15), 4.13–4.12 (m, 2H, H-10), 3.66–3.65 (m, 2H, H-9), 3.58–3.56 (m, 6H, H-4, H-6, H-7), 3.49 (m, 2H, H-3), 3.33 (s, 3H, H-1), 2.41 (s, 3H, H-17); <sup>13</sup>C NMR (150 MHz, CDCl<sub>3</sub>) δ 144.9 (C-13), 133.1 (C-16), 130.0 (C-15), 128.1 (C-14), 72.0 (C-3), 70.8 (C-4/C-6/C-7), 70.7 (C-4/C-6/C-7), 70.6 (C-4/C-6/C-7), 69.4 (C-10), 68.8 (C-9), 59.1 (C-1), 21.8 (C-17); IR (thin film) 2877, 1598, 1452 cm<sup>-1</sup>.



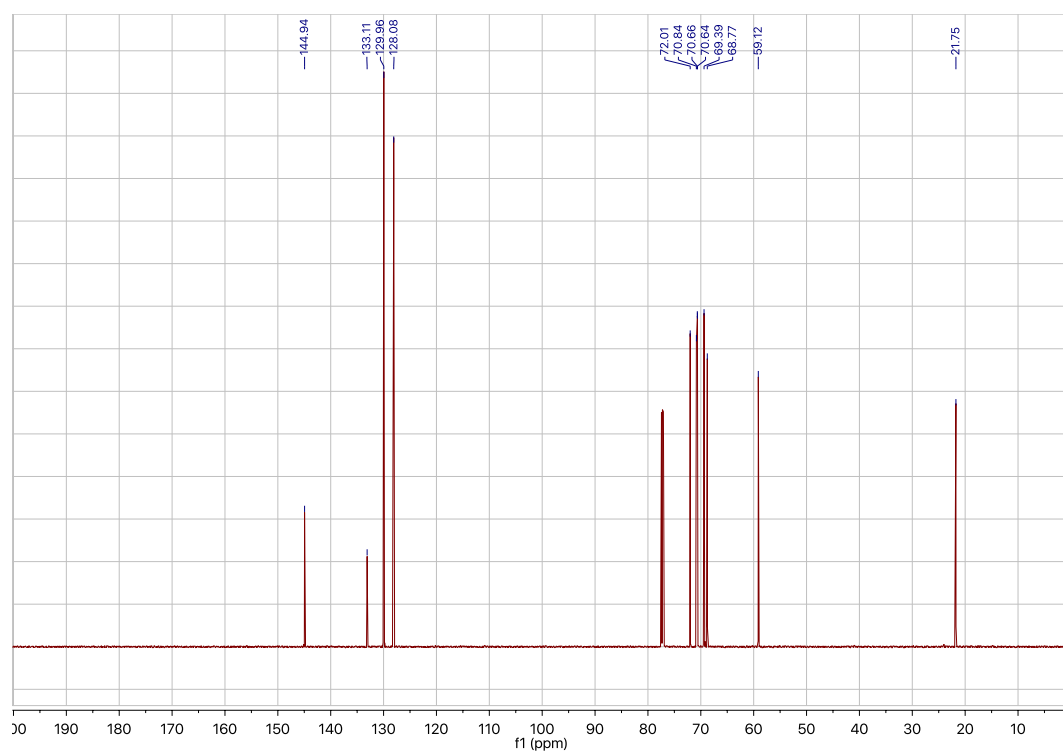
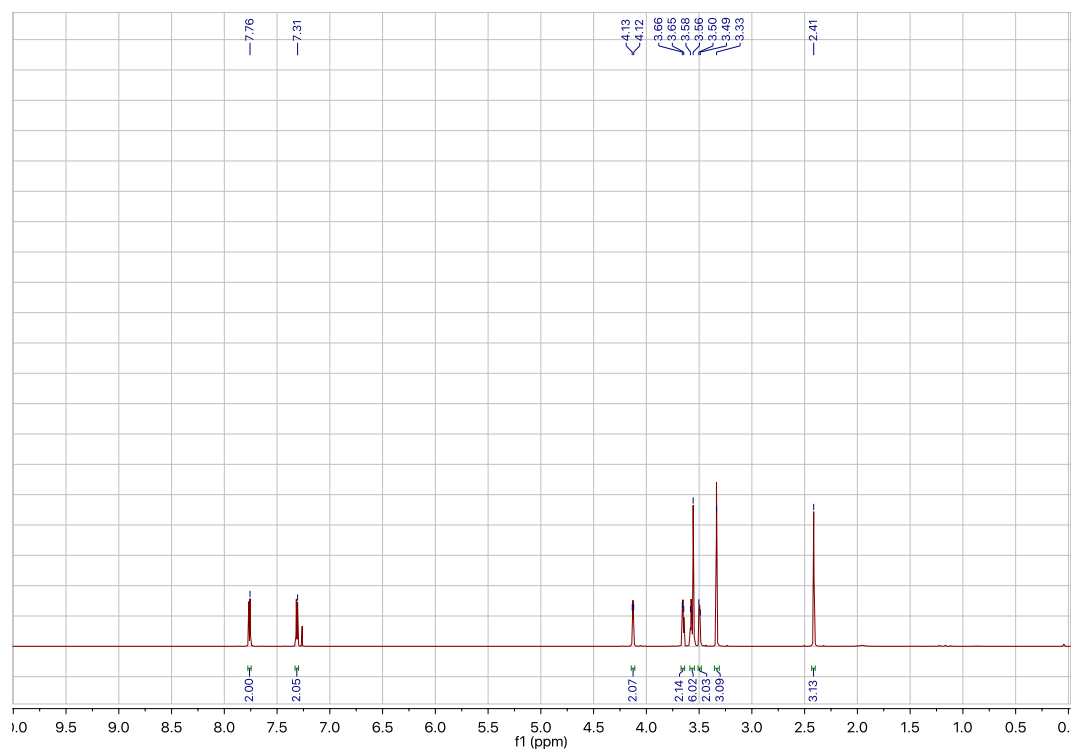
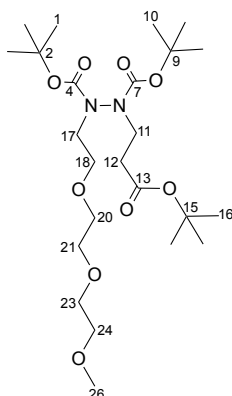


Figure S98.  $^1\text{H}$  and  $^{13}\text{C}$  NMR spectra for 2-(2-(2-methoxyethoxy)ethoxy)ethyl 4-methylbenzenesulfonate **76**.

## Tri-*tert*-butyl 2,5,8-trioxa-11,12-diazatetradecane-11,12,14-tricarboxylate **56**



To a solution of di-*tert*-butyl 1-(3-(*tert*-butoxy)-3-oxopropyl)hydrazine-1,2-dicarboxylate **72** (0.77 g, 2.1 mmol) and cesium carbonate (1.04 g, 3.19 mmol) in DMF (8 mL), was added 2-(2-(2-methoxyethoxy)ethoxy)ethyl 4-methylbenzenesulfonate **76** (1.02 g, 3.21 mmol), and the reaction mixture was stirred at 21 °C for 72 h. Following this, the reaction mixture was diluted with water (8 mL) and extracted with EtOAc (3 × 15 mL). The organic extracts were combined and subsequently washed sat. aq. LiCl solution (15 mL). The organic phase was then dried over MgSO<sub>4</sub>, concentrated *in vacuo* and the crude residue was purified by flash column chromatography (20–50% EtOAc/Pet.). The appropriate fractions were then combined and concentrated *in vacuo* to afford tri-*tert*-butyl 2,5,8-trioxa-11,12-diazatetradecane-11,12,14-tricarboxylate (0.92 g, 1.8 mmol, 85%) as a colourless oil. <sup>1</sup>H NMR (600 MHz, CDCl<sub>3</sub>, rotamers) δ 3.78–3.59 (m, 12H, H-11, H-17, H-18, H-20, H-21, H-23), 3.56–3.53 (m, 2H, H-24), 3.37 (s, 3H, H-26), 2.61 (t, *J* = 7.8 Hz, 2H, H-12), 1.48–1.42 (m, 27H, H-1, H-10, H-16); <sup>13</sup>C NMR (150 MHz, CDCl<sub>3</sub>) δ 171.4 (C-13), 171.2 (C-13), 171.1 (C-13), 155.8 (C-4/C-7), 155.2 (C4/C-7), 155.2 (C-4/C-7), 155.0 (C-4/C-7), 154.6 (C-4/C-7), 154.5 (C-4/C-7), 81.6 (C-2/C-9/C-15), 81.5 (C-2/C-9/C-15), 81.4 (C-2/C-9/C-15), 81.4 (C-2/C-9/C-15), 81.2 (C-2/C-9/C-15), 81.2 (C-2/C-9/C-15), 81.1 (C-2/C-9/C-15), 80.7 (C-2/C-9/C-15), 80.6 (C-2/C-9/C-15), 80.4 (C-2/C-9/C-15), 72.0 (C-24), 70.7 (C-23/C-21/C-20), 70.7 (C-23/C-21/C-20), 70.7 (C-23/C-21/C-20), 70.6 (C-23/C-21/C-20), 70.5 (C-23/C-21/C-20), 70.4 (C-23/C-21/C-20), 68.7 (C-18), 68.5 (C-18), 59.1 (C-26), 51.2 (C-17), 50.5 (C-17), 50.3 (C-17), 47.2 (C-11), 46.1 (C-11), 46.0 (C-11), 34.4 (C-12), 33.9 (C-12), 33.9 (C-12), 28.4 (C-1/C-10/C-16), 28.4 (C-1/C-

10/C-16), 28.3 (C-1/C-10/C-16), 28.2 (C-1/C-10/C-16), 28.2 (C-1/C-10/C-16); IR (thin film) 2973, 2928, 2872, 1705  $\text{cm}^{-1}$ ; LRMS (ES+) 507 (100,  $[\text{M}+\text{H}]^+$ ); HRMS (ES+) calcd for  $\text{C}_{25}\text{H}_{46}\text{N}_2\text{O}_9$   $[\text{M}+\text{H}]^+$  507.3282, observed 507.3272.

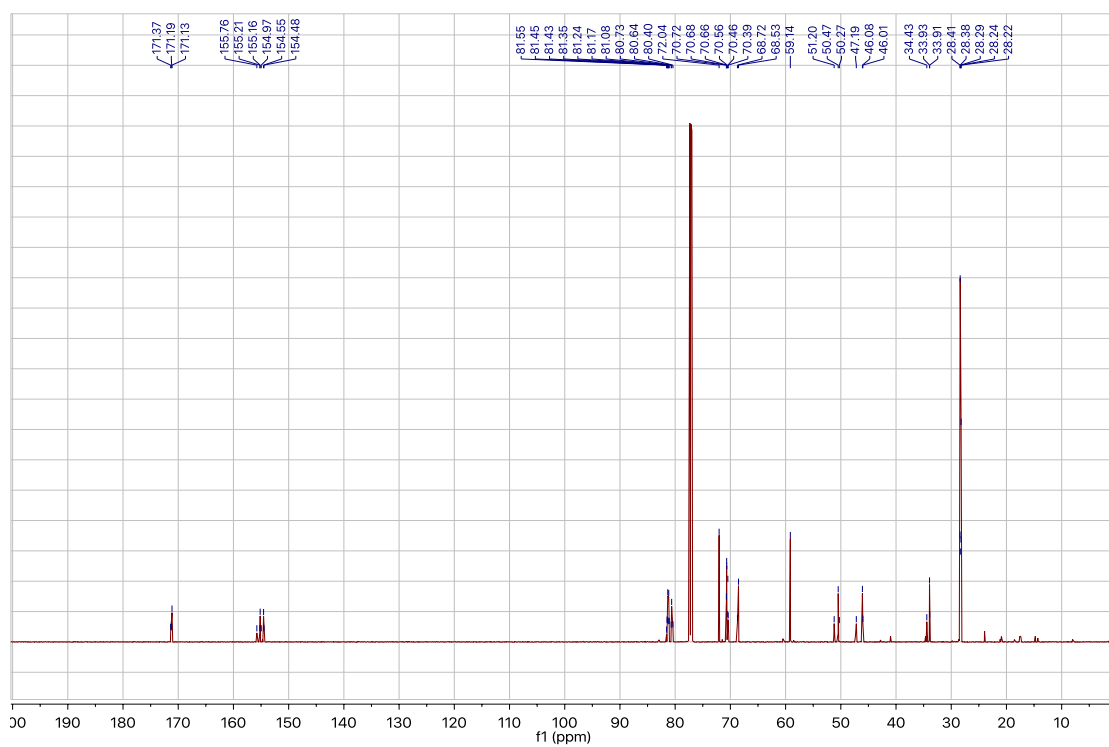
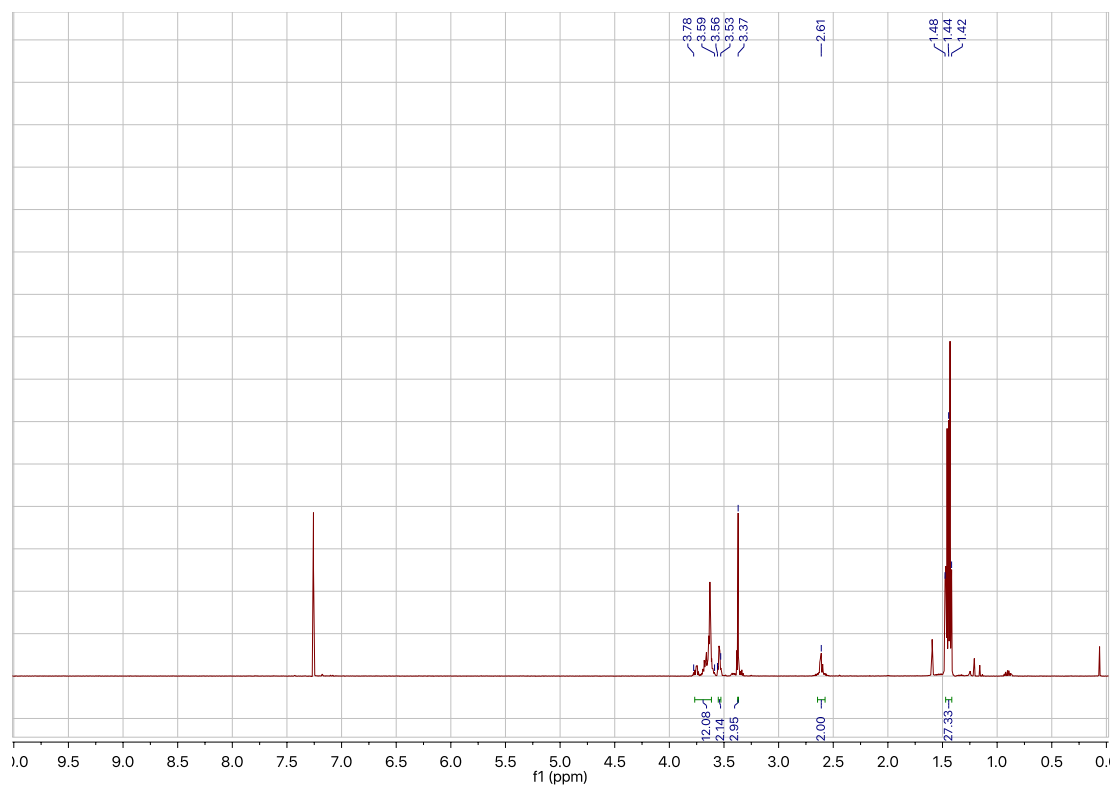


Figure S99.  $^1\text{H}$  and  $^{13}\text{C}$  NMR spectra for tri-*tert*-butyl 2,5,8-trioxa-11,12-diazatetradecane-11,12,14-tricarboxylate **56**.



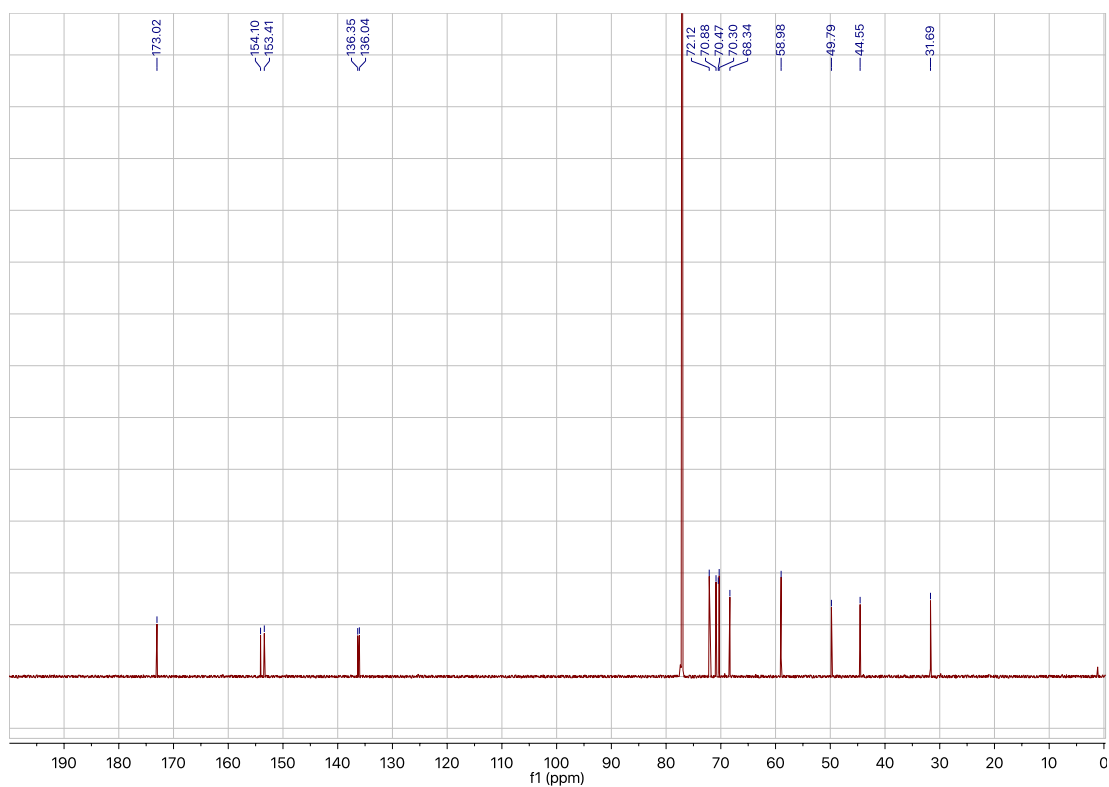
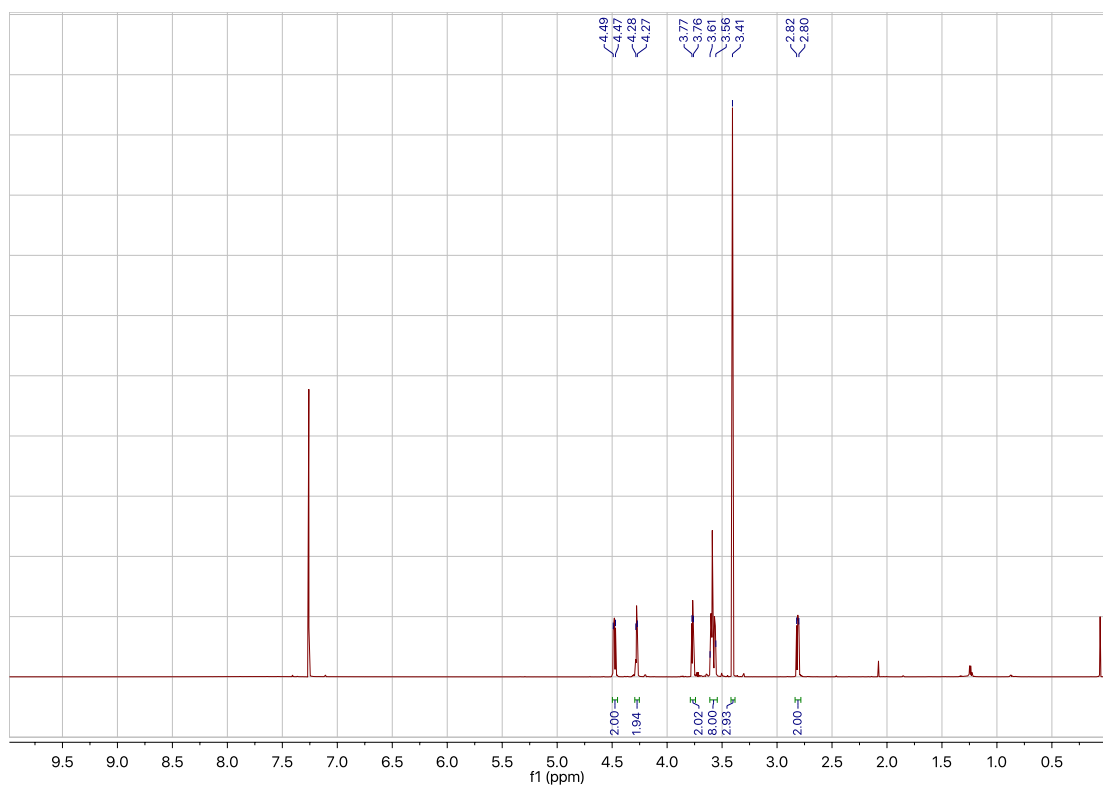
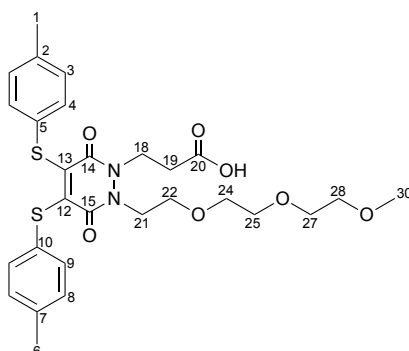


Figure S100.  $^1\text{H}$  and  $^{13}\text{C}$  NMR spectra for 3-(4,5-dibromo-2-(2-(2-(2-methoxyethoxy)ethoxy)ethyl)-3,6-dioxo-3,6-dihydropyridazin-1(2*H*)-yl)propanoic acid **77**.

**3-(2-(2-(2-(2-Methoxyethoxy)ethoxy)ethyl)-3,6-dioxo-4,5-bis(*p*-tolylthio)-3,6-dihydropyridazin-1(2*H*)-yl)propanoic acid 55**



To a solution of 4-methylbenzenethiol **36** (0.02 g, 0.2 mmol) and triethylamine (0.03 mL, 0.2 mmol) in CH<sub>2</sub>Cl<sub>2</sub> (1.5 mL) at 21 °C, was added 3-(4,5-dibromo-2-(2-(2-(2-methoxyethoxy)ethoxy)ethyl)-3,6-dioxo-3,6-dihydropyridazin-1(2*H*)-yl)propanoic acid **77** (0.03 g, 0.06 mmol) in CH<sub>2</sub>Cl<sub>2</sub> (0.5 mL), and the reaction mixture was stirred for 19 h. Following this, water (10 mL) was added and the resulting mixture's pH was adjusted to 3.0 with 1 M HCl. Following this, CH<sub>2</sub>Cl<sub>2</sub> (6 mL) was added and the mixture was washed with water (3 × 8 mL) and brine (8 mL). The organic phase was dried over MgSO<sub>4</sub>, concentrated *in vacuo* and the crude residue was purified by flash column chromatography (0–10% MeOH/CH<sub>2</sub>Cl<sub>2</sub>). The appropriate fractions were then combined and concentrated *in vacuo* to afford 3-(2-(2-(2-(2-methoxyethoxy)ethoxy)ethyl)-3,6-dioxo-4,5-bis(*p*-tolylthio)-3,6-dihydropyridazin-1(2*H*)-yl)propanoic acid (0.02 g, 0.03 mmol, 58%) as a yellow oil. <sup>1</sup>H NMR (600 MHz, CDCl<sub>3</sub>) δ 7.16–7.14 (m, 4H, H-4, H-9), 7.08–7.06 (m, 4H, H-3, H-8), 4.31 (t, *J* = 7.3 Hz, 2H, H-18), 4.09 (t, *J* = 5.0 Hz, 2H, H-21), 3.70 (t, *J* = 5.0 Hz, 2H, H-22), 3.62–3.55 (m, 8H, H-24, H-25, H-27, H-28), 3.40 (s, 3H, H-30), 2.73 (t, *J* = 7.3 Hz, 2H, H-19), 2.32 (app. d, 6H, H-1, H-6); <sup>13</sup>C NMR (150 MHz, CDCl<sub>3</sub>) δ 173.4 (C-20), 157.2 (C-15), 156.3 (C-14), 142.6 (C-12/C-13), 142.0 (C-12/C-13), 138.1 (C-2/C-7), 138.1 (C-2/C-7), 131.4 (C-4/C-9), 131.3 (C-4/C-9), 130.0 (C-3/C-8), 129.9 (C-3/C-8), 129.2 (C-5/C-10), 129.2 (C-5/C-10), 72.1 (C-28), 70.8 (C-24/C-25/C-27), 70.6 (C-24/C-25/C-27), 70.4 (C-24/C-25/C-27), 68.5 (C-22), 59.0 (C-30), 48.7 (C-21), 43.3 (C-18), 31.5 (C-19), 21.4 (C-1, C-6); IR (thin film) 3455, 3020, 2920, 2870, 1729, 1625 cm<sup>-1</sup>; LRMS (ES<sup>+</sup>) 575 (100, [M+H]<sup>+</sup>); HRMS (ES<sup>+</sup>) calcd for C<sub>28</sub>H<sub>35</sub>N<sub>2</sub>O<sub>7</sub>S<sub>2</sub> [M+H]<sup>+</sup> 575.1880, observed 575.1881.

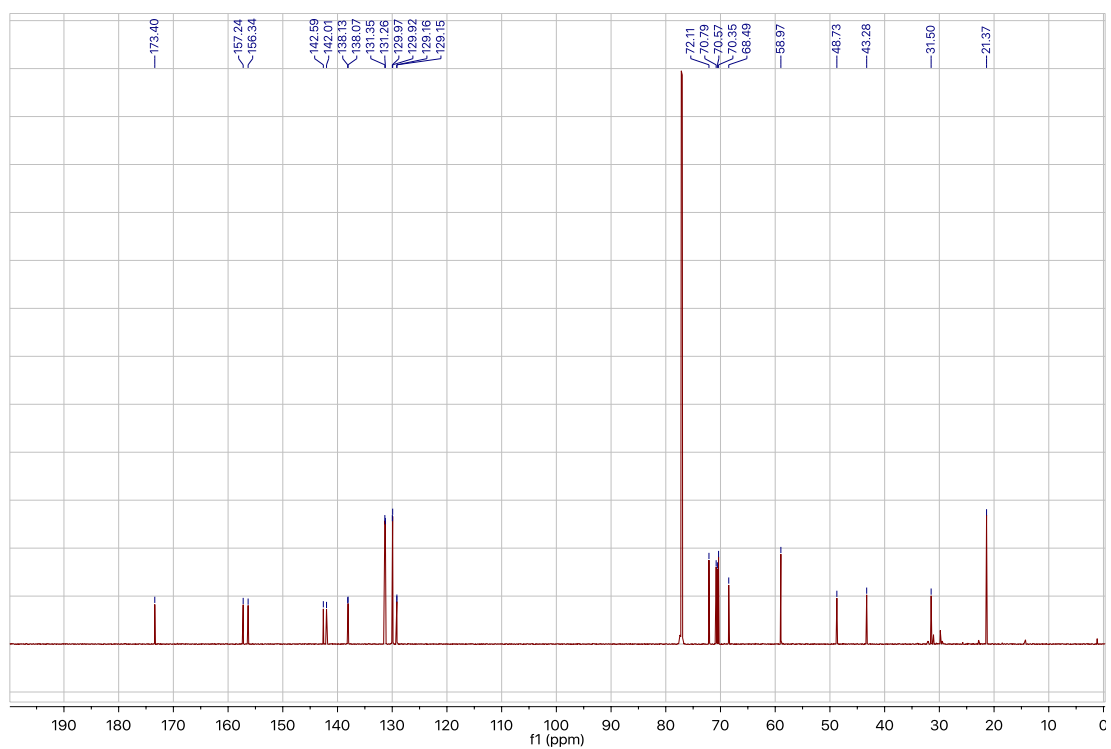
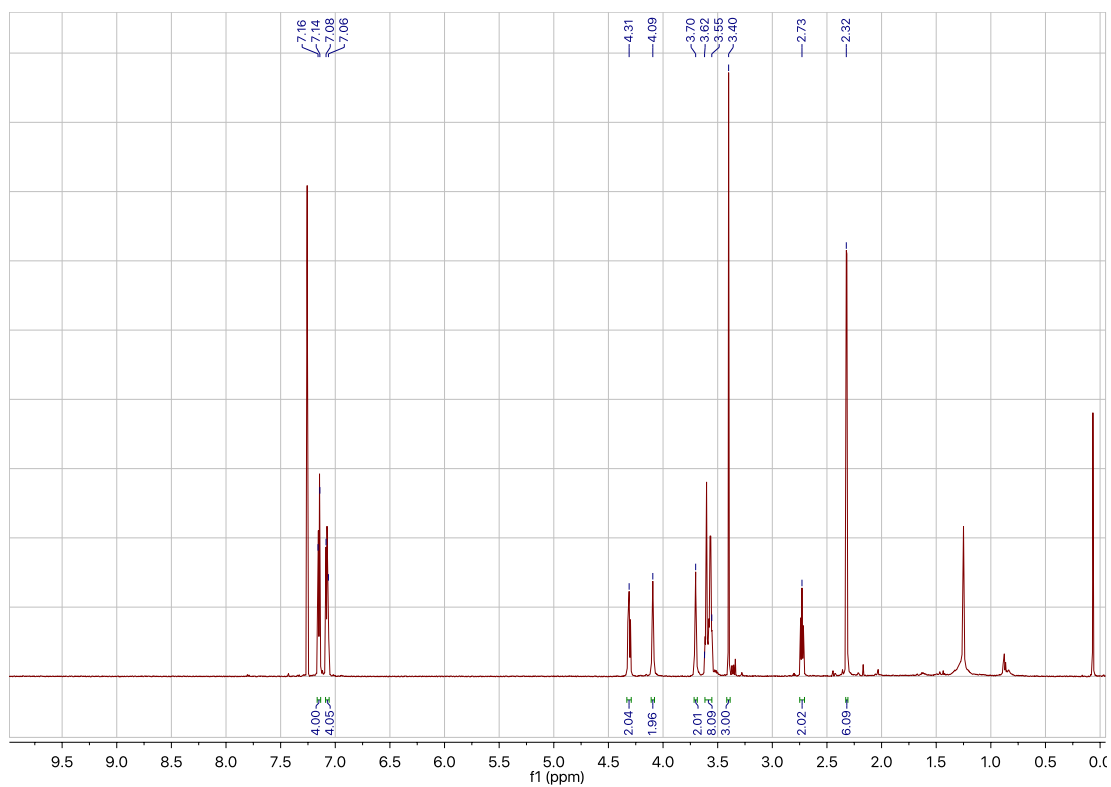
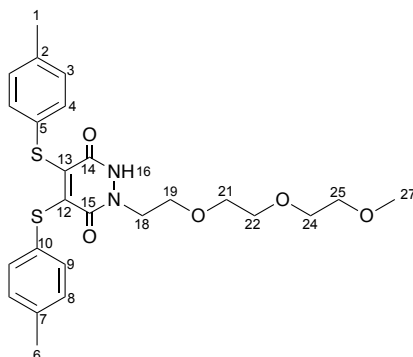


Figure S101. <sup>1</sup>H and <sup>13</sup>C NMR spectra for 3-(2-(2-(2-(2-methoxyethoxy)ethoxy)ethyl)-3,6-dioxo-4,5-bis(*p*-tolylthio)-3,6-dihydropyridazin-1(2*H*)-yl)propanoic acid **55**.

## 1-(2-(2-(2-Methoxyethoxy)ethoxy)ethyl)-4,5-bis(*p*-tolylthio)-1,2-dihydropyridazine-3,6-dione **78**



A solution of 3-(2-(2-(2-(2-methoxyethoxy)ethoxy)ethyl)-3,6-dioxo-4,5-bis(*p*-tolylthio)-3,6-dihydropyridazin-1(*2H*)-yl)propanoic acid **55** (0.11 g, 0.19 mmol) in THF (5 mL) was cooled to 0 °C and stirred for 10 mins. To this was added EDC·HCl (0.06 g, 0.3 mmol) and the resulting solution was stirred at 0 °C for 30 mins. After this time DMAP (0.04 g, 0.3 mmol) and *tert*-butanol **41** (0.18 mL, 1.9 mmol) were added and the solution was stirred at 21 °C for 21 h. Following this, the reaction mixture was diluted with EtOAc (10 mL) and washed with 0.5% citric acid (3 × 10 mL), distilled water (10 mL) and brine (10 mL). The organic phase was dried over MgSO<sub>4</sub>, concentrated *in vacuo* and the crude residue was purified by flash column chromatography (0–10% MeOH/CH<sub>2</sub>Cl<sub>2</sub>). The appropriate fractions were then combined and concentrated *in vacuo* to afford 1-(2-(2-(2-methoxyethoxy)ethoxy)ethyl)-4,5-bis(*p*-tolylthio)-1,2-dihydropyridazine-3,6-dione (0.04 g, 0.08 mmol, 42%) as a yellow solid. m.p. 81–84 °C; <sup>1</sup>H NMR (700 MHz, CDCl<sub>3</sub>) δ 7.23–7.20 (m, 4H, H-4, H-9), 7.09–7.06 (m, 4H, H-3, H-8), 4.13 (t, *J* = 5.1 Hz, 2H, H-18), 3.78 (t, *J* = 5.1 Hz, 2H, H-19), 3.64–3.63 (m, 2H, H-24), 3.60 (app. s, 4H, H-21, H-22), 3.54–3.53 (m, 2H, H-25), 3.33 (s, 3H, H-27), 2.32 (app. d, 6H, H-1, H-6); <sup>13</sup>C NMR (150 MHz, CDCl<sub>3</sub>) δ 156.7 (C-15), 150.4 (C-14), 144.0 (C-12, C-13), 138.0 (C-2/C-7), 137.9 (C-2/C-7), 131.3 (C-4/C-9), 130.9 (C-4/C-9), 130.0 (C-3/C-8), 129.9 (C-3/C-8), 129.6 (C-5/C-10), 129.6 (C-5/C-10), 72.2 (C-25), 70.8 (C-21/C-22), 70.4 (C-21/C-22), 70.4 (C-24), 68.6 (C-19), 59.01 (C-27), 50.5 (C-18), 21.4 (C-1/C-6), 21.3 (C-1/C-6); IR (solid) 3053, 3019, 2919, 2863, 1739, 1644 cm<sup>-1</sup>;



LRMS (ES+) 503 (100, [M+H]<sup>+</sup>); HRMS (ES+) calcd for C<sub>25</sub>H<sub>31</sub>N<sub>2</sub>O<sub>5</sub>S<sub>2</sub> [M+H]<sup>+</sup> 503.1674, observed 503.1662.

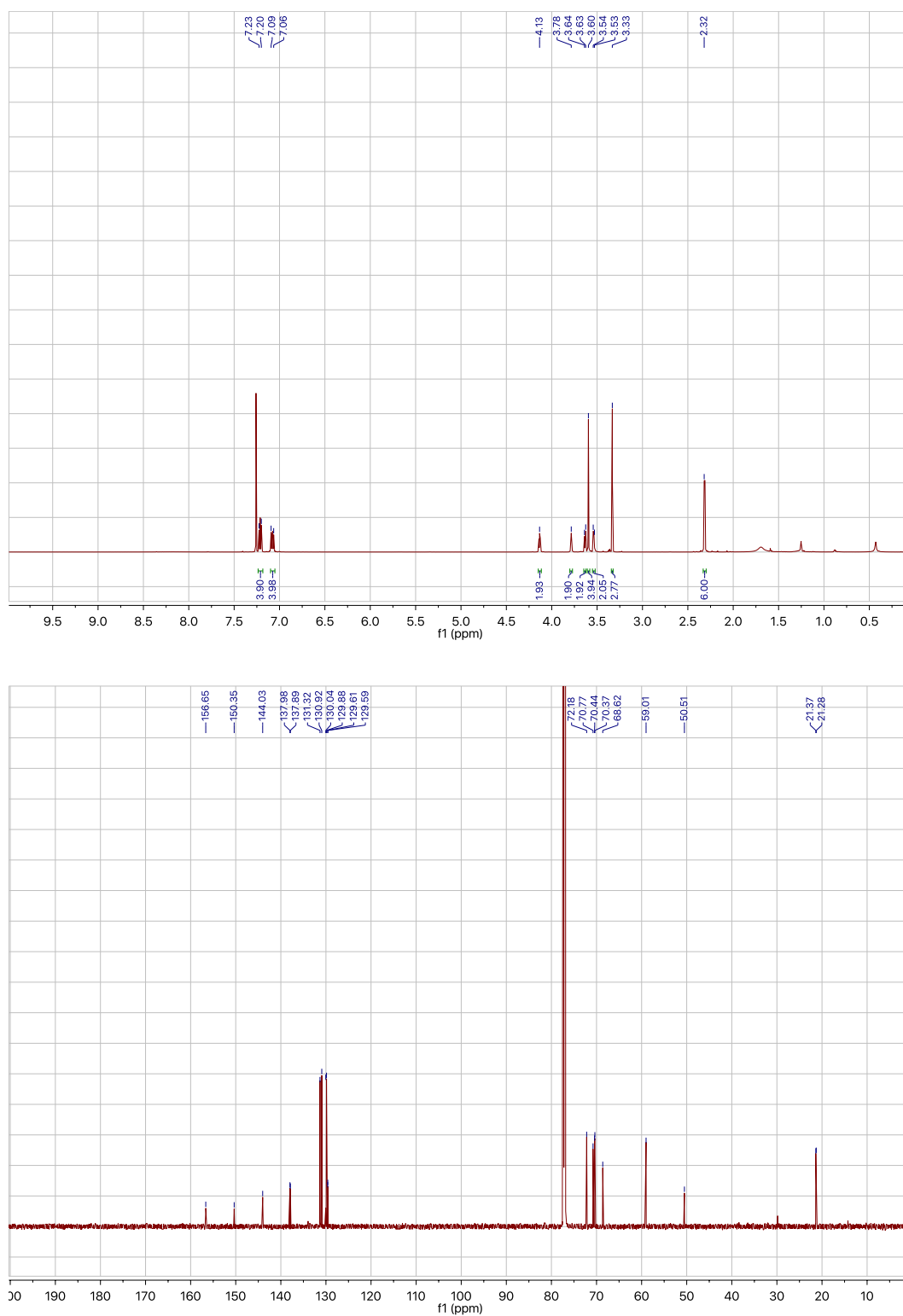
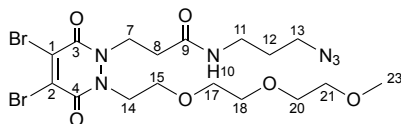


Figure S102. <sup>1</sup>H and <sup>13</sup>C NMR spectra for 1-(2-(2-(2-methoxyethoxy)ethoxy)ethyl)-4,5-bis(*p*-tolylthio)-1,2-dihydropyridazine-3,6-dione **78**.

***N*-(3-Azidopropyl)-3-(4,5-dibromo-2-(2-(2-(2-methoxyethoxy)ethoxy)ethyl)-3,6-dioxo-3,6-dihydropyridazin-1(2*H*)-yl)propanamide 80**



To a solution of 3-(4,5-dibromo-2-(2-(2-(2-methoxyethoxy)ethoxy)ethyl)-3,6-dioxo-3,6-dihydropyridazin-1(2*H*)-yl)propanoic acid **77** (0.15 g, 0.31 mmol) in THF (4 mL) stirring at 0 °C was added DCC (0.08 g, 0.4 mmol), and the reaction mixture was stirred at 0 °C for 30 mins. After this time, 3-azido-1-propanamine **79** (0.04 g, 0.4 mmol) was added, and the reaction mixture was stirred at 21 °C for a further 23 h. Following this, the reaction mixture was filtered to remove insolubles and underwent 3 rounds of successive cooling on acetone/dry ice and filtrations before being concentrated *in vacuo*. The crude residue was purified by flash column chromatography (0–5% MeOH/CH<sub>2</sub>Cl<sub>2</sub>). The appropriate fractions were then combined and concentrated *in vacuo* to afford *N*-(3-azidopropyl)-3-(4,5-dibromo-2-(2-(2-(2-methoxyethoxy)ethoxy)ethyl)-3,6-dioxo-3,6-dihydropyridazin-1(2*H*)-yl)propanamide (0.09 g, 0.2 mmol, 51%) as a clear brown oil. <sup>1</sup>H NMR (700 MHz, CDCl<sub>3</sub>) δ 6.40 (app. s, 1H, H-10), 4.46 (t, *J* = 7.0 Hz, 2H, H-7), 4.36 (t, *J* = 4.9 Hz, 2H, H-14), 3.74 (t, *J* = 4.9 Hz, 2H, H-15), 3.58–3.56 (m, 6H, H-17, H-18, H-20), 3.53–3.51 (m, 2H, H-21), 3.36 (s, 3H, H-23), 3.35 (app. d, 2H, H-13), 3.31 (q, *J* = 6.7 Hz, 2H, H-11), 2.66 (t, *J* = 7.0 Hz, 2H, H-8), 1.76 (p, *J* = 6.7 Hz, 2H, H-12); <sup>13</sup>C NMR (150 MHz, CDCl<sub>3</sub>) δ 170.0 (C-9), 153.8 (C-4), 153.4 (C-3), 136.1 (C-1/C-2), 136.0 (C-1/C-2), 72.0 (C-21), 70.6 (C-17/C-18/C-20), 70.5 (C-17/C-18/C-20), 70.5 (C-17/C-18/C-20), 67.9 (C-15), 59.1 (C-23), 49.4 (C-13), 48.8 (C-14), 45.1 (C-7), 37.4 (C-11), 33.9 (C-8), 28.9 (C-12); IR (thin film) 2923, 2874, 2094, 1631 cm<sup>-1</sup>; LRMS (ES<sup>+</sup>) 571 (100, [[M<sup>81</sup>Br<sup>79</sup>Br]+H]<sup>+</sup>); HRMS (ES<sup>+</sup>) calcd for C<sub>17</sub>H<sub>27</sub>N<sub>6</sub>O<sub>6</sub>Br<sub>2</sub> [[M<sup>81</sup>Br<sup>79</sup>Br]+H]<sup>+</sup> 571.0333, observed 571.0337.

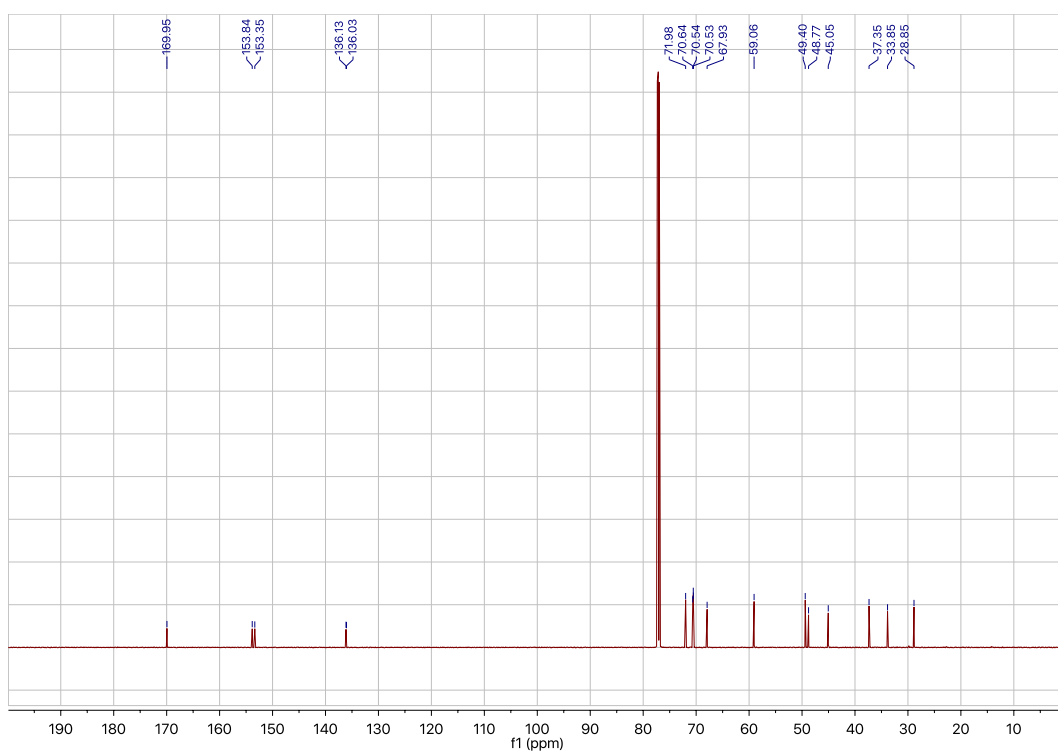
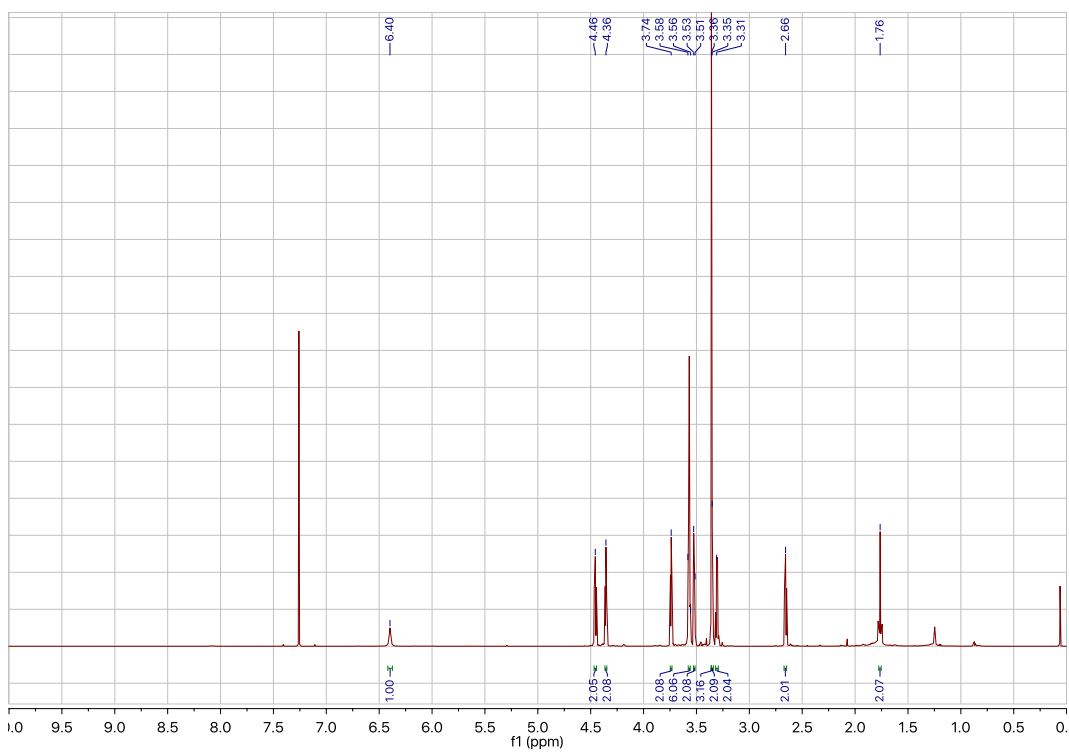
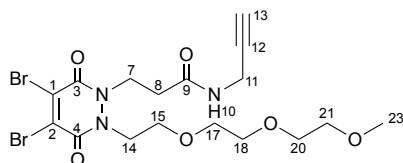


Figure S103.  $^1\text{H}$  and  $^{13}\text{C}$  NMR spectra for *N*-(3-azidopropyl)-3-(4,5-dibromo-2-(2-(2-(2-methoxyethoxy)ethoxy)ethyl)-3,6-dioxo-3,6-dihydropyridazin-1(2*H*)-yl)propanamide **80**.

**3-(4,5-Dibromo-2-(2-(2-(2-methoxyethoxy)ethoxy)ethyl)-3,6-dioxo-3,6-dihydropyridazin-1(2H)-yl)-N-(prop-2-yn-1-yl)propanamide 82**



To a solution of 3-(4,5-dibromo-2-(2-(2-(2-methoxyethoxy)ethoxy)ethyl)-3,6-dioxo-3,6-dihydropyridazin-1(2H)-yl)propanoic acid **77** (0.10 g, 0.21 mmol) in THF (4 mL) stirring at 0 °C was added DCC (0.05 g, 0.2 mmol), and the reaction mixture was stirred at 0 °C for 30 mins. After this time, propargylamine **81** (15  $\mu$ L, 0.23 mmol) was added, and the reaction mixture was stirred at 21 °C for a further 20 h. Following this, the reaction mixture was filtered to remove insolubles and underwent 3 rounds of successive cooling on acetone/dry ice and filtrations before being concentrated *in vacuo*. The crude residue was purified by flash column chromatography (0–15% MeOH/CH<sub>2</sub>Cl<sub>2</sub>). The appropriate fractions were then combined and concentrated *in vacuo* to afford 3-(4,5-dibromo-2-(2-(2-(2-methoxyethoxy)ethoxy)ethyl)-3,6-dioxo-3,6-dihydropyridazin-1(2H)-yl)-N-(prop-2-yn-1-yl)propanamide (0.06 g, 0.1 mmol, 55%) as a green oil. <sup>1</sup>H NMR (700 MHz, CDCl<sub>3</sub>)  $\delta$  6.78 (app. s, 1H, H-10), 4.46 (t, *J* = 7.1 Hz, 2H, H-7), 4.33 (t, *J* = 4.8 Hz, 2H, H-14), 4.00 (dd, *J* = 5.4, 2.5 Hz, 2H, H-11), 3.74 (t, *J* = 4.8 Hz, 2H, H-15), 3.59–3.56 (m, 6H, H-17, H-18, H-20), 3.53–3.52 (m, 2H, H-21), 3.36 (s, 3H, H-23), 2.71 (t, *J* = 7.1 Hz, 2H, H-8), 2.20 (t, *J* = 2.5 Hz, 1H, H-13); <sup>13</sup>C NMR (150 MHz, CDCl<sub>3</sub>)  $\delta$  169.8 (C-9), 153.8 (C-4), 153.3 (C-3), 136.2 (C-1/C-2), 136.0 (C-1/C-2), 79.7 (C-12), 72.0 (C-21), 71.5 (C-13), 70.6 (C-17/C-18/C-20), 70.5 (C-17/C-18/C-20), 70.5 (C-17/C-18/C-20), 68.0 (C-15), 59.0 (C-23), 49.1 (C-14), 45.1 (C-7), 33.3 (C-8), 29.2 (C-11); IR (thin film) 2873, 1629 cm<sup>-1</sup>; LRMS (ES+) 526 (100, [[M<sup>81</sup>Br<sup>79</sup>Br]+H]<sup>+</sup>); HRMS (ES+) calcd for C<sub>17</sub>H<sub>24</sub>N<sub>3</sub>O<sub>6</sub>Br<sub>2</sub> [[M<sup>81</sup>Br<sup>79</sup>Br]+H]<sup>+</sup> 526.0006, observed 526.0007.

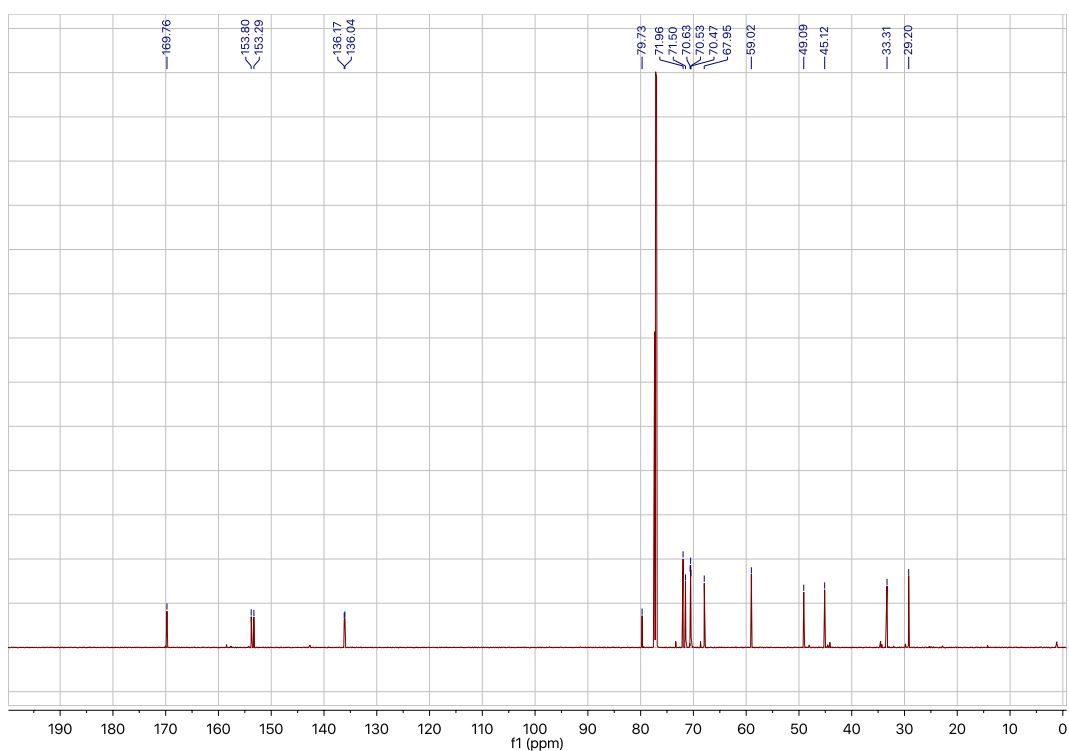
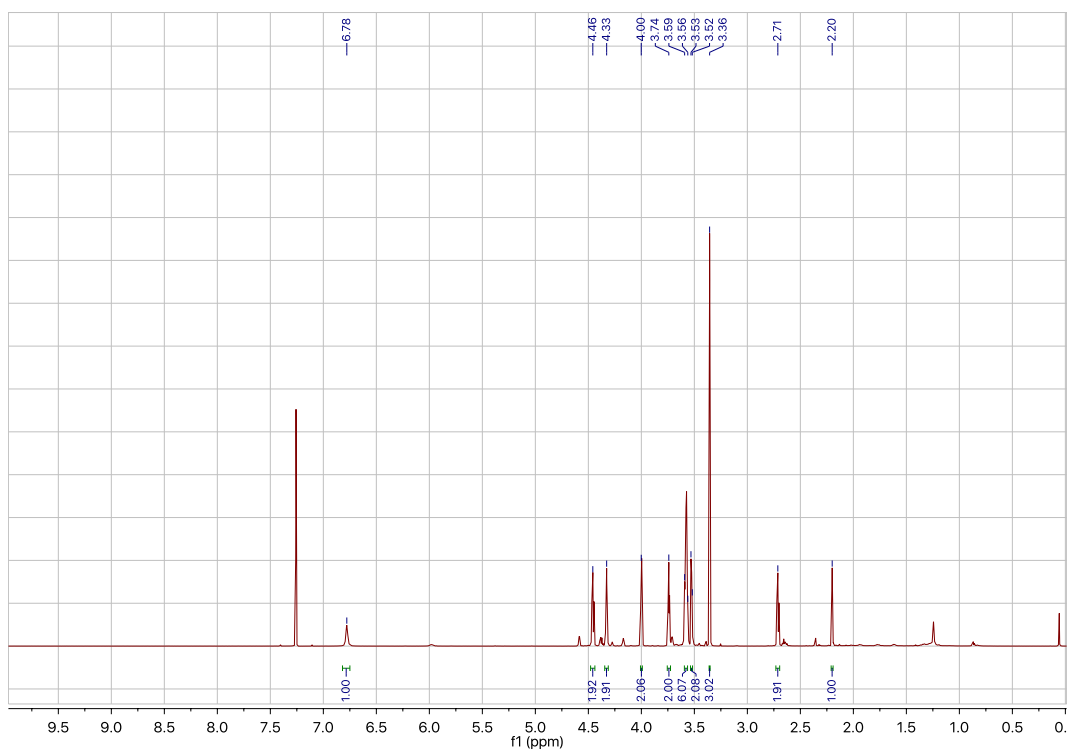
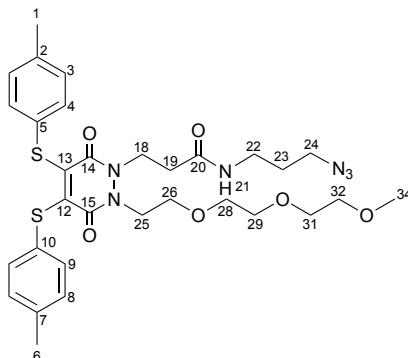


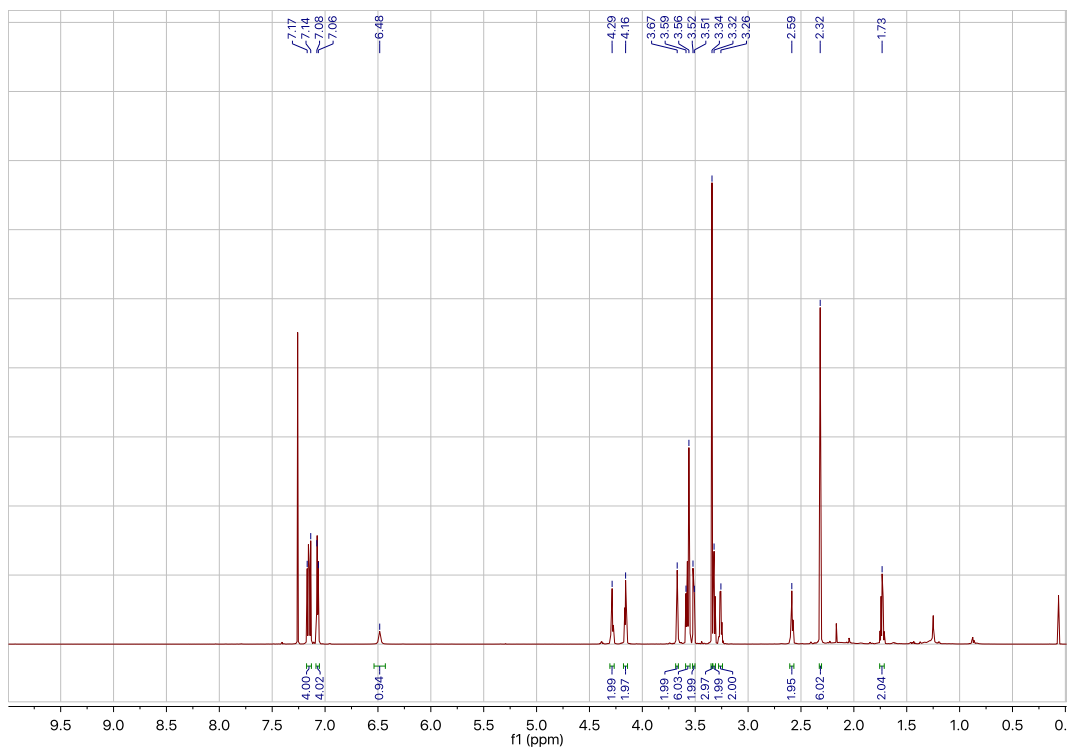
Figure S104.  $^1\text{H}$  and  $^{13}\text{C}$  NMR spectra for 3-(4,5-dibromo-2-(2-(2-(2-methoxyethoxy)ethoxy)ethyl)-3,6-dioxo-3,6-dihydropyridazin-1(2*H*)-yl)-*N*-(prop-2-yn-1-yl)propanamide **82**.

***N*-(3-Azidopropyl)-3-(2-(2-(2-(2-methoxyethoxy)ethoxy)ethyl)-3,6-dioxo-4,5-bis(*p*-tolylthio)-3,6-dihydropyridazin-1(2*H*)-yl)propanamide 83**



To a solution of 4-methylbenzenethiol **36** (0.03 g, 0.2 mmol) and triethylamine (75  $\mu$ L, 0.54 mmol) in  $\text{CH}_2\text{Cl}_2$  (2 mL) at 21  $^\circ\text{C}$ , was added *N*-(3-azidopropyl)-3-(4,5-dibromo-2-(2-(2-(2-methoxyethoxy)ethoxy)ethyl)-3,6-dioxo-3,6-dihydropyridazin-1(2*H*)-yl)propanamide **80** (0.05 g, 0.09 mmol), and the reaction mixture was stirred for 10 mins. Following this, the reaction mixture was diluted with  $\text{CH}_2\text{Cl}_2$  (8 mL) and washed with water (3  $\times$  8 mL) and brine (8 mL). The organic phase was then dried over  $\text{MgSO}_4$ , concentrated *in vacuo* and the crude residue was purified by flash column chromatography (0–5% MeOH/ $\text{CH}_2\text{Cl}_2$ ). The appropriate fractions were then combined and concentrated *in vacuo* to afford *N*-(3-azidopropyl)-3-(2-(2-(2-(2-methoxyethoxy)ethoxy)ethyl)-3,6-dioxo-4,5-bis(*p*-tolylthio)-3,6-dihydropyridazin-1(2*H*)-yl)propanamide (0.05 g, 0.08 mmol, 85%) as a yellow oil.  $^1\text{H}$  NMR (700 MHz,  $\text{CDCl}_3$ )  $\delta$  7.17–7.14 (m, 4H, H-4, H-9), 7.08–7.06 (m, 4H, H-3, H-8), 6.48 (app. s, 1H, H-21), 4.29 (t,  $J = 6.9$  Hz, 2H, H-18), 4.16 (t,  $J = 5.0$  Hz, 2H, H-25), 3.67 (t,  $J = 5.0$  Hz, 2H, H-26), 3.59–3.56 (m, 6H, H-28, H-29, H-31), 3.52–3.51 (m, 2H, H-32), 3.34 (s, 3H, H-34), 3.32 (t,  $J = 6.6$  Hz, 2H, H-24), 3.26 (q,  $J = 6.6$  Hz, 2H, H-22), 2.59 (t,  $J = 6.9$  Hz, 2H, H-19), 2.32 (s, 6H, H-1, H-6), 1.73 (p,  $J = 6.6$  Hz, 2H, H-23);  $^{13}\text{C}$  NMR (150 MHz,  $\text{CDCl}_3$ )  $\delta$  170.3 (C-20), 156.9 (C-15), 156.4 (C-14), 142.3 (C-12/C-13), 142.1 (C-12/C-13), 138.1 (C-2/C-7), 138.1 (C-2/C-7), 131.3 (C-4/C-9), 131.2 (C-4/C-9), 129.9 (C-3, C-8), 129.3 (C-5/C-10), 129.1 (C-5/C-10), 72.0 (C-32), 70.6 (C-28/C-29/C-31), 70.6 (C-28/C-29/C-31), 70.5 (C-28/C-29/C-31), 68.1 (C-26), 59.0 (C-34), 49.3 (C-24), 47.8 (C-25), 43.9 (C-18), 37.3 (C-22), 34.0 (C-19), 28.8

(C-23), 21.4 (C-1, C-6); IR (thin film) 2921, 2869, 2094, 1621  $\text{cm}^{-1}$ ; LRMS (ES+) 657 (100,  $[\text{M}+\text{H}]^+$ ); HRMS (ES+) calcd for  $\text{C}_{31}\text{H}_{41}\text{N}_6\text{O}_6\text{S}_2$   $[\text{M}+\text{H}]^+$  657.2524, observed 657.2527.



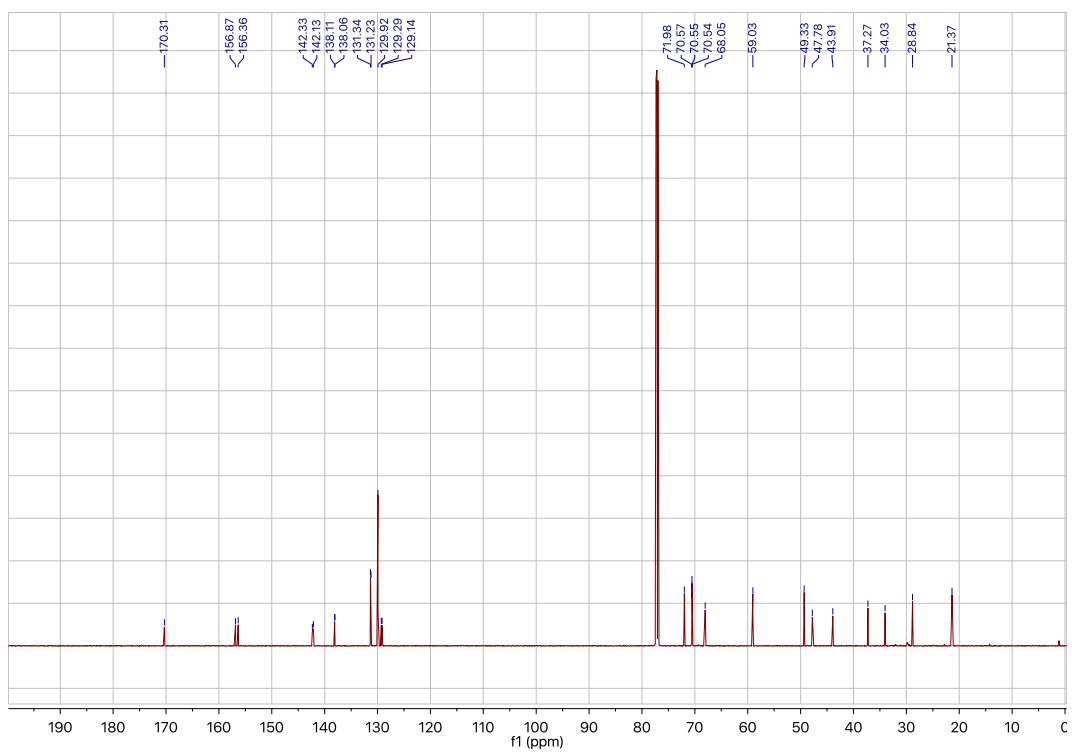
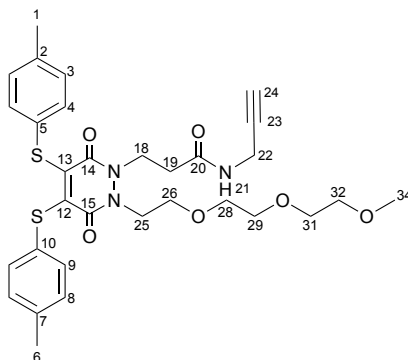


Figure S105.  $^1\text{H}$  and  $^{13}\text{C}$  NMR spectra for *N*-(3-azidopropyl)-3-(2-(2-(2-(2-methoxyethoxy)ethoxy)ethyl)-3,6-dioxo-4,5-bis(*p*-tolylthio)-3,6-dihydropyridazin-1(2*H*)-yl)propanamide **83**.

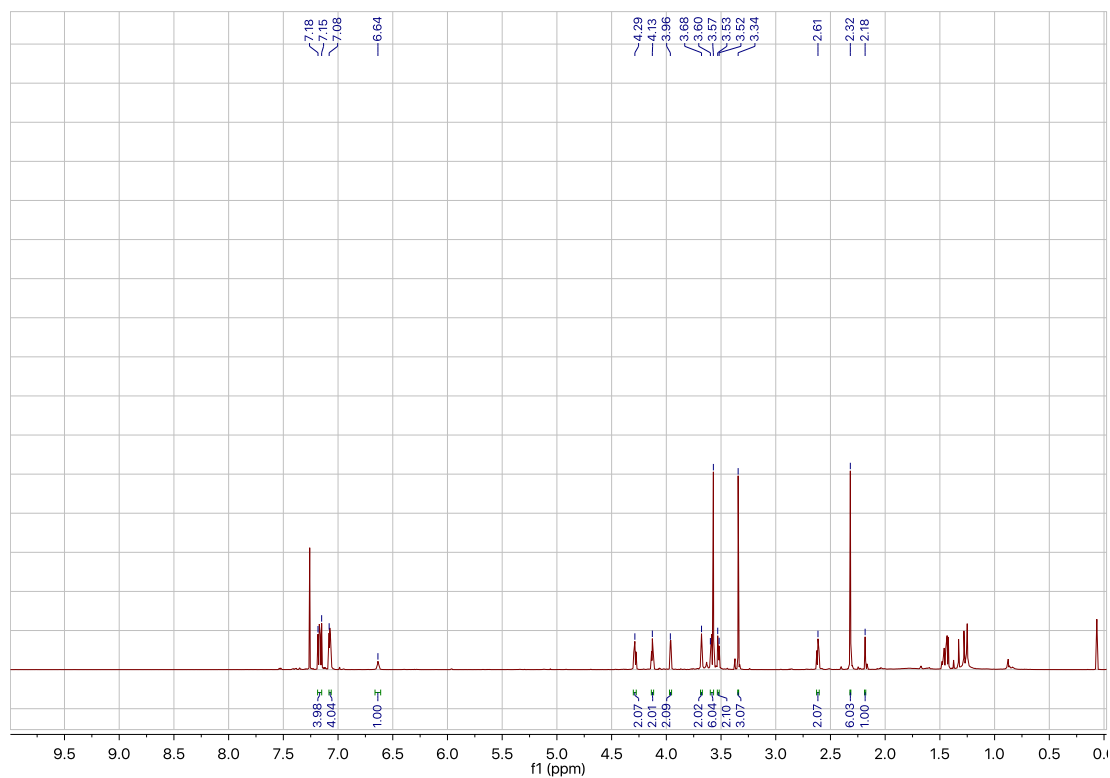


**3-(2-(2-(2-(2-Methoxyethoxy)ethoxy)ethyl)-3,6-dioxo-4,5-bis(*p*-tolylthio)-3,6-dihydropyridazin-1(2*H*)-yl)-*N*-(prop-2-yn-1-yl)propanamide **84****



To a solution of 4-methylbenzenethiol **36** (0.01 g, 0.08 mmol) and triethylamine (17  $\mu$ L, 0.12 mmol) in  $\text{CH}_2\text{Cl}_2$  (3 mL) at 21  $^\circ\text{C}$ , was added 3-(4,5-dibromo-2-(2-(2-(2-methoxyethoxy)ethoxy)ethyl)-3,6-dioxo-3,6-dihydropyridazin-1(2*H*)-yl)-*N*-(prop-2-yn-1-yl)propanamide **82** (0.01 g, 0.02 mmol), and the reaction mixture was stirred for 10 mins. Following this, the reaction mixture was diluted with  $\text{CH}_2\text{Cl}_2$  (8 mL) and washed with water (3  $\times$  8 mL) and brine (8 mL). The organic phase was then dried over  $\text{MgSO}_4$ , concentrated *in vacuo* and the crude residue was purified by flash column chromatography (0–5% MeOH/ $\text{CH}_2\text{Cl}_2$ ). The appropriate fractions were then combined and concentrated *in vacuo* to afford 3-(2-(2-(2-(2-methoxyethoxy)ethoxy)ethyl)-3,6-dioxo-4,5-bis(*p*-tolylthio)-3,6-dihydropyridazin-1(2*H*)-yl)-*N*-(prop-2-yn-1-yl)propanamide (0.01 g, 0.02 mmol, 82%) as a yellow oil.  $^1\text{H}$  NMR (700 MHz,  $\text{CDCl}_3$ ) $\delta$  7.18–7.15 (m, 4H, H-4, H-9), 7.08–7.06 (m, 4H, H-3, H-8), 6.64 (app. s, 1H, H-21), 4.29 (t,  $J = 7.0$  Hz, 2H, H-18), 4.13 (t,  $J = 4.9$  Hz, 2H, H-25), 3.96 (dd,  $J = 5.3, 2.5$  Hz, 2H, H-22), 3.68 (t,  $J = 4.9$  Hz, 2H, H-26), 3.60–3.57 (m, 6H, H-28, H-29, H-31), 3.53–3.52 (m, 2H, H-32), 3.34 (s, 3H, H-34), 2.61 (t,  $J = 7.0$  Hz, 2H, H-19), 2.32 (s, 6H, H-1, H-6), 2.18 (t,  $J = 2.5$  Hz, 1H, H-24);  $^{13}\text{C}$  NMR (150 MHz,  $\text{CDCl}_3$ )  $\delta$  169.9 (C-20), 156.9 (C-15), 156.3 (C-14), 142.4 (C-12/C-13), 142.3 (C-12/C-13), 138.1 (C-2/C-7), 138.0 (C-2/C-7), 131.3 (C-4/C-9), 131.3 (C-4/C-9), 129.9 (C-3/C-8), 129.9 (C-3/C-8), 129.4 (C-5/C-10), 129.3 (C-5/C-10), 79.8 (C-23), 72.0 (C-32), 71.5 (C-24), 70.5 (C-28/C-29/C-31), 70.5 (C-28/C-29/C-31), 68.2 (C-26), 59.0 (C-34), 48.4 (C-25), 44.1 (C-18), 33.5 (C-19), 29.2 (C-22), 21.4 (C-1, C-

6); IR (thin film) 2921, 2869, 1621  $\text{cm}^{-1}$ ; LRMS (ES+) 612 (100,  $[\text{M}+\text{H}]^+$ ); HRMS (ES+) calcd for  $\text{C}_{31}\text{H}_{38}\text{N}_3\text{O}_6\text{S}_2$   $[\text{M}+\text{H}]^+$  612.2197, observed 612.2198.



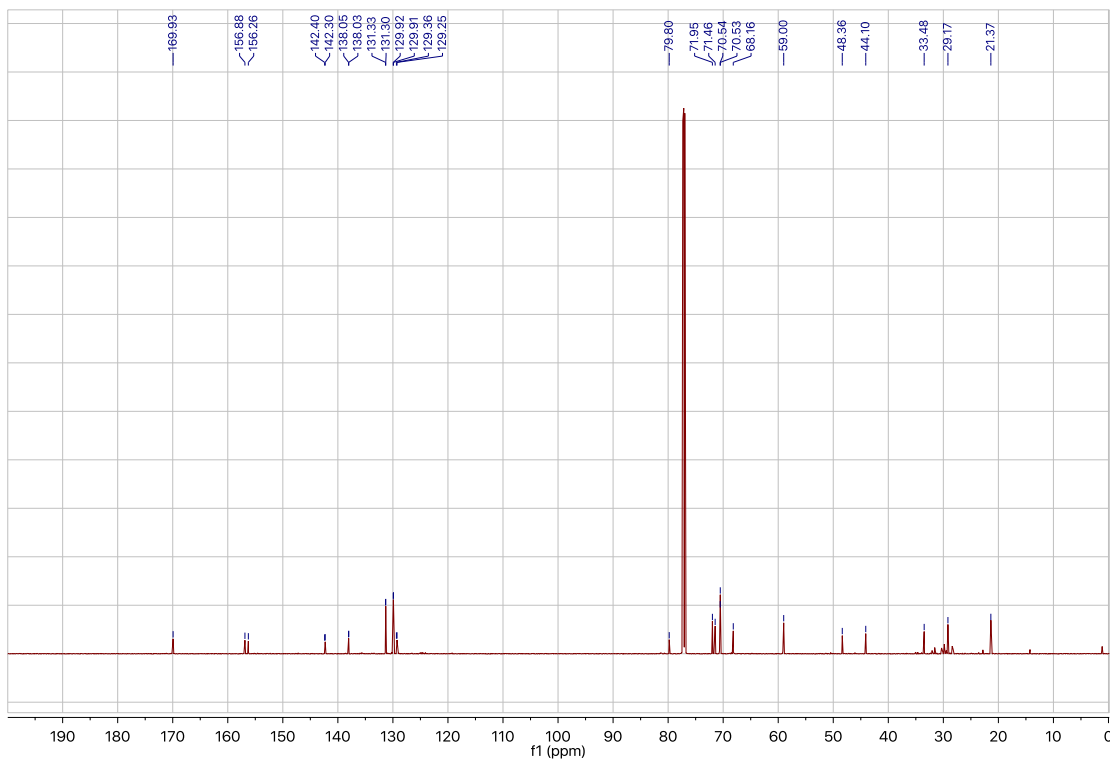


Figure S106.  $^1\text{H}$  and  $^{13}\text{C}$  NMR spectra for 3-(2-(2-(2-(2-methoxyethoxy)ethoxy)ethyl)-3,6-dioxo-4,5-bis(*p*-tolylthio)-3,6-dihydropyridazin-1(2*H*)-yl)-*N*-(prop-2-yn-1-yl)propanamide **84**. \*Mixture of impurities at 1.48–1.25 ppm.

# References

- 1 J. D. Seitz, J. G. Vineberg, E. Herlihy, B. Park, E. Melief and I. Ojima, *Bioorg. Med. Chem.*, 2015, **23**, 2187–2194.
- 2 R. Siegel, E. Ward, O. Brawley and A. Jemal, *CA Cancer J. Clin.*, 2011, **61**, 212–236.
- 3 R. V. Chari, M. L. Miller and W. C. Widdison, *Angew. Chem., Int. Ed.*, 2014, **53**, 3796–3827.
- 4 B. A. Chabner and T. G. Roberts, *Nat. Rev. Cancer*, 2005, **5**, 65–72.
- 5 L. Wills, P. Clutterbuch and B. D. F. Evans, *Biochem. J.*, 1937, **31**, 2136–2147.
- 6 M. C. Li, R. Hertz and D. M. Berganstal, *N. Engl. J. Med.*, 1958, **259**, 66–74.
- 7 M. J. Osborn, M. Freeman and F. M. Huennekens, *Proc. Soc. Exp. Biol. Med.*, 1958, **97**, 429–431.
- 8 M. J. Osborn and F. M. Huennekens, *J. Biol. Chem.*, 1958, **233**, 969–974.
- 9 G. A. Curt, N. J. Clendeninn and B. A. Chabner, *Cancer Treat. Rep.*, 1984, **68**, 87–99.
- 10 E. 3rd Frei, M. Karon, R. H. Levin, E. J. Freireich, R. J. Taylor, J. Hananian, O. Selawry, J. F. Holland, B. Hoogstraten, I. J. Wolman, E. Abir, A. Sawitsky, S. Lee, S. D. Mills, E. O. J. Burgert, C. L. Spurr, R. B. Patterson, F. G. Ebaugh, G. W. 3rd James and J. H. Moon, *Blood*, 1965, **26**, 642–656.
- 11 J. H. 3rd Moxley, V. T. De Vita, K. Brace and E. 3rd Frei, *Cancer Res.*, 1967, **27**, 1258–1263.
- 12 V. T. De Vita, A. A. Serpick and P. P. Carbone, *Ann. Intern. Med.*, 1970, **73**, 881–895.
- 13 B. Rosenberg, L. VanCamp, J. E. Trosko and V. H. Mansour, *Nature*, 1969,

222, 385–386.

- 14 A. V. Klein and T. W. Hambley, in *Ligand Design in Medicinal Inorganic Chemistry*, ed. T. Storr, John Wiley & Sons, Online, 2014, pp. 9–45.
- 15 M. Galanski, M. A. Jakupec and B. K. Keppler, *Curr. Med. Chem.*, 2005, **12**, 2075–2094.
- 16 N. J. Wheate, S. Walker, G. E. Craig and R. Oun, *Dalt. Trans.*, 2010, **39**, 8113–8127.
- 17 N. R. Patel, A. Piroyan, A. H. Nack, C. A. Galati, M. McHugh, S. Orosz, A. W. Keeler, S. O’Neal, W. C. Zamboni, B. Davis and T. P. Coleman, *Mol. Pharm.*, 2016, **13**, 1996–2009.
- 18 G. Casi and D. Neri, *Mol. Pharm.*, 2015, **12**, 1880–1884.
- 19 A. Dal Corso, D. Neri and S. Cazzamalli, *J. Control. Release*, 2017, **246**, 39–45.
- 20 J. D. Seitz, J. G. Vineberg, L. Wei, J. F. Khan, B. Lichtenthal, C. F. Lin and I. Ojima, *J. Fluor. Chem.*, 2015, **171**, 148–161.
- 21 N. Krall, F. Pretto and D. Neri, *Chem. Sci.*, 2014, **5**, 3640–3644.
- 22 N. Krall, F. Pretto, W. Decurtins, G. J. L. Bernardes, C. T. Supuran and D. Neri, *Angew. Chem., Int. Ed.*, 2014, **53**, 4231–4235.
- 23 E. Valeur, L. Knerr, M. Ölwegård-Halvarsson and M. Lemurell, *Drug Discov. Today*, 2017, **22**, 841–847.
- 24 D. G. Maloney, A. J. Grillo-Lopez, C. A. White, D. Bodkin, R. J. Schilder, J. A. Neidhart, N. Janakiraman, K. A. Foon, T. M. Liles, B. K. Dallaire, K. Wey, I. Royston, T. Davis and R. Levy, *Blood*, 1997, **90**, 2188–2195.
- 25 J. A. Ledermann, S. Canevari and T. Thigpen, *Ann. Oncol.*, 2015, **26**, 2034–2043.
- 26 M. Fernández, F. Javaid and V. Chudasama, *Chem. Sci.*, 2018, **9**, 790–810.

- 27 D. K. Armstrong, A. J. White, S. C. Weil, M. Phillips and R. Coleman, *Gynecol. Oncol.*, 2013, **129**, 452–458.
- 28 J. Pfisterer, M. Plante, I. Vergote, A. du Bois, H. Hirte, A. J. Lacave, U. Wagner, A. Stähle, G. Stuart, R. Kimmig, S. Olbricht, T. Le, J. Emerich, W. Kuhn, J. Bentley, C. Jackisch, H. J. Lück, J. Rochon, A. H. Zimmermann and E. Eisenhauer, *J. Clin. Oncol.*, 2006, **24**, 4699–4707.
- 29 G. Bolis, G. Scarfone, G. Giardina, A. Villa, G. Mangili, M. Melpignano, M. Presti, S. Tateo, M. Franchi and F. Parazzini, *Gynecol. Oncol.*, 2001, **81**, 3–9.
- 30 A. J. González-Martín, E. Calvo, I. Bover, M. J. Rubio, A. Arcusa, A. Casado, B. Ojeda, C. Balañá, E. Martínez, A. Herrero, B. Pardo, E. Adrover, J. Rifá, M. J. Godes, A. Moyano and A. Cervantes, *Ann. Oncol.*, 2005, **16**, 749–755.
- 31 I. Vergote and C. P. Leamon, *Ther. Adv. Med. Oncol.*, 2015, **7**, 206–218.
- 32 P. D. Senter, *Curr. Opin. Chem. Biol.*, 2009, **13**, 235–244.
- 33 M. Srinivasarao, C. V. Galliford and P. S. Low, *Nat. Rev. Drug Discov.*, 2015, **14**, 203–219.
- 34 C. Peters and S. Brown, *Biosci. Rep.*, 2015, **35**, 1–20.
- 35 J. Christiansen and A. K. Rajasekaran, *Mol. Cancer Ther.*, 2004, **3**, 1493–1501.
- 36 Y. V Kovtun and V. S. Goldmacher, *Cancer Lett.*, 2007, **255**, 232–240.
- 37 G. Casi and D. Neri, *J. Med. Chem.*, 2015, **58**, 8751–8761.
- 38 M. Carrasco-Triguero, J. H. Yi, R. Dere, Z. J. Qiu, C. Lei, Y. Li, C. Mahood, B. Wang, D. Leipold, K. A. Poon and S. Kaur, *Bioanalysis*, 2013, **5**, 1007–1023.
- 39 T. Rohrer, *Chim. Oggi Chem. Today*, 2012, **30**, 76–79.
- 40 A. Kumar, T. Mastren, B. Wang, J. T. Hsieh, G. Hao and X. Sun, *Bioconjugate Chem.*, 2016, **27**, 1681–1689.

- 41 M. S. Dennis, H. Jin, D. D, R. Yang, L. McFarkand, A. Ogasawara, S. Williams, M. J. Cole, S. Ross and R. Schwall, *Cancer Res.*, 2007, **67**, 254–261.
- 42 A. Azvolinsky, *J. Natl. Cancer Inst.*, 2013, **105**, 1765–1766.
- 43 C. S. Kue, A. Kamkaew, K. Burgess, L. V Kiew, L. Y. Chung and H. B. Lee, *Med. Res. Rev.*, 2016, **36**, 494–575.
- 44 N. Krall, J. Scheuermann and D. Neri, *Angew. Chem., Int. Ed.*, 2013, **52**, 1384–1402.
- 45 I. R. Vlahov and C. P. Leamon, *Bioconjugate Chem.*, 2012, **23**, 1357–1369.
- 46 K. Simons and S. D. Fuller, *Annu. Rev. Cell Biol.*, 1985, **1**, 243–288.
- 47 S. Azzi, J. K. Hebda and J. Gavard, *Front. Oncol.*, 2013, **3**, 1–14.
- 48 H. Maeda, *Proc. Jpn. Acad., Ser. B*, 2012, **88**, 53–71.
- 49 G. Anilkumar, S. A. Rajasekaran, S. Wang, O. Hankinson, N. H. Bander and A. K. Rajasekaran, *Cancer Res.*, 2003, **63**, 2645–2648.
- 50 H. Liu, A. K. Rajasekaran, P. Moy, Y. Xia, S. Kim, V. Navarro, R. Rahmati and N. H. Bander, *Cancer Res.*, 1998, **58**, 4055–4060.
- 51 J. S. Ross, C. E. Sheehan, H. A. Fisher, R. P. Kaufman, P. J. Kaur, K. Gray, I. Webb, G. S. Gray, R. Mosher and B. V Kallakury, *Clin. Cancer Res.*, 2003, **9**, 6357–6362.
- 52 J. K. Troyer, M. L. Beckett and G. L. J. Wright, *Int. J. Cancer*, 1995, **62**, 552–558.
- 53 G. L. Wright, C. Haley, M. L. Beckett and P. F. Schellhammer, *Urol. Oncol.*, 1995, **1**, 18–28.
- 54 J. T. Pinto, B. P. Suffoletto, T. M. Berzin, C. H. Qiao, S. Lin, W. P. Tong, F. May, B. Mukherjee and W. D. Heston, *Clin. Cancer Res.*, 1996, **2**, 1445–1451.

- 55 B. S. Slusher, J. J. Vornov, A. G. Thomas, P. D. Hurn, I. Harukuni, A. Bhardwaj, R. J. Traystman, M. B. Robinson, P. Britton, X. C. Lu, F. C. Tortella, K. M. Wozniak, M. Yudkoff, B. M. Potter and P. F. Jackson, *Nat. Med.*, 1999, **5**, 1396–1402.
- 56 V. Yao, C. E. Berkman, J. K. Choi, D. S. O’Keefe and D. J. Bacich, *Prostate*, 2010, **7**, 305–316.
- 57 S. A. Kularatne, K. Wang, H. K. Santhapuram and P. S. Low, *Mol. Pharm.*, 2009, **6**, 780–789.
- 58 S. M. Hillier, K. P. Maresca, F. J. Femia, J. C. Marquis, C. A. Foss, N. Nguyen, C. N. Zimmerman, J. A. Barrett, W. C. Eckelman, M. G. Pomper, J. L. Joyal and J. W. Babich, *Cancer Res.*, 2009, **69**, 6932–6940.
- 59 K. P. Maresca, S. M. Hillier, F. J. Femia, D. Keith, C. Barone, J. L. Joyal, C. N. Zimmerman, A. P. Kozikowski, J. A. Barrett, W. C. Eckelman and J. W. Babich, *J. Med. Chem.*, 2009, **52**, 347–357.
- 60 J. A. Barrett, R. E. Coleman, S. J. Goldsmith, S. Vallabhajosula, N. A. Petry, S. Cho, T. Armor, J. B. Stubbs, K. P. Maresca, M. G. Stabin, J. L. Joyal, W. C. Eckelman and J. W. Babich, *J. Nucl. Med.*, 2013, **54**, 380–387.
- 61 K. P. Maresca, J. C. Marquis, S. M. Hillier, G. Lu, F. J. Femia, C. N. Zimmerman, W. C. Eckelman, J. L. Joyal and J. W. Babich, *Bioconjugate Chem.*, 2010, **21**, 1032–1042.
- 62 S. M. Hillier, K. P. Maresca, G. Lu, R. D. Merkin, J. C. Marquis, C. N. Zimmerman, W. C. Eckelman, J. L. Joyal and J. W. Babich, *J. Nucl. Med.*, 2013, **54**, 1369–1376.
- 63 J. Zavada, Z. Zavadova, S. Pastorekova, F. Ciampor, J. Pastorek and V. Zelnik, *Int. J. Cancer*, 1993, **54**, 268–274.
- 64 C. T. Supuran, *Nat. Rev. Drug Discov.*, 2008, **7**, 168–181.
- 65 S. Pastorekova, S. Parkkila, A. K. Parkkila, R. Opavsky, V. Zelnik, J. Saarnio and J. Pastorek, *Gastroenterology*, 1997, **112**, 398–408.



- 66 S. A. Hussain, R. Ganesan, G. Reynolds, L. Gross, A. Stevens, J. Pastorek, P. G. Murray, B. Perunovic, M. S. Anwar, L. Billingham, N. D. James, D. Spooner, C. J. Poole, D. W. Rea and D. H. Palmer, *Br. J. Cancer*, 2007, **96**, 104–109.
- 67 A. M. Niemela, P. Hynninen, J. P. Mecklin, T. Kuopio, A. Kokko, L. Aaltonen, A. K. Parkkila, S. Pastorekova, J. Pastorek, A. Waheed, W. S. Sly, T. F. Orntoft, M. Kruhoffer, H. Haapasalo, S. Parkkila and A. J. Kivela, *Cancer Epidemiol. Biomarkers Prev.*, 2007, **16**, 1760–1766.
- 68 M. A. Proescholdt, M. J. Merrill, E. M. Stoerr, A. Lohmeier, F. Pohl and A. Brawanski, *Neurooncology*, 2012, **14**, 1357–1366.
- 69 N. Krall, F. Pretto, W. Decurtins, G. J. Bernardes, C. T. Supuran and D. Neri, *Angew Chem. Int. Ed. Engl.*, 2014, **53**, 4231–4235.
- 70 N. Krall, F. Pretto and D. Neri, *Chem. Sci.*, 2014, **5**, 3640–3644.
- 71 S. Bhuniya, S. Maiti, E. J. Kim, H. Lee, J. L. Sessler, K. S. Hong and J. S. Kim, *Angew. Chem., Int. Ed.*, 2014, **53**, 4469–4474.
- 72 S. Luo, V. S. Kansara, X. Zhu, N. K. Mandava, D. Pal and A. K. Mitra, *Mol. Pharm.*, 2006, **3**, 329–339.
- 73 A. D. Vadlapudi, R. K. Vadlapatla, D. Pal and A. K. Mitra, *AAPS J.*, 2012, **14**, 832–842.
- 74 G. Russell-Jones, K. McTavish, J. McEwan, J. Rice and D. Nowotnik, *J. Inorg. Biochem.*, 2004, **98**, 1625–1633.
- 75 S. Chen, X. Zhao, J. Chen, J. Chen, L. Kuznetsova, S. S. Wong and I. Ojima, *Bioconjugate Chem.*, 2010, **21**, 979–987.
- 76 J. G. Vineberg, E. S. Zuniga, A. Kamath, Y. J. Chen, J. D. Seitz and I. Ojima, *J. Med. Chem.*, 2014, **57**, 5777–5791.
- 77 S. Quici, A. Casoni, F. Foschi, L. Armelao, G. Bottaro, R. Seraglia, C. Bolzati, N. Salvatorese, D. Carpanese and A. Rosato, *J. Med. Chem.*, 2015, **58**, 2003–

- 2014.
- 78 T. Mironava, M. Simon, M. H. Rafailovich and B. Rigas, *Toxicol. Vitro.*, 2013, **27**, 882–889.
- 79 W. Xia, A. R. Hilgenbrink, E. L. Matteson, M. B. Lockwood, J.-X. Cheng and P. S. Low, *Blood*, 2009, **113**, 438–446.
- 80 C. M. Paulos, M. J. Turk, G. J. Breur and P. S. Low, *Adv. Drug Deliv. Rev.*, 2004, **56**, 1205–1217.
- 81 K. Siwowska, S. Haller, F. Bortoli, M. Benešová, V. Groehn, P. Bernhardt, R. Schibli and C. Müller, *Mol. Pharm.*, 2017, **14**, 523–532.
- 82 T. Betzel, C. Müller, V. Groehn, A. Müller, J. Reber, C. R. Fischer, S. D. Krämer, R. Schibli and S. M. Ametamey, *Bioconjugate Chem.*, 2013, **24**, 205–214.
- 83 C. M. Paulos, J. A. Reddy, C. P. Leamon, M. J. Turk and P. S. Low, *Mol. Pharmacol.*, 2004, **66**, 1406–1414.
- 84 W. Xia and P. S. Low, *J. Med. Chem.*, 2010, **53**, 6811–6824.
- 85 J. Yang, H. Chen, I. R. Vlahov, J.-X. Cheng and P. S. Low, *Proc. Natl. Acad. Sci. USA*, 2006, **103**, 13872–13877.
- 86 R. J. Lee, S. Wang and P. S. Low, *Biochim. Biophys. Acta*, 1996, **1312**, 237–242.
- 87 C. P. Leamon, I. R. Vlahov, J. A. Reddy, M. Vetzal, H. K. Santhapuram, F. You, A. Bloomfield, R. Dorton, M. Nelson, P. Kleindl, J. F. Vaughn and E. Westrick, *Bioconjugate Chem.*, 2014, **25**, 560–568.
- 88 J. A. Ledermann, S. Canevari and T. Thigpen, *Ann. Oncol.*, 2015, **26**, 2034–2043.
- 89 M. Bartouskova, B. Melichar and B. Mohelnikova-Duchonova, *Pteridines*, 2015, **26**, 1–12.

- 90 C. P. Leamon and J. A. Reddy, *Adv. Drug Deliv. Rev.*, 2004, **56**, 1127–1141.
- 91 C. A. Ladino, R. V. Chari, L. A. Bourret, N. L. Kedersha and V. S. Goldmacher, *Int. J. Cancer*, 1997, **73**, 859–864.
- 92 J. A. Reddy, E. Westrick, I. R. Vlahov, S. J. Howard, H. K. Santhapuram and C. P. Leamon, *Cancer Chemother. Pharmacol.*, 2006, **58**, 229–236.
- 93 C. P. Leamon, J. A. Reddy, I. R. Vlahov, E. Westrick, A. Dawson, R. Dorton, M. Vetzal, H. K. Santhapuram and Y. Wang, *Mol. Pharm.*, 2007, **4**, 659–667.
- 94 C. P. Leamon, J. A. Reddy, M. Vetzal, R. Dorton, E. Westrick, N. Parker, Y. Wang and I. R. Vlahov, *Cancer Res.*, 2008, **68**, 9839–9844.
- 95 J. A. Reddy, R. Dorton, A. Dawson, M. Vetzal, N. Parker, J. S. Nicoson, E. Westrick, P. J. Klein, Y. Wang, I. R. Vlahov and C. P. Leamon, *Mol. Pharm.*, 2009, **6**, 1518–1525.
- 96 W. A. Henne, S. A. Kularatne, J. Hakenjos, J. D. Carron and K. L. Henne, *Bioorg. Med. Chem. Lett.*, 2013, **23**, 5810–5813.
- 97 J. Alsarraf, E. Péraudeau, P. Poinot, I. Tranoy-Opalinski, J. Clarhaut, B. Renoux and S. Papot, *Chem. Commun.*, 2015, **51**, 15792–15795.
- 98 P. V. Paranjpe, S. Stein and P. J. Sinko, *Anticancer Drugs*, 2005, **16**, 763–775.
- 99 J. Y. Lu, D. A. Lowe, M. D. Kennedy and P. S. Low, *J. Drug Target.*, 1999, **7**, 43–53.
- 100 F. M. F. Santos, A. I. Matos, A. E. Ventura, J. Gonçalves, L. F. Veiros, H. F. Florindo and P. M. P. Gois, *Angew. Chem., Int. Ed.*, 2017, **56**, 9346–9350.
- 101 R. H. Mizzoni and P. E. Spoerri, *J. Am. Chem. Soc.*, 1951, **73**, 1873–1874.
- 102 A. Maruani, M. E. B. Smith, E. Miranda, K. A. Chester, V. Chudasama and S. Caddick, *Nat. Commun.*, 2015, **6**, 6645–6654.
- 103 V. Chudasama, M. E. B. Smith, F. F. Schumacher, D. Papaioannou, G. Waksman, J. R. Baker and S. Caddick, *Chem. Commun.*, 2011, **47**, 8781–

8783.

- 104 M. F. Debets, J. C. M. van Hest and F. P. J. T. Rutjes, *Org. Biomol. Chem.*, 2013, **11**, 6439–6455.
- 105 L. Castañeda, Z. V. F. Wright, C. Marculescu, T. M. Tran, V. Chudasama, A. Maruani, E. A. Hull, J. P. M. Nunes, R. J. Fitzmaurice, M. E. B. Smith, L. H. Jones, S. Caddick and J. R. Baker, *Tetrahedron Lett.*, 2013, **54**, 3493–3495.
- 106 E. Robinson, J. P. M. Nunes, V. Vassileva, A. Maruani, J. C. F. Nogueira, M. E. B. Smith, R. B. Pedley, S. Caddick, J. R. Baker and V. Chudasama, *RSC Adv.*, 2017, **7**, 9073–9077.
- 107 M. T. W. Lee, A. Maruani, D. A. Richards, J. R. Baker, S. Caddick and V. Chudasama, *Chem. Sci.*, 2017, **8**, 2056–2060.
- 108 J. P. M. Nunes, V. Vassileva, E. Robinson, M. Morais, M. E. B. Smith, R. B. Pedley, S. Caddick, J. R. Baker and V. Chudasama, *RSC Adv.*, 2017, **7**, 24828–24832.
- 109 E. Robinson, J. P. M. Nunes, V. Vassileva, A. Maruania, J. C. F. Nogueira, M. E. B. Smith, R. B. Pedley and S. Caddick, *RSC Adv.*, 2017, **7**, 9073–9077.
- 110 I. R. Vlahov, H. K. R. Santhapuram, Y. Wang, P. J. Kleindl, F. You, S. J. Howard, E. Westrick, J. A. Reddy and C. P. Leamon, *J. Org. Chem.*, 2007, **72**, 5968–5972.
- 111 A. Maruani, S. Alom, P. Canavelli, M. T. W. Lee, R. E. Morgan, V. Chudasama and S. Caddick, *Chem. Commun.*, 2015, **51**, 5279–5282.
- 112 C. Bahou, D. A. Richards, A. Maruani, E. A. Love, F. Javaid, S. Caddick, J. R. Baker and V. Chudasama, *Org. Biomol. Chem.*, 2018, **16**, 1359–1366.
- 113 F. Kratz, A. Warnecke, K. Scheuermann, C. Stockmar, J. Schwab, P. Lazar, P. Drückes, N. Esser, J. Drevs, D. Rognan, C. Bissantz, C. Hinderling, G. Folkers, I. Fichtner and C. Unger, *J. Med. Chem.*, 2002, **45**, 5523–5533.
- 114 N. Forte, M. Livanos, E. Miranda, M. Morais, X. Yang, V. S. Rajkumar, K. A.

- Chester, V. Chudasama and J. R. Baker, *Bioconjug. Chem.*, 2018, **29**, 486–492.
- 115 M. E. B. Smith, M. B. Caspersen, E. Robinson, M. Morais, A. Maruani, J. P. M. Nunes, K. Nicholls, M. J. Saxton, S. Caddick, J. R. Baker and V. Chudasama, *Org. Biomol. Chem.*, 2015, **13**, 7946–7949.
- 116 D. Feng, Y. Song, W. Shi, X. Li and H. Ma, *Anal. Chem.*, 2013, **85**, 6530–6535.
- 117 M. H. Lee, J. Y. Kim, J. H. Han, S. Bhuniya, J. L. Sessler, C. Kang and J. S. Kim, *J. Am. Chem. Soc.*, 2012, **134**, 12668–12674.
- 118 J. G. Vineberg, E. S. Zuniga, A. Kamath, Y. J. Chen, J. D. Seitz and I. Ojima, *J. Med. Chem.*, 2014, **57**, 5777–5791.
- 119 J. X. Lu, Y. C. Song, W. Shi, X. H. Li and H. Ma, *Sens. Actuators B*, 2012, **161**, 615–620.
- 120 S. J. Wang, H. M. Ma, J. Li, X. Q. Chen, Z. J. Bao and S. N. Sun, *Talanta*, 2006, **70**, 518–521.
- 121 S. Santra, C. Kaittanis, O. J. Santiesteban and J. M. Perez, *J. Am. Chem. Soc.*, 2011, **133**, 16680–16688.
- 122 Y.-B. Hu, E. B. Dammer, R.-J. Ren and G. Wang, *Transl. Neurodegener.*, 2015, **4**, 1–10.
- 123 G. H. Diering and M. Numata, *Front. Physiol.*, 2014, **4**, 1–7.
- 124 J. Huotari and A. Helenius, *EMBO J.*, 2011, **30**, 3481–3500.
- 125 M. J. Geisow and W. H. Evans, *Exp. Cell Res.*, 1984, **150**, 36–46.
- 126 A. E. Lanterna, M. González-Béjar, M. Frenette and J. C. Scaiano, *Photochem. Photobiol. Sci.*, 2017, **16**, 1284–1289.
- 127 K. G. Reddie, W. H. Humphries, C. P. Bain, C. K. Payne, M. L. Kemp and N. Murthy, *Org. Lett.*, 2012, **14**, 680–683.

- 128 Y. Chen, H. R. Liu, H. S. Liu, M. Cheng, P. Xia, K. D. Qian, P. C. Wu, C. Y. Lai, Y. Xia, Z. Y. Yang, S. L. Morris-Natschke and K. H. Lee, *Eur. J. Med. Chem.*, 2012, **49**, 74–85.
- 129 W. Ji, N. Li, D. Chen, X. Qi, W. Sha, Y. Jiao, Q. Xu and J. Lu, *J. Mater. Chem. B*, 2013, **1**, 5942–5949.
- 130 P. Klan, T. Solomek, C. G. Bochet, A. Blanc, R. Givens, M. Rubina, V. Popik, A. Kostikov and J. Wirz, *Chem. Rev.*, 2013, **113**, 119–191.
- 131 B. D. Wagner, *Molecules*, 2009, **14**, 210–237.
- 132 C. L. Tung, H. Y. Lam, J. Xu and X. Li, *Chem. Commun.*, 2014, **50**, 5298–5300.
- 133 H. Woo, Y. You, T. Kim, G.-J. Jhon and W. Nam, *J. Mater. Chem.*, 2012, **22**, 17100–17112.
- 134 E. González-García, V. Helaine, G. Klein, M. Schuermann, G. A. Sprenger, W.-D. Fessner and J.-L. Reymond, *Chem.–Eur. J.*, 2003, **9**, 893–899.
- 135 G. C. Van de Bittner, E. A. Dubikovskaya, C. R. Bertozzi and C. J. Chang, *PNAS*, 2010, **107**, 21316–21321.
- 136 E. A. Abu-Gharib, R. M. EL-Khatib, L. A. E. Nassr and A. M. Abu-Dief, *J. Korean Chem. Soc.*, 2011, **55**, 346–353.
- 137 R. Baba, Y. Hori and K. Kikuchi, *Chem. Eur. J.*, 2015, **21**, 4695–4702 (Supporting Information).
- 138 A. Maruani, H. Savoie, F. Bryden, S. Caddick, R. Boyle and V. Chudasama, *Chem. Commun.*, 2015, **51**, 15304–15307.
- 139 M. T. Lee, A. Maruani, J. R. Baker and S. Caddick, *Chem. Sci.*, 2016, **7**, 799–802.
- 140 H. C. Kolb, M. G. Finn and K. B. Sharpless, *Angew. Chem., Int. Ed.*, 2001, **40**, 2004–2021.

- 141 R. A. Evans, *Aust. J. Chem.*, 2007, **60**, 384–395.
- 142 C. D. Spicer and B. G. Davis, *Nat. Commun.*, 2014, **5**, 4740–4754.
- 143 V. Chudasama, A. Maruani and S. Caddick, *Nat. Chem.*, 2016, **8**, 114–119.
- 144 S. Hamura, S. Shimosato and H. Okada, JP Pat. 5754133 B2, 2015.
- 145 Y. Iwasawa, K. Nonoshita and K. Tomimoto, *Tetrahedron Lett.*, 1995, **36**, 7459–7462.
- 146 P. A. Clarke, R. L. Davie and S. Peace, *Tetrahedron Lett.*, 2002, **43**, 2753–2756.
- 147 M. Escudero-Casao and E. Juaristi, *Helv. Chim. Acta*, 2012, **95**, 1714–1722.
- 148 K. Oe, Y. Ohfuné and T. Shinada, *Org. Lett.*, 2014, **16**, 2550–2553.
- 149 L. Ducry and B. Stump, *Bioconjugate Chem.*, 2009, **21**, 5–13.
- 150 J. Ling, M. Z. Rong and M. Q. Zhang, *J. Mater. Chem.*, 2011, **21**, 18373–18380.
- 151 US Pat., 7 456 205, 2008.
- 152 K. Fukase, M. Takashina, Y. Hori, D. Tanaka, K. Tanaka and S. Kusumoto, *Synlett*, 2005, 2342–2346.
- 153 S. Kohmoto, E. Mori and K. Kishikawa, *J. Am. Chem. Soc.*, 2007, **129**, 13364–13365.